

Boundary formulations for discrete lattices to describe the non-smooth dynamic response of solid media in the time domain

Hoving, J.S.

10.4233/uuid:5f0de4f7-fe12-4859-9044-483586266f5a

Publication date

Document Version Final published version

Citation (APA)

Hoving, J. S. (2025). Boundary formulations for discrete lattices: to describe the non-smooth dynamic response of solid media in the time domain. [Dissertation (TU Delft), Delft University of Technology]. https://doi.org/10.4233/uuid:5f0de4f7-fe12-4859-9044-483586266f5a

Important note

To cite this publication, please use the final published version (if applicable). Please check the document version above.

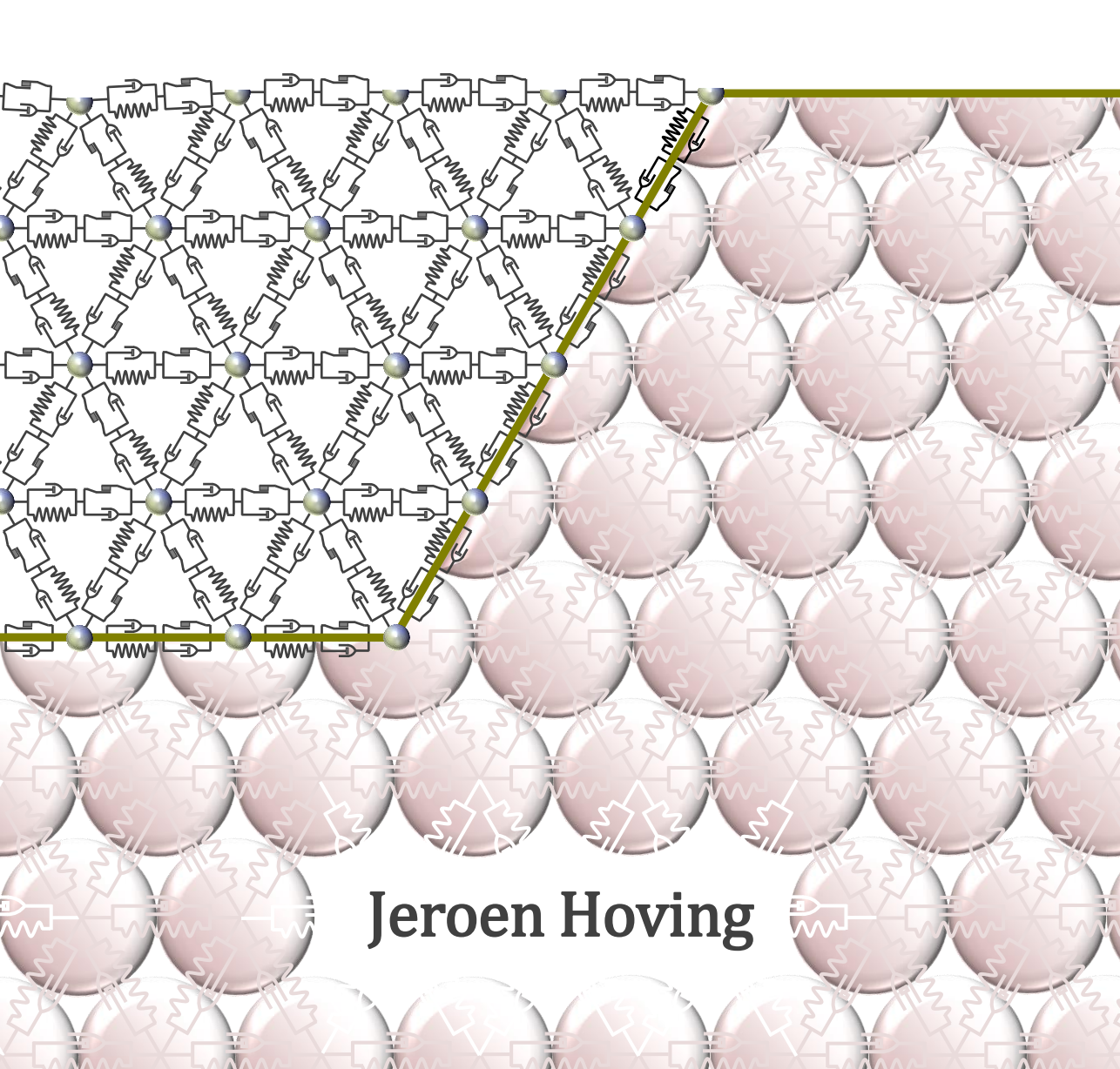
Copyright

Other than for strictly personal use, it is not permitted to download, forward or distribute the text or part of it, without the consent of the author(s) and/or copyright holder(s), unless the work is under an open content license such as Creative Commons.

Please contact us and provide details if you believe this document breaches copyrights. We will remove access to the work immediately and investigate your claim.

Boundary formulations for discrete lattices

to describe the non-smooth dynamic response of solid media in the time domain



Boundary formulations for discrete lattices

to describe the non-smooth dynamic response of solid media in the time domain

Boundary formulations for discrete lattices

to describe the non-smooth dynamic response of solid media in the time domain

Dissertation

for the purpose of obtaining the degree of doctor
at Delft University of Technology
by the authority of the Rector Magnificus Prof. dr.ir. T.H.J.J. van der Hagen,
Chair of the Board for Doctorates,
to be defended publicly on
Thursday 22 May 2025 at 12:30 hours

by

Jeroen Sebastiaan HOVING

Master of Science in Civil Engineering, Delft University of Technology, the Netherlands born in Den Helder, the Netherlands This dissertation has been approved by the promotors.

Composition of the doctoral committee:

Rector Magnificus, chairperson

Prof.dr. A.V. Metrikine, Delft University of Technology, promotor Dr.ir. K.N. van Dalen, Delft University of Technology, promotor

Independent members:

Prof.dr.ir. H.E.J.G. Schlangen, Delft University of Technology Dr.ir. W.T. van Horssen, Delft University of Technology

Prof. dr.ir. H. Askes, University of Twente, the Netherlands

Prof. dr. P. Galvín, Universidad de Sevilla, Spain

Dr. O. Dorival, Université Paul Sabatier Toulouse III, France

Prof.dr.ir. M.A.N. Hendriks, Delft University of Technology, Norwegian University

of Science and Technology, reserve member



Keywords: Boundary formulations, discrete lattice, non-smooth dynamics, solid media,

frequency domain versus time domain, Green's functions, stick-slip behaviour, wave propagation, wave reflections, numerical modelling, boundary in-

tegral equations, dynamic stiffness, dynamic compliance.

Printed by: Gildeprint – www.gildeprint.nl

Artwork by: Jeroen Hoving

Copyright © 2025 by J.S. Hoving

ISBN 978-94-6518-055-7

An electronic version of this dissertation is available at: repository.tudelft.nl

"There is nothing in the stars, if you fail to move"

Iggy Pop

Preface

The work presented in this thesis was carried out at the Faculty of Civil Engineering and Geosciences of Delft University of Technology, first as a PhD-candidate at the section of Structural Mechanics, and later as a researcher, lecturer, assistant professor, and currently as a senior lecturer at the section Offshore Engineering. This thesis marks the culmination of a somewhat extended period of research into the dynamic behaviour of solid media, during which I have delved much longer and deeper into the fascinating topics of non-smooth dynamics, lattice modelling, and boundary integral methods then I had originally planned.

This journey would not have been possible without the support and guidance of many individuals to whom I owe gratitude. First and foremost, I would like to thank my daily supervisor turned promotor, colleague and friend, Prof.dr. Andrei Metrikine, for sharing his knowledge, for his trust and support without reservation, for taking the time to listen and discuss, and for always trying to give me useful and practical advice, not only in the field of structural dynamics, but also on a personal level, for teaching me how to do things (right) and also, in some cases, how to not do things, and for consistently challenging me to become the best version of myself. I am also sincerely grateful to dr.ir. Karel van Dalen, who joined as a promotor at a relatively late stage, but whose analytical thinking, constructive feedback and committed supervision were of tremendous value and proved to be absolutely essential in bringing this thesis to completion.

I would also like to express my sincere gratitude to Prof.ir. Ton Vrouwenvelder and Prof.dr.ir. Frans Molenkamp, who were originally intended to be my promoters. Although they both retired before the completion of this thesis, their encouragement and guidance during my years as a PhD-candidate laid the foundation for this work and are warmly acknowledged. In addition, I would like to extend my sincere appreciation to the members of the doctoral committee for their willingness to review this work and for investing their valuable time and expertise.

Special thanks go to my parents, for always being there and always supporting me, to Michiel and Folco for being my paranymphs and to all the other people who are close to me and whom I can count among my loved ones and friends. You know who you are.

Finally, I am deeply grateful to my wife Dara for her endless encouragement and patience. The pursuit of this PhD has spanned a significant part of our adult lives together, during which we have both started careers, got married and had three children. Her belief in me has been a constant source of motivation, and without her support, I would never have been able to cross the finish line with such determination and pride.

Jeroen Hoving Delft, April 2025

Summary

The dynamic interaction between a structure and its surrounding medium plays a pivotal role in numerous engineering applications. In cases where a dynamically loaded medium exhibits non-smooth behaviour, such as in dynamic soil-structure or ice-structure interaction, any model for that medium must account for nonlinear phenomena to accurately capture the response of the medium. To minimize calculation times, it is desirable to keep the domain of the model that is able to account for these nonlinearities as small as possible. This thesis addresses the development of a modelling framework that enables an efficient and robust description of the non-smooth dynamic response of a solid medium in the time domain.

To this end, the medium is subdivided into two domains: a sophisticated near-field domain in the region of interaction with a dynamic load source that is able to account for non-linear phenomena, and a surrounding far-field domain at such distance from the load that its response is linear. The near field is modelled using discrete lattice systems that are able to accommodate non-smooth dynamic phenomena by incorporating stick-slip behaviour and inelastic collisions. The far field is represented by a boundary integral formulation, that describes the response of the far-field domain exclusively at its interface with the near-field while accounting for the behaviour and properties of the far-field domain beyond this interface. This approach allows for an accurate yet computationally efficient inclusion of a finite, an infinite or semi-infinite far-field domain, enabling accurate wave transmission and minimal reflection at the interface between the near field and the far field domains.

The discrete lattice modelling in the near field employs so-called Bingham-Kelvin-Voigt (BKV) elements, consisting of a combination of springs, dashpots and dry-friction elements. Due to the presence of these dry-friction elements, as well as accounting for the possible occurrence of inelastic collisions, the response of such lattices is characterised by transitions between different motion states, such as stick, slip and lock, that are governed by the dynamic excitation and the thresholds of these rheological elements.

To incorporate the linear far-field response, boundary integral equations (BIEs) are derived for both continuous and discrete representations of the far field. While BIEs for continuous domains are well-established in literature, this thesis presents one of the first derivations of BIEs for a far-field domain that is described as a finite or semi-infinite system of discrete particles. These BIEs are generally expressed in terms of the dynamic stiffness or, inversely, in terms of the dynamic compliance, that describe a force-displacement relation in the Laplace domain. For one-dimensional systems, expressions for the Laplace domain relations can often be derived analytically, but time domain responses must generally be evaluated numerically, in which case the use of the dynamic compliance is preferred over the use of the dynamic stiffness. For two-dimensional systems, the formulation of the BIEs is based on the Green's functions of the respective media and numerical boundary methods are required to obtain the corresponding dynamic compliance matrices. Since the Green's functions are not always known and often cannot be obtained straightforwardly, determining the Green's

functions is a key difficulty when formulating the BIEs.

Recognising the computational challenges associated with time domain simulations of non-linear systems, a mixed time-frequency domain (MTFD) method is developed. This hybrid approach leverages the efficiency of frequency-domain techniques during periods of linear behaviour, while accounting for the changing properties of the lattice over time whenever a nonlinear event occurs. The presented methodology has the potential to significantly improve computational performance, especially in systems where nonlinear phenomena occur intermittently.

The results presented in this thesis demonstrate the effectiveness of discrete lattice models in capturing non-smooth dynamic phenomena, and highlight the critical importance of accurate boundary representations to ensure reliable simulations. The comparison between discrete-continuous and fully discrete systems illustrates the impact of the far-field representation on the overall dynamic response. When applied to lattice models, BIEs based on discrete far-field systems outperform continuum-based BIEs particularly in terms of compatibility and the undisturbed wave propagation through the interface. Future studies should explore adaptations of the discrete lattice models to determine their influence on the formulation of the BIEs, for example by changing the lattice configuration from hexagonal to square, incorporating interactions between second neighbours or introducing additional rheological elements to account for transverse and rotational interactions. The performance of the discrete-based BIEs however, is greatly influenced by the quality of the numerical implementation and further improvements to the numerical implementation should be made to make it more robust and make it more widely applicable.

In addition, while the common understanding is that any model that accounts for nonlinear phenomena must be evaluated in the time domain, the non-iterative MTFD method offers a promising way to extend the applicability of frequency domain approaches to describe the non-smooth dynamic response of solid media the time domain.

In conclusion, this thesis provides both the theoretical foundations and the numerical tools to enable efficient modelling of nonlinear wave propagation and thereby contributes to advancing the state-of-the-art in modelling the non-smooth dynamic responses of solid media in the time domain, with the potential of contributing to improved design and analysis in a broad range of civil, geotechnical, and offshore engineering applications.

Table of Contents

1	Introduction	1
1.1	Dividing a medium into a linear and a nonlinear domain	2
1.2	Discrete lattice models for non-smooth dynamic phenomena	
1.3	Boundary integral equations to account for the far-field domain	
1.4	The time domain versus the frequency domain	10
1.5	Numerical implementation and application of BIEs	11
1.6	Aims and novelty of the thesis	12
1.7	Reading guide	13
2	One- and two-dimensional lattice models	15
2.1	Lagrange's formalism for lattice models	16
2.2	Rheological elements for lattice models in dynamics	18
2.3	One-dimensional lattice models	19
2.3.1	The one-dimensional Bingham-Kelvin-Voigt (BKV) lattice	20
2.3.2	'Stick' in the one-dimensional BKV lattice	21
2.3.3	'Slip' in the one-dimensional BKV lattice	22
2.3.4	'Lock' in the one-dimensional BKV lattice	24
2.3.5	State-transitions in the one-dimensional BKV lattice	26
2.4	Two-dimensional lattices	31
2.4.1	The hexagonal Bingham-Kelvin-Voigt (BKV) lattice	31
2.4.2	Kinematics of BKV elements in a two-dimensional lattice	35
2.4.3	'Stick' in the hexagonal BKV lattice	39
2.4.4	'Slip' in the hexagonal BKV lattice	40
2.4.5	'Lock' in the hexagonal BKV lattice	41
2.4.6	State-transitions in the hexagonal BKV lattice	
2.4.7	Geometrical and material randomness in the hexagonal lattice	
2.5	Material properties of one- and two-dimensional media	44
2.6	Response of the hexagonal lattice with elementary boundaries	
2.6.1	Elementary boundaries for two-dimensional lattices	
2.6.2	Accuracy of linearizations applied to two-dimensional lattices	46
2.6.3	Response of the hexagonal BKV lattice with a fixed boundary	51
3	One- and two-dimensional discrete-continuous systems	57
3.1	Dynamic stiffness and dynamic compliance	
3.2	The one-dimensional discrete-continuous BKV system	
3.2.1	Matching the parameters of the lattice and the continuous rod	
3.2.2	Dimensionless boundary equation in the Laplace domain	
3.2.3	Governing boundary integral equation in the time domain	66

3.2.4	Governing equations for the 1D discrete-continuous BKV system	70
3.2.5	Response of the one-dimensional discrete-continuous BKV system	71
3.3	An evaluation of several 1D discrete-continuous systems	74
3.3.1	Dynamic compliances for several kinds of semi-infinite rods	74
3.3.2	Wave propagation in 1D discrete-continuous systems	75
3.4	Wave propagation in a finite discrete-continuous system in 1D	86
3.5	Boundary formulation for a continuous far-field domain in 2D	90
3.5.1	An indirect boundary formulation for a continuous far-field domain	92
3.5.2	The dynamic compliance matrix for a continuum with surface cavity	97
3.5.3	Green's functions for the continuum displacements and stresses	99
3.5.4	Unit load distributions in the Laplace-wavenumber domain	109
3.6	The two-dimensional discrete-continuous BKV system	111
3.6.1	Matching the parameters of the lattice and the continuum	113
3.6.2	Governing equations for the 2D discrete-continuous BKV system	114
3.6.3	Discussion on the two-dimensional discrete-continuous system	118
4	One- and two-dimensional fully discrete systems	121
4.1	The one-dimensional fully discrete BKV system	122
4.1.1	Matching the parameters of the lattice and the cascade	
4.1.2		
4.1.3	Governing boundary integral equation in the time domain	
4.1.4	Governing equations for the fully discrete BKV system	
4.1.5	Nonlinear response of the 1D fully discrete BKV system	
4.2	Fully discrete versus discrete-continuous systems in 1D	
4.2.1	Dynamic compliance of semi-infinite cascades and rods	
4.2.2	Wave dispersion in semi-infinite cascades and semi-infinite rods	
4.2.3	Wave reflection in one-dimensional systems	137
4.2.4	Reflection coefficients for one-dimensional fully discrete systems	143
4.3	Two-dimensional fully discrete particle systems	145
4.3.1	A direct boundary formulation for discrete particle systems	146
4.3.2	The dynamic compliance matrix for a discrete particle system	151
4.4	Green's functions for the viscoelastic half-plane of particles	153
4.4.1	Displacements and reaction forces in the half-plane of particles	153
4.4.2	Boundary conditions for the half-plane of particles	163
4.4.3	Green's displacements in the half-plane of particles	164
4.4.4	Green's reaction forces in the half-plane of particles	166
4.5	An equivalent 1D-response of the half-plane of particles	167
4.5.1	Governing equations for an infinitely-long uniform load	
4.5.2	Matching the parameters of the 1D and 2D discrete particle systems	173
4.5.3	Green's displacements of the semi-infinite viscoelastic cascade	176
4.5.4	Green's reaction forces in the semi-infinite viscoelastic cascade	178
4.5.5	Equivalent response of the half-plane of particles and the cascade	180

4.6	The half-plane of particles versus the continuum	185
4.6.1	Wave dispersion in the half-plane of particles and in the continuum	186
4.6.2	Direction-dependent polarization of body waves	190
4.7	The two-dimensional fully discrete BKV system	195
4.7.1	Interface properties of the fully discrete system	197
4.7.2	System of boundary integral equations	199
4.7.3	Equations of motion for interior and surface particles	201
4.7.4	Linear response of the fully discrete BKV system	205
4.7.5	Nonlinear response of the fully discrete BKV system	211
5	A mixed time-frequency domain approach for 1D systems	s 221
5.1	Methodology of the mixed time-frequency domain approach	222
5.2	The MTFD-method applied to 1D discrete-continuous systems	
5.2.1	Boundary formulation in the Laplace domain for nonzero ICs	223
5.2.2	Governing equations for the discrete-continuous Hooke system	228
5.2.3	Transformation to the time domain accounting for nonzero ICs	230
5.2.4	Response of the 1D Hooke system using the MTFD-method	238
5.3	The MTFD-method applied to a discrete-continuous BKV system	240
5.3.1	Boundary formulation for the BKV system with nonzero ICs	241
5.3.2	Governing Laplace domain equations for the 1D BKV-lattice	247
5.3.3	Response of the 1D BKV system using the MTFD-method	248
5.3.4	Advantages and disadvantages of the MTFD-method	255
6	Conclusions and Recommendations	259
6.1	Discrete lattice models for non-smooth dynamic phenomena	260
6.2	Boundary integral formulations to account for the far-field domain	
6.2.1	Two-dimensional discrete-continuous systems	263
6.2.2	Two-dimensional fully discrete systems	
6.3	The time domain versus the frequency domain	266
List of	f references	269
Apper	ndices	275
Same	nvatting	407
Curric	culum Vitae	409
Public	ations	411

$oldsymbol{1}$ Introduction

The dynamic interaction between structures and their surroundings is an important aspect of many engineering problems and a proper understanding of these interaction problems is often a necessity to take appropriate measures. For construction work in urban areas for example, a thorough understanding of the interaction between the structures involved and the underlying soil is vital to prevent vibration nuisance to people living and working near the construction site. Another example is the dynamic interaction of wind turbines, both on- and offshore, with the soil. Due to the rotor motion and the rotor blades passing the turbine tower, waves are emitted that propagate along the turbine tower and into the soil. As the fatigue life is design driving for wind turbine foundations, it is important to understand how much vibration energy is lost due to the dynamic interaction of the wind turbine with the soil. For these examples, the soil can be assumed to behave linearly and may therefore be described as a linear-elastic solid medium.

In many other situations, the interaction of a structure with another medium may not be described using linear models, especially when applied dynamic loads inflict damage to that medium. For example, high-speed trains pose serious concerns because of the high level of vibrations they generate and the potential occurrence of quick dynamic soil settlements under a railway track. This is especially an issue in soft and water-saturated soils, which are widely spread in northern European countries like the Netherlands; in these soils, the Rayleigh wave velocity is easily exceeded by modern high-speed trains, thereby causing high-amplitude vibrations of the soil at a wide frequency band. The use of high-speed trains in countries with an abundance of soft and water-saturated soils is therefore problematic; for example, high-speed trains in the Netherlands are enforced to speed limits to prevent potential derailment and deterioration of the railway track, due to dynamic wheel-rail interaction as depicted in Figure 1.1a. Not only railway companies, but also owners and residents of buildings near high-speed lines, with a view to preventing damage to their belongings, benefit from a thorough understanding of the dynamic interaction between the train, the railway track and the





Figure 1.1: a) Railway track deterioration due to dynamic wheel-rail interaction on waterlogged soil [Kaewunruen and Remennikov, 2016]; b) An offshore wind support structure in the IJsselmeer interacting with ice.

underlying soil.

Next to problems involving dynamic soil-structure interaction, dynamic interactions that involve nonlinear phenomena are found in cold regions engineering. While the demand for energy remains persistently high, the energy transition has significantly boosted the offshore renewable energy sector. Because easily accessible areas suitable for the development of offshore renewables are limited, the offshore energy industry has expanded its activities into more remote and difficult areas of operation such as the Arctic and other cold regions. In these cold regions, seas are covered by ice that may grow up to significant thicknesses and often include much thicker ice ridges. Offshore structures installed in these areas, have been designed to withstand the corresponding ice loads. Yet, the interaction between offshore structures and the surrounding sea ice is not at all well understood. Past measurements at offshore structures in cold regions have shown that the topsides of these structures may experience severe vibrations due to ice-structure interaction [Haverkamp, 2008]. These iceinduced vibrations do not only disturb the well-being of people working on the platform, but may also lead to fatigue damage of the structure. Accordingly, ice-induced vibrations may also lead to fatigue concerns for offshore wind turbines installed in ice-infested areas, such as the offshore wind support structure depicted in Figure 1.1b. In these ice-structure interaction problems, the interaction is highly nonlinear as the ice crushes and breaks against the structure, driven by wind and currents. While recent research shows an improved understanding of the physical mechanism that leads to ice-induced vibrations, the state-of-the-art models available are phenomenological in nature rather than physics-based [Hendrikse and Nord, 2019]. To improve the understanding of the fundamental physics underlying dynamic icestructure interaction, as well as to improve the models that describe this interaction, thereby allowing a better design of offshore structures for cold regions, insight into the nonlinear dynamic behaviour of the ice surrounding these structures is necessary.

1.1 Dividing a medium into a linear and a nonlinear domain

To determine the loads on a structure due to the dynamic interaction of that structure with a medium, it is vital to correctly model the response of that medium. In literature, several thorough reviews of the available analytical and numerical methods for the dynamic interaction

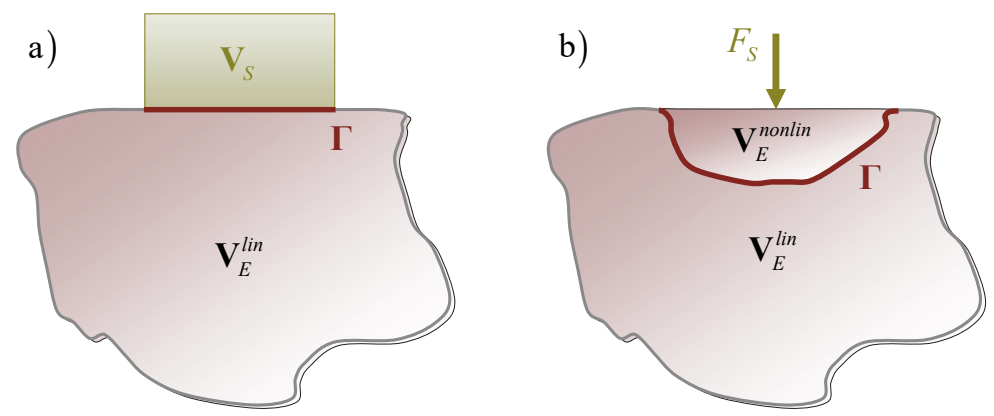


Figure 1.2: a) Interaction between a structure and a medium; b) Interaction between the linear and nonlinear domains of a solid medium due to a structure-induced load.

between structures and elastic media are available. For example, Clouteau et al. [2013] mainly consider interaction problems of structures interacting with unbounded linear-elastic media, where the structure is included in the models that describe the interaction. An impression of this is depicted in Figure 1.2a.

In this thesis, we focus on the response of the medium and only include the interaction with the structure as a load, or as a set of loads, externally applied to the medium. Near the load, the behaviour of the medium may be governed by nonlinear phenomena and therefore any model for the medium must be able to account for these. Such nonlinear phenomena typically occur in the examples of soil-structure and ice-structure interaction depicted in Figure 1.1. From a numerical point of view, it is desirable to keep the domain of the medium that is able to account for nonlinearities as small as possible to minimize the required calculation time. This is especially important when considering two- or three-dimensional models. Therefore, we divide the medium into two separate domains as shown in Figure 1.2b: a sophisticated domain V_E^{nonlin} in the region of interaction with the structure that is able to account for nonlinearities, here referred to as the near field, and a domain V_E^{lin} at such distance from the interaction point that its response is linear, here referred to as the far field. While our main interest is the response of the nonlinear part of the medium in the near field, its behaviour depends on the response of the linear far-field domain which must therefore be correctly accounted for. Additionally, the behaviour of the linear domain of the medium may also be of interest to, for example, study vibrations at a substantial distance from the region of interaction with the structure.

1.2 Discrete lattice models for non-smooth dynamic phenomena

Nonlinear phenomena, such as dry-friction or fracture, are difficult to capture by continuum models. For example, in finite element analysis, nonlinearities are often incorporated employing the theory of elastoplasticity and thus by incorporating a nonlinear stress-strain relation, e.g. Pavlatos and Beskos [1994]; von Estorff and Firuziaan [2000]. As such, nonlinear material behaviour is introduced through transient properties that smoothly change over time.

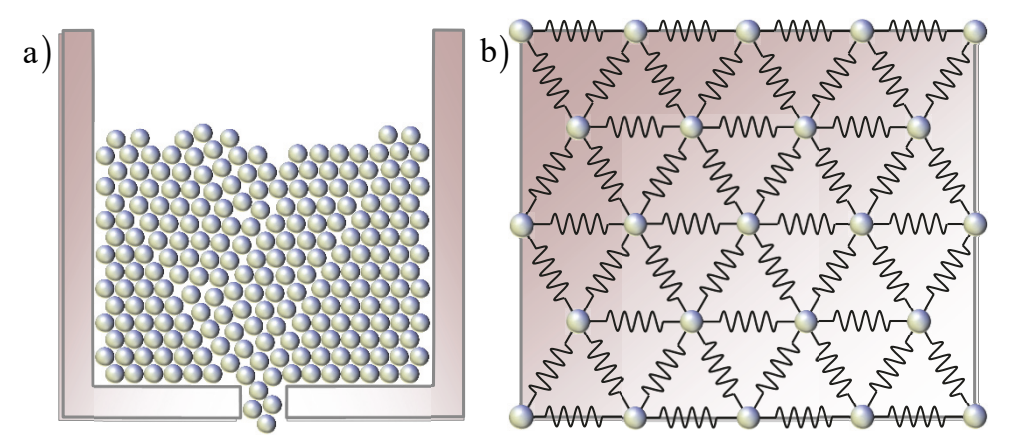


Figure 1.3: a) Example of discrete element modelling: flow of granular material in a hopper (left); b) Example of a lattice model: a square structural element represented by a triangular or hexagonal lattice (right)

In reality however, many nonlinear phenomena are not smooth at all. Another major difficulty of continuum models is the lack of an internal length property causing mesh sensitivity in finite element analysis [Fakhimi, 2009]. Discrete models by definition incorporate an internal length through the dimension of its discrete particles, and as it is straightforward to let these particles behave independently from each other, these discrete approaches can conveniently be used to incorporate non-smooth dynamic behaviour of a medium.

Depending on the scale of the problem under consideration, different discrete modelling approaches exist. In their review, Bolander et al. [2021] categorize the discrete mechanical models that are available; while this review specifically focuses on applications in fracture mechanics, the proposed classification of discrete models is generally applicable and therefore adopted here. The discrete modelling approaches that are identified are: I) classical or conventional lattice models, II) particle-based lattice or hybrid-lattice-particle models and III) distinct or discrete element methods (DEM). Note here that particle-based lattice models (II) combine certain properties from the classical lattice models (I) and DEM (III) as will be explained later in this section.

The commonality between the three modelling approaches is that they all define a material or a medium by a collection of nodes, where each node represents a material particle or a small fragment of the considered medium that interacts with adjacent nodes. Here, the term lattice is used when the connectivity between the nodes is determined a priori and remains the same throughout, as opposed to DEM where the connectivity between the particles is allowed to change with time and depends on contact laws. As a consequence, nodal displacements in lattice models are generally limited as they have a certain restriction on the freedom of movement due to the connectivity between adjacent particles, while particles in DEM may roam freely through a medium and can easily cope with large displacements [Bićanić, 2004]. This is consistent with the idea that particles in lattice models are generally considered at the meso-scale, while DEM is particularly effective to model the behaviour and interaction of large numbers of small particles [Cundall, 1971] and is often used to describe media on a

micro-scale level. For example, Radjai and Dubois [2011] show that DEM is used to address problems in granular and discontinuous media in many different scientific fields. A typical application of the discrete element method is depicted in Figure 1.3a, showing the flow of a granular material in a hopper. Here, the granular material is represented as a collection of spherical particles, but DEM also allows for the use of other, usually polyhedral, shapes, e.g. Boon et al. [2012]. Other examples of discrete micro-scale modelling that are generally considered to be similar to DEM are found in molecular dynamics (MD), non-smooth contact dynamics (NSCD) and granular element method (GEM). Although the involved physics may be fundamentally different, these methods are similar to discrete element modelling in its formal analogy [Kafashan et al., 2019].

While these micro-scale methods mimic reality well, a large disadvantage is the amount of calculation time needed. With the ongoing increase of computational power, the scale at which DEM may be applied has increased as well. At present however, the amount of particles for which, for example, granular media problems can be properly calculated using the discrete element method represents only a few handfuls of sand, which is insufficient to determine the large-scale dynamic behaviour involved in the interaction of a medium with a structure. In this thesis, we therefore choose to model the nonlinear domain as a lattice instead.

The concept of one-dimensional mass-spring systems was first introduced by Lagrange [1759]. Lattice modelling only took off much later when Hrennikoff [1940, 1941] proposed a so-called framework method to solve elasticity problems, in which he uses a plane framework of bars, later commonly known as truss elements, for plane stress applications and to model bending of thin plates. Shortly thereafter, McHenry [1942, 1943] applied this method in a more general sense to two-dimensional stress problems in elastic bodies and is the first, to the author known, example in literature that refers to this method as a lattice. In the 1970s and 1980s, lattice modelling was successfully applied to simulate fracture behaviour in heterogeneous materials, e.g. Herrmann et al. [1989]; Ziman [1979]. Since then, many applications of lattice models are found in the fields of fracture mechanics and micromechanics, e.g. Bolander et al. [1996]; Kale and Ostoja-Starzewski [2022]; Ostoja-Starzewski [2002]; Schlangen and van Mier [1992].

In the early lattice models, the interaction between adjacent lattice nodes is generally described by truss elements that allow for axial translation only. One of the main limitations of these lattice models is that, to match the lattice parameters with the macromaterial properties of the medium it represents, its constant connectivity yields a fixed Poisson's ratio. This is extensively discussed in literature, e.g. Maradudin et al. [1971]; Z. Pan et al. [2018]. The limitation of the Poisson's ratio in lattices can be addressed by adding nodal degrees of freedom or by adding nodal interactions using beam or frame elements, which refer to elements that allow for respectively bending interaction only and for combined axial and bending interaction, e.g. Roux and Guyon [1985]; Schlangen and Garboczi [1997]. This advance in lattice modelling is quite similar to the introduction of enhanced continuum formulations such as the Cosserat continuum [Cosserat and Cosserat, 1909] as a modification of the standard Boltzmann continuum by introducing rotational degrees of freedom. According to the

classification of discrete models adopted from Bolander et al. [2021], the lattice models where the interaction between nodes is either described by truss, beam or frame elements belong to the classical lattice models. In addition to these, modelling approaches where the interaction between nodes is described through springs or other reversible or irreversible elements are also included in this class of lattice models [Nikolić et al., 2018].

Ostoja-Starzewski et al. [1996] introduced a lattice model as a so-called two-dimensional spring network to model the fracture of elastic composites and polycrystals. Figure 1.3b shows an example of a linear lattice model applied to a structural element, where the interaction between neighbouring particles is described by springs. Together with Sahimi and Goddard [1986], Herrmann and Roux [1990] and Delaplace et al. [1996], the work of Ostoja-Starzewski et al. [1996] belongs to the first appearances of spring lattice models. Representing material behaviour using springs, or other rheological elements [Ostoja-Starzewski, 2002] such as dashpots, instead of truss, beam or frame elements both has advantages and disadvantages. As a result of using such rheological elements in lattice models, the behaviour of the medium represented is exclusively known at the nodes, while using truss, beam or frame elements, the behaviour of the medium may also be (partly) known in between the nodes, albeit in an approximate sense. While this somewhat limits the abilities of these lattice models, they require less computational effort. Additionally, using rheological elements, the axial translation, shear translation and rotation in the interaction of adjacent nodes can be, but do not necessarily have to be, decoupled. The advantage of decoupling the interaction between adjacent nodes is for example illustrated by Suiker et al. [2001b] and Zhao and Zhao [2012], where the limitation of the Poisson's ratio is partially addressed by including both axial and shear springs into the lattice model. Other advantages of using rheological elements in lattice models are that dynamic phenomena, such as wave propagation, can conveniently be accounted for and that, incorporating irreversible rheological elements, nonlinear or nonsmooth interactions between adjacent particles can straightforwardly be implemented. Both are advantages that are specifically relevant for this research making these lattice models very suitable for application in this thesis.

In their analysis of one-dimensional mass-spring systems, also known as cascades, Bavinck et al. [1994] and Dieterman et al. [1995] show that the wave propagation in one-dimensional spring-type lattice models is different from the wave propagation in corresponding continuous models due to the differences in their dispersive properties, especially at high frequencies. Next to considering one-dimensional systems, Mühlhaus and Oka [1996] regard the differences for three-dimensions and show that using higher-order displacement gradients in continuum models may diminish these differences. Corresponding developments regarding wave propagation in lattice models are related to the improvement of gradient elasticity theories, i.e. to provide extensions to the classical equations of elasticity with additional higher-order spatial derivatives of strains, stresses and sometimes accelerations. A thorough and in-depth overview on this is given by Askes and Aifantis [2011]. These gradient elasticity models are often derived from discrete lattice models, because the classical continuum mechanics theory does not necessarily suffice for an accurate and detailed description of corresponding deformation phenomena, such as size effect, while discrete models are well suited

to describe material behaviour at small scales. For example, Metrikine and Askes [2002] and Askes and Metrikine [2002] discuss one-dimensional dynamically consistent gradient elasticity models derived from discrete lattices, while Suiker et al. [2001a] compare the wave propagation characteristics of two-dimensional lattices with a corresponding Cosserat continuum. Among other aspects, Askes and Metrikine [2004] address the issue of periodicity and the inherent anisotropy in higher-order continua derived from discrete lattices. This approach shows that isotropy in a discrete lattice can be obtained by including both nearest, or first, neighbours as well as second neighbours into the particle equations of motions, and assuming different spring stiffnesses for the interaction with first and second neighbours. The idea of including second neighbours was also proposed by Ostoja-Starzewski [2002], but without addressing the isotropy. Shortly thereafter, Metrikine and Askes [2006] present the derivation of an isotropic dynamically consistent gradient elasticity model from a two-dimensional lattice.

Next to the abundance of literature focused on the fundamentals of wave propagation in lattice and continuum models, there are also many examples of literature that explore wave propagation in lattices for practical applications. For example, lattice models have been used to analyse wave propagation in railway tracks at high-speed lines, e.g. Suiker et al. [2001b, 2001c], to model the dynamic behaviour of ballasted railway tracks, e.g. Ricci et al. [2005], as well as to model settlement of ballast in railway track transition zones, e.g. de Oliveira Barbosa et al. [2021]; de Oliveira Barbosa et al. [2022], but have also been applied in the field of ice-structure interaction, e.g. Dorival et al. [2008]; van Vliet and Metrikine [2018]. Furthermore, Wang et al. [2009] consider wave-propagation induced fracture of solids. Instead of using a classical lattice model however, the latter work presents a so-called hybrid-lattice-particle modelling approach.

Especially within the field of fracture mechanics, limitations of classical lattice models have become apparent as these models have difficulty to capture the effect of random local material inhomogeneities and therefore do not satisfactory mimic the fracture process in rocky or aggregate materials such as concrete [Bažant et al., 1990]. This has led to the development of particle-based lattice models, which can be considered a cross-over between the classical lattice models and DEM; as for the classical lattice models, the connectivity between the nodes is constant, but in accordance with DEM the nodes are represented as particles for which properties, such as geometry, structure and particle linkage, are accounted for. Particle-based lattice modelling is mainly applied to model fracture in concrete as it is well capable to represent the concrete mesostructure by accounting for its aggregate particles [Bažant et al., 1990]. This class of lattice models can be divided into two types being the rigid-body-spring models (RBSM) also referred to as irregular lattice models, e.g. Hwang et al. [2016]; Kim and Lim [2011]; Y. Pan et al. [2017] and lattice discrete particle models (LDPM), e.g. Cusatis et al. [2011a]; Cusatis et al. [2011b]; Wang et al. [2009].

In this thesis, the focus is placed on the overall dynamic response of solid media, and specifically on the interaction between near-field and far-field domains during wave propagation induced by the occurrence of non-smooth phenomena in the near-field domain. As such, it is not our aim to realistically mimic micro-scale phenomena, such as fracture, for

which the particle-based lattice models (II) and DEM (III) are specifically suitable. For our application, it is sufficient to model our medium as a classical or conventional lattice (I) consisting of a collection of discrete meso-scale particles, where each particle represents a small portion or volume of that medium. The possibly non-smooth behaviour between adjacent particles in the lattice model is included by introducing sophisticated nonlinear rheological models obtained by combining reversible and irreversible rheological elements such as springs, dashpots and dry-friction elements.

1.3 Boundary integral equations to account for the far-field domain

When modelling the nonlinear dynamic response of a medium by dividing that medium into a nonlinear domain in the near field and a linear domain in the far field, the response of the nonlinear domain does not only depend on the properties of the nonlinear model itself, but is also governed by its interaction with the surrounding linear domain. In general, if the surrounding medium is infinite in the direction of wave propagation, or may be assumed infinite by approximation, the response of the linear domain must satisfy the radiation condition, such that correctly accounting for this domain disables any wave reflections at the boundary of the nonlinear domain. Figure 1.4a depicts an example of a three-dimensional soil-structure-interaction problem where the half-space acts as a silent or non-reflective boundary to the nonlinear domain it surrounds. As an example of a surrounding medium with finite dimensions, consider the ice sheet depicted in Figure 1.4b. Here, wave reflections may occur at the outer edges of the ice that may ultimately propagate back into the nonlinear domain. Correctly accounting for the linear far-field domain in this case should allow for wave reflections at the outer edges of the linear domain, while there are no reflections when any propagating waves are transmitted between the nonlinear and linear domains.

Now, if we are exclusively interested in the response of the near-field domain, the only part of the far-field response that we must necessarily account for is its response at the interface with the near-field domain, but only if the response of the far-field domain at this interface correctly accounts for the behaviour and properties of the far-field domain beyond this interface. This can be done by using a boundary integral equation (BIE) that describes the

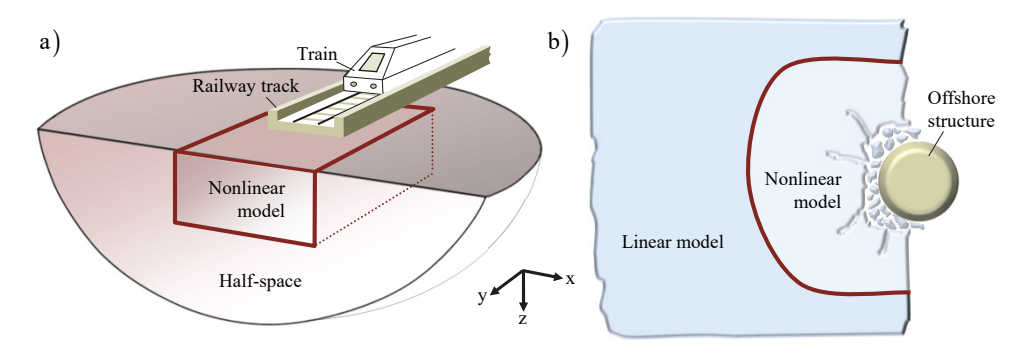


Figure 1.4: Interaction between the nonlinear and linear domains of: a) the soil due to interaction with a high-speed train; b) sea ice due to interaction with an offshore structure.

response of the far-field domain using an integral equation that is defined only at its boundary with the near-field domain, while it accounts for the behaviour and the properties of the whole far-field domain. If the sole purpose of a boundary formulation is to absorb the energy of incident waves and thereby supress wave reflections and act as a silent boundary, techniques other than the use of BIEs are available, such as introducing a perfectly matched layer (PML), e.g. Bérenger [1994]; Kausel and de Oliveira Barbosa [2012]. Although using PMLs is numerically very efficient when an absorbing boundary is required, this numerical technique may not be applied when the surrounding medium has finite dimensions and reflected waves passing through the boundary should be accounted for.

In few particular cases and principally only for one-dimensional domains, BIEs can be derived directly from the balance of forces at the boundary, or from the one-dimensional wave equation, for example by using d'Alembert's solution [D'Alembert, 1747]. For two-and three-dimensional systems however, the BIEs are generally obtained by employing the dynamic reciprocal work theorem, e.g. de Hoop [1966], Achenbach [2004]. Starting from the dynamic reciprocal work theorem, the BIEs may be described in terms of the fundamental or Green's functions of that domain. Since the Green's functions are not always known and cannot always be derived, determining the Green's functions is generally the key difficulty in deriving BIEs. Thereby, these approaches can only be applied successfully for domains of which the Green's functions are known or can be determined.

As we intend to model the nonlinear near-field domain as a discrete lattice, it is most appropriate to model the linear far-field domain as a discrete system as well. Surely, to achieve a perfect boundary formulation such that there is no unwanted wave reflections at the boundary, the far-field domain should at least match the discrete nature of the near-field domain. While there is some literature available regarding Green's functions for discrete lattice models, e.g. Katsura et al. [1971]; Maradudin et al. [1971]; Martin [2006], to the knowledge of the author of this thesis, there are no publications that specifically explore the derivation of BIEs for discrete lattice models. Moreover, the development of hybrid schemes involving discrete lattices and corresponding boundary formulations are very sparse in literature. The paper by Cai et al. [2000] describes the coupling of two linear domains described by matching linear square lattices to resolve a problem in molecular dynamics. The approach described is numerically demanding and cannot be easily adapted for different geometries. Later contributions by Karpov et al. [2005] and Carpio and Tapiador [2010] present more generic approaches to determine non-reflecting boundary conditions in molecular dynamics by employing the concept of lattice dynamics Green's functions [Maradudin et al., 1971]. In correspondence with using PMLs, the approaches in these contributions are aimed at developing non-reflective boundaries, rather than at developing a truthful representation of the farfield domain and its properties.

Given the limited availability of literature that treats the derivation of BIEs for discrete lattices, it is relevant to note that a boundary formulation does not necessarily have to be perfect as long as any wave reflections that do occur at the boundary are not significant and only marginally influence the response of the near-field domain. Based on this, it is not an absolute necessity to model the far-field domain as a discrete system and other options can

be regarded. Because of its relative and apparent straightforward way of representing reality, a popular alternative is the continuum, which has been abundantly used to model far-field domains, especially when the near-field domain is also considered as a continuum. Accordingly, there have been ample studies considering the Green's functions for continuous media and there are abundant derivations and applications of BIEs for continuous media available in literature. Therefore in this thesis, we will derive BIEs from a discrete representation of the far-field domain and compare their performance to those of BIEs derived from continuous representations. Here, do note that implementing BIEs for a continuous far field at the boundary of a discrete near field poses additional challenges due to differences in their fundamental properties.

1.4 The time domain versus the frequency domain

In dynamics, a boundary integral equation that describes the dynamic response of a far-field domain at its boundary and thus at the interface with the near-field domain, generally follows from the convolution of force and displacement at this interface resulting in an integral force-displacement relation in the time domain. In the frequency domain, the corresponding algebraic relation is commonly known as the *dynamic stiffness*. In two- and three-dimensional problems, the discretisation of the boundary, which is required when the far-field domain is modelled as a continuum, and the application of the boundary element method yields this force-displacement relation in the form of the so-called dynamic stiffness matrix.

Depending on the properties of the lattice model and the boundary formulation used to incorporate the far-field response, the resulting time domain system of differential equations can sometimes be fully derived analytically. In principal, this is only the case for linear-elastic one-dimensional models; as soon as multiple dimensions are considered, or for example if damping is included, the system of equations of motion can no longer be directly obtained analytically in the time domain. The full system of equations of motion for the near-field lattice that includes the boundary formulation, is therefore generally derived in the frequency domain as a set of algebraic equations. The inversion into the time domain almost always has to be done numerically as analytical solutions of the involved integrals are generally unknown. Nevertheless, the numerical inversion of the algebraically obtained frequency domain response requires severely less numerical effort than solving the corresponding time domain system of differential equations numerically.

Although the advantage in numerical effort makes frequency domain approaches preferable over time domain approaches, the presence of nonlinear phenomena in the near field implies the necessity to work in the time domain rather than in the frequency domain. This is because the involved nonlinearities are often steered by time domain processes and cannot always be captured by considering all frequencies separately, which is essentially done in frequency domain approaches. Consequently, the occurring nonlinear phenomena cannot be easily described in the frequency domain and any model that attempts to incorporate these nonlinear phenomena generally has to be solved in the time domain. However, the behaviour of a medium or a system is often not continuously nonlinear. Instead, nonlinear phenomena may be initiated by the surpassing of a certain threshold. Consider for example an object

lying on a table; this object will only start sliding over the table surface when the force exerted on the object surpasses the friction threshold. The overall behaviour of this object is thus nonlinear only because of the instantaneous transition to another mode or state of behaviour at a certain moment in time, while both before and after the object has started to slide the object behaves linearly. With the aim to minimize the required computational effort, in this thesis options will be explored to utilize the advantage of frequency domain approaches for those periods in time where a medium or system behaves linearly, even though the overall response of the system may be nonlinear.

1.5 Numerical implementation and application of BIEs

In virtually all applications of boundary integral equations (BIEs), numerical techniques are required to solve BIEs and describe the response of a domain at its boundary, which in turn requires the boundary to be discretized. The numerical implementation of techniques to solve BIEs is commonly referred to as the boundary element method (BEM). It is noted here that while the applied numerical techniques are an important aspect of solving BIEs, this thesis does not focus on the development or improvement of existing boundary elements methods and merely uses commonly known boundary methods as a means to implement BIEs. Nevertheless, it is worth reviewing existing applications of BEM in dynamics to determine the options for numerical implementation of BIEs in this research.

The papers of Friedman and Shaw [1962] and Banaugh and Goldsmith [1963] represent the first applications of BEM in dynamics in the time and frequency domain, respectively. The work by Rizzo [1967] on boundary value problems in elastostatics introduced the direct BEM leading to a wide application of the method in applied mechanics. Since then, both direct and indirect BEM approaches have been formulated for elastodynamic applications, as can be identified by the books of Banerjee and Butterfield [1981], Wolf [1985] and Dominguez [1993].

The dynamic stiffness matrix that is obtained by applying the conventional direct BEM, through the employment of the dynamic reciprocal work theorem or the method of weighted residuals, is generally non-symmetric. The indirect BEM however, where the dynamic stiffness matrix is obtained by assuming fictitious sources at a small distance from the considered boundary to avoid singularities, always yields a symmetric dynamic stiffness matrix [Wolf and Darbre, 1984a, 1984b]. Since the dynamic stiffness matrix is by definition a full matrix, it is beneficial to work with a symmetric dynamic stiffness matrix rather than a non-symmetric one to improve computational effort. To limit the computational effort as much as possible, in this thesis, the indirect BEM approach by Wolf and Darbre [1984a] is adopted to derive a symmetric dynamic stiffness matrix for the continuous far-field domain, while for the discrete representation of the far-field domain the conventional method suffices. More recent work, for example that of Coulier [2014], shows that it is also possible to reduce the computational effort of BEM by rearranging the dynamic stiffness matrix, but this options will not be further explored in this thesis.

Despite extensive research of improved elastodynamic formulations for BEM, many issues still remain unsolved [Frangi and Novati, 1999]. For example, according to Dominguez

[1993] and Peirce and Siebrits [1997] BIEs are often unstable in the time domain when finite media are considered. For a more thorough and in-depth overview of the development of the Boundary Element Methods reference is made to the reviews by Beskos [1987, 1997] and specifically for applications in acoustics to the more recent review by Kirkup [2019].

1.6 Aims and novelty of the thesis

This thesis deals with the modelling of the nonlinear response of a solid medium to loads induced by its dynamic interaction with a structure and the resulting wave propagation through that medium. Here, the structure and its response are not included and the interaction of the structure with the solid medium is represented by an external time-dependent force.

To efficiently model its response, we divide the solid medium into a detailed nonlinear domain close to the structure, i.e. the near field, and a linear domain at an appropriate distance from the structure, i.e. the far-field. The near-field is modelled as a discrete lattice capable of describing nonlinear phenomena in the time domain, while the far-field is accounted for by a boundary representation to limit the dimensions of the medium to the near-field domain. To correctly describe the response of the near-field domain, the boundary representation must correctly account for the response of the far-field domain. The main objective of this thesis therefore is:

To develop a methodology capable of efficiently describing the nonlinear time domain response of a medium in the near field, while properly accounting for its response in the far field.

Properly accounting for the response of the far-field in this case emphasizes the objective of waves travelling through the boundary with as minimal as possible disturbance or alteration due to the boundary formulation. To judge the proper integration of the linear far-field domain at the boundary of the near-field domain, we consider both continuous and discrete representations of the linear far-field domain. As there are abundant derivations and applications of BIEs for continuous media available in literature, we first consider the behaviour of a discrete-continuous medium composed of a discrete lattice in the near field and for which the boundary formulation is derived from a continuous linear far-field domain. Second, corresponding BIEs are derived by considering the linear far-field domain as a system of particles that matches the discrete properties of the near-field domain. Subsequently, the time domain response of the nonlinear near-field domain is compared for both the continuous and discrete far-field representations. Before considering two-dimensional versions of these discrete-continuous and fully discrete representations, corresponding one-dimensional models are considered to identify the characteristic properties and behaviour. Note here that three-dimensional media are not considered in this study.

This study includes one of the first attempts to derive a boundary integral formulation for a far-field domain described as a finite or semi-infinite system of discrete particles. Additionally, the application of such a boundary formulation to a nonlinear discrete lattice in the near field has not been executed before. Thus, emphasizing the novelty of this thesis.

Additionally, a novel mixed time-frequency domain method is introduced to simulate the nonlinear response of a medium in the time domain by utilising much faster frequency domain approaches and thereby improve its numerical performance.

1.7 Reading guide

As shown by the flow-chart of the thesis structure in Figure 1.5, this dissertation is divided into six chapters. The current chapter gives a general introduction to lattices and their boundary formulations and thereby clarifies the context, as well as the practical and scientific relevance of this study. Additionally, the ambitions and novelties of this study are clarified.

Before presenting the detailed development of boundary formulations to represent the far field in the time domain, Chapter 2 gives a qualitative description of the one- and two-dimensional discrete lattice models and their capability to describe the desired nonlinear response in the region of interaction with a structure, i.e. in the near field. First, the equations of motion for the considered nonlinear lattice are derived using Lagrange's formalism, after which the states and state transitions that appear in the lattice elements are discussed. Chapter 2 is concluded by considering the response of the one- and two-dimensional lattice models with elementary boundaries incorporated and a discussion of the linearizations that are applied for two-dimensional lattices.

Chapters 3 and 4 treat the derivation of the boundary integral equations and the development of the corresponding integrated models by representing the far-field domain as a semi-infinite continuum and a system of discrete particles respectively. In both chapters, the concept of the boundary integral approach is explained and the characteristic properties are identified by first considering one-dimensional models. Subsequently, the development of the corresponding two-dimensional models is treated, including a discussion of the relevant boundary formulation and the derivation of the valid Green's functions. Finally, at the end of Chapter 4, an exemplary nonlinear response of a two-dimensional fully discrete medium is presented and discussed.

Subsequently, Chapter 5 is devoted to improving the time domain simulation for the oneand two-dimensional media through a so-called mixed time-frequency domain method. The main purpose of this method is the optimisation of the numerical calculation time by employing frequency domain approaches, while allowing nonlinearities to occur in the time domain.

Finally, Chapter 6 summarizes the main results and conclusions of this study and addresses the future perspectives of incorporating boundary formulations in lattice modelling.

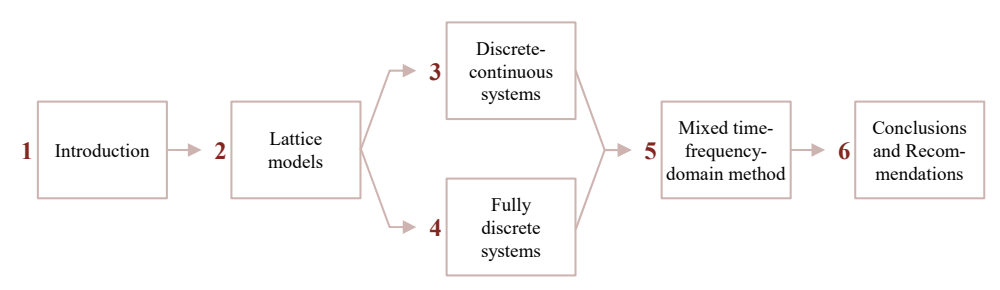


Figure 1.5: Structure of the thesis.

One- and two-dimensional lattice models

This chapter presents the one- and two-dimensional discrete lattice models and demonstrates their capability to describe the nonlinear dynamic response of a medium close to a load source or in the region of interaction with a structure, i.e. in the near-field domain.

The first section of this chapter presents Lagrange's formalism as a consistent approach to derive the equations of motion for any particle in a one- or two-dimensional lattice by taking into account the interaction between that particle and its adjacent particles. Thereby, Lagrange's formalism allows for the derivation of the complete system of equations of motion for any lattice model independent of its parameters and thus allowing for the variation of properties throughout the lattice. The different rheological elements or models, consisting of different combinations of springs, dashpots and dry-friction elements, that describe the interaction between adjacent lattice particles are discussed in Section 2.2. Then, in Sections 2.3 and 2.4, we respectively derive the governing equations for the one- and two-dimensional discrete lattices accounting for the different motion states according to which the rheological models in these lattices may behave. In these sections, additionally, the conditions under which any transitions between these motion states occur are discussed. Subsequently, Section 2.5 addresses the macromaterial properties for which the responses of the one- and two-dimensional lattices are presented in this thesis. Finally, in Section 2.6, we consider the response of both a linear and a nonlinear hexagonal lattice to an externally applied dynamic load. The lattices considered here have so-called elementary boundaries, meaning that the particles at the lattice boundary are supported using rheological elements, such as springs or dashpots. Thereby, the particles along the boundary behave independently from each other and their response is not derived from the behaviour of the surrounding medium. Additionally in this final section, the performance and accuracy of the two-dimensional lattice modelling is assessed by evaluating the response of a linear-elastic two-dimensional lattice and comparing the results obtained using a frequency domain approach with the results obtained for three different time domain approaches.

2.1 Lagrange's formalism for lattice models

To derive the equations of motion for a particle in a lattice model, there are different options available. For simple geometries, the equations of motion can be straightforwardly obtained from the equilibrium of forces at the considered particle. This is known as the Newtonian approach. Alternatively, we can use the Lagrangian approach, where the equations of motion are derived from the kinetic and potential energy in the system using Lagrange's formalism [Goldstein et al., 2002; Lanczos, 1966; Landau and Lifshitz, 1976]. Especially for more complicated geometries, such as multi-dimensional lattices, it becomes difficult to apply the Newtonian approach in an orderly way and therefore becomes sensitive to errors. Although the Lagrangian approach is rather laborious for simple problems, it is unambiguous and consistent and therefore particularly suitable for more complicated geometries.

To find the equations of motion of a particle in a linear or nonlinear lattice, and thereby to determine the full system of equations for the whole lattice, we here apply Lagrange's formalism. Lagrange's formalism states that the equation of motion for any degree of freedom in a system can be found by applying the Euler-Lagrange differential equations for that degree of freedom [Landau and Lifshitz, 1976]. Note that throughout this thesis, properties of lattice particles are denoted using boldface notation superscript to distinguish it from regular notation superscript that would imply exponentiation. Consistently, lattice particles themselves are also denoted in boldface. Thereby, the Euler-Lagrange differential equation for a particle **n** in a one-dimensional lattice reads:

$$\frac{\partial L^{\mathbf{n}}}{\partial u^{\mathbf{n}}} - \frac{d}{dt} \left(\frac{\partial L^{\mathbf{n}}}{\partial \dot{u}^{\mathbf{n}}} \right) = 0 \tag{2.1}$$

Here, $L^{\mathbf{n}}$ is the Lagrangian of the cell of particle **n**. In this dissertation, dot notation, or Newton's notation, is used for differentiation to time, so while $u^{\mathbf{n}}$ denotes the displacement of particle **n**, $\dot{u}^{\mathbf{n}}$ denotes the velocity of particle **n**.

Now, let us assume that the interaction between any two adjacent particles is described

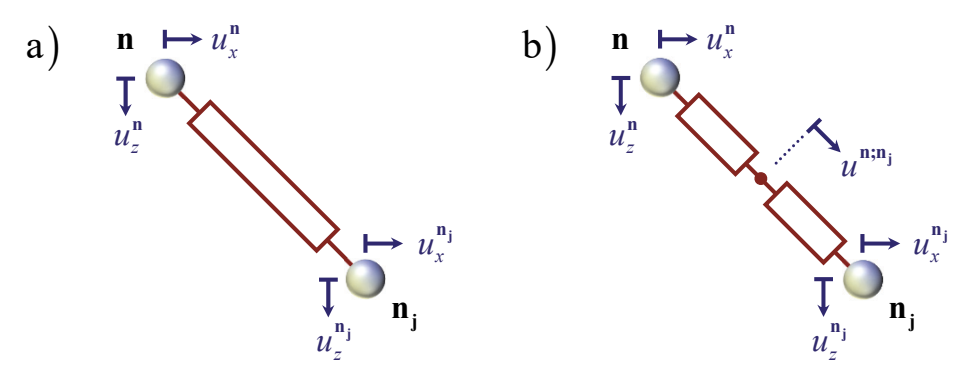


Figure 2.1: a) A single or direct relation between two particles; b) A dual relation between two particles.

by rheological elements that either represent a single relation as depicted in Figure 2.1a, or by a dual relation as depicted in Figure 2.1b. Independent of the nature of the interaction between these particles, the equations of motion of particle $\bf n$ in x- and z-directions are obtained from equation (2.1) by respectively inserting u_x^n and u_z^n as the degree of freedom instead of u^n . For lattices that solely incorporate rheological elements that describe a single or direct relation according to Figure 2.1a, the complete system of equations of motion for the lattice is then straightforwardly obtained by collecting the Euler-Lagrange differential equations for all degrees of freedom in the lattice. For lattices where the interaction between adjacent particles is described according to the dual relation depicted in Figure 2.1b however, each rheological element provides an additional degree of freedom, and thereby an additional equation of motion, to the lattice. These additional equations of motion are obtained by applying the Euler-Lagrange differential equation for the displacement $u^{n;n_j}$ of the node intermediate particles $\bf n$ and $\bf n_j$, which is found in accordance with equations (2.1) as:

$$\frac{\partial L^{\mathbf{n}}}{\partial u^{\mathbf{n};\mathbf{n}_{j}}} - \frac{d}{dt} \left(\frac{\partial L^{\mathbf{n}}}{\partial \dot{u}^{\mathbf{n};\mathbf{n}_{j}}} \right) = 0 \tag{2.2}$$

Note here that the intermediate node between the particles \mathbf{n} and $\mathbf{n_j}$ to which the displacement $u^{\mathbf{n_i}\mathbf{n_j}}$ and the velocity $u^{\mathbf{n_i}\mathbf{n_j}}$ refer, has no mass and therefore has no inertia. Furthermore, the node intermediate particles \mathbf{n} and $\mathbf{n_j}$ should always remain on the straight line between the particles \mathbf{n} and $\mathbf{n_j}$. The motion of this node can therefore be described one-dimensionally along the straight line between the particles \mathbf{n} and $\mathbf{n_j}$ and by a single degree of freedom.

The Lagrangian of the cell of particle **n** is defined as the difference between the kinetic energy $E_{kin}^{\mathbf{n}}$ of the particle **n** itself and the potential energy $E_{pot}^{\mathbf{n}}$ that is contained in the interaction of particle **n** with all its adjacent particles:

$$L^{\mathbf{n}} = E_{kin}^{\mathbf{n}} - E_{pot}^{\mathbf{n}} \tag{2.3}$$

In this case, the potential energy E_{pot}^{n} follows from the elongations of all rheological elements in the cell of particle \mathbf{n} . The way we describe these elongations follows from their magnitude; when the elongations and the corresponding particle displacements remain small, we consider these elongations and displacements relative to their initial state. For large elongations however, we consider the elongations and the corresponding particle displacements relative to their prior state. As we consider both linear and nonlinear material behaviour in this thesis, both small and large elongations may occur and are accounted for. Furthermore, to obtain the system of equations of motion for a two-dimensional lattice as a set of linear ordinary differential equations, we linearize the expressions for the elongations. Appendix A treats the linearizations for both small and large elongations of the rheological elements in two-dimensional lattices. Here, note that the elongations of rheological elements in one-dimensional lattices do not require linearization.

2.2 Rheological elements for lattice models in dynamics

The rheological element that can generally be considered as the most common is the Hooke element [Hooke, 1678]. The Hooke element, named after the 17th century physicist Robert Hooke, describes a purely elastic relation and is thus represented in Figure 2.2a by a spring. Another common linear element used to describe material behaviour is the well-known Kelvin-Voigt element [Thomson and Tait, 1867; Voigt, 1887] that is named after the British physicist Lord Kelvin and the German physicist Woldemar Voigt. The Kelvin-Voigt element describes a viscoelastic relation and consists of a spring and a dashpot, or Newton element, in parallel, as shown in Figure 2.2b. The Kelvin-Voigt element can alternatively be considered as a Hooke element with damping. The rheological element depicted in Figure 2.2c is known as the Bingham element [Bingham, 1922] and is named after Prof. Eugene Bingham, one of the founders of the Society of Rheology in 1929. The Bingham element describes a nonlinear viscoplastic relation, by a parallel combination of a dashpot and a dry-friction or Saint-Venant element [Coulomb, 1821]. Note here that the Hooke, Kelvin-Voigt and Bingham elements are examples of the single relation previously depicted in Figure 2.1a.

Combining the Hooke element with a dry-friction element in series, we obtain a nonlinear elastoplastic relation that is known as the Prandtl element [Prandtl, 1904]. This serial configuration of a spring and a dry-friction element is depicted in Figure 2.2d. The rheological element depicted in Figure 2.2e is composed of a Kelvin-Voigt and a Bingham element in series and is therefore referred to as the Bingham-Kelvin-Voigt element or, in short, the BKV element. Due to the placement of two rheological elements in series, both the Prandtl and BKV elements are examples of the dual relation that was previously depicted by Figure 2.1b.

While the Hooke and Kelvin-Voigt elements are both linear elements, the Bingham, Prandtl and BKV elements are nonlinear, as they each incorporate a dry-friction element. Dry-friction elements are activated only when the force working on the dry-friction element is larger than a constant threshold force, which is referred to as the critical friction force. If the force on the dry-friction element is smaller than the threshold, the dry-friction element is not activated and can therefore be considered as a rigid element. For example, if the dry-friction element is not activated, the Bingham element can be considered to be rigid and the

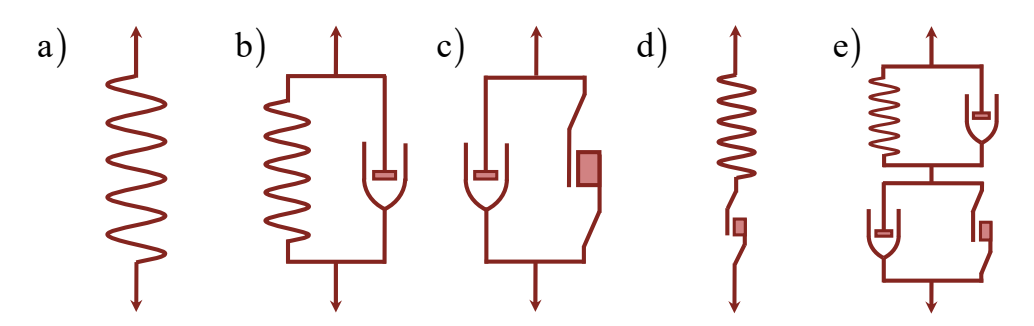


Figure 2.2: Rheological elements: a) the Hooke element; b) the Kelvin-Voigt element; c) the Bingham element; d) the Prandtl element; e) the Bingham-Kelvin-Voigt element

Prandtl element behaves as a spring or Hooke element. The rheological elements that feature dry-friction elements thus behave differently depending on whether the dry-friction element is activated or not. The motion state of these nonlinear rheological elements where the dry-friction element is not activated is referred to as 'stick', while the motion state for which the dry-friction element is activated is referred to as 'slip'. Consequently, stick and slip can only occur in rheological elements that feature a dry friction element.

Next to stick and slip, we also consider a motion state referred to as 'lock'. This lock-state considers the inelastic collision of two particles; if two particles collide their relative motion is impeded and the rheological element between these particles can be considered rigid until their relative motion is reversed. This lock-state is not represented graphically in Figure 2.2 as the behaviour of this motion state is independent of the configuration of the rheological element. Each of the three motion states that we distinguish, being stick, slip and lock, yields different equations of motion depending on the rheological element in which these motion states occurs.

In this thesis, we primarily consider lattices featuring the BKV-element depicted in Figure 2.2e, because it allows us to describe the viscoelastic behaviour of the near-field domain by means of the Kelvin-Voigt element, as well as the possibly nonlinear behaviour of the near-field domain by means of the Bingham element. In addition, the BKV-element can be considered as a generic rheological element since all other elements depicted in Figure 2.2 can straightforwardly be derived from the BKV-element by tuning its parameters.

Before addressing the two-dimensional lattice, in the following we will first evaluate the behaviour of the BKV element in a one-dimensional lattice to gain insight in the behaviour and properties of this element in the different motion states. Subsequently, the transitions that occur between the different motion states, and the conditions under which these transitions occur are discussed.

2.3 One-dimensional lattice models

The one-dimensional lattice is obtained by lining up a number of rheological elements in series, with particles between subsequent rheological elements. In this section, we will derive the governing equations of motion for particles inside the one-dimensional lattice, in particular for the one-dimensional lattice that consists of nonlinear BKV-elements. The equations of motion for respectively the linear-elastic Hooke and viscoelastic Kelvin-Voigt lattices, as well as for the nonlinear Prandtl lattice, may be straightforwardly derived from the equations of motion for the BKV lattice by smartly choosing the corresponding material and geometrical properties.

To allow for large elongations in the one-dimensional lattice, the elongation of the rheological element between particles $\bf n$ and $\bf n+1$ is, in accordance with Appendix A.2, generally described as:

$$e^{\mathbf{n},\mathbf{n}+1} = u^{\mathbf{n}+1} - u^{\mathbf{n}} + \varepsilon^{\mathbf{n},\mathbf{n}+1} \tag{2.4}$$

Here, u^{n} and u^{n+1} are the displacements of particles **n** and **n+1** that occur during the current

time step dt and $\varepsilon^{n,n+1}$ describes the elongation of the rheological element between particles **n** and **n+1** at time t-dt. Thereby, $\varepsilon^{n,n+1}$ is constant during the current time step. According to this definition of the elongation, the displacements u^n and u^{n+1} are small compared to the total elongation of the rheological element, while global deformations in the lattice, i.e. deformations that correspond to the total elongations of its rheological elements, may still be large.

2.3.1 The one-dimensional Bingham-Kelvin-Voigt (BKV) lattice

A fragment of the one-dimensional BKV lattice is depicted in Figure 2.3. A particle $\bf n$, with a mass $M^{\bf n}$, in the interior of the one-dimensional BKV lattice interacts with particles $\bf n-1$ and $\bf n+1$ through BKV elements. The BKV element between the particles $\bf n$ and $\bf n+1$ consists of a Kelvin-Voigt element with a stiffness coefficient $K_e^{\bf n,n+1}$ and a damping coefficient $C_e^{\bf n,n+1}$, and a Bingham element with a damping coefficient $C_f^{\bf n,n+1}$ and a critical friction force $F_{cr}^{\bf n,n+1}$, in series. The properties of the BKV element between any other two adjacent particles are described accordingly.

The equations of motion for a particle $\bf n$ in the one-dimensional BKV lattice are obtained using Lagrange's formalism. Since Lagrange's formalism describes the motion of a particle through the law of conservation of energy, only conservative forces are taken into account. Non-conservative forces, i.e. forces that add energy to, or take energy from a particle, such as external loads or friction, are not part of the equations of motion obtained through the Lagrangian approach. Nevertheless, since any equation of motion obtained through the Lagrangian approach, is in fact an equilibrium of forces, we are allowed to introduce non-conservative forces to that equation of motion as long as the equilibrium is maintained [Lanczos, 1966]. To enable the application of Lagrange's formalism, we consider the Kelvin-Voigt and Bingham elements featured in the BKV element as springs for which the stiffness is described through the operators $\hat{K}_e^{{\bf n},{\bf n}+1}$ and $\hat{K}_f^{{\bf n},{\bf n}+1}$ respectively. For the Kelvin-Voigt element, this operator is defined as $\hat{K}_e^{{\bf n},{\bf n}+1} = K_e^{{\bf n},{\bf n}+1} + C_e^{{\bf n},{\bf n}+1} \frac{\partial}{\partial t}$ and for the Bingham element this operator is defined as $\hat{K}_f^{{\bf n},{\bf n}+1} = C_f^{{\bf n},{\bf n}+1} \frac{\partial}{\partial t}$. The force in the dry-friction element, which is non-conservative, is added to the equations of motion at a later stage. Thus, the Lagrangian $L^{\bf n}$ for the cell of particle ${\bf n}$ in the interior of the one-dimensional BKV lattice reads:

$$L^{\mathbf{n}} = \frac{1}{2} M^{\mathbf{n}} \left(\dot{u}^{\mathbf{n}} \right)^{2} - \frac{1}{2} \hat{K}_{e}^{\mathbf{n}-\mathbf{1},\mathbf{n}} \left(e_{KV}^{\mathbf{n}-\mathbf{1},\mathbf{n}} \right)^{2} - \frac{1}{2} \hat{K}_{f}^{\mathbf{n}-\mathbf{1},\mathbf{n}} \left(e_{B}^{\mathbf{n}-\mathbf{1},\mathbf{n}} \right)^{2} - \frac{1}{2} \hat{K}_{e}^{\mathbf{n},\mathbf{n}+\mathbf{1}} \left(e_{KV}^{\mathbf{n},\mathbf{n}+\mathbf{1}} \right)^{2} - \frac{1}{2} \hat{K}_{f}^{\mathbf{n},\mathbf{n}+\mathbf{1}} \left(e_{B}^{\mathbf{n},\mathbf{n}+\mathbf{1}} \right)^{2}$$
 (2.5)

Here, $e_{KV}^{n-1,n}$ and $e_B^{n-1,n}$ are the elongations of respectively the Kelvin-Voigt and Bingham

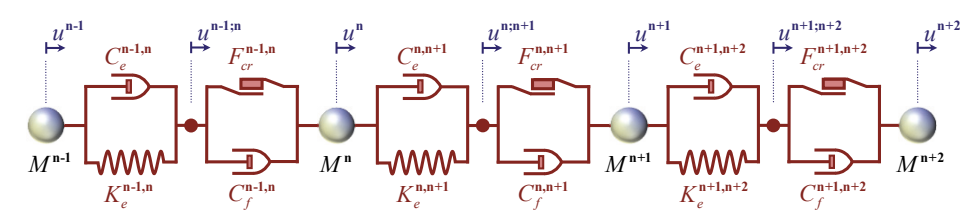


Figure 2.3: A fragment of the one-dimensional BKV lattice.

elements between particles **n-1** and **n**. Furthermore, $e_{KV}^{n,n+1}$ and $e_{R}^{n,n+1}$ are the elongations of respectively the Kelvin-Voigt and Bingham element between particles n and n+1. Substituting the Lagrangian Lⁿ into the Euler-Lagrange differential equations then yields the equation of motion for particle n. To allow for large displacements, the elongations of respectively the Kelvin-Voigt and Bingham elements between particles n and n+1 are defined in accordance with equation (2.4) as:

$$e_{KV}^{\mathbf{n},\mathbf{n}+1} = u^{\mathbf{n};\mathbf{n}+1} - u^{\mathbf{n}} + \varepsilon_{KV}^{\mathbf{n},\mathbf{n}+1}$$

$$e_{R}^{\mathbf{n},\mathbf{n}+1} = u^{\mathbf{n}+1} - u^{\mathbf{n};\mathbf{n}+1} + \varepsilon_{R}^{\mathbf{n},\mathbf{n}+1}$$
(2.6)

$$e_R^{\mathbf{n},\mathbf{n}+1} = u^{\mathbf{n}+1} - u^{\mathbf{n};\mathbf{n}+1} + \varepsilon_R^{\mathbf{n},\mathbf{n}+1} \tag{2.7}$$

Here, $u^{n;n+1}$ denotes the displacement of the massless node intermediate particles **n** and **n+1**.

Due to the presence of the dry-friction element, every BKV element within the one-dimensional BKV lattice behaves according to one of three admissible motion states: stick, slip or lock. Consequently, the equations of motion for each particle in the lattice may differ depending on the motion states of the BKV elements. In the following, the governing equations for a particle **n** in the BKV lattice are therefore derived separately for each of the motion states. First, we derive the equations of motion for a particle **n** in the BKV lattice assuming that all BKV elements in its cell are in stick and subsequently we will derive the corresponding equations of motion assuming that the involved BKV elements are in slip. Next, we will derive the equations of motion for particle n in the BKV lattice assuming that the BKV element between particles n and n+1 is in lock-state. To conclude this section, we will discuss the transitions that exist between the different motion states.

2.3.2 'Stick' in the one-dimensional BKV lattice

Stick is the motion state that occurs in a BKV element, when the forces working on the Bingham element are not large enough to overcome the critical friction force of the dry-friction element, so that the dry-friction element 'sticks' and the Bingham element is not activated. Figure 2.4a shows the forces in a BKV element during stick. In this motion state, the elongation of the Bingham element is impeded, but as the Bingham element may have been activated prior to its current stick-state, the elongation is not necessarily equal to zero. Thus, as long as the BKV element is in a stick-state, the Bingham element can be considered as a rigid bar with a constant elongation, so that the elongation of the Bingham element $e_B^{n,n+1}$ is equal to its elongation-constant $\varepsilon_B^{n,n+1}$. Due to the rigidity of the Bingham element, the elongation rate of the BKV element is always equal to the elongation rate of the Kelvin-Voigt element, that is, as long as the BKV element remains in the stick-state. Thus, while the BKV element is in a stick-state, the elongations of the Kelvin-Voigt and Bingham elements between particles n and n+1 may be expressed as:

$$e_{KV}^{\mathbf{n},\mathbf{n}+1} = e^{\mathbf{n},\mathbf{n}+1} - \varepsilon_B^{\mathbf{n},\mathbf{n}+1} \tag{2.8}$$

$$e_R^{\mathbf{n},\mathbf{n}+1} = \varepsilon_R^{\mathbf{n},\mathbf{n}+1} \tag{2.9}$$

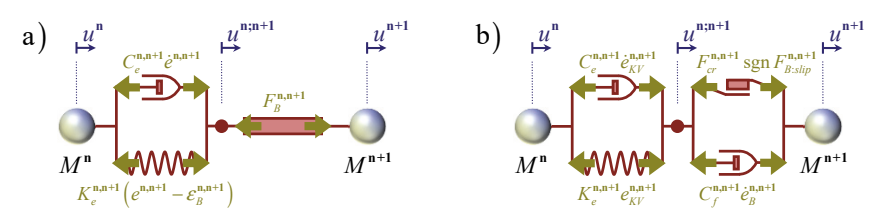


Figure 2.4: Forces in the BKV element during: a) stick; b) slip.

Here, $e^{\mathbf{n},\mathbf{n}+1}$ is the elongation of the BKV element between particles \mathbf{n} and $\mathbf{n}+1$ as defined by equation (2.4). Note here that by writing the elongation of the Kelvin-Voigt element according to equation (2.8), the displacement of the node intermediate particles \mathbf{n} and $\mathbf{n}+1$, which does not act as a degree of freedom during stick, does not appear in the system of equation of motions. The actual displacement $u^{\mathbf{n};\mathbf{n}+1}$ of the node intermediate particles \mathbf{n} and $\mathbf{n}+1$ during stick-state must be equal to the displacement of particle $\mathbf{n}+1$, i.e. $u^{\mathbf{n};\mathbf{n}+1}=u^{\mathbf{n}+1}$.

To obtain the equation of motion for an arbitrary particle \mathbf{n} in the one-dimensional BKV lattice, we substitute equations (2.8) and (2.9), respectively for the BKV element between particles \mathbf{n} -1 and \mathbf{n} , and for the BKV element between particles \mathbf{n} and \mathbf{n} +1, into equation (2.5) for the Lagrangian $L^{\mathbf{n}}$. Then, we apply the Euler-Lagrange differential equation (2.1) and substitute the expressions for the operators $\hat{K}_{\varepsilon}^{\mathbf{n}-\mathbf{1},\mathbf{n}}$ and $\hat{K}_{\varepsilon}^{\mathbf{n},\mathbf{n}+\mathbf{1}}$. This yields the equation of motion for a particle \mathbf{n} in the one-dimensional BKV lattice, for the situation where all BKV elements in its cell are in stick, as:

$$M^{\mathsf{n}}\ddot{u}^{\mathsf{n}} + C_{e}^{\mathsf{n}-\mathsf{1},\mathsf{n}}\dot{e}^{\mathsf{n}-\mathsf{1},\mathsf{n}} + K_{e}^{\mathsf{n}-\mathsf{1},\mathsf{n}} \left(e^{\mathsf{n}-\mathsf{1},\mathsf{n}} - \varepsilon_{B}^{\mathsf{n}-\mathsf{1},\mathsf{n}} \right) - C_{e}^{\mathsf{n},\mathsf{n}+\mathsf{1}}\dot{e}^{\mathsf{n},\mathsf{n}+\mathsf{1}} - K_{e}^{\mathsf{n},\mathsf{n}+\mathsf{1}} \left(e^{\mathsf{n},\mathsf{n}+\mathsf{1}} - \varepsilon_{B}^{\mathsf{n},\mathsf{n}+\mathsf{1}} \right) = 0 \ (2.10)$$

As long as the Bingham elements are not activated, and the elongation-constants $\mathcal{E}_B^{\mathbf{n},\mathbf{n}+\mathbf{n}}$ and $\mathcal{E}_B^{\mathbf{n},\mathbf{n}+\mathbf{1}}$ remain equal to zero, the one-dimensional BKV lattice behaves purely viscoelastic and exactly resembles the Kelvin-Voigt lattice. The equation of motion for a particle \mathbf{n} in the one-dimensional Kelvin-Voigt lattice is thus obtained from equation (2.10) by setting the elongation-constants $\mathcal{E}_B^{\mathbf{n}-\mathbf{1},\mathbf{n}}$ and $\mathcal{E}_B^{\mathbf{n},\mathbf{n}+\mathbf{1}}$ to zero. By additionally choosing the value of the damping coefficients equal to zero, i.e. $C_e^{\mathbf{n}-\mathbf{1},\mathbf{n}}=C_e^{\mathbf{n},\mathbf{n}+\mathbf{1}}=0$, the equation of motion for a particle \mathbf{n} in the one-dimensional Hooke lattice is obtained. The equation of motion for a particle \mathbf{n} in the one-dimensional Prandtl lattice with all Prandtl elements in stick, follows from substituting $C_e^{\mathbf{n},\mathbf{n}+\mathbf{1}}=0$ and $\mathcal{E}_B^{\mathbf{n},\mathbf{n}+\mathbf{1}}=\mathcal{E}_f^{\mathbf{n},\mathbf{n}+\mathbf{1}}$ for all elements into equation (2.10), where $\mathcal{E}_f^{\mathbf{n},\mathbf{n}+\mathbf{1}}$ denotes the elongation of the involved dry friction element.

2.3.3 'Slip' in the one-dimensional BKV lattice

When the forces that work on a Bingham element are large enough to overcome the critical friction force of its dry-friction element, i.e. the maximum friction force that the element can handle, the dry-friction element in the BKV element 'slips' [Tipler, 1998], and the Bingham element is activated. In this motion state, both the Kelvin-Voigt and Bingham elements are active and the BKV element may be described by the dual relation given in Figure 2.1b.

For the situation where the involved BKV elements are in a slip-state, the equation of

motion for particle **n** is obtained by substituting the Lagrangian $L^{\mathbf{n}}$, given by equation (2.5), into the Euler-Lagrange differential equations (2.1). Next, we substitute the expressions for the operators $\hat{K}_e^{\mathbf{n}-\mathbf{1},\mathbf{n}}$, $\hat{K}_f^{\mathbf{n}-\mathbf{1},\mathbf{n}}$, $\hat{K}_e^{\mathbf{n},\mathbf{n}+\mathbf{1}}$ and $\hat{K}_f^{\mathbf{n},\mathbf{n}+\mathbf{1}}$, and we include the critical friction force $F_{cr}^{\mathbf{n}-\mathbf{1},\mathbf{n}}$ in the dry friction element, without jeopardizing the equilibrium of forces [Lanczos, 1966]. Here, we assume that when a dry friction element is in slip, the force in the dry friction element is constant and equal to the critical friction force. Thereby, we do not account for the differences between static and the kinetic friction. The equation of motion for a particle **n** in the one-dimensional BKV lattice with the BKV elements in its cell in slip, then reads:

$$M^{\mathbf{n}}\ddot{u}^{\mathbf{n}} + C_{f}^{\mathbf{n}-\mathbf{1},\mathbf{n}}\dot{e}_{B}^{\mathbf{n}-\mathbf{1},\mathbf{n}} + F_{cr}^{\mathbf{n}-\mathbf{1},\mathbf{n}}\operatorname{sgn}F_{B:slip}^{\mathbf{n}-\mathbf{1},\mathbf{n}} - C_{e}^{\mathbf{n},\mathbf{n}+\mathbf{1}}\dot{e}_{KV}^{\mathbf{n},\mathbf{n}+\mathbf{1}} - K_{e}^{\mathbf{n},\mathbf{n}+\mathbf{1}}e_{KV}^{\mathbf{n},\mathbf{n}+\mathbf{1}} = 0$$
(2.11)

Here, $F_{B:slip}^{\mathbf{n-1,n}}$ denotes the force that is applied to the Bingham element to initiate the current instance of slip. Additionally, sgn is an abbreviation of signum, so that $\operatorname{sgn} F_{B:slip}^{\mathbf{n-1,n}}$ determines the sign of the critical friction force $F_{cr}^{\mathbf{n-1,n}}$ based on whether the current instance of slip was initiated in tension of in compression. Note here that the sign of the critical friction force must remain the same throughout each instance of slip.

When the BKV element between particles **n** and **n+1** is in slip, the node intermediate particles **n** and **n+1** is a degree of freedom. As the node intermediate particles **n** and **n+1**, alternatively denoted as a slip-node, has no mass and therefore no kinetic energy, its Lagrangian is found as:

$$L^{\mathbf{n},\mathbf{n}+1} = -\frac{1}{2} \hat{K}_{e}^{\mathbf{n},\mathbf{n}+1} \left(e_{KV}^{\mathbf{n},\mathbf{n}+1} \right)^{2} - \frac{1}{2} \hat{K}_{f}^{\mathbf{n},\mathbf{n}+1} \left(e_{B}^{\mathbf{n},\mathbf{n}+1} \right)^{2}$$
(2.12)

Substitution into the Euler-Lagrange differential equation (2.2), as well as substituting the expressions for the operators $\hat{K}_e^{\mathbf{n},\mathbf{n}+1}$ and $\hat{K}_f^{\mathbf{n},\mathbf{n}+1}$, and including the critical friction force, the equation of motion for the slip-node intermediate particles \mathbf{n} and $\mathbf{n}+1$ becomes:

$$C_e^{\mathbf{n},\mathbf{n}+1}\dot{e}_{KV}^{\mathbf{n},\mathbf{n}+1} + K_e^{\mathbf{n},\mathbf{n}+1}e_{KV}^{\mathbf{n},\mathbf{n}+1} - C_f^{\mathbf{n},\mathbf{n}+1}\dot{e}_B^{\mathbf{n},\mathbf{n}+1} - F_{cr}^{\mathbf{n},\mathbf{n}+1}\operatorname{sgn} F_{B:slip}^{\mathbf{n},\mathbf{n}+1} = 0$$
(2.13)

As depicted in Figure 2.4b, equation of motion (2.13) describes the equilibrium of forces at the slip-node of a BKV element in slip and is valid for any slip-node in a BKV element in slip. The corresponding equation of motion for the slip-node intermediate particles **n-1** and **n** is thus obtained by adapting the superscripts that refer to the involved particles.

The system of equations of motion for the one-dimensional Prandtl lattice with its elements in slip is found by substituting $C_e^{\mathbf{n},\mathbf{n}+1} = C_f^{\mathbf{n},\mathbf{n}+1} = 0$ and $F_{B:slip}^{\mathbf{n},\mathbf{n}+1} = F_{f:slip}^{\mathbf{n},\mathbf{n}+1}$ into equations (2.11) and (2.13) for all elements in the lattice. Here, $F_{f:slip}^{\mathbf{n},\mathbf{n}+1}$ denotes the force that is applied to the involved dry friction element to initiate the current instance of slip. As the slip-state does not occur in the Hooke and Kelvin-Voigt lattices, corresponding equations do not exist for these lattices.

2.3.4 'Lock' in the one-dimensional BKV lattice

The situation where a rheological element between two particles 'locks', can physically be considered as an inelastic collision between these particles that occurs when the distance between the two particles becomes smaller than a certain threshold. When this threshold is reached, the two particles collide and any further decrease of the distance between these particles is impeded. Consequently, lock only occurs in rheological elements that are in compression. Assuming that the relative motion between the two involved particles is fully obstructed in lock, rheological elements that are in lock-state can be represented by a rigid bar.

For the case that the BKV element between particles **n** and **n+1** is in lock and is thus represented by a rigid bar, the equation of motion for both particles n and n+1 must depend on the state of the element between particles **n-1** and **n**, and on the state of the element between particles n+1 and n+2. This dependency is illustrated in Figure 2.5. In fact, by modelling the BKV element in lock as a rigid bar, the motions of the particles n and n+1 become identical. For every adjacent BKV element that is also in lock, another particle will have the same equation of motion, and in that equation of motion the interaction described by the first successive non-locked BKV-element are to be taken into account. Additionally note that, as a consequence, for every element in lock the number of degrees of freedom in the system is reduced by one. Although it is fairly straightforward to implement the lock-state in a onedimensional lattice by considering locked elements as rigid bars, this is not as straightforward for two- or three-dimensional lattices. Not only will it be very laborious to incorporate the lock-state by means of rigid bars in, for example, the two-dimensional lattice for all possible combinations of motion states in the different elements, it is also significantly less straightforward as these rigid bars may still rotate, which means that the number of degrees of freedom does not simply reduce, but the equations of motion involved with these degrees of freedom change. In this thesis therefore, we will not use rigid bars to model the lock-state in our lattices. To illustrate the approach however, the equations of motion for an arbitrary particle **n** with the BKV element between particles **n** and **n+1** in lock-state represented by a rigid bar, are derived in Appendix C.2, while the lock-state by means of a rigid bar is further discussed for the hexagonal BKV lattice in Appendix C.3.

Instead of representing the interaction between two particles for the lock-state by a rigid bar, we introduce lock by adding a spring parallel to the BKV element with a stiffness that is significantly larger than the stiffness of the spring present in the BKV element. Here, note that as lock only occurs in compression, the spring that is introduced during lock only yields a stiffness increase while the involved rheological element remains in compression. Furthermore, note that while adding a spring with a large stiffness does not fully impede the movement between the particles $\bf n$ and $\bf n+1$, the relative motions will be severely reduced. Except that this approach is far more straightforward to implement, it is physically also more realistic than using a rigid bar as a collision between two objects is not usually completely inelastic in reality. The application of the lock-state by using a high-stiffness spring in parallel is illustrated by Figure 2.5 for the BKV element between particles $\bf n$ and $\bf n+1$. Figure 2.5a shows the situation where the lock-state does not occur; as the total distance between particles $\bf n$ and $\bf n+1$ is larger than a certain minimum allowed distance $D_{\rm min}^{\bf n,n+1}$, and a certain gap remains, i.e.

 $\Delta D^{\mathbf{n},\mathbf{n}+1}>0$, the parallel spring is not activated and the motion of the BKV element is unrestricted. However, when the distance between particles \mathbf{n} and $\mathbf{n}+\mathbf{1}$ reduces to the threshold distance and the gap closes, i.e. $\Delta D^{\mathbf{n},\mathbf{n}+1}=0$, the parallel spring with stiffness $K_{lock}^{\mathbf{n},\mathbf{n}+1}$ is activated and the relative motion between the particles \mathbf{n} and $\mathbf{n}+\mathbf{1}$ is opposed by the axial force in the parallel spring. The latter situation is depicted in Figure 2.5b.

To determine the equations of motion of a particle **n** for the case that the element between particles **n** and **n+1** is in lock-state, we must first establish what happens in the BKV element when the lock-state occurs. Principally, the behaviour of a BKV element during lock follows from its motion state before the lock-state is initiated. For the case that lock occurs while the BKV element is in a stick-state, it is evident that the Bingham element remains inactive during the lock-state. As a consequence, after a stick-to-lock transition and for the duration of the lock-state, the displacement of the intermediate node is equal to the displacement of particle **n+1** and the BKV element behaves as a Kelvin-Voigt element.

When lock occurs while the BKV element is in slip, it follows that the Bingham element is active at the onset of lock. Clearly as lock sets in, the elongation rate of the BKV element is severely reduced, i.e. $\dot{e}^{n,n+1} \approx 0$, and the elongation of the whole element becomes constant by approximation. This however does not mean that the Bingham element immediately stops being active as confirmed by the discussion of the slip-to-stick transition in Section 2.3.5. Principally, the Bingham element may be expected to remain active until the velocity of the node intermediate particles **n** and **n+1** changes direction. Now, as the intermediate node has no inertia, it is quite reasonable to assume that the Bingham element becomes inactive quite quickly after the initiation of lock. Therefore, independent from the motion state before lock, we may generally assume that, as depicted in Figure 2.5b, during the lock-state the Bingham element is inactive and that during lock the BKV element behaves as a Kelvin-Voigt element. Consequently, the equation of motion of the particle **n** for the case that the element between particles n and n+1 is in lock-state is, after all, independent from the motion state that occurs prior to lock. Nevertheless, the magnitude of the constant elongation $\varepsilon_B^{n,n+1}$ of the involved Bingham element during and after lock does depend on the motion state prior to lock. During a stick-to-lock transition, the elongation $\varepsilon_B^{\mathbf{n},\mathbf{n}+1}$ remains constant and equal to its value prior to lock, while after a slip-to-lock transition, the elongation $\varepsilon_R^{n,n+1}$ follows from the forceequilibrium at the slip-node intermediate particles **n** and **n+1** as derived in Appendix C.2.

Noting that the BKV elements adjacent to a BKV element in lock, may either be in stick, slip or lock, multiple combinations of motion states may occur in the cell of a particle **n**. Here, let us consider the example that the BKV element between particles **n-1** and **n** is in stick-state and the BKV element between particles **n** and **n+1** is in lock-state. The equation of motion for the particle **n** then follows from equation (2.10) by including the axial force in the parallel spring as:

$$\begin{split} M^{\mathsf{n}}\ddot{u}^{\mathsf{n}} + C_{e}^{\mathsf{n-1},\mathsf{n}}\dot{e}^{\mathsf{n-1},\mathsf{n}} + K_{e}^{\mathsf{n-1},\mathsf{n}} \left(e^{\mathsf{n-1},\mathsf{n}} - \varepsilon_{B}^{\mathsf{n-1},\mathsf{n}} \right) \\ - C_{e}^{\mathsf{n,\mathsf{n+1}}}\dot{e}^{\mathsf{n,\mathsf{n+1}}} - K_{e}^{\mathsf{n,\mathsf{n+1}}} \left(e^{\mathsf{n,\mathsf{n+1}}} - \varepsilon_{B}^{\mathsf{n,\mathsf{n+1}}} \right) - K_{lock}^{\mathsf{n,\mathsf{n+1}}} \left(e^{\mathsf{n,\mathsf{n+1}}} + \Delta D_{0}^{\mathsf{n,\mathsf{n+1}}} \right) = 0 \end{split} \tag{2.14}$$

The axial force in the parallel spring, in Figure 2.5 denoted as $F_{lock}^{\mathbf{n},\mathbf{n}+1}$, straightforwardly follows from the elongation of the spring and its stiffness, where the elongation of the parallel spring in turn follows from the elongation $e^{\mathbf{n},\mathbf{n}+1}$ of the element between particles \mathbf{n} and $\mathbf{n}+1$ and the allowed shortening of this element $\Delta D_0^{\mathbf{n},\mathbf{n}+1}$ at which the lock-state occurs and the spring is activated. The allowed shortening of the element between particles \mathbf{n} and $\mathbf{n}+1$ is given by the difference between the initial distance $D_0^{\mathbf{n},\mathbf{n}+1}$ between the particles, or the initial length of this element, and the threshold distance $D_{\min}^{\mathbf{n},\mathbf{n}+1}$ at which the lock-state is initiated, i.e. $\Delta D_0^{\mathbf{n},\mathbf{n}+1} = D_0^{\mathbf{n},\mathbf{n}+1} - D_{\min}^{\mathbf{n},\mathbf{n}+1}$. Here note that the stiffness of the parallel spring is chosen to be a factor φ_{lock} larger than the stiffness in the Kelvin-Voigt element, i.e. $K_{lock}^{\mathbf{n},\mathbf{n}+1} = \varphi_{lock} K_e^{\mathbf{n},\mathbf{n}+1}$, where for example a value of $\varphi_{lock} = 5$ is more than sufficient to significantly reduce the relative motion between the particles.

The equation of motion for a particle **n** with the BKV element between particles **n** and **n+1** in lock and the BKV element between particles **n-1** and **n** in slip, follows from equation (2.11) by including the contribution of the parallel spring as:

$$M^{n}\ddot{u}^{n} + C_{f}^{n-1,n}\dot{e}_{B}^{n-1,n} + F_{cr}^{n-1,n}\operatorname{sgn}F_{B:slip}^{n-1,n} - C_{e}^{n,n+1}\dot{e}^{n,n+1} - K_{e}^{n,n+1}\left(e^{n,n+1} - \varepsilon_{B}^{n,n+1}\right) - K_{lock}^{n,n+1}\left(e^{n,n+1} + \Delta D^{n,n+1}\right) = 0$$

$$(2.15)$$

The corresponding equations of motion for a particle **n** in the one-dimensional Kelvin-Voigt lattice follow from equation (2.14) by choosing the constants $\mathcal{E}_B^{\mathbf{n}-\mathbf{1},\mathbf{n}}$ and $\mathcal{E}_B^{\mathbf{n},\mathbf{n}+\mathbf{1}}$ equal to zero and the corresponding equations of motion for the one-dimensional Hooke lattice are then found by additionally choosing the damping coefficients $C_{\varepsilon}^{\mathbf{n}-\mathbf{1},\mathbf{n}}$ and $C_{\varepsilon}^{\mathbf{n},\mathbf{n}+\mathbf{1}}$ equal to zero.

2.3.5 State-transitions in the one-dimensional BKV lattice

Every rheological element in the one-dimensional BKV lattice separately behaves according to either one of the three admissible motion states. While all elements in a cell can be

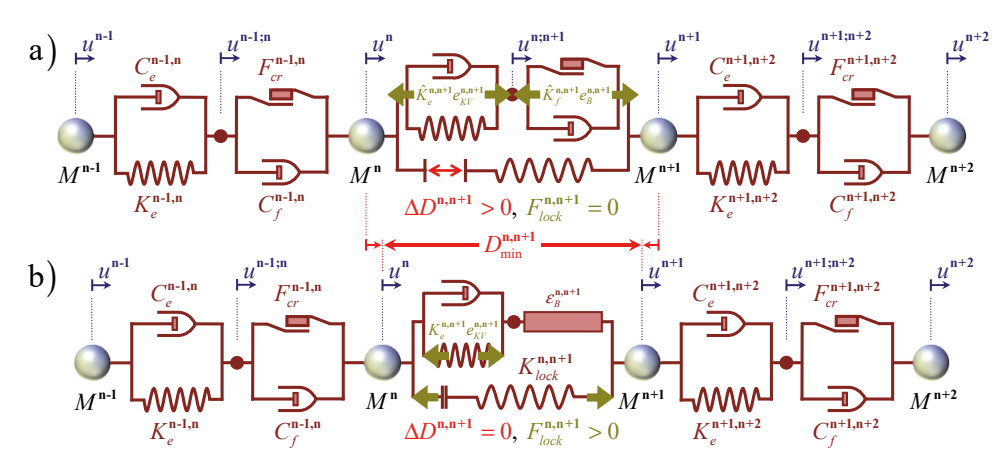


Figure 2.5: Segment of the one-dimensional BKV lattice with a lock-element added to the BKV element between particles **n** and **n+1**: a) while not in lock-state; b) during lock-state.

expected to be in the same state at certain time intervals, the case that adjacent elements behave according to different motion states at the same time should be accounted for. Therefore, the motion states of all elements in the lattice must be actively monitored. To do this, we first need to understand how transitions between the motion states occur. Figure 2.6a shows a diagram where arrows depict the admissible transitions between the different motion states in a BKV element.

In the following, we will successively discuss the stick-to-slip and slip-to-stick transitions, as well as the transitions into and out of lock. These transitions are represented in Figure 2.6a by the dark-red, light-red, dark-green and light-green arrows respectively. The absence of the lock-to-slip transition in Figure 2.6a is explained in the subsection that regards the transition out of lock.

Stick-to-slip transition

For the transition from stick to slip in a BKV element between two adjacent particles $\bf n$ and $\bf n+1$, let us consider the forces in the Bingham element during stick that are depicted in Figure 2.6b. During stick, the dashpot in the Bingham element is idle and the corresponding force equal to zero, so that the force in the dry friction element, denoted as the friction force $F_p^{\bf n,n+1}$, is equal to the total force that is applied to the Bingham element, denoted as $F_B^{\bf n,n+1}$. However, once the force applied to the Bingham element exceeds the threshold of the dry-friction element, previously denoted as the critical friction force $F_{cr}^{\bf n,n+1}$, the Bingham element is activated and the motion state in the BKV element transits from stick to slip. As the Bingham element may be activated in both tension and compression in the same manner, the stick-to-slip transition in the BKV element between particles $\bf n$ and $\bf n+1$ occurs when:

$$|F_B^{\mathbf{n},\mathbf{n}+1}| > F_{cr}^{\mathbf{n},\mathbf{n}+1}$$
 (2.16)

At any given time, and thus also during stick, the force that is applied to the Bingham element, can straightforwardly be derived from the force equilibrium at the massless slip-node intermediate particles $\bf n$ and $\bf n+1$ as:

$$F_B^{\mathbf{n},\mathbf{n}+1} = C_e^{\mathbf{n},\mathbf{n}+1} \dot{e}^{\mathbf{n},\mathbf{n}+1} + K_e^{\mathbf{n},\mathbf{n}+1} \left(e^{\mathbf{n},\mathbf{n}+1} - \varepsilon_B^{\mathbf{n},\mathbf{n}+1} \right)$$
 (2.17)

Alternatively, the force $F_B^{n,n+1}$ may be obtained from the force equilibrium at particle n+1. Note here that during stick, the friction force, i.e. the force in the dry friction element, is equal to the force applied to the Bingham element, ergo $F_{fr}^{n,n+1} = F_B^{n,n+1}$. Once the Bingham element is activated however, the friction force is equal to the critical friction force. During slip, the direction of this force can be related to the elongation rate $\dot{e}_B^{n,n+1}$. At the moment that the stick-to-slip transition occurs however, this elongation rate is equal to zero and cannot be used to determine the direction of the friction force at that time. The direction of the force applied to the Bingham element however is known and can therefore be used to account for the direction of the motion. Consequently, at the time an instance of slip is initiated, the

friction force during the following time interval in which the element remains in slip can be determined as $F_{fr}^{\mathbf{n},\mathbf{n}+1} = F_{cr}^{\mathbf{n},\mathbf{n}+1} \operatorname{sgn} F_{B;slip}^{\mathbf{n},\mathbf{n}+1}$, where $F_{B;slip}^{\mathbf{n},\mathbf{n}+1}$ is the force applied to the Bingham element specifically at the time of the stick-to-slip transition.

Slip-to-stick transition

For rheological elements that consist of a dry friction element with no other element in parallel, such as the Prandtl element, the moment at which the transition from slip to stick occurs cannot be determined by monitoring the force working on that element. This is because, as long as the element remains in slip, it follows from force equilibrium that the applied force must be equal to the critical friction force and thus constant.

Instead, we determine the transition from slip to stick by monitoring the relative motion between the two degrees of freedom for which the dry friction element describes the interaction. Now, consider the case that during slip the two degrees of freedom involved move in opposite directions. Once the two degrees of freedom no longer move in opposing directions, i.e. their relative motion becomes equal to zero or changes sign, the dry friction element will stick, because the relative motion can only exist in the opposite direction when the corresponding critical friction force is overcome. Hypothetically, it is possible that, over the course of a single time step, the force applied to the dry friction element in the opposite direction is large enough to immediately induce slip in the opposite direction. Nevertheless, choosing the time step small enough prevents this from happening and assures a smooth transition between the motion states.

Thus in general, instead of depending on the applied friction force, the transition from slip to stick is governed by the relative velocity of the degrees of freedom involved, which in this case is described by the elongation rate of the dry-friction element. This is also testified by, for example, Popp et al. [1996], Andreaus and Casini [2001] and Cheng and Zu [2004]. Consequently, for the BKV element between particles $\bf n$ and $\bf n+1$, the transition from slip to stick occurs when the elongation rate of the Bingham element becomes equal to zero or changes sign. At this moment, the sign of the elongation rate of the Bingham element, denoted as $\dot{e}_B^{\bf n,n+1}$, no longer matches the sign of the force that was applied to the Bingham element to initiate the current instance of slip, i.e. $F_{B.slip}^{\bf n,n+1}$. As the Bingham element may be activated in both tension and compression, the slip-to-stick transition of the BKV element

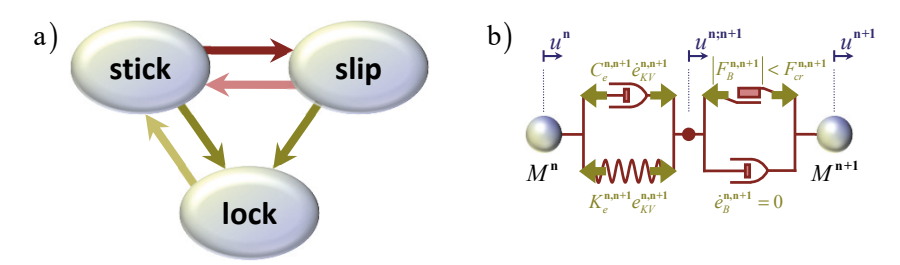


Figure 2.6: a) Possible transitions between motion states in a BKV element; b) Forces in the Bingham-Kelvin-Voigt element during stick.

between particles **n** and **n+1** occurs when:

$$\operatorname{sgn} \dot{e}_{B}^{\mathbf{n},\mathbf{n}+1} \neq \operatorname{sgn} F_{B:slip}^{\mathbf{n},\mathbf{n}+1} \tag{2.18}$$

One might now state that, even though equation (2.18) holds, the current force applied to the Bingham element, previously denoted as $F_B^{n,n+1}$, may still be larger than the critical friction force, for example due to an externally applied load, and that equation (2.16) should be checked before stating that the slip-to-stick transition has definitively occurred. This check is not required however, as it can be straightforwardly shown that if equation (2.18) holds, the force on the Bingham element must be smaller than the critical friction force.

To prove this, let us consider the forces inside the Bingham element during slip. The force equilibrium at either particle $\bf n$ or at the node intermediate particles $\bf n$ and $\bf n+1$ dictates that:

$$F_B^{\mathbf{n},\mathbf{n}+1} = C_f^{\mathbf{n},\mathbf{n}+1} \dot{e}_B^{\mathbf{n},\mathbf{n}+1} + F_{cr}^{\mathbf{n},\mathbf{n}+1} \operatorname{sgn} F_{B:sliv}^{\mathbf{n},\mathbf{n}+1}$$
(2.19)

Now, let us arbitrarily assume that during this instance of slip $\operatorname{sgn} F_{B:slip}^{\mathbf{n},\mathbf{n}+1} > 0$, so that the critical friction force in equation (2.19) has a positive sign. As long as this instance of slip lasts, it must be that $\operatorname{sgn} \dot{e}_B^{\mathbf{n},\mathbf{n}+1} > 0$, so that the force in the dashpot is positive as well, i.e. $C_f^{\mathbf{n},\mathbf{n}+1} = \mathbf{n} =$

Transition into lock

Whether lock occurs in a rheological element is not related to its configuration, and as a consequence, the transition into lock is not related to the prior motion state of that element. Therefore, the stick-to-lock and slip-to-lock transitions are induced in the same manner.

As the lock-state in a rheological element physically represents an inelastic collision between the two involved particles, lock occurs when the distance between the two particles becomes smaller than a certain threshold. Let us denote $D^{\mathbf{n},\mathbf{n}+1}$ as the distance between particles \mathbf{n} and $\mathbf{n}+\mathbf{1}$, and $D_{\min}^{\mathbf{n},\mathbf{n}+1}$ as the threshold distance, i.e. the minimum distance allowed between particles \mathbf{n} and $\mathbf{n}+\mathbf{1}$. The transition of the element between particles \mathbf{n} and $\mathbf{n}+\mathbf{1}$ into lock thus occurs when:

$$D^{n,n+1} \le D_{\min}^{n,n+1} \tag{2.20}$$

By assuming that at least $D_{\min}^{n,n+1} > 0$, we impose that each particle in a one-dimensional lattice remains between its adjacent particles at all times.

Transition out of lock

Consider a BKV element between two adjacent particles that is in a lock-state. Since the lock-state describes the collision of two particles, a BKV element will remain in lock as long as the involved particles are pushed against each other and the BKV element is in compression. The element between these particles can only undergo a transition out of lock when the two particles are pulled away from each other and thereby results from a reversal of the forces working on the BKV element. Due to the inertia of the two colliding particles, the critical friction force of the dry friction element can never be overcome instantaneously after the reversal of forces. Consequently, when a BKV element undergoes a transition out of lock, it will always undergo a transition into stick, so that the lock-to-slip transition does not occur. Here note that, to capture the moment in time at which the lock-to-stick transition occurs in a numerical simulation, the time step should be carefully chosen.

To determine when the lock-to-stick transition occurs, let us consider a BKV element between two adjacent particles n and n+1 that is in lock. Due to the applied compression there is a force inside the BKV element that attempts to push the particles n and n+1 apart from each other, let us denote this as the internal force $F_{int}^{n,n+1}$. Additionally, let us denote the total force applied on the BKV element between particles \mathbf{n} and $\mathbf{n+1}$ by adjacent elements as the external force $F_{ext}^{n,n+1}$. Principally, during lock, the relative motion between the particles n and n+1 is impeded, so that these particles are supposed to move in unison and the elongation of the BKV element is constant. Nevertheless, since we model the lock-state by a spring with a large but not infinite stiffness K_{lock} , there will always be some relative motion between the particles n and n+1, even though it will be very small. Therefore, if the external force working on a BKV element in lock-state is larger than its internal forces, i.e. $F_{ext}^{n,n+1} > F_{int}^{n,n+1}$, the element will become slightly shorter, while if the internal forces of the locked BKV element overcome the external force, i.e. $F_{int}^{n,n+1} > F_{ext}^{n,n+1}$, there will be a very small but positive elongation. We may then state that, as soon as the internal force overcomes the external force, i.e. $F_{int}^{n,n+1} > F_{ext}^{n,n+1}$, and all forces working internally and externally on this BKV element together no longer compress this element, lock-to-stick transition occurs. As we model the lock-state by adding a spring parallel to the original BKV element, the point at which the lock-to-stick transition for an element between particles **n** and **n+1** occurs when that element obtains a positive elongation rate:

$$\dot{e}^{\mathbf{n},\mathbf{n}+1} \ge 0 \tag{2.21}$$

Alternatively, we can describe the lock-to-stick-transition through the total resulting axial force $F_{lock}^{\mathbf{n},\mathbf{n}+1}$ that causes the BKV element to remain in lock, which is given by the difference between the external force $F_{ext}^{\mathbf{n},\mathbf{n}+1}$ and the internal force $F_{int}^{\mathbf{n},\mathbf{n}+1}$. If, instead of using a large stiffness spring, we would model the lock-state by using rigid bars, the only way to determine the occurrence of the lock-to-stick transition is by monitoring the total axial force $F_{lock}^{\mathbf{n},\mathbf{n}+1}$.

The case where we model the lock-state in the one-dimensional BKV lattice using a rigid bar is discussed in Appendix C.2.

2.4 Two-dimensional lattices

In the previous section, we have obtained the governing equations for the nonlinear onedimensional Bingham-Kelvin-Voigt (BKV) lattice and showed how the governing equations for the one-dimensional Kelvin-Voigt and Hooke lattices can be derived from these. In the following, we will discuss the corresponding two-dimensional lattices.

Figure 2.7a depicts a medium that is composed of equal-sized, circular particles. These particles are set in a hexagonal configuration, so that any particle is surrounded by six adjacent particles and the distance between the centre of gravity of each two adjacent particles is exactly equal. The interaction between adjacent particles may be described by any of the rheological elements that were previously depicted in Figure 2.2. The hexagonal configuration of particles and rheological elements is commonly known as the triangular or hexagonal lattice [Metrikine and Askes, 2006; Suiker et al., 2001a]. As the rheological elements featured in Figure 2.7b are springs, or Hooke elements, this particular lattice is denoted as the hexagonal Hooke lattice.

A particle together with the rheological elements that describe the interactions with any adjacent particles, is denoted as a cell. As depicted in Figure 2.7, three main cell configurations can be distinguished: inner cells, boundary cells and surface cells. Inner cells are cells situated in the interior of the lattice and always consist of a particle and six rheological elements that describe the interaction of that particle with its adjacent particles. Boundary cells are the cells of particles located at the boundary of the lattice, which may coincide with the interface between the near-field lattice and the surrounding far-field domain. Lastly, surface cells are all cells situated at the surface of the lattice. Depending on their location, boundary and surface cells may feature two, three or four rheological elements to describe the interaction between the involved particles.

In the following, we will derive the equations of motion for the hexagonal Bingham-Kelvin-Voigt (BKV) lattice, i.e. a hexagonal lattice consisting of Bingham-Kelvin-Voigt elements. Note here that the equations of motion for each particle depend on the cell configuration of that particle. In accordance with the one-dimensional lattices, the governing equations for the hexagonal Hooke, Kelvin-Voigt and Prandtl lattices can be derived from the governing equations for the hexagonal BKV lattice and are therefore not separately discussed.

2.4.1 The hexagonal Bingham-Kelvin-Voigt (BKV) lattice

In principle, the chosen geometry for the domain of the hexagonal BKV lattice is arbitrary, as long as the hexagonal configuration of the lattice is maintained. As stated in Section 1.6 however, our aim is to efficiently account for the nonlinear response of a medium in the near field, while correctly accounting for the linear far field response. To accomplish this, the interface between the near- and far-field domains must always be chosen in the region of the medium that behaves linearly throughout its response. The geometry of the hexagonal BKV

lattice is chosen in accordance with Figure 2.8, such that its horizontal surface coincides with the x-axis, while the distance between the particle at the origin, being the application point of the load, and the particles at the lattice boundary Γ is equal in all directions in the sense that the path from the origin to any particle at the boundary can always be bridged by the same number of BKV elements. As a consequence, the hexagonal BKV lattice, i.e. the near-field domain, always has the shape of the lower half of a hexagon.

As previously stated, in any hexagonal lattice, several cell configurations exist. The different cell configurations that appear in the hexagonal BKV lattice are depicted in Figure 2.9. The most common cell configuration is the inner cell, depicted in Figure 2.9a, consisting of a particle with discrete, or nodal, coordinates \mathbf{m} , \mathbf{n} and six BKV elements that describe the interaction of the particle \mathbf{m} , \mathbf{n} with its adjacent particles. Here, the nodal coordinates \mathbf{m} and \mathbf{n} are integers that respectively correspond to the x- and z-coordinate of a particle \mathbf{m} , \mathbf{n} as $x = \mathbf{m}\ell/2$ and $z = \mathbf{n}\ell\sqrt{3}/2$, where ℓ denotes the unit length of the lattice.

To consider an inner cell as a unit cell, and thus to allow us to describe the equations of motion for a particle **m,n** in the interior of the hexagonal BKV lattice in such a manner that its equations of motion are generally applicable to all inner cells in the hexagonal BKV lattice, the orientation of the BKV elements has been chosen as depicted in Figure 2.9a. To distinguish between different BKV elements appearing in the cell of a particle **m,n**, the numerator *j* is used. The orientation of the BKV elements has been consistently applied to all cells in the hexagonal BKV lattice in accordance with the inner cell of Figure 2.9a, as can be seen in Figure 2.8. Note here, that for hexagonal lattices consisting of rheological elements

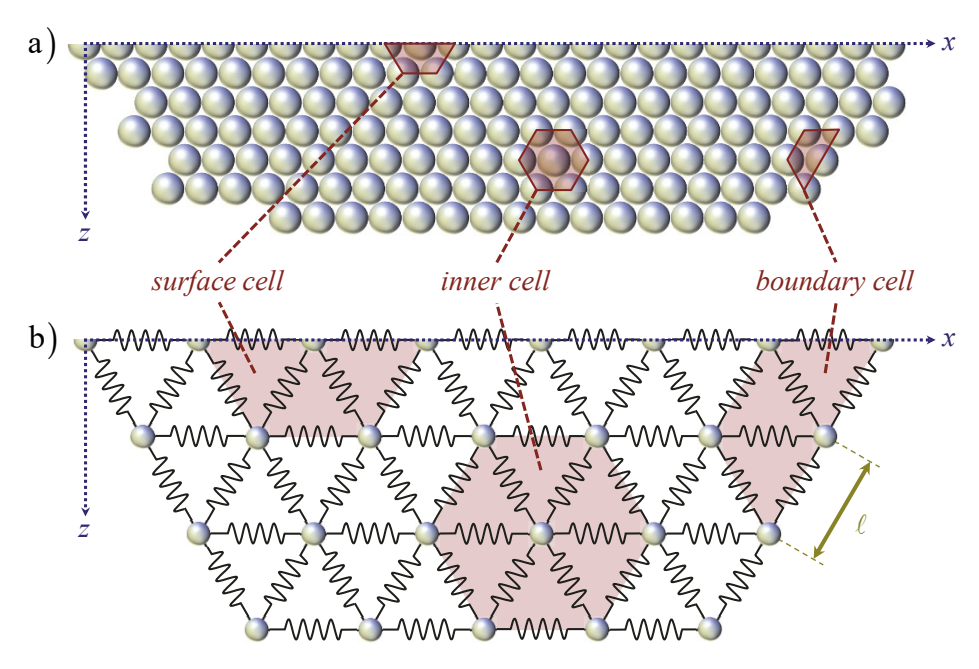


Figure 2.7: a) A material divided in equal-sized particles in a hexagonal configuration; b) A hexagonal Hooke lattice with springs between adjacent particles.

that describe a single relation between adjacent particles according to Figure 2.1a, the orientation of all elements is the same as shown by Figure 2.7b for the hexagonal Hooke lattice.

The configuration of all other cells in the hexagonal BKV lattice, and thus their equations of motion, can be derived from that of the inner cell depending on the number of particles adjacent to particle \mathbf{m} , \mathbf{n} , and thus by the number of BKV elements in the cell. Figure 2.9d, Figure 2.9e and Figure 2.9f show the three types of boundary cells that appear on the left side of the lattice boundary Γ . Note here that the corresponding boundary cells at the right side of the lattice boundary are not exact mirror images of the cells on the left side of the lattice due to the orientation of the BKV elements in the lattice. The boundary cell at the bottom of the hexagonal lattice depicted in Figure 2.9b however, is the exact mirror image of the surface cell depicted in Figure 2.9c.

In fact, as the surface cell and the bottom boundary cells both represent half the space of an inner cell, and the orientation of their elements respectively coincide with the lower and upper halves of an inner cell, these two cells combined exactly comprise an inner cell. As a consequence, the properties of the surface and bottom boundary cells must be such that, attached to one another, they match the properties of an inner cell. Therefore, the properties of the surface and the bottom boundary cells, respectively depicted in Figure 2.9b and Figure 2.9c, can straightforwardly be derived by adding their equations of motion and comparing the result to the equations of motion for the inner cell depicted in Figure 2.9a. For the lattice to be homogeneous, we find that the particles at the surface and at the bottom boundary of the hexagonal lattice have the same mass and that its mass is equal to half the mass of a particle in the interior of the lattice. Next to the difference in mass of the particles that exist at respectively the boundary and the interior of the lattice, also the properties of the BKV elements are different depending on whether they exist at the surface, the boundary or in the interior of the lattice. From the equations of motion for the inner, surface and bottom boundary cells, it follows that the stiffness and damping of the surface elements and the BKV elements at the bottom boundary, must respectively be equal to half the stiffness and half the damping of a BKV element in the interior of the lattice.

Following the same analogy, the corner and surface boundary cells given in respectively Figure 2.9e and Figure 2.9f together comprise the boundary cell in Figure 2.9d. The masses of these and other particles along the sloped boundary of the hexagonal lattice follow from the space they occupy and therefore depend on the shape of the lattice boundary. As discussed later, for example in Section 3.5.1, the shape of this part of the lattice boundary is not necessarily defined by the configuration of the near-field lattice alone and may also depend on the properties of the far-field medium. In relation to this, the masses of the different boundary particles and other interface properties are discussed in Sections 3.6.1 and 4.7.1 for far-field domains represented by a continuous layer and a half-plane of particles respectively.

To find the system of equations of motion for the hexagonal BKV lattice, we here apply Lagrange's formalism in accordance with the approach for the one-dimensional lattice [Goldstein et al., 2002; Lanczos, 1966; Landau and Lifshitz, 1976]. Before deriving the equations of motion however, we will first discuss the kinematics of the BKV elements in the hexagonal lattice.

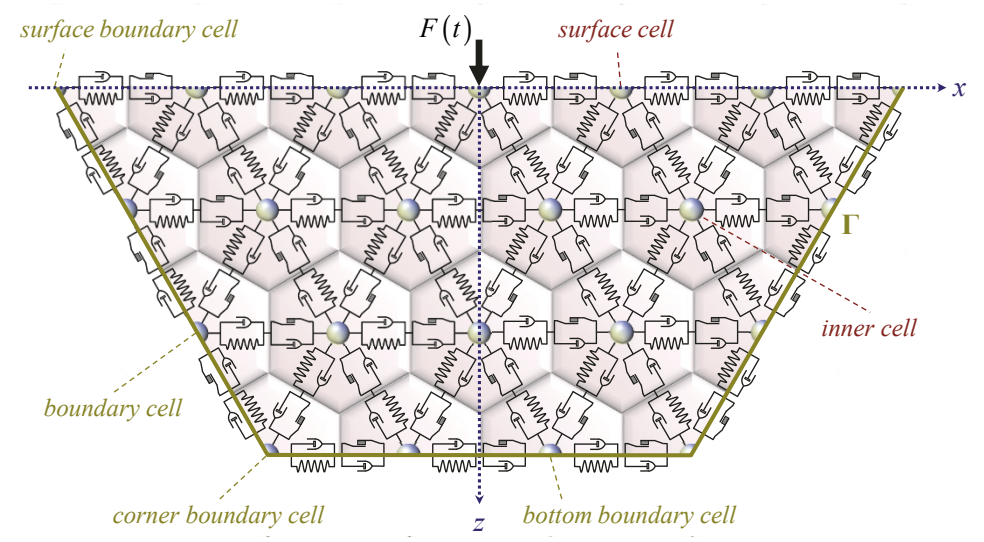


Figure 2.8: The hexagonal BKV lattice.

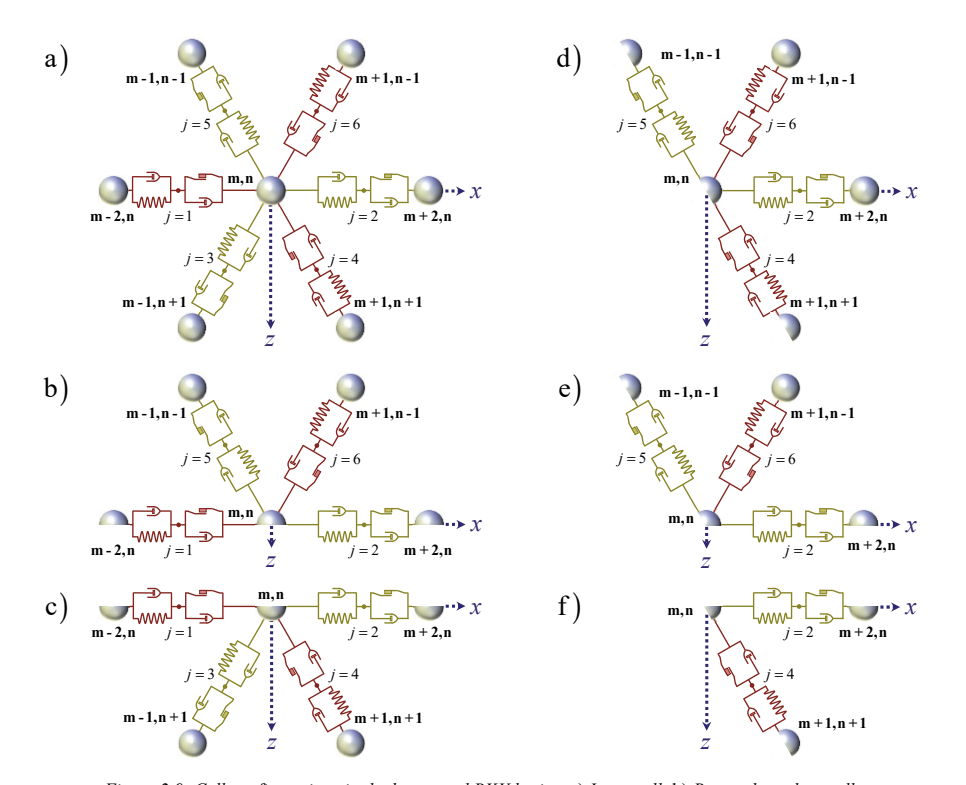


Figure 2.9: Cell configurations in the hexagonal BKV lattice: a) Inner cell; b) Bottom boundary cell; c) Surface cell; d) Left boundary cell; e) Left corner boundary cell; f) Left surface boundary cell.

2.4.2 Kinematics of BKV elements in a two-dimensional lattice

Due to the dual nature of the BKV element, the interaction between a particle \mathbf{m}_i , \mathbf{n}_i and an adjacent particle \mathbf{m}_i , \mathbf{n}_i is not only described by the motion of these particles, but also by the motion of the massless slip-node intermediate particles \mathbf{m}_i , \mathbf{n}_i and \mathbf{m}_i , \mathbf{n}_i . Here, note that the slip-node in a BKV element may only move along the straight line between the particles \mathbf{m}_i , and \mathbf{m}_i , \mathbf{n}_i . Consequently, while each particle in the lattice adds two degrees of freedom to the system of equations of motion, each slip-node only provides a single degree of freedom to the system. In Figure 2.10a, all degrees of freedom that exist in an inner cell of the hexagonal BKV lattice are depicted by black arrows.

Figure 2.10b depicts the elongation and rotation of a BKV element between particles \mathbf{m}_i , and \mathbf{m}_i , \mathbf{n}_i , due to the displacement of particle \mathbf{m}_i , \mathbf{n}_i . Describing the elongations of the rheological elements as they move and rotate in two-dimensional space exactly would yield the corresponding system of equations of motion as a set of nonlinear differential equations. To obtain a set of linear differential equations, we linearize the expressions for the elongations of the rheological elements. This linearization is applied differently depending on whether the elongations are small or large. The difference is that the linearization for small elongations accounts for the elongations and particle displacements relative to their initial state, while the linearization for large elongations accounts for the elongations and particle displacements relative to their position before the current time step. The expressions for the elongations that result from these assumptions are derived in Appendices A.1 and A.2 respectively. Due to the nonlinear nature of BKV elements, elongations in these elements may be expected to become large. For the two-dimensional BKV lattice, we therefore apply the linearization for large elongations. According to Appendix A.2, the elongation of a rheological element between particles \mathbf{m} , \mathbf{n} and \mathbf{m}_i , \mathbf{n} may thus be approximated as:

$$e_j^{\mathbf{m},\mathbf{n}} = \left(u_x^{\mathbf{m}_j,\mathbf{n}_j} - u_x^{\mathbf{m},\mathbf{n}}\right)\cos\alpha_j^{\mathbf{m},\mathbf{n}} + \left(u_z^{\mathbf{m}_j,\mathbf{n}_j} - u_z^{\mathbf{m},\mathbf{n}}\right)\sin\alpha_j^{\mathbf{m},\mathbf{n}} + \varepsilon_j^{\mathbf{m},\mathbf{n}}$$
(2.22)

Here, $u_x^{\mathbf{m},\mathbf{n}}$, $u_z^{\mathbf{m},\mathbf{n}}$, $u_x^{\mathbf{m}_j,\mathbf{n}_j}$ and $u_z^{\mathbf{m}_j,\mathbf{n}_j}$ denote the displacements of particles \mathbf{m},\mathbf{n} and $\mathbf{m}_j,\mathbf{n}_j$ in

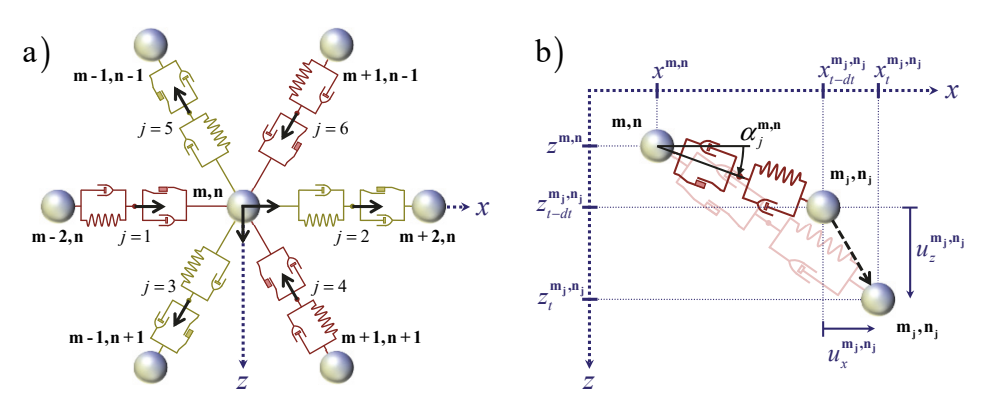


Figure 2.10: a) The degrees of freedom of an inner cell in the hexagonal BKV lattice; b) The relative displacement of particle $m_i n_j$ with respect to particle $m_i n_j$.

respectively x- and z-direction during the current time step dt. Furthermore, $\varepsilon_j^{\mathbf{m},\mathbf{n}}$ describes the elongation of the considered rheological element between particles \mathbf{m},\mathbf{n} and $\mathbf{m}_j,\mathbf{n}_j$ before the current time step, so at time t-dt, which is thus constant during the current time step. Finally, $\alpha_j^{\mathbf{m},\mathbf{n}}$ is the angle of the rheological element between particles \mathbf{m},\mathbf{n} and $\mathbf{m}_j,\mathbf{n}_j$. The kinematics of this angle are discussed at the end of this section.

The elongations of the Kelvin-Voigt and Bingham elements, that together comprise the BKV element, are obtained by separately applying the linearization for large elongations according to Appendix A.2 for each of these elements. The resulting expressions for the elongations of the two elements depend on the orientation of the considered BKV element. For the BKV elements that have their orientation such that the Kelvin-Voigt element is closest to the particle \mathbf{m} , \mathbf{n} , i.e. the elements j = 2,3,5 in Figure 2.10a, the elongations of the Kelvin-Voigt and Bingham elements are respectively found as:

$$e_{KV;j}^{\mathbf{m},\mathbf{n}} = u^{\mathbf{m},\mathbf{n};\mathbf{m}_{j},\mathbf{n}_{j}} - u_{x}^{\mathbf{m},\mathbf{n}} \cos \alpha_{j}^{\mathbf{m},\mathbf{n}} - u_{z}^{\mathbf{m},\mathbf{n}} \sin \alpha_{j}^{\mathbf{m},\mathbf{n}} + \varepsilon_{KV;j}^{\mathbf{m},\mathbf{n}}$$

$$(2.23)$$

$$e_{B;j}^{\mathbf{m},\mathbf{n}} = u_x^{\mathbf{m}_j,\mathbf{n}_j} \cos \alpha_j^{\mathbf{m},\mathbf{n}} + u_z^{\mathbf{m}_j,\mathbf{n}_j} \sin \alpha_j^{\mathbf{m},\mathbf{n}} - u_z^{\mathbf{m},\mathbf{n};\mathbf{m}_j,\mathbf{n}_j} + \varepsilon_{B;j}^{\mathbf{m},\mathbf{n}}$$
(2.24)

Here, $u^{\mathbf{m},\mathbf{n};\mathbf{m}_{j},\mathbf{n}_{j}}$ is the displacement of the slip-node intermediate particles \mathbf{m},\mathbf{n} and $\mathbf{m}_{j},\mathbf{n}_{j}$ at the current time step dt in the direction of the depicted degrees of freedom in Figure 2.10a.

For the other BKV elements, being those that have their orientation such that the Bingham element is closest to the particle \mathbf{m} , \mathbf{n} , i.e. the elements j = 1, 4, 6 in Figure 2.10a, the degree of freedom for the slip-node intermediate particles \mathbf{m} , \mathbf{n} and $\mathbf{m}_{\mathbf{j}}$, $\mathbf{n}_{\mathbf{j}}$ points into the opposite direction. The respective elongations of the Kelvin-Voigt and Bingham elements thus become:

$$e_{KV;j}^{\mathbf{m},\mathbf{n}} = u_x^{\mathbf{m}_j,\mathbf{n}_j} \cos \alpha_j^{\mathbf{m},\mathbf{n}} + u_z^{\mathbf{m}_j,\mathbf{n}_j} \sin \alpha_j^{\mathbf{m},\mathbf{n}} + u_z^{\mathbf{m},\mathbf{n};\mathbf{m}_j,\mathbf{n}_j} + \varepsilon_{KV;j}^{\mathbf{m},\mathbf{n}}$$
(2.25)

$$e_{B,i}^{\mathbf{m},\mathbf{n}} = -u^{\mathbf{m},\mathbf{n};\mathbf{m}_{i},\mathbf{n}_{i}} - u_{x}^{\mathbf{m},\mathbf{n}} \cos \alpha_{i}^{\mathbf{m},\mathbf{n}} - u_{z}^{\mathbf{m},\mathbf{n}} \sin \alpha_{i}^{\mathbf{m},\mathbf{n}} + \varepsilon_{B,i}^{\mathbf{m},\mathbf{n}}$$
(2.26)

In equations (2.23) to (2.26), $\varepsilon_{KV;j}^{\mathbf{m,n}}$ and $\varepsilon_{B;j}^{\mathbf{m,n}}$ respectively denote the elongations of the Kelvin-Voigt and Bingham element between particles $\mathbf{m,n}$ and $\mathbf{m_{j},n_{j}}$ before the current time step, so at time t-dt, that are constants during the current time step. Note that by adding the elongations of the Kelvin-Voigt and Bingham elements, i.e. by adding either equations (2.23) and (2.24) or equations (2.25) and (2.26), we always obtain the elongation of the BKV element given by equation (2.22).

Kinematics of the rheological element angle

As the lattice deforms, the coordinates of all particles in the lattice change over time and the angles of all rheological elements in the lattice do so as well. For small deformations, the influence of this so-called geometrical nonlinearity is small and may be neglected. In the hexagonal BKV lattice however, the displacements and elongations can become significant and the geometrical nonlinearities must be accounted for. To do this, we could consider the

element angles as degrees of freedom of the lattice. While this would not only significantly increase the total number of degrees of freedom in the lattice, this also causes the set of differential equations to become nonlinear due to the involved trigonometric terms. To account for large deformations and to make sure that the equations of motion remain as a set of linear differential equations, we instead assume that the angles of all rheological elements are constant during each time step. Additionally, we update the angles of the rheological elements after each time step based on the coordinates of the lattice particles that follow from solving the set of linear differential equations at the previous time step.

Denoting $\Delta x_j = x^{\mathbf{m_j},\mathbf{n_j}} - x^{\mathbf{m,n}}$ and $\Delta z_j = z^{\mathbf{m_j},\mathbf{n_j}} - z^{\mathbf{m,n}}$ as shown in Figure 2.11a, the angle $\alpha_j^{\mathbf{m,n}}$ of a rheological element j between particles $\mathbf{m,n}$ and $\mathbf{m_j,n_j}$ at any time step straightforwardly follows from the geometry of the lattice as:

$$\alpha_j^{\mathbf{m},\mathbf{n}} = \arccos\left(\frac{\Delta x_j}{\sqrt{\Delta x_j^2 + \Delta z_j^2}}\right) \operatorname{sgn}(\Delta z_j)$$
 (2.27)

Here, sgn is an abbreviation of signum, so that $\operatorname{sgn}(\Delta z_j)$ gives the sign of Δz_j . According to equation (2.27), the angle $\alpha_j^{\mathbf{m},\mathbf{n}}$ of an element between particles \mathbf{m},\mathbf{n} and $\mathbf{m}_j,\mathbf{n}_j$ can always be expressed in terms of the coordinates, and thus the displacements, of particles \mathbf{m},\mathbf{n} and $\mathbf{m}_j,\mathbf{n}_j$.

Since the displacements of particles \mathbf{m} , \mathbf{n} and $\mathbf{m}_{\mathbf{j}}$, $\mathbf{n}_{\mathbf{j}}$ are degrees of freedom of the system of equations of motion, their positions in the lattice are correctly determined at every time step. The displacement of the slip-node intermediate particles \mathbf{m} , \mathbf{n} and $\mathbf{m}_{\mathbf{j}}$, $\mathbf{n}_{\mathbf{j}}$ however is determined based on the angle $\alpha_{j}^{\mathbf{m},\mathbf{n}}$ and thereby follows from the positions of the particles \mathbf{m} , \mathbf{n} and $\mathbf{m}_{\mathbf{j}}$, $\mathbf{n}_{\mathbf{j}}$ prior to the current time step. As a consequence, the slip-node intermediate particles \mathbf{m} , \mathbf{n} and $\mathbf{m}_{\mathbf{j}}$, $\mathbf{n}_{\mathbf{j}}$ does not remain exactly on the straight line between particles \mathbf{m} , \mathbf{n} and $\mathbf{m}_{\mathbf{j}}$, $\mathbf{n}_{\mathbf{j}}$ after the current time step dt. This is exaggeratedly depicted in Figure 2.11b. Here, the angle of the element between particles \mathbf{m} , \mathbf{n} and $\mathbf{m}_{\mathbf{j}}$, $\mathbf{n}_{\mathbf{j}}$ that is assumed to be constant during the current time step dt and that follows from the position of particles \mathbf{m} , \mathbf{n} and $\mathbf{m}_{\mathbf{j}}$, $\mathbf{n}_{\mathbf{j}}$ prior to the current time step is denoted as $\alpha_{\mathbf{j}}^{\mathbf{m},\mathbf{n}} = \alpha_{\mathbf{j};dt}^{\mathbf{m},\mathbf{n}}$, while the corresponding angle after the current time step is denoted as $\alpha_{\mathbf{j};dt}^{\mathbf{m},\mathbf{n}} = \alpha_{\mathbf{j};dt}^{\mathbf{m},\mathbf{n}}$, while the corresponding angle after the current time step is denoted as $\alpha_{\mathbf{j};dt}^{\mathbf{m},\mathbf{n}} = \alpha_{\mathbf{j};dt}^{\mathbf{m},\mathbf{n}}$.

The error in the position of the slip-nodes depends on the chosen time step dt, and thus, the time step dt must be chosen small enough to assure the accuracy of the model. Additionally, to make sure that this error does not accumulate, we correct the coordinates for the slip-node intermediate particles \mathbf{m} , \mathbf{n} and $\mathbf{m}_{\mathbf{j}}$, $\mathbf{n}_{\mathbf{j}}$ a posteriori, i.e. after every time step, using the global coordinates of the particles \mathbf{m} , \mathbf{n} and $\mathbf{m}_{\mathbf{j}}$, $\mathbf{n}_{\mathbf{j}}$ that result from the current time step. In Figure 2.11b, the erroneous lengths of the Bingham and Kelvin-Voigt elements that follow from solving the equations of motion with the assumed constant angle $\alpha_{j}^{\mathbf{m},\mathbf{n}}$, are respectively denoted as λ_{B} and λ_{KV} . Furthermore, l_{B} and l_{KV} denote the correct lengths of respectively the Bingham and Kelvin-Voigt element at the end of the current time step. When the considered BKV-element is in stick-state and the Bingham element is not activated, the Bingham element is rigid with a constant length. Hence, we then find the length l_{B} of the Bingham element

$$l_B = \lambda_B \tag{2.28}$$

When the BKV-element is in slip-state and the Bingham element is activated, we determine the length l_B of the Bingham element from the ratio between the erroneous length λ_B of the Bingham element and the total erroneous length of the BKV element, i.e. the sum of λ_{KV} and λ_B , as:

$$l_B = \frac{\lambda_B}{\lambda_{KV} + \lambda_B} D_j^{\mathbf{m,n}} \tag{2.29}$$

Here, $D_i^{m,n}$ is the distance between particles m,n and m_j,n_j at the end of time step dt. Using the previously introduced notation for the element angle after the current time step dt as $\alpha_{i:dt}^{m,n}$, the x- and z-coordinates of the slip-node intermediate particles \mathbf{m} , \mathbf{n} and \mathbf{m}_{i} , \mathbf{n}_{j} respectively become:

$$x^{\mathbf{m},\mathbf{n};\mathbf{m}_{j},\mathbf{n}_{j}} = x^{\mathbf{m},\mathbf{n}} + l_{B}\cos\alpha_{i:dt^{+}}^{\mathbf{m},\mathbf{n}}$$

$$(2.30)$$

$$x^{\mathbf{m},\mathbf{n};\mathbf{m}_{j},\mathbf{n}_{j}} = x^{\mathbf{m},\mathbf{n}} + l_{B} \cos \alpha_{j;dt^{+}}^{\mathbf{m},\mathbf{n}}$$

$$z^{\mathbf{m},\mathbf{n};\mathbf{m}_{j},\mathbf{n}_{j}} = z^{\mathbf{m},\mathbf{n}} + l_{B} \sin \alpha_{j;dt^{+}}^{\mathbf{m},\mathbf{n}}$$
(2.30)

The BKV elements in the hexagonal BKV lattice behave in accordance with the BKV elements in the one-dimensional BKV lattice. Consequently, each BKV element in the hexagonal BKV lattice is always in either stick-, slip- or lock-state. The characteristics of the BKV element for each of these motion states were previously discussed for the one-dimensional BKV lattice in respectively Sections 2.3.2 to 2.3.4. In the following, we will therefore only discuss those properties of the motion states that are particular for BKV elements in the hexagonal lattice. Although the motion state of each BKV element in a cell of the hexagonal

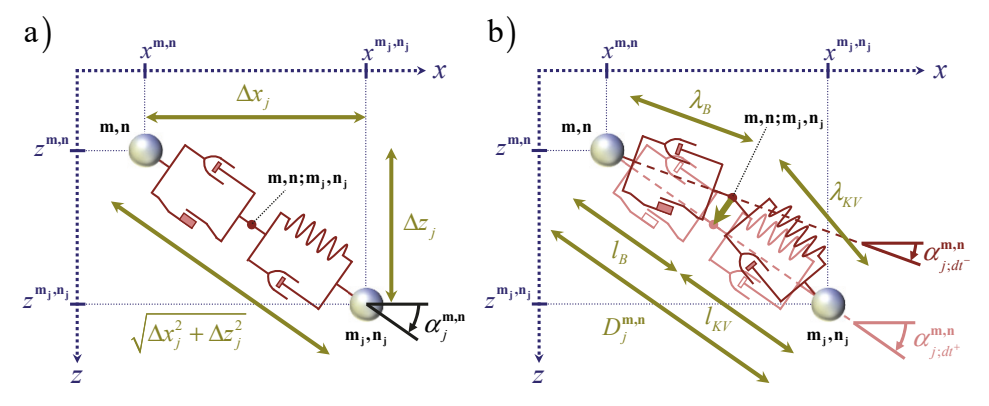


Figure 2.11: a) A Bingham-Kelvin-Voigt element in the two-dimensional lattice; b) The error and the actual position of the slip-node.

BKV lattice may be different, we will here state the equations of motion for an inner cell with all BKV elements in either of the three motion states to illustrate the approach.

2.4.3 'Stick' in the hexagonal BKV lattice

Let us consider the inner cell of the hexagonal BKV lattice depicted in Figure 2.12a. As all BKV elements are in stick-state, the Bingham elements are not activated and therefore depicted as rigid bars. Although the BKV elements in the depicted inner cell have different orientations, all elements behave in exactly the same way as long as all elements are in a stick-state. Note here that, although the elongations of the Bingham elements will not change during a stick-state, they are not necessarily equal to zero, for example if, preceding the current stick-state, slip has occurred in the BKV element. Thus, when all elements are in stick-state, the elongations of the Kelvin-Voigt and Bingham elements are for either orientation of the BKV elements respectively found as:

$$e_{KV;j}^{\mathbf{m},\mathbf{n}} = e_j^{\mathbf{m},\mathbf{n}} - \varepsilon_{B;j}^{\mathbf{m},\mathbf{n}} \tag{2.32}$$

$$e_{B;j}^{\mathbf{m},\mathbf{n}} = \varepsilon_{B;j}^{\mathbf{m},\mathbf{n}} \tag{2.33}$$

Applying Lagrange's formalism by considering the Kelvin-Voigt elements as springs for which the stiffness is described by the operator $\hat{K}^{\mathbf{m,n}}_{e:j}$, where $\hat{K}^{\mathbf{m,n}}_{e:j} = K^{\mathbf{m,n}}_{e:j} + C^{\mathbf{m,n}}_{e:j} \partial/\partial t$, and respectively employing the Euler-Lagrange differential equations for the horizontal and vertical displacements of particle $\mathbf{m,n}$, i.e. $u^{\mathbf{m,n}}_x$ and $u^{\mathbf{m,n}}_z$, the equations of motion for a particle $\mathbf{m,n}$ in an inner cell of the hexagonal BKV lattice with all BKV elements in stick, read:

$$M^{\mathbf{m},\mathbf{n}} \dot{u}_{x}^{\mathbf{m},\mathbf{n}} - \sum_{i=1}^{6} C_{e;j}^{\mathbf{m},\mathbf{n}} \dot{e}_{j}^{\mathbf{m},\mathbf{n}} \cos \alpha_{j}^{\mathbf{m},\mathbf{n}} - \sum_{i=1}^{6} K_{e;j}^{\mathbf{m},\mathbf{n}} \left(e_{j}^{\mathbf{m},\mathbf{n}} - \varepsilon_{B;j}^{\mathbf{m},\mathbf{n}} \right) \cos \alpha_{j}^{\mathbf{m},\mathbf{n}} = 0$$
(2.34)

$$M^{\mathbf{m},\mathbf{n}}\ddot{u}_{z}^{\mathbf{m},\mathbf{n}} - \sum_{j=1}^{6} C_{e,j}^{\mathbf{m},\mathbf{n}} \dot{e}_{j}^{\mathbf{m},\mathbf{n}} \sin \alpha_{j}^{\mathbf{m},\mathbf{n}} - \sum_{j=1}^{6} K_{e,j}^{\mathbf{m},\mathbf{n}} \left(e_{j}^{\mathbf{m},\mathbf{n}} - \varepsilon_{B,j}^{\mathbf{m},\mathbf{n}} \right) \sin \alpha_{j}^{\mathbf{m},\mathbf{n}} = 0$$
 (2.35)

Here, $K_{e;j}^{\mathbf{m},\mathbf{n}}$ and $C_{e;j}^{\mathbf{m},\mathbf{n}}$ are respectively the stiffness and damping coefficients of the Kelvin-Voigt element between a particle \mathbf{m},\mathbf{n} and an adjacent particle $\mathbf{m}_{\mathbf{j}},\mathbf{n}_{\mathbf{j}}$.

While the position of particle \mathbf{m} , \mathbf{n} in the inner cell of the hexagonal BKV lattice, with all BKV elements in stick, follows from the equations of motion (2.34) and (2.35), the positions of the slip-nodes in an inner cell are derived from the position of the particle to which they are rigidly connected. Thus, the coordinates of the slip-nodes in elements j = 1, 4, 6 are found using equations (2.30) and (2.31), while the coordinates of the slip-nodes in elements j = 2, 3, 5 follow from the equivalent equations for the respective particles $\mathbf{m}_j, \mathbf{n}_j$.

The complete system of equations of motion for the hexagonal BKV lattice with all BKV elements in stick, follows from applying equations (2.34) and (2.35) to all particles in the lattice. Disregarding external forces, equations (2.34) and (2.35) can be applied to all existing cell geometries in the hexagonal BKV lattice, taking into account that the mass $M^{m,n}$, the stiffness coefficient $K_{e:j}^{m,n}$ and the damping coefficient $C_{e:j}^{m,n}$, as well as the domain of the

numerator *j*, may vary per cell configuration. Do note here that, as the boundary must exist at such a distance from the load source that its response is linear, all boundary elements must behave linearly at all times and thus always remain in stick.

The systems of equations of motion for the hexagonal Kelvin-Voigt and hexagonal Hooke lattices may be obtained from equations (2.34) and (2.35) by substituting $\mathcal{E}_{B;j}^{\mathbf{m},\mathbf{n}} = 0$ and $C_{e;j}^{\mathbf{m},\mathbf{n}} = 0$ for all elements appearing in the considered cell. The system of equations of motion for the Prandtl lattice with all Prandtl elements in stick can be obtained from equations (2.34) and (2.35) by substituting $\mathcal{E}_{B;j}^{\mathbf{m},\mathbf{n}} = \mathcal{E}_{f;j}^{\mathbf{m},\mathbf{n}}$ and $C_{e;j}^{\mathbf{m},\mathbf{n}} = 0$ for all elements. Here, $\mathcal{E}_{f;j}^{\mathbf{m},\mathbf{n}}$ denotes the elongation of the dry friction element in the Prandtl element that is constant during stick.

2.4.4 'Slip' in the hexagonal BKV lattice

Figure 2.12b depicts an inner cell of the hexagonal BKV lattice with all its elements in slip-state, i.e. with all Bingham elements activated. To obtain the corresponding equations of motion, we again apply Lagrange's formalism by considering the adjacent Kelvin-Voigt and Bingham elements as equivalent springs for which the stiffness is described by the operators $\hat{K}_{e;j}^{\mathbf{m},\mathbf{n}}$ and $\hat{K}_{f;j}^{\mathbf{m},\mathbf{n}}$, where $\hat{K}_{e;j}^{\mathbf{m},\mathbf{n}} = K_{e;j}^{\mathbf{m},\mathbf{n}} + C_{e;j}^{\mathbf{m},\mathbf{n}}$ and $\hat{K}_{f;j}^{\mathbf{m},\mathbf{n}} = C_{f;j}^{\mathbf{m},\mathbf{n}}$. Employing the Euler-Lagrange differential equations for the particle displacements in x- and z-direction respectively, the equations of motion for particle \mathbf{m},\mathbf{n} in an inner cell of the hexagonal BKV lattice with all BKV elements in slip, are found as:

$$M^{\mathbf{m},\mathbf{n}}\ddot{u}_{x}^{\mathbf{m},\mathbf{n}} - \sum_{j \in j_{KT}^{\mathbf{m},\mathbf{n}}} \left(C_{e;j}^{\mathbf{m},\mathbf{n}} \dot{e}_{KV;j}^{\mathbf{m},\mathbf{n}} + K_{e;j}^{\mathbf{m},\mathbf{n}} e_{KV;j}^{\mathbf{m},\mathbf{n}} \right) \cos \alpha_{j}^{\mathbf{m},\mathbf{n}} - \sum_{j \in j_{B}^{\mathbf{m},\mathbf{n}}} \left(C_{f;j}^{\mathbf{m},\mathbf{n}} \dot{e}_{B;j}^{\mathbf{m},\mathbf{n}} + F_{cr;j}^{\mathbf{m},\mathbf{n}} \operatorname{sgn} F_{B:slip;j}^{\mathbf{m},\mathbf{n}} \right) \cos \alpha_{j}^{\mathbf{m},\mathbf{n}} = 0 \quad (2.36)$$

$$M^{\mathbf{m},\mathbf{n}}\ddot{u}_{z}^{\mathbf{m},\mathbf{n}} - \sum_{j \in J_{KV}^{\mathbf{m},\mathbf{n}}} \left(C_{e;j}^{\mathbf{m},\mathbf{n}} \dot{e}_{KV;j}^{\mathbf{m},\mathbf{n}} + K_{e;j}^{\mathbf{m},\mathbf{n}} e_{KV;j}^{\mathbf{m},\mathbf{n}} \right) \sin \alpha_{j}^{\mathbf{m},\mathbf{n}} - \sum_{j \in J_{B}^{\mathbf{m},\mathbf{n}}} \left(C_{f;j}^{\mathbf{m},\mathbf{n}} \dot{e}_{B;j}^{\mathbf{m},\mathbf{n}} + F_{cr;j}^{\mathbf{m},\mathbf{n}} \operatorname{sgn} F_{B:slip;j}^{\mathbf{m},\mathbf{n}} \right) \sin \alpha_{j}^{\mathbf{m},\mathbf{n}} = 0 \qquad (2.37)$$

Here, $j_{KV}^{\mathbf{m},\mathbf{n}}$ denotes the set of BKV elements in the cell that have the Kelvin-Voigt element connected to the particle \mathbf{m},\mathbf{n} , while $j_B^{\mathbf{m},\mathbf{n}}$ is the set of BKV elements for which the Bingham element is connected to the particle \mathbf{m},\mathbf{n} . Furthermore, $K_{e;j}^{\mathbf{m},\mathbf{n}}$ and $C_{e;j}^{\mathbf{m},\mathbf{n}}$ are respectively the stiffness and damping in the Kelvin-Voigt elements, and $C_{f;j}^{\mathbf{m},\mathbf{n}}$ is the damping in the Bingham

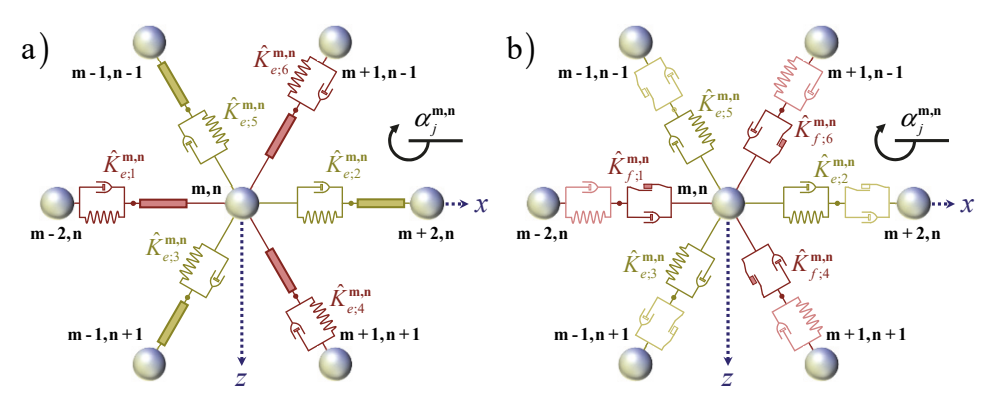


Figure 2.12: An inner cell of the hexagonal BKV lattice, with: a) all BKV elements in stick; b) all BKV elements in slip.

elements. Furthermore, $\operatorname{sgn} F_{B:\operatorname{slip};j}^{\mathbf{m},\mathbf{n}}$, being the sign of the force on the Bingham element that initiated the considered instance of slip, determines the direction of the corresponding critical friction forces.

The equations of motion for the slip-nodes in an inner cell are found by substituting their respective Lagrangians into the corresponding Euler-Lagrange differential equations. For all BKV elements in an inner cell, i.e. for j = 1...6, the equation of motion for the slip-node reads:

$$C_{e;j}^{\mathbf{m,n}} \dot{e}_{KV;j}^{\mathbf{m,n}} + K_{e;j}^{\mathbf{m,n}} e_{KV;j}^{\mathbf{m,n}} - C_{f;j}^{\mathbf{m,n}} \dot{e}_{B;j}^{\mathbf{m,n}} - F_{cr;j}^{\mathbf{m,n}} \operatorname{sgn} F_{B:slip;j}^{\mathbf{m,n}} = 0$$
(2.38)

By adapting the numerator j to the considered cell geometry, and disregarding external forces, equations of motion (2.36) to (2.38) apply to all cell geometries that exist in the hexagonal BKV lattice.

The system of equations of motion for the Prandtl lattice with all Prandtl elements in slip follows from equations (2.36) to (2.38) by substituting $C_{e;j}^{\mathbf{m},\mathbf{n}} = C_{f;j}^{\mathbf{m},\mathbf{n}} = 0$ and $F_{B:slip;j}^{\mathbf{m},\mathbf{n}} = F_{f:slip;j}^{\mathbf{m},\mathbf{n}}$ for all elements. Here, $F_{f:slip;j}^{\mathbf{m},\mathbf{n}}$ denotes the force applied to the involved dry friction element to initiate the current instance of slip. As the slip-state does not occur in the hexagonal Hooke and Kelvin-Voigt lattices, corresponding equations cannot be derived for these lattices.

2.4.5 'Lock' in the hexagonal BKV lattice

To incorporate lock into the system of equations of motion for the hexagonal lattice, the same approach as for the one-dimensional lattice is used. This means that the lock-state is incorporated into the hexagonal lattice by adding a spring parallel to a BKV element with a spring stiffness that is significantly larger than the stiffness of the spring present in the BKV element. The system of equations of motion for an inner particle \mathbf{m}, \mathbf{n} with a single BKV element in its cell in lock and its other BKV elements in stick, can be straightforwardly obtained from equations (2.34) and (2.35), being the equations of motion for an inner particle with all BKV elements in its cell in stick, by including the additional parallel spring in the corresponding equation of motion. Accounting for the additional parallel spring, in this case, means including a term $-K_{lock;j}^{\mathbf{m},\mathbf{n}}\left(e_j^{\mathbf{m},\mathbf{n}} + \Delta D_{0;j}^{\mathbf{m},\mathbf{n}}\right)$, where $K_{lock;j}^{\mathbf{m},\mathbf{n}}$ is the large stiffness of the parallel spring, $e_j^{\mathbf{m},\mathbf{n}}$ is the elongation of the element and $\Delta D_{0;j}^{\mathbf{m},\mathbf{n}}$ is the allowed shortening of the element at which the lock-state occurs. Note here that choosing the stiffness of the parallel spring five times larger than the stiffness in the Kelvin-Voigt element is more than sufficient for an element to behave rigidly compared to its surrounding elements.

In accordance with the one-dimensional lattice, we assume that Bingham elements in the hexagonal lattice are inactive during lock, so that any BKV elements that experience lock behave viscoelastically. The magnitude of the constant elongation $\varepsilon_{B;j}^{\mathbf{m},\mathbf{n}}$ of the involved Bingham element during and after lock however depends on the motion states prior to lock. After a stick-to-lock transition, the elongation $\varepsilon_{B;j}^{\mathbf{m},\mathbf{n}}$ remains constant and equal to its value prior to lock, while after a slip-to-lock transition, the elongation follows from the force-equilibrium at the slip-node in the corresponding Bingham element as derived in Appendix C.3.

Alternatively, we can choose to model the lock-state of a BKV element in the hexagonal

lattice by considering that BKV element as a rigid bar. As explained in Section 2.3.4, obtaining the corresponding equations of motion for the hexagonal lattice is far more laborious and less straightforward than for the one-dimensional BKV lattice. This is testified by Appendix C.3 regarding the derivation of the system of equations of motion for an inner particle **m,n** where the single element in its cell that is in lock-state is represented by a rigid bar.

For reasons previously explained, the angle $\alpha_j^{\mathbf{m},\mathbf{n}}$ of a BKV element j between particles \mathbf{m},\mathbf{n} and $\mathbf{m}_j,\mathbf{n}_j$ is considered as a constant during the current time step. The angle $\alpha_j^{\mathbf{m},\mathbf{n}}$ thereby fixes the direction of the axial forces in a locked element during a single time step. Especially for locked elements in a two-dimensional lattice rotations may be significant, and additionally these rotations may occur quickly. To make sure that the angle $\alpha_j^{\mathbf{m},\mathbf{n}}$ may be considered to be constant during the current time step, and to thereby assure the accuracy of the corresponding system of equations of motion, the time step dt must be carefully chosen.

Finally, note that the systems of equations of motion for the hexagonal Kelvin-Voigt, hexagonal Hooke and hexagonal Prandtl lattices with elements in lock can be straightforwardly derived from their systems of equations of motion by making the appropriate substitutions.

2.4.6 State-transitions in the hexagonal BKV lattice

The transitions between the three admissible motion states have previously been discussed for BKV elements appearing in the one-dimensional BKV lattice in Section 2.3.5. The transitions between motion states of a BKV element in the hexagonal BKV lattice principally occur under the same conditions as the state-transitions in the one-dimensional lattice and therefore the diagram given by Figure 2.6 also holds for state-transitions in the hexagonal BKV lattice. Although, the dimension of the lattice does not influence the nature of the state-transitions, the expressions for the transitions do depend on the dimension and configuration of the considered lattice.

Stick-to-slip transition

The transition from stick to slip, of a BKV element between particles \mathbf{m} , \mathbf{n} and \mathbf{m}_{j} , \mathbf{n}_{j} , occurs when the total force that is applied to the Bingham element, denoted as $F_{B;j}^{\mathbf{m},\mathbf{n}}$ exceeds the threshold of the dry friction element, given by the critical friction force $F_{cr;j}^{\mathbf{m},\mathbf{n}}$. As the Bingham element may be activated in both tension or compression accordingly, the stick-to-slip transition in the element j between particles \mathbf{m} , \mathbf{n} and \mathbf{m}_{j} , \mathbf{n}_{j} occurs when:

$$\left|F_{B;j}^{\mathbf{m,n}}\right| > F_{cr;j}^{\mathbf{m,n}} \tag{2.39}$$

The force equilibrium at the massless slip-node intermediate particles \mathbf{m} , \mathbf{n} and \mathbf{m}_{j} , \mathbf{n}_{j} yields the force on the Bingham element $F_{B;j}^{\mathbf{m},\mathbf{n}}$ during stick as:

$$F_{B;j}^{\mathbf{m,n}} = C_{e;j}^{\mathbf{m,n}} \dot{e}_{j}^{\mathbf{m,n}} + K_{e;j}^{\mathbf{m,n}} \left(e_{j}^{\mathbf{m,n}} - \varepsilon_{B;j}^{\mathbf{m,n}} \right) \tag{2.40}$$

Slip-to-stick transition

The transition of a BKV element between particles \mathbf{m} , \mathbf{n} and $\mathbf{m}_{\mathbf{j}}$, $\mathbf{n}_{\mathbf{j}}$ from slip to stick occurs when the elongation rate of the Bingham element becomes equal to zero or changes sign. When this occurs, the sign of the elongation rate of the Bingham element no longer matches the sign of the force applied to initiate the current instance of slip. Considering that the Bingham element may be activated in both tension and compression, the slip-to-stick transition of a BKV element between particles \mathbf{m} , \mathbf{n} and $\mathbf{m}_{\mathbf{j}}$, $\mathbf{n}_{\mathbf{j}}$ occurs when:

$$\operatorname{sgn} \dot{e}_{B;j}^{\mathbf{m},\mathbf{n}} \neq \operatorname{sgn} F_{B:slip;j}^{\mathbf{m},\mathbf{n}} \tag{2.41}$$

Transition into lock

As stated before, the occurrence of lock in an element is independent of its configuration, independent of its prior motion state and physically represents the collision of the two involved particles. Thus, in accordance with the one-dimensional case, the transition into lock of an element in the hexagonal BKV lattice occurs when:

$$D_i^{\mathbf{m,n}} \le D_{\min;i}^{\mathbf{m,n}} \tag{2.42}$$

Here, $D_j^{\mathbf{m},\mathbf{n}}$ is the distance between particles \mathbf{m},\mathbf{n} and $\mathbf{m}_{\mathbf{j}},\mathbf{n}_{\mathbf{j}}$ and $D_{\min;j}^{\mathbf{m},\mathbf{n}}$ is the minimum or threshold distance between particles \mathbf{m},\mathbf{n} and $\mathbf{m}_{\mathbf{j}},\mathbf{n}_{\mathbf{j}}$.

Transition out of lock

As explained in Section 2.3.5, an element that undergoes a transition out of lock will afterwards always be in stick-state and the transition from lock to slip can never occur. Independent of the configuration of a rheological element, the transition of an element from lock to stick occurs when all forces working together at the considered element stop compressing that element. Representing the lock-state by means of a rigid bar, Appendix C.3 shows that we can derive the exact axial force on any BKV element in lock. Then, noting that an element in lock is unable to transmit tensile forces, we can use this axial force to determine when the lock-to-stick transition occurs. As explained in Section 2.3.4 however, we apply the lock-state in an element of the hexagonal BKV lattice by adding a spring with a significantly larger stiffness than the springs appearing in the BKV elements. As a result, any locked element will always have a certain, albeit very small, elongation. Because an element only remains in lock as long as the involved particles are pushed toward each other, the transition out of lock occurs when the involved particles move apart, i.e. when the locked element obtains a positive elongation rate. The lock-to-stick transition for a BKV element between particles \mathbf{m} , and \mathbf{m}_i , \mathbf{n}_i therefore occurs when:

$$\dot{e}_j^{\mathbf{m},\mathbf{n}} \ge 0 \tag{2.43}$$

Note that, due to modelling lock by a spring with a large stiffness, the transition out of lock may occur while the distance between particles \mathbf{m} , \mathbf{n} and $\mathbf{m}_{\mathbf{j}}$, $\mathbf{n}_{\mathbf{j}}$ is slightly smaller than the threshold distance $D_{\min,j}^{\mathbf{m},\mathbf{n}}$. To assure that, after a transition out of lock, an element does not instantly undergo a transition back into lock, the threshold distance is set to be equal to the smallest distance observed between particles \mathbf{m} , \mathbf{n} and $\mathbf{m}_{\mathbf{j}}$, $\mathbf{n}_{\mathbf{j}}$ until the actual distance becomes larger than the threshold.

2.4.7 Geometrical and material randomness in the hexagonal lattice

To capture the physics of material behaviour well, the random heterogeneity of the material throughout the medium must be accounted for. Absence of this randomness yields a significant mesh dependency in the response of two- and three-dimensional lattices as any occurring waves will propagate along the directions privileged by the regular mesh, thereby losing the unstructured character of material behaviour. This is specifically relevant for models that allow for nonlinear phenomena and that yield large displacements.

In this thesis, the random heterogeneity of the lattice is achieved by randomly perturbing the initial location of the particles in the lattice. The results from applying this geometrical randomness is depicted in Figure 2.13. Here, Figure 2.13a shows a hexagonal lattice with a regular arrangement of the particles in the lattice, while Figure 2.13b shows the same hexagonal lattice, but now with an irregular or randomized particle arrangement. Note here that the locations of the particles located at the surface and the boundary of the lattice have not been randomized.

Alternatively, or additionally, the random heterogeneity of the considered material may also be achieved by randomly varying the lattice parameters, such as the mass of the particles and the stiffness of the springs, for example using a Gaussian distribution. The random variation of these parameters throughout the hexagonal lattice has not been applied in this thesis as a general case, but is addressed specifically when applied.

2.5 Material properties of one- and two-dimensional media

To show the workings of the one- and two-dimensional models in this thesis, the chosen values for the macromaterial properties are of no immediate relevance, although physically realistic values should be used. For ease of comparison of their results, all models are chosen to represent the same material, so that a single set of macromaterial properties is used throughout this thesis. The parameters of the one- and two-dimensional lattices then follow from the chosen macromaterial properties and their geometry. The relations between the macromaterial properties and the parameters of the one-dimensional lattice are discussed in Section 3.2.1, while the parameters of the hexagonal lattice are derived in Appendix C.1 and discussed in Section 3.6.1.

The macromaterial, or continuum, properties considered in this thesis are the mass density ρ , the Young's modulus E, the Poisson's ratio v and the damping coefficient ζ_e that describes the viscous material damping in relation to the material elasticity. As an example of how the damping coefficient ζ_e is applied, consider the dynamic modulus of elasticity \hat{E} as an operator that describes the viscoelastic material behaviour through the Young's modulus and the

damping coefficient as $\hat{E} = E(1 + \zeta_e \frac{\partial}{\partial t})$.

In this thesis, we generally assume a mass density $\rho = 2000 \text{ kg/m}^3$ and a Young's modulus E = 20 MPa, which are typical values for a non-cohesive soft soil [Kézdi, 1974]. Furthermore, the Poisson's ratio is chosen as $v = \frac{1}{4}$ because, as shown in Appendix C.1, only for this Poisson's ratio the parameters of the hexagonal lattice that accounts for axial interactions only can be matched to the macromaterial properties. In some cases, the damping in this thesis is given dimensionally in terms of the damping coefficient ζ_e but in most cases the dimensionless damping ratio ζ is used that describes the material damping as a fraction of the critical damping. Note here that the value of the damping is not fixed and thereby varies throughout this thesis.

2.6 Response of the hexagonal lattice with elementary boundaries

Before considering the response of the hexagonal lattice that includes a boundary formulation to account for a far-field domain with properties that are equivalent to the near-field lattice, we will here first consider the response of the hexagonal lattice with several so-called elementary boundaries. The different types of elementary boundaries that are considered in this thesis are discussed in Section 2.6.1. Subsequently, in Section 2.6.2, we will discuss the methods that are available to obtain the response of a hexagonal lattice from the system of equations of motion. Additionally, we will here address the accuracy of the linearizations for small- and large elongations by comparing the response of the hexagonal lattice to a time-dependent load for the different linearizations applied. Finally, we will consider the nonlinear response of a hexagonal BKV lattice with a fixed boundary to an externally applied time-dependent load in Section 2.6.3.

2.6.1 Elementary boundaries for two-dimensional lattices

An elementary boundary here means that each particle at the boundary of the lattice is independently supported by a single rheological element in respectively horizontal and vertical direction. Consider for example the hexagonal lattice with a linear-elastic boundary depicted in Figure 2.14a. Here, each particle at the lattice boundary is supported by one spring in horizontal direction and one spring in vertical direction, both with a spring stiffness K_b that has the same order of magnitude as the spring stiffness of the elements inside the hexagonal lattice. Additional examples of elementary boundaries are the viscous boundary, depicted in Figure 2.14b, consisting of horizontal and vertical dashpots with damping coefficient C_b at

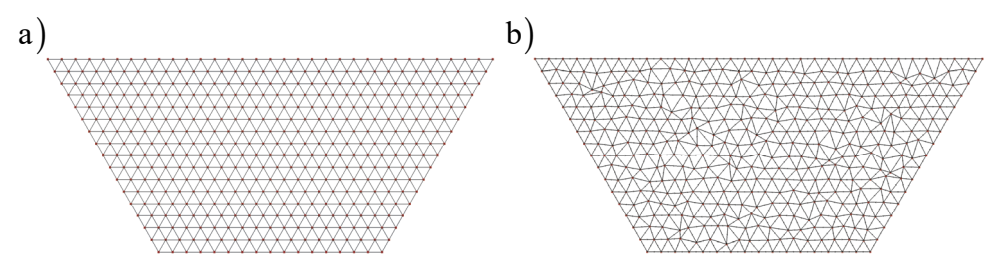


Figure 2.13: A hexagonal lattice with: a) a regular mesh; b) an irregular or randomized mesh.

every boundary particle, or a viscoelastic boundary, which features a Kelvin-Voigt element in both horizontal and vertical directions at each of the boundary particles. Additionally, the free boundary, i.e. the situation where the boundary particles are not supported at all, and the fixed boundary, i.e. the situation where the boundary particles are fixed in-place, are also examples of elementary boundaries.

Note that for the elementary boundaries that are introduced by adding horizontal and vertical rheological elements we do not actually specify the location of the point at which these elements are supported, nor do we specify the length of the elements. Instead, we assume that the horizontal support elements remain horizontal at all times and accordingly that the vertical support elements remain vertical at all times. Because of this, their angles are constant at all times and their elongations match the displacements of the boundary particles.

To model the fixed boundary, it is most accurate to simply fix the boundary particles inplace and thereby remove the corresponding degrees of freedom from the system of equations
of motion. This reduces the size of the problem to be solved and thereby reduces the calculation time. For implementation convenience however, the so-called fixed boundary is here
modelled by supporting the boundary particles with a horizontal and a vertical spring that
both have a spring stiffness K_b^{∞} , which is significantly larger than the spring stiffness of the
elements featured in the hexagonal lattice. This means that the boundary particles are maintained as degrees of freedom and the total number of degrees of freedom for the lattice with
a fixed boundary is the same as the number of degrees of freedom for a lattice with any of
the other elementary boundaries. As such, the linear-elastic and fixed boundaries are essentially the same as they only differ in magnitude of the stiffness. Here, note that the stiffness K_b^{∞} should not be chosen abundantly large as a very stiff boundary may yield large computation times; to simulate the fixed behaviour by means of springs with a large spring stiffness,
it is more than sufficient to choose the stiffness of the boundary springs for example ten times
larger than the stiffness of the springs in the lattice, i.e. $K_b^{\infty} = 10K_b$.

2.6.2 Accuracy of linearizations applied to two-dimensional lattices

As stated previously in Sections 2.1 and 2.4.2, the expressions for the elongations of the rheological elements in a two-dimensional lattice are linearized to obtain the corresponding system of equations of motion as a set of linear ordinary differential equations. The reason that this linearization is required is that in two-dimensional space the rheological elements do not only become longer or shorter, but they also rotate and taking this rotation into account in the expressions for their elongations yields the system of equations of motion as a set of nonlinear differential equations. In fact, for rheological elements with a constant angle, i.e. no rotation, it can straightforwardly be shown that the linearizations for both small- and large-elongations, respectively discussed in Appendices A.1 and A.2, are exact and without error. Note that this is independent of whether linear or nonlinear rheological elements are considered. Evidently, as the angles of all rheological elements in a one-dimensional lattice are always constant, linearization of their elongations is not required for one-dimensional lattices.

Since the linearizations for small and large elongations are different simplifications of the

same analytically exact expression, the magnitude of their errors is different. For both linearizations, the expressions for the elongation of the rheological element between particles \mathbf{m} , \mathbf{n} and $\mathbf{m}_{\mathbf{j}}$, $\mathbf{n}_{\mathbf{j}}$ are derived in Appendix A by applying a truncated Taylor approximation. Consequently, for both cases, the error partly follows from neglecting higher-order terms in the expression for the elongation to which the Taylor expansion is applied and partly follows from neglecting higher-order terms of the Taylor expansion itself. The advantage of the linearization for large elongations is that its error is proportional to the size of the applied time step, because it accounts for the displacements of the particles over the current time step. As a consequence, the error of the response that follows from applying the linearization for large elongations reduces by decreasing the time step. This error reduction is attributed to the fact that the terms of the Taylor series that are being neglected are smaller at smaller time steps. Thus, by decreasing the time step, the response of the lattice that is obtained using the linearization for large elongations will improve its approximation of the exact response.

In Appendix A.3, a higher-order approach for large elongations is presented that reduces the error of the linearization for large elongations by including higher-order terms in the Taylor expansion. As we are already able to approximate the exact response of a hexagonal lattice well using the linearization for large elongations according to Appendix A.2, the higher-order approach presented in Appendix A.3 is not aimed at improving the accuracy of the response, but is considered in an attempt to increase the step size and thereby reduce the number of time steps, and thus reduce the calculation time, required to obtain a similarly accurate response.

Solving the equations of motion in the time domain or in the frequency domain

The response of the hexagonal lattice can generally be obtained by solving the corresponding system of equations of motion either in the time domain or in the frequency domain. In general, frequency domain solutions require significantly less computational effort than time

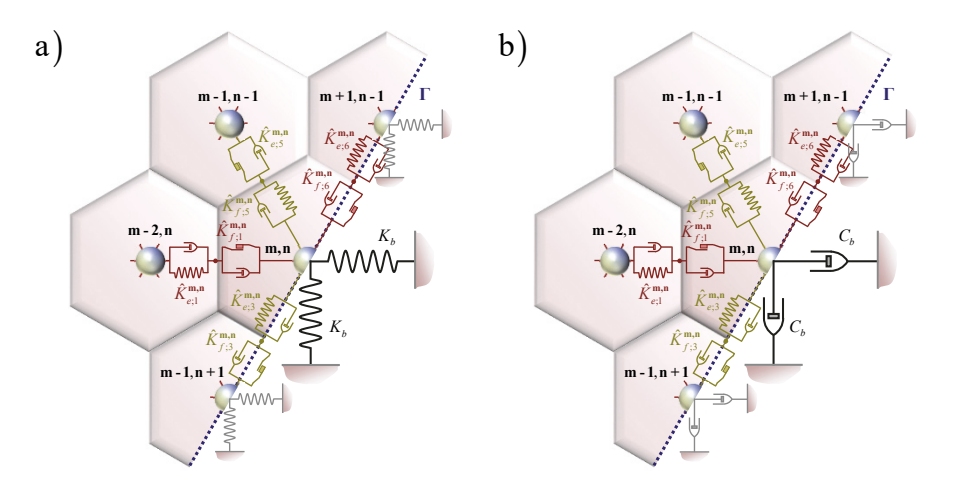


Figure 2.14: a) Linear-elastic boundary with horizontal and vertical springs at every boundary particle; b) Viscous boundary with horizontal and vertical dashpots at every boundary particle.

domain solutions. While the system of ordinary differential equations for the time domain approach must be solved at every time step using iterative methods, the algebraic system of equations of motion for the frequency domain is evaluated for all frequencies once, after which the frequency domain response is transformed to the time domain by numerically evaluating an integral transform at every time step. As a result of this, the elongations of the rheological elements can only be determined with respect to their original lengths, and the lattice geometry cannot be updated over time. Thus, in order to use the frequency domain approach, we sacrifice the possibility of incorporating the linearization for large elongations and of updating the angle at every time step.

Once the hexagonal lattice incorporates any rheological elements that allow for physically nonlinear behaviour, for example by incorporating slip or lock, the elongations of these rheological elements are large and the system of equations of motion must generally be evaluated in the time domain. In the time domain approach, we therefore generally apply the linearization for large strains. Alternatively however, for example to compare the time domain response with the frequency domain response, also the linearization for small elongations may be applied in the time domain approach. Furthermore, as the time domain solution does allow the geometry of the hexagonal lattice to be updated over time, we principally account for the geometrical nonlinearity in the time domain approach. To this purpose, the angles of the rheological elements in the lattice are assumed constant only during each time step to solve the corresponding system of equations as a system of linear ODEs, and are updated after each time step based on the lattice response.

Comparison of linearizations applied for two-dimensional lattices

To assess the accuracy of the different approaches presented in Appendix A, we here compare the responses of a linear-elastic hexagonal Hooke lattice with a linear-elastic boundary to an externally applied time-dependent load for the following cases:

- Frequency domain (FD) solution incorporating the linearization for small elongations;
- Time domain (TD) solution incorporating the linearization for small elongations;
- Time domain (TD) solution incorporating the linearization for large elongations;
- Time domain (TD) solution using the higher-order approach for large elongations.

For both solutions that incorporate the linearization for small elongations, the geometrical nonlinearity is not accounted for so that the angles of all rheological elements in the lattice are assumed constant and equal to their initial value for the full duration of the response. For the two time domain solutions that respectively incorporate the linearization for large elongations and the higher-order approach for large elongations, the geometrical nonlinearity is accounted for and the angles of all rheological elements in the lattice are thus updated at every time step. As the validity of the different approaches depends on the magnitude of the elongations and therefore on the magnitude of the load, we here compare the above models for different magnitudes of the applied loading.

The considered hexagonal Hooke lattice with a linear-elastic boundary is depicted in Figure 2.15 and consists of 25 particles with a mass M and 82 Hooke elements with a stiffness K_e . Note here that the geometry of the hexagonal Hooke lattice has not been randomized to

make sure that the responses for the four models described here are all obtained for the exact same geometry. In addition, Figure 2.15 shows the hexagonal area that each particle inside the lattice represents. To be able to match the parameters of the two-dimensional lattice with the macromaterial properties discussed in Section 2.5, we assume a unit third dimension dy. Based on the hexagonal area each particle represents and accounting for the unit third dimension, the mass of a particle in the interior of the homogeneous hexagonal lattice is found as $M = \frac{\sqrt{3}}{2} \rho \ell^2 dy$, where ρ is the mass density and ℓ is the distance between adjacent particles in the lattice. Furthermore, the relation between the stiffness of the springs in the homogeneous hexagonal Hooke lattice and the Young's modulus is derived in Appendix C.1 as $K_e = \frac{8}{5\sqrt{3}} E dy$.

As stated in Section 2.5, we here assume that the hexagonal Hooke lattice represents a non-cohesive soft soil with a density $\rho = 2000 \,\mathrm{kg/m^3}$, a Young's modulus $E = 20 \,\mathrm{MPa}$ and a Poisson's ratio $v = \frac{1}{4}$. Noting that the lattice models are intended to describe a solid medium at the meso-scale, the interparticle distance in the hexagonal lattice is chosen as $\ell = 0.2 \,\mathrm{m}$. Based on the chosen interparticle distance and the given macromaterial properties, the mass of the inner particles is obtained as $M = 69.28 \,\mathrm{kg}$, while the stiffness of the springs in the hexagonal Hooke lattice are obtained as $K_e = 18.48 \,\mathrm{MN/m}$. Furthermore, the spring stiffness of the linear-elastic boundary is chosen to be equal to the stiffness of the Hooke elements inside the lattice, i.e. $K_b = K_e$.

For each of the four solutions given at the start of this section, a pulse load F(t) is applied at the surface particle 0,0 that consists of a single sinus period and may be expressed as:

$$F(t) = \overline{F}\sin(\omega_F t)H(T_F - t)H(t).$$

Here, \bar{F} is the amplitude, T_F is the period of the sinus in the pulse load and ω_F is the corresponding angular frequency, chosen as $\omega_F = 80 \text{ rad/s}$.

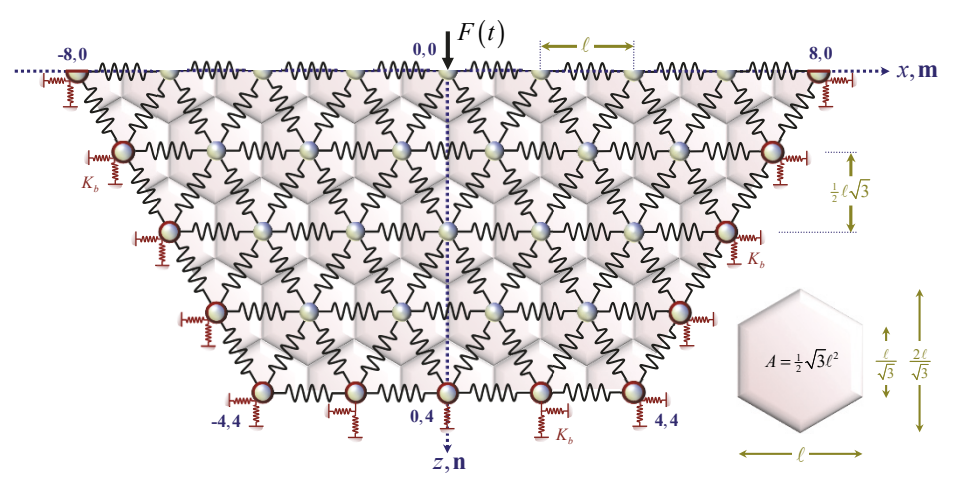


Figure 2.15: The hexagonal Hooke lattice with a linear-elastic boundary.

The response of the linear-elastic Hooke lattice is presented in Figure 2.16 for all four solutions by means of the normalized vertical displacement of particle 0.0 as a function of time, where the displacements are normalized with respect to the unit particle distance ℓ . Here, Figure 2.16a shows the vertical displacement of particle 0.0 due to the given pulse load for an amplitude $\bar{F} = 0.1 \, \text{MN}$, while Figure 2.16b shows the vertical displacement of the same particle, but now for an amplitude $\bar{F} = 1 \text{ MN}$. For the linearization that assumes small elongations, the vertical displacements of particle 0,0, given in Figure 2.16 by the dashed blue line and the continuous light blue line for the time domain and the frequency domain solutions respectively, are approximately the same for both magnitudes of the amplitude. Between the responses obtained for these two models, a very small difference, which is not distinguishable in Figure 2.16, remains that is due to the numerical errors embedded in the different solution methods applied. Although the frequency domain solution solves the system of equations of motion algebraically, and is therefore numerically exact up to the chosen precision of its variables, the resulting response is obtained in the frequency domain. The time domain displacements are then obtained by numerically applying an inverse integral transform over a truncated domain of the frequency domain displacements and therefore includes a certain small numerical error. On the other hand, in the time domain solution the system of ordinary differential equations is solved by means of the Runge-Kutta method, which is an iterative method and therefore prone to certain small numerical errors as well.

The difference between the responses to the pulse load with amplitude $\bar{F}=0.1\,\mathrm{MN}$, obtained by respectively applying the linearizations for small and large elongations given by Figure 2.16a, is only visible at the extremes and may overall be considered to be negligible. We can therefore state that for the pulse load with amplitude $\bar{F}=0.1\,\mathrm{MN}$, the elongations of the rheological elements in the hexagonal lattice are within the range at which the linearization for small elongations is valid. Evidently, as shown by Figure 2.16b, increasing the amplitude of the pulse load to $\bar{F}=1\,\mathrm{MN}$ increases the elongations of the rheological elements, and thereby increases the error of this linearization to such an extent that assuming small elongations is no longer valid. By further increasing the magnitude of the loading, all similarity between the responses obtained using the linearization for small and large

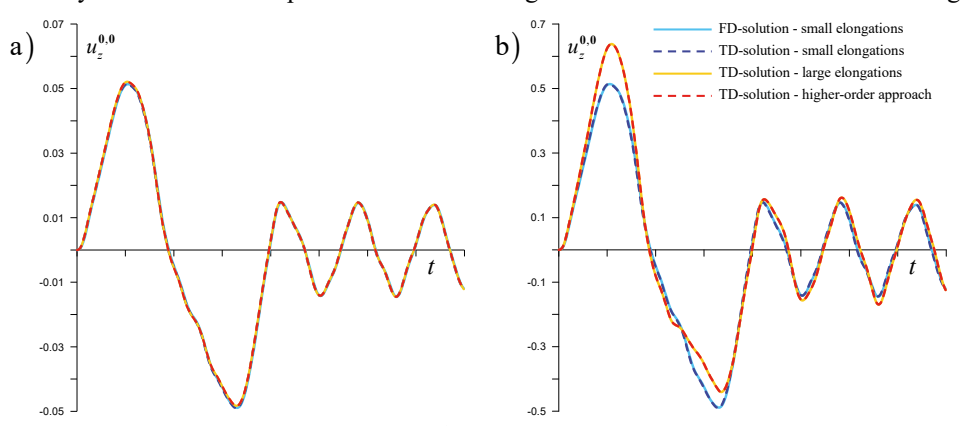


Figure 2.16: Normalized vertical displacement of the loaded particle at the lattice origin due to a pulse load for different approaches: a) with an amplitude of 0.1 MN; b) with an amplitude of 1.0 MN.

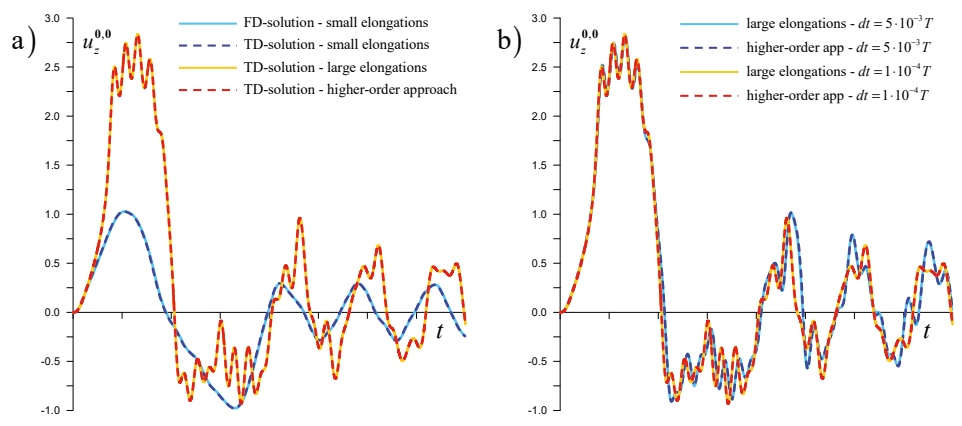


Figure 2.17: Vertical displacement of the loaded particle due to a pulse load with an amplitude of 2.0 MN: a) approaches for small and large elongations; b) approaches for large elongations for different sizes of the time step dt.

elongations is lost. This is demonstrated by Figure 2.17a, which shows the normalized response obtained for the pulse load with an amplitude $\bar{F} = 2 \text{ MN}$.

The two time domain solutions that incorporate the linearization and the higher-order approach for large elongations, for which the responses are given in Figure 2.16 and Figure 2.17a by the continuous yellow line and the dashed red line respectively, give the same vertical displacements of particle 0,0. For the same size of the time step dt, the differences between the two responses are negligible. Figure 2.17b again shows the responses obtained using linearization and higher-order approach for large elongations for a pulse load with an amplitude $\overline{F} = 2$ MN, but now for different sizes of the time step dt. As the responses obtained for both approaches are the same for both sizes of the time step, it follows from Figure 2.17b that using the higher-order approach for large elongations only marginally improves the accuracy. In fact, the influence of reducing the time step is much larger than the influence of using higher-order terms in the expression for the elongation. From this it can be concluded that the error induced by assuming that the angle is constant for the duration of each time step is significantly larger than the error induced by neglecting the higher order terms in the expression for the elongation of the rheological elements. Consequently, using the higherorder approach for large elongations does not necessarily warrant an increase in size of the time step as an option to reduce calculation time.

2.6.3 Response of the hexagonal BKV lattice with a fixed boundary

To demonstrate the characteristic nonlinear response of the BKV lattice to an externally applied time-dependent load, we here consider the hexagonal BKV lattice with a fixed boundary that is depicted in Figure 2.18. A time-dependent pulse load F(t) is applied at particle $\mathbf{0}$, $\mathbf{0}$ at the origin of the lattice that, as before, consists of a single sinus with an angular frequency ω_F , a period T_F and an amplitude \overline{F} . In this case, the angular frequency and amplitude are respectively chosen as $\omega_F = 200 \, \text{rad/s}$ and $\overline{F} = 2 \, \text{MN}$.

The size of the hexagonal lattice is described by the number of rheological elements N that is at least required to connect the particle 0,0 at the origin of the lattice with any particle

at the boundary. For the regular hexagonal BKV lattice depicted in Figure 2.18, the value of **N** is equal to 4, because the distance between the particle **0**,**0** at the origin of the lattice and, for example, particle **N**,**N** at the boundary of the lattice consists of four BKV elements. In this case however, we will present and discuss the nonlinear response obtained for the irregular hexagonal BKV lattice with a dimension **N** equal to 8 for which the mesh is depicted in Figure 2.19. The considered BKV lattice principally consists of 117 particles and 308 BKV elements. However, since we consider a fixed boundary, the involved boundary particles are fixed in place and should therefore not be considered as degrees of freedom of the system. Accordingly, the BKV elements along the fixed boundary are not activated. Disregarding the particles and the elements at the fixed boundary, there are 92 particles and 284 BKV elements in the lattice.

The parameters of the hexagonal BKV lattice are chosen to match the macromaterial properties stated in Section 2.5, and are thus in accordance with the parameters of the hexagonal Hooke lattice previously considered in Section 2.6.2. The interparticle distance in the lattice is thus chosen as $\ell=0.2$ m, the mass of the inner particles is equal to M=69.28 kg and the stiffness of the springs in the BKV elements is equal to $K_e=18.48$ MN/m . Arbitrarily choosing a damping coefficient of $\zeta_e=1\cdot 10^{-3}$ s, the damping constants of the dashpots in the BKV elements are obtained as $C_e=C_f=18.48$ kNs/m . Additionally, the critical friction force of the dry friction elements in the BKV elements is chosen relative to the amplitude of the applied pulse load as $F_{cr}=0.4\bar{F}$. As previously explained in Section 2.4.1, it follows from the geometry of respectively the boundary and the surface cells that the mass of the boundary and surface particles, as well as the damping and the stiffness of the BKV elements at the boundary and the surface of the lattice, depicted in Figure 2.19 by the blue line segments, are half of those of the regular particles and BKV elements.

To induce additional occurrences of nonlinear behaviour, the considered irregular BKV lattice has a cluster of weak BKV elements, depicted in Figure 2.19 by the red line segments. The values for the parameters of these weak elements are chosen to be equal to 20% of the

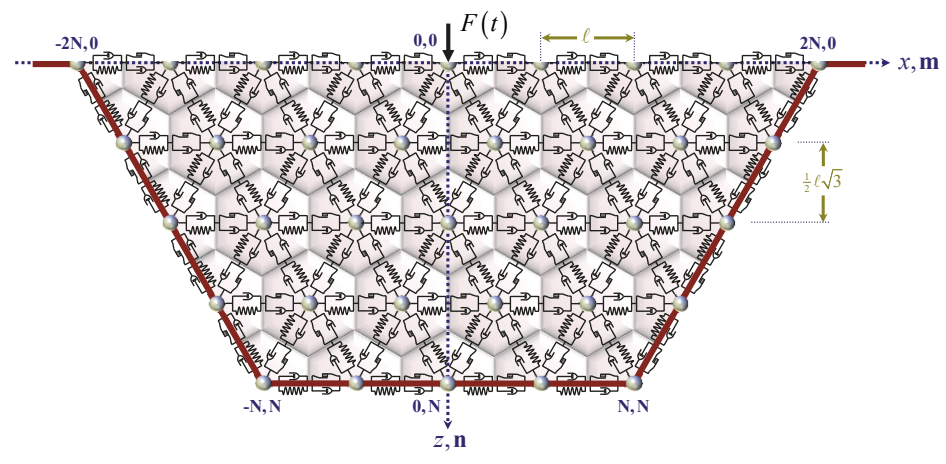


Figure 2.18: The hexagonal BKV lattice with a fixed boundary of dimension N equal to 4.

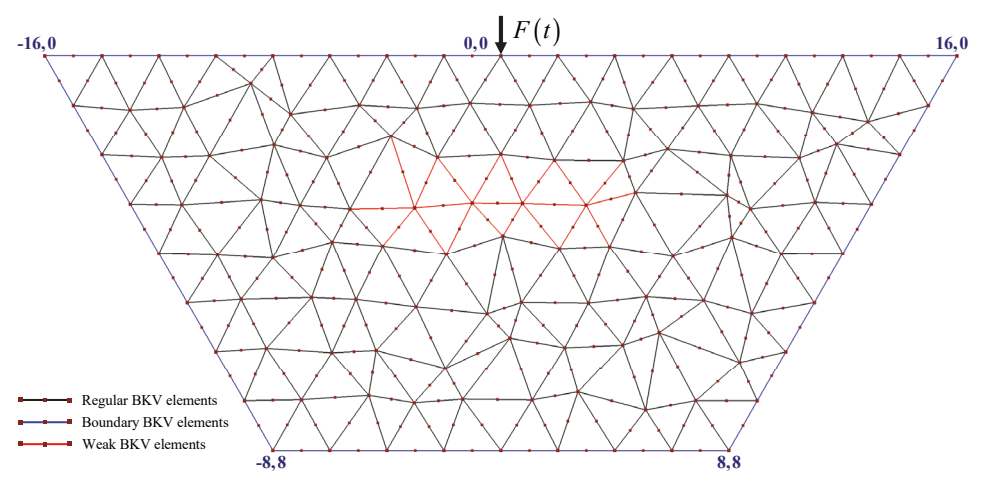


Figure 2.19: The irregular BKV lattice of dimension N equal to 8 with a cluster of weak BKV elements.

corresponding values for the regular elements, given in Figure 2.19 by the black line segments. Thus, the springs in the weak BKV elements have a stiffness coefficient $K_e^{weak} = 0.2 K_e = 3.695 \text{ MN/m}$ and the corresponding dashpots have a damping coefficient $C_e^{weak} = C_f^{weak} = 0.2 C_e = 3.695 \text{ kNs/m}$. Additionally, the critical friction force of the weak BKV elements is chosen as $F_{cr}^{weak} = 0.2 F_{cr} = 0.16 \overline{F}$.

Figure 2.20a and Figure 2.20b respectively depict the horizontal and vertical response of the loaded particle at the origin of the lattice, i.e. particle $\bf 0,0$, to the single sinus pulse load applied at that particle, as a function of time. Here, the displacements are again normalized by dividing the actual displacements by the unit particle distance ℓ . In both figures, the continuous red line gives the displacement response of particle $\bf 0,0$ in the irregular BKV lattice depicted in Figure 2.19. Additionally, the continuous blue line gives the response of a corresponding Kelvin-Voigt lattice, thus with a fixed boundary, the same irregular particle arrangement, the same viscoelastic properties and including the same cluster of weak elements. This corresponding Kelvin-Voigt lattice may be directly obtained from the irregular BKV lattice depicted in Figure 2.19 by choosing the properties of the BKV elements such that the slip- and lock-states do not occur. This can for example be achieved by choosing the critical friction force of the dry friction elements to be significantly larger than the amplitude of the applied loading and choosing the threshold distance at which lock occurs to be equal to zero for all BKV elements.

In Figure 2.20, the time domain of the horizontal axes, has been chosen such that any nonlinear phenomena in the BKV lattice, being the occurrence of the slip- and/or lock-states in the BKV elements, occur within its domain. Here, only the initial displacement response of the loaded particle in respectively the BKV and Kelvin-Voigt lattices is given; beyond the domain of the response given in Figure 2.20, both the Kelvin-Voigt and BKV lattices behave exclusively viscoelastic until eventually all oscillations are damped out. The dashed red lines in Figure 2.20a and Figure 2.20b respectively give the final horizontal and vertical displacements of the loaded particle that remain after all oscillations and reflections have dissipated

and the hexagonal BKV lattice has come to rest. As the Kelvin-Voigt lattice only behaves linearly, eventually all particles in the lattice return to their starting positions and thus the final horizontal and vertical displacements of the loaded particle in the Kelvin-Voigt lattice are equal to zero. Note here that although a nonzero final displacement of the loaded particle is evidence of the occurrence of nonlinear behaviour in the BKV lattice, a zero final displacement does not necessarily mean that there have been no occurrences of nonlinear behaviour in the lattice.

Regarding Figure 2.20a, note that the nonzero horizontal displacement of the loaded particle occurs exclusively due to the irregular particle arrangement of both the Kelvin-Voigt and BKV lattice; if the lattices were chosen to be regular, they would be symmetric and the loaded particle would at all times remain exactly at the symmetry line and not displace horizontally. Despite the irregular particle arrangement of the lattices however, do note that for the loaded particle in both lattices, the horizontal displacements are significantly smaller than the vertical displacements.

The first time one of the elements in the BKV elements transits to a slip- or lock state can be identified as the time moment at the which the response of the loaded particle in the BKV lattice starts to deviate from the response of the same particle in the Kelvin-Voigt lattice. To evaluate the nonlinear behaviour of the BKV lattice let us consider Figure 2.21a and Figure 2.21b showing snapshots of the Kelvin-Voigt and BKV lattices at respectively time t_1 and time t_2 . The points in the simulation at which the time moments t_1 and t_2 occur are given in Figure 2.20b. In Figure 2.21, the black line segments represent BKV elements that are in stick-state, which is clearly the majority of the elements in the BKV lattice. Furthermore, the blue line-segments represent BKV elements in slip-state, while the red line-segments represent BKV elements in lock-state. The elements of the Kelvin-Voigt lattice, which are not subject to the variation of motion states, are represented by the grey line segments. Here, the elements of the BKV lattice are shown in front of the Kelvin-Voigt lattice, so that if a Kelvin-Voigt element is not visible, its position and angle coincides with the corresponding element

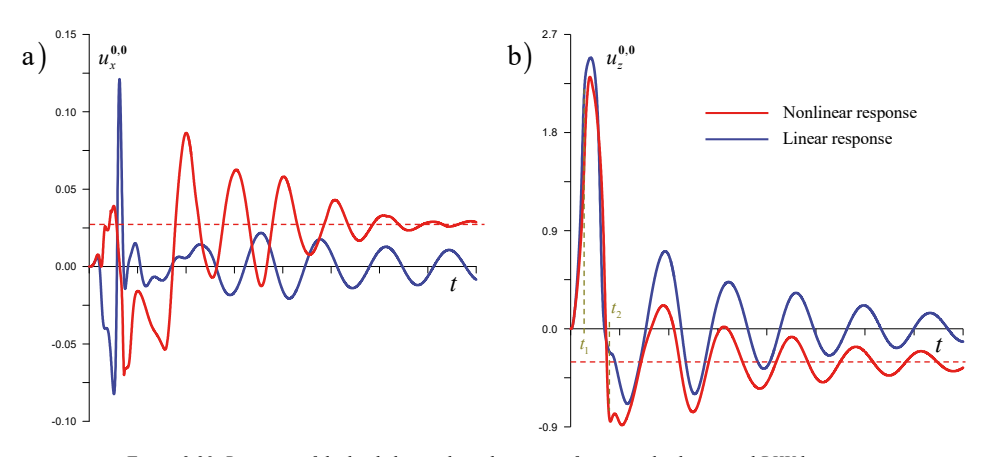


Figure 2.20: Response of the loaded particle at the origin of an irregular hexagonal BKV lattice to a pulse load: a) horizontal displacement; b) vertical displacement.

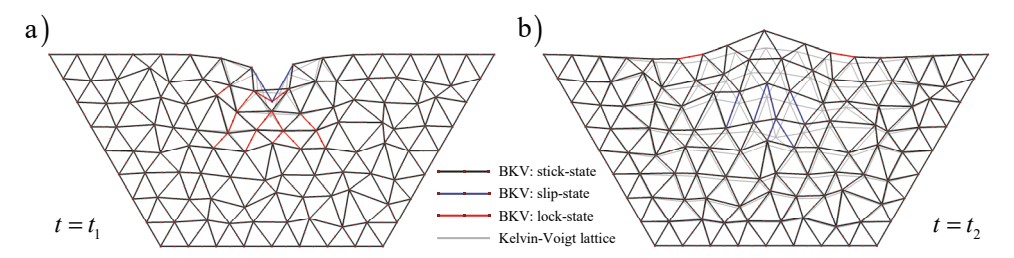


Figure 2.21: The motion-states in the BKV-lattice at a) time moment $t=t_1$; b) time moment $t=t_2$.

in the BKV lattice.

In Figure 2.21a, which is the snapshot for time moment t_1 , the applied load and the particle motion is directed downwards, which coincides with the positive direction of the z-axis. Here, we can see that nonlinear phenomena primarily occur right underneath the applied load, as well as in the cluster of weak elements. In this snapshot, there are two BKV elements in slipmode, which are the two surface elements connected to the loaded particle. Furthermore, there are thirteen BKV elements in lock-state of which two are inner elements directly connected to the loaded particle and nine locked elements are located in the compressed cluster of weak BVK elements. Note here that lock generally occurs in elements that are being compressed, because the lock-state occurs when the distance between two particles becomes smaller than a certain threshold. Now, when slip occurs in an element under compression the shortening rate of that element increases significantly and therefore generally the threshold for lock is quickly reached thereafter. Thus, in compression, the magnitude of the slip-displacements in the BKV elements is limited by the occurrence of lock, while in tension this is not the case. As a logical consequence, the resulting slip displacements in tension are much larger than those in compression, or one might say that slip occurs much more often in tension than in compression. This is illustrated by Figure 2.21b, which is the snapshot for time moment t_2 , where the applied load and the particle motion are directed upwards, coinciding with the negative direction of the z-axis. Here, six of the BKV elements in the weak cluster are in a slip-state due to the tension in these elements. Additionally, there are two surface elements in a lock-state due to the bending of the lattice surface.

Because the lattice only describes the interaction between a particle and up to six particles that are directly adjacent in its initial configuration, we do not account for any interactions between any two particles that initially are not directly adjacent. From Figure 2.21a, we can see that this may lead to unwanted issues: at the time moment of this snapshot, the loaded particle does not interact with the particle directly underneath and closest by. In fact, the displacement of the loaded particle during this snapshot is not yet at its maximum and during this simulation the two involved particles will eventually overlap. If the interaction between the two particles would have been described by a rheological element, the occurrence of lock in that element would prevent the overlap from occurring. Such an issue can for example be resolved by considering a so-called extended hexagonal lattice [Askes and Metrikine, 2004] in which, next to the rheological elements that describe the interaction of an inner particle with its six closest neighbours, an additional six rheological elements are included for every

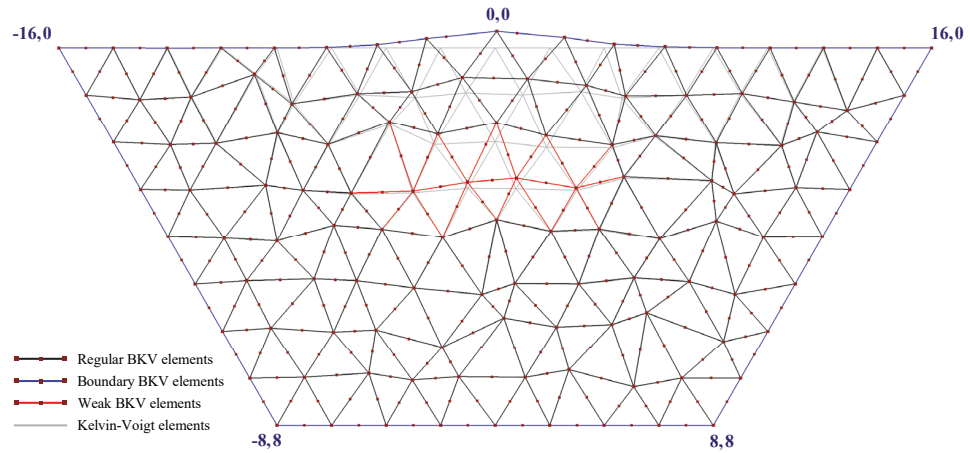


Figure 2.22: Final position of all particles and elements in the Kelvin-Voigt and BKV lattices.

inner particle to describe its interaction with the next six particles closest by. In this thesis however, we do not further consider the extended hexagonal lattice.

Figure 2.22 shows the final position of all particles and elements in both the Kelvin-Voigt and BKV lattices. In accordance with Figure 2.19, the regular BKV elements, the boundary and surface elements, and the weak BKV elements are respectively given by the black, blue and red line segments. The elements in the Kelvin-Voigt lattice are given in grey. Whereas the Kelvin-Voigt lattice returns to its initial position, the BKV lattice does not. From Figure 2.22 we can see that the largest deformations, i.e. the largest lasting elongations, have occurred in the BKV elements directly connected to the loaded particle and those located in the cluster of weak BKV elements. Here, note that the final and permanent displacement of the lattice particles is upward, because the magnitude of the slip-displacements that have occurred in the weak BKV elements are larger in tension than in compression. This can be explained by noting that the magnitude of the slip-displacements in the BKV elements is limited by the occurrence of lock, while in tension there is no limit to the slip-displacements.

3

One- and two-dimensional discrete-continuous systems

As discussed in Section 1.1, it is our aim to describe the response of a medium to a dynamic load source by dividing that medium into a nonlinear domain in the vicinity of the load, i.e. the near field, and a linear domain that represents the far field of the medium. Whereas the preceding chapter discusses the one- and two-dimensional discrete lattice models used to describe the possible nonlinear response of the near-field domain, Chapters 3 and 4 specifically focus on the derivation and the performance of boundary integral equations used to represent the behaviour of the linear far-field domain at the interface with the near-field domain. In this chapter, we specifically focus on media for which the linear far-field domain is represented by a continuum, while Chapter 4 regards the linear far-field domain as a system of particles.

The far-field domain is ideally represented if the corresponding interface conditions are formulated in such a way that any waves propagating through the discrete near-field lattice are not reflected at the interface. In the time domain, this boundary formulation consists of an integral force-displacement relation that represents the behaviour of the far-field domain at the interface with the near-field domain. In the frequency domain, or alternatively in the Laplace domain, this relation is commonly known as the *dynamic stiffness* relation, or inversely as the *dynamic compliance* relation. In Section 3.1, we further explain the concepts of dynamic stiffness and dynamic compliance, and discuss the corresponding force-displacement relations for both one- and two-dimensional media. Subsequently, in Section 3.2, we consider a one-dimensional system composed of a one-dimensional BKV lattice in the near field and a one-dimensional continuum in the far field with the main aim to discuss the concept and typical issues of accounting for the far field by a boundary formulation. In Section 3.3, we discuss several one-dimensional discrete-continuous systems and their boundary formulations. Here, additionally, the performance of the corresponding models is evaluated and compared qualitatively by considering the wave reflection at the discrete-continuous interface. Then, in Section 3.4, we consider a discrete-continuous system for which the far-field

domain consists of a continuous rod of finite length and evaluate the performance of its boundary formulation to show that our approach is also applicable for media with finite dimensions.

Section 3.5 considers the derivation of a boundary formulation for two-dimensional discrete-continuous systems. Here, the integral force-displacement relations along the boundary of the near field domain are derived by modelling the far-field domain as a linear two-dimensional continuum. Finally, in Section 3.6, the full system of equations of motion is derived for the two-dimensional discrete-continuous BKV system. Since we have not managed to successfully implement the boundary integral equations for the two-dimensional discrete-continuous system, only the approach to derive the boundary formulation from modelling the far-field domain as a two-dimensional continuum is presented here, and actual results for the two-dimensional discrete-continuous BKV system are not included. Section 3.6 concludes with a discussion of the issues involved with the numerical implementation of a boundary formulation for a discrete near-field lattice, specifically when the far-field domain is modelled as a two-dimensional continuum.

3.1 Dynamic stiffness and dynamic compliance

The dynamic interaction between two arbitrary media, thus independent of whether we are considering two lattices, two continua or a lattice and a continuum, can always be described using the so-called dynamic stiffness, or using its inverse known as the dynamic compliance.

To explain the concept of dynamic stiffness, let us consider the interaction between the nonlinear and linear domains of an elastic medium due to a point load depicted in Figure 3.1. If we know the exact relation between the forces working on, and the displacements of, the linear-elastic medium \mathbf{V}_E^{lin} at the interface Γ , we can describe the response of the linear-elastic medium \mathbf{V}_E^{lin} at the interface Γ , to loads applied at the nonlinear medium \mathbf{V}_E^{nonlin} , by this force-displacement relation. Statically, a force-displacement relation is described by the commonly known Hooke's Law, where the ratio between force and displacement is given by

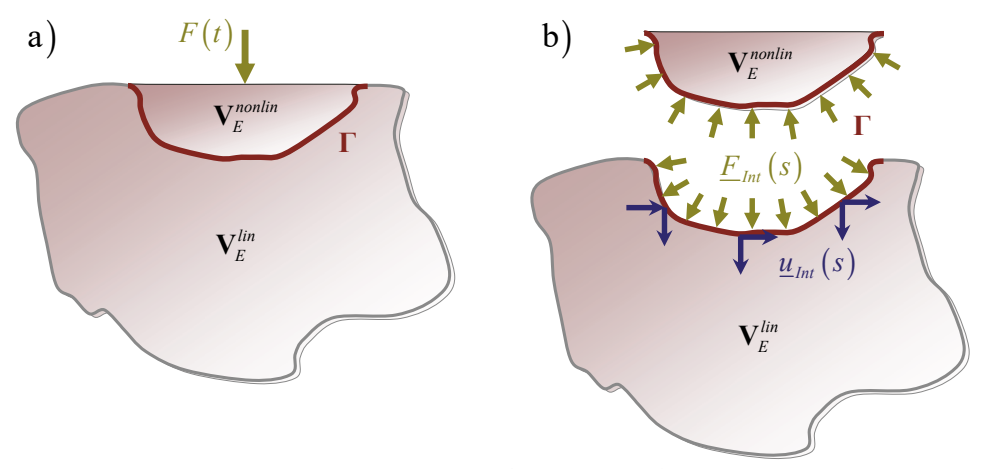


Figure 3.1: a) A dynamic load applied to a medium; b) Laplace domain force-displacement relation at the interface between the linear and nonlinear domains of the medium.

the stiffness. In dynamics, the relation between an applied dynamic force and the corresponding displacement response is commonly described in the frequency or, as implemented in this thesis, in the Laplace domain by a force-displacement ratio known as the dynamic stiffness. For a pointwise contact between two one-dimensional media, this scalar relation reads:

$$\tilde{F}_{Int}(s) = -\tilde{\chi}(s)\,\tilde{u}_{Int}(s) \tag{3.1}$$

Here, the tilde over a variable denotes a variable in the Laplace domain and s is the complex-valued Laplace parameter, so that $\tilde{F}_{lnt}(s)$ and $\tilde{u}_{lnt}(s)$ respectively denote the force on and the displacement of the interface in the Laplace domain, and $\tilde{\chi}(s)$ is the dynamic stiffness.

For two-dimensional and three-dimensional media, the interface between any two systems is respectively described by a line and a plane. In the particular case where at least one of the two involved systems is a discrete particle system, the interface between the two systems is described by a set of points, either along a line or along a plane. The forces on, and the displacements of, the interface Γ due to the dynamic interaction of a linear and a nonlinear system are depicted in Figure 3.1b for the two-dimensional case. The Laplace domain force-displacement relation at the interface of any two systems in either two- or three-dimensional space may be described by the dynamic stiffness matrix:

$$\underline{\underline{\tilde{F}}}_{Int}(s) = -\underline{\underline{\tilde{\chi}}}(s)\underline{\tilde{u}}_{Int}(s) \tag{3.2}$$

Here, $\underline{\tilde{F}}_{Int}(s)$ and $\underline{\tilde{u}}_{Int}(s)$ are force and displacement vectors that respectively contain the forces applied at, and the displacements of, the set of points along the interface.

As stated at the beginning of this section, the force-displacement relation described by the dynamic stiffness may alternatively be described by its inverse known as the dynamic compliance. The dynamic compliance generally describes the Laplace domain force-displacement relation in terms of the displacement at an interface $\tilde{u}_{Int}(s)$ and the force at that interface $\tilde{F}_{Int}(s)$ as:

$$\tilde{u}_{lnt}(s) = -\tilde{\beta}(s)\tilde{F}_{lnt}(s) \tag{3.3}$$

The dynamic compliance $\tilde{\beta}(s)$ is either a scalar or a matrix depending on the dimensions of the system considered and is the inverse of the dynamic stiffness.

For many one-dimensional systems, expressions for both the dynamic stiffness and the dynamic compliance can be derived analytically from classical elastodynamics. In some rare cases the corresponding time domain expressions can also be derived analytically, but in most cases these time domain relations must be evaluated numerically. In this thesis, we will derive analytical expressions for the dynamic stiffness and dynamic compliance for several of these one-dimensional systems. Additionally, we will show that for the numerical evaluation of these systems the use of the dynamic compliance is generally preferred over the use of the dynamic stiffness.

For two- and three-dimensional systems, there are some rare occasions where analytical expressions for the dynamic stiffness and dynamic compliance relations can be derived from known analytical expressions for the Green's functions. Generally however, numerical boundary methods are required to obtain the dynamic stiffness and compliance matrices. For the two-dimensional continua discussed in Sections 3.5 and 3.6, we derive these dynamic stiffness and compliance matrices by means of the indirect Boundary Element Method starting from the dynamic reciprocal work theorem [de Hoop, 1966].

3.2 The one-dimensional discrete-continuous BKV system

As an example of a medium that describes the behaviour near a load source by a nonlinear model, while at an appropriate distance the behaviour is described linearly, in this section we describe the near field as a one-dimensional lattice composed of nonlinear BKV elements, while the far field is described by a semi-infinite viscoelastic rod. The resulting one-dimensional discrete-continuous system is depicted in Figure 3.2. The one-dimensional BKV lattice consists of N particles and N-1 BKV elements, where each particle n has a mass M^n and the distance between any two adjacent particles is denoted as ℓ . The semi-infinite viscoelastic rod has a density ρ , cross-section area A, Young's modulus E and damping coefficient ζ_e . The one-dimensional BKV lattice and the semi-infinite viscoelastic rod are connected at the particle N, which is fixed to the viscoelastic rod at coordinate $x = x_{Int}$. The semi-infinite viscoelastic rod must be located at such a distance from the applied load F(t), that nonlinear phenomena occur only in the one-dimensional BKV lattice and do not reach the rod. Therefore, the number of particles N is chosen large enough to assure that no sliding occurs in the BKV element between particles N-1 and N. In accordance with the designation of particles and cells in the hexagonal lattice as introduced in Section 2.4, we respectively refer to particle 1, at the tip of the BKV system, and particle N, at the lattice-rod interface, as the surface particle and the boundary particle.

The equation of motion for the semi-infinite viscoelastic rod is the commonly known one-dimensional wave equation in which the Young's modulus E is replaced by the so-called dynamic modulus of elasticity \hat{E} , which describes the viscoelastic behaviour of the rod through the operator $\hat{E} = E\left(1 + \zeta_e \frac{\partial}{\partial t}\right)$. The one-dimensional wave equation for the viscoelastic rod may thus be written as:

$$\rho A\ddot{u}(x,t) - EA\zeta_e \dot{u}''(x,t) - EAu''(x,t) = 0$$
(3.4)

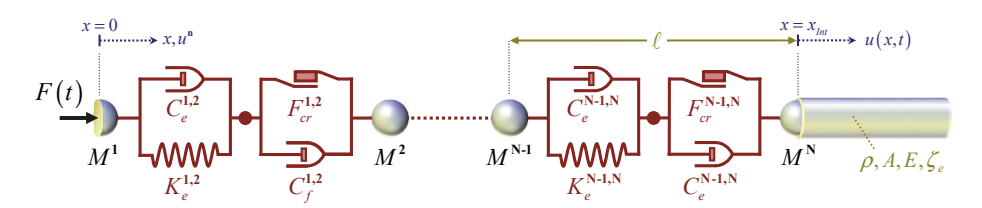


Figure 3.2: The one-dimensional semi-infinite discrete-continuous BKV system.

Here, u(x,t) is the axial displacement in the semi-infinite rod at a coordinate x, where $x > x_{lnt}$, and ζ_e is a coefficient that describes the viscous material damping in the rod. Furthermore, Newton's or dot notation is used for differentiation to time and Lagrange's notation, or prime notation, is used for differentiation to space.

The interaction between the semi-infinite viscoelastic rod and the lattice is described by two interface conditions respectively describing the balance of forces and the displacement continuity at the lattice-rod interface. Here, the force that the lattice applies upon the semi-infinite rod follows from the equation of motion of particle **N** excluding the rod, while the force that the rod applies upon the lattice is given by the normal force at the tip of the rod. The two interface conditions at the lattice-continuum interface at coordinate $x = x_{lnt}$ thus read:

$$M^{N}\ddot{u}^{N} + C_{e}^{N-1,N}\dot{e}^{N-1,N} + K_{e}^{N-1,N}e^{N-1,N} = EA\zeta_{e}\dot{u}'(x_{lnt},t) + EAu'(x_{lnt},t)$$
(3.5)

$$u^{N} = u(x_{lnt}, t) \tag{3.6}$$

Here, $e^{N-1,N}$ and $\dot{e}^{N-1,N}$ are respectively the elongation and the elongation rate of the BKV element between particles **N-1** and **N** as defined by equation (2.4). Note here that the elongation constant $\varepsilon_B^{N-1,N}$ of the Bingham element between particles **N-1** and **N** is omitted because the involved BKV element is not allowed to behave nonlinearly and the Bingham element may therefore not be activated.

In the following, we will first discuss the relations between the parameters of the one-dimensional BKV lattice and the viscoelastic rod that allow us to consider the one-dimensional discrete-continuous system as a homogeneous system at low frequencies. Subsequently, in Section 3.2.2, we will derive the dynamic stiffness for the viscoelastic rod as well as a Laplace domain boundary relation that describes the reaction of the viscoelastic rod to the motion of the boundary particle. Then, the corresponding time domain relations are derived in Section 3.2.3 and the governing system of equations of motion is presented in Section 3.2.4. Finally, we will discuss the resulting longitudinal response of the one-dimensional discrete-continuous BKV system to an arbitrary applied dynamic load in Section 3.2.5.

3.2.1 Matching the parameters of the lattice and the continuous rod

To correctly describe the behaviour of a homogeneous medium that is partly modelled by a lattice and partly by a continuum, any waves propagating through the medium should ideally not be aware of the interface between the lattice and the continuum. Their interaction must thus be such that waves do not reflect at the lattice-continuum interface, or any reflections that do occur should at least be minimal. Since we model the viscoelastic rod to be semi-infinite, the ideal lattice-continuum interface is silent and the viscoelastic rod should provide a non-reflective boundary to the one-dimensional lattice.

In the one-dimensional BKV lattice, previously discussed in Section 2.3, the parameters of the particles and rheological elements are associated with particle numbers to allow us to differentiate the material parameters along the lattice. Even though both lattice and

continuum represent the same material and must principally have the same physical properties, the one-dimensional BKV lattice allows for nonlinearities and therefore a certain variability of the parameters along the lattice is allowed for. However, to minimize any wave reflections, the one-dimensional discrete-continuous BKV system comprised of lattice and rod together must be homogeneous in the region of the lattice-continuum interface. Therefore, close to the interface, the BKV lattice must be linear and the mass of the lattice particles, as well as the stiffness and the damping of the involved BKV elements, with the exception of any particle or element directly located at the interface, are constant and respectively denoted as M, K_e and C_e . The relations between these constant parameters of the one-dimensional BKV lattice and the material properties of the viscoelastic rod are found noting that the equations of motion for the one-dimensional BKV lattice must in the long-wave limit reduce to the equations of motion for the viscoelastic rod [Maradudin et al., 1971; Suiker et al., 2001a]. Note here that for comparison with the viscoelastic rod, only the linear behaviour of the one-dimensional BKV lattice should be considered. The equation of motion for a particle **n** in the linearly behaving one-dimensional BKV lattice may therefore be obtained from equation (2.10) by assuming that all BKV elements always remain in stick. This means that the Bingham elements are not activated and their elongation-constants, denoted in equation (2.10) as $\varepsilon_B^{n-1,n}$ and $\varepsilon_B^{n,n+1}$, are equal to zero at all times and may be omitted. By considering the long-wave limit, we assume small elongations and may use the expression for the elongations of the BKV elements according to Appendix A.1. The equation of motion for a particle **n** in the linearly behaving homogeneous one-dimensional BKV lattice thus reads:

$$M\ddot{u}^{n} + C_{e} \left(2\dot{u}^{n} - \dot{u}^{n-1} - \dot{u}^{n+1} \right) + K_{e} \left(2u^{n} - u^{n-1} - u^{n+1} \right) = 0$$
(3.7)

To obtain the behaviour in the long-wave limit, we continualize the above homogeneous equation of motion by replacing the particle displacement u^n by a displacement u(x,t) and subsequently applying a Taylor series expansion with respect to this displacement. The displacements u^{n-1} and u^{n+1} of adjacent particles n-1 and n+1 are then replaced by second order Taylor polynomials of the displacement u(x,t), and read:

$$u^{n\pm 1} = u(x \pm \ell, t) = u(x, t) \pm \ell u'(x, t) + \frac{\ell^2}{2} u''(x, t).$$

Here, ℓ is the distance between two adjacent particles in the one-dimensional BKV lattice. The Taylor expansion of the homogeneous equation for particle \mathbf{n} yields the equations of motion for the linearly behaving homogeneous one-dimensional BKV lattice in the long-wave limit as:

$$M\ddot{u}(x,t) - C_e \ell^2 \dot{u}''(x,t) - K_e \ell^2 u''(x,t) = 0$$
 (3.8)

As the lattice and the rod describe the same homogeneous medium, their mass per unit length

must be equal. From the geometry of the discrete-continuous system depicted in Figure 3.3, it follows that the mass per unit length in the lattice and the rod match when $M = \rho A \ell$. Thus, the one-dimensional wave equation for the viscoelastic rod, given by equation (3.4), and the equation of motion for the homogeneous one-dimensional BKV lattice in the long-wave limit, given by equation (3.8), coincide when the following relations are satisfied:

$$M = \rho A \ell, \quad C_e = \zeta_e \frac{EA}{\ell}, \quad K_e = \frac{EA}{\ell}.$$
 (3.9)

Note here that the coefficient ζ_e , which was originally introduced to describe the material damping of the viscoelastic rod, can also be used to relate the damping and stiffness of the rheological elements in the one-dimensional BKV lattice.

By choosing the tip of the rod, and thus the point of interaction between the lattice and the viscoelastic rod, to be located at a particle as depicted in Figure 3.3a, both the surface and the boundary particle $\bf N$ geometrically only represent half the unit length. To maintain a homogeneous distribution of the mass along the lattice, the masses M^1 and M^N of respectively the surface and the boundary particle are half the mass of a particle $\bf n$ in the interior of the one-dimensional lattice. Due to this distribution of the particles along the lattice, the properties of all rheological elements in the one-dimensional lattice are equal.

Alternatively, as depicted in Figure 3.3b, we may also choose to distribute the lattice particles along the one-dimensional lattice such that the masses of all particles are equal. In that case, there will not be a particle at the tip of the one-dimensional system, nor at the lattice-rod interface. It then follows from the geometry of the lattice that the lengths of the rheological elements at the tip of the system and at the lattice-rod interface are equal to half the unit length, i.e. $\frac{1}{2}\ell$. For the tip and interface elements to behave in accordance with the rheological elements in the interior of the one-dimensional lattice, the stiffness and damping of these elements must be twice the stiffness and damping of the interior elements. This can be straightforwardly verified by comparing the behaviour of two of these half-springs in

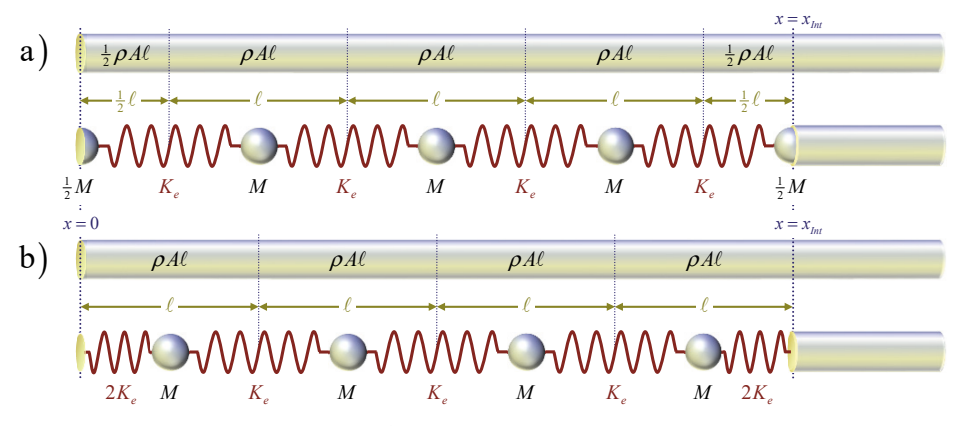


Figure 3.3: Distribution of particles along the one-dimensional lattice, where: a) all springs have equal properties; b) all particles have equal masses.

series, each with a length $\frac{1}{2}\ell$, with the behaviour of a single spring with length ℓ . Here, note that due to a lack of a mass and thus a lack of inertia at the tip of the system, any force applied at this tip yields an equal reaction force in the corresponding rheological element, thereby applying the same force on the first, i.e. leftmost, particle. Applying a load at the tip of the system depicted in Figure 3.3b, is thus equivalent to applying that load at the first particle.

The above is confirmed by Metrikine et al. [2014], where the wave reflection at the interface between a semi-infinite one-dimensional Hooke lattice and a semi-infinite linear-elastic rod is considered. In this contribution, it is shown that there will be no reflection in the long-wave limit as long as the stiffness of the spring at the interface, denoted as $K_e^{\rm N-I,N}$, and the mass of the boundary particle $M^{\rm N}$ satisfy the following relation:

$$K_e^{N-I,N} = \frac{2K_e M}{M + 2M^N}$$
 (3.10)

Equation (3.10) gives the relation between the spring stiffness and the interface mass at the interface in its dimensional form, while in the original contribution by Metrikine et al. [2014], this relation is given in its dimensionless form.

The two alternatives depicted in Figure 3.3a and in Figure 3.3b respectively assume either that $M^{\rm N}=\frac{1}{2}M$ and $K_e^{\rm N-1,N}=K_e$, or that $M^{\rm N}=0$ and $K_e^{\rm N-1,N}=2K_e$. Both suggested combinations of mass and stiffness at the lattice-continuum interface satisfy equation (3.10), but it should be noted that these are only two particular cases and, depending on the properties of the considered one-dimensional continuum, other combinations of these parameters may be more appropriate. Metrikine et al. [2014] for example show that for a system consisting of a one-dimensional Hooke lattice and a one-dimensional undamped second-order gradient continuum, minimal reflection in the long-wave limit is achieved for $M^{\rm N}=0.4079M$ and $K_e^{\rm N-1,N}=1.1014K_e$.

The reflection and transmission of waves at the discrete-continuous interface is further discussed in Section 3.3 for several one-dimensional discrete-continuous media.

3.2.2 Dimensionless boundary equation in the Laplace domain

To consider the fundamental properties of the discrete-continuous BKV system, we normalize it by introducing the following dimensionless parameters as derived in Appendix B.1:

$$t = t_{\text{dim}}\omega_0, \quad u^{\mathbf{n}} = \frac{u_{\text{dim}}^{\mathbf{n}}}{\ell}, \quad M^{\mathbf{n}} = \frac{M_{\text{dim}}^{\mathbf{n}}}{\rho A \ell}, \quad \zeta = \frac{1}{2}\zeta_e\omega_0, \quad C_e^{\mathbf{n},\mathbf{n}+1} = \frac{C_{e;\text{dim}}^{\mathbf{n},\mathbf{n}+1}}{C_{crit}}, \quad K_e^{\mathbf{n},\mathbf{n}+1} = \frac{K_{e;\text{dim}}^{\mathbf{n},\mathbf{n}+1}\ell}{2EA}.$$

Here, ω_0 and C_{crit} are respectively the so-called particle frequency and critical particle damping of the homogeneous one-dimensional BKV lattice in its linear regime that respectively describe the natural frequency and the critical damping of the lattice particles for the case that the motion of its adjacent particles is impeded. As derived in Appendix B.4, the particle frequency and critical particle damping of the homogeneous one-dimensional viscoelastic lattice are respectively obtained as $\omega_0 = \sqrt{2K_e/M}$ and $C_{crit} = M\omega_0$. Furthermore, ζ is the

damping ratio of the one-dimensional BKV lattice in its linear regime, so that $\zeta = C_e/C_{crit}$. To keep the number of variables in this thesis to a minimum, the same notations are adopted for both dimensional and dimensionless variables. In their direct relations however, the dimensional variables are given the subscript dim.

Using the above dimensionless variables, the dimensionless wave equation for the viscoelastic rod, valid only for $x > x_{Int}$, and the two dimensionless interface conditions, respectively describing the force equilibrium and the displacement continuity at the lattice-continuum interface, previously described by equations (3.4) to (3.6) respectively, now read:

$$\ddot{u}(x,t) - \zeta \dot{u}''(x,t) - \frac{1}{2}u''(x,t) = 0 \tag{3.11}$$

$$M^{N} \ddot{u}^{N} + C_{e}^{N-1,N} \dot{e}^{N-1,N} + K_{e}^{N-1,N} e^{N-1,N} = \zeta \dot{u}'(x_{lnt},t) + \frac{1}{2} u'(x_{lnt},t)$$
(3.12)

$$u^{N} = u(x_{lnt}, t) \tag{3.13}$$

To determine the dynamic stiffness of the rod, we apply the Laplace integral transform with respect to time assuming zero initial conditions. This yields equations (3.11) to (3.13) in the Laplace domain as:

$$s^{2}\tilde{u}(x,s) - \frac{1}{2}(1 + 2\zeta s)\tilde{u}''(x,s) = 0 \tag{3.14}$$

$$M^{N} s^{2} \tilde{u}^{N} + \left(C_{e}^{N-1,N} s + K_{e}^{N-1,N}\right) \tilde{e}^{N-1,N} = \frac{1}{2} (1 + 2\zeta s) \tilde{u}'(x_{lnt}, s)$$
(3.15)

$$\tilde{u}^{N} = \tilde{u}\left(x_{lnt}, s\right) \tag{3.16}$$

Introducing $s_{\zeta} = s/\sqrt{1+2\zeta s}$, the general solution to equation (3.14) reads:

$$\tilde{u}(x,s) = A_1 e^{-s_{\varsigma}\sqrt{2}x} + A_2 e^{+s_{\varsigma}\sqrt{2}x} \tag{3.17}$$

Here, A_1 and A_2 are unknowns that follow from the rod's boundary conditions. Since the complex-valued Laplace parameter s in terms of the dimensionless frequency Ω is known as $s = i\Omega + \sigma$ and σ is a small positive real value, it follows that Re(s) > 0. Then, the damping ratio ζ is by definition positive and real, so that $\text{Re}(1+2\zeta s) > 0$. If we then choose the square root in s_{ζ} such that its real part is positive, i.e. $\text{Re}(\sqrt{1+2\zeta s}) > 0$, it can be proven mathematically that the real part of s_{ζ} is also always positive, i.e. $\text{Re}(s_{\zeta}) > 0$. Thereby, the first term in equation (3.17) satisfies the infinity condition, i.e. the wave amplitude decays with increasing distance from the source, while the second term does not. Thus, by requiring that the displacement $\tilde{u}(x,s)$ must be zero at a positive infinite distance from the interface, the general solution to equation (3.14) becomes:

$$\tilde{u}(x,s) = A_1 e^{-s\zeta\sqrt{2}x} \tag{3.18}$$

Here, the amplitude A_1 is not relevant for the dynamic stiffness of the rod, because the

derivative of equation (3.18) with respect to space at $x = x_{lnt}$ may be expressed as:

$$\tilde{u}'(x_{lnt},s) = -s_{\mathcal{L}}\sqrt{2}A_{l}e^{-s_{\mathcal{L}}\sqrt{2}x_{lnt}} = -s_{\mathcal{L}}\sqrt{2}\tilde{u}(x_{lnt},s)$$
(3.19)

Substituting the interface displacement relation (3.16) into equation (3.19) and subsequently substituting the remainder into equation (3.15) allows us to express the equation of motion of particle N at the one-dimensional lattice-continuum interface in the Laplace domain as:

$$M^{N} s^{2} \tilde{u}^{N} + \left(C_{e}^{N-1,N} s + K_{e}^{N-1,N}\right) \tilde{e}^{N-1,N} + \tilde{\chi}(s) \tilde{u}^{N} = 0$$
(3.20)

Here, the dynamic stiffness $\tilde{\chi}(s)$ for the viscoelastic rod is found as:

$$\tilde{\chi}(s) = \frac{1}{2}s_{\zeta}\sqrt{2}\left(1 + 2\zeta s\right) = \frac{1}{2}s\sqrt{2 + 4\zeta s} \tag{3.21}$$

Equation (3.20) is the Laplace domain boundary formulation that describes the interaction between the one-dimensional BKV lattice and the viscoelastic rod at their interface. Herein, the behaviour and the properties of the viscoelastic rod are effectively represented by the dynamic stiffness as given by equation (3.21). This dynamic stiffness is in turn derived from the boundary value problem for the semi-infinite viscoelastic rod at the interface between lattice and rod such that the response of the rod, i.e. the linear far-field domain, does not separately have to be accounted for.

3.2.3 Governing boundary integral equation in the time domain

Applying the inverse Laplace integral transform to the force-displacement relation (3.20) yields the equation of motion for the boundary particle N in the time domain as:

$$M^{N}\ddot{u}^{N} + C_{e}^{N-1,N}\dot{e}^{N-1,N} + K_{e}^{N-1,N}e^{N-1,N} + \int_{0}^{t} \chi(t-\tau)u^{N}(\tau)d\tau = 0$$
(3.22)

In few cases, the time domain function $\chi(t)$, found as the inverse Laplace transform of the dynamic stiffness, can be derived analytically. For example, for the linear-elastic rod, discussed in Appendix D.1, the dynamic stiffness is found as $\tilde{\chi}(s) = \frac{1}{2} s \sqrt{2}$. In the time domain, the linear-elastic rod may therefore be considered as a dashpot with a dimensionless damping coefficient $C_{rod} = \frac{1}{2} \sqrt{2}$ and the corresponding boundary formulation becomes an ordinary differential equation. For the viscoelastic rod however, the time domain function $\chi(t)$ cannot be derived analytically and must be obtained numerically instead.

Application of the inverse Laplace transform requires integration over the semi-infinite domain of the Laplace parameter *s* and thus, to obtain the inverse Laplace transform numerically, we truncate its domain of integration. Truncating the domain of integration of any integral, is only allowed if the integrand properly converges within the truncated domain.

Ergo, noting the dependency of the Laplace parameter on frequency, we can only directly apply the inverse Laplace transform numerically if the dynamic stiffness $\tilde{\chi}(s)$ decreases sufficiently fast for increasing frequencies, and as depicted by Figure 3.4a, the dynamic stiffness given by equation (3.21) grows with frequency. Here note that for some cases, the inverse Laplace transform may still be evaluated numerically, but only if we are able to subtract an expression from the dynamic stiffness for which the inverse transform may be obtained analytically, and the remaining integrand converges within the truncated domain. For the dynamic stiffness of the viscoelastic rod however, at least to the knowledge of the author of this thesis, such an expression is not available.

To overcome this, we divide the equation of motion for particle **N** at the one-dimensional lattice-continuum interface in the Laplace domain, given by equation (3.20), by the dynamic stiffness $\tilde{\chi}(s)$. This yields the interface equation of motion as:

$$\tilde{u}^{N} + \tilde{\beta}(s) \left\{ M^{N} s^{2} \tilde{u}^{N} + \left(C_{e}^{N-1,N} s + K_{e}^{N-1,N} \right) \tilde{e}^{N-1,N} \right\} = 0$$
(3.23)

Here, $\tilde{\beta}(s)$ is the dynamic compliance of the viscoelastic rod, which is the inverse of the dynamic stiffness $\tilde{\chi}(s)$ given by equation (3.21), and is found for the viscoelastic rod as:

$$\tilde{\beta}(s) = \frac{2}{s\sqrt{2+4\zeta s}} \tag{3.24}$$

The dynamic compliance of the semi-infinite viscoelastic rod, given by equation (3.24), is depicted in Figure 3.4b as a function of dimensionless frequency by substituting $s = i\Omega$ for an arbitrary damping ratio $\zeta = 0.5$. Figure 3.4 shows that while the dynamic stiffness increases for increasing frequencies, the dynamic compliance decreases and tends to zero for increasing frequencies.

Applying the inverse Laplace transform to equation (3.23) now yields the equation of motion for the particle **N** in the time domain, i.e. the boundary integral equation, as:

$$u^{N} + \int_{0}^{t} \beta(t-\tau) \left\{ M^{N} \ddot{u}^{N} + C_{e}^{N-1,N} \dot{e}^{N-1,N} + K_{e}^{N-1,N} e^{N-1,N} \right\} (\tau) d\tau = 0$$
(3.25)

Although we are unable to obtain a time domain expression from the dynamic stiffness given by equation (3.21) analytically, we can analytically obtain a time domain expression by applying the inverse Laplace transform to the expression for the dynamic compliance $\tilde{\beta}(s)$ given by equation (3.24). Within the domain of the integral in equation (3.25), this yields:

$$\beta(t) = \sqrt{2}\operatorname{erf}\sqrt{\frac{t}{2\zeta}} \tag{3.26}$$

Here, erf(...) is the error function, or Gauss error function.

To include equation (3.25) in an explicit system of ordinary differential equations that can be evaluated numerically, we isolate the terms that describe the acceleration of particle **N** at time t. Solving the convolution integral in equation (3.25) by for example using the trapezium rule, or any higher order quadrature rule, we can isolate the acceleration term \ddot{u}^N at the current time t. This acceleration term is then multiplied by the time domain expression for the dynamic compliance $\beta(t-\tau)$ at $\tau=t$, i.e. $\beta(t=0)$. Unfortunately, the value of the time domain expression for the dynamic compliance of the viscoelastic rod at t=0 follows from equation (3.26) as $\beta(t=0)=0$, so that this acceleration term is removed from equation (3.25). Instead, we therefore differentiate equation (3.25) to time. Using Leibniz' integral rule for differentiation of integrals [Abramowitz and Stegun, 1972; Woods, 1926], and taking into account that $\beta(t=0)=0$, the boundary integral equation becomes:

$$\dot{u}^{N} + \int_{0}^{t} \dot{\beta}(t-\tau) \Big\{ M^{N} \ddot{u}^{N} + C_{e}^{N-1,N} \dot{e}^{N-1,N} + K_{e}^{N-1,N} e^{N-1,N} \Big\} (\tau) d\tau = 0$$
(3.27)

Here, $\dot{\beta}(t)$ is the time derivative of the time domain expression for the dynamic compliance as given by equation (3.26), which follows directly from the definition of the error function. Within the domain of the integral in equation (3.27), the expression for $\dot{\beta}(t)$ is found as:

$$\dot{\beta}(t) = \frac{e^{-\frac{1}{2}t/\zeta}}{\sqrt{\pi\zeta t}} \tag{3.28}$$

Note here that the time derivative of the time domain expression for the dynamic compliance can be considered as a time domain expression for the (mechanical) admittance, or inversely for the (mechanical) impedance, in the sense that this expression may also be obtained as the inverse Laplace transform of a force-velocity relation in the Laplace domain. The time

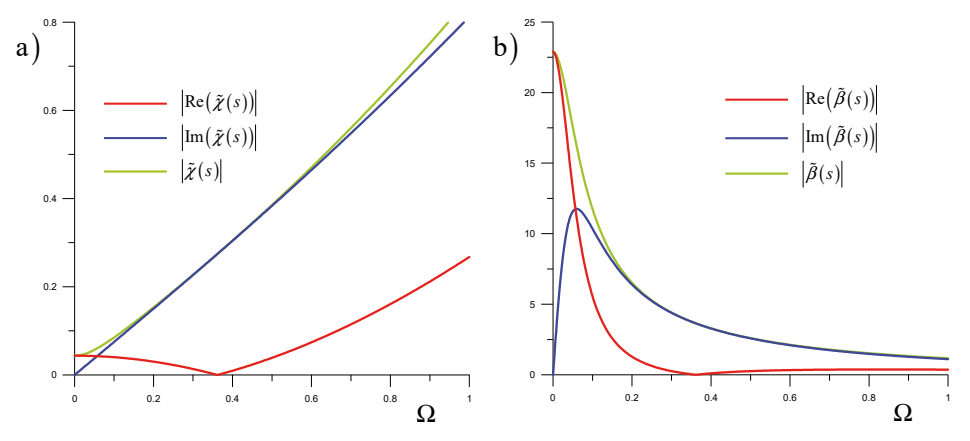


Figure 3.4: a) The dynamic stiffness of the semi-infinite viscoelastic rod; b) The dynamic compliance of the semi-infinite viscoelastic rod.

dependencies of the time domain expressions given by equation (3.26) and (3.28), which we henceforth refer to as the time domain dynamic compliance and the time domain admittance respectively, are given by Figure 3.6 in Section 3.3.1, in which the time domain dynamic compliances and admittances for several semi-infinite rods are compared.

It follows from equation (3.28) that the time domain admittance is singular at t = 0, but integrable. Thus, despite its singularity, the convolution integral in the interface equation of motion given by (3.27) may still be evaluated. To isolate the terms that describe the motion of particle N at time t, we rewrite equation (3.27) as:

$$\dot{u}^{N} + \int_{0}^{t-\Delta t} \dot{\beta}(t-\tau) F^{N}(\tau) d\tau + \int_{t-\Delta t}^{t} \dot{\beta}(t-\tau) F^{N}(\tau) d\tau = 0$$
(3.29)

Here, $F^{N}(t)$ denotes the force applied by the lattice onto the viscoelastic rod at the lattice-continuum interface, which in equation (3.27) equals the term between accolades. Furthermore, evaluating the integral on the domain $\tau = [0, t - \Delta t]$ numerically using for example the trapezium rule, where Δt is the applied time interval. The integral over the domain $\tau = [t - \Delta t, t]$ however, is solved analytically by assuming that the force $F^{N}(\tau)$ within this domain may be described as a linear function $a\tau + b$. This is well within the error of applying the trapezium rule, for which the whole integrand is assumed to be linear between any two integration points.

Substituting equation (3.28) into the rightmost term, as well as assuming the given linear function for the force $F^{N}(\tau)$ yields the equation of motion of the boundary particle N as:

$$\dot{u}^{N} + \int_{0}^{t-\Delta t} \dot{\beta}(t-\tau) F^{N}(\tau) d\tau + \int_{t-\Delta t}^{t} \frac{e^{-\frac{1}{2}(t-\tau)/\zeta}}{\sqrt{\pi \zeta(t-\tau)}} (a\tau + b) d\tau = 0$$
(3.30)

By assuming that the force is linear and found as $F^{N}(t) = at + b$, it must logically follow that at time t- Δt , the corresponding force is found as $F^{N}(t - \Delta t) = a(t - \Delta t) + b$. From this we can obtain expressions for the unknowns a and b respectively as:

$$a = \frac{F^{N}(t) - F^{N}(t - \Delta t)}{\Delta t}, \quad b = \frac{tF^{N}(t - \Delta t) - (t - \Delta t)F^{N}(t)}{\Delta t}.$$

Substituting the above expressions for the unknowns a and b into equation (3.30) and solving the rightmost integral analytically yields the equation of motion of the particle \mathbf{N} at the lattice-continuum interface in the one-dimensional discrete-continuous Kelvin-Voigt system as:

$$\dot{u}^{N} + B_{1} \left(M^{N} \ddot{u}^{N} + C_{e}^{N-1,N} \dot{e}^{N-1,N} + K_{e}^{N-1,N} e^{N-1,N} \right) + B_{2} F^{N} \left(t - \Delta t \right) + \int_{0}^{t-\Delta t} \dot{\beta} \left(t - \tau \right) F^{N} \left(\tau \right) d\tau = 0$$
 (3.31)

Here, the terms B_1 and B_2 are respectively found as:

$$B_1 = \sqrt{2}\operatorname{erf}\sqrt{\frac{\Delta t}{2\zeta}} - B_2, \quad B_2 = \frac{\zeta\sqrt{2}}{\Delta t}\operatorname{erf}\sqrt{\frac{\Delta t}{2\zeta}} - 2\sqrt{\frac{\zeta}{\pi\Delta t}}e^{-\frac{\Delta t}{2\zeta}}.$$

Equation (3.31) can be considered as an ordinary second-order differential equation because the term $B_2F^{N}(t-\Delta t)$, as well as the remaining integral, only consider the motion of the boundary particle **N** prior to time t and are therefore constants during the current time step.

Since the expressions for the equation of motion for the boundary particle according to equations (3.25) and (3.27) are very similar, the approach that yields the final equation of motion (3.31) from equation (3.27) may also seem applicable to equation (3.25). This however is not the case, because the time domain expression for the dynamic compliance $\beta(t-\tau)$ at $\tau=t$ in equation (3.25) is equal to zero, i.e. $\beta(t=0)=0$, so that the contribution of the integral over the domain $\tau=[t-\Delta t,t]$ is very small. In fact, compared to the contribution of the integral over the domain $\tau=[0,t-\Delta t]$, the contribution of the current time step can be considered negligible. In any system of equations of motion, even a small multiplicator of the acceleration at the current time step yields an ill-conditioned mass matrix, so that the almost negligible multiplicator of the acceleration according to equation (3.25) consequently leads to numerical instability. On the other hand, the contribution of the integral in equation (3.27) over the domain $\tau=[t-\Delta t,t]$ is significant as the time domain admittance approaches infinity in the limit of $t \to 0$, while the corresponding convolution integral over this domain is still integrable and yields a finite non-zero value.

3.2.4 Governing equations for the 1D discrete-continuous BKV system

The equations of motion for the one-dimensional BKV lattice were previously derived in Section 2.3 for each of the admissible motion states separately, i.e. with respectively all elements in either one of the admissible motion states. As each BKV element in the one-dimensional BKV lattice may behave according to different motion states, we here introduce a more general version of the system of equations of motion allowing for the variation of motion states along the one-dimensional BKV lattice. Including the time-dependent force F(t) applied to particle 1, the dimensionless equations of motion for particles $\mathbf{n} = 1...\mathbf{N-1}$ are generally expressed as:

$$M^{1}\ddot{u}^{1} - C_{e}^{1,2}\dot{e}_{state}^{1,2} - K_{e}^{1,2}e_{state}^{1,2} - F_{lock}^{1,2} = F(t)$$
(3.32)

$$M^{n}\ddot{u}^{n} + F_{state}^{n-1,n} + F_{lock}^{n-1,n} - C_{e}^{n,n+1} \dot{e}_{state}^{n,n+1} - K_{e}^{n,n+1} e_{state}^{n,n+1} - F_{lock}^{n,n+1} = 0$$
(3.33)

These equations are normalized using the dimensionless parameters specified at the start of Section 3.2.2. In addition, note that the dimensionless external force is related to its dimensional counterpart as $F(t) = F_{\text{dim}}(t)/2EA$. Depending on the motion state, $e_{\text{state}}^{\mathbf{n},\mathbf{n}+1}$ gives the relevant elongation of the element between particles \mathbf{n} and $\mathbf{n}+1$ and $F_{\text{state}}^{\mathbf{n}-1,\mathbf{n}}$ describes the force that is applied to particle \mathbf{n} by the BKV element between particles $\mathbf{n}-1$ and \mathbf{n} , while $F_{lock}^{\mathbf{n}-1,\mathbf{n}}$

and $F_{lock}^{\mathbf{n},\mathbf{n}+1}$ give the forces in the parallel springs that are activated only when the corresponding BKV elements are in lock-state.

Expressions for Stick

For a BKV element between particles **n** and **n+1** that is in stick-state, we find:

$$e_{state}^{\mathbf{n},\mathbf{n}+1} = e^{\mathbf{n},\mathbf{n}+1} - \varepsilon_{R}^{\mathbf{n},\mathbf{n}+1}, \qquad F_{state}^{\mathbf{n},\mathbf{n}+1} = C_{e}^{\mathbf{n},\mathbf{n}+1} \dot{e}_{state}^{\mathbf{n},\mathbf{n}+1} + K_{e}^{\mathbf{n},\mathbf{n}+1} e_{state}^{\mathbf{n},\mathbf{n}+1}, \qquad F_{lock}^{\mathbf{n},\mathbf{n}+1} = 0.$$

Here, note that the expression for $e_{state}^{n,n+1}$ is also incorporated in the expression for $F_{state}^{n,n+1}$.

Expressions for Slip

Accordingly, for a BKV element between particles **n** and **n+1** that is in slip-state, we find:

$$e_{state}^{\mathbf{n},\mathbf{n}+1} = e_{KV}^{\mathbf{n},\mathbf{n}+1}, \qquad F_{state}^{\mathbf{n},\mathbf{n}+1} = C_f^{\mathbf{n},\mathbf{n}+1} \dot{e}_B^{\mathbf{n},\mathbf{n}+1} + F_{cr}^{\mathbf{n},\mathbf{n}+1} \operatorname{sgn} F_{Bsdin}^{\mathbf{n},\mathbf{n}+1}, \qquad F_{lock}^{\mathbf{n},\mathbf{n}+1} = 0.$$

Here, the dimensionless parameters for the damping and the critical friction force in the Bingham element are respectively related to their dimensional counterparts as:

$$C_f^{\mathbf{n},\mathbf{n}+1} = \frac{C_{f;\text{dim}}^{\mathbf{n},\mathbf{n}+1}}{C_{crit}}, \qquad F_{cr}^{\mathbf{n},\mathbf{n}+1} = \frac{F_{cr;\text{dim}}^{\mathbf{n},\mathbf{n}+1}}{2EA}.$$

For any BKV element that is in slip, the equation of motion for the corresponding slip-node must be added to the system of equations of motion. For the slip-node intermediate particles $\bf n$ and $\bf n+1$, the dimensionless equation of motion follows from equation (2.13) as:

$$C_e^{\mathbf{n},\mathbf{n}+1}\dot{e}_{KV}^{\mathbf{n},\mathbf{n}+1} + K_e^{\mathbf{n},\mathbf{n}+1}e_{KV}^{\mathbf{n},\mathbf{n}+1} - C_f^{\mathbf{n},\mathbf{n}+1}\dot{e}_B^{\mathbf{n},\mathbf{n}+1} - F_{cr}^{\mathbf{n},\mathbf{n}+1}\operatorname{sgn}F_{B:slip}^{\mathbf{n},\mathbf{n}+1} = 0$$
(3.34)

Expressions for Lock

Finally, for a BKV element between particles n and n+1 that is in lock-state, we find:

$$e_{state}^{\mathbf{n},\mathbf{n}+1} = e_{state}^{\mathbf{n},\mathbf{n}+1} - \varepsilon_B^{\mathbf{n},\mathbf{n}+1}, \qquad F_{state}^{\mathbf{n},\mathbf{n}+1} = C_e^{\mathbf{n},\mathbf{n}+1} \dot{e}_{state}^{\mathbf{n},\mathbf{n}+1} + K_e^{\mathbf{n},\mathbf{n}+1} e_{state}^{\mathbf{n},\mathbf{n}+1}, \qquad F_{lock}^{\mathbf{n},\mathbf{n}+1} = K_{lock}^{\mathbf{n},\mathbf{n}+1} \left(e^{\mathbf{n},\mathbf{n}+1} + \Delta D_0^{\mathbf{n},\mathbf{n}+1} \right).$$

Equations (3.32) to (3.34), together with the equation of motion for particle N given by equation (3.31), describe the full system of equations for the one-dimensional discrete-continuous BKV system. Note here that since the lattice must be linear in the region of the interface, the equation of motion for the boundary particle N is not subject to the variation of motion states.

3.2.5 Response of the one-dimensional discrete-continuous BKV system

Figure 3.5 shows the longitudinal response of a one-dimensional discrete-continuous BKV system consisting of 80 particles at ten consecutive time moments to an applied pulse load.

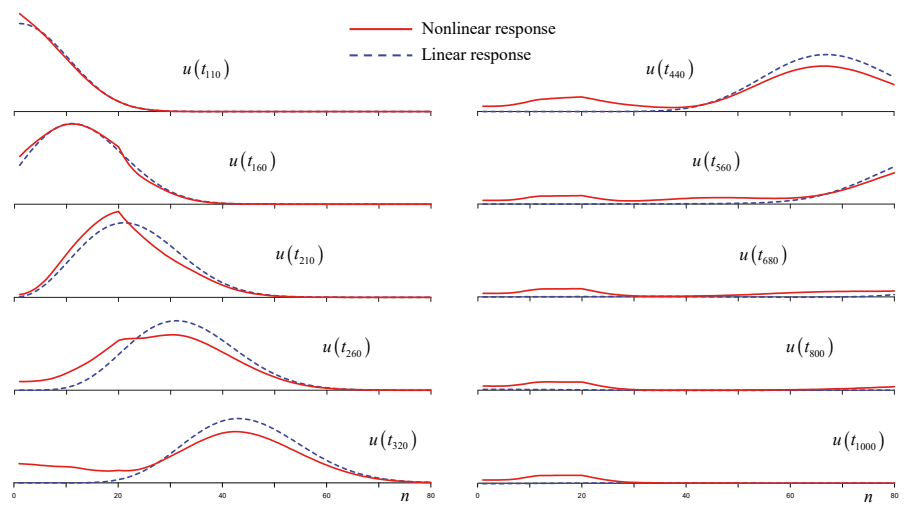


Figure 3.5: Displacement along the one-dimensional discrete-continuous BKV system at successive time moments due to a single sinus pulse load.

As stated in Section 2.5, the material properties of the one- and two-dimensional media considered in this thesis are chosen to represent a non-cohesive soft soil. The Young's modulus of the continuum is thus equal to E=20 MPa and has a mass density $\rho=2000 \, \mathrm{kg/m^3}$, so that the longitudinal wave velocity in the rod is found as $c=100 \, \mathrm{m/s}$. Additionally, the cross-sectional area of the rod follows from assuming unit second and third dimensions dy and dz, so that the cross-sectional are is equal to $A=dy\cdot dz=1 \, \mathrm{m^2}$. Furthermore, we choose a rather high damping ratio of $\zeta=0.75$ to emphasize the influence of the damping on the response of the one-dimensional discrete-continuous BKV system. Choosing the interparticle distance in the one-dimensional BKV lattice as $\ell=0.2$ m and additionally substituting the continuum material properties into equation (3.9), the mass of the particles and the stiffness of the springs in the one-dimensional BKV lattice are respectively obtained as $M=400 \, \mathrm{kg}$ and $K_e=100 \, \mathrm{MN/m}$. Consequently, the particle frequency is obtained as $\omega_0=707.1 \, \mathrm{rad/s}$ and the critical particle damping in the lattice is obtained as $C_{crit}=282.8 \, \mathrm{kNs/m}$. The given damping ratio thus corresponds to a damping coefficient $C_e=C_f=212.1 \, \mathrm{kNs/m}$ in the dashpots of the lattice.

At particle 1, a pulse load F(t) is applied that consists of a single sinus period. In its dimensionless form, this pulse load may be expressed as:

$$F(t) = \overline{F}\sin(\Omega_F t)H(T_F - t)H(t).$$

Here, \overline{F} is the dimensionless force amplitude, while Ω_F and T_F are the dimensionless angular frequency and the period of the sinus in the pulse load, respectively. The dimensional force amplitude and the angular frequency of the pulse load are chosen as $\overline{F}_{\text{dim}}=1\,\text{MN}$ and $\omega_F=80\,\text{rad/s}$ respectively. The latter corresponds to a dimensionless frequency of the sinus in the applied single-sinus pulse load of $\Omega_F=0.113$.

The dashed blue lines in Figure 3.5 show the response of the discrete-continuous BKV system, where the critical friction force of all nonlinear Bingham elements is chosen as $F_{cr} > \overline{F}$. For this situation, the Bingham elements are not activated and all BKV elements remain in stick, so that the response is exclusively viscoelastic. It can be seen from Figure 3.5 that the propagating wave is transmitted almost completely into the semi-infinite viscoelastic rod. As verified upon closer examination, there is a small reflection at the discretecontinuous interface. Due to the relatively large damping, this reflection quickly dissipates in the one-dimensional BKV system. Although the system of equations of motion for the considered BKV system involves the numerical evaluation of a convolution integral, the reflection at the discrete-continuous interface is only marginally influenced by the consequent numerical error. Instead, the reflection is largely induced by the differences between the discrete one-dimensional BKV lattice and the continuous viscoelastic rod. This can analytically be verified for an equivalent undamped system, denoted as the one-dimensional discretecontinuous Hooke system, where this reflection is more pronounced. The reflection coefficients for the discrete-continuous interface in respectively the one-dimensional Hooke and BKV systems are further discussed in Section 3.3.

The continuous red lines in Figure 3.5 show the response of the one-dimensional discrete-continuous BKV system, where the BKV elements generally have a critical friction force $F_{cr}=0.8\overline{F}$ to allow for the activation of the nonlinear Bingham elements. To amplify occurrences of nonlinear behaviour in the one-dimensional BKV lattice a segment of weak BKV elements is introduced between particles $\mathbf{n}=20...40$. For these BKV elements, the critical friction force and the damping coefficient are respectively chosen as $F_{cr}^{\mathbf{n},\mathbf{n}+1}=0.4\overline{F}$ and $C_e^{\mathbf{n},\mathbf{n}+1}=C_f^{\mathbf{n},\mathbf{n}+1}=169.7$ kNs/m . The latter corresponds to a damping ratio of $\zeta=0.6$, which is 80 percent of the damping in the other BKV elements.

Figure 3.5 shows that the wave induced by the applied pulse load is partly reflected at the weak segment of the one-dimensional BKV lattice, which is due to the different properties of the elements between particles $\mathbf{n}=20...40$. The initial wave induced by the applied pulse load, as well as the secondary wave after full reflection at particle 1, are fully transmitted into the semi-infinite viscoelastic rod. Independent of whether nonlinearities are present or not, Figure 3.5 thus shows that the wave reflection at the discrete-continuous interface is minimal. For the nonlinear response of the one-dimensional BKV system, approximately the first 30 particles remain displaced after the pulse load has passed and is dissipated from the system. These irreversible displacements testify the occurrence of nonlinear events within this domain of the one-dimensional BKV lattice. In fact, for this particular simulation, in total 108 nonlinear events occurred, which means that 108 times a BKV element within the one-dimensional BKV lattice was subject to a state-transition.

The numerical simulation to obtain Figure 3.5 was performed using Fortran, where the initial-value problem of the corresponding system of ordinary differential equations was solved with the Runge-Kutta method by means of the Fortran-library RK-suite [Brankin and Gladwell, 1997].

3.3 An evaluation of several 1D discrete-continuous systems

The preceding section extensively discusses the one-dimensional discrete-continuous BKV system, consisting of a one-dimensional BKV lattice in the near field and a semi-infinite viscoelastic rod in the far field, and the derivation of a boundary integral equation to replace the viscoelastic rod. The systems of equations of motion for equivalent one-dimensional systems that are composed of a one-dimensional Hooke or a Prandtl lattice in the near field and a linear-elastic rod in the far field, or of a one-dimensional Kelvin-Voigt lattice in the near field and a viscoelastic rod in the far field, can be straightforwardly derived from the equations for the discrete-continuous BKV system. The resulting one-dimensional semi-infinite discrete-continuous systems are individually discussed in Appendix D. Note here that Appendix D additionally considers several discrete-continuous dispersive systems, i.e. systems on an elastic foundation.

In the following, the performance of several one-dimensional semi-infinite discrete-continuous systems is evaluated and compared. First, the dynamic compliances of the involved semi-infinite rods are presented in Section 3.3.1, after which the quality of the corresponding boundary integral equations is evaluated by considering the reflection of an incident wave at the discrete-continuous interface for each of these systems in Section 3.3.2.

3.3.1 Dynamic compliances for several kinds of semi-infinite rods

The equation of motion of the boundary particle **N** in any one-dimensional discrete-continuous system considered in Appendix D can generally be described in both the Laplace and the time domains using the dynamic compliance. Therefore, we here consider the expressions for the dynamic compliance of the involved semi-infinite rods, i.e. the one-dimensional continua used to model the far-field domain in these systems, rather than using the dynamic stiffness, which in most cases is only available in the frequency or Laplace domain.

The expressions for the dynamic compliances of the considered semi-infinite rods, as well as the corresponding time domain dynamic compliances and time domain admittances are given in Table 3.1. These expressions have all been derived separately in Appendix D that regards the corresponding one-dimensional discrete-continuous systems. More specifically,

	$ ilde{eta}(s)$	$\beta(t), t \ge 0$	$\dot{\beta}(t), t \ge 0$
Linear-elastic rod	$\frac{2}{s\sqrt{2}}$	$\sqrt{2}$	0
Viscoelastic rod	$\frac{2}{s\sqrt{2+4\zeta s}}$	$\sqrt{2}\operatorname{erf}\sqrt{\frac{t}{2\zeta}}$	$\frac{e^{-\frac{1}{2}t/\xi}}{\sqrt{\pi \zeta t}}$
Linear-elastic dispersive rod	$\frac{2}{\sqrt{2(s^2 + \Omega_d^2)}}$	$\sqrt{2}J_{0}\left(\Omega_{d}t ight)$	$-\sqrt{2}\Omega_d J_1 (\Omega_d t)$
Viscoelastic dispersive rod	$\frac{2}{\sqrt{s^2 + \Omega_d^2} \sqrt{2 + 4\zeta s}}$	$\int\limits_{0}^{t}J_{0}\left(\Omega_{d}\left(t-\tau\right)\right)\frac{e^{-\frac{1}{2}\tau/\zeta}}{\sqrt{\pi\zeta\tau}}d\tau$	$\frac{e^{-\frac{1}{2}t/\xi}}{\sqrt{\pi\zetat}} - \Omega_d \int_0^t J_1\left(\Omega_d\left(t-\tau\right)\right) \frac{e^{-\frac{1}{2}\tau/\xi}}{\sqrt{\pi\zeta\tau}}d\tau$

Table 3.1: Expressions for the dynamic compliances in the Laplace domain, as well as for the time domain dynamic compliances and the time domain admittances for several semi-infinite rods.

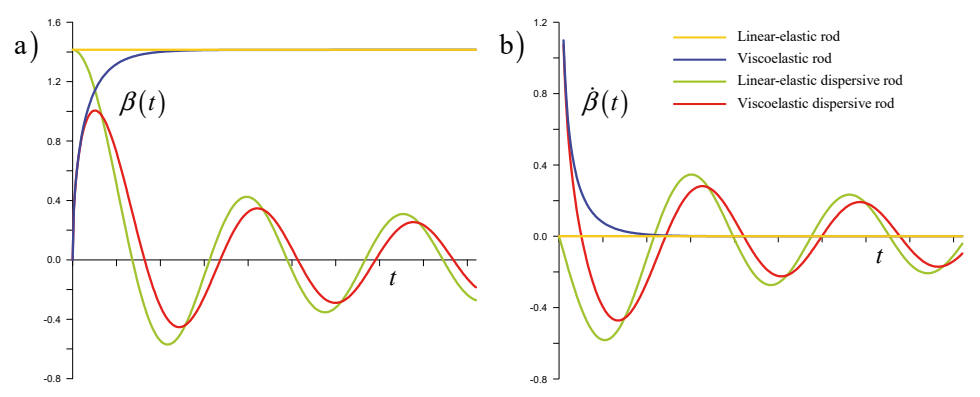


Figure 3.6: a) Time domain dynamic compliances for several semi-infinite rods; b) Time domain admittances for several semi-infinite rods.

the linear-elastic rod is featured in the one-dimensional Hooke system discussed in Appendix D.1, while the viscoelastic rod is featured in the one-dimensional BKV system previously discussed in Section 3.2. Furthermore, the so-called linear-elastic and viscoelastic dispersive rods are featured in the elastically supported one-dimensional dispersive Hooke and Kelvin-Voigt systems respectively discussed in Appendices D.2 and D.5. These semi-infinite continua are here referred to as dispersive rods because the incorporated elastic support causes the wave propagation in these rods to be dispersive.

Figure 3.6a and Figure 3.6b respectively show the time domain dynamic compliances and the time domain admittances as functions of time t for the considered semi-infinite rods. Here, the yellow lines give the constant time domain dynamic compliance and time domain admittance for the linear-elastic rod, while the blue lines give the time domain dynamic compliance and time domain admittance for the viscoelastic rod that both converge to the corresponding time domain expressions for the linear-elastic rod with time. The time domain dynamic compliances for the linear-elastic and viscoelastic dispersive rods, given in Figure 3.6 by respectively the green and red lines, both tend to zero for large $t \to \infty$. Note here that the dynamic compliances of the viscoelastic and dispersive viscoelastic rod in Figure 3.6, both obtained for an arbitrary damping ratio $\zeta = 0.75$, are equal to zero at t = 0, while the time domain admittances are infinite at t = 0.

3.3.2 Wave propagation in 1D discrete-continuous systems

The performance of the boundary integral equations derived for several linear far-field domains can be evaluated by considering the reflection and transmission of an incident wave at the interface between the near-field lattice and a continuum far field. Since the lattice response must be linear in the vicinity of the discrete-continuous interface, the performance of the boundary integral equations can be evaluated by considering fully linear systems, rather than systems that partly allow for nonlinear phenomena. In this section, we therefore consider the wave propagation in the one-dimensional discrete-continuous Kelvin-Voigt system. Figure 3.7 depicts the directions of propagation of the incident, reflected and transmitted waves in the one-dimensional Kelvin-Voigt system.

Let us assume a harmonic incident wave in the homogeneous Kelvin-Voigt lattice that propagates in the direction of the lattice-continuum interface at particle **N**. The dimensionless displacement of a particle **n** in the interior of the near-field lattice due to this incident wave may then be described as $u^{\mathbf{n}} = Ae^{i(\Omega u - \kappa \mathbf{n})}$. Here, A is the dimensionless amplitude of the incident wave, while Ω and κ are respectively the dimensionless angular frequency and the dimensionless wavenumber of the incident wave. Substituting the displacement $u^{\mathbf{n}}$ into the equation of motion for a particle in the interior of the one-dimensional Kelvin-Voigt lattice, previously given in its dimensional form by equation (3.7), yields the corresponding dispersion relation as:

$$-\Omega^2 + \left(1 + 2i\zeta\Omega\right)2\sin^2\frac{\kappa}{2} = 0\tag{3.35}$$

From this dispersion relation, the following useful relations between the dimensionless frequency Ω and dimensionless wavenumber κ can be derived:

$$\cos \kappa = 1 - \frac{\Omega^2}{1 + 2i\zeta\Omega}, \quad \sin \kappa = \frac{\Omega}{1 + 2i\zeta\Omega} \sqrt{2 + 4i\zeta\Omega - \Omega^2}.$$
 (3.36)

Equation (3.36) shows that, by incorporating damping, the relation between the dimension-less wavenumber and the dimensionless frequency is complex-valued for all nonzero frequencies, while for an undamped medium this relation is either real or imaginary depending on the frequency. The latter statement can straightforwardly be verified by substituting $\zeta = 0$ into equation (3.36). As we here consider harmonic incident waves, we assume that the angular frequency of the incident wave is real and, as a consequence, the wavenumber must be complex-valued for nonzero damping.

The incident wave may be partly reflected back into the one-dimensional lattice and partly transmitted into the linear-elastic rod. In the particular case that the linear-elastic rod is semi-infinite, the rod should ideally behave as a perfectly non-reflective boundary so that the incident wave is fully transmitted into the linear-elastic rod and no wave reflection exists. Due to the inherent differences in nature of the discrete lattice and the continuous rod however, the corresponding boundary formulation will never be ideal and a small reflection must remain. To quantify the reflection and transmission of an incident wave, we use the so-called reflection and transmission coefficients that can be described in terms of either the amplitude or the energy.

Amplitude reflection coefficient

The amplitude reflection coefficient is here defined as the ratio between the amplitudes of the reflected and the incident waves. Principally, the amplitude reflection coefficient can be obtained at any particle in the lattice, but here we specifically consider the amplitude reflection coefficient at the discrete-continuous interface and thus at the boundary particle N of the one-dimensional Kelvin-Voigt lattice.

The amplitude reflection coefficient for the wave that reflects from the discrete-continuous interface in the one-dimensional Kelvin-Voigt system may be obtained from the equation of motion for the boundary particle \mathbf{N} , previously given in the time domain by equation (3.12). As previously explained in Section 3.2.1, the dimensionless mass of the boundary particle \mathbf{N} is found as $M^{\mathbf{N}} = \frac{1}{2}$ to make sure that the discrete-continuous Kelvin-Voigt system is homogeneous and thereby assure that there is no wave reflection in the long wave limit. Accordingly, the dimensionless damping and stiffness coefficients of the Kelvin-Voigt element between particles \mathbf{N} -1 and \mathbf{N} are respectively found as $C_e^{\mathbf{N}$ -1, $\mathbf{N}} = \zeta$ and $K_e^{\mathbf{N}}$ -1, $\mathbf{N}} = \frac{1}{2}$. Rearranging equation (3.12), the equation of motion for the boundary particle \mathbf{N} in the discrete-continuous Kelvin-Voigt system thus reads:

$$\ddot{u}^{N} + 2\zeta(\dot{u}^{N} - \dot{u}^{N-1}) + u^{N} - u^{N-1} = 2\zeta\dot{u}'(x_{Int}, t) + u'(x_{Int}, t)$$
(3.37)

The displacement of an arbitrary particle \mathbf{n} in the one-dimensional Kelvin-Voigt lattice is due to both the incident and the reflected waves, while the displacement along the linear-elastic rod can only be due to the transmitted wave. Assuming the incident, reflected and transmitted waves to be harmonic, we describe the displacement of a particle \mathbf{n} inside the lattice and the displacement at a coordinate x in the rod respectively as:

$$u^{\mathbf{n}} = A_{inc}e^{\mathrm{i}(\Omega t - \kappa \mathbf{n})} + A_{ref}e^{\mathrm{i}(\Omega t + \kappa \mathbf{n})}$$
(3.38)

$$u(x,t) = A_{tra}e^{i(\Omega t - \kappa_{rod}x)}$$
(3.39)

Here, A_{inc} , A_{ref} and A_{tra} are the complex amplitudes of respectively the incident, reflected and transmitted waves. Furthermore, the dimensionless angular frequency Ω is real-valued, while the dimensionless wavenumber κ of the incident and reflected waves in the lattice, as well as the dimensionless wavenumber κ_{rod} of the transmitted wave in the viscoelastic rod, are generally complex-valued. The relation between the angular frequency Ω and the wavenumber κ of the lattice is given by the dispersion relation (3.35). As shown by Appendix E.1, substituting equation (3.39) into the equation of motion for the viscoelastic rod, previously given by equation (3.11), yields the dimensionless wavenumber for the viscoelastic rod as $\kappa_{rod} = \Omega \sqrt{2} / \sqrt{1 + 2i \zeta \Omega}$. Note here that, to assure the proper wave decay for the incident, the reflected and the transmitted waves, the square roots in the expressions for the wavenumbers in the lattice and the rod are chosen such that their imaginary parts are negative, i.e. $\text{Im}(\kappa) < 0$ and $\text{Im}(\kappa_{rod}) < 0$.

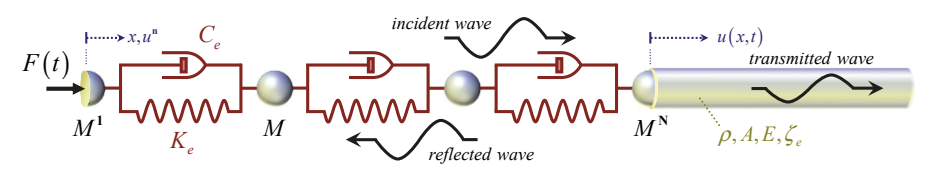


Figure 3.7: The incident, reflected and transmitted waves in the one-dimensional Kelvin-Voigt system.

Substituting equation (3.39) into equation (3.37), as well as inserting the dispersion relation for the viscoelastic rod and noting that the displacements of the lattice and the rod must be the same at the discrete-continuous interface, allows us to express the boundary equation exclusively in terms of the displacement of the boundary particle N. Then, substituting equation (3.38), employing Euler's formula and inserting the dispersion relations, as well as introducing $z = 2 + 4i\zeta\Omega$, the ratio between the amplitudes of the reflected and the incident waves may be obtained as:

$$\frac{A_{ref}e^{+i\kappa N}}{A_{linc}e^{-i\kappa N}} = \frac{\sqrt{z - \Omega^2} - \sqrt{z}}{\sqrt{z - \Omega^2} + \sqrt{z}}$$
(3.40)

Noting that A_{inc} and A_{ref} are the complex amplitudes of respectively the incident and reflected wave at the surface particle, i.e. for $\mathbf{n}=0$, it follows that $A_{inc}e^{-i\kappa\mathbf{N}}$ and $A_{ref}e^{+i\kappa\mathbf{N}}$ are the complex amplitudes of respectively the incident and reflected waves at the boundary particle \mathbf{N} . Consequently, the amplitude reflection coefficient at the boundary particle \mathbf{N} of the one-dimensional discrete-continuous Kelvin-Voigt system reads:

$$R_A^{\mathbf{N}} = \left| \frac{A_{ref}^{\mathbf{N}}}{A_{inc}^{\mathbf{N}}} \right| = \left| \frac{A_{ref} e^{+i\kappa \mathbf{N}}}{A_{inc} e^{-i\kappa \mathbf{N}}} \right| = \left| \frac{\sqrt{z - \Omega^2} - \sqrt{z}}{\sqrt{z - \Omega^2} + \sqrt{z}} \right|$$
(3.41)

The amplitude reflection coefficient R_4^N is depicted in Figure 3.8a, as a function of the dimensionless angular frequency Ω and for several values of the damping ratio ζ . Note here that for the particular case that $\zeta=0$, waves do not propagate in the one-dimensional lattice at frequencies higher than the dimensionless cutoff frequency. Appendix E.4, regarding the reflection coefficients for the corresponding linear-elastic system, shows that this cutoff frequency is found as $\Omega_{co}=\sqrt{2}$. For nonzero damping ratios, Figure 3.8a shows that the

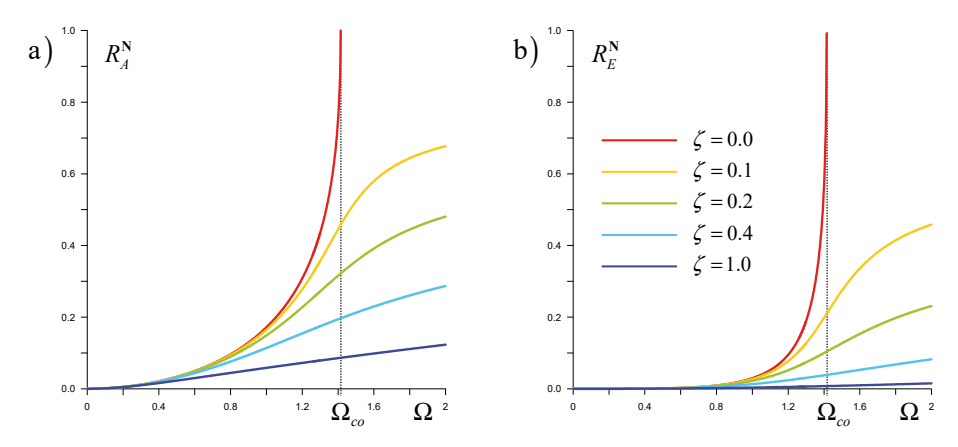


Figure 3.8: Reflection coefficients for different values of the damping ratio:
a) Amplitude reflection coefficient; b) Energy reflection coefficient.

amplitude reflection coefficients increase with frequency, while the amplitude reflection coefficients reduce with increase of the damping ratio. Figure 3.8a furthermore shows that the one-dimensional viscoelastic rod only serves as a non-reflective boundary for the one-dimensional Kelvin-Voigt lattice in the long-wave limit.

Energy reflection coefficient

For a medium without damping, the energy of an incident or a reflected wave can be determined by either considering the energy density over a domain of the medium at a certain moment in time, or by considering the energy flux at a certain point in the medium over a period of time. Due to the dissipation of energy in a medium that includes damping, the energy density along such a medium is not constant and thereby it is not straightforward to obtain the total energy of the considered wave in such a medium using the energy density. For the Kelvin-Voigt system therefore, we consider the energy flux, and define the energy reflection coefficient as the ratio between the energy fluxes over a single period of the reflected and the incident waves. Here, we specifically consider the energy reflection coefficient at the discrete-continuous interface and thus at the boundary particle N of the one-dimensional Kelvin-Voigt lattice.

It is most straightforward to separately obtain the energy fluxes due to respectively an isolated incident wave and an isolated reflected wave, rather than to attempt to obtain the energy flux when the incident and reflected wave appear simultaneously and thereby interfere. The energy flux that a Kelvin-Voigt element transfers to a particle $\bf n$ is here defined as the force in the corresponding spring multiplied by the velocity of particle $\bf n$. Thereby note that in our analysis of the energy reflection, we choose to disregard the contribution of the force in the dashpot. Thus, by considering the energy flux of an isolated incident wave as it is transferred by the Kelvin-Voigt element between particles $\bf n$ -1 and $\bf n$ to the particle $\bf n$ from the Kelvin-Voigt element between particles $\bf n$ and $\bf n$ +1, denoted as $S_{ref}^{\bf n}$, the dimensionless energy fluxes of an isolated incident and an isolated reflected wave at a particle $\bf n$ in the one-dimensional Kelvin-Voigt lattice, are respectively obtained as:

$$S_{inc}^{\mathbf{n}} = \frac{1}{2} \left(u_{inc}^{\mathbf{n}} - u_{inc}^{\mathbf{n}-\mathbf{1}} \right) \dot{u}_{inc}^{\mathbf{n}} \tag{3.42}$$

$$S_{ref}^{\mathbf{n}} = \frac{1}{2} \left(u_{ref}^{\mathbf{n}} - u_{ref}^{\mathbf{n+1}} \right) \dot{u}_{ref}^{\mathbf{n}} \tag{3.43}$$

Here, u_{inc}^{n} and u_{rej}^{n} denote the displacement of particle **n** due to respectively the isolated incident wave and the isolated reflected wave. To make sure that the expressions for these displacements are real-valued, we include displacement terms related to both the complex wavenumber κ and to its complex conjugate. Assuming the incident and reflected waves to be harmonic, these displacements are respectively described as:

$$u_{inc}^{\mathbf{n}} = \frac{1}{2} \left\{ A_{inc} e^{\mathrm{i}(\Omega t - \kappa \mathbf{n})} + \overline{A}_{inc} e^{-\mathrm{i}(\Omega t - \overline{\kappa} \mathbf{n})} \right\}$$
(3.44)

$$u_{ref}^{\mathbf{n}} = \frac{1}{2} \left\{ A_{ref} e^{i(\Omega t + \kappa \mathbf{n})} + \overline{A}_{ref} e^{-i(\Omega t + \overline{\kappa} \mathbf{n})} \right\}$$
(3.45)

Here, \overline{A}_{inc} and \overline{A}_{ref} are the complex conjugates of the amplitudes A_{inc} and A_{ref} of the incident and reflected waves respectively and $\overline{\kappa}$ is the complex conjugate of the dimensionless wavenumber κ . As the square roots in the expression for the wavenumber κ are chosen such that its imaginary part is negative, i.e. $\operatorname{Im}(\kappa) < 0$, it follows that the imaginary part of the complex conjugate wavenumber $\overline{\kappa}$ is positive, i.e. $\operatorname{Im}(\overline{\kappa}) > 0$.

Respectively substituting equations (3.44) and (3.45) into equations (3.42) and (3.43), including the dispersion relations for the wavenumber κ and its complex conjugate as derived in Appendix E.3, as well as averaging the energy fluxes over a single period of the harmonic incident wave yields the energy fluxes for the harmonic incident and reflected waves as:

$$S_{inc}^{\mathbf{n}} = \frac{1}{8} i\Omega \left(e^{+i\kappa} - e^{-i\bar{\kappa}} \right) A_{inc} \overline{A}_{inc} e^{-i(\kappa - \bar{\kappa})\mathbf{n}}$$
(3.46)

$$S_{ref}^{\mathbf{n}} = \frac{1}{8} i\Omega \left(e^{+i\kappa} - e^{-i\overline{\kappa}} \right) A_{ref} \overline{A}_{ref} e^{+i(\kappa - \overline{\kappa})\mathbf{n}}$$
(3.47)

Here, note that the particle number **n** present in the exponents in the equations above describes the decay of the wave amplitude at that particle relative to the wave amplitudes A_{inc} and A_{ref} at the tip of the system, i.e. at particle **1**. Thereby, $A_{inc}e^{-i\kappa \mathbf{n}}$ and $A_{ref}e^{+i\kappa \mathbf{n}}$ are the wave amplitudes of the incident and reflected waves at particle **n**, while $\overline{A}_{inc}e^{+i\kappa \overline{\mathbf{n}}}$ and $\overline{A}_{ref}e^{-i\kappa \overline{\mathbf{n}}}$ are the complex conjugates of the corresponding wave amplitudes at a particle **n**.

Obtaining the energy reflection coefficient as the ratio between the energy fluxes of the reflected and incident waves at the boundary particle **N** from equations (3.46) and (3.47), denoting the wave amplitudes of the incident and reflected waves at the boundary particle respectively as A_{inc}^{N} and A_{ref}^{N} , and substituting the amplitude reflection coefficient R_{A}^{N} given by equation (3.41), the energy reflection coefficient at the boundary particle **N** reads:

$$R_E^{\mathbf{N}} = \left| \frac{S_{ref}^{\mathbf{N}}}{S_{lnc}^{\mathbf{N}}} \right| = \left| \frac{A_{ref} e^{+i\kappa \mathbf{N}} \overline{A}_{ref} e^{-i\kappa \overline{\mathbf{N}}}}{A_{lnc} e^{-i\kappa \mathbf{N}} \overline{A}_{lnc} e^{+i\kappa \overline{\mathbf{N}}}} \right| = \left| \frac{A_{ref}^{\mathbf{N}}}{A_{lnc}^{\mathbf{N}}} \right|^2 = \left| \frac{2z - \Omega^2 - 2\sqrt{z}\sqrt{z - \Omega^2}}{2z - \Omega^2 + 2\sqrt{z}\sqrt{z - \Omega^2}} \right|$$
(3.48)

Figure 3.8b depicts the energy reflection coefficient R_E^N as a function of the dimensionless angular frequency Ω for several values of the damping ratio ζ . Figure 3.8b shows that the dependency of the energy reflection coefficient on the damping ratio is similar to the dependency of the amplitude reflection coefficient depicted in Figure 3.8a, so that the energy reflection coefficients reduce with an increase of the damping ratio. Figure 3.8b furthermore shows that the energy flux of the waves that are reflected by the semi-infinite viscoelastic rod are negligible for frequencies lower than half the cutoff frequency, i.e. for $\Omega < \frac{1}{2}\Omega_{co}$.

Reflection of an incident wave due to a single-sinus pulse load

To verify that the total energy of an isolated incident wave is constant while it fully resides in the Hooke lattice and that it reduces in the Kelvin-Voigt system due to the damping, Figure 3.9a shows the total energy in a one-dimensional Kelvin-Voigt lattice due to a single sinus pulse load, as a function of time for different values of the damping ratio ζ . Here, the total energy in the lattice is obtained by summation of the kinetic energy of all particles and the potential energy of all rheological elements in the lattice. The considered Kelvin-Voigt lattice consists of N = 80 particles and the single sinus pulse load is described as:

$$F(t) = \overline{F}\sin(\Omega t)H(T_F - t)H(t).$$

Here, \overline{F} , Ω and T_F are respectively the dimensionless amplitude, the dimensionless angular frequency and the dimensionless period of the sinus. The angular frequency Ω of the sinus pulse is here arbitrarily chosen as $\Omega = 0.2$.

The red line in Figure 3.9a shows that the total energy E_{tot} in the particles of the onedimensional Hooke lattice, i.e. the one-dimensional Kelvin-Voigt lattice for the particular case that $\zeta = 0$, due to the pulse load is constant and at its maximum as soon as the pulse load has stopped acting, i.e. for time $t > T_F$, and until the time t_{Int} at which the front of the incident wave reaches the discrete-continuous interface. This is exactly the time period in which the isolated incident wave resides fully inside the lattice so that the constant total energy during this period equals the energy of the isolated incident wave. Accordingly, the energy of the isolated reflected wave can be obtained as the constant total energy in the lattice during the time period in which only the reflected wave fully resides in the system. This occurs as soon as the incident wave has been fully transmitted into the linear-elastic rod, i.e. for time $t > t_{Int} + T_F$, and until the time $3t_{Int}$ at which the front of the reflected wave returns to the discrete-continuous interface and after fully reflecting from the tip of the system. Due to the absence of damping in the Hooke lattice, the ratio between the constant total energy of the isolated reflected wave and the constant total energy of the isolated incident wave gives a measure of the magnitude of the reflected energy and can thereby be considered as an energy reflection coefficient. Thus, by dividing the total energy in the lattice during the period

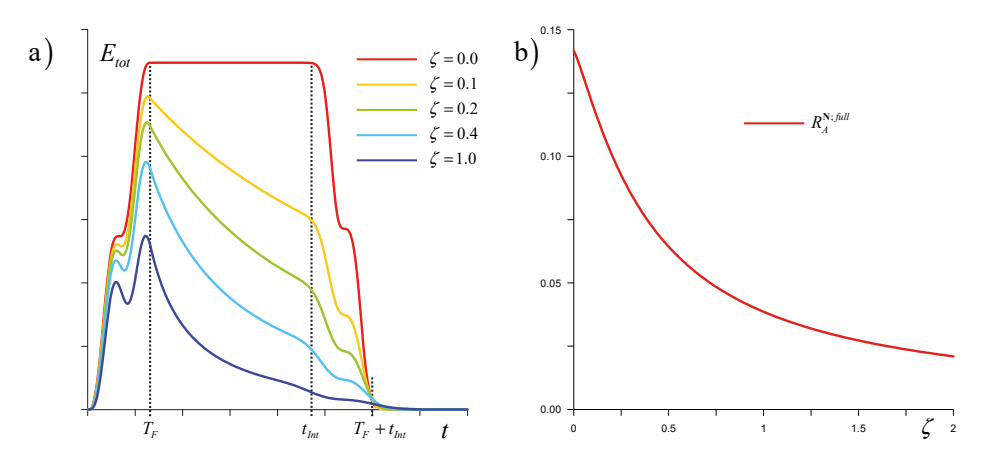


Figure 3.9: a) Total energy in the one-dimensional Kelvin-Voigt lattice over time; b) Amplitude and energy reflection coefficients of an incident wave as a function of the damping ratio.

at which the isolated reflected wave fully resides in the lattice by the total energy in the lattice during the period at which the isolated incident wave resides fully in the lattice, the energy reflection coefficient of the one-dimensional discrete-continuous Hooke system is obtained as $R_E = 4.0 \cdot 10^{-4}$.

Next to the total energy in the one-dimensional Hooke lattice, Figure 3.9a additionally depicts the total energy in the one-dimensional Kelvin-Voigt lattice as a function of time for several nonzero values of the damping ratio ζ . As opposed to the total energy in the Hooke lattice, the energy dissipation due to the damping causes the total energy in the Kelvin-Voigt lattice to clearly decay over time during the time period $t = T_F \dots t_{Int}$. And, as is to be expected, the energy dissipation during this period increases with the magnitude of the damping ratio. Furthermore it should be noted that, due to the damping, the waves do not have a sharp front. Both the energy dissipation and the absence of a sharp front make it impossible to determine an energy reflection coefficient for the discrete-continuous Kelvin-Voigt system as a ratio between the energies of the isolated incident wave and the isolated reflected wave.

The amplitude reflection coefficient for the Kelvin-Voigt system has previously been obtained as equation (3.41) by considering the energy flux at the boundary particle N for a harmonic incident wave. Whereas a harmonic incident wave is sinusoidal in time, an incident wave induced by a pulse load features a range of frequencies and this frequency spectrum should be accounted for. Although this frequency spectrum is not flat, as an upper limit, the amplitude reflection coefficient for an incident wave induced by a pulse load may be obtained by integrating the amplitude reflection coefficient for harmonic incident waves over the frequency range at which waves propagate through the Kelvin-Voigt system. Thereby, we thus assume an equal contribution to the pulse load by all frequencies within the considered range. This yields the amplitude reflection coefficient for an incident wave induced by a pulse load as a function of the damping ratio ζ as:

$$R_{A;pulse}^{N}\left(\zeta\right) = \frac{1}{\Omega_{co}} \int_{0}^{\Omega_{co}} \frac{\sqrt{z - \Omega^{2}} - \sqrt{z}}{\sqrt{z - \Omega^{2}} + \sqrt{z}} d\Omega \tag{3.49}$$

Figure 3.9b shows the resulting amplitude reflection coefficient for the discrete-continuous Kelvin-Voigt system for an incident wave due to a pulse load as a function of the damping ratio ζ .

By substituting the cutoff frequency $\Omega_{co} = \sqrt{2}$ and $\zeta = 0$, i.e. z = 2, into equation (3.49), we obtain the amplitude reflection coefficient for zero damping as $R_{A;pulse}^N(\zeta = 0) = 0.142$. Due to the existing viscous damping, there is no cutoff frequency in the one-dimensional Kelvin-Voigt system. Nevertheless, at frequencies larger than the cutoff frequency Ω_{co} , an incident wave induced by a single-sinus pulse load with a frequency $\Omega < 1$, i.e. a frequency lower than the particle frequency, may be expected to not significantly influence the motion of the discrete-continuous interface. Therefore, in Figure 3.9b, we have approximated the corresponding amplitude reflection for the one-dimensional Kelvin-Voigt system by equation (3.49) using the cutoff frequency $\Omega_{co} = \sqrt{2}$ defined for the system without damping. The

amplitude reflection coefficients due to an arbitrary dynamic load may be obtained in a more exact manner by multiplying the integrand in equation (3.49) with the frequency spectrum of the applied load.

Interference between the incident and the reflected waves

The energy reflection coefficient given by equation (3.48) describes the ratio between the energy fluxes of an isolated reflected wave and an isolated incident wave at the boundary particle **N** in the one-dimensional discrete-continuous Kelvin-Voigt system over a single period of an applied harmonic load. The incident and reflected waves due to a harmonic load applied at the tip of the Kelvin-Voigt system however, are not isolated at all, but exist simultaneously and, in the case of nonzero damping, principally interfere everywhere along the lattice. In the following, we will therefore evaluate the interference between the incident and the reflected waves in the lattice to determine whether it has a significant influence on the response of the lattice and, if so, how this interference must be accounted for in discrete-continuous systems.

To evaluate the interference between the incident and the reflected wave in the lattice near its boundary, we consider the energy exchange at the discrete-continuous interface in the one-dimensional Kelvin-Voigt system. By multiplying the balance between the forces of the lattice and the rod at their interface, i.e. the equation of motion for the boundary particle N given by equation (3.37), with the velocity of the interface, we obtain the following dimensionless energy balance that describes the energy exchange at the interface between the lattice and the rod:

$$\ddot{u}^{N}\dot{u}^{N} + 2\zeta(\dot{u}^{N} - \dot{u}^{N-1})\dot{u}^{N} + (u^{N} - u^{N-1})\dot{u}^{N} = 2\zeta\dot{u}'(x_{lnt}, t)\dot{u}(x_{lnt}, t) + u'(x_{lnt}, t)\dot{u}(x_{lnt}, t)$$
(3.50)

In the energy balance given by equation (3.50), the first term on the left-hand side describes the change in kinetic energy of the boundary particle over time, while the third term on the left-hand side gives the energy flux through the lattice-rod interface due to both the incident and the reflected wave. Accordingly, the second term on the right-hand side describes the energy flux through the lattice-rod interface due to the transmitted wave. The second term on the left-hand side and the first term on the right-hand side describe the energy dissipation due to the damping in respectively the lattice and the rod over time.

To simultaneously consider the incident, the reflected and the transmitted waves, we include components related to both the incident and the reflected waves in the expression for the displacement of the boundary particle **N**, while the displacement of the viscoelastic rod is described in terms of the transmitted wave. Furthermore, to make sure that the expressions for the displacements in the lattice and the rod are real-valued, we include displacement terms related to both the complex wavenumbers and to their complex conjugates. The displacements of the lattice particles and the viscoelastic rod therefore read:

$$u^{\mathbf{n}} = \frac{1}{2} \left\{ A_{inc} e^{\mathrm{i}(\Omega t - \kappa \mathbf{n})} + \overline{A}_{inc} e^{-\mathrm{i}(\Omega t - \overline{\kappa} \mathbf{n})} \right\} + \frac{1}{2} \left\{ A_{ref} e^{\mathrm{i}(\Omega t + \kappa \mathbf{n})} + \overline{A}_{ref} e^{-\mathrm{i}(\Omega t + \overline{\kappa} \mathbf{n})} \right\}$$
(3.51)

$$u(x,t) = \frac{1}{2} \left\{ A_{tra} e^{i(\Omega t - \kappa_{rod} x)} + \overline{A}_{tra} e^{-i(\Omega t - \overline{\kappa}_{rod} x)} \right\}$$
(3.52)

Here, the amplitudes \overline{A}_{inc} , \overline{A}_{ref} and \overline{A}_{tra} are the complex conjugates of the dimensionless amplitudes A_{inc} , A_{ref} and A_{tra} of the incident, reflected and transmitted waves respectively. Furthermore, the wavenumbers $\overline{\kappa}$ and $\overline{\kappa}_{rod}$ are the complex conjugates of the dimensionless wavenumbers κ and κ_{rod} in respectively the lattice and the viscoelastic rod.

Appendix E.5 shows that substituting equations (3.51) and (3.52) into equation (3.50), as well as averaging the energy balance over a single period of the harmonic incident wave, and introducing both $z = 2 + 4i\zeta\Omega$ and its complex conjugate $\bar{z} = 2 - 4i\zeta\Omega$, yields the energy balance at the discrete-continuous interface of the one-dimensional Kelvin-Voigt system as:

$$\left| \frac{A_{ref}^{N}}{A_{inc}^{N}} \right|^{2} + \frac{\sqrt{z - \Omega^{2}} - \sqrt{\overline{z} - \Omega^{2}}}{\sqrt{z - \Omega^{2}} + \sqrt{\overline{z} - \Omega^{2}}} \left(\frac{\overline{A}_{inc}^{N} A_{ref}^{N}}{\left| A_{inc}^{N} \right|^{2}} - \frac{A_{inc}^{N} \overline{A}_{ref}^{N}}{\left| A_{inc}^{N} \right|^{2}} \right) + \frac{\sqrt{z} + \sqrt{\overline{z}}}{\sqrt{z - \Omega^{2}} + \sqrt{\overline{z} - \Omega^{2}}} \left| \frac{A_{tra}^{x_{int}}}{A_{inc}^{N}} \right|^{2} = 1 \quad (3.53)$$

Here, $A_{inc}^{\mathbf{N}} = A_{inc}e^{-\mathrm{i}\kappa\mathbf{N}}$, $A_{ref}^{\mathbf{N}} = A_{ref}e^{+\mathrm{i}\kappa\mathbf{N}}$ and $A_{tra}^{x_{int}} = A_{tra}e^{-\mathrm{i}\kappa_{rod}x_{int}}$ are respectively the amplitudes of the incident, reflected and transmitted wave at the lattice-rod interface. Furthermore, $\overline{A}_{inc}^{\mathbf{N}} = \overline{A}_{inc}e^{+\mathrm{i}\kappa\mathbf{N}}$ and $\overline{A}_{ref}^{\mathbf{N}} = \overline{A}_{ref}e^{-\mathrm{i}\kappa\mathbf{N}}$ are the complex conjugates of the incident and reflected wave amplitudes at the lattice-rod interface respectively.

The first term in equation (3.53) exactly matches the energy reflection coefficient, as given by equation (3.48), that describes the ratio between the energy flux of the reflected wave and the energy flux of the incident wave, both obtained for isolated incident and reflected waves. As the third term in equation (3.53) in a similar manner relates the energy of the transmitted wave to the energy of the incident wave, it is safe to assume that this term describes the ratio between the energy flux of the transmitted wave and the energy flux of the incident wave. Therefore, we will refer to this term as the energy transmission coefficient. Then, as the second term in equation (3.53) includes cross terms of the amplitudes of the incident and the reflected waves, but is not related to the transmitted wave, this term can only exist when and where the incident and the reflected wave exist simultaneously, and therefore, this term must in some way be related to the interference between the incident and the reflected waves. Analysing the mathematical derivation that leads to equation (3.53), we find that this interference term partially originates from the energy flux at the lattice-rod interface due to both the incident and the reflected wave, and partially originates from the energy dissipation in the lattice. Furthermore, note that this interference term only appears in the energy balance when damping is included; for zero damping it follows that $\overline{z} = z$, so that the interference term in equation (3.53) is equal to zero. This is verified by considering the energy exchange at the lattice-rod interface for the discrete-continuous Hooke system, given in Appendix E.4, which lacks an interference term. As the interference term in equation (3.53) is expressed as a ratio versus the energy flux of the incident wave, we henceforth refer to this term as the energy interference coefficient.

To determine the magnitude of the energy contained in the interference between the

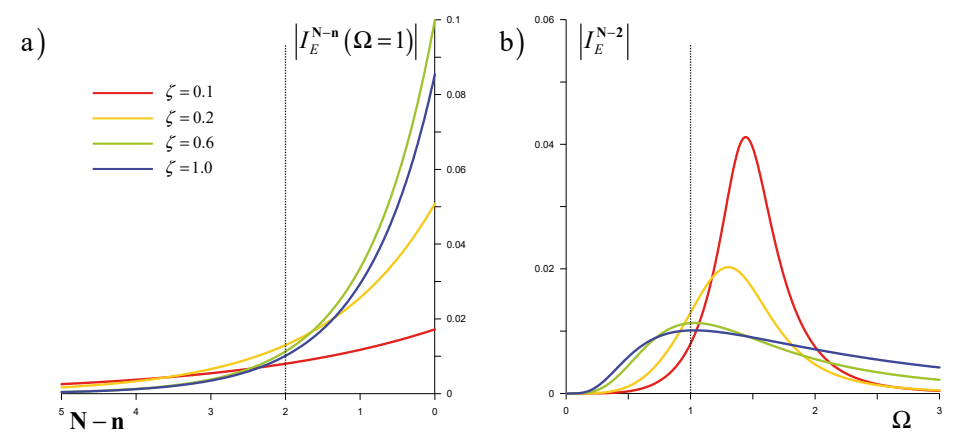


Figure 3.10: The trend of the energy interference coefficient, i.e. without oscillatory components: a) Decay with increasing distance from the boundary particle \mathbf{N} at frequency Ω =1; b) as a function of frequency at particle \mathbf{n} = \mathbf{N} -2.

incident and reflected waves and to determine where along the lattice its magnitude is significant, we express the wave amplitudes of the incident and reflected waves at a particle $\bf n$ in terms of its distance to the boundary particle $\bf N$. Thereby, the wave amplitudes of the incident and reflected waves at a particle $\bf n$ in terms of the wave amplitudes at the lattice boundary read $A_{inc}^{\bf n}=A_{inc}^{\bf N}e^{+i\kappa({\bf N}-{\bf n})}$ and $A_{ref}^{\bf n}=A_{ref}^{\bf N}e^{-i\kappa({\bf N}-{\bf n})}$. Furthermore, noting that the amplitude cross terms in equation (3.53) reduce to the amplitude ratios $A_{ref}^{\bf N}/A_{inc}^{\bf N}$ and $A_{ref}^{\bf N}/A_{inc}^{\bf N}$, for which the expressions are respectively given by equation (3.40) and derived in Appendix E.5, we can express the energy interference coefficient at a particle $\bf n$ in the Kelvin-Voigt lattice as:

$$I_{E}^{\mathbf{n}} = \frac{\sqrt{z - \Omega^{2}} - \sqrt{\overline{z} - \Omega^{2}}}{\sqrt{z - \Omega^{2}} + \sqrt{\overline{z} - \Omega^{2}}} \left(\frac{\sqrt{z - \Omega^{2}} - \sqrt{z}}{\sqrt{z - \Omega^{2}} + \sqrt{z}} e^{-2i\kappa(\mathbf{N} - \mathbf{n})} - \frac{\sqrt{\overline{z} - \Omega^{2}} - \sqrt{\overline{z}}}{\sqrt{\overline{z} - \Omega^{2}} + \sqrt{\overline{z}}} e^{+2i\overline{\kappa}(\mathbf{N} - \mathbf{n})} \right)$$
(3.54)

As noted before, the square root in the expression for the wavenumber κ is chosen such that its imaginary part is negative, i.e. $\operatorname{Im}(\kappa) < 0$, and as a consequence, the imaginary part of the complex conjugate wavenumber $\bar{\kappa}$ is positive, i.e. $\operatorname{Im}(\bar{\kappa}) > 0$. Thereby, it follows from equation (3.54) that the energy interference coefficient decays exponentially with increasing distance from the boundary particle \mathbf{N} . This is confirmed by Figure 3.10a that depicts the energy interference coefficient as a function of \mathbf{N} - \mathbf{n} , i.e. the distance between particle \mathbf{n} and the boundary particle \mathbf{N} , for different damping ratios. To obtain these results, we considered a harmonic incident wave with a frequency equal to the particle frequency, i.e. $\Omega = 1$, and removed the oscillatory components in the energy interference coefficient. Furthermore, Figure 3.10b depicts the corresponding energy interference coefficient at particle $\mathbf{n} = \mathbf{N} - 2$ as a function of the dimensionless frequency Ω . Here, note that the dashed line in Figure 3.10a denotes the case depicted by Figure 3.10b, and vice versa, the dashed line in Figure 3.10b denotes the case depicted by Figure 3.10a.

According to Figure 3.10a the reduction of the energy interference coefficient with increasing distance from the boundary appears to be proportional to the damping ratio. This

makes sense because the damping ratio determines the reduction of the amplitudes of, and thus of the energy contained in, the incident and the reflected waves during their propagation along the lattice. Figure 3.10a furthermore shows that the largest magnitude of the energy interference coefficient at the boundary particle N is found for a damping ratio $\zeta = 0.6$, while for both larger and smaller damping ratios, the magnitude of the energy interference is less. Additionally, note that the magnitude of the energy interference coefficient at the boundary particle N is significantly reduced for small damping ratios, which coincides with our previous finding that for zero damping there is no energy contained in the interference between the incident and reflected waves. Figure 3.10b however shows that the magnitude of the energy interference coefficient very much depends on the frequency of the incident wave and that, for certain frequencies, even small damping ratios may yield significant magnitudes of the energy interference coefficient. Figure 3.10b furthermore shows that by reducing the damping, the frequency spectrum of the energy interference coefficient becomes more narrow and its peak value increases. In fact, for zero damping, the frequency spectrum of the energy interference coefficient becomes infinitely narrow and infinitely large at the cutoff frequency $\Omega_{co} = \sqrt{2}$, while for all other frequencies at which waves can propagate in the undamped system, i.e. for $\Omega < \Omega_{co}$, the energy interference coefficient is equal to zero.

From the results presented by Figure 3.10, we may conclude that the energy interference is most pronounced at the boundary particle N and, due to the damping in the Kelvin-Voigt lattice, reduces with increasing distance from the boundary. To minimize the influence of the wave reflection on the nonlinear near-field response of the BKV lattice, we must account for the spatial domain of the lattice near the boundary particle N where the energy contained in the interference between the incident and reflected waves is significant. The BKV lattice should thus be considered to effectively consist of two domains: a near-field domain consisting of a lattice with BKV elements that allows for nonlinearities, and a linear domain consisting of a lattice with Kelvin-Voigt elements in the vicinity of the discrete-continuous interface. As the energy contained in the interference between the incident and the reflected wave decays exponentially with the distance from the boundary, the required size of the linear domain of the lattice is, in general, limited to only a few particles. Nevertheless, even though the energy interference at the boundary particle is limited for small damping ratios, the decay of the energy interference with increasing distance from the boundary for these small damping ratios is relatively slow and may therefore require a larger linear domain in the lattice. Furthermore, it is important to emphasize that the energy interference only occurs when there is a reflected wave present, so that the magnitude of the energy interference depends on the level of reflection from the lattice boundary and thereby depends on the chosen model for the far-field domain of the considered medium. Finally, note that in two-dimensional discretecontinuous systems, the magnitude of the energy interference may be expected to be smaller due to the geometrical damping that exist in these systems.

3.4 Wave propagation in a finite discrete-continuous system in 1D

In the preceding sections, we have exclusively considered boundary formulations for semiinfinite far-field domains that ideally behave as a silent or non-reflective boundary to the onedimensional lattice. As stated in Section 1.3, non-reflective boundaries may also be obtained using numerical techniques, such as using a perfectly matched layer (PML) [Bérenger, 1994; Kausel and de Oliveira Barbosa, 2012]. The principle of using a PML is to absorb the energy of any waves that propagate to the boundary of a medium and into the PML. Consequently, such techniques may only be applied when the wave propagation in the far-field domain is of no consequence to the response of the near-field domain. This is generally the case when the far-field domain may be considered to be infinite in the direction of wave-propagation and thereby satisfies the radiation condition. Nevertheless, if the far-field domain is not infinite, wave reflections in the far-field domain may propagate back into the near-field domain and should be accounted for. The advantage of using the boundary formulation proposed in this thesis over for example PMLs, is its capability to account for wave reflections in the far-field domain and thereby correctly model the dynamic response of a system with finite dimensions. To illustrate this, let us consider the discrete-continuous system depicted in Figure 3.11 that is composed of a one-dimensional Hooke lattice in the near field and a linear-elastic finite rod with a fixed boundary in the far field.

The dimensionless relations at the interface between the Hooke lattice and the finite linear-elastic rod are the same as the corresponding relations for the semi-infinite discrete-continuous Hooke system considered in Appendix D.1, or may alternatively be derived from the corresponding relations for the Kelvin-Voigt system, given by equations (3.14) to (3.16), by choosing the damping ratio ζ equal to zero. The difference between the finite and semi-infinite systems follows from the formulation of the general solution for the rod. For semi-infinite systems the proper behaviour of the far-field domain for $x \to \infty$ is accounted for by only considering waves propagating away from the load, while for finite systems the propagation of both incident and reflected waves must be accounted for. The general solution to the dimensionless equation of motion for the finite linear-elastic rod therefore reads:

$$\tilde{u}(x,s) = A_1 e^{+s\sqrt{2}x} + A_2 e^{-s\sqrt{2}x}$$
(3.55)

Noting that the finite linear-elastic rod is fixed at coordinate x_B , where $x_B > x_{lnt}$, we denote the dimensionless boundary conditions of the finite linear-elastic rod as:

$$M^{\mathsf{N}} s^2 \tilde{u}^{\mathsf{N}} + K_e^{\mathsf{N-1},\mathsf{N}} \tilde{e}^{\mathsf{N-1},\mathsf{N}} = -\tilde{F}^{\mathsf{N}} = \frac{1}{2} \tilde{u}'(x_{\mathit{Int}},s), \qquad \qquad \tilde{u}(x_B,s) = 0.$$

Here, the left boundary condition follows from the force equilibrium at the discrete-

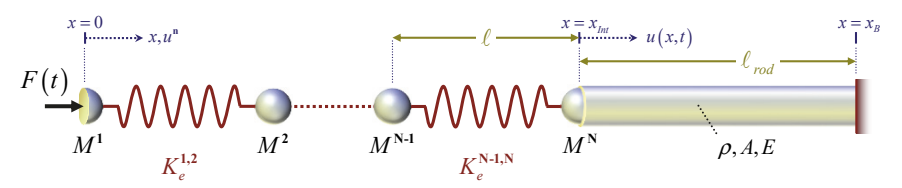


Figure 3.11: The one-dimensional finite discrete-continuous Hooke system.

continuous interface. The expressions for the unknown wave amplitudes A_1 and A_2 may now be obtained by substituting equation (3.55) into the given boundary conditions. Noting that the length of the finite rod is found as $\ell_{rod} = x_B - x_{Int}$, then yields the Laplace domain displacement of the finite rod as:

$$\tilde{u}(x,s) = \frac{\tilde{F}^{N}\sqrt{2}}{s} \frac{e^{+s\sqrt{2}(x_{B}-x)} - e^{-s\sqrt{2}(x_{B}-x)}}{e^{+s\sqrt{2}\ell_{rod}} + e^{-s\sqrt{2}\ell_{rod}}}$$
(3.56)

Taking into account that, at the discrete-continuous interface, the displacements of the finite rod and the boundary particle **N** are equal, i.e. $\tilde{u}(x_{lnt},s) = \tilde{u}^{N}$, the dynamic compliance of the finite linear-elastic rod at the discrete-continuous interface is obtained as:

$$\tilde{\beta}(s) = \frac{\tilde{u}^{N}}{\tilde{F}^{N}} = \frac{\sqrt{2}}{s} \tanh\left(s\sqrt{2}\ell_{rod}\right)$$
(3.57)

For comparison, Figure 3.12a depicts the dynamic compliance of both the finite and the semi-infinite linear-elastic rod as a function of the dimensionless frequency Ω . The dynamic compliance of the finite linear-elastic rod according to equation (3.57) is given by the continuous red line, while the dynamic compliance of the semi-infinite rod, derived as $\tilde{\beta}(s) = s^{-1}\sqrt{2}$ in Appendix D.1, is given by the dashed blue line. Applying the inverse Laplace transform to equation (3.57), we obtain the following time domain expression for the dynamic compliance, henceforth referred to as the time domain dynamic compliance, of the finite linear-elastic rod at $t \ge 0$ as:

$$\beta(t) = \begin{cases} +\sqrt{2}, & \text{if} \quad t \mod 2T_{rod} < T_{rod} \\ -\sqrt{2}, & \text{if} \quad t \mod 2T_{rod} \ge T_{rod} \end{cases}$$
(3.58)

Here, T_{rod} is the dimensionless time that is required for an incident wave to travel from the discrete-continuous interface to the point of fixation at coordinate x_B and back again, which is found as $T_{rod} = 2\sqrt{2}\ell_{rod}$. The corresponding time domain dynamic compliances of the semi-infinite and finite linear-elastic rods are shown in the Figure 3.12b as a function of time. Again, the continuous red line gives the time domain dynamic compliance for the finite linear-elastic rod, while the dashed blue line gives the time domain dynamic compliance for the semi-infinite linear-elastic rod. Figure 3.12b clearly shows that, at every period T_{rod} , the time domain dynamic compliance of the finite rod alternately jumps from $\beta(t) = +\sqrt{2}$ to $\beta(t) = -\sqrt{2}$ and vice versa.

In correspondence with the semi-infinite discrete-continuous Hooke system, the equation of motion for the boundary particle in the finite discrete-continuous Hooke system reads:

$$\tilde{u}^{N} + \tilde{\beta}(s) \left(M^{N} s^{2} \tilde{u}^{N} + K_{e}^{N-1,N} \tilde{e}^{N-1,N} \right) = 0$$
(3.59)

Applying the inverse Laplace integral transform to equation (3.59) and using Leibniz' integral rule for differentiation of integrals yields the boundary integral equation for the finite Hooke system as:

$$\dot{u}^{N} + \sqrt{2} \left\{ M^{N} \ddot{u}^{N} + K_{e}^{N-1,N} e^{N-1,N} \right\} + \int_{0}^{t} \dot{\beta} (t - \tau) \left\{ M^{N} \ddot{u}^{N} + K_{e}^{N-1,N} e^{N-1,N} \right\} (\tau) d\tau = 0$$
 (3.60)

From Figure 3.12b it follows that the time domain admittance, i.e. the time derivative of the time domain dynamic compliance, of the finite rod is equal to zero during the time periods between any two jumps of the time domain dynamic compliance. The jumps in the time domain dynamic compliance that occur at every T_{rod} however, are represented in the time domain admittance by Dirac delta functions. Within the domain of the integral in equation (3.60), i.e. for $t \ge 0$, and given that the time domain admittance repeats every $2T_{rod}$, the time domain admittance thus reads:

$$\dot{\beta}(t) = \begin{cases} 0, & \text{if} \quad t \mod T_{rod} \neq 0\\ -2\sqrt{2}\delta(t), & \text{if} \quad t \mod 2T_{rod} = T_{rod}\\ +2\sqrt{2}\delta(t), & \text{if} \quad t \mod 2T_{rod} = 0 \end{cases}$$

$$(3.61)$$

Here, note that mod in equation (3.61) is an abbreviation of modulo.

Figure 3.13 shows the longitudinal response of the one-dimensional finite discrete-continuous Hooke system to an applied pulse load at 30 different time moments. Note here that only the response of the Hooke lattice is shown. The pulse load applied at the tip of the one-dimensional Hooke system coincides with the pulse load F(t) that was previously applied to obtain Figure 3.5, giving the response of the semi-infinite discrete-continuous BKV system. Each frame of Figure 3.13 depicts the response to the pulse load at two successive time

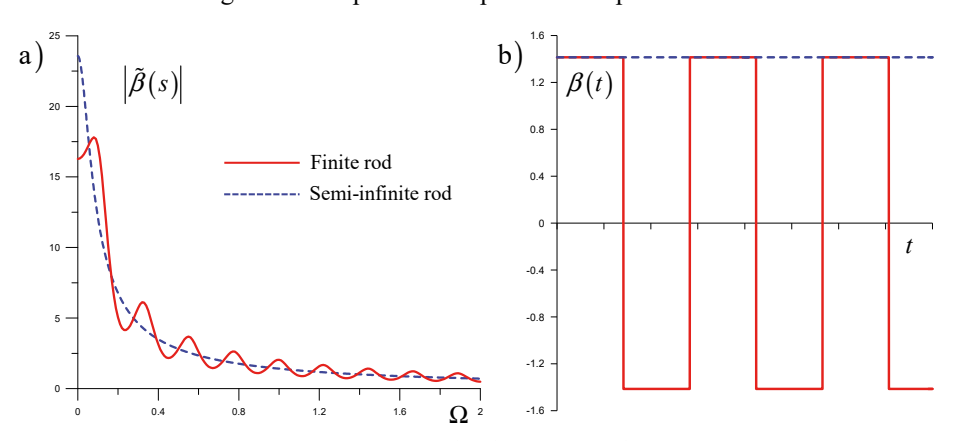


Figure 3.12: The dynamic compliance of the finite and semi-infinite linear-elastic rods:
a) absolute value in the frequency domain; b) in the time domain.

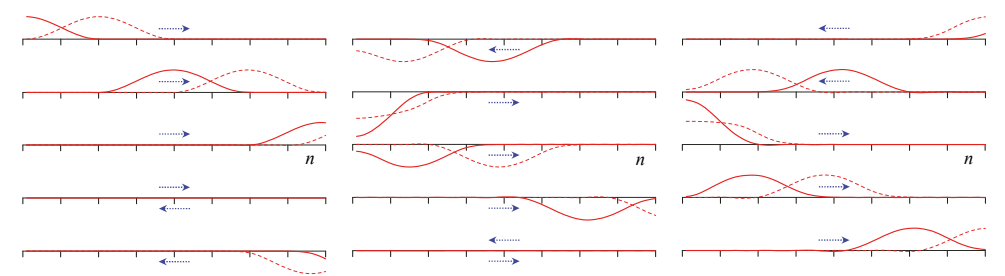


Figure 3.13: Longitudinal response of the finite discrete-continuous Hooke system to a sinus pulse load.

moments. Here, the blue arrows give the direction of wave propagation for the considered time frame, so that the continuous red line always corresponds to the first time moment, while the dashed red line corresponds to a slightly later moment in time. It can be seen from Figure 3.13 that the propagated wave is first transmitted completely into the finite rod and only returns to the lattice after the wave is reflected at the fixed boundary. Subsequently, the wave is again reflected at the tip of the system after which it bounces hence and forth between the tip of the system and the fixed boundary of the rod.

3.5 Boundary formulation for a continuous far-field domain in 2D

After evaluating several one-dimensional discrete-continuous systems and comparing the performance of the involved boundary integral equations, derived for different representations of the far-field domain, this section focuses on the derivation of boundary formulations in application of two-dimensional discrete-continuous systems. In this section, we particularly focus on deriving a boundary formulation for a far-field domain that is modelled as a two-dimensional continuum.

The two-dimensional discrete-continuous BKV system consisting of a hexagonal BKV lattice and a two-dimensional viscoelastic continuum is depicted in Figure 3.14. The hexagonal BKV lattice was previously discussed in Section 2.4, where the equations of motion for all particles at the surface and in the interior of the hexagonal lattice were derived. Whereas the interaction between the one-dimensional lattice and the continuous rod is described at a single point of contact, the interaction between the hexagonal lattice and the two-dimensional continuum is described at all particles along the lattice boundary. Noting that the Green's functions are commonly known for the continuous half-plane, it would be most convenient to model the far field as a semi-infinite medium and divide it into a near- and a far-field domain by sub-structuring along a horizontal interface [Kausel and Roësset, 1981]. As such, the linear far-field domain would conveniently remain as a half-plane or a half-space. Nevertheless, the horizontal sub-structuring also yields the nonlinear near-field domain to be semi-infinite, which does not only impose difficulties to modelling this nonlinear near-field domain numerically, but also goes against the desire to keep the domain of the nonlinear part of the model as small as possible to minimize calculation time.

The interaction between these boundary particles and the two-dimensional continuum is in the Laplace domain described by the system of force-displacement relations, previously given by equation (3.2). In correspondence with the boundary formulation for the one-

dimensional discrete-continuous system treated in Section 3.2.3, at least the diagonal terms of the dynamic stiffness matrix will increase for $\Omega \to \infty$, and we may therefore not obtain the corresponding interface equations in the time domain by numerically applying the inverse Laplace transform. To overcome this, we describe the Laplace domain relations at the lattice-continuum interface in terms of the dynamic compliance. Pre-multiplying equation (3.2) by the dynamic compliance matrix $\tilde{\beta}(s)$, i.e. the inverse of the dynamic stiffness matrix, yields the displacement of the boundary particles in the Laplace domain as:

$$\underline{\tilde{u}}_{Int}(s) = -\underline{\tilde{\beta}}(s)\underline{\tilde{F}}_{Int}(s) \tag{3.62}$$

Here, the force vector $\underline{\tilde{F}}_{bu}(s)$ contains the forces of the discrete lattice that are applied to the continuum at the lattice-continuum interface and follow from the configuration of the respective boundary particles. Note here that both the dynamic stiffness and dynamic compliance matrices are full matrices that consists of physical relations between all boundary particles through the two-dimensional continuum and must therefore be well-defined.

In the following section, we will first employ the dynamic reciprocal work theorem and apply the indirect Boundary Element Method (iBEM) [Dominguez, 1993; Wolf, 1985] to obtain the dynamic stiffness and compliance relations at the lattice-continuum interface. Subsequently, the resulting dynamic stiffness and dynamic compliance matrices are presented in Section 3.5.2. Then, in Section 3.5.3, the Green's functions for the two-dimensional continuum are derived that appear in the dynamic stiffness and compliance matrices. Finally, in Section 3.5.4, several different shapes of unit load distributions are discussed that are used to convert the point loads from the near-field lattice to tractions along the boundary of the continuous far-field domain. This is of importance because the chosen distribution for the unit loads influences the convergence of the Green's functions in the wavenumber domain.

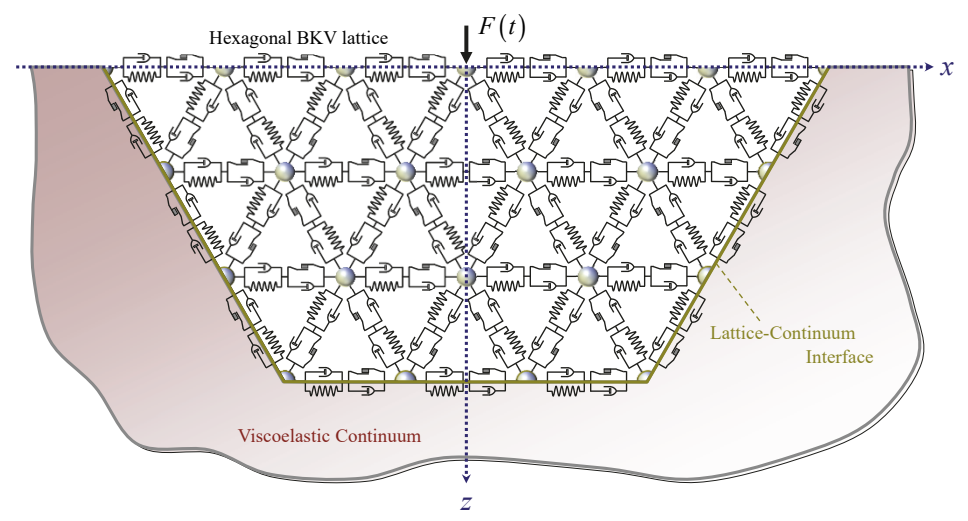


Figure 3.14: The two-dimensional discrete-continuous BKV system

3.5.1 An indirect boundary formulation for a continuous far-field domain

The basis of finding the force-displacement relation at the boundary of the discrete lattice originates from the theorem of reciprocal work. The dynamic reciprocal work theorem is an into dynamics extended version of the elastostatic reciprocal work theorem of Maxwell-Betti [de Hoop, 1966] and describes the relationship between the displacements of, and the tractions on, a body in two different elastodynamic states.

Consider two arbitrary but different elastodynamic states of a body \mathbf{V} with boundary $\mathbf{\Gamma}$ depicted in Figure 3.15. Suppose that one elastodynamic state of the body \mathbf{V} is described by internal displacements $\underline{u}(\mathbf{v})$, body forces $\rho\underline{b}(\mathbf{v})$, surface displacements $\underline{u}(\xi)$ and tractions $\underline{t}(\xi)$ as depicted in Figure 3.15a. Here, \mathbf{v} and ξ are coordinates that describe the position respectively inside the body and along its boundary. Figure 3.15b depicts another state of the same body \mathbf{V} , for example due to an external load \underline{P} , that is described by internal displacements $\underline{u}_P(\mathbf{v})$ and body forces $\rho\underline{b}_P(\mathbf{v})$, as well as by surface displacements $\underline{u}_P(\xi)$ and tractions $\underline{t}_P(\xi)$. The dynamic reciprocal work theorem now states that, in the frequency domain, and thus in the Laplace domain, the following relation between the two elastodynamic states must hold:

$$\int_{\mathbf{V}} \rho \underline{b}(\mathbf{v})^{\mathsf{T}} \underline{u}_{P}(\mathbf{v}) d\mathbf{v} + \int_{\Gamma} \underline{t}(\xi)^{\mathsf{T}} \underline{u}_{P}(\xi) d\xi = \int_{\mathbf{V}} \rho \underline{b}_{P}(\mathbf{v})^{\mathsf{T}} \underline{u}(\mathbf{v}) d\mathbf{v} + \int_{\Gamma} \underline{t}_{P}(\xi)^{\mathsf{T}} \underline{u}(\xi) d\xi$$
(3.63)

Equation (3.63) states that the work done by the tractions $\underline{t}(\xi)$ and the body forces $\rho\underline{b}(v)$ through the displacements $\underline{u}_P(v)$ and $\underline{u}_P(\xi)$ is equal to the work done by the tractions $\underline{t}_P(\xi)$ and the body forces $\rho\underline{b}_P(v)$ through the displacements $\underline{u}(v)$ and $\underline{u}(\xi)$. Note here that for clarity of the derivation presented, any reference to either the frequency or the Laplace parameter in this section are omitted.

In this thesis, we are interested in describing the response of a medium to an externally applied load, due to for example its interaction with a structure. As stated before, this medium is composed of a lattice in the near field, i.e. near the load source, and a continuum in the far field. As the interaction between lattice and continuum only exists along the lattice-continuum interface, body forces are absent and therefore equation (3.63) reduces to:

$$\int_{\Gamma} \underline{t} (\xi)^{\mathsf{T}} \underline{u}_{P}(\xi) d\xi = \int_{\Gamma} \underline{t}_{P}(\xi)^{\mathsf{T}} \underline{u}(\xi) d\xi \tag{3.64}$$

As we consider a two-dimensional solid medium, all displacements and tractions in the dynamic reciprocal work theorem are vectors with components in x- and z-directions. However note that equation (3.64) is an equality between scalars and not between vectors or matrices.

To find the force-displacement relation at the lattice-continuum interface, we here apply the dynamic reciprocal work theorem to a two-dimensional viscoelastic continuum with a horizontal surface at the x-axis and a surface cavity that matches the shape of the discrete lattice in the near-field, denoted as the far-field body \mathbf{V} . The so-called *unknown elastody-namic state* of the far-field body \mathbf{V} , depicted in Figure 3.16a, is described by the displacements $\underline{u}(\xi)$ and the tractions $\underline{t}(\xi)$ along the boundary Γ . Note here that the shape of the

surface cavity, and thus the shape of the boundary Γ , can be freely chosen as long as all particles of the near-field lattice at the lattice-continuum interface are included. The most straightforward way to obtain the boundary Γ is thus to connect the boundary particles using straight lines as shown in Figure 3.14 and Figure 3.16.

Additionally, let the elastodynamic state described by the surface displacements $\underline{u}_P(\xi)$ and tractions $\underline{t}_P(\xi)$ refer to an elastodynamic state of the continuum for which we are able to describe the displacements and the tractions along the boundary Γ . This state of the continuum is then considered as the *known elastodynamic state*. Through the dynamic reciprocal work theorem, the displacements $\underline{u}_P(\xi)$ and tractions $\underline{t}_P(\xi)$ are then used to find the unknown relation between the displacements $\underline{u}(\xi)$ and the tractions $\underline{t}(\xi)$. Once the relation between displacements $\underline{u}(\xi)$ and tractions $\underline{t}(\xi)$ is known, the force-displacement relation at the boundary Γ , and thus the dynamic stiffness and dynamic compliance matrices can be derived.

The known elastodynamic state: The viscoelastic continuum without a cavity

Due to the cavity, there are no Green's functions, or fundamental solutions, available for the displacements and tractions along the boundary Γ of the continuum due to an externally applied load. For a continuum without a surface cavity however, the Green's function can be derived from the two-dimensional elastodynamic wave equation. As the dynamic reciprocal work theorem applies to different elastodynamic states of the same body, we divide this continuum into two separate bodies for which the interface exactly matches the boundary Γ . As depicted in Figure 3.16b, we then remain with a far-field body V that exactly matches the shape of the continuum with the surface cavity and a near-field, or cavity, body V_{cav} that exactly matches the shape of the near-field lattice.

According to Huygens' principle [Huygens, 1690], also known as the Huygens-Fresnel principle, the response of the far-field body V is indifferent to whether the cavity body V_{cav} is present or not, as long as the response of the far-field body V is the same in both situations. Now, consider the cavity body V_{cav} in Figure 3.16b to have a boundary Γ_{cav} that is offset from the boundary Γ with an infinitesimal distance and assume a load distribution $P(\xi)$ along Γ_{cav} for which we can determine the displacements $P_{cav}(\xi)$ and tractions $P_{cav}(\xi)$ along the

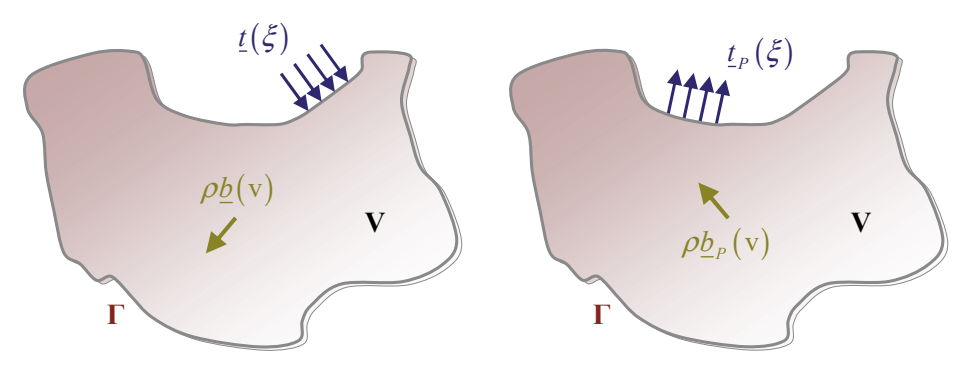


Figure 3.15: Two arbitrary but different elastodynamic states of the same body

boundary Γ of the body V, i.e. the known state. Knowing the tractions $\underline{t}(\xi)$ along the boundary Γ of the body V in the unknown state then allows us to determine the displacements $\underline{u}(\xi)$ along the boundary Γ of the body V, through the dynamic reciprocal work theorem that describes the relation between the known and unknown elastodynamic states depicted in Figure 3.16, while we in fact compare two different bodies.

As the distance between the boundary Γ and the cavity boundary Γ_{cav} is assumed to be infinitesimal, we can consider the load distribution $\underline{P}(\xi)$ to describe the interaction between the bodies \mathbf{V} and \mathbf{V}_{cav} . The displacements $\underline{u}_P(\xi)$ and the tractions $\underline{t}_P(\xi)$ along the boundary Γ due to the load distribution $\underline{P}(\xi)$ along the boundary Γ are expressed in terms of their respective Green's functions, or fundamental solutions, as:

$$\underline{u}_{P}(\xi) = \int_{\Gamma} \underline{g}_{u}(\xi') \underline{P}(\xi - \xi') d\xi' \tag{3.65}$$

$$\underline{t}_{P}(\xi) = \int_{\Gamma} \underline{g}_{i}(\xi') \underline{P}(\xi - \xi') d\xi' \tag{3.66}$$

Here, $\underline{g}_{u}(\xi)$ and $\underline{g}_{t}(\xi)$ are matrices that contain the Green's functions for respectively the displacements and \overline{th} tractions along the boundary Γ , which we will henceforth refer to as the Green's displacements and Green's tractions respectively. Furthermore, the load distribution $\underline{P}(\xi)$ contains the x- and z-components $P_{x}(\xi)$ and $P_{z}(\xi)$, the displacement vector $\underline{u}_{P}(\xi)$ contains the horizontal and vertical displacements $u_{P,x}(\xi)$ and $u_{P,z}(\xi)$ along Γ , and accordingly the traction vector $\underline{t}_{P}(\xi)$ contains the horizontal and vertical tractions $t_{P,x}(\xi)$ and $t_{P,z}(\xi)$ along Γ .

Equations (3.65) and (3.66) describe a continuous relation between the load distribution $\underline{P}(\xi)$ and the displacements $\underline{u}_P(\xi)$ and tractions $\underline{t}_P(\xi)$ along the boundary Γ . To instead find the relation between the lattice particles at the lattice-continuum interface and the continuum, we divide the boundary Γ into a number of subdomains, which is equal to the number of particles at the lattice-continuum interface. It then follows that the load distribution $\underline{P}(\xi)$ along the boundary Γ is equal to the sum of the load distributions at the subdomains of the boundary Γ of all \mathbf{N}_{Int} particles. We can describe this as:

$$\underline{P}(\xi) = \sum_{i=1}^{N_{\text{Int}}} \underline{p}^{i}(\xi)$$

Here, $\underline{p}^{i}(\xi)$ is the load distribution that belongs to the subdomain of the particle i on the boundary Γ and contains the horizontal and vertical load distributions $p_x^{i}(\xi)$ and $p_z^{i}(\xi)$. Now, if we describe each load distribution $\underline{p}^{i}(\xi)$ at particle i as a multiplication of an arbitrary unit distribution $p_1^{i}(\xi)$ and a load magnitude vector \underline{P}^{i} , we can describe the total load distribution $\underline{P}(\xi)$ along Γ as:

$$\underline{P}(\xi) = \underline{p_1}(\xi)\,\underline{P} \tag{3.67}$$

Here, the vector \underline{P} contains the horizontal and vertical load magnitudes P_z^i and P_z^i for all particles and thus for all subdomains, i.e. for $\mathbf{i}=1...\mathbf{N}_{Int}$. Consequently, $p_1(\xi)$ is a $2\times 2\mathbf{N}_{Int}$ -matrix that contains the unit distributions $p_1^i(\xi)$ for all \mathbf{N}_{Int} subdomains. Here, a unit distribution is defined by the property that the integral of that distribution over Γ is equal to one, i.e. $\int_{\Gamma} p_1^i(\xi) d\xi = 1$. This implies that the unit distribution $p_1^i(\xi)$ may also be a point load, which we can describe as a distribution over Γ using the Dirac delta function, ergo $p_1^i(\xi) = \delta(\xi)$.

Substituting equation (3.67) into equations (3.65) and (3.66) allows us to express the displacements $\underline{u}_P(\xi)$ and the tractions $\underline{t}_P(\xi)$ in terms of the load magnitude vector \underline{P} as:

$$\underline{u}_{P}(\xi) = u_{1}(\xi)\underline{P} \tag{3.68}$$

$$\underline{t}_{P}(\xi) = t_{1}(\xi)\underline{P} \tag{3.69}$$

Here, $\underline{u_1}(\xi)$ and $\underline{t_1}(\xi)$ are $2 \times 2 \mathbf{N_{Int}}$ -matrices that, when $p_1^i(\xi)$ is a unit point load, are equal to the Green's function matrices $g_u(\xi)$ and $g_t(\xi)$. If $p_1^i(\xi)$ is given as a unit load distribution however, the matrices $\underline{u_1}(\xi)$ and $\underline{t_1}(\xi)$ are related to respectively the Green's displacements $g_u(\xi)$ and Green's tractions $g_t(\xi)$ as:

$$\underline{u_1}(\xi) = \int_{\Gamma} g_u(\xi') p_1(\xi - \xi') d\xi' \tag{3.70}$$

$$\underline{\underline{t_1}}(\xi) = \int_{\Gamma} \underline{g_t}(\xi') \underline{p_1}(\xi - \xi') d\xi' \tag{3.71}$$

Henceforth, we will respectively refer to the matrices $\underline{u_1}(\xi)$ and $\underline{t_1}(\xi)$ as the modified Green's displacement matrix and the modified Green's traction matrix. The modified Green's function matrices $\underline{u_1}(\xi)$ and $\underline{t_1}(\xi)$ respectively consist of the displacements and the tractions along the boundary Γ due to unit load distributions $\underline{p_1}^i(\xi)$ at all particles i along the boundary Γ .

The unknown elastodynamic state: The continuum with a surface cavity

In the dynamic reciprocal work theorem, the so-called unknown elastodynamic state is described through the displacements $\underline{u}(\xi)$ and tractions $\underline{t}(\xi)$ along the boundary Γ . As

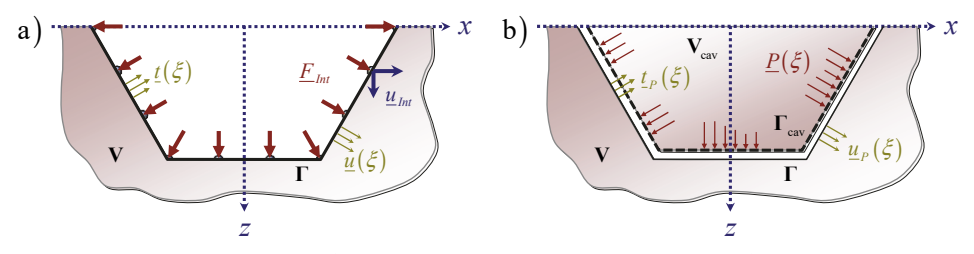


Figure 3.16: a) The continuum with a surface cavity that matches the lattice boundary, i.e. the unknown elastodynamic state; b) The continuum without a cavity, composed of the continuum with the cavity and a cavity body.

depicted in Figure 3.16a however, at the locations of the boundary particles along Γ , the continuum is subject to the lattice forces \underline{F}_{Int} , while the displacements of the boundary particles along Γ are collected in the displacement vector \underline{u}_{Int} . Thus, we require a relation between the particle displacement vector \underline{u}_{Int} and the displacements $\underline{u}(\xi)$ along Γ , as well as a relation between the boundary particle force vector \underline{F}_{Int} and the tractions $\underline{t}(\xi)$ along Γ . Note here that neither the vectors \underline{u}_{Int} and $\underline{u}(\xi)$ nor the vectors \underline{F}_{Int} and $\underline{t}(\xi)$ have the same dimensions; in fact, the displacement vector \underline{u}_{Int} and the force vector \underline{F}_{Int} respectively contain the horizontal and vertical displacements of, and forces on, all boundary particles, while the displacement vector $\underline{u}(\xi)$ and the traction vector $\underline{t}(\xi)$ respectively describe the horizontal and vertical displacements and tractions along the whole boundary Γ . Therefore, we consider the boundary Γ on \mathbf{N}_{Int} subdomains, where \mathbf{N}_{Int} is equal to the number of particles at the lattice-continuum interface. Choosing a geometrically logical and even division of the boundary Γ yields the subdomain of Γ for a particle \mathbf{j} as $\{\xi_{\mathbf{j}} - \Delta \xi \dots \xi_{\mathbf{j}} + \Delta \xi\}$. Here, $\xi_{\mathbf{j}}$ is the position of particle \mathbf{j} on Γ and $2\Delta \xi$ is the distance between any two particles on the boundary Γ .

To describe the relation between the displacements $\underline{u}^{\mathbf{j}}(\xi)$ of the boundary Γ on the domain of particle \mathbf{j} and the displacement $\underline{u}^{\mathbf{j}}_{lnt}$ of that particle any shape functions can be chosen. In this case, choosing the Heaviside function as a shape function, we find the following relation:

$$\underline{u}^{i}(\xi) = H(\Delta \xi - |\xi_{i} - \xi|) \underline{u}_{bt}^{i}$$
(3.72)

The relation between the displacements $\underline{u}(\xi)$ along Γ and the interface displacements \underline{u}_{lm} is then found as the summation of all displacements $\underline{u}^{i}(\xi)$ along the boundary Γ , and thus:

$$\underline{u}(\xi) = \underline{H}(\xi)\underline{u}_{Int} \tag{3.73}$$

Here, $\underline{\underline{H}}(\xi)$ is a $2 \times 2 \mathbf{N}_{\text{Int}}$ -matrix composed of Heaviside functions related to the respective domains of each particle $\mathbf{j} = 1 \dots \mathbf{N}_{\text{Int}}$ on the boundary Γ . Equation (3.73) gives a rather crude representation of the displacement field as it implies that the displacements $\underline{u}(\xi)$ are discontinuous along the boundary Γ . This however, is not a problem as we aim for a force-displacement relation of the discrete set of lattice particles along the boundary Γ and not for a continuous force-displacement relation along this boundary.

To find the relation between the boundary particle force vector \underline{F}_{Int} and the tractions $\underline{t}(\xi)$ along the boundary Γ , let us first consider the relation between the forces on a particle \mathbf{i} and the tractions on the domain of the boundary Γ that corresponds particle \mathbf{i} . The domain of the boundary Γ that corresponds to a particle \mathbf{i} is described as $\{\xi_{\mathbf{i}} - \Delta \xi ... \xi_{\mathbf{i}} + \Delta \xi\}$, where $\xi_{\mathbf{i}}$ is the position of particle \mathbf{i} on the boundary Γ and $2\Delta \xi$ is the distance between any two particles on the boundary Γ . The tractions on the domain of particle \mathbf{i} may then be expressed in terms of the tractions $\underline{t}(\xi)$ using the Heaviside function $H(\Delta \xi - |\xi_{\mathbf{i}} - \xi|)$ as depicted in Figure 3.17. The resultant of the tractions on the domain of particle \mathbf{i} , must be equal and

opposite to the exerted forces \underline{F}_{lnt}^{i} at particle **i**. Assuming that the boundary Γ has a unit width in the third dimension, the force \underline{F}_{lnt}^{i} at particle **i** is found in terms of the tractions as:

$$\underline{F}_{lnt}^{i} = -\int_{\Gamma} H\left(\Delta \xi - \left|\xi_{i} - \xi\right|\right) \underline{t}(\xi) d\xi \tag{3.74}$$

Here, \underline{F}_{lnt}^{i} contains the forces $F_{lnt,x}^{i}$ and $F_{lnt,z}^{i}$. Collecting the forces \underline{F}_{lnt}^{i} for all particles $\mathbf{i} = \mathbf{1} \dots \mathbf{N}_{Int}$ in the force vector \underline{F}_{lnt} yields the following relation between the force vector \underline{F}_{lnt} and the tractions $\underline{t}(\xi)$ along the boundary Γ :

$$\underline{F}_{lnt} = -\int_{\Gamma} \underline{H}(\xi)^{\mathrm{T}} t(\xi) d\xi \tag{3.75}$$

Here, $\underline{\underline{H}}(\xi)$ is a $2 \times 2N_{Int}$ -matrix composed of Heaviside functions related to the respective domains of each particle $\mathbf{i} = 1...N_{Int}$ on the boundary Γ .

To apply the dynamic reciprocal work theorem using the so-called known and unknown elastodynamic states depicted in Figure 3.16, we have assumed that the displacements and tractions along the boundary Γ of the far-field body V are the same in both states. Consequently, the tractions $\underline{t}(\xi)$ on the boundary Γ of the continuum with the cavity are equal to the tractions $\underline{t}_P(\xi)$ on the interface Γ due to the load distribution $\underline{P}(\xi)$ in the continuum without the cavity:

$$\underline{t}(\xi) = \underline{t}_{P}(\xi) = \underline{t}_{1}(\xi)\underline{P} \tag{3.76}$$

Substituting equation (3.76) into equation (3.75), yields the relation between the boundary particle force vector \underline{F}_{Int} and the load magnitude vector \underline{P} as:

$$\underline{\underline{F}}_{Int} = -\int_{\Gamma} \underline{\underline{\underline{H}}} \left(\xi\right)^{\mathrm{T}} \underline{\underline{t}}_{\underline{\underline{I}}} \left(\xi\right) d\xi \, \underline{\underline{P}} \tag{3.77}$$

3.5.2 The dynamic compliance matrix for a continuum with surface cavity

Substituting equations (3.68) and (3.69) for the known elastodynamic state, and equations (3.73) and (3.76) for the unknown elastodynamic state, into equation (3.64) for the dynamic

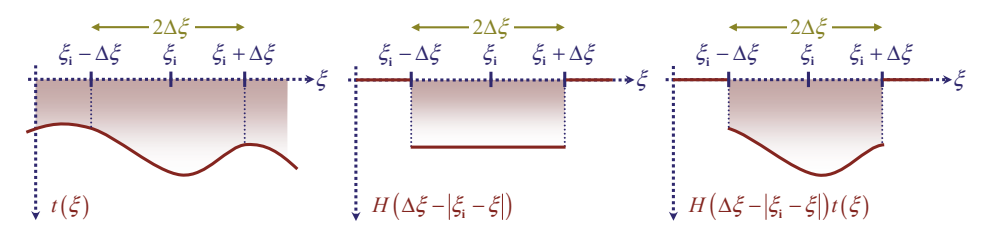


Figure 3.17: The traction at the boundary Γ on the domain of a particle i.

reciprocal work theorem, yields the following relation between the load magnitude vector $\underline{\mathbf{P}}$ and the boundary particle displacement vector $\underline{\mathbf{u}}_{lnt}$:

$$\underline{\underline{P}}^{\mathsf{T}} \int_{\Gamma} \underline{\underline{t}}_{1}(\xi)^{\mathsf{T}} \underline{\underline{u}}_{1}(\xi) d\xi \, \underline{\underline{P}} = \underline{\underline{P}}^{\mathsf{T}} \int_{\Gamma} \underline{\underline{t}}_{1}(\xi)^{\mathsf{T}} \, \underline{\underline{\underline{H}}}(\xi) d\xi \, \underline{\underline{u}}_{lnt}$$
(3.78)

As the above equation must hold for any load magnitude vector \underline{P} , we may remove the vector term \underline{P}^T from equation (3.78) without violating the equality. Solving the remainder for \underline{P} , the force-displacement relation at the boundary Γ of the continuum with a corresponding cavity follows from substitution into equation (3.77) as:

$$\underline{\underline{F}}_{lnt} = -\int_{\Gamma} \underline{\underline{H}}(\xi)^{\mathsf{T}} \underline{t_1}(\xi) d\xi \left(\int_{\Gamma} \underline{t_1}(\xi)^{\mathsf{T}} \underline{\underline{u}}_{1}(\xi) d\xi \right)^{-1} \int_{\Gamma} \underline{t_1}(\xi)^{\mathsf{T}} \underline{\underline{H}}(\xi) d\xi \underline{\underline{u}}_{lnt}$$
(3.79)

Here, note that equation (3.79) is derived from the dynamic reciprocity theorem that is generally valid in the Laplace domain and therefore equation (3.79) also describes a relation in the Laplace domain. Thus, including the reference to the Laplace parameter s that we previously omitted and comparing equation (3.79) to the dynamic stiffness relation previously described by equation (3.62) in the Laplace domain, we find the dynamic stiffness matrix as:

$$\underline{\tilde{\chi}}(s) = \underline{\tilde{T}}(s)^{\mathrm{T}} \underline{\tilde{G}}(s)^{-1} \underline{\tilde{T}}(s) \tag{3.80}$$

Consequently, the corresponding dynamic compliance matrix is found as:

$$\tilde{\underline{\beta}}(s) = \left(\tilde{\underline{\underline{T}}}(s)^{\mathsf{T}} \tilde{\underline{\underline{G}}}^{-1}(s)\tilde{\underline{\underline{T}}}(s)\right)^{-1} = \tilde{\underline{\underline{T}}}(s)^{-1} \tilde{\underline{\underline{G}}}(s)\left(\tilde{\underline{\underline{T}}}^{-1}(s)\right)^{\mathsf{T}}$$
(3.81)

Here, the matrices $\underline{\tilde{T}}(s)$ and $\underline{\tilde{G}}(s)$ are respectively found as:

$$\underline{\underline{T}}(s) = \int_{\Gamma} \underline{\tilde{t}}_{1}(\xi, s)^{T} \underline{\underline{H}}(\xi) d\xi \tag{3.82}$$

$$\underline{\tilde{G}}(s) = \int_{\mathbb{R}} \tilde{t}_1(\xi, s)^{\mathrm{T}} \, \tilde{u}_1(\xi, s) \, d\xi \tag{3.83}$$

The matrix $\tilde{\underline{T}}(s)$ is sometimes referred to as the strain-displacement matrix [Wolf and Darbre, 1984a], but it is also known as the lumping matrix [Coda et al., 1999; Pinto and Prato, 2006], because it follows from the so-called lumping procedure that is used to approximate the displacement field along Γ by the discrete interface displacement vector according to equation (3.73). The matrix $\underline{\tilde{G}}(s)$ is a symmetric matrix that is commonly known as the flexibility matrix; its symmetry follows directly from the dynamic reciprocal work theorem as proven in Appendix F.2. The expressions for the terms appearing in the lumping matrix $\underline{\tilde{T}}(s)$ and the flexibility matrix $\underline{\tilde{G}}(s)$ are respectively discussed in Appendices F.1 and F.2. Since the flexibility matrix $\underline{\tilde{G}}(s)$ is a symmetric matrix, it follows from equations (3.80)

and (3.81) that the dynamic stiffness and compliance matrices are symmetric as well. This symmetry is induced by our choice of using the Heaviside function for both the relation between the continuous displacement field along Γ and the interface displacement vector given by equation (3.73), and for the relation between the tractions along Γ and the interface force vector given by equation (3.75). Although the Heaviside function is very straightforward, we may also use other shape functions to describe the relations given by equations (3.73) and (3.75) without breaking the symmetry of the dynamic stiffness matrix, given the condition that these relations are chosen accordingly.

According to equations (3.82) and (3.83), the lumping and flexibility matrices follow from the so-called modified Green's displacement and modified Green's traction matrices, respectively denoted as $\underline{\tilde{u}}_1(\xi,s)$ and $\underline{\tilde{t}}_1(\xi,s)$. Both these matrices include corresponding horizontal and vertical Green's functions due to the horizontal and vertical unit load distributions, denoted as $p_{1,x}^i(\xi)$ and $p_{1,z}^i(\xi)$. Here, the numerator i refers to the boundary particle on Γ at which the unit load distributions are applied that generate the considered modified Green's function along Γ .

The tractions at the boundary Γ , which for the full continuum describes the interface between the bodies V and V_{cav} , can be expressed in terms of stresses at this interface using Cauchy's stress principle. Expressing Cauchy's stress tensor in its components in x- and z-direction, the modified Green's tractions due to a unit load distribution at particle i on the boundary Γ in respectively x- and z-direction follow from the modified Green's stresses as:

$$\tilde{t}_{1,xx}^{i}(\xi,s) = n_{x}(\xi)\tilde{\sigma}_{1,xxx}^{i}(\xi,s) + n_{z}(\xi)\tilde{\sigma}_{1,xxx}^{i}(\xi,s)$$
(3.84)

$$t_{1,xz}^{i}\left(\xi,s\right) = n_{x}\left(\xi\right)\sigma_{1,xxz}^{i}\left(\xi,s\right) + n_{z}\left(\xi\right)\sigma_{1,xxz}^{i}\left(\xi,s\right) \tag{3.85}$$

$$t_{1,zx}^{i}(\xi,s) = n_x(\xi)\sigma_{1,zxx}^{i}(\xi,s) + n_z(\xi)\sigma_{1,zzx}^{i}(\xi,s)$$

$$(3.86)$$

$$t_{1,zz}^{i}\left(\xi,s\right) = n_{x}\left(\xi\right)\sigma_{1,zzz}^{i}\left(\xi,s\right) + n_{z}\left(\xi\right)\sigma_{1,zzz}^{i}\left(\xi,s\right) \tag{3.87}$$

Here, the modified Green's traction $\tilde{t}_{1,ab}^i\left(\xi,s\right)$ gives the traction along Γ in the direction of index a due to the unit load distribution at particle \mathbf{i} in the direction of index b. Accordingly, the modified Green's stress $\tilde{\sigma}_{1,abc}^i\left(\xi,s\right)$ describes the normal or shear stress, depending on whether indices a and b are equal or not, in the direction of index b due to the unit load distribution at particle \mathbf{i} in the direction of index c. Furthermore, $n_x\left(\xi\right)$ and $n_z\left(\xi\right)$ are respectively the x- and z-components of the outward normal along the boundary Γ , which are defined by the angle $\theta(\xi)$ between the x-axis and outward normal of Γ at coordinate ξ , so that $n_x\left(\xi\right) = \cos\theta\left(\xi\right)$ and $n_z\left(\xi\right) = \sin\theta\left(\xi\right)$.

The modified Green's displacements and modified Green's stresses, resulting in the modified Green's tractions according to equations (3.84) to (3.87), that yield the lumping and flexibility matrices and thus the dynamic compliance matrix are derived in the following.

3.5.3 Green's functions for the continuum displacements and stresses

In the previous section, starting from the dynamic reciprocal work theorem, we have obtained an expression for the dynamic compliance at the boundary Γ of a continuum with a cavity

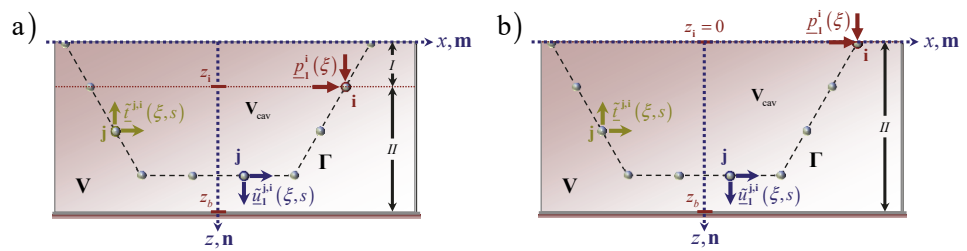


Figure 3.18: a) A unit load applied at a particle **i** inside the continuous layer; b) A unit load applied at a particle **i** at the surface of the continuous layer.

that matches the near-field lattice using the so-called modified Green's displacements and stresses of the full continuum, thus without a cavity. In this section, we will first derive the modified Green's displacements and stresses along the boundary Γ inside the full continuum in the Laplace-wavenumber domain. Subsequently, the expressions for these Green's functions are transformed to the Laplace domain using the residue theorem, providing us with the necessary expressions for the modified Green's displacement matrix $\underline{\tilde{u}}_1(\xi,s)$ and the modified Green's traction matrix $\underline{\tilde{t}}_1(\xi,s)$ in the Laplace domain, finally yielding the dynamic stiffness and compliance matrices.

To find the modified Green's functions at the boundary Γ , we model the continuum as a layer with a fixed bottom to allow for the application of dynamic loads with a nonzero mean, i.e. loads with a static component. Note here that a continuous half-plane is not suitable for this, because half-planes are statically indeterminate, so that any half-plane loaded by a static force will move wholly and undisturbed to infinity. The continuous layer with its fixed bottom is depicted in Figure 3.18. Here, the horizontal surface of the continuous layer is chosen as the x-axis and the horizontal rigid bottom is located at the z-coordinate $z = z_b$, so that the continuous layer has a constant thickness equal to z_b . To determine the Green's displacements and stresses in the continuous layer, we consider its displacements and stresses due to a unit load applied at an arbitrary point. Let us, as a general case, consider this unit load to be applied at a particle i on the boundary Γ located inside the continuous layer as depicted in Figure 3.18a. To obtain its governing equations, the continuous layer is divided into two horizontal sublayers; a surface and a bottom layer. The surface layer, denoted by roman numeral I, is the part of the continuous layer between the layer surface and the z-coordinate of particle i, i.e. $z = z_i$. The bottom layer, denoted by roman numeral II, consists of the remainder of the continuous layer and is located between the z-coordinate of particle i, i.e. $z = z_i$, and the rigid bottom at z-coordinate $z = z_b$. To minimize the influence of wave reflections from the bottom of the continuous layer on the domain of the lattice, the thickness of the bottom layer, denoted as h_{II} , is chosen to exceed the thickness h_{I} of the surface layer by a significant margin, i.e. $h_{II} >> h_{I}$. Important to note here is that the continuous layer is considered to be homogeneous and therefore both horizontal sublayers must represent the same material and have the same material properties.

Figure 3.18b depicts the situation where the unit load is applied at the surface of the continuous layer. The governing equations for this case are obtained directly, i.e. without dividing the continuous layer into horizontal sublayers.

Governing equations for the continuous layer in the Laplace-wavenumber domain

Assuming plane-strain conditions, the system of equations of motion for a continuum with a mass density ρ , Young's modulus E and Poisson's ratio v, is described by the well-known two-dimensional elastodynamic equation [Achenbach, 1973]:

$$\rho \underline{\ddot{u}}(x,z,t) - (\hat{\lambda} + \hat{\mu}) \nabla_{x,z} (\nabla_{x,z} \cdot \underline{u}(x,z,t)) - \hat{\mu} \nabla_{x,z}^{2} \underline{u}(x,z,t) = 0$$
(3.88)

Here, $\underline{u}(x,z,t)$ is a displacement vector consisting of the horizontal and vertical continuum displacements, respectively denoted as $u_x(x,z,t)$ and $u_z(x,z,t)$. As before, Newton's notation implies a time derivative and thus $\underline{\ddot{u}}(x,z,t)$ is the corresponding acceleration vector. Furthermore, $\hat{\lambda}$ and $\hat{\mu}$ are Lamé operators that describe the viscoelastic behaviour of the continuous layer through the relations $\hat{\lambda} = \lambda \left(1 + \zeta_e \frac{\partial}{\partial t}\right)$ and $\hat{\mu} = \mu \left(1 + \zeta_e \frac{\partial}{\partial t}\right)$. Here, λ and μ are the Lamé constants that describe the elastic properties of the material through the Young's modulus E and the Poisson's ratio v respectively as $\lambda = vE/(1-2v)/(1+v)$ and $\mu = E/2/(1+v)$, and ζ_e is a coefficient that represents the material damping in the continuous layer.

Applying Helmholtz' orthogonal decomposition by expressing the displacement vector \underline{u} through the Lamé vector potential $\underline{\psi} = (0, -\psi)$ and the Lamé scalar potential ϕ in their common form, i.e. $\underline{u}(x,z,t) = \nabla \times \underline{\psi} + \nabla \phi$, the two-dimensional elastodynamic equation (3.88) splits into the following uncoupled equations:

$$\ddot{\psi} - \hat{c}_S^2 \left(\frac{\partial^2 \psi}{\partial x^2} + \frac{\partial^2 \psi}{\partial z^2} \right) = 0 \tag{3.89}$$

$$\ddot{\phi} - \hat{c}_P^2 \left(\frac{\partial^2 \phi}{\partial x^2} + \frac{\partial^2 \phi}{\partial z^2} \right) = 0 \tag{3.90}$$

Here, \hat{c}_S^2 and \hat{c}_P^2 are respectively described as $\hat{c}_S^2 = c_S^2 \left(1 + \zeta_e \frac{\partial}{\partial t}\right)$ and $\hat{c}_P^2 = c_P^2 \left(1 + \zeta_e \frac{\partial}{\partial t}\right)$, where c_S and c_P are respectively the shear and compressional wave velocity, and ζ_e is the damping coefficient. The shear and compressional wave velocities are related to the Lamé constants as $c_S^2 = \mu/\rho$ and $c_P^2 = (\lambda + 2\mu)/\rho$ respectively. The expressions for \hat{c}_S^2 and \hat{c}_P^2 may be described likewise using the Lamé operators $\hat{\lambda}$ and $\hat{\mu}$.

Applying the Fourier transform with respect to space and the Laplace transform with respect to time yields equations (3.89) and (3.90) in the Laplace-wavenumber domain. The Lamé potentials that satisfy equations (3.89) and (3.90) in the Laplace -wavenumber domain are then found for respectively the surface and bottom layers as:

$$\tilde{\tilde{\psi}}_{I} = A_{1}e^{+R_{5}z} + A_{2}e^{-R_{5}z}, \qquad \qquad \tilde{\tilde{\phi}}_{I} = A_{3}e^{+R_{P}z} + A_{4}e^{-R_{P}z}.$$
(3.91)

$$\tilde{\tilde{\psi}}_{II} = A_5 e^{+R_S z} + A_6 e^{-R_S z}, \qquad \tilde{\tilde{\phi}}_{II} = A_7 e^{+R_P z} + A_8 e^{-R_P z}. \tag{3.92}$$

Previously, a single tilde placed over a variable was used to denote a variable as its Laplace transform. Accordingly, the double tilde denotes a variable as its the Fourier-Laplace transform, thus describing the considered variable in the Laplace-wavenumber domain.

The expressions for R_S and R_P are respectively found as $R_S^2 = k^2 + s^2/\hat{c}_S^2$ and $R_P^2 = k^2 + s^2/\hat{c}_P^2$, where k and s are respectively the wavenumber and the complex-valued Laplace parameter. To fix the sign of the square roots of R_S and R_P , we assume $\text{Re}(R_S, R_P) \ge 0$. Here, note that in a homogeneous continuum, the expressions for R_S and R_P in the surface and bottom layers are the same.

From Helmholtz' decomposition, we find the displacements of the continuous layer in terms of the Lamé potentials. The corresponding stresses are then straightforwardly derived from the elasticity theory. Respectively applying the Fourier and Laplace transforms with respect to space and time, as well as substituting the Lamé potentials according to equations (3.91) yields the Laplace-wavenumber domain displacements and stresses in the surface layer as:

$$\tilde{\tilde{u}}_{x,I}(k,z,s) = R_S \left(A_1 e^{+R_S z} - A_2 e^{-R_S z} \right) + ik \left(A_3 e^{+R_P z} + A_4 e^{-R_P z} \right) \tag{3.93}$$

$$\tilde{\tilde{u}}_{z,l}(k,z,s) = -ik(A_1 e^{+R_S z} + A_2 e^{-R_S z}) + R_P(A_3 e^{+R_P z} - A_4 e^{-R_P z})$$
(3.94)

$$\tilde{\tilde{\sigma}}_{xx,I}(k,z,s) = 2\hat{\mu}ikR_S(A_1e^{+R_Sz} - A_2e^{-R_Sz}) - \hat{\mu}\gamma_P(A_3e^{+R_Pz} + A_4e^{-R_Pz})$$
(3.95)

$$\tilde{\tilde{\sigma}}_{zx,I}(k,z,s) = \hat{\mu}\gamma_s \left(A_1 e^{+R_S z} + A_2 e^{-R_S z} \right) + 2\hat{\mu} i k R_P \left(A_3 e^{+R_P z} - A_4 e^{-R_P z} \right)$$
(3.96)

$$\tilde{\tilde{\sigma}}_{zz,l}(k,z,s) = -2\hat{\mu}ikR_{S}(A_{1}e^{+R_{S}z} - A_{2}e^{-R_{S}z}) + \hat{\mu}\gamma_{S}(A_{3}e^{+R_{P}z} + A_{4}e^{-R_{P}z})$$
(3.97)

Accordingly, substituting the Lamé potentials given by equations (3.92) yields the Laplace-wavenumber displacements and stresses in the bottom layer as:

$$\tilde{\tilde{u}}_{x,H}(k,z,s) = R_S \left(A_5 e^{+R_S z} - A_6 e^{-R_S z} \right) + ik \left(A_7 e^{+R_P z} + A_8 e^{-R_P z} \right)$$
(3.98)

$$\tilde{\tilde{u}}_{z,H}(k,z,s) = -ik(A_5 e^{+R_S z} + A_6 e^{-R_S z}) + R_P(A_7 e^{+R_P z} - A_8 e^{-R_P z})$$
(3.99)

$$\tilde{\tilde{\sigma}}_{xx,II}(k,z,s) = 2\hat{\mu}ikR_S \left(A_5 e^{+R_S z} - A_6 e^{-R_S z} \right) - \hat{\mu}\gamma_P \left(A_7 e^{+R_P z} + A_8 e^{-R_P z} \right)$$
(3.100)

$$\tilde{\tilde{\sigma}}_{zx,II}(k,z,s) = \hat{\mu}\gamma_{S}(A_{5}e^{+R_{S}z} + A_{6}e^{-R_{S}z}) + 2\hat{\mu}ikR_{P}(A_{7}e^{+R_{P}z} - A_{8}e^{-R_{P}z})$$
(3.101)

$$\tilde{\tilde{\sigma}}_{zz,II}(k,z,s) = -2\hat{\mu}ikR_S(A_5e^{+R_Sz} - A_6e^{-R_Sz}) + \hat{\mu}\gamma_S(A_7e^{+R_Pz} + A_8e^{-R_Pz})$$
(3.102)

Here, the variables γ_S and γ_P are respectively found as $\gamma_S = 2R_S^2 - s^2/\hat{c}_S^2$ and $\gamma_P = 2R_P^2 - s^2/\hat{c}_S^2$. Note here that i denotes the imaginary unit and should not be mistaken for the particle numerator i. The derivation of the above expressions is given in Appendix F.3.

Boundary conditions for the continuous layer

The expressions for the unknowns A_1 to A_8 in equations (3.93) to (3.102) follow from the boundary conditions of the two horizontal sublayers in the Laplace-wavenumber domain.

The boundary conditions at the surface and at the bottom of the continuous layer respectively follow from the fact that stresses at an unloaded surface do not exist and that the bottom is fixed. In the Laplace-wavenumber domain, the application of a load inside the continuous layer therefore yields the following boundary conditions at the layer surface and bottom as:

$$\left. \tilde{\tilde{\sigma}}_{zx,l} \left(k, z, s \right) \right|_{z=0} = \left. \tilde{\tilde{\sigma}}_{zz,l} \left(k, z, s \right) \right|_{z=0} = 0 \tag{3.103}$$

$$\tilde{u}_{x,H}(k,z,s)\Big|_{z=z_k} = \tilde{u}_{z,H}(k,z,s)\Big|_{z=z_k} = 0$$
 (3.104)

The four remaining boundary conditions are found at the interface between the horizontal sublayers, whose position is defined by the location of particle **i** at which the considered unit load is applied. Clearly, the displacements of the surface and bottom layers must coincide at the interface between both layers and thus, the corresponding boundary conditions read:

$$\tilde{\tilde{u}}_{x,II}\left(k,z,s\right)\Big|_{z=z} - \tilde{\tilde{u}}_{x,I}\left(k,z,s\right)\Big|_{z=z} = 0 \tag{3.105}$$

$$\left. \tilde{\tilde{u}}_{z,II} \left(k, z, s \right) \right|_{z=z_1} - \tilde{\tilde{u}}_{z,I} \left(k, z, s \right) \right|_{z=z_1} = 0 \tag{3.106}$$

The two remaining boundary conditions follow from the equilibrium of stresses at the interface between the horizontal sublayers at the z-coordinate z_i of the load applied at a particle **i** and must therefore include the applied load.

In Section 3.5.1, it was noted that a load along the boundary Γ must either be applied as a point load or as a load distribution. A well-known property of the two-dimensional continuum is that the displacement under a point load is infinite. Therefore, we apply the load at particle \mathbf{i} as a distributed load. Independent of its direction, a horizontally distributed unit load at particle \mathbf{i} may generally be described in the space-time domain as $p_1^{\mathbf{i}}(x,t) = p_1(x-x_{\mathbf{i}})\delta(t)$. Here, $p_1(x-x_{\mathbf{i}})$ describes the shape of the distribution at a particle \mathbf{i} along Γ that must satisfy the property $\int p_1(x-x_{\mathbf{i}})dx = 1$. Respectively applying the Fourier and Laplace transforms with respect to space and time, we obtain the Laplace-wave-number domain unit load distribution at a particle \mathbf{i} as $\tilde{p}_1^{\mathbf{i}}(k) = \tilde{p}_1(k)e^{-ikx_{\mathbf{i}}}$. Consequently, the two boundary conditions at the interface of the horizontal sublayers at the z-coordinate $z_{\mathbf{i}}$ of the load applied at a particle \mathbf{i} are found as:

$$\tilde{\tilde{\sigma}}_{zx,II}\left(k,z,s\right)\Big|_{z=z_{i}} - \tilde{\tilde{\sigma}}_{zx,I}\left(k,z,s\right)\Big|_{z=z_{i}} = \tilde{\tilde{p}}_{1,x}\left(k\right)e^{-ikx_{i}}$$

$$(3.107)$$

$$\left. \tilde{\sigma}_{zz,II}\left(k,z,s\right) \right|_{z=z_{1}} - \tilde{\sigma}_{zz,I}\left(k,z,s\right) \right|_{z=z_{1}} = \left. \tilde{p}_{1,z}\left(k\right)e^{-ikx_{1}} \right. \tag{3.108}$$

Here, $\tilde{p}_{1,x}(k)$ and $\tilde{p}_{1,z}(k)$ respectively denote the horizontal and vertical load distributions at particle **i**, that are described exclusively in terms of the wavenumber k, since their time dependence, given by the Dirac delta function $\delta(t)$, is removed by the transformation to the Laplace-wavenumber domain. Consequently, $\tilde{p}_{1,z}(k)$ and $\tilde{p}_{1,z}(k)$ describe the wave-

number dependency on the chosen shape of the unit load distribution and thereby determine the convergence of the Green's functions in the wavenumber domain. This is further discussed in Section 3.5.4 for several shapes of the unit distribution.

Equations (3.103) to (3.108) give the complete set of boundary conditions for a horizontally distributed load inside the continuous layer. Substituting equations (3.93) to (3.102) into the given set of boundary conditions yields the system of eight algebraic equations of motion that may be solved for the unknown wave amplitudes A_1 to A_8 . The resulting system of boundary conditions is given in terms of the wave amplitudes A_1 to A_8 in Appendix F.4.

In accordance with equations (3.107) and (3.108), the boundary conditions for a load applied inside a continuous layer must always be described along the horizontal interface of its sublayers. Therefore, if we wish to determine the displacements and stresses in the continuum due to a distributed load, this load must be distributed horizontally. To satisfy the reciprocal work theorem, and thereby allowing the use of the dynamic stiffness and compliance matrices as derived in equations (3.80) and (3.81), any unit load must be applied at or along the boundary Γ . Consequently, the boundary Γ must always be horizontal at the domain of particle i at which a distributed load is applied. As previously specified in Section 3.5.1, the shape of the boundary Γ may be freely chosen as long as all particles at the lattice-continuum interface are part of the boundary Γ . The path of the boundary Γ is therefore adapted such that it has a horizontal domain at all particles on the interface resulting in the boundary depicted in Figure 3.19. Note here that the domain of particle i on the boundary Γ at which the unit load distribution is applied, described as $\{x_i - \Delta x \dots x_i + \Delta x\}$, does not have the same size for all particles along Γ .

Green's functions for the lumping and flexibility matrices

To construct the lumping and flexibility matrices, we require separate expressions for the displacements and stresses due to unit loads that are either applied in horizontal or vertical direction respectively. To this purpose, the system of boundary conditions, given by equations (3.93) to (3.102), is solved for $\tilde{p}_{1,x}(k) = 1$ and $\tilde{p}_{1,z}(k) = 0$ first and the expressions for the resulting wavenumbers A_1 to A_8 are denoted as $A_{x:1}^i$ to $A_{x:8}^i$. This yields the Green's expressions for the displacements and stresses due to an exclusive horizontal load at a particle i. The Green's expressions for the displacements and stresses due to an exclusive vertical load at a particle **i** are found by solving the system of boundary conditions for $\hat{p}_{1,x}(k) = 0$ and $\tilde{p}_{1,z}(k) = 1$, and denoting the resulting expressions for the wavenumbers A_1 to A_8 as $A_{z;1}^i$ to $A_{z,8}^{i}$. The so-called modified Green's displacements and modified Green's stresses, i.e. the displacements and stresses due to a unit load distribution, are now obtained by multiplying the Green's displacements and Green's stresses due to the horizontal and vertical loads by the expression for the unit load distribution in the Laplace-wavenumber domain, denoted as $\tilde{p}_1(k)$. Omitting the directional indices, the modified Green's displacements and modified Green's stresses along Γ due to a unit load distribution at a particle i may generally thus be described in the Laplace-wavenumber domain as:

$$\tilde{\tilde{u}}_{1}^{i}(k,z,s) = \tilde{\tilde{g}}_{u}^{i}(k,z,s)\,\tilde{\tilde{p}}_{1}(k) \tag{3.109}$$

$$\tilde{\tilde{\sigma}}_{1}^{i}(k,z,s) = \tilde{\tilde{g}}_{\sigma}^{i}(k,z,s)\,\tilde{\tilde{p}}_{1}(k) \tag{3.110}$$

Here, $\tilde{g}_u^i(k,z,s)$ and $\tilde{g}_\sigma^i(k,z,s)$ respectively refer to the Green's displacements and Green's stresses that are obtained by separately solving the system of boundary conditions (3.103) to (3.108) for either a horizontal or a vertical unit load at a particle **i** on the boundary Γ .

The expressions for the Green's displacements and Green's stresses due to respectively horizontally and vertically applied unit loads at a particle $\bf i$ located inside the continuous layer, derived from the system of boundary conditions, are given in Appendix F.4. Note here that the exponent $e^{-ik\alpha}$, related to the position of the particle $\bf i$, is included in these expressions. For the particular case that the particle $\bf i$ is located at the surface, the system of four algebraic equations of motion, as well as the resulting expressions for the Green's displacements and Green's stresses are derived and given in Appendix F.5.

Modified Green's functions for the continuous layer in the Laplace domain

Applying the inverse Fourier transform with respect to the wavenumber k to the modified Green's displacements and stresses in equations (3.109) and (3.110) yields the modified Green's displacements and stresses in the Laplace domain as:

$$\tilde{u}_{1}^{i}(x,z,s) = \frac{1}{2\pi} \int_{-\infty}^{+\infty} \tilde{\tilde{g}}_{u}^{i}(k,z,s) \, \tilde{\tilde{p}}_{1}(k) e^{ikx} dk \tag{3.111}$$

$$\tilde{\sigma}_{1}^{i}(x,z,s) = \frac{1}{2\pi} \int_{-\infty}^{+\infty} \tilde{g}_{\sigma}^{i}(k,z,s) \, \tilde{p}_{1}(k) e^{ikx} dk \qquad (3.112)$$

To evaluate the inverse Fourier transforms in above equations, we apply contour integration by means of the residue theorem [Ahlfors, 1966], which is also referred to as Cauchy's residue theorem. Thus, we first extend the integrand to the complex plane and we subsequently choose a closed contour that consists of the real axis as well as a semicircle in either the upper or lower half of the complex plane. The integral over the closed contour is then obtained

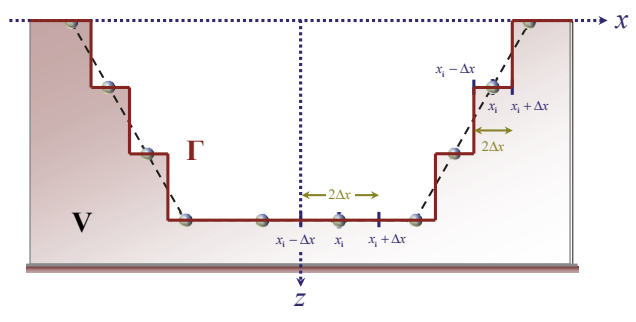


Figure 3.19: The path of the boundary Γ with horizontal domains at all boundary particles.

through its residues.

In Appendix I.1, this approach is exemplified by applying the contour integration to evaluate the inverse Fourier transform of an arbitrary complex-valued function $\tilde{f}(k)$ in the wavenumber domain. By means of the residue theorem, and assuming that all the poles are simple, it follows that the inverse Fourier transform of this function may be obtained as:

$$\frac{1}{2\pi} \int_{-\infty}^{+\infty} \tilde{f}(k) e^{ikx} dk = \pm i \sum_{j} \frac{N(\tilde{f}, k_{j}^{\times})}{\frac{\partial}{\partial k} \Delta(\tilde{f}, k) \Big|_{k=k_{j}^{\times}}} e^{ik_{j}^{\times} x}$$

Here, $N(\tilde{f},k)$ and $\Delta(\tilde{f},k)$ respectively denote the numerator and denominator of the considered expression, while k_j^{\times} denotes the poles, or singularities, of the function $\tilde{f}(k)$ within a closed contour that encompasses all the poles.

Applying the contour integration by means of the residue theorem to evaluate the inverse Fourier transforms in equations (3.111) and (3.112), the modified Green's displacements and stresses in the Laplace domain become:

$$\tilde{u}_{1}^{i}(x,z,s) = \pm i \sum_{j} \frac{N\left(\tilde{\tilde{g}}_{u}^{i}, k_{j}^{\times}\right)}{\frac{\partial}{\partial k} \Delta(k) \Big|_{k=k_{j}^{\times}}} \tilde{\tilde{p}}_{1}\left(k_{j}^{\times}\right) e^{ik_{j}^{\times}x} \pm i \sum_{j} \tilde{\tilde{g}}_{u}^{i}\left(k_{j}^{\otimes}, z, s\right) \frac{N\left(\tilde{\tilde{p}}_{1}, k_{j}^{\otimes}\right)}{\frac{\partial}{\partial k} \Delta\left(\tilde{\tilde{p}}_{1}, k\right) \Big|_{k=k^{\otimes}}} e^{ik_{j}^{\otimes}x}$$
(3.113)

$$\tilde{\sigma}_{1}^{i}(x,z,s) = \pm i \sum_{j} \frac{N\left(\tilde{\tilde{g}}_{\sigma}^{i}, k_{j}^{\times}\right)}{\frac{\partial}{\partial k} \Delta(k) \Big|_{k=k_{j}^{\times}}} \tilde{\tilde{p}}_{1}\left(k_{j}^{\times}\right) e^{ik_{j}^{\times}x} \pm i \sum_{j} \tilde{\tilde{g}}_{\sigma}^{i}\left(k_{j}^{\otimes}, z, s\right) \frac{N\left(\tilde{\tilde{p}}_{1}, k_{j}^{\otimes}\right)}{\frac{\partial}{\partial k} \Delta\left(\tilde{\tilde{p}}_{1}, k\right) \Big|_{k=k_{j}^{\otimes}}} e^{ik_{j}^{\otimes}x}$$
(3.114)

Note here that, since the Green's displacements $\tilde{g}_u^i(k,z,s)$ and the Green's stresses $\tilde{g}_\sigma^i(k,z,s)$ both originate from the system of equations of motion for the continuous layer, they have the same denominator, which is here denoted as $\Delta(k)$. Consequently, both displacements and stresses have the same poles in the complex k-plane, that are denoted as k_j^* . Furthermore, $\Delta(\tilde{p}_1,k)$ and k_j^* , respectively denote the denominator and the poles of the unit load distribution $\tilde{p}_1(k)$.

It is important to emphasize that the numerators $N\left(\tilde{g}_{u}^{i},k\right)$ and $N\left(\tilde{g}_{\sigma}^{i},k\right)$, and the common denominator $\Delta(k)$ must here be chosen such that either function is single-valued. The single-valued common denominator is obtained from the determinant of the system of equations of motion for the continuous layer as:

$$\Delta(k) = 4k^{2}R_{P}R_{S}\gamma_{S} + k^{2}\left(4R_{P}^{2}R_{S}^{2} + \gamma_{S}^{2}\right)\sinh R_{P}z_{b}\sinh R_{S}z_{b} - R_{P}R_{S}\left(4k^{4} + \gamma_{S}^{2}\right)\cosh R_{P}z_{b}\cosh R_{S}z_{b}$$
(3.115)

The numerators $N(\tilde{g}_u^i, k)$ and $N(\tilde{g}_\sigma^i, k)$ are now straightforwardly obtained by omitting the denominator $\Delta(k)$ from the expressions for the Green's displacements and Green's stresses

in the Laplace-wavenumber domain as given in Appendices F.4 and F.5.

The signs in equations (3.113) and (3.114) are positive when the contour is chosen over the upper half of the complex k-plane, and negative when the contour is chosen over the lower half of the complex k-plane. Whether to choose the contour over the upper or lower half of the complex k-plane follows from the requirement that the contribution of the semicircle-segment to the contour integral must fade when the radius of the semicircle goes to infinity, so that only the real-axis segment of the contour integral remains. Note here that, due to the hyperbolic functions appearing in the expression for the common denominator $\Delta(k)$, the number of roots, or zeroes, of the denominator, i.e. the number of poles of the Green's functions, is infinite within the contour in the limit that the radius of the semicirclesegment of the contour goes to infinity. Consequently, as the contribution of the semicirclesegment to the contour integral must fade with an increase of the semicircle radius, so must the contribution of a residue fade as the imaginary part of the corresponding root increases. In other words, if the imaginary part of a root goes to infinity, the contribution of its residue to the contour integral must go to zero. Consequently, the contour is chosen over the half of the complex k-plane for which the exponents in equations (3.113) and (3.114) go to zero. It follows that, for $x > x_i$, the modified Green's displacements and stresses converge if the imaginary part of the roots go to positive infinity, and thus the contour is chosen over the upper half of the complex k-plane. Accordingly, for $x < x_i$, the imaginary part of the roots must go to negative infinity and the contour is therefore chosen over the lower half of the complex k-plane. The number of roots that are to be taken into account are then chosen such that the contribution of an additional root is negligible.

For the particular case that $x = x_i$, the exponents disappear from equations (3.113) and (3.114) and do not contribute to the convergence of these equations. As a consequence, choosing the contour over either the upper or lower half of the complex k-plane is arbitrary for this case. Noting that the residues in equations (3.113) and (3.114) do not necessarily converge for large imaginary parts of a pole k_j^* , the convergence of these equations is exclusively determined by the shape and therefore by the equation for the chosen unit load distribution in the Laplace-wavenumber domain, denoted as $\tilde{p}_1(k)$. This unit load distribution is generally chosen such that it has a finite amount of its own residues that are taken into account separately by the second term on the right-hand side of equations (3.113) and (3.114). To assure the convergence of the modified Green's displacements and stresses, the poles corresponding to the residues of the unit load distribution must all be located within the applied contour.

Essential to applying the contour integration by means of the residue theorem, and thus to obtain the modified Green's displacements and stresses in the Laplace domain through equations (3.113) and (3.114), is to correctly determine their poles, and thus to correctly determine the roots, or zeroes, of the denominator $\Delta(k)$ in the complex k-plane. To this purpose, we have developed a numerical algorithm to find the roots of the common denominator in the complex k-plane, which is extensively discussed in Appendix I.2. In summary, the algorithm to find the roots of an arbitrary frequency-dependent function within a contour in the complex k-plane consists of the following steps. First, we determine the number of roots

within the domain of the considered contour for a single frequency by applying Cauchy's Argument Principle [Krantz, 1999] and we order the roots using the heapsort method [Williams, 1964]. Next, we divide this domain into subdomains, such that each subdomain contains exactly one root. Then, we use a minimization algorithm, in this case the Nelder-Mead algorithm [Nelder and Mead, 1965], to determine the exact location of the root within each subdomain. Once the locations of the roots for one frequency are known, the roots may be straightforwardly determined for other frequencies, as from one frequency to the next, the roots only shift slightly within the complex *k*-plane.

Figure 3.20a and Figure 3.20b show the first 26 roots of the common denominator $\Delta(k)$ in the positive half of the complex k-plane for respectively a damping ratio $\zeta = 0.1$ and a damping ratio $\zeta = 0.75$. Here, the black crosses, the red plusses and the blue diamonds respectively refer to the roots of the common denominator at frequencies $\omega = 1.0 \text{ rad/s}$, $\omega = 20 \text{ rad/s}$ and $\omega = 50 \text{ rad/s}$. For the frequency $\omega = 1.0 \text{ rad/s}$, it can be seen from Figure 3.20 that the locations of all roots in the complex k-plane are nearly the same for both damping ratio's. In fact, as there is no influence of the damping in the static case, the position of the roots for both damping ratios must be exactly the same at zero frequency. The symmetry of the root-positions with respect to the imaginary axis at zero frequency is due to the homogeneity of the continuous layer. With increasing frequency, the roots first move towards the real axis and then move parallel to the real axis in the negative direction. For zero damping, these roots would be located exactly on the real axis and it is therefore logically explained that for a damping ratio $\zeta = 0.1$, the roots along the real axis are much closer to this axis than the corresponding roots for a damping ratio $\zeta = 0.75$. Note here that Appendix I.2 includes a figure showing the paths of the first six roots of the denominator $\Delta(k)$ as a function of frequency in the complex k-plane for both damping ratio's.

With the roots of the common denominator $\Delta(k)$ known, only the roots of the unit load distribution remain to determine the modified Green's displacements and stresses (3.113) and (3.114) as a function of frequency and thus as a function of the Laplace parameter s.

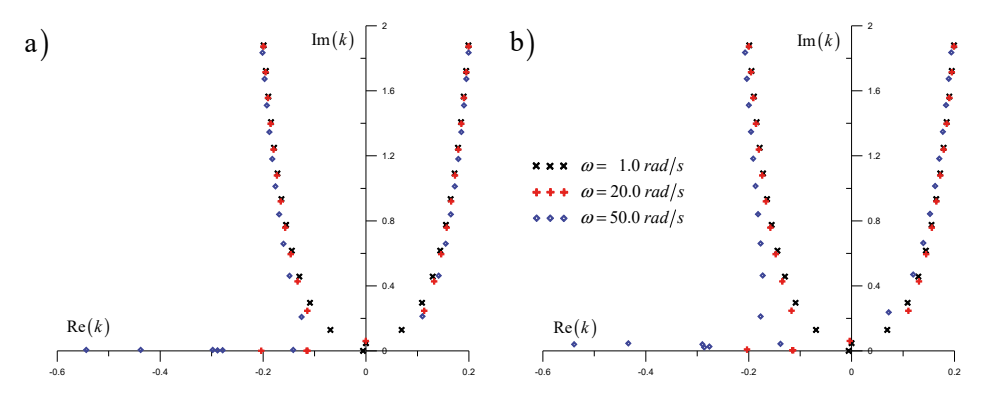


Figure 3.20: The first 26 roots of the denominator $\Delta(k)$ in the complex plane: a) for a damping ratio $\zeta = 0.1$; b) for a damping ratio $\zeta = 0.75$.

3.5.4 Unit load distributions in the Laplace-wavenumber domain

As previously noted, a unit load is a load for which the resultant of its distribution equals one, and any unit load distribution applied at a particle must always be distributed horizontally to comply with the boundary conditions for a horizontally distributed load applied inside the continuous layer, given by equations (3.103) to (3.108). The shape of the unit load distribution at a particle **i** may thus be denoted in space as $p_1(x-x_i)$. According to equations (3.107) and (3.108), the location of particle **i** is in the Laplace-wavenumber domain incorporated in the exponent e^{-ikx_i} . Thereby, it influences the choice over which half of the complex k-plane the contour is chosen, but the location of a particle **i** does not influence the convergence of the modified Green's displacements and stresses. This is especially true for the particular case that $x = x_i$ for which the exponents in equations (3.113) and (3.114) disappear. The convergence of these Green's functions is however influenced by the shape of the unit load distribution, which is independent from the location of particle **i**, and is thus denoted in the space-time domain as $p_1(x,t) = p_1(x)\delta(t)$.

Figure 3.21 shows the unit point load together with three possible shapes for the unit load distribution: the constant load distribution, an exponentially decaying load distribution and a bell-shaped load distribution. As noted previously, the point load causes significant issues when applied to a two-dimensional continuum and is therefore not further discussed here. In the Laplace-wavenumber domain, the piecewise constant load distribution is found as $\tilde{p}_1(k) = 2\sin(k\Delta x)/k$ and thus provides an additional convergence of k^{-1} . Due to the differentiation of the denominator with respect to the wavenumber k in the expression for the residues however, this additional convergence is insufficient to assure the convergence of equations (3.113) and (3.114) for the particular case that $x = x_i$. The shape of the unit load distribution should thus be chosen to have a higher rate of convergence in the Laplace-wavenumber domain. This can for example be achieved by introducing a unit load distribution that decays exponentially in space:

$$p_1(x) = \frac{a}{2}e^{-a|x|} \tag{3.116}$$

Here, a is a positive real constant that determines the decay of the load distribution in space and the factor a/2 is included to make sure that equation (3.116) is, in fact, a unit distribution. Applying the Fourier and Laplace transforms with respect to respectively space and time over the resulting expression for $p_1(x,t)$ yields the exponentially decaying unit load distribution in the Laplace-wavenumber domain as:

$$\tilde{\tilde{p}}_{1}(k) = \frac{a^{2}}{k^{2} + a^{2}} \tag{3.117}$$

The exponentially decaying unit load distribution converges a factor k^2 faster than the unit point load. For this unit load distribution, the modified Green's functions in equations (3.113) and (3.114) thus converge with a rate k^{-1} . Furthermore it follows from equation (3.117) that,

by applying the exponentially decaying load distribution, we introduce one additional pole within the applied contour over either the upper half or the lower half of the complex k-plane. The corresponding poles are respectively found as $k_1^{\otimes} = +ia$ or $k_1^{\otimes} = -ia$.

To further improve the performance of the modified Green's functions, we can principally choose any distribution that causes the modified Green's functions to converge faster with the wavenumber k. In this case, we choose the unit distribution in the Laplace-wavenumber domain as:

$$\tilde{\tilde{p}}_{1}(k) = \frac{a^{2}b^{2}c^{2}}{(k^{2} + a^{2})(k^{2} + b^{2})(k^{2} + c^{2})}$$
(3.118)

The unit load distribution given by equation (3.118) causes the modified Green's functions in equations (3.113) and (3.114) to converge with a rate k^5 . The additional poles in either half of the complex k-plane that are introduced by applying the above load distribution are respectively found as $k_1^{\otimes} = \pm ia$, $k_2^{\otimes} = \pm ib$ and $k_3^{\otimes} = \pm ic$.

Applying the inverse Fourier transform with respect to the wavenumber yields a so-called bell-shaped unit load distribution in the space domain as:

$$p_{1}(x) = \frac{a}{2} \frac{b^{2} c^{2} e^{-a|x|}}{(b^{2} - a^{2})(c^{2} - a^{2})} + \frac{b}{2} \frac{a^{2} c^{2} e^{-b|x|}}{(a^{2} - b^{2})(c^{2} - b^{2})} + \frac{c}{2} \frac{a^{2} b^{2} e^{-c|x|}}{(a^{2} - c^{2})(b^{2} - c^{2})}$$
(3.119)

Here, a, b and c are positive real constants that determine the spatial decay of the bell-shaped distribution.

Whereas the unit point load and the piecewise constant unit load distribution at a particle **i** both exactly fit the horizontal domain $\{x_i - \Delta x ... x_i + \Delta x\}$ of that particle along the boundary Γ , the exponentially decaying and bell-shaped load distributions are not restricted to this domain. We may however apply both distributions if the contribution of the load outside the domain of the considered particle is negligible. It thus follows that, according to respectively

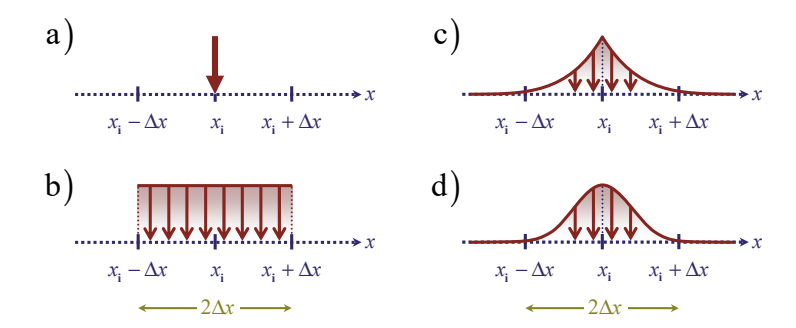


Figure 3.21: a) the unit point load; b) the constant unit load distribution; c) the exponentially decaying unit load distribution; d) the bell-shaped unit load distribution.

equations (3.116) and (3.119), the value of the exponentially decaying and bell-shaped unit load distributions at $x = \pm \Delta x$ must be significantly smaller than its value at x = 0. For example, demanding the decay such that its value at $x = \pm \Delta x$ is 1% of the peak value, i.e. $p_1(\Delta x) = 10^{-2} p_1(0)$, yields the constant a for the exponentially decaying function by approximation as $a = 4.61/\Delta x$. For this a, the resulting segment of the exponentially decaying unit load distribution that is included within the horizontal domain of a particle is found as:

$$a = \frac{4.61}{\Delta x} \rightarrow \int_{-\Delta x}^{+\Delta x} p_1(x) dx = \int_{-\Delta x}^{+\Delta x} \frac{a}{2} e^{-a|x|} dx = 0.9900$$
 (3.120)

For the bell-shaped unit load distribution, we find many possible combinations for the constants a, b and c that yield the same decay. An example of a combination of these constants that satisfies the given decay is found as $a = 7.6/\Delta x$, $b = 8.0/\Delta x$ and $c = 8.6/\Delta x$. The part of the bell-shaped unit load distribution at a particle i that is included within the horizontal domain $\{x_i - \Delta x ... x_i + \Delta x\}$ is in this case found as:

$$a = \frac{7.6}{\Delta x}; b = \frac{8.0}{\Delta x}; c = \frac{8.6}{\Delta x}; \rightarrow \int_{-\Delta x}^{+\Delta x} p_1(x) dx = 0.9954$$
 (3.121)

Thus, the bell-shaped unit load distribution does not only yield a better convergence for the modified Green's functions than the exponentially decaying unit load distribution, but it also includes a larger part of the unit distribution within the horizontal domain along Γ that belongs to the corresponding particle. This is important because any part of the unit distribution that is applied outside the horizontal domain $\{x_i - \Delta x ... x_i + \Delta x\}$ of particle i is, in many cases, not applied along the boundary Γ at all and thereby violates the reciprocal work theorem. Ergo, reducing the magnitude of the unit distributions that are applied outside the horizontal domain of the corresponding particles, reduces the error in the derived dynamic stiffness and compliance matrices.

Finally note that all three given poles of the bell-shaped unit load distribution are located further away from the origin of the complex k-plane than the single pole of the exponentially decaying unit load distribution. For the particular case that $x = x_i$, this directly influences the required size of the contour and thus the number of roots of the common denominator $\Delta(k)$ that must be accounted for in the contour integration to accurately obtain the modified Green's functions. While this also influences the size of the required contour when $x \neq x_i$, this influence is less significant due to the convergence of the modified Green's displacements and stresses as a function of the wavenumber.

3.6 The two-dimensional discrete-continuous BKV system

The two-dimensional discrete-continuous BKV system that is composed of a hexagonal BKV lattice and a two-dimensional continuous layer is depicted in Figure 3.22. Any external time-dependent load, denoted as F(t), is applied at the particle with nodal coordinates 0,0, located

at the origin of the lattice. Any particle with nodal coordinates \mathbf{m} , \mathbf{n} has a mass $M^{\mathbf{m},\mathbf{n}}$ and the distance of the lattice is denoted by ℓ . Each BKV element between adjacent particles \mathbf{m} , \mathbf{n} and \mathbf{m}_j , \mathbf{n}_j consist of a Kelvin-Voigt element with a stiffness coefficient $K_{e;j}^{\mathbf{m},\mathbf{n}}$ and a damping coefficient $C_{e;j}^{\mathbf{m},\mathbf{n}}$ and a Bingham element with a damping coefficient $C_{f;j}^{\mathbf{m},\mathbf{n}}$ and a critical friction force $F_{cr;j}^{\mathbf{m},\mathbf{n}}$. The distance from the loaded particle to either particle at the lattice boundary is bridged by an equal number of BKV elements, and thus by an equal number of particles, in all directions. The size of the hexagonal lattice can therefore be described by, for example, the number of particle rows in the lattice. Denoting the row of particles at the horizontal boundary of the lattice as \mathbf{N} , the hexagonal lattice is found to consists of $\frac{\mathbf{N}+1}{2}(3\mathbf{N}+2)$ particles and the number of BKV elements in the hexagonal lattice follows as $\frac{\mathbf{N}}{2}(9\mathbf{N}+5)$. At its boundary, the lattice is connected to a viscoelastic continuous layer with a thickness z_b and a unit width dy, which is thus the dimension of the continuum in the y-direction. Furthermore, the continuous layer has a mass density ρ , a Young's modulus E, a Poisson's ratio v and a damping coefficient ζ_e . The interface between the hexagonal BKV lattice and the continuous layer is denoted as Γ .

In the following, we will first discuss the parameters for which the material properties of the hexagonal BKV lattice and the viscoelastic continuous layer match. Then, in Section 3.6.2, we will present the governing system of equations of motion for the two-dimensional discrete-continuous system by first specifically deriving the equations of motion for the particles at the lattice-continuum interface both in the Laplace and in the time domain. Subsequently, guidance is given on how to determine the equations of motion for the particles in the interior of the hexagonal BKV lattice. Finally, Section 3.6.3 discusses the difficulties related to the numerical implementation of the two-dimensional discrete-continuous system and explains why deriving a boundary formulation from a continuum far-field does not serve well for the hexagonal BKV lattice.

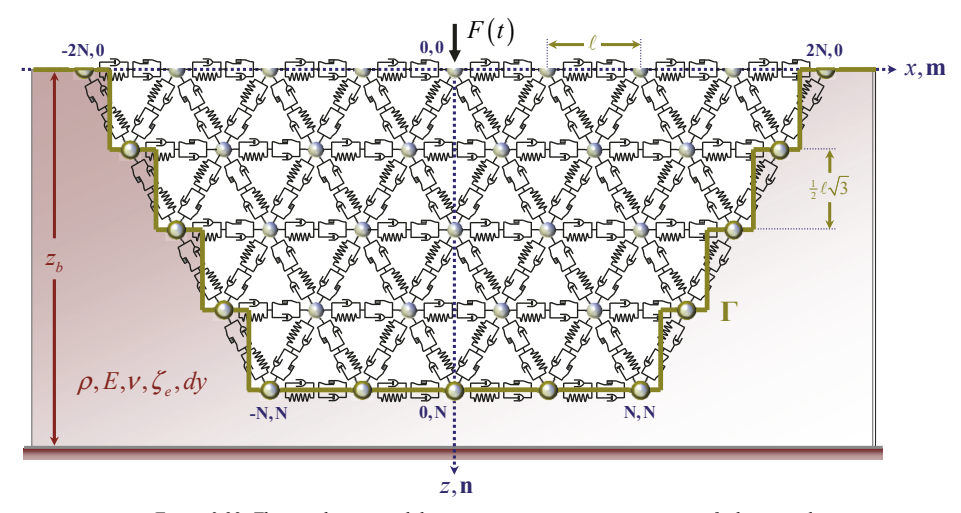


Figure 3.22: The two-dimensional discrete-continuous system consisting of a hexagonal BKV lattice and a viscoelastic continuous layer.

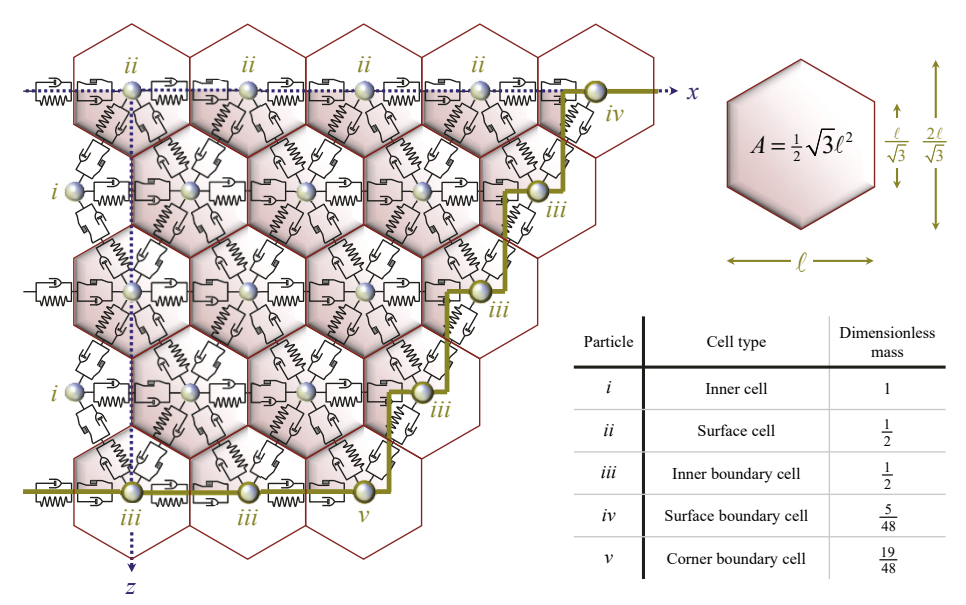


Figure 3.23: The masses of the particles in the hexagonal lattice correspond to the space their cells occupy,

3.6.1 Matching the parameters of the lattice and the continuum

As previously discussed with regard to the one-dimensional discrete-continuous BKV system in Section 3.2.1, the behaviour of a homogeneous medium modelled by a lattice in the near field and a continuum in the far field can only be described correctly when the parameters of the lattice and the continuum represent the same material. For the two-dimensional system consisting of a hexagonal BKV lattice and a two-dimensional continuum, this additionally requires the BKV elements to behave linearly at the lattice-continuum interface.

For both parts of the BKV system to represent the same material, first of all the mass per unit volume in the hexagonal BKV lattice and in the continuous layer must be equal. Figure 3.23 shows the area that the particles in the interior of the hexagonal lattice represent as a hexagon. Assuming the continuous layer to have a unit width dy in the third dimension, the mass of a particle in the interior of the hexagonal lattice is straightforwardly obtained from the dimensions of the hexagon and the unit width dy as $M = \frac{\sqrt{3}}{2} \rho \ell^2 dy$. Here, ρ is the mass density and ℓ is the distance between adjacent particles in the lattice. Figure 3.23 additionally shows that the particles at both the surface of the hexagonal lattice and at the lattice-continuum interface only represent a part of the unit hexagon area, and must therefore have smaller masses. The ratio of the masses of these particles at the edge of the lattice versus the mass of a particle in the interior of the lattice, i.e. the normalized or dimensionless mass, follows directly from the part of the unit hexagon that each of these particles represent. In the table accompanying Figure 3.23, the dimensionless mass is given for all different particles types existing in the hexagonal lattice.

To obtain the relations between the parameters of the hexagonal BKV lattice and the

continuum properties, we may consider the hexagonal lattice to consist of viscoelastic Kelvin-Voigt elements rather than nonlinear BKV elements. In Appendix C.1, the parameters of the hexagonal Kelvin-Voigt lattice are derived from the macromaterial, or continuum, properties by noting that the homogeneous equations of motion for the hexagonal Kelvin-Voigt lattice must in the long-wave limit reduce to the equations of motion for the viscoelastic continuum [Maradudin et al., 1971; Suiker et al., 2001a]. From the comparison between the models, it follows that the material properties of the hexagonal lattice and the continuous layer can only match if the Poisson's ratio is equal to $\nu = \frac{1}{4}$. By taking the previously derived relation between the parameters of the hexagonal BKV lattice and the material properties of the continuous layer follow as:

$$M = \frac{\sqrt{3}}{2} \rho \ell^2 dy, \quad C_e = \zeta_e \frac{8}{5\sqrt{3}} E dy, \quad K_e = \frac{8}{5\sqrt{3}} E dy$$
 (3.122)

Furthermore, note that the shear and compressional wave velocities in the hexagonal BKV lattice may respectively be expressed in terms of the Young's modulus and the density of the continuous layer as $c_s^2 = \frac{2}{5}E/\rho$ and $c_p^2 = \frac{6}{5}E/\rho$, so that $c_p = c_s\sqrt{3}$.

3.6.2 Governing equations for the 2D discrete-continuous BKV system

In accordance with the approach for the one-dimensional discrete-continuous system, we normalize the governing system of equations of motion by introducing dimensionless parameters for time, space and mass. For the two-dimensional discrete-continuous BKV system, these are:

$$t=t_{\mathrm{dim}}\omega_0\,,\quad u^{\mathbf{m},\mathbf{n}}=\frac{u_{\mathrm{dim}}^{\mathbf{m},\mathbf{n}}}{\ell}\,,\quad M^{\mathbf{m},\mathbf{n}}=\frac{M_{\mathrm{dim}}^{\mathbf{m},\mathbf{n}}}{\frac{\sqrt{5}}{2}\rho\ell^2dy}.$$

Here, ω_0 is the particle frequency of the homogeneous hexagonal BKV lattice, which is derived in Appendix B.4 as $\omega_0 = \sqrt{3K_e/M}$. Furthermore, we introduce the dimensionless damping in the form of the damping ratio $\zeta = C_e/C_{crit}$, where C_{crit} is the critical particle damping, derived in Appendix B.4 as $C_{crit} = \frac{2}{3}M\omega_0$. According to Appendix B.2, this yields the damping ratio, the damping and the stiffness of the BKV elements in the lattice, as well as the dimensionless force, in terms of their dimensional counterparts as:

$$\zeta = \frac{1}{2} \zeta_e \omega_0, \quad C_{e;j}^{\mathbf{m,n}} = \frac{C_{e;j,\text{dim}}^{\mathbf{m,n}}}{\frac{3}{2} C_{crit}}, \quad K_{e;j}^{\mathbf{m,n}} = \frac{K_{e;j,\text{dim}}^{\mathbf{m,n}}}{\frac{8\sqrt{3}}{5} E dy} = \frac{K_{e;j,\text{dim}}^{\mathbf{m,n}}}{3K_e}, \quad F^{\mathbf{m,n}} = \frac{F_{\text{dim}}^{\mathbf{m,n}}}{\frac{8\sqrt{3}}{5} E dy \ell} = \frac{F_{\text{dim}}^{\mathbf{m,n}}}{3K_e \ell}.$$

Here, the numerator j denotes the rheological element between the particle \mathbf{m} , \mathbf{n} and an adjacent particle \mathbf{m}_j , \mathbf{n}_j . Furthermore, the expressions for M, C_e and K_e are given by equation (3.122). To reduce the number of variables in this thesis, the same notations are used for both

dimensional and dimensionless variables. In the direct relations between these variables given here however, the dimensional variables are given the subscript 'dim'.

In the two-dimensional discrete-continuous BKV system, the far-field domain is described by a continuous layer. As an example, Figure 3.24 shows a boundary cell along the horizontal segment of the lattice-continuum interface. Since the location of the interface Γ is chosen in the region of the lattice where its response is linear, the Bingham elements in a boundary cell are not activated, and the corresponding BKV elements may be considered as Kelvin-Voigt elements. As previously explained in Section 2.4.1, any rheological elements at the interface have half the stiffness and half the damping of the elements in the interior of the lattice. Taking equation (3.122) into account, it follows that the inner elements of a boundary cell have a dimensionless stiffness $K_{e;j}^{\mathbf{m},\mathbf{n}} = \frac{1}{3}$ and a dimensionless damping coefficient $C_{e;j}^{\mathbf{m},\mathbf{n}} = \frac{2}{3} \zeta$, while the rheological elements along the interface Γ have a dimensionless stiffness $K_{e;j}^{\mathbf{m},\mathbf{n}} = \frac{1}{3} \zeta$.

Disregarding the force-displacement relation at the lattice-continuum interface, the equations of motion for any boundary particle \mathbf{m} , \mathbf{n} may be obtained from equations (2.34) and (2.35) by accounting for the correct number of rheological elements and noting that the elongations of any involved Bingham elements are equal to zero. As the number of elements is not equal for all boundary cells, the number of rheological elements in the cell of an boundary particle \mathbf{m} , \mathbf{n} is here denoted as $n_e^{\mathbf{m},\mathbf{n}}$. Including the forces that are applied to the boundary particle \mathbf{m} , \mathbf{n} by the interaction with the continuous layer in x- and z-direction, respectively denoted as $\tilde{F}_{int,x}^{\mathbf{m},\mathbf{n}}(s)$ and $\tilde{F}_{int,x}^{\mathbf{m},\mathbf{n}}(s)$, the equations of motion for a particle at the lattice-continuum interface may be expressed in the Laplace domain as:

$$M^{\mathbf{m},\mathbf{n}} s^{2} \tilde{u}_{x}^{\mathbf{m},\mathbf{n}} - \sum_{j=1}^{n_{e}^{\mathbf{m},\mathbf{n}}} \left(C_{e,j}^{\mathbf{m},\mathbf{n}} s + K_{e,j}^{\mathbf{m},\mathbf{n}} \right) \tilde{e}_{j}^{\mathbf{m},\mathbf{n}} \cos \alpha_{j}^{\mathbf{m},\mathbf{n}} + \tilde{F}_{Int,x}^{\mathbf{m},\mathbf{n}} \left(s \right) = 0$$
(3.123)

$$M^{m,n} s^{2} \tilde{u}_{z}^{m,n} - \sum_{j=1}^{n_{e}^{m,n}} \left(C_{e;j}^{m,n} s + K_{e;j}^{m,n} \right) \tilde{e}_{j}^{m,n} \sin \alpha_{j}^{m,n} + \tilde{F}_{Int,z}^{m,n} \left(s \right) = 0$$
(3.124)

The interaction forces $\tilde{F}_{lnt,x}^{\mathbf{m,n}}(s)$ and $\tilde{F}_{lnt,z}^{\mathbf{m,n}}(s)$ in equations (3.123) and (3.124) are expressed in terms of the displacements of all particles along the interface Γ through the dynamic

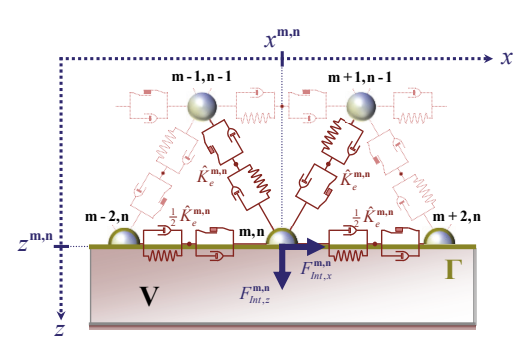


Figure 3.24: A boundary cell at the horizontal segment of the lattice-continuum interface.

stiffness relation given by equation (3.2). Collecting the equations for all boundary particles into a single expression and including the dynamic stiffness relation, the governing system of interface equations reads:

$$\underline{\underline{M}}_{Int} s^2 \underline{\tilde{u}}_{Int} + \left(\underline{\underline{C}}_{Int} s + \underline{\underline{K}}_{Int}\right) \underline{\tilde{u}} + \underline{\tilde{\chi}}(s) \underline{\tilde{u}}_{Int} = 0$$
(3.125)

Here, $\underline{\underline{M}}_{Int}$, $\underline{\underline{C}}_{Int}$ and $\underline{\underline{K}}_{Int}$ are respectively the mass, damping and stiffness matrices for the particles along the lattice boundary, i.e. along the lattice-continuum interface. Furthermore, the displacement vector $\underline{\tilde{u}}_{Int}$ contains the horizontal and vertical displacements of the particles at the lattice-continuum interface, while the displacement vector $\underline{\tilde{u}}$ contains the displacements of all particles that are present in the boundary cells of the hexagonal BKV lattice.

Because the terms in the dynamic stiffness matrix increase for $\Omega \to \infty$, we pre-multiply (3.125) by the dynamic compliance matrix $\tilde{\beta}(s)$. The system of interface equations of motion for the hexagonal BKV lattice in the Laplace domain thus reads:

$$\underline{\tilde{u}}_{Int} + \underline{\tilde{\beta}}(s) \left(\underline{\underline{M}}_{Int} s^2 \underline{\tilde{u}}_{Int} + \left(\underline{\underline{C}}_{Int} s + \underline{\underline{K}}_{Int}\right) \underline{\tilde{u}}\right) = 0$$
(3.126)

Here, note that the interface displacement vector $\underline{\tilde{u}}_{Int}$ is a subset of the displacement vector $\underline{\tilde{u}}$, so that both equations (3.125) and (3.126) may be rearranged into the form $\underline{\underline{A}}(s)\underline{\tilde{u}}=0$. Applying the inverse Laplace transform to equation (3.126) then yields:

$$\underline{\underline{u}}_{lnt} + \int_{0}^{t} \underline{\underline{\beta}} (t - \tau) \Big(\underline{\underline{M}}_{lnt} \underline{\underline{u}}_{lnt} + \underline{\underline{C}}_{lnt} \underline{\underline{u}} + \underline{\underline{K}}_{lnt} \underline{\underline{u}} \Big) (\tau) d\tau = 0$$
(3.127)

Here, $\beta(t)$ is the time domain dynamic compliance matrix. In correspondence with the approach used for the one-dimensional discrete-continuous system in Section 3.2.3, we differentiate equation (3.127) using Leibniz' rule for differentiation of integrals [Abramowitz and Stegun, 1972; Woods, 1926] with the purpose of obtaining a nonzero acceleration term at the current time step that allows us to numerically solve the system of ordinary differential equations for the near-field lattice in the time domain. This yields the time domain system of interface equations as:

$$\underline{\dot{u}}_{Int} + \underline{\beta}(0) \left(\underline{\underline{M}}_{Int} \underline{\ddot{u}}_{Int} + \underline{\underline{C}}_{Int} \underline{\dot{u}} + \underline{\underline{K}}_{Int} \underline{u} \right) + \int_{0}^{t} \underline{\dot{\beta}}(t - \tau) \left\{ \underline{\underline{M}}_{Int} \underline{\ddot{u}}_{Int} + \underline{\underline{C}}_{Int} \underline{\dot{u}} + \underline{\underline{K}}_{Int} \underline{u} \right\} (\tau) d\tau = 0$$
 (3.128)

Here, $\beta(0)$ is the time domain dynamic compliance matrix at t = 0, while $\dot{\beta}(t)$ is the time domain admittance matrix that equals the time derivative of the time domain dynamic compliance matrix. Note here that, in correspondence with the dynamic compliances for the viscoelastic rod and the viscoelastic dispersive rod, the dynamic compliance matrix for the viscoelastic continuous layer may also very well be equal to zero. Nevertheless, as discussed in

the upcoming Section 3.6.3, we failed to numerically obtain the modified Green's functions for the continuous layer and therefore the behaviour of the time domain dynamic compliances for $t \to 0$ cannot be verified.

To properly account for large deflections in the nonlinear BKV lattice, we here apply the linearization for large elongations according to Appendix A.2. In this approach, the total elongation of the rheological elements in the lattice at time t is described in terms of the particle displacements during the last time step dt prior to time t and the elongation of the rheological elements at time t-dt, which are constant during the current time step. In this way, the particle displacements can be tuned to remain small as their magnitude depends on the size of the time step dt, while the total elongation of the rheological elements can be large.

In the system of interface equations described by equation (3.128), the elongations of the rheological elements are embedded in the stiffness term $\underline{\underline{K}}_{lnt}\underline{u}$. To apply the linearization for large elongations, we replace this stiffness term by a stiffness term that includes the particle displacements during the current time step dt and a force vector related to the elongation of the rheological elements at time t-dt, i.e. $\underline{\underline{K}}_{lnt}\underline{u} \to \underline{\underline{K}}_{lnt}\underline{u} + \underline{F}_{\varepsilon,lnt}$. Accounting for the linearization for large elongations, the system of interface equations thus becomes:

$$\underline{\dot{u}}_{Int} + \underline{\beta}(0) \Big(\underline{\underline{M}}_{Int} \underline{\ddot{u}}_{Int} + \underline{\underline{C}}_{Int} \underline{\dot{u}} + \underline{\underline{K}}_{Int} \underline{u} + \underline{F}_{\varepsilon,Int} \Big)
+ \int_{0}^{t} \underline{\dot{\beta}}(t-\tau) \Big\{ \underline{\underline{M}}_{Int} \underline{\ddot{u}}_{Int} + \underline{\underline{C}}_{Int} \underline{\dot{u}} + \underline{\underline{K}}_{Int} \underline{u} + \underline{F}_{\varepsilon,Int} \Big\} (\tau) d\tau = 0$$
(3.129)

Here, the displacement vector \underline{u} now includes the particle displacements as they occur during the current time step dt, while the force vector $\underline{F}_{\varepsilon,lnt}$ contains the stiffness contribution of the elongations of all BKV elements at or attached to the interface Γ , before the current time step, i.e. at time t-dt. Note here that during the current time step dt, any quantity described at time t-dt is a constant so that the force vector $\underline{F}_{\varepsilon,lnt}$ is also constant during the time step dt. Furthermore, since the location of the lattice boundary is by definition chosen at such a distance from the origin, i.e. from an applied load, that any nonlinearities occurring in the lattice do not reach the boundary, it follows that any BKV elements at or attached to the interface Γ must behave viscoelastically. Therefore, the stiffness contribution of the BKV elements at or attached to the interface at time t-dt can be expressed in terms of the elongation of the whole BKV element. Denoting the elongation of the BKV element between particles \mathbf{m} , \mathbf{n} and $\mathbf{m}_{\mathbf{j}}$, $\mathbf{n}_{\mathbf{j}}$ at time t-dt as $\varepsilon_{\mathbf{j}}^{\mathbf{m},\mathbf{n}}$, the terms of the force vector $\underline{F}_{\varepsilon,lnt}$ related to the boundary particle \mathbf{m} , \mathbf{n} are respectively obtained in x- and z-direction as:

$$F_{\varepsilon,x}^{\mathbf{m},\mathbf{n}} = \sum_{j=1}^{n_{\varepsilon}^{\mathbf{m},\mathbf{n}}} K_{e;j}^{\mathbf{m},\mathbf{n}} \varepsilon_{j}^{\mathbf{m},\mathbf{n}} \cos \alpha_{j}^{\mathbf{m},\mathbf{n}}$$
(3.130)

$$F_{\varepsilon,z}^{\mathbf{m},\mathbf{n}} = \sum_{j=1}^{n_{\varepsilon}^{\mathbf{m},\mathbf{n}}} K_{\varepsilon,j}^{\mathbf{m},\mathbf{n}} \varepsilon_{j}^{\mathbf{m},\mathbf{n}} \sin \alpha_{j}^{\mathbf{m},\mathbf{n}}$$
(3.131)

Equation (3.129) gives the general system of equations of motion for the boundary particles of the hexagonal BKV lattice. Inserting the time domain dynamic compliance matrix for the continuous layer obtained by applying the inverse Laplace transform to the dynamic compliance matrix given by equation (3.81) completes the interface relations for the two-dimensional discrete-continuous system.

The system of equations of motion for the hexagonal lattice is completed by adding the equations of motion for all particles in the interior and at the surface of the hexagonal lattice. The equations of motion for particles in the interior of the hexagonal lattice with all BKV elements in either stick, slip and lock were previously derived and discussed in Sections 2.4.3, 2.4.4 and 2.4.5 respectively. At any given moment in time however, different BKV elements in the lattice may simultaneously behave according to different motion states. The resulting system of equations of motion for the hexagonal BKV lattice must therefore be continuously updated to correctly incorporate the variation of motion states over time. A full description of the governing system of equations of motion for the hexagonal BKV lattice that accounts for the variation in motion states over time is given in Section 4.7.3.

3.6.3 Discussion on the two-dimensional discrete-continuous system

Unfortunately, the numerical implementation of the boundary formulations for the near-field lattice derived from a continuous layer in the far field was unsuccessful and therefore no results are presented here. Although much was learned from attempts made, the decision was taken to discontinue our efforts aimed at the successful numerical implementation of the two-dimensional discrete continuous system. Several of the arguments that support this decision are here addressed briefly.

First of all, let us conclude that due to a mismatch in their dispersive properties, the continuous layer can never yield a perfectly non-reflective boundary for the hexagonal lattice. For the one-dimensional discrete-continuous systems this is testified for example by Figure 3.8, showing the corresponding nonzero amplitude and energy reflection coefficients. Deriving a boundary formulation from the far-field continuum that is applicable to the near-field lattice imposes additional difficulties in two dimensions. First and foremost, the forces that are applied by the hexagonal lattice to the continuum at the lattice-continuum interface are point loads and it is commonly known that the response of a two-dimensional continuum under a point load cannot be determined. To be able to properly describe the interaction between the lattice and the continuum, we must therefore translate the forces in the particles of the lattice to tractions along the continuous interface, and vice versa translate the tractions along the continuous interface of the continuous far-field to reaction forces that can be applied at the particles of the near-field lattice. To straightforwardly do this, we have introduced shape functions that allow for the integration over a certain representative domain of the interface, consequently describing the force-displacement relation at the discrete-continuous interface in an average sense. Noting that these shape functions must be distributed horizontally to be able to solve the system of equations of motion for the continuous layer and thereby obtain the displacements and tractions along its boundary, as well as to try and obtain a continuum response that performs reasonably well for the applied point loads, we have chosen

these shape functions as narrow bell-shaped functions. While this makes sense when considering the balance of forces at the interface, the resulting tractions along the face of the continuous far field do not likely resemble the tractions for the case that the near field would also consist of a continuum. Moreover, by using narrow shape functions, the amount of poles required to obtain sufficient convergence of the modified Green's displacements and modified Green's stresses using the contour integration is still very large, thereby dramatically increasing computation time. Additionally, we encountered severe precision problems when attempting to accurately determine the poles located far from the origin of the complex *k*-plane. Not only does this lead to a degradation of the dynamic compliance matrix, thereby reducing the non-reflectiveness and thus the quality of the boundary formulation, but it also induces numerical instability and further increases calculation time.

Despite the difficulties encountered, we still believe that it is possible to obtain the modified Green's displacements and modified Green's stresses for the continuous layer such that they can be used to describe a boundary formulation in a numerically robust manner. To this purpose, it would be useful to further investigate the interaction along the discrete-continuous interface. For example, determining the actual displacements and tractions along a boundary inside a fully continuous system may provide insight on the shape functions that should be used to more realistically describe the interaction between the forces that are applied to the boundary of the far-field domain by the near-field lattice and the tractions along this boundary. Assuming such relatively smooth traction and displacement fields along the discretecontinuous interface surely improves the numerical performance, but at this time we can only guess what the quality of the corresponding boundary formulation would be. Additionally, such an approach would yield challenges with respect to the nonzero traction fields along the vertical segments of the discrete-continuous interface, which, as explained in Section 3.5.3, are not accounted for in the set of boundary conditions used to solve the system of equations of motion for the continuum and are thereby used to derive the displacements and tractions along the boundary. Based on this, it may be worth to investigate alternative approaches to obtain the Green's displacements and Green's tractions along the interface, or alternatively look at different shapes for the discrete-continuous interface. Finally, instead of using the indirect boundary element method, which is presented in Section 3.5 and requires several assumptions to derive the boundary formulation for the continuum, the direct boundary approach, which is successfully applied for the fully discrete system and presented in Section 4.3.1, could be used.

Rather than further investigating the available options however, we have decided that it is more appropriate to derive a boundary formulation for a far-field system that more closely matches the discrete properties of the near-field. In particular, this far-field system should be capable of properly handling point loads at its interface with the lattice. In the next chapter, we therefore describe the far field by a system of discrete particles that matches the discrete properties of the hexagonal lattice and is thereby expected to provide a satisfactory boundary formulation.

4

One- and two-dimensional fully discrete systems

To describe the response of a medium to a dynamic load, we again divide that medium into a nonlinear domain in the near field and a linear domain in the far field. In accordance with the discrete-continuous systems discussed in Chapter 3, the near-field domain is described by a nonlinear discrete lattice, but in this chapter, the linear far-field domain is described by a system of discrete particles. Here, the configuration of the system of discrete particles is matched with the configuration of the lattice model, such that the nonlinear near-field domain and the linear far-field domain are analogous discrete lattices with a corresponding grid of particles. This means that when nonlinear events do not occur in the near-field domain and the medium is considered homogeneous, the cells in the near- and far-field lattices are identical. Matching the grid of both discrete systems eliminates the need for any artificial operations to transfer the point loads from the near-field to the far-field domain, which is one of the disadvantages of the discrete-continuous systems. A boundary formulation for the nonlinear discrete lattice that is derived from a matching system of discrete particles is thereby expected to yield a much better non-reflective behaviour at the boundary of the nonlinear near-field lattice compared to a boundary formulation derived from a continuous far-field domain.

In accordance with the approach for the discrete-continuous system in the previous chapter, the interaction between the nonlinear near-field lattice and the linear far-field system of particles is described by the force-displacement relation that is commonly known in the frequency and Laplace domains as the *dynamic stiffness* relation, previously discussed in Section 3.1, or inversely by the *dynamic compliance* relation. In Section 4.1, we first consider a one-dimensional fully discrete system composed of a one-dimensional BKV lattice and a matching semi-infinite particle system, which is followed by a comparison of the responses of the one-dimensional fully discrete systems with the corresponding one-dimensional discrete-continuous systems in Section 4.2.

In section 4.3 a direct boundary formulation is derived for the hexagonal near-field lattice

from a matching two-dimensional system of particles, while Section 4.4 presents the Green's functions for this viscoelastic half-plane of particles. To verify that the expressions for the displacements and reaction forces of the half-plane of particles are obtained and implemented correctly, Section 4.5 considers the equivalent one-dimensional response of the half-plane of particles to an infinitely long uniform line load at its surface and compares it to the response of the corresponding one-dimensional cascade. Subsequently, Section 4.6 reviews the dynamic behaviour of the half-plane of particles by considering its dispersive and direction-dependent wave propagation properties in comparison with the continuous layer. Finally, Section 4.7 considers the two-dimensional fully discrete BKV system, composed of a hexagonal BKV lattice in the near field and a viscoelastic system of particles in the far field. First, its governing equations are presented, after which the response of the fully discrete BKV system to an applied dynamic load is presented and the reflection at its boundary is evaluated for both a linear and a nonlinear hexagonal lattice.

4.1 The one-dimensional fully discrete BKV system

The fully discrete system comprised of a one-dimensional BKV lattice and a semi-infinite viscoelastic discrete particle system is depicted in Figure 4.1. In correspondence with the discrete-continuous BKV system treated in Section 3.2, the one-dimensional BKV lattice consists of **N** particles and **N-1** BKV elements, where each particle **n** has a mass M^n and the distance between any two adjacent particles is denoted as ℓ . The semi-infinite discrete particle system, henceforth referred to as a semi-infinite cascade [Bavinck and Dieterman, 2000; Dieterman and Metrikine, 1997], is chosen to match the properties of the linearly behaving one-dimensional BKV lattice, such that the distance between any two adjacent particles in the cascade is also equal to ℓ and the mass of all particles in the interior of the cascade is equal to M. Additionally, the interaction between adjacent particles in the cascade is described by Kelvin-Voigt elements with a damping coefficient C_e and a stiffness coefficient K_e .

The one-dimensional BKV lattice and the semi-infinite viscoelastic cascade are connected at the particle with coordinate $x = x_{lnt}$. To distinguish between the particles of the one-dimensional BKV lattice and the semi-infinite cascade, a particle in the BKV lattice is referred to as a particle \mathbf{n} , while a particle in the semi-infinite cascade is referred to as a particle \mathbf{p} . Consequently, the sub-particle at the lattice-cascade interface, which belongs to the one-dimensional BKV lattice is referred to as particle \mathbf{N} , while the sub-particle at the lattice-cascade interface that belongs to the cascade is referred to as particle \mathbf{P} . In accordance

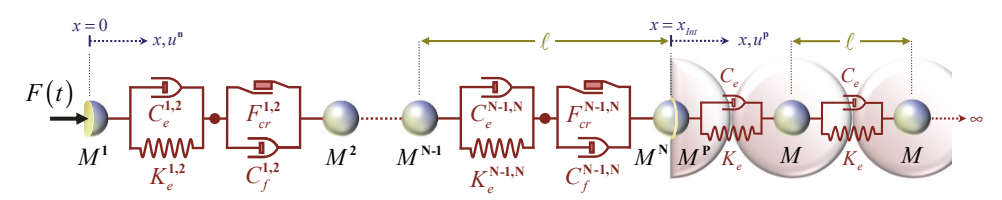


Figure 4.1: The one-dimensional fully discrete BKV system.

with the one-dimensional discrete-continuous systems presented in Section 3.2, the location of the lattice-cascade interface is chosen at such a distance from the applied time-dependent load F(t), that nonlinear phenomena occur only in the one-dimensional BKV lattice and do not reach the lattice-cascade interface and the BKV element between particles N-1 and N behaves exclusively linear.

To obtain a boundary formulation for the one-dimensional BKV lattice that accounts for the far-field domain by modelling it as a semi-infinite viscoelastic cascade, we consider the lattice-cascade interaction at coordinate $x = x_{Int}$ as a boundary value problem for the semi-infinite viscoelastic cascade. As part of this boundary value problem, let us first consider the behaviour of a particle **p** in the interior of the semi-infinite cascade. Its equation of motion is found as:

$$M\ddot{u}^{p} + C_{e} \left(2\dot{u}^{p} - \dot{u}^{p-1} - \dot{u}^{p+1} \right) + K_{e} \left(2u^{p} - u^{p-1} - u^{p+1} \right) = 0$$

$$(4.1)$$

Here, $u^{\mathbf{p}}$ is the axial displacement of a particle \mathbf{p} in the interior of the semi-infinite viscoelastic cascade, where $\mathbf{p} \ge \mathbf{P}$.

At the interface between the one-dimensional lattice and the viscoelastic cascade, we find two interface conditions that respectively describe the equilibrium of forces between the subparticles **N** and **P**, and the continuity of the displacements of both sub-particles at the interface. The two conditions at the lattice-cascade interface thus read:

$$M^{N}\ddot{u}^{N} + C_{e}^{N-1,N}\dot{e}^{N-1,N} + K_{e}^{N-1,N}e^{N-1,N} = -M^{P}\ddot{u}^{P} - C_{e}\left(\dot{u}^{P} - \dot{u}^{P+1}\right) - K_{e}\left(u^{P} - u^{P+1}\right)$$
(4.2)

$$u^{N} = u^{P} \tag{4.3}$$

Here, $e^{N-1,N}$ and $\dot{e}^{N-1,N}$ are respectively the elongation and the elongation rate of the BKV element between particles **N-1** and **N** as defined by equation (2.4). Note here that the BKV element between particles **N-1** and **N** may only behave linearly and that the corresponding Bingham element may not be activated.

In the following, we first discuss the parameters for which the material properties of the one-dimensional BKV lattice and the viscoelastic cascade match. Subsequently, in Section 4.1.2, we derive the dynamic stiffness for the semi-infinite cascade and obtain the corresponding dimensionless boundary formulation in the Laplace domain, after which we derive the corresponding time domain relation in Section 4.1.3. Section 4.1.4 regards the governing system of equation of motion for the one-dimensional fully discrete BKV system as well as an in-depth discussion of the numerical performance of different instances of the boundary formulation used. Finally, in Section 4.1.5, we present and discuss the response of the one-dimensional fully discrete BKV system to an applied pulse load.

4.1.1 Matching the parameters of the lattice and the cascade

As discussed previously, any waves propagating through the interface between the near- and far-field domains should ideally not be reflected, or at least the reflection should be minimal.

Although the BKV lattice allows for nonlinearities and for a variation of parameters along the lattice, at least in the region of the lattice-cascade interface, the response of the fully discrete BKV system must be linear and the material properties of the lattice and the viscoelastic cascade must match.

Compared to matching the parameters in the discrete-continuous systems, the matching of the parameters in the lattice-cascade system is rather trivial; since the mass per unit length must coincide and the distance in both parts of the system is equal to ℓ , it follows that the particle mass in the homogeneous part of the one-dimensional BKV lattice and the semi-infinite viscoelastic cascade must be the same and equal to M. Additionally, since the Bingham elements in the vicinity of the lattice-cascade interface may not be activated, the BKV elements in this region of the lattice behave viscoelastically. Consequently, by choosing the damping and stiffness coefficients of the rheological elements in the BKV lattice near the lattice-cascade interface equal to the damping coefficient C_e and the stiffness coefficient K_e in the viscoelastic cascade, the fully discrete BKV system represents a homogeneous medium. Nevertheless, as previously discussed for the discrete-continuous system in Section 3.2.1, the exact properties of the masses and rheological elements at the lattice-cascade interface, depend on the chosen location of their interface.

By choosing the interface between the lattice and the cascade at a particle in accordance with Figure 4.1, we find that the sub-particle ${\bf N}$ geometrically represents half a unit length. It is therefore intuitive to choose the mass $M^{\bf N}$ of this sub-particle as $M^{\bf N}=\frac{1}{2}M$. Accordingly, the sub-particle ${\bf P}$ also represents half a unit length and its mass $M^{\bf P}$ is accordingly chosen as $M^{\bf P}=\frac{1}{2}M$. Nevertheless, from Figure 4.2a it straightforwardly follows that, to match the material parameters of the lattice and the cascade at the lattice-cascade interface, the masses $M^{\bf N}$ and $M^{\bf P}$ of the sub-particles ${\bf N}$ and ${\bf P}$ may be freely chosen as long as they together satisfy the following constraint:

$$M^{N} + M^{P} = M (4.4)$$

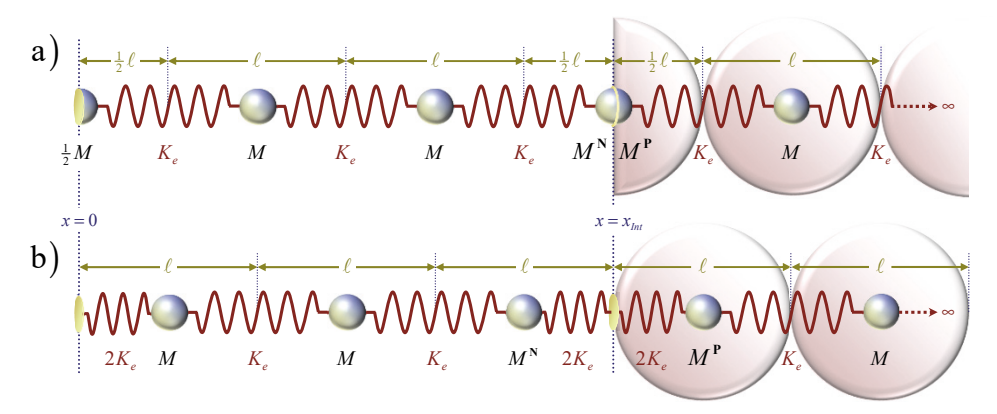


Figure 4.2: The one-dimensional fully discrete system consisting of a lattice and a cascade, where:
a) all springs have equal properties; b) all particles have equal masses.

Alternatively, we can choose the lattice-cascade interface in-between the particles **N** and **P** as depicted in Figure 4.2b, which are then conveniently chosen to be exactly one unit length apart and therefore both have a mass M. To find the stiffness of the interface springs for which the fully discrete system is homogeneous at the lattice-cascade interface, we insert the equation of motion for the massless interface into the equation of motion for the particle **N** and compare the resulting expression to the equation of motion for any particle in the interior of either the lattice or the cascade. The derivation in Appendix D.4 shows that, to match the material parameters of the lattice and the cascade at the lattice-cascade interface, and by assuming the interface springs in both lattice and cascade to have equal stiffnesses, their stiffness must be chosen as $2K_e$.

4.1.2 Dimensionless boundary equation in the Laplace domain

To regard the fundamental properties of the one-dimensional fully discrete BKV system, and to allow for a comparison of these properties with those of the corresponding discrete-continuous system discussed in the previous chapter, we normalize the BKV system by introducing the following dimensionless parameters for time, space, mass, damping and stiffness as derived in Appendix B.3:

$$t = t_{\dim} \omega_0, \quad u^{\mathbf{n}} = \frac{u_{\dim}^{\mathbf{n}}}{\ell}, \quad M^{\mathbf{n}} = \frac{M_{\dim}^{\mathbf{n}}}{M}, \quad C_e^{\mathbf{n},\mathbf{n}+1} = \frac{C_{e,\dim}^{\mathbf{n},\mathbf{n}+1}}{C_{crit}}, \quad K_e^{\mathbf{n},\mathbf{n}+1} = \frac{K_{e;\dim}^{\mathbf{n},\mathbf{n}+1}}{M\omega_0^2} = \frac{K_{e;\dim}^{\mathbf{n},\mathbf{n}+1}}{2K_e}.$$

Here, ω_0 is the so-called particle frequency, which denotes the natural frequency of particles in the interior of a homogeneous lattice for the particular case that the motion of adjacent particles is impeded. Furthermore, C_{crit} is the corresponding critical particle damping. For a particle in a homogeneous one-dimensional lattice, the particle frequency and the critical particle damping are derived in Appendix B.4 and respectively found as $\omega_0 = \sqrt{2K_e/M}$ and $C_{crit} = M\omega_0$. Finally, note that we use the same notations for both dimensional and dimensionless variables to minimize the number of different variables within the thesis. Nevertheless, in the given relations with the dimensionless variables, the dimensional variables are denoted using the subscript dim.

Incorporating the above dimensionless variables into equations (4.1) to (4.3), the dimensionless equation of motion for any particle \mathbf{p} in the interior of the semi-infinite viscoelastic cascade and the two dimensionless interface conditions at the lattice-cascade interface, respectively become:

$$\ddot{u}^{p} + \zeta \left(2\dot{u}^{p} - \dot{u}^{p-1} - \dot{u}^{p+1} \right) + \frac{1}{2} \left(2u^{p} - u^{p-1} - u^{p+1} \right) = 0 \tag{4.5}$$

$$M^{N} \ddot{u}^{N} + C_{e}^{N-1,N} \dot{e}^{N-1,N} + K_{e}^{N-1,N} e^{N-1,N} = -M^{P} \ddot{u}^{P} - \zeta \left(\dot{u}^{P} - \dot{u}^{P+1} \right) - \frac{1}{2} \left(u^{P} - u^{P+1} \right)$$
(4.6)

$$u^{N} = u^{P} \tag{4.7}$$

Here, ζ is the damping ratio, i.e. $\zeta = C_e/C_{crit}$, where C_e is the damping in the homogeneous cascade. Furthermore, note here that the mass of the boundary particle **P**, denoted as M^P ,

differs from the other masses in the cascade. To determine the dynamic stiffness of the cascade for trivially zero initial conditions, we apply the Laplace integral transform to equations (4.5) to (4.7) with respect to time. This yields:

$$s^{2}\tilde{u}^{p} + \frac{1}{2}(1 + 2\zeta s)(2\tilde{u}^{p} - \tilde{u}^{p-1} - \tilde{u}^{p+1}) = 0$$
(4.8)

$$M^{N}s^{2}\tilde{u}^{N} + \left(C_{e}^{N-1,N}s + K_{e}^{N-1,N}\right)\tilde{e}^{N-1,N} = -M^{P}s^{2}\tilde{u}^{P} - \frac{1}{2}(1 + 2\zeta s)(\tilde{u}^{P} - \tilde{u}^{P+1})$$

$$\tag{4.9}$$

$$\tilde{u}^{N} = \tilde{u}^{P} \tag{4.10}$$

Here, note that equation (4.8) is the dimensionless equation of motion of the semi-infinite cascade in the Laplace domain, while equations (4.9) and (4.10) respectively give the Laplace domain force and displacement relations at the lattice-cascade interface.

Assuming the solution to the equation of motion of the cascade, given by equation (4.8), in the form of harmonic waves and accounting for the proper behaviour of the viscoelastic cascade at infinity, we describe the Laplace domain displacement of a particle $\bf p$ in the interior of the semi-infinite cascade as $\tilde{u}^{\bf p}=Ae^{-i\kappa \bf p}$. Here, κ is the dimensionless wavenumber of the propagating wave and A is the wave amplitude. Substituting the expression for the Laplace domain displacement into the displacement relation at the interface, given by equation (4.10), yields the wave amplitude as $A=\tilde{u}^{\bf N}e^{+i\kappa \bf P}$. Consequently, the Laplace domain displacement of a particle $\bf p$ in the interior of the semi-infinite cascade may be expressed as:

$$\tilde{u}^{\mathbf{p}} = \tilde{u}^{\mathbf{N}} e^{-i\kappa(\mathbf{p} - \mathbf{P})} \tag{4.11}$$

Substituting the Laplace domain displacement for the particle \mathbf{p} , given by equation (4.11), into the force relation at the lattice-cascade interface, given in the Laplace domain by equation (4.9), yields the equation of motion of the particle \mathbf{N} at the lattice-cascade interface in the Laplace domain as:

$$M^{N} s^{2} \tilde{u}^{N} + \left(C_{e}^{N-1,N} s + K_{e}^{N-1,N}\right) \tilde{e}^{N-1,N} + \tilde{\chi}(s) \tilde{u}^{N} = 0$$
(4.12)

Here, $\tilde{\chi}(s)$ is the dynamic stiffness of the semi-infinite viscoelastic cascade that is found as:

$$\tilde{\chi}(s) = M^{\mathbf{P}} s^2 + \frac{1}{2} (1 + 2\zeta s) (1 - e^{-i\kappa}) \tag{4.13}$$

The expression for the dynamic stiffness of the semi-infinite viscoelastic cascade given by equation (4.13) includes a term related to the dimensionless wavenumber κ , while for example in the expression for the dynamic stiffness of the semi-infinite viscoelastic rod, given in Section 3.2.2, such a term is not present. The term related to the wavenumber can be removed from equation (4.13), by expressing the wavenumber κ in terms of the complex-valued Laplace parameter s using the dispersion relation for the viscoelastic cascade. This dispersion relation is derived in Appendix E.3 and yields the following relations between the

dimensionless wavenumber κ and the dimensionless Laplace parameter s:

$$\cos \kappa = 1 + \frac{s^2}{1 + 2\zeta s}, \quad \sin \kappa = \frac{-is}{1 + 2\zeta s} \sqrt{2 + 4\zeta s + s^2}. \tag{4.14}$$

Note here that, to obtain the correct sine relation from the given cosine relation, the square root must be chosen such that the imaginary part of the wavenumber κ is negative and thereby corresponds to the forward propagating wave that fades for $\mathbf{p} \to \infty$.

Rearranging equation (4.13) using Euler's formula and substituting the relations from equation (4.14), we find the dynamic stiffness of the semi-infinite cascade as:

$$\chi(s) = \left(M^{P} - \frac{1}{2}\right)s^{2} + \frac{1}{2}s\sqrt{2 + 4\zeta s + s^{2}}$$
(4.15)

Equation (4.15) describes the dynamic stiffness of the semi-infinite cascade for the case that the location of the lattice-cascade interface is chosen at a particle as depicted in both Figure 4.1 and Figure 4.2a. According to equation (4.15), the dynamic stiffness of the semi-infinite cascade depends on the dimensionless mass M^P of the sub-particle P. The contribution by Dieterman and Metrikine [1997] investigates the response of a linear-elastic semi-infinite cascade by varying its boundary mass, which in the fully discrete system equals the mass of the sub-particle P. However, for a homogeneous system consisting of a one-dimensional lattice and a semi-infinite cascade, the investigation of the boundary mass and its influence on the response of the semi-infinite cascade is irrelevant. To explain this, let us consider that, as an alternative, we may choose to extract the boundary mass, i.e. the mass of the sub-particle P, from the expression for the dynamic stiffness, given in equation (4.15), and incorporate it directly into equation (4.12). This yields the equation of motion for the boundary particle P as:

$$(M^{N} + M^{P})s^{2}\tilde{u}^{N} + (C_{e}^{N-1,N}s + K_{e}^{N-1,N})e^{N-1,N} + \chi_{alt}(s)\tilde{u}^{N} = 0$$
(4.16)

The corresponding dynamic stiffness of the semi-infinite cascade then becomes:

$$\tilde{\chi}_{alt}(s) = -\frac{1}{2}s^2 + \frac{1}{2}s\sqrt{2 + 4\zeta s + s^2}$$
(4.17)

Taking the constraint (4.4) into account, which states that the masses of the sub-particles **N** and **P** together must equal the mass M, equation (4.16) shows that the response of the particle at the lattice-cascade interface is independent of how you divide the mass M over the sub-particles **N** and **P**.

To allow for a comparison between the boundary formulations that follow from modelling the one-dimensional far-field domain of the one-dimensional BKV system as a viscoelastic rod and cascade respectively, and noting that the sub-particle **P** does not exist in a viscoelastic

rod, we use the boundary formulation for the cascade according to equations (4.12) and (4.13). Here, we conveniently choose the dimensionless mass of the sub-particles \mathbf{N} and \mathbf{P} to be equal, so that $M^{\mathbf{N}} = M^{\mathbf{P}} = \frac{1}{2}$. As such, the sub-particle \mathbf{N} has the same mass in both the fully discrete and discrete-continuous systems and the homogeneous distribution of mass along the BKV system is maintained. From equation (4.15), the dynamic stiffness of the semi-infinite cascade then follows as:

$$\tilde{\chi}(s) = \frac{1}{2}s\sqrt{2 + 4\zeta s + s^2} \tag{4.18}$$

Comparing the expression for the dynamic stiffness of the semi-infinite viscoelastic cascade according to equation (4.18) with the dynamic stiffness of the semi-infinite viscoelastic rod, previously given by equation (3.21), we find that the dynamic stiffness of the semi-infinite viscoelastic cascade features an additional term s^2 under the square root.

4.1.3 Governing boundary integral equation in the time domain

The equation of motion of the particle N at the lattice-cascade interface may be obtained by applying the inverse Laplace transform directly to equation (4.12) that incorporates the dynamic stiffness. However, since we can generally not obtain the time domain expression for the dynamic stiffness analytically and must therefore apply the inverse Laplace transform numerically, it is more convenient to use the inverse force-displacement relation that gives the equation of motion of the particle N at the lattice-cascade interface in terms of the dynamic compliance. As previously explained in Section 3.2.3, this is because the dynamic compliance decreases sufficiently fast for large frequencies, while the dynamic stiffness does not decrease with frequency at all. This is also testified by Figure 4.3a and Figure 4.3b, that respectively show the dynamic stiffness and dynamic compliance for the semi-infinite viscoelastic cascade and the semi-infinite viscoelastic rod as a function of dimensionless frequency Ω by substituting $s = i\Omega$. For comparison, the corresponding dynamic stiffness and dynamic

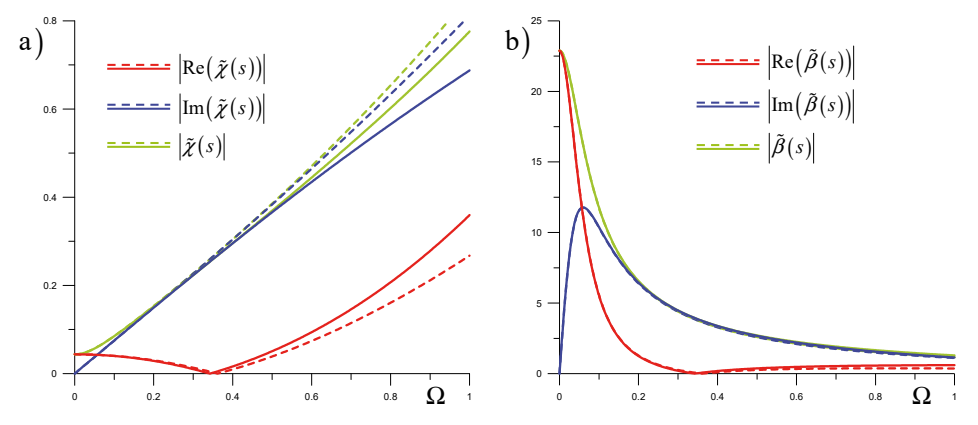


Figure 4.3: Frequency domain force-displacement relations for the viscoelastic cascade (solid lines) and the viscoelastic rod (dashed lines): a) dynamic stiffness; b) dynamic compliance.

compliance of the semi-infinite viscoelastic rod are here given by dashed lines. Note here that, for small frequencies, the dynamic stiffness and dynamic compliance of the rod and the cascade are approximately equal, while for large frequencies the difference between the rod and the cascade is more significant. As a consequence, the differences between the semi-infinite viscoelastic rod and the semi-infinite viscoelastic cascade are clearly visible for the dynamic stiffness that increases with frequency, while for the dynamic compliance, which decreases with frequency, the differences are not clearly distinguishable. Note here furthermore that the similarity between the dynamic stiffnesses and compliances of the rod and the cascade depend on damping; for smaller values of the damping the differences are more pronounced as confirmed by the comparison of the dynamic stiffnesses and dynamic compliances of the semi-infinite linear-elastic rod and cascade that is presented in Appendix D.2.

To express the equation of motion of the particle N at the lattice-cascade interface in the Laplace domain in terms of the dynamic compliance, we divide equation (4.12) by the dynamic stiffness, or alternatively we multiply equation (4.12) by the dynamic compliance. This yields:

$$\tilde{u}^{N} + \tilde{\beta}(s) \left\{ M^{N} s^{2} \tilde{u}^{N} + \left(C_{e}^{N-1,N} s + K_{e}^{N-1,N} \right) \tilde{e}^{N-1,N} \right\} = 0$$
(4.19)

Here, $\beta(s)$ is the dynamic compliance of the semi-infinite viscoelastic cascade that reads:

$$\tilde{\beta}(s) = \frac{2}{s\sqrt{2 + 4\zeta s + s^2}} \tag{4.20}$$

The dynamic compliance of the semi-infinite viscoelastic cascade given by equation (4.20) is depicted in Figure 4.3b as a function of frequency by substituting $s = i\Omega$.

While we are not able to obtain an analytical time domain expression for the dynamic stiffness by applying the inverse Laplace transform to equation (4.18), applying the inverse Laplace transform to equation (4.20) does yield an analytical time domain expression for the dynamic compliance. Within the relevant domain of the resulting boundary integral equation, i.e. for $t \ge 0$, the inverse Laplace transform of the dynamic compliance of the semi-infinite cascade and its time derivative are respectively obtained as:

$$\beta(t) = 2 \int_{0}^{t} e^{-2\zeta \tau} J_{0}\left(\tau \sqrt{2 - 4\zeta^{2}}\right) d\tau, \qquad \dot{\beta}(t) = 2e^{-2\zeta t} J_{0}\left(t \sqrt{2 - 4\zeta^{2}}\right). \tag{4.21}$$

Here, $J_0(...)$ denotes the Bessel functions of the first kind of order zero. Note here that for a damping ratio $\zeta > \frac{1}{2}\sqrt{2}$, the argument of the Bessel functions in equations (4.21) becomes complex-valued. Consequently, for $\zeta > \frac{1}{2}\sqrt{2}$, we may alternatively express equations (4.21) in terms of the modified Bessel function of the first kind. Furthermore, note that the time derivative of the time domain expression for the dynamic compliance can be considered as a time domain expression for the (mechanical) admittance, or inversely for the (mechanical)

impedance, because it corresponds to a force-velocity relation in the Laplace domain. The time dependencies of the time domain expressions given by equations (4.21), that we will henceforth refer to as the time domain dynamic compliance and the time domain admittance, are given by Figure 4.5 in Section 4.2.1, in which the time domain dynamic compliances and time domain admittances are compared for several models of the semi-infinite far-field domain

To obtain the equation of motion for the particle N at the lattice-cascade interface in the time domain, we first apply the inverse Laplace transform to equation (4.19). This yields the boundary integral equation in the form of equation (3.25), previously obtained for the discrete-continuous system in Section 3.2.3. To include this boundary integral equation in an explicit system of second order ordinary differential equations for the lattice that can be evaluated numerically, we attempt to isolate the acceleration of particle N at time t in this equation. However, because the time domain expression for the dynamic compliance of the semi-infinite cascade, as given in equation (4.21), is equal to zero at t = 0, i.e. $\beta(t = 0) = 0$, this acceleration term is removed from equation (3.25) causing the corresponding system of ordinary differential equations to become numerically unstable. To obtain a nonzero acceleration term at the current time step, we instead differentiate the boundary integral equation (3.25) using Leibniz' rule for differentiation of integrals [Abramowitz and Stegun, 1972; Woods, 1926].

Taking into account that the time domain dynamic compliance of the semi-infinite cascade is equal to zero at t = 0, this yields the equation of motion for the particle **N** at the lattice-cascade interface in the time domain as:

$$\dot{u}^{N} + \int_{0}^{t} \dot{\beta}(t-\tau) \left\{ M^{N} \ddot{u}^{N} + C_{e}^{N-1,N} \dot{e}^{N-1,N} + K_{e}^{N-1,N} e^{N-1,N} \right\} (\tau) d\tau = 0$$
(4.22)

Note here that, in contrast to the semi-infinite viscoelastic rod, the time domain admittance of the semi-infinite cascade is not singular at any value for time t. In fact, whereas the time domain admittance of the semi-infinite viscoelastic rod is infinite in the limit $t \to 0$, the corresponding time domain admittance of the semi-infinite viscoelastic cascade at t = 0 is found as $\dot{\beta}(t = 0) = 2$.

To numerically evaluate the convolution integral in equation (4.22), we may, for example, apply the composite trapezium rule. Dividing the domain of the convolution integral in H equal time intervals, and denoting the time interval as Δt , as well as assuming trivially zero initial conditions then yields the time domain equation of motion for the boundary particle N as:

$$\dot{u}^{N} + \Delta t \left\{ M^{N} \ddot{u}^{N} + C_{e}^{N-1,N} \dot{e}^{N-1,N} + K_{e}^{N-1,N} e^{N-1,N} \right\} + \Delta t \sum_{h=1}^{H-1} \dot{\beta} \left(t_{H-h} \right) F^{N} \left(t_{h} \right) = 0$$
(4.23)

Here, $F^{N}(t_h)$ is the force applied by the lattice to the viscoelastic cascade at the lattice-

cascade interface at time t_h , where the time moment t_h is obtained as $t_h = h\Delta t$. Accordingly, the time moment t_{H-h} is obtained as $t_{H-h} = (H-h)\Delta t$. Here, note that equation (4.23) is an ordinary second-order differential equation because the summation only includes history terms related to the motion of the boundary particle **N** prior to time t and must therefore be constant during the current time step.

Improved representation of the governing interface equation in the time domain

Equation (4.23) shows that the contribution of the convolution integral that is related to the motion of the boundary particle at the current time step is proportional to the time step Δt . Thereby, the contribution of the particle acceleration, which we numerically solve the corresponding system of differential equations for, may become very small and cause the corresponding mass-matrix to be ill-conditioned. However, because the time domain admittance, i.e. the time derivative of the dynamic compliance, of the semi-infinite viscoelastic cascade at time t=0 is found to be both non-infinite and non-zero, we can obtain a nonzero acceleration term at the current time step outside the convolution integral by differentiating the equation of motion for the boundary particle a second time, and thereby improve its numerical performance significantly. Note here that for the interface equation of the discrete-continuous system previously discussed in Section 3.2.3, the time differentiation could not straightforwardly be applied a second time, because the time domain admittance of the involved semi-infinite viscoelastic rod is singular at t=0.

Applying the time differentiation to the equation of motion for the particle N at the lattice-cascade interface, given by equation (4.22), using Leibniz' rule for differentiation of integrals, the equation of motion for the boundary particle becomes:

$$\ddot{u}^{N} + \dot{\beta}(0) \left(M^{N} \ddot{u}^{N} + C_{e}^{N-1,N} \dot{e}^{N-1,N} + K_{e}^{N-1,N} e^{N-1,N} \right) + \int_{0}^{t} \ddot{\beta}(t-\tau) F^{N}(\tau) d\tau = 0$$
(4.24)

Here, the time domain admittance of the semi-infinite viscoelastic cascade at t=0 was previously found as $\dot{\beta}(0)=2$ and the force $F^{N}(t)$ describes the force applied by the lattice to the viscoelastic cascade at the lattice-cascade interface. Furthermore, $\ddot{\beta}(t)$ is the second time derivative of the time domain expression for the dynamic compliance $\beta(t)$, derived from equation (4.21) as:

$$\ddot{\beta}(t) = -2e^{-2\zeta t} \left(2\zeta J_0 \left(t\sqrt{2 - 4\zeta^2} \right) + \sqrt{2 - 4\zeta^2} J_1 \left(t\sqrt{2 - 4\zeta^2} \right) \right) \tag{4.25}$$

Here, $J_0(...)$ and $J_1(...)$ are the Bessel functions of the first kind of respectively order zero and of order one. It is here important to emphasize that equation (4.25) is obtained by applying time differentiation to the time domain expression for the mechanical admittance given in equation (4.21) and does not correspond to the time domain expression that follows from the force-acceleration relation in the Laplace domain. Applying the inverse Laplace transform to this force-acceleration relation, sometimes referred to as accelerance or inertance,

yields an additional Dirac-delta term $2\delta(t)$ on the right-hand side of equation (4.25). As a result of using Leibniz' rule for differentiation of integrals, the contribution of this term to the interface equation of motion is already included in equation (4.24).

For damping ratios $\zeta > \frac{1}{2}\sqrt{2}$, the argument of the Bessel functions in equations (4.25) are complex-valued, so that we may alternatively express equation (4.25) for these damping ratios as:

$$\ddot{\beta}(t) = -2e^{-2\zeta t} \left(2\zeta I_0 \left(t\sqrt{4\zeta^2 - 2} \right) - \sqrt{4\zeta^2 - 2} I_1 \left(t\sqrt{4\zeta^2 - 2} \right) \right)$$

Here, $I_0(...)$ and $I_1(...)$ are the modified Bessel function of the first kind of respectively order zero and order one.

4.1.4 Governing equations for the fully discrete BKV system

The governing system of equations of motion for the one-dimensional fully discrete BKV system consists of the equations of motion for all particles inside the one-dimensional BKV lattice, i.e. the particles $n = 1 \dots N - 1$, together with the equation of motion for the boundary particle N.

The governing equations of motion for particles $\mathbf{n} = 1...\mathbf{N-1}$ that allow for the variation of motion states in each of the rheological elements inside the one-dimensional BKV lattice were previously given by equations (3.32) to (3.34) in Section 3.2.4 and are therefore not repeated here. The equation of motion for the boundary particle \mathbf{N} is not subject to the variation of motion states, because nonlinear phenomena may not occur at the lattice-cascade interface, and may either be given by equation (4.22) or by equation (4.24). While equations (4.22) and (4.24) are two different, but both analytically correct, versions of the boundary integral equation, the numerical performance of using either of these equations as the equation of motion for the boundary particle is quite different. The two versions of the boundary integral equation and their numerical performance are further discussed in Section 4.2.3, in which the wave reflection of both these boundary formulations are assessed in comparison with the reflections that occur in the discrete-continuous system.

4.1.5 Nonlinear response of the 1D fully discrete BKV system

Figure 4.4 depicts the response of the one-dimensional fully discrete BKV system to a single-sinus pulse load, with an amplitude $\bar{F}=1$ MN , at ten consecutive time moments. In correspondence with the corresponding discrete-continuous system, for which the response is discussed in Section 3.2.5, we here consider the response along a one-dimensional BKV lattice consisting of 80 particles with mass M=400 kg at an interparticle distance of $\ell=0.2$ m. The springs in the BKV elements have a stiffness equal to $K_e=100$ MN/m, which yields the particle frequency and the critical particle damping in the BKV lattice to be the same as those found in Sections 3.2.5 and 4.1.4, so that they are respectively obtained as $\omega_0=707.1$ rad/s and $C_{crit}=282.8$ kNs/m.

For the sake of not presenting the exact same response twice, Figure 4.4 gives the

response of the one-dimensional fully discrete BKV system to a pulse load with a dimension-less load frequency $\Omega_F=0.5$ and a damping ratio in the BKV elements of $\zeta=0.1$. The given dimensionless frequency of the pulse corresponds to a frequency $\omega_F=353.6~{\rm rad/s}$, while the given damping ratio corresponds to damping coefficients $C_e=C_f=28.3~{\rm kNs/m}$. Here note that the response of the corresponding discrete-continuous system that we previously presented in Figure 3.5 depicted was obtained for $\Omega_F=0.113~{\rm and}~\zeta=0.75$.

The continuous red and green lines in Figure 4.4 respectively give the nonlinear and linear response of the one-dimensional fully discrete BKV system. To obtain the linear response, the critical friction force of all BKV elements is chosen as $F_{cr} > \overline{F}$, so that the nonlinear Bingham elements are not activated. To obtain the nonlinear response, the critical friction force of the BKV elements in the lattice is generally chosen as $F_{cr} = 0.8\overline{F}$, while particularly for the elements between particles $\mathbf{n} = 20...40$, the critical friction force is reduced to $F_{cr}^{\mathbf{n},\mathbf{n}+1} = 0.4\overline{F}$. Additionally, to amplify nonlinear effects, the damping ratio of the BKV elements between particles $\mathbf{n} = 20...40$ is reduced to $C_{e}^{\mathbf{n},\mathbf{n}+1} = C_{f}^{\mathbf{n},\mathbf{n}+1} = 22.63 \,\mathrm{kNs/m}$, which coincides with a damping ratio of $\zeta = 0.08$. The dashed blue line shows the corresponding nonlinear response for the one-dimensional discrete-continuous BKV system, verifying that, at the scale of these graphs, the differences between the response of the fully discrete and the discrete-continuous BKV systems cannot be distinguished.

In correspondence with Figure 3.5, Figure 4.4 shows that for the nonlinear response, the incident wave, induced by the single-sinus pulse load, is partially reflected at the edges of the weaker segment of the one-dimensional BKV lattice and causes a secondary wave. After this secondary wave is reflected from the tip of the system and is transmitted into the semi-infinite viscoelastic cascade, the first segment of the one-dimensional BKV lattice remains displaced due to the occurrence of nonlinear events within this segment. As the final displacements are the same for a large number of particles in the middle of this segment, it must be that the

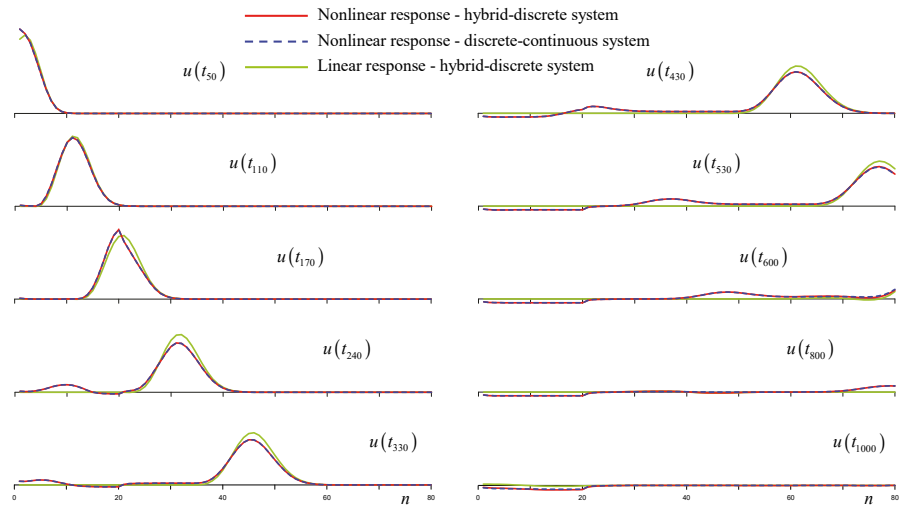


Figure 4.4: Displacement along the one-dimensional BKV system at successive time moments due to a single-sinus pulse load.

nonlinearities have mainly occurred at the edges of this segment. In fact, for this particular simulation, all 50 nonlinear events, i.e. state-transitions, occurred in the particles n = 1...4 and in the particles n = 20...29.

For both the linear and the nonlinear response of the one-dimensional fully discrete BKV system in Figure 4.4, all waves arriving at the lattice boundary, are (almost) fully transmitted into the far-field domain. This is also true for waves arriving at the discrete-continuous interface of the corresponding discrete-continuous system. At the scale of Figure 4.4, any existing reflections due to incident waves arriving at the interface with the far-field domain are not visible and therefore the differences between the fully discrete and the discrete-continuous BKV systems cannot be identified from Figure 4.4. Nevertheless, if we verify by zooming in and consider the response of both the fully discrete and discrete-continuous BKV systems at a scale at which possible wave reflections are visible, we will see a clear difference between the wave reflections in the two systems. The wave reflections in respectively the one-dimensional fully discrete BKV system and the corresponding discrete-continuous system are qualitatively compared in the following section.

4.2 Fully discrete versus discrete-continuous systems in 1D

After having extensively discussed the one-dimensional fully discrete BKV system in the preceding section, and the corresponding discrete-continuous system in Section 3.2, we do here evaluate and compare the boundary formulations in which we account for the far-field domain by respectively modelling it as a cascade and a rod. Note here that both systems are generic in the sense that corresponding systems with different properties can be derived from it. For example, by choosing the critical friction force of the Bingham elements larger than the load amplitude, i.e. $F_{cr} > \overline{F}$, and thereby preventing the occurrence of nonlinear events, any BKV system reduces to a purely viscoelastic Kelvin-Voigt system. By additionally choosing zero damping, i.e. $\zeta = 0$, we respectively obtain the linear-elastic fully discrete and discrete-continuous Hooke systems. Each of these systems has been individually discussed in Appendix D.

Because the interface between the near-field and the far-field is chosen in the domain where the response is linear, the occurrence of nonlinear events does not affect the performance of the boundary formulations. In this section, we therefore exclusively consider linear-elastic and viscoelastic systems. While the frequency dependence of the dynamic compliances for the viscoelastic rod and viscoelastic cascade were already compared in Figure 4.3, section 4.2.1 compares the time domain dynamic compliances and time domain admittances for semi-infinite linear-elastic and viscoelastic rods and cascades. Subsequently, Section 4.2.2 discusses and compares the dispersive properties of the semi-infinite rods and cascades, while Section 4.2.3, the performance of the boundary formulations for the fully discrete and discrete-continuous systems are compared in detail by evaluating the wave reflection at respectively the lattice-cascade and lattice-rod interface. Finally, Section 4.2.4 analytically derives the reflection coefficient for harmonic incident waves in one-dimensional fully discrete systems, showing that the lattice-cascade interface is perfectly non-reflective.

4.2.1 Dynamic compliance of semi-infinite cascades and rods

The dynamic interaction of the one-dimensional lattice with both the semi-infinite cascade and the semi-infinite rod are described by the corresponding equation of motion of the boundary particle **N**. For reasons abundantly explained in Sections 3.2 and 4.1, the equation of motion of the boundary particle **N** is described in both the Laplace and the time domain by means of the dynamic compliance. The expressions for the dynamic compliances of the linear-elastic and viscoelastic semi-infinite rods, as well as those for the linear-elastic and viscoelastic semi-infinite cascades are given in Table 4.1 in both the Laplace domain and the time domain. Additionally, Table 4.1 gives the time derivative of the corresponding time domain dynamic compliances, which are also referred to as the time domain admittances. Note here that the second time derivative of the dynamic compliance, or the time derivative of the time domain admittance, is not included in the table or the comparison, as it is exclusively used for boundary formulations that involve the viscoelastic cascade.

The given expressions for the linear-elastic rod and the linear-elastic cascade are derived in Appendices D.1 and D.3, which respectively regard the one-dimensional discrete-continuous and fully discrete Hooke systems. Note here that Appendix D.4 also discusses the one-dimensional fully discrete Hooke system, but for an alternative location of the lattice-cascade interface chosen in-between two particles rather than at a particle. Although the different location of the lattice-cascade interface yields a different dynamic compliance, its expression is not included in Table 4.1 as this table exclusively regards systems with the interface between the near-field and far-field domains located at a particle. The expressions for the viscoelastic rod and the viscoelastic cascade given in Table 4.1 were previously derived in Sections 3.2 and 4.1, regarding the one-dimensional discrete-continuous and fully discrete BKV systems respectively. Note here that for zero damping, i.e. for $\zeta = 0$, the equations given in Table 4.1 for the viscoelastic rod and the viscoelastic cascade reduce to the equations for respectively the linear-elastic rod and the linear-elastic cascade.

Figure 4.5a and Figure 4.5b respectively give the time domain dynamic compliances and the time domain admittances for the one-dimensional semi-infinite systems as a function of time. Here, the yellow and green lines respectively correspond to the linear-elastic rod and

table 4.1: Expressions for the dynamic compilances in the Laplace domain, the time domain dynamic compilances and	тпе тте
domain admittances, for the one-dimensional semi-infinite linear-elastic and viscoelastic systems.	

	$\tilde{eta}(s)$	$\beta(t), t \ge 0$	$\dot{\beta}(t), t \ge 0$
Linear-elastic rod	$\frac{2}{s\sqrt{2}}$	$\sqrt{2}$	0
Linear-elastic cascade	$\frac{2}{s\sqrt{2+s^2}}$	$2\int\limits_0^t J_0\left(\sqrt{2}\tau\right)d\tau$	$2J_{0}\left(\sqrt{2}t ight)$
Viscoelastic rod	$\frac{2}{s\sqrt{2+4\zeta s}}$	$\sqrt{2}\operatorname{erf}\sqrt{\frac{t}{2\zeta}}$	$\frac{e^{-\frac{1}{2}t/\zeta}}{\sqrt{\pi\zetat}}$
Viscoelastic cascade	$\frac{2}{s\sqrt{2+4\zeta s+s^2}}$	$2\int_{0}^{t}e^{-2\zeta\tau}J_{0}\left(\tau\sqrt{2-4\zeta^{2}}\right)d\tau$	$2e^{-2\zeta t}J_0\left(t\sqrt{2-4\zeta^2}\right)$

the linear-elastic cascade, while the blue and red lines respectively correspond to the viscoelastic rod and the viscoelastic cascade, where in both cases the damping ratio is arbitrarily chosen as $\zeta = 0.2$. Here, the time domain dynamic compliances of the viscoelastic rod and cascade respectively converge to the time domain dynamic compliances of the linear-elastic rod and cascade for $t \to \infty$. According to the final value theorem, this shows that in the longwave limit there is no difference between either of the rods and the cascades, which is well-documented in literature [Maradudin et al., 1971; Suiker et al., 2001a]. Furthermore note that, although the time domain dynamic compliances of the linear-elastic cascade, viscoelastic cascade and viscoelastic rod are equal to zero for t = 0, the time domain dynamic compliance of the linear-elastic rod is not equal to zero for t = 0. Then, for both the linear-elastic and the viscoelastic rod, the time domain admittance is infinite at t = 0. For the linear-elastic rod this is due to the jump in the dynamic compliance at t = 0, incorporated in the time domain admittance using the Dirac delta function, while for the viscoelastic rod, this originates from a division by zero for t = 0. For the linear-elastic and the viscoelastic cascades the time domain admittance is finite at t = 0 and in both cases found as $\dot{\beta}(t = 0) = 2$.

4.2.2 Wave dispersion in semi-infinite cascades and semi-infinite rods

Because of the similar geometry and equations of motion, the dispersive properties of the semi-infinite cascades in the far field are identical to those of the corresponding one-dimensional lattices in the near field. For the discrete-continuous systems on the other hand, the dispersive properties of the discrete lattices in the near field and the continuous far-field are quite different. Because the differences in their dispersive properties are especially relevant for the interaction between the near-field lattice and the far-field continuum, their dispersive properties have previously been discussed in 3.3.2. To provide an overview, Figure 4.6 presents the dispersion relations for all four one-dimensional far-field models considered in this thesis. Assuming that the frequency Ω is real-valued, Figure 4.6a and Figure 4.6b respectively give the real and imaginary parts of the wavenumber κ as a function of frequency. Here, note that the dispersion relations for the linear-elastic and the viscoelastic rod are both derived in

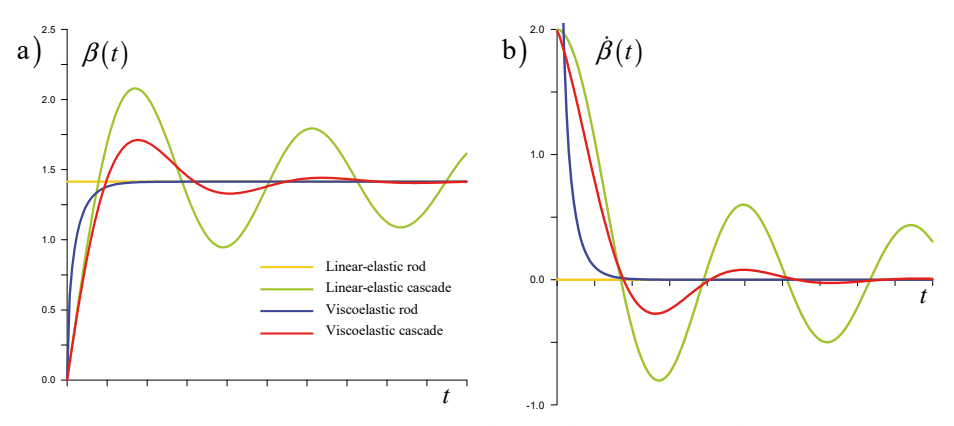


Figure 4.5: a) Time domain dynamic compliances for semi-infinite rods and semi-infinite cascades; b) Time domain admittances for semi-infinite rods and semi-infinite cascades.

Appendix E.1, while the dispersion relations for the linear-elastic and viscoelastic cascades are derived in Appendices E.2 and E.3 respectively.

The dispersion relation for the linear-elastic rod, given by the yellow line, is real for all frequencies, while the dispersion relation for the linear-elastic cascade, given by the green line, only yields real wavenumbers for $\Omega \leq \sqrt{2}$ and purely imaginary wavenumbers for $\Omega > \sqrt{2}$, insinuating the existence of a stop band above $\Omega = \sqrt{2}$. The dispersion relations for the viscoelastic rod, given by the blue lines, and for the viscoelastic cascade, given by the red lines, are complex-valued for all frequencies. Here, the dispersion relations for both viscoelastic rod and cascade are given for two values of the damping ratio, i.e. for $\zeta = 0.1$ and $\zeta = 0.2$, to illustrate the influence of the damping.

4.2.3 Wave reflection in one-dimensional systems

To assess the performance of the different boundary formulations for the one-dimensional lattice, in which we account for the far-field domain by either modelling it as a semi-infinite rod or as a semi-infinite cascade, we do here compare the reflection of an incident wave at the lattice boundary for the corresponding one-dimensional systems. For this purpose, the parameters and properties are chosen to coincide with those of the BKV systems for which the response was depicted by Figure 4.4 and we consider the reflection of an incident wave due to the same single-sinus pulse load. This means that the considered viscoelastic lattice has an interparticle distance $\ell = 0.2$ m, a particle frequency $\omega_0 = 707.1$ rad/s and a damping ratio $\zeta = 0.1$. While the pulse load has an amplitude $\overline{F} = 1$ MN and a dimensionless angular frequency $\Omega_F = 0.5$, which thus corresponds to a frequency $\omega_F = 353.6$ rad/s.

The reflection of the incident wave at the lattice-cascade and the lattice-rod interface of respectively the one-dimensional fully discrete and discrete-continuous Kelvin-Voigt systems is depicted in Figure 4.7 for four consecutive time moments. The first, or upper, graph in Figure 4.7 shows the longitudinal response along the lattice at the time moment at which the incident wave is almost completely transmitted into the far-field, while the last graph shows the reflected wave as it reaches the tip of the system. Here, Figure 4.7a, shows the

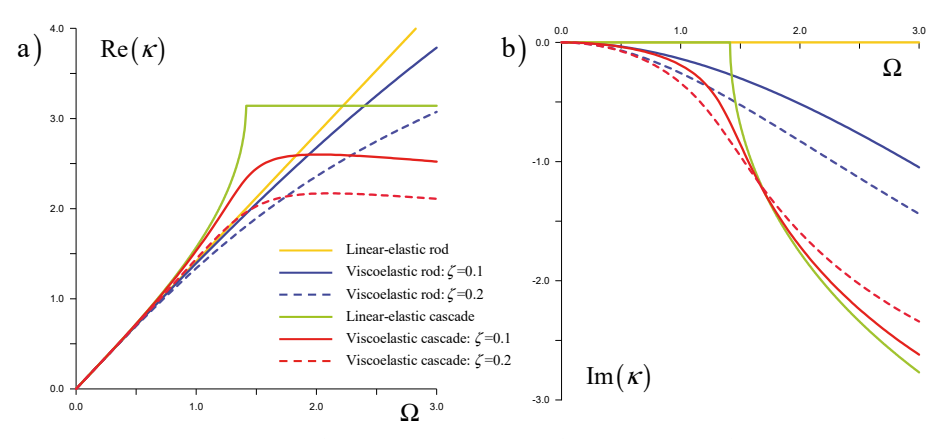


Figure 4.6: Dispersion relations for the one-dimensional semi-infinite rods and semi-infinite cascades as a function of frequency: a) Real part of the wavenumber; b) Imaginary part of the wavenumber.

response of the Kelvin-Voigt systems using the time domain approach that was previously used to obtain Figure 3.5 and Figure 4.4 for the corresponding nonlinear BKV systems. This means that the reflections in Figure 4.7a are obtained by numerically evaluating the governing time domain system of ordinary differential equations using a Runge-Kutta scheme. Figure 4.7b depicts the time domain response of both the one-dimensional discrete-continuous and the one-dimensional fully discrete Kelvin-Voigt systems that follows from the frequency domain solution, that in this case consists of solving the governing systems of equations in the Laplace domain and using the Laplace integral transform to obtain the time domain response at every time step.

In Figure 4.7a, the dashed green line shows the reflected wave for the one-dimensional fully discrete Kelvin-Voigt system where equation (4.22) is used as the interface equation, while the continuous red line shows the reflected wave for the corresponding system using equation (4.24) as the interface equation. Both responses correspond to the linear response of the fully discrete BKV system given by the yellow line in Figure 4.4. Furthermore, the dashed blue lines in Figure 4.7 give the corresponding response for the one-dimensional discrete-continuous Kelvin-Voigt system. On the scale of Figure 4.4, the differences between the responses for the fully discrete Kelvin-Voigt system using either equation (4.22) or equation (4.24) as the interface equation, are not visible. However, if we consider the reflected wave on the scale of Figure 4.7, which is 40 times smaller than the scale of the longitudinal response depicted in Figure 4.4, the differences between using equation (4.22) or (4.24) are clearly visible and are further discussed below.

Either way, for all three depicted reflections, the convolution integral was numerically evaluated using the alternative extended Simpson's rule [Press et al., 1989]. The numerical evaluation of the convolution integral is here applied using a Simpson's rule instead of the

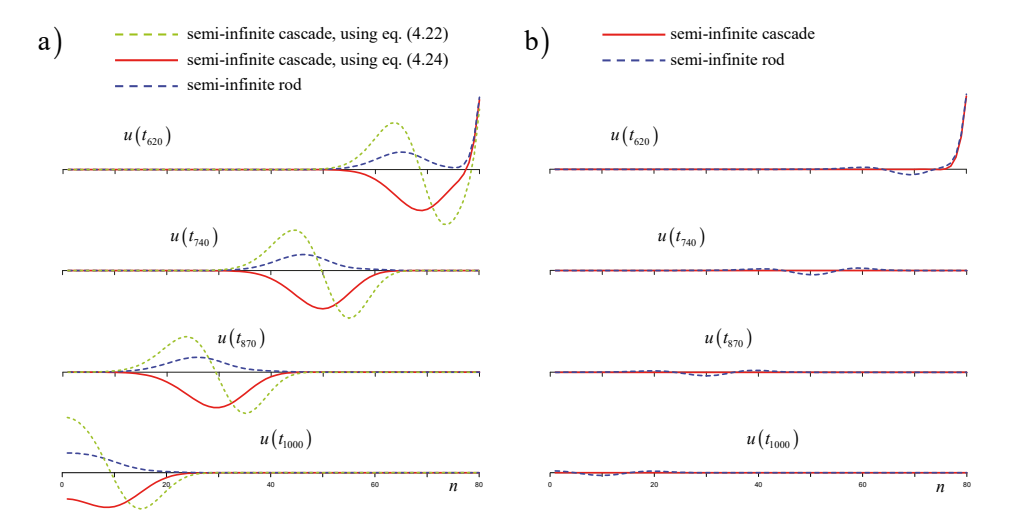


Figure 4.7: Reflection of a longitudinal incident wave in the one-dimensional BKV system with the far field described by respectively a semi-infinite cascade and a semi-infinite rod: a) time domain solution; b) frequency domain solution.

trapezium rule, which was previously used to obtain equation (4.23) from equation (4.22), because the response is well described by a second order polynomial. The alternative extended Simpson's rule is used because the number of time steps involved in the convolution integral continuously increases; the regular composite Simpson's rule does not suffice as it is only available for an odd number of datapoints, i.e. for an even number of time steps, and is thus not applicable for all possible numbers of time steps.

Comparison of the reflections at the lattice-cascade and lattice-rod interface

Let us first consider the reflections in the fully discrete and discrete-continuous Kelvin-Voigt systems for the time domain solution depicted in Figure 4.7a. Comparing the reflections from the lattice-cascade interface that employ interface equations (4.22) and (4.24), given by respectively the green dashed line and the continuous red line, we find that the reflection obtained for the system with interface equation (4.22) is somewhat larger than the reflection obtained for the system with interface equation (4.24). This is according to expectation, as in equation (4.24), the contribution of the acceleration of the boundary particle at the current time step is separated from the convolution integral, while in equation (4.22), this contribution is embedded in the convolution integral and can only be separated from the convolution integral by applying numerical integration.

Next, comparing the reflections at the lattice-cascade interface with the reflections at the lattice-rod interface in the time domain solution, it is quite remarkable that, for both interface equations, the reflection at the lattice-cascade interface is larger than the reflection at the lattice-rod interface. After all, since the lattice and the continuous rod are fundamentally different media with different dispersive properties, as shown by the dispersion relations depicted in Figure 4.6, some reflection of an incident wave from the lattice-rod interface should be expected. On the other hand, the discrete nature of the lattice and the cascade are identical and have the same dispersive properties, so that any reflections from the lattice-cascade interface would be expected to be much smaller than the reflections at the lattice-rod interface. The latter is verified by the frequency domain solution for the one-dimensional fully discrete Kelvin-Voigt system in Figure 4.7b, in which the lattice-cascade interface appears to be completely non-reflective, while for the corresponding discrete-continuous system a reflected wave remains. In fact, as the lattice-cascade is analytically proven to be non-reflective in Section 4.2.4, we can conclude that the larger reflections from the lattice-cascade interface in the time domain solution, depicted in Figure 4.7a, must be due to numerical errors.

As both the time domain and frequency domain solutions include the numerical application of the inverse Laplace transform, the reflections displayed by Figure 4.7a must either be due to a numerical error in the Runge-Kutta scheme used to solve the involved system of differential equations in the time domain, or due to the numerical evaluation of the convolution integral. The fact that for the time domain solution, the reflection of an incident wave at the lattice-cascade interface is larger than the reflection at the lattice-rod interface, can partly be explained by comparing the corresponding boundary formulations. For the fully discrete system the equation of motion for the boundary particle **N** is given by either equation (4.22) or (4.24), while for the discrete-continuous system the equation of motion for particle **N** is

given by equation (3.31). While the contribution of the convolution integral to the current time step for both boundary formulations of the fully discrete system are obtained numerically, the contribution of the convolution integral to the current time step in the boundary formulation for the discrete-continuous system is, in an approximate sense, obtained analytically. As a consequence, the numerical error for the discrete-continuous system is relatively small and the obtained time domain response is numerically quite precise.

From the comparison of the reflections obtained by the time domain and the frequency domain solutions, it is legitimate to state that, even when considering one-dimensional linear-elastic and viscoelastic systems, the governing system of equations of motion should preferably be evaluated in the frequency domain rather than in the time domain. Nevertheless, in the following, we will discuss the numerical performance of using either equation (4.22) or (4.24) in further depth.

Numerical performance of using either equation (4.22) or equation (4.24)

Figure 4.8 compares the displacement response of the loaded surface particle in the one-dimensional fully discrete BKV system for the different equations of motion for the boundary particle N, respectively given by equations (4.22) and (4.24). Here, nonlinearities are excluded and the properties of the lattice and the cascade correspond with each other, so that the medium is homogeneous and viscoelastic, and correspond with the macromaterial properties used throughout this thesis. In this case, the response is given for a lattice that consists of 20 particles, each with a mass $M=400~{\rm kg}$ at an interparticle distance of $\ell=0.2~{\rm m}$. Here, the size of the lattice is deliberately chosen smaller as before to enhance any occurring reflections. The springs in the lattice again have a stiffness equal to $K_e=100~{\rm MN/m}$, so that the particle frequency and the critical damping are respectively obtained as $\omega_0=707.1~{\rm rad/s}$ and $C_{crit}=282.8~{\rm kNs/m}$. Furthermore, the damping ratio is chosen as $\zeta=0.1$, so that the dashpots in the lattice have a damping coefficient $C_e=28.3~{\rm kNs/m}$.

Figure 4.8a and Figure 4.8b both present the response to a single-sinus pulse load with an amplitude $\bar{F}=1.0$ MN and a load frequency $\omega_F=353.6$ rad/s, which corresponds to a dimensionless load frequency $\Omega_F=0.5$. Here, the continuous blue line gives the response of the fully discrete system for the frequency domain solution. This means that this response is obtained by solving the algebraic system of equations in the Laplace domain, and by subsequently applying the inverse Laplace transform to the resulting Laplace domain displacements at every time step. Because there are no reflections in the displacement response obtained by the frequency domain solution, Figure 4.8 confirms that the semi-infinite viscoelastic cascade yields a perfectly non-reflective far-field system for the BKV lattice.

The continuous green and red lines both give displacement responses of the fully discrete system that follow from solving the corresponding system of ordinary differential equations in the time domain. Here, the continuous green line gives the response that incorporates equation (4.22) as the equation of motion for the boundary particle **N**, while the continuous red line give the corresponding response that uses equation (4.24) as the boundary integral equation. While initially, the three responses in Figure 4.8a overlap, it is clear that both equations yield significant wave reflection from the lattice-cascade interface. Figure 4.8b zooms in on

these reflections that occur in the displacement response due to numerical errors when using the time domain solution.

As stated before, the system of ODEs in this thesis are generally solved using the Runge-Kutta method by means of the Fortran-library RK-suite by Brankin and Gladwell [1997]. After scrutinizing the numerical implementation and its results, it was found that the applied numerical method yields a small numerical error in the displacement response for all particles in the lattice. This numerical error by itself is rather insignificant, and would not be visible by the naked eye at the scale of either Figure 4.8a or Figure 4.8b. The occurrence of this numerical error has been confirmed by considering the response of a one-dimensional Hooke lattice to a pulse load, which shows that despite the absence of damping, the amplitude of the incident wave reduces slightly and that the magnitude of this numerical error depends on the time interval used. Now, due to the presence of the convolution integral in the boundary formulation for the fully discrete system, we integrate over the full time domain history of the response and thereby this otherwise insignificant numerical error in the response accumulates to an error in the interface equation that is significant enough to induce reflections from any incident waves that arrives at this interface. As a consequence, it must follow that the magnitude of this error also depends on the numerical integration scheme used to evaluate the convolution integral.

As shown by Figure 4.8b, the magnitude and shape of the reflected waves are quite different depending on whether we use equation (4.22) or equation (4.24) as the interface equation. Here, the continuous green and red lines show the respective reflections for the case that the time step Δt of the numerical simulations is chosen as $\Delta t = T/100$, where T is the load period, and the numerical evaluation of the convolution integral has been performed using the composite Trapezium rule. While the response that follows from using equation (4.22) is sinusoidal in shape, with both a positive and a negative peak, the response that follows from using equation (4.24) only has a negative peak, but yields a constant offset from the particles' equilibrium position after the reflected wave has passed.

The fact that these reflections are due to numerical errors indicates that the performance

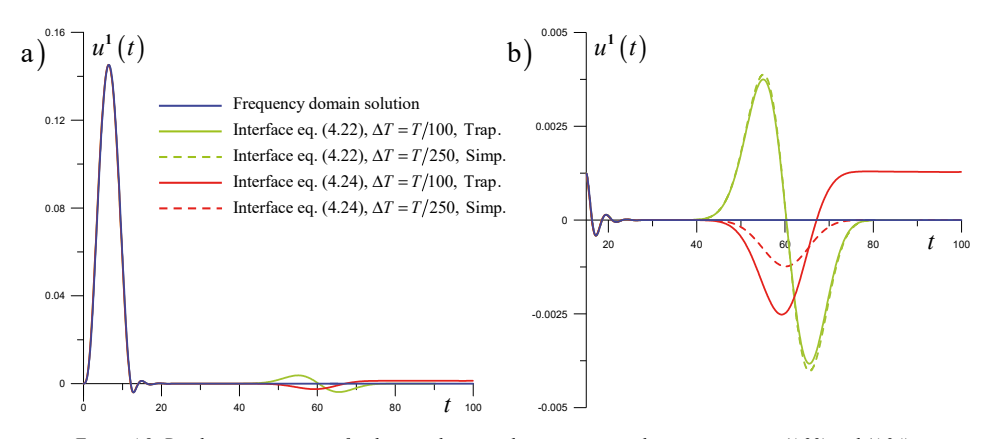


Figure 4.8: Displacement response for the time domain solutions respectively using equations (4.22) and (4.24):
a) Time domain versus frequency domain solution; b) Reflection from the boundary for different approaches.

of the numerical implementation can be improved by reducing the time step and thereby increasing both the number of points at which the system of ODEs is solved and the number of points over which the convolution integral is obtained. To show this, the dashed green and red lines in Figure 4.8b depict the response of the loaded surface particle for the case that the time step Δt is chosen as $\Delta t = T/250$. In addition to reducing the time step, for both the resulting responses the convolution integral was numerically evaluated using the alternative extended Simpson's rule [Press et al., 1989]. The influence of reducing the time step and applying an improved integration scheme for the convolution integral are clearly visible for the time domain solution that incorporates equation (4.24) as the interface equation. While reducing the time step reduces both the peak of this reflection as well as its constant offset, applying these numerical improvements separately has shown that the constant offset is primarily due to using the composite trapezium rule and that this offset disappears when we use a higher-order scheme for numerical evaluation of the convolution integral.

While the proposed numerical improvements clearly reduce the reflections from the interface for the system that uses interface equation (4.24), Figure 4.8b shows that this effect is not present when we use equation (4.22) instead. This can be explained by first considering that we numerically solve the corresponding system of ODEs for the acceleration, and second noting that as shown by equation (4.23), the interaction force that includes the acceleration, is present only as a part of the convolution integral, so that its contribution to the current time step depends on the size of the time step Δt . Consequently, by reducing the time step, we also reduce the contribution of the particle acceleration to the current integration step in the Runge Kutta-scheme, which in turn makes it more difficult to obtain a robust numerical response using equation (4.22) as the interface equation. As a consequence, the reflection for the system that includes equation (4.22) does not reduce when we reduce the time step.

In addition to the size of the time step and the chosen integration scheme for the convolution integral, the magnitude of the reflection due to this numerical error also depends on the chosen load frequency. This dependency is depicted by Figure 4.9, which gives the displacement response of the loaded surface particle for three different load frequencies. Here, the fully discrete system has the same material properties as before, with the exception of the damping coefficient that is chosen as $\zeta = 0.2$. The amplitude of the applied single-sinus pulse load is the same for all three responses depicted and equal to $\bar{F} = 0.1$ MN . Unlike the load amplitudes, the magnitudes of the displacement response are quite different for the three load frequencies, which is a consequence of the duration of the pulses applied. From Figure 4.9a, we observe that the magnitude of the displacement response is inversely proportional to the load frequency Ω_F . Here, the responses for the three load frequencies are obtained numerically in the time domain for the system of ODEs that incorporates equation (4.24) for the boundary particle N and a time step Δt chosen as $\Delta t = T/1000$.

Any reflections in the displacement response that occur due to the numerical error in the interface equation are hardly visible at the scale of Figure 4.9a, but are clearly visible in Figure 4.9b in which the occurring reflections are magnified a hundred times compared to Figure 4.9a. The magnitudes of these reflections are not proportional to the magnitude of the initial displacement response depicted in Figure 4.9a, but are found to be proportional to the

area under the initial displacement response. This is in line with the previous observation that the numerical error accumulates due to numerical evaluation of the convolution integral, because the area under the integrand of the convolution integral must reduce proportional to the area under the displacement response.

The analysis of the numerical performance of the two instances of the equation of motion for the boundary particle N, has clarified that using equation (4.24) as the interface equation is preferred over using equation (4.22). In addition, this analysis has provided several tools to tune the numerical implementation and minimize any reflections from the boundary caused by numerical errors that are due to the numerical evaluation of the convolution integral in the interface equation. In addition, note that the identity of the inverse Laplace transform, for which different options are presented in Appendix J.4, used to numerically determine the dynamic compliance and its derivatives in the time domain should be carefully chosen depending on their value at t = 0. This is discussed in further detail in Section 5.2.3, which addresses the application of the inverse Laplace transform for nonzero initial conditions.

4.2.4 Reflection coefficients for one-dimensional fully discrete systems

As shown in Figure 4.7b for the frequency domain solution, the lattice-cascade interface is completely non-reflective. As the one-dimensional Kelvin-Voigt lattice and the semi-infinite viscoelastic cascade are identical discrete models and therefore have the exact same dispersive properties, this notion seems to be quite evident. Nevertheless, the non-reflectiveness of the lattice-cascade interface can be proven analytically by deriving the reflection and transmission coefficients of a harmonic incident wave arriving at the lattice-cascade interface.

The amplitude reflection and transmission coefficients of an incident wave at the lattice-cascade interface are analytically obtained starting from the equation of motion of the boundary particle N, which for the one-dimensional fully discrete Kelvin-Voigt system is previously given by equation (4.6). Noting that the elongation of the rheological element between the boundary particle N and its adjacent particle N-1 may be expressed in terms of the corresponding particle displacements as $e^{N-1,N} = u^N - u^{N-1}$, we find the dimensionless interface

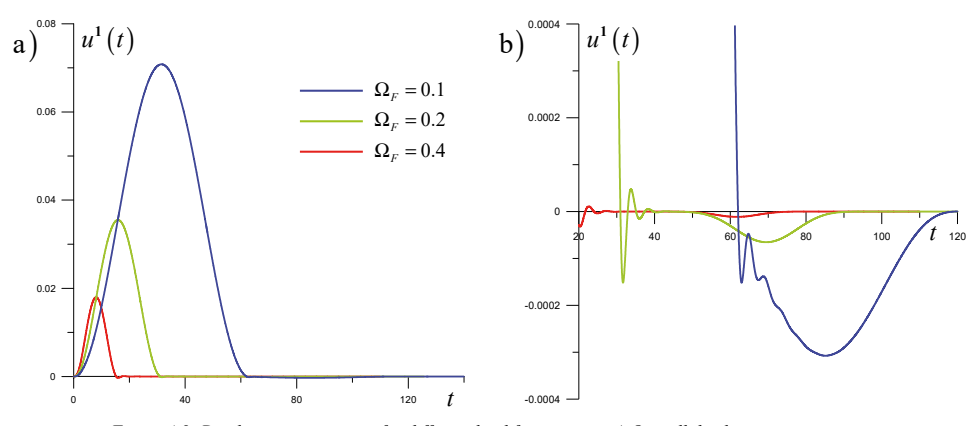


Figure 4.9: Displacement response for different load frequencies: a) Overall displacement response; b) Reflections from the lattice boundary due to numerical errors.

equation as:

$$M^{N}\ddot{u}^{N} + C_{e}^{N-1,N} \left(\dot{u}^{N} - \dot{u}^{N-1} \right) + K_{e}^{N-1,N} \left(u^{N} - u^{N-1} \right) = -M^{P} \ddot{u}^{P} - \zeta \left(\dot{u}^{P} - \dot{u}^{P+1} \right) - \frac{1}{2} \left(u^{P} - u^{P+1} \right)$$
(4.26)

Whereas the displacement of a particle inside the one-dimensional Kelvin-Voigt lattice may be due to both the incident and possibly a reflected wave, the displacement of a particle in the semi-infinite viscoelastic cascade can only be due to the transmitted wave. Therefore, assuming that the incident, reflected and transmitted waves are all harmonic, the displacements of any particles **n** and **p** in their domains are respectively described as:

$$u^{\mathbf{n}} = A_{inc}e^{\mathrm{i}(\Omega t - \kappa \mathbf{n})} + A_{ref}e^{\mathrm{i}(\Omega t + \kappa \mathbf{n})}$$

$$\tag{4.27}$$

$$u^{\mathbf{p}} = A_{tra}e^{\mathrm{i}(\Omega t - \kappa \mathbf{p})} \tag{4.28}$$

Here, A_{inc} , A_{ref} and A_{tra} are the wave amplitudes of respectively the incident, the reflected and the transmitted waves. Furthermore, note that the wavenumber κ is the same in both domains.

According to equation (4.28), the displacement and the velocity of the particle **P+1** in the viscoelastic cascade may be expressed in terms of the adjacent boundary particle **P** as $u^{P+1} = u^P e^{-i\kappa}$ and $\dot{u}^{P+1} = \dot{u}^P e^{-i\kappa}$ respectively. Additionally, since the half-particles **N** and **P** together form the same boundary particle, their displacements, velocities and accelerations must be equal. Substituting these relations into equation (4.26) allows us to express the right-hand side of equation (4.26), related to the motion of the particles **P** and **P+1**, fully in terms of the motion of the boundary particle **N**. The resulting equation was previously obtained in the Laplace domain by equation (4.12). Subsequently, substituting equation (4.27) for the particles **N** and **N-1** in the remainder and rearranging yields the amplitude ratio of the reflected and incident waves in the Laplace domain as:

$$\frac{A_{ref}e^{+i\kappa N}}{A_{inc}e^{-i\kappa N}} = \frac{\Omega^{2}\left(M^{N} + M^{P}\right) - \left(K_{e}^{N-1,N} + i\Omega C_{e}^{N-1,N}\right)\left(1 - e^{+i\kappa}\right) - \frac{1}{2}\left(1 + 2i\zeta\Omega\right)\left(1 - e^{-i\kappa}\right)}{-\Omega^{2}\left(M^{N} + M^{P}\right) + \left\{K_{e}^{N-1,N} + i\Omega C_{e}^{N-1,N} + \frac{1}{2}\left(1 + 2i\zeta\Omega\right)\right\}\left(1 - e^{-i\kappa}\right)}$$
(4.29)

Since A_{inc} and A_{ref} are the complex amplitudes of the incident and reflected waves at the surface particle, i.e. for $\mathbf{n}=0$, $A_{inc}^{\mathbf{N}}=A_{inc}e^{-i\kappa\mathbf{N}}$ and $A_{ref}^{\mathbf{N}}=A_{ref}e^{+i\kappa\mathbf{N}}$ respectively describe the complex amplitudes of the incident and reflected waves at the boundary particle \mathbf{N} . Using Euler's formula and the dispersion relations for the Kelvin-Voigt lattice derived in Appendix E.3, we thus find the amplitude reflection coefficient for the lattice-cascade interface as:

$$\frac{A_{ref}^{N}}{A_{inc}^{N}} = \frac{\left(M^{N} + M^{P} - \frac{K_{e}^{N-1,N} + i\Omega C_{e}^{N-1,N}}{1 + 2i\zeta\Omega} - \frac{1}{2}\right)\Omega^{2} + \left(\frac{K_{e}^{N-1,N} + i\Omega C_{e}^{N-1,N}}{1 + 2i\zeta\Omega} - \frac{1}{2}\right)i\Omega\sqrt{2 + 4i\zeta\Omega - \Omega^{2}}}{-\left(M^{N} + M^{P} - \frac{K_{e}^{N-1,N} + i\Omega C_{e}^{N-1,N}}{1 + 2i\zeta\Omega} - \frac{1}{2}\right)\Omega^{2} + \left(\frac{K_{e}^{N-1,N} + i\Omega C_{e}^{N-1,N}}{1 + 2i\zeta\Omega} + \frac{1}{2}\right)i\Omega\sqrt{2 + 4i\zeta\Omega - \Omega^{2}}}$$
(4.30)

Noting that the Kelvin-Voigt lattice and the viscoelastic cascade represent the same material, it straightforwardly follows from Appendix B.3 that the dimensionless damping coefficient and the dimensionless stiffness coefficient of the boundary element in the lattice are respectively obtained as $C_e^{\text{N-I,N}} = \zeta$ and $K_e^{\text{N-I,N}} = \frac{1}{2}$. For the Kelvin-Voigt system, the Laplace domain amplitude reflection coefficient thus reduces to:

$$\frac{A_{ref}^{N}}{A_{inc}^{N}} = \frac{\left(M^{N} + M^{P} - 1\right)\Omega^{2}}{-\left(M^{N} + M^{P} - 1\right)\Omega^{2} + i\Omega\sqrt{2 + 4i\zeta\Omega - \Omega^{2}}}$$
(4.31)

According to equation (4.31), we find that there will be no wave reflection, if we choose the collective dimensionless mass of the boundary particles \mathbf{N} and \mathbf{P} as $M^{\mathbf{N}} + M^{\mathbf{P}} = 1$. This equality is exactly equal to the constraint previously given by equation (4.4) in its dimensional form. Consequently, for using the boundary formulation for the one-dimensional Kelvin-Voigt lattice that considers the far-field domain as a semi-infinite viscoelastic cascade, there will be no reflections at the lattice-cascade interface.

Ergo, consistent with the reflections at the lattice-cascade interface obtained by the frequency domain solution depicted in Figure 4.7b, the amplitude reflection coefficient for the one-dimensional fully discrete Kelvin-Voigt system is analytically found as $R_A = 0$. Furthermore, note that the nonzero reflection from the lattice-rod interface of the corresponding discrete-continuous system, depicted for the frequency domain solution in Figure 4.7b, corresponds to the analytically derived nonzero amplitude and energy reflection coefficients for the discrete-continuous interface that are given by respectively equations (3.41) and (3.48) in Section 3.3.2.

4.3 Two-dimensional fully discrete particle systems

Although the derivation and implementation of a boundary formulation that accounts for a continuous far-field domain does not yield any insuperable difficulties for one-dimensional systems, as explained in Section 3.6.3, we were unsuccessful in implementing a boundary formulation for the hexagonal lattice that models the far-field domain as a two-dimensional continuum. Amongst others, this was due to the difference in geometry between the lattice and the continuum, specifically at their interface. Replacing the two-dimensional continuum by a system of particles that is geometrically equivalent to the hexagonal lattice removes these dissimilarities.

Figure 4.10 depicts the two-dimensional fully discrete system that consists of the hexagonal BKV lattice in the near field and a semi-infinite two-dimensional viscoelastic system of particles in the far field. The properties of the hexagonal BKV lattice and the equations of motion for all its non-boundary particles are discussed in Section 2.4. The interaction of the hexagonal lattice and the linear two-dimensional system of particles along the lattice-lattice interface may generally be described by the dynamic stiffness matrix that follows from the system of Laplace domain force-displacement relations previously given by equation (3.2) in Section 3.1. Due to the increase of the involved dynamic stiffnesses for $\Omega \to \infty$ and the fact

that the corresponding time domain relations may only be obtained numerically, the forcedisplacement relations at the lattice-lattice interface are described in the Laplace domain by means of the dynamic compliance matrix as:

$$\underline{\tilde{u}}_{Int}(s) = -\underline{\tilde{\beta}}(s)\underline{\tilde{F}}_{Int}(s) \tag{4.32}$$

In accordance with the approach for the two-dimensional discrete-continuous system, the dynamic compliance matrix that describes the interaction of the two-dimensional near-field and far-field lattices at their interface, is derived starting from the dynamic reciprocal work theorem. While the derivation of the dynamic compliance relation at the discrete-continuous interface requires an indirect approach that makes certain assumptions regarding the interaction between the lattice and the continuum, the dynamic compliance matrix at the interface of the hexagonal lattice and the two-dimensional system of particles may be derived from the dynamic reciprocal work theorem without making any assumptions. The corresponding direct boundary formulation and the resulting dynamic compliance matrix are respectively presented in Sections 4.3.1 and 4.3.2.

4.3.1 A direct boundary formulation for discrete particle systems

In this section, we will first rearrange the dynamic reciprocal work theorem such that it is applicable for systems, or bodies, that consist of multiple particles and thereby have a discrete nature. Henceforth, we will refer to these systems, or bodies, as *discrete particle systems*. Employing the resulting dynamic reciprocal work theorem for discrete particle systems, we will then derive the dynamic stiffness and dynamic compliance matrices for a discrete particle system with a cavity that exactly matches the shape of the hexagonal BKV-lattice, and which

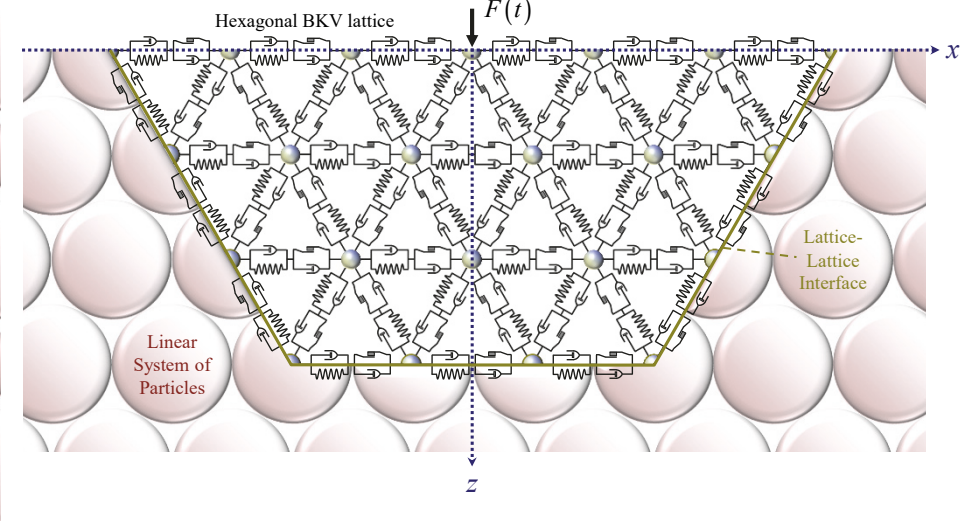


Figure 4.10: The two-dimensional fully discrete BKV system.

is derived from the known relations for a corresponding discrete particle system without a cavity.

The dynamic reciprocal work theorem for discrete particle systems

As previously discussed in Section 3.1, the dynamic reciprocal work theorem is derived from the elastostatic reciprocal work theorem of Maxwell-Betti [de Hoop, 1966] by extending it into dynamics, and describes the frequency or Laplace domain relation between the displacements of, and the tractions on, a continuous body in two different elastodynamic states. Disregarding internal body forces and assuming that one elastodynamic state of the body is described in the Laplace domain by surface displacements $\underline{\tilde{u}}(\xi,s)$ and surface tractions $\underline{\tilde{t}}(\xi,s)$, as well as assuming that another elastodynamic state of the same body is described by surface displacements $\underline{\tilde{u}}_P(\xi,s)$ and surface tractions $\underline{\tilde{t}}_P(\xi,s)$ due to an externally applied arbitrary load \underline{P} , the dynamic reciprocal work theorem yields the following relation between the two elastodynamic states:

$$\int_{\Gamma} \underline{\tilde{t}}(\xi, s)^{\mathsf{T}} \, \underline{\tilde{u}}_{P}(\xi, s) \, d\xi = \int_{\Gamma} \underline{\tilde{t}}_{P}(\xi, s)^{\mathsf{T}} \, \underline{\tilde{u}}(\xi, s) \, d\xi$$

Here, we consider a two-dimensional solid medium, and therefore all displacements and tractions in the dynamic reciprocal work theorem are vectors that contain components in *x*- and *z*-directions.

Since the considered discrete particle system is a body made up of point masses and rheological elements, neither tractions nor stresses exist as they require a continuous surface or boundary. Accordingly, the continuous traction and displacement fields that appear in the dynamic reciprocal work theorem do not exist either. Nevertheless, as the resultant of a traction field over a certain area yield a force, we may alternatively express the dynamic reciprocal work theorem in terms of forces on, and displacements of, a set of discrete points along the boundary of a body, that is as long as the work-energy balance of the two considered elastodynamic states is maintained. In other words, integrating the multiplied traction and displacement fields over a boundary Γ is equivalent to the summation of the forces working on the set of particles at the boundary Γ multiplied by the displacements of those particles. In the Laplace domain, we can write the theorem of dynamic reciprocal work for discrete particle systems as:

$$\sum_{i} \underline{\tilde{R}}^{i}(s)^{T} \underline{\tilde{u}}_{P}^{i}(s) = \sum_{i} \underline{\tilde{R}}_{P}^{i}(s)^{T} \underline{\tilde{u}}^{i}(s)$$

$$(4.33)$$

Here, the vectors $\underline{\tilde{u}}^{\mathbf{j}}(s)$ and $\underline{\tilde{R}}^{\mathbf{j}}(s)$ respectively contain the horizontal and vertical displacements of, and the horizontal and vertical reaction forces at, a particle \mathbf{j} along the boundary of a discrete particle system in an arbitrary elastodynamic state. Furthermore, the vectors $\underline{\tilde{u}}_{P}^{\mathbf{j}}(s)$ and $\underline{\tilde{R}}_{P}^{\mathbf{j}}(s)$ respectively describe the horizontal and vertical displacements of, and the horizontal and vertical reaction forces at, particle \mathbf{j} along the boundary of a discrete particle system in the elastodynamic state due to an applied load \underline{P} . Collecting the reaction forces for

all particles $\mathbf{j} = 1..\mathbf{N}_{\text{Int}}$, where \mathbf{N}_{Int} denotes the number of particles at the boundary Γ , per elastodynamic state into the force vectors $\underline{\tilde{R}}(s)$ and $\underline{\tilde{R}}_P(s)$ respectively, as well as collecting the corresponding displacements for all particles $\mathbf{j} = 1..\mathbf{N}_{\text{Int}}$ into the displacement vectors $\underline{\tilde{u}}(s)$ and $\underline{\tilde{u}}_P(s)$, we can now generally express the dynamic reciprocal work theorem for discrete particle systems as:

$$\underline{\tilde{R}}(s)^{\mathsf{T}}\underline{\tilde{u}}_{P}(s) = \underline{\tilde{R}}_{P}(s)^{\mathsf{T}}\underline{\tilde{u}}(s) \tag{4.34}$$

For our case, the dynamic reciprocal work theorem according to equation (4.34) applies to the particle system with a cavity that matches the near-field lattice and is denoted as the discrete particle system V. As the vectors $\underline{\tilde{u}}(s)$, $\underline{\tilde{u}}_P(s)$, $\underline{\tilde{R}}(s)$ and $\underline{\tilde{K}}_P(s)$ respectively include both horizontal and vertical displacements and reaction forces, they each have a length $2N_{\text{Int}}$. Figure 4.11a shows the discrete particle system with the cavity subject to the force vector $\underline{F}_{Int}(s)$ and with displacements $\underline{\tilde{u}}_{Int}(s)$, between which we aim to find the relation described by the dynamic compliance matrix according to equation (4.32). Because of the cavity, we are not able to find this relation along the boundary Γ directly and therefore we refer to this elastodynamic state as the so-called *unknown elastodynamic state*.

For a discrete particle system without a cavity, such as a half-plane or a layer of particles, we can find the displacements of, and reaction forces at, any particle in the system due to an arbitrary load applied at any particle in the system using the corresponding Green's functions. In this case, we consider the system without the cavity as an assembly of a discrete particle system that exactly matches the shape of the far-field system V, i.e. with the surface cavity, and a particle system that exactly matches the shape of the cavity, denoted as the cavity system V_{cav} . The full discrete particle system composed of the particle systems V and V_{cav} is depicted in Figure 4.11b. Note here that the interface between V and V_{cav} exactly matches the boundary Γ . For an arbitrary load applied inside the cavity system V_{cav} , we can determine the resulting displacements and reaction forces for all particles located at the boundary Γ using the corresponding Green's functions for the complete particle system. According to Huygens' principle [Huygens, 1690], the response of the far-field system V is indifferent to whether a load is applied inside the cavity system V_{cav} or at the boundary Γ , as long as the response of the system at the boundary Γ is the same for both situations. Consequently, knowing the displacements of and the reaction forces at the particles along the boundary Γ due to an arbitrary load applied inside the cavity system V_{cav} , we may remove the cavity system V_{cav} as long as the displacements and reaction forces along the boundary Γ are maintained. Doing so, we remain with the far-field system V in an elastodynamic state for which we know the displacements and reaction forces along Γ , i.e. the so-called *known elastodynamic state*.

Denoting the displacements of, and the reaction forces at, the particles along the boundary Γ in the unknown elastodynamic state by the vectors $\underline{u}(s)$ and $\underline{R}(s)$ respectively, and denoting the corresponding displacements and reaction forces in the known elastodynamic state by the vectors $\underline{u}_P(s)$ and $\underline{R}_P(s)$, we can now employ the dynamic reciprocal work theorem for discrete particle systems according to equation (4.34) to determine the force-displacement relation for the unknown elastodynamic state of the far-field system V. Before deriving this

force-displacement relation, commonly known as the dynamic stiffness or dynamic compliance, from the dynamic reciprocal work theorem, we will first elaborate on the so-called known and unknown elastodynamic states of the far-field system **V**.

The known elastodynamic state: A discrete particle system without a cavity

The known elastodynamic state, depicted in Figure 4.11b, describes the state of the far-field system V for which the displacements of, and reaction forces at, the particles along the boundary Γ due to an external load, or an arbitrary set of external loads, can be obtained from the corresponding Green's functions of the discrete particle system without a cavity, which is an assembly of the far-field system V and the cavity system V_{cav} .

Now let us assume a load vector \underline{P} that describes a set of loads that are applied at all particles along the boundary Γ , yet assume that these loads are applied at the sub-particles that belong to the cavity system \mathbf{V}_{cav} . Alternatively, we can thus consider that the load vector \underline{P} is applied along the face Γ_{cav} that belongs to the cavity system \mathbf{V}_{cav} and matches the shape of the boundary Γ . Denoting the load applied at a particle \mathbf{i} along the boundary Γ_{cav} as $\underline{P}^{\mathbf{i}}$, which consists of the horizontal and vertical point loads $P_x^{\mathbf{i}}$ and $P_z^{\mathbf{i}}$, the displacements of, and the reaction forces at, a particle \mathbf{j} along the boundary Γ due to the applied load are found through the corresponding Green's functions as:

$$\underline{\tilde{u}}_{P}^{\mathbf{j},\mathbf{i}}(s) = \tilde{g}_{u}^{\mathbf{j},\mathbf{i}}(s)\underline{P}^{\mathbf{i}} \tag{4.35}$$

$$\underline{\tilde{R}}_{P}^{j,i}(s) = \tilde{g}_{R}^{j,i}(s)\underline{P}^{i} \tag{4.36}$$

Here, $\underline{\tilde{u}}_{P}^{j,i}(s)$ and $\underline{\tilde{R}}_{P}^{j,i}(s)$ are respectively the displacement and reaction force vector for a particle \mathbf{j} that each contain their respective horizontal and vertical components. Thus, the Green's displacement matrix $\underline{\tilde{g}}_{u}^{j,i}(s)$ and the Green's reaction force matrix $\underline{\tilde{g}}_{R}^{j,i}(s)$, are both 2×2-matrices.

The total displacements of, and total reaction forces at, particle **j** in respectively horizontal and vertical direction are obtained by superimposing the displacements of, and reaction forces at, particle **j** due to all loads along the boundary Γ_{cav} that are contained in the load vector \underline{P} , i.e. by summarizing the contributions of the point loads on all particles **i**, where $\mathbf{i} = 1..\mathbf{N}_{\text{Int}}$, to the displacement of, and the reaction forces at, particle **j**. Consequently, the

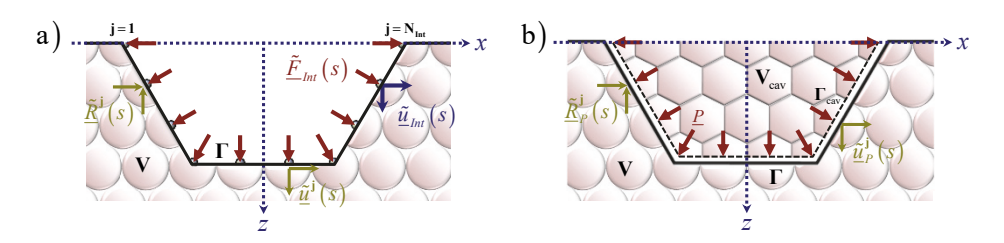


Figure 4.11: a) The discrete particle system with a cavity, i.e. the unknown elastodynamic state; b) The full discrete particle system composed of the particle system with the cavity and a cavity system.

displacements of, and the reaction forces at, particle i are respectively found as:

$$\underline{\tilde{u}}_{P}^{j}(s) = \sum_{i=1}^{N_{\text{Int}}} \underline{\tilde{u}}_{P}^{j,i}(s) = \sum_{i=1}^{N_{\text{Int}}} \underline{\tilde{g}}_{u}^{j,i}(s) \underline{P}^{i}$$

$$\underline{\underline{\tilde{R}}_{P}^{j}}(s) = \sum_{i=1}^{N_{\text{Int}}} \underline{\underline{\tilde{R}}_{P}^{j,i}}(s) = \sum_{i=1}^{N_{\text{Int}}} \underline{\underline{\tilde{g}}_{R}^{j,i}}(s) \underline{\underline{P}}^{i}$$

Collecting the displacements and the reaction forces for all particles \mathbf{j} along the boundary Γ into respectively the displacement vector $\underline{\tilde{u}}_P$ and the reaction force vector $\underline{\tilde{R}}_P$, ultimately yields:

$$\underline{\tilde{u}}_{P}(s) = \tilde{g}_{u}(s)\underline{P} \tag{4.37}$$

$$\underline{\tilde{R}}_{P}(s) = \underline{\tilde{g}}_{R}(s)\underline{P} \tag{4.38}$$

Here, $\underline{\tilde{g}_u}(s)$ and $\underline{\tilde{g}_R}(s)$ are square matrices with dimension $2N_{\text{Int}}$ that respectively contain the Green's displacements and Green's reaction forces for all particles along Γ due to the point loads at all particles along Γ_{cav} . Accordingly, the displacement vector $\underline{\tilde{u}}_P$, the reaction force vector $\underline{\tilde{R}}_P$ and the load vector \underline{P} are vectors with length $2N_{\text{Int}}$.

The unknown elastodynamic state: A discrete particle system with a cavity

The unknown elastodynamic state, depicted in Figure 4.11a, refers to the elastodynamic state of the far-field system V for which the relation between the displacements $\underline{\tilde{u}}_{Int}(s)$ of the particles along the boundary Γ and the force vector $\underline{\tilde{F}}_{Int}(s)$ is unknown and that we wish to solve for. In the dynamic reciprocal work theorem, the unknown elastodynamic state is described by the displacements $\underline{\tilde{u}}(s)$ and the reaction forces $\underline{\tilde{R}}(s)$ for all particles along the boundary Γ .

As the vectors $\underline{\tilde{u}}(s)$ and $\underline{\tilde{u}}_{lnt}(s)$ both describe the two-dimensional displacement field of all particles of the far-field system V along the boundary Γ , they are one and the same. Ergo:

$$\underline{\tilde{u}}(s) = \underline{\tilde{u}}_{lnt}(s) \tag{4.39}$$

Accordingly, the exerted force vector $\underline{\tilde{F}}_{lnt}(s)$ consists of forces applied along the boundary Γ that are exactly equal but opposite to the reaction forces described by the vector $\underline{\tilde{R}}(s)$. Consequently, the relation between the force vectors $\underline{\tilde{F}}_{lnt}(s)$ and $\underline{\tilde{R}}(s)$ reads:

$$\tilde{R}(s) = -\tilde{F}_{loc}(s) \tag{4.40}$$

Both equations (4.39) and (4.40) are very straightforward as long as the location of the particles along the boundary Γ match for the far-field system V and the cavity system V_{cav} .

4.3.2 The dynamic compliance matrix for a discrete particle system

Substituting the Green's relations (4.37) and (4.38) for the known elastodynamic state and the force and displacement relations for the unknown elastodynamic state given by equations (4.39) and (4.40) into the dynamic reciprocal work theorem, given by equation (4.34), and rearranging the remainder noting that the dynamic reciprocal work theorem is an equality between scalars, yields the following force-displacement relation:

$$\underline{P}^{\mathsf{T}} \underline{\tilde{g}_{u}} \left(s \right)^{\mathsf{T}} \underline{\tilde{F}}_{lnt} \left(s \right) = \underline{P}^{\mathsf{T}} \underline{\tilde{g}}_{R} \left(s \right)^{\mathsf{T}} \underline{\tilde{u}}_{lnt} \left(s \right) \tag{4.41}$$

Since the applied load can be arbitrarily chosen such that all terms in the load vector \underline{P} are nonzero and noninfinite, we may replace the load vector by the unit vector, which essentially removes the vector term \underline{P}^T from equation (4.41), without violating the equality. Solving the remaining equation for the force vector \underline{F}_{Int} yields the force-displacement relation along the boundary Γ as:

$$\underline{\underline{\tilde{F}}}_{Int}(s) = -\left(\underline{\underline{\tilde{g}}}_{u}(s)^{\mathsf{T}}\right)^{-1}\underline{\underline{\tilde{g}}}_{R}(s)^{\mathsf{T}}\underline{\tilde{u}}_{Int}(s) \tag{4.42}$$

Consequently, we find the corresponding dynamic stiffness matrix as:

$$\underline{\underline{\tilde{z}}}(s) = \left(\underline{\underline{\tilde{g}}_u}(s)^{\mathsf{T}}\right)^{-1} \underline{\underline{\tilde{g}}_R}(s)^{\mathsf{T}} = \left(\underline{\underline{\tilde{g}}_R}(s)\underline{\underline{\tilde{g}}_u}(s)^{-1}\right)^{\mathsf{T}}$$
(4.43)

And accordingly, the dynamic compliance matrix is found as:

$$\underline{\underline{\tilde{\beta}}}(s) = \left(\underline{\underline{\tilde{g}}_R}(s)^{\mathsf{T}}\right)^{-1} \underline{\underline{\tilde{g}}_u}(s)^{\mathsf{T}} = \left(\underline{\underline{\tilde{g}}_u}(s)\underline{\underline{\tilde{g}}_R}(s)^{-1}\right)^{\mathsf{T}}$$
(4.44)

According to equations (4.43) and (4.44), the dynamic stiffness and compliance matrices for the discrete particle system with a cavity follow from the Green's displacement matrix and the Green's reaction force matrix for the system without a cavity. The corresponding Green's functions for the discrete particle system without a cavity are derived in the following section.

Note that, in the boundary formulation presented here, no assumptions are made regarding the displacements of, or the reaction forces at, the boundary Γ of the discrete particle system. Consequently, the resulting force-displacement relation given by either the dynamic stiffness matrix in equation (4.43), or the dynamic compliance matrix in equation (4.44), is exact, which is in strong contrast with the force-displacement relation obtained by applying the indirect boundary element method for the discrete-continuous system in Section 3.5.1. Additionally, to determine the dynamic compliance matrix for the discrete particle system, we require the Green's functions exclusively at the boundary particles along the boundary Γ . This is again unlike the discrete-continuous system, for which the Green's functions are

required along the full continuous boundary Γ . Consequently, to obtain the particle response at the interface of the fully discrete system, the corresponding Green's functions do not have to be integrated over the boundary Γ as a function of the coordinate ξ , neither do we have to introduce any load distributions or Heaviside functions at the lattice-continuum interface to transform the forces at these particles into tractions, and vice versa. Furthermore, while the dynamic stiffness and compliance matrices obtained for the continuous far-field were found through the lumping and flexibility matrices, which each require the integration of the so-called modified Green's matrices over the boundary Γ , the dynamic stiffness and compliance matrices for the discrete particle system, given by equations (4.43) and (4.44), are expressed in terms of the Green's matrices $\underline{\tilde{g}}_u(s)$ and $\underline{\tilde{g}}_R(s)$ directly. The fact that the boundary formulation for the discrete particle system lacks these integrals is clearly beneficial for the numerical implementation and will significantly improve the involved calculation times.

Application to a two-dimensional discrete particle system

To describe the interaction between the discrete near-field lattice and a two-dimensional discrete particle system using the dynamic compliance matrix according to equation (4.44), we need to determine the Green's displacements and the Green's reaction forces at the particles along Γ . These Green's functions may be obtained from the governing equations for a corresponding discrete particle system without a cavity.

The corresponding discrete far-field system is modelled as a half-plane of particles, as this allows us to account for the dispersive character of the medium, without introducing unnecessary complications associated with wave reflections from a bottom. The half-plane of particles is depicted in Figure 4.12. Here, the *x*-axis is chosen at the surface of the half-plane of particles and the *z*-axis is chosen at the symmetry line of the cavity system V_{cav} , which coincides with the vertical symmetry line of the hexagonal lattice in the combined system. Figure 4.12a shows the displacements $\tilde{u}_{p}^{j,i}(s)$ of a particle **j**, and additionally the reaction forces $\tilde{R}_{p}^{j,i}(s)$ along the boundary Γ at another particle **j**, due to a load \underline{P}^{i} at a particle **i** located inside the half-plane of particles. These displacements and reaction forces are obtained by means of the corresponding Green's functions according to respectively equations (4.35) and (4.36). To obtain the expressions for the Green's displacements and the Green's reaction forces for all particles along the boundary Γ , we consider the half-plane of particles to be composed of two subsystems, where the horizontal interface between the two

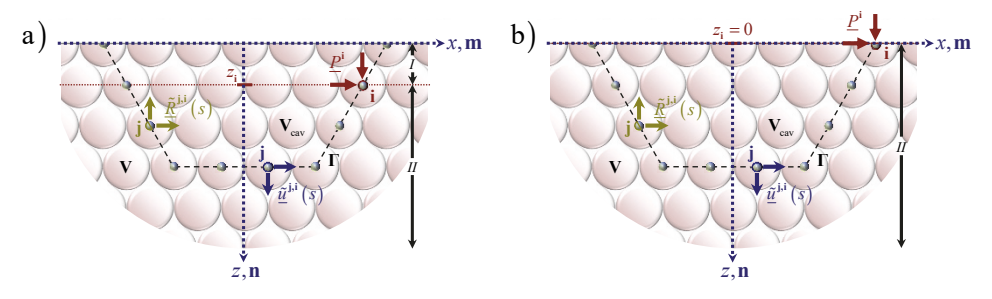


Figure 4.12: The displacements of, and reaction forces at, a particle **j** for a load applied a particle **i** located: a) inside the half-plane of particles; b) at the surface of the half-plane of particles.

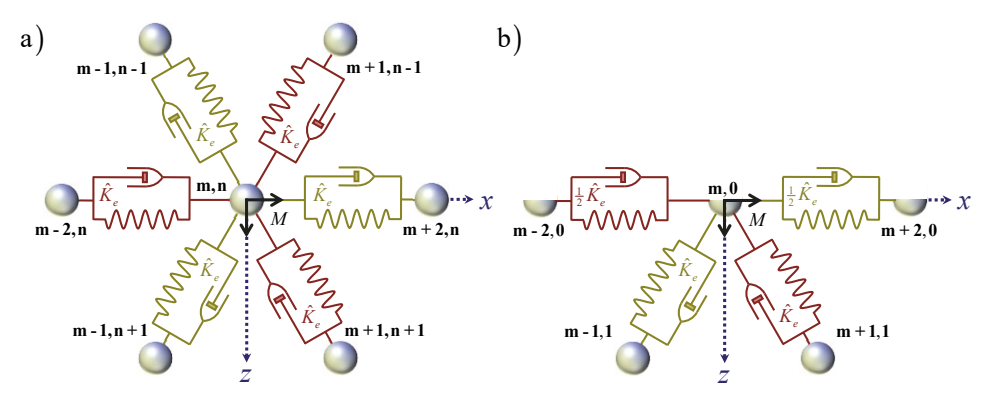


Figure 4.13: Cell configuration of: a) a particle **m,n** in the interior of the viscoelastic half-plane of particles; b) a particle **m,0** at the surface of the viscoelastic half-plane of particles;

subsystems is given by the z-coordinate of the loaded particle i, i.e. $z = z_i$. Here, the layer of particles between the surface of the half-plane and the z-coordinate of the loaded particle is denoted by roman numeral I and must allow for both upward and downward propagating waves. The remainder of the half-plane, which itself is again a half-plane of particles, only needs to account for downward propagating waves and is denoted by roman numeral II. For the particular case that the loaded particle i is located at the surface of the half-plane of particles, as depicted in Figure 4.12b, only downward propagating waves need to be accounted for, so that we can consider the half-plane of particles as a single system.

4.4 Green's functions for the viscoelastic half-plane of particles

In this section, we derive the Laplace domain expressions for the Green's displacements and the Green's reaction forces in the viscoelastic half-plane of particles as they appear in the expressions for the dynamic stiffness matrix and the dynamic compliance matrix, given by equations (4.43) and (4.44) respectively. In Section 4.4.1, we will first derive the governing Laplace domain displacements and reaction forces from the equations of motion for the particles in the viscoelastic half-plane. Subsequently, Section 4.4.2 presents the boundary conditions for a load applied at either a particle at the surface, or a particle in the interior of the half-plane, required to obtain the wave amplitudes that appear in the expressions for the Green's functions. Then, Section 4.4.3 and Section 4.4.4 respectively present the Laplace domain displacements and the Laplace domain reaction forces for the viscoelastic half-plane of particles.

4.4.1 Displacements and reaction forces in the half-plane of particles

In accordance with the approach used for the lattice models in Section 2.1, we derive the equations of motion for a particle in the half-plane of particles by applying Lagrange's formalism. The involved Euler-Lagrange differential equations for the two degrees of freedom of that particle, for which the location is described by the discrete, or nodal, coordinates \mathbf{m} and \mathbf{n} , follow from equation (2.1) by respectively replacing the displacement variable $u^{\mathbf{n}}$ by the horizontal and vertical displacements of particle \mathbf{m} , denoted as $u_x^{\mathbf{m},\mathbf{n}}$ and $u_z^{\mathbf{m},\mathbf{n}}$. The

Lagrangian of the cell of particle m,n appearing in the Euler-Lagrange differential equations, follows from the kinetic energy of particle m,n and the total potential energy enclosed in all rheological elements in its cell, in accordance with equation (2.3). As shown by Figure 4.13, the discrete particle half-plane is chosen to match the configuration of the hexagonal nearfield lattice so that the x- and z-coordinates for particle \mathbf{m} , \mathbf{n} are obtained as $x = \frac{1}{2} \mathbf{m} \ell$ and $z = \frac{1}{2} \mathbf{n} \ell \sqrt{3}$. The cells of the interior and surface particles include the rheological elements that describe the interaction of these particles with their adjacent particles. For a proper boundary formulation, i.e. a formulation that allows for the undisturbed wave propagation through the interface of the near-field lattice with the far-field domain, the half-plane of particles must at least be homogeneous and purely viscoelastic. Therefore, all particles in the interior of the half-plane have the same mass M and the interaction between all adjacent particles is described by Kelvin-Voigt elements with the same properties.

To satisfy the law of conservation of energy such that we are allowed to use the Euler-Lagrange differential equations [Lanczos, 1966], we consider the Kelvin-Voigt elements as springs for which the equivalent stiffness is described by the operator $\hat{K}_e = K_e + C_e \frac{\partial}{\partial t}$. Here, K_e and C_e are respectively the stiffness and damping coefficients of the Kelvin-Voigt element, while the partial time derivative implies a differentiation of the corresponding displacement with respect to time. Consequently, the Lagrangian for a particle m,n inside the discrete particle half-plane becomes:

$$L^{\mathbf{m},\mathbf{n}} = \frac{1}{2} M \left(\dot{u}_x^{\mathbf{m},\mathbf{n}} \right)^2 + \frac{1}{2} M \left(\dot{u}_z^{\mathbf{m},\mathbf{n}} \right)^2 - \frac{1}{2} \hat{K}_e \sum_{j=1}^6 \left(e_j^{\mathbf{m},\mathbf{n}} \right)^2$$
(4.45)

Furthermore, $e_i^{m,n}$ is the elongation of the j-th element in the cell of particle m,n. Since we consider the purely viscoelastic response of the half-plane of particles, we may apply the linearization for small elongations and express the elongation $e_i^{m,n}$ as given in Appendix A.1.

Applying Lagrange's formalism by substituting equation (4.45) into the Euler-Lagrange differential equations for the displacements $u_x^{m,n}$ and $u_z^{m,n}$ respectively, and successively accounting for the evenly divided angles of the Kelvin-Voigt elements in the corresponding cell, yields the equations of motion for the interior particle m,n depicted in Figure 4.13a as:

$$M\ddot{u}_{x}^{\mathbf{m,n}} + \hat{K}_{e} \begin{pmatrix} 3u_{x}^{\mathbf{m,n}} - u_{x}^{\mathbf{m-2,n}} - u_{x}^{\mathbf{m+2,n}} - \frac{1}{4} \left(u_{x}^{\mathbf{m-1,n+1}} + u_{x}^{\mathbf{m+1,n+1}} + u_{x}^{\mathbf{m-1,n-1}} + u_{x}^{\mathbf{m+1,n-1}} \right) \\ + \frac{\sqrt{3}}{4} \left(u_{z}^{\mathbf{m-1,n+1}} - u_{z}^{\mathbf{m+1,n+1}} - u_{z}^{\mathbf{m-1,n-1}} + u_{z}^{\mathbf{m+1,n-1}} \right) \end{pmatrix} = 0$$
 (4.46)

$$M\ddot{u}_{x}^{\mathbf{m,n}} + \hat{K}_{e} \begin{pmatrix} 3u_{x}^{\mathbf{m,n}} - u_{x}^{\mathbf{m-2,n}} - u_{x}^{\mathbf{m+2,n}} - \frac{1}{4} \left(u_{x}^{\mathbf{m-1,n+1}} + u_{x}^{\mathbf{m+1,n+1}} + u_{x}^{\mathbf{m-1,n-1}} + u_{x}^{\mathbf{m+1,n-1}} \right) \\ + \frac{\sqrt{3}}{4} \left(u_{z}^{\mathbf{m-1,n+1}} - u_{z}^{\mathbf{m+1,n+1}} - u_{z}^{\mathbf{m-1,n-1}} + u_{z}^{\mathbf{m+1,n-1}} \right) \end{pmatrix} = 0 \qquad (4.46)$$

$$M\ddot{u}_{z}^{\mathbf{m,n}} + \hat{K}_{e} \begin{pmatrix} 3u_{z}^{\mathbf{m,n}} + \frac{\sqrt{3}}{4} \left(u_{x}^{\mathbf{m-1,n+1}} - u_{x}^{\mathbf{m+1,n+1}} - u_{x}^{\mathbf{m-1,n-1}} + u_{x}^{\mathbf{m+1,n-1}} \right) \\ - \frac{3}{4} \left(u_{z}^{\mathbf{m-1,n+1}} + u_{z}^{\mathbf{m+1,n+1}} + u_{z}^{\mathbf{m-1,n-1}} + u_{z}^{\mathbf{m+1,n-1}} \right) \end{pmatrix} = 0 \qquad (4.47)$$

Together, equations (4.46) and (4.47) describe the two-dimensional behaviour of particles in the discrete half-plane in the time domain. These equations are the discrete equivalent of the two-dimensional elastodynamic equation for the continuum, previously given by equation (3.88).

Applying Lagrange's formalism for the particle **m,0** located at the surface of the viscoelastic half-plane of particles, depicted in Figure 4.13b, yields its equations of motion as:

$$\frac{1}{2}M\ddot{u}_{x}^{\mathbf{m},0} + \frac{1}{2}\hat{K}_{e}\left(3u_{x}^{\mathbf{m},0} - u_{x}^{\mathbf{m}-2,0} - u_{x}^{\mathbf{m}+2,0} - \frac{1}{2}\left(u_{x}^{\mathbf{m}-1,1} + u_{x}^{\mathbf{m}+1,1}\right) + \frac{\sqrt{3}}{2}\left(u_{z}^{\mathbf{m}-1,1} - u_{z}^{\mathbf{m}+1,1}\right)\right) = 0 \quad (4.48)$$

$$\frac{1}{2}M\ddot{u}_{z}^{\mathbf{m},0} + \frac{1}{2}\hat{K}_{e}\left(3u_{z}^{\mathbf{m},0} - \frac{3}{2}\left(u_{z}^{\mathbf{m}-1,1} + u_{z}^{\mathbf{m}+1,1}\right) + \frac{\sqrt{3}}{2}\left(u_{x}^{\mathbf{m}-1,1} - u_{x}^{\mathbf{m}+1,1}\right)\right) = 0 \quad (4.49)$$

Dimensionless equations of motion for a particle in the half-plane of particles

In accordance with the approach for the one-dimensional lattices, and as opposed to the derivation of the governing equations for the two-dimensional continuum in Section 3.5, we here derive the governing equations of motion for the half-plane of particles in their dimensionless form. To normalize the equations for the half-plane of particles, the following dimensionless parameters for respectively time and space are introduced:

$$t = t_{\text{dim}} \omega_0, \quad u^{\mathbf{m},\mathbf{n}} = \frac{u_{\text{dim}}^{\mathbf{m},\mathbf{n}}}{\ell}.$$

Here, ω_0 is the particle frequency, i.e. the natural frequency of a particle in hexagonal BKV lattice for the particular case that the motion of any adjacent particles is impeded. As shown by Appendix B.4, this so-called particle frequency for a particle in a hexagonal lattice is found as $\omega_0 = \sqrt{3K_e/M}$ and is thereby different from the particle frequency of the homogeneous one-dimensional cascade.

Inserting the dimensionless parameters for space and time into equations (4.46) and (4.47), including the expression for the operator $\hat{K}_e = K_e + C_e \frac{\partial}{\partial t}$, dividing the remainder by $M \omega_0^2 \ell$ and subsequently applying the Laplace transform with respect to time, the Laplace domain equations of motion for a particle \mathbf{m} , \mathbf{n} in the viscoelastic half-plane of particles become:

$$s^{2}\tilde{u}_{x}^{\mathbf{m},\mathbf{n}} + \frac{1}{3}(1 + 2\zeta s) \begin{pmatrix} 3\tilde{u}_{x}^{\mathbf{m},\mathbf{n}} - \tilde{u}_{x}^{\mathbf{m}-2,\mathbf{n}} - \tilde{u}_{x}^{\mathbf{m}-2,\mathbf{n}} - \frac{1}{4}(\tilde{u}_{x}^{\mathbf{m}-1,\mathbf{n}+1} + \tilde{u}_{x}^{\mathbf{m}+1,\mathbf{n}+1} + \tilde{u}_{x}^{\mathbf{m}-1,\mathbf{n}-1} + \tilde{u}_{x}^{\mathbf{m}+1,\mathbf{n}-1}) \\ + \frac{\sqrt{3}}{4}(\tilde{u}_{z}^{\mathbf{m}-1,\mathbf{n}+1} - \tilde{u}_{z}^{\mathbf{m}+1,\mathbf{n}+1} - \tilde{u}_{z}^{\mathbf{m}-1,\mathbf{n}-1} + \tilde{u}_{z}^{\mathbf{m}+1,\mathbf{n}-1}) \end{pmatrix} = 0$$
 (4.50)

$$s^{2}\tilde{u}_{\varepsilon}^{\mathbf{m},\mathbf{n}} + \frac{1}{3}(1 + 2\zeta s) \begin{pmatrix} 3\tilde{u}_{\varepsilon}^{\mathbf{m},\mathbf{n}} + \frac{\sqrt{3}}{4} \left(\tilde{u}_{x}^{\mathbf{m}-\mathbf{1},\mathbf{n}+\mathbf{1}} - \tilde{u}_{x}^{\mathbf{m}+\mathbf{1},\mathbf{n}+\mathbf{1}} - \tilde{u}_{x}^{\mathbf{m}-\mathbf{1},\mathbf{n}-\mathbf{1}} + \tilde{u}_{x}^{\mathbf{m}+\mathbf{1},\mathbf{n}-\mathbf{1}} \right) \\ -\frac{3}{4} \left(\tilde{u}_{\varepsilon}^{\mathbf{m}-\mathbf{1},\mathbf{n}+\mathbf{1}} + \tilde{u}_{\varepsilon}^{\mathbf{m}+\mathbf{1},\mathbf{n}+\mathbf{1}} + \tilde{u}_{\varepsilon}^{\mathbf{m}-\mathbf{1},\mathbf{n}-\mathbf{1}} + \tilde{u}_{\varepsilon}^{\mathbf{m}+\mathbf{1},\mathbf{n}-\mathbf{1}} \right) \end{pmatrix} = 0 \quad (4.51)$$

Here, ζ is the damping ratio obtained as $\zeta = C_e/C_{crit}$, where C_{crit} is the critical particle damping, which, as shown by Appendix B.4, is obtained for a hexagonal lattice as $C_{crit} = \frac{2}{3}M\omega_0$.

Note here that the form of equations (4.50) and (4.51) is similar to that of the equation of motion of a particle in the one-dimensional cascade, previously given by equation (4.8).

Governing Laplace domain displacements in the half-plane of particles

To describe the wave propagation in the half-plane of particles, we here seek a solution to

equations (4.50) and (4.51) by describing the Laplace domain displacements of the particle **m,n** in the form of a superposition of plane harmonic waves [Suiker et al., 2001b]. Before doing so however, let us first consider the source of the wave propagation through the halfplane, i.e. the applied load.

As shown previously by Figure 4.12, we consider a load \underline{P}^i applied at a particle i along a boundary Γ that matches the interface between the nonlinear hexagonal lattice and the viscoelastic half-plane. Application of this force to a two-dimensional continuum as a point load yields singular displacements in the continuum. For the half-plane of particles, the resulting displacement is finite as the point force matches the discrete nature of the lattice. To describe the response of the half-plane of particles to a load at particle i, we must describe the corresponding boundary conditions along the horizontal level of particles with nodal coordinate n_i . The load is then incorporated in the boundary conditions using the Kronecker Delta δ_{m_im} , which is defined to be equal to one when $m = m_i$ and equal to zero when $m \neq m_i$. The load \underline{P}^i , applied at particle i along a horizontal level of particles, may thus be expressed in terms of the Kronecker delta as $\underline{P}^i = \underline{P}\delta_{m_im}$.

To consider plane harmonic waves in the half-plane of particles due to a load applied at particle **i**, we describe the Kronecker delta by an integral identity in terms of the dimensionless horizontal wavenumber κ_x . Accounting for the horizontal spacing of the particles by describing the dimensionless x-coordinate of a particle in terms of the horizontal nodal coordinate **m** as $x = \frac{1}{2}$ **m**, the Kronecker Delta may be expressed using the following integral representation:

$$\delta_{\mathbf{m}_{i}\mathbf{m}} = \frac{1}{4\pi} \int_{-2\pi}^{+2\pi} e^{\frac{1}{2}i\kappa_{x}(\mathbf{m}_{i}-\mathbf{m})} d\kappa_{x}$$

$$(4.52)$$

The integral identity for the Kronecker Delta is chosen as such to properly account for the geometry and the infinite horizontal domain of the half-plane of particles.

To find a solution to equations (4.50) and (4.51) that satisfies the boundary conditions for a point load applied at a particle **i**, the Laplace domain displacements of any particle **m,n** inside the half-plane are described in accordance with the integral representation for the Kronecker Delta given by equation (4.52). The two-dimensional wave propagation is accounted for by incorporating a term related to the vertical wavenumber κ_z , in which the dimensionless z-coordinate of a particle with vertical nodal coordinate **n** is found as $z = \frac{\sqrt{3}}{2}$ **n**. Note here that according to the integral identity for the Kronecker Delta, the horizontal wavenumber κ_x must be real, while the vertical wavenumber κ_z can be complex-valued and is dependent on the horizontal wavenumber κ_x . The horizontal and vertical displacements of a particle **m,n** are thus assumed in the Laplace domain as:

$$\tilde{u}_x^{\mathbf{m},\mathbf{n}}\left(s\right) = \int_{-2\pi}^{+2\pi} A^{\mathbf{i}} e^{-\frac{1}{2}\mathbf{i}\kappa_x \mathbf{m}} e^{+\frac{\sqrt{2}}{2}\mathbf{i}\kappa_z \mathbf{n}} d\kappa_x \tag{4.53}$$

$$\tilde{u}_{z}^{\mathbf{m},\mathbf{n}}\left(s\right) = \int_{2\pi}^{+2\pi} B^{\mathbf{i}} e^{-\frac{1}{2}\mathbf{i}\kappa_{x}\mathbf{m}} e^{+\frac{\sqrt{2}}{2}\mathbf{i}\kappa_{z}\mathbf{n}} d\kappa_{x} \tag{4.54}$$

Here, A^{i} and B^{i} are unknown wave amplitudes that follow from solving the system of boundary conditions for the point load \underline{P}^{i} applied at a particle **i**. Furthermore, the argument of the exponent related to the horizontal wavenumber κ_{x} is chosen in accordance with the expression for the Kronecker Delta in equation (4.52). The properties of the vertical wavenumber κ_{z} itself as well as the sign of the exponent argument and the corresponding direction of wave propagation are further discussed below.

Equations (4.53) and (4.54) are novel expressions for the Laplace domain displacements of lattice particles, where the integral representation used is similar to applying the inverse Fourier integral transform with respect to the horizontal wavenumber used for continua. Thereby, the integrands in equations (4.53) and (4.54) can respectively be considered as the horizontal and vertical displacements in the Laplace-wavenumber domain.

Substituting the Laplace domain displacements according to equations (4.53) and (4.54) into equations of motion (4.50) and (4.51) for particle \mathbf{m} , \mathbf{n} , as well as for all particles adjacent to particle \mathbf{m} , \mathbf{n} , yields the following system of equations for the wave amplitudes A^{i} and B^{i} :

$$\left(3\left(1+\frac{s^{2}}{1+2\zeta s}\right)-2\cos\kappa_{x}-\cos\frac{\kappa_{x}}{2}\cos\frac{\kappa_{z}\sqrt{3}}{2}\right)A^{i}-\sqrt{3}\sin\frac{\kappa_{x}}{2}\sin\frac{\kappa_{z}\sqrt{3}}{2}B^{i}=0$$

$$-\sqrt{3}\sin\frac{\kappa_{x}}{2}\sin\frac{\kappa_{z}\sqrt{3}}{2}A^{i}+3\left(1+\frac{s^{2}}{1+2\zeta s}-\cos\frac{\kappa_{x}}{2}\cos\frac{\kappa_{z}\sqrt{3}}{2}\right)B^{i}=0$$
(4.55)

The above system of homogeneous algebraic equations has a non-trivial solution if, and only if, its determinant is equal to zero. Provided that the Laplace parameter s is replaced by $i\omega$, the resulting equality gives the dispersion relation for the viscoelastic half-plane of particles with a hexagonal configuration and reads:

$$\left(3\left(1+\frac{s^2}{1+2\zeta s}\right)-2\cos\kappa_x-\cos\frac{\kappa_x}{2}\cos\frac{\kappa_z\sqrt{3}}{2}\right)\left(1+\frac{s^2}{1+2\zeta s}-\cos\frac{\kappa_x}{2}\cos\frac{\kappa_z\sqrt{3}}{2}\right)-\sin^2\frac{\kappa_x}{2}\sin^2\frac{\kappa_z\sqrt{3}}{2}=0 \quad (4.56)$$

Solving equation (4.56) for the cosine-term related to the vertical wavenumber κ_z using the quadratic formula, yields:

$$\left(\cos\frac{\kappa_{z}\sqrt{3}}{2}\right)_{1,2} = \left(2\left(1 + \frac{s^{2}}{1 + 2\zeta s}\right) - \cos\kappa_{x}\right)\cos\frac{\kappa_{x}}{2} \\
\pm \frac{1}{1 + 2\zeta s}\sqrt{s^{4}\left(2\cos\kappa_{x} - 1\right) - 2s^{2}\left(1 + 2\zeta s\right)\left(\cos\kappa_{x} - 1\right)^{2} + \frac{1}{2}\left(1 + 2\zeta s\right)^{2}\left(\cos\kappa_{x} - 1\right)^{3}} \tag{4.57}$$

In contrast to the two-dimensional continuum and the discrete particle system with a square

configuration [Suiker et al., 2001b], it follows from equation (4.57) that, for the discrete particle system with a hexagonal configuration, the shear and compressional waves cannot be isolated.

Next, note that equation (4.57) gives two expressions for $\cos\left(\frac{\sqrt{3}}{2}\kappa_z\right)$ and that each of these expressions yields one wavenumber that belongs to the first Brillouin zone of the lattice [Brillouin, 1953]. We denote the wavenumbers for each of these expressions as $\kappa_z^{(1)}$ and $\kappa_z^{(2)}$ respectively. Using Euler's formula and the Pythagorean trigonometric identity, we find the exponents of the forward and backward propagating waves for either wavenumber $\kappa_z^{(h)}$, with h=1..2, as:

$$e^{\pm \frac{\sqrt{5}}{2} i \kappa_z^{(h)}} = \cos \frac{\kappa_z^{(h)} \sqrt{3}}{2} \pm i \sqrt{1 - \cos^2 \frac{\kappa_z^{(h)} \sqrt{3}}{2}}$$
(4.58)

In equations (4.53) and (4.54), we have posed the Laplace domain displacements of a particle \mathbf{m} , \mathbf{n} in the half-plane of particles to have only one characteristic wavenumber in z-direction and we have only considered one direction for the wave propagation. Clearly, there are two characteristic wavenumbers in z-direction and, depending on the boundary conditions, waves propagating in both positive and negative z-direction should be considered. Therefore, the expressions for the Laplace domain displacements $\tilde{u}_x^{\mathbf{m},\mathbf{n}}(s)$ and $\tilde{u}_z^{\mathbf{m},\mathbf{n}}(s)$ of particle \mathbf{m} , \mathbf{n} must be adapted to incorporate both wavenumbers and, depending on the location of particle \mathbf{m} , \mathbf{n} compared to the location of the loaded particle \mathbf{i} , waves travelling in both directions. Note here that the positive sign of the exponents' argument related to the vertical wavenumber $\kappa_z^{(h)}$ in equations (4.53) and (4.54) does not correspond to wave propagation in a certain direction, as this direction depends on the sign of the imaginary part of the vertical wavenumber $\kappa_z^{(h)}$. Nevertheless, if the positive argument of the exponent related to the vertical wavenumber $\kappa_z^{(h)}$ corresponds to a wave travelling in positive z-direction, the same exponent with a negative argument must always correspond to a wave travelling in negative z-direction.

Thus, accounting for the two characteristic wavenumbers and accounting for waves travelling in both positive and negative z-direction, the horizontal and vertical displacements of a particle \mathbf{m} , \mathbf{n} due to a load at a particle \mathbf{i} are, in a general sense, described as:

$$\tilde{u}_{x}^{\mathbf{m},\mathbf{n}}\left(s\right) = \int_{-2\pi}^{+2\pi} \left(\sum_{h=1}^{2} A_{1}^{\mathbf{i},(h)} e^{+\frac{\sqrt{5}}{2}\mathbf{i}\kappa_{z}^{(h)}\mathbf{n}} + \sum_{h=1}^{2} A_{2}^{\mathbf{i},(h)} e^{-\frac{\sqrt{5}}{2}\mathbf{i}\kappa_{z}^{(h)}\mathbf{n}}\right) e^{-\frac{1}{2}\mathbf{i}\kappa_{x}\mathbf{m}} d\kappa_{x}$$

$$(4.59)$$

$$\tilde{u}_{z}^{\mathbf{m},\mathbf{n}}\left(s\right) = \int_{-2\pi}^{+2\pi} \left(\sum_{h=1}^{2} B_{1}^{\mathbf{i},(h)} e^{+\frac{\sqrt{5}}{2}\mathbf{i}\kappa_{z}^{(h)}\mathbf{n}} + \sum_{h=1}^{2} B_{2}^{\mathbf{i},(h)} e^{-\frac{\sqrt{5}}{2}\mathbf{i}\kappa_{z}^{(h)}\mathbf{n}}\right) e^{-\frac{1}{2}\mathbf{i}\kappa_{x}\mathbf{m}} d\kappa_{x}$$

$$(4.60)$$

Henceforth, we choose the square roots in equations (4.57) and (4.58) such that the positive argument of the exponent related to the vertical wavenumber $\kappa_z^{(h)}$ corresponds to the wave propagating in positive z-direction, while the negative argument of the same exponent corresponds to the wave propagating in negative z-direction. Consequently, $A_1^{i,(h)}$ and $B_1^{i,(h)}$ are

respectively the horizontal and vertical wave amplitudes of the waves propagating in positive z-direction, while $A_2^{\mathbf{i},(h)}$ and $B_2^{\mathbf{i},(h)}$ are respectively the horizontal and vertical wave amplitudes of the waves propagating in negative z-direction, both with wavenumber $\kappa_z^{(h)}$.

Each wavenumber $\kappa_z^{(h)}$ corresponds to two components of the eigenvector, respectively denoted as $D_1^{(h)}$ for the wave propagating in positive z-direction and as $D_2^{(h)}$ for the wave propagating in negative z-direction. The expressions for the second component of each eigenvector are respectively obtained as the amplitude ratios $B_1^{\mathbf{i},(h)}/A_1^{\mathbf{i},(h)}$ and $B_2^{\mathbf{i},(h)}/A_2^{\mathbf{i},(h)}$, and follow from the system of algebraic equations for the corresponding exponents of the vertical wavenumber $\kappa_z^{(h)}$. Here, the system of algebraic equations for waves travelling in positive z-direction is given by equation (4.55), while the corresponding system for waves travelling in negative z-direction is the same but with a positive sign for the off-diagonal terms. As a consequence, and for each vertical wavenumber, the resulting expressions for the two eigenvector terms are found to be related as $D_1^{(h)} = D_2^{(h)}$. Thus, introducing $D_1^{(h)} = D_1^{(h)} = -D_2^{(h)}$, we obtain:

$$D^{(h)} = \frac{B_1^{\mathbf{i},(h)}}{A_1^{\mathbf{i},(h)}} = -\frac{B_2^{\mathbf{i},(h)}}{A_2^{\mathbf{i},(h)}} = \frac{\frac{1}{3}\sqrt{3}\sin\frac{\kappa_x}{2}\sin\frac{\kappa_z^{(h)}\sqrt{3}}{2}}{1 + \frac{s^2}{1 + 2\zeta s} - \cos\frac{\kappa_x}{2}\cos\frac{\kappa_z^{(h)}\sqrt{3}}{2}}$$
(4.61)

Note here that, although the wave amplitudes $A_1^{\mathbf{i},(h)}$, $A_2^{\mathbf{i},(h)}$, $B_1^{\mathbf{i},(h)}$ and $B_2^{\mathbf{i},(h)}$ depend on the location of the loaded particle \mathbf{i} , the corresponding eigenvector components do not. Using equation (4.61), the vertical wave amplitudes of the waves in positive and negative z-direction may respectively be expressed in terms of the horizontal wave amplitudes as $B_1^{\mathbf{i},(h)} = D^{(h)}A_1^{\mathbf{i},(h)}$ and $B_2^{\mathbf{i},(h)} = -D^{(h)}A_2^{\mathbf{i},(h)}$. Here, note that while equation (4.61) follows from the equation of motion in z-direction, i.e. the second equation in the system of algebraic equations (4.55), the expression for $D^{(h)}$ may also be derived from the equation of motion in x-direction, being the first equation in (4.55).

Assuming that the loaded particle \mathbf{i} is located in the interior of the half-plane of particles, as previously depicted in Figure 4.12a, we must separately describe the response of the two subsystems the half-plane is composed of. Although both subsystems represent the same material and thus allow for the same characteristic wavenumbers $\kappa_z^{(h)}$, they do not allow for the same waves. As a dynamic load at a particle \mathbf{i} in the interior of the half-plane yields wave reflections at the half-plane surface, the response of a particle \mathbf{m} , \mathbf{n} in subsystem I, i.e. any particle for which $\mathbf{n} \in [0...\mathbf{n_i}]$, must account for waves travelling in both positive and negative z-directions. On the other hand, to satisfy the infinity condition and thus to describe the proper behaviour of the half-plane at $z \to \infty$, the response of a particle \mathbf{m} , \mathbf{n} in subsystem II, i.e. any particle for which $\mathbf{n} \in [\mathbf{n_i} ... \infty]$, only has to account for waves travelling in positive z-direction.

Incorporating the contributions due to both wavenumbers $\kappa_z^{(h)}$, with h=1..2, as well as the contributions of waves travelling in both positive and negative z-directions, the horizontal and vertical displacements of a particle \mathbf{m} , \mathbf{n} in subsystem I due to a load at a particle \mathbf{i}

respectively become:

$$\tilde{u}_{x,I}^{\mathbf{m},\mathbf{n}}\left(s\right) = \int_{2\pi}^{+2\pi} \left(\sum_{h=1}^{2} A_{1}^{\mathbf{i},(h)} e^{+\frac{\sqrt{2}}{2}\mathbf{i}\kappa_{z}^{(h)}\mathbf{n}} + \sum_{h=1}^{2} A_{2}^{\mathbf{i},(h)} e^{-\frac{\sqrt{2}}{2}\mathbf{i}\kappa_{z}^{(h)}\mathbf{n}}\right) e^{-\frac{1}{2}\mathbf{i}\kappa_{x}\mathbf{m}} d\kappa_{x}$$

$$(4.62)$$

$$\tilde{u}_{z,I}^{\mathbf{m},\mathbf{n}}\left(s\right) = \int_{-2\pi}^{+2\pi} \left(\sum_{h=1}^{2} D^{(h)} A_{1}^{\mathbf{i}.(h)} e^{+\frac{\sqrt{5}}{2} \mathrm{i} \kappa_{z}^{(h)} \mathbf{n}} - \sum_{h=1}^{2} D^{(h)} A_{2}^{\mathbf{i}.(h)} e^{-\frac{\sqrt{5}}{2} \mathrm{i} \kappa_{z}^{(h)} \mathbf{n}}\right) e^{-\frac{1}{2} \mathrm{i} \kappa_{x} \mathbf{m}} d\kappa_{x}$$

$$(4.63)$$

Accordingly, incorporating the contributions due to both wavenumbers $\kappa_z^{(h)}$, with h = 1...2, but only accounting for waves travelling in positive z-direction, the horizontal and vertical displacements of a particle \mathbf{m} , \mathbf{n} in subsystem II due to a load at a particle \mathbf{i} are respectively described as:

$$\tilde{u}_{x,H}^{m,n}(s) = \int_{-2\pi}^{+2\pi} \left(\sum_{h=1}^{2} A_3^{\mathbf{i},(h)} e^{+\frac{\sqrt{5}}{2} \mathbf{i} \kappa_z^{(h)} \mathbf{n}} \right) e^{-\frac{1}{2} \mathbf{i} \kappa_x \mathbf{m}} d\kappa_x$$
(4.64)

$$\tilde{u}_{z,II}^{\mathbf{m},\mathbf{n}}(s) = \int_{-2\pi}^{+2\pi} \left(\sum_{h=1}^{2} D^{(h)} A_3^{\mathbf{i},(h)} e^{+\frac{\sqrt{5}}{2} i \kappa_z^{(h)} \mathbf{n}} \right) e^{-\frac{1}{2} i \kappa_x \mathbf{m}} d\kappa_x$$
(4.65)

For the particular case that the loaded particle i is located at the surface of the half-plane, subsystem I does not exist and the horizontal and vertical displacements of any particle m,n in the half-plane are described exclusively by equations (4.64) and (4.65) respectively.

The method to obtain the governing displacements for the half-plane of particles employed here, is somewhat different from the approach for the two-dimensional continuum in Section 3.5.3, where we employ Helmholtz' decomposition. Alternatively however, the governing displacements for the two-dimensional continuum may also be obtained by analogy of the approach for the half-plane of particles presented here.

Governing Laplace domain reaction forces in the half-plane of particles

Equivalent to stresses existing at the interface between two continuous bodies, reaction forces exist at particles located at or along the interface between two discrete particle systems. Thereby, the reaction forces do not only depend on the location of the considered particle, but also on the shape and the orientation of the interface at the involved particle. As an example of this, consider the reaction forces along two different orientations of a straight interface depicted in Figure 4.14. For both situations, the reaction forces describe the interaction between two half-particles, even though the shape of the interface, and thereby the shape of the two sub-particles, is the same for both, the different orientations of the interface yield different expressions for the reaction forces. Additionally, the expressions for the reaction forces also depend on the shape of the interface; consider for example that the expressions for a particle along a straight interface will be different to those obtained for a particle at the corner of an interface, where two straight segments of that interface meet. While we are able to generally determine reaction forces at any particle in the half-plane of particles by arbitrarily assuming an interface for each of these particles, it is useful to here specifically

consider the reaction forces along the interface Γ between the cavity system V_{cav} and the discrete particle system V, of which the Green's functions are required to construct the dynamic stiffness and compliance matrix according to equations (4.43) and (4.44).

As an example of how to determine the reaction forces, consider a particle \mathbf{m} , \mathbf{n} located along the horizontal path of the interface Γ , depicted by Figure 4.14a. The particle \mathbf{m} , \mathbf{n} at the interface Γ consists of two half-particles: an upper half-particle that is part of the cavity system \mathbf{V}_{cav} , and a lower half-particle that belongs to the discrete particle system \mathbf{V} . The reaction forces at either half-particle are then opposite to the horizontal and vertical forces that describe the interaction of the two half-particles. The horizontal and vertical reaction forces at a particle \mathbf{m} , \mathbf{n} , respectively denoted as $\tilde{R}_x^{\mathbf{m},\mathbf{n}}(s)$ and $\tilde{R}_z^{\mathbf{m},\mathbf{n}}(s)$, then follow directly from the corresponding equations of motion of either half-particle.

Here, it is important to emphasize that the dynamic reciprocal work theorem according to equation (4.34) considers the displacements and reaction forces along the boundary Γ of the discrete particle system V, and not the reaction forces along the face Γ_{cav} of the cavity system V_{cav} . Although the displacements of the two half-particles that make up particle m,n must always be the same, and even the reaction forces at the two half-particles are the same if the particle is not loaded, the reaction forces at the two half-particles are not the same when there is a load is applied at the particle m,n. Therefore, the reaction forces must always be determined at the boundary Γ and thus from the equations of motion of the sub-particle in the discrete particle system V.

The expressions for the horizontal and vertical reaction forces at the lower half-particle \mathbf{m} , \mathbf{n} along the horizontal part of the boundary Γ , depicted in Figure 4.14a, are equal in magnitude but opposite in direction to the left-hand side of the equations of motion for the surface particle \mathbf{m} , $\mathbf{0}$, previously given by equations (4.48) and (4.49). Introducing the common dimensionless parameters and applying the Laplace transform with respect to time then yields the corresponding Laplace domain reaction forces. Subsequently substituting the expressions for the corresponding Laplace domain displacements, given by equations (4.62) to (4.65), we can express the reaction forces in terms of the wave amplitudes $A_1^{i,(h)}$, $A_2^{i,(h)}$ and $A_3^{i,(h)}$.

Generally, the final expressions for the reaction forces at a particle \mathbf{m} , \mathbf{n} depend on the shape of the interface Γ and on the location of particle \mathbf{m} , \mathbf{n} compared to the loaded particle \mathbf{i} . For any particle \mathbf{m} , \mathbf{n} that is located in the interior of subsystem I, i.e. for $\mathbf{n} < \mathbf{n}_i$, all particles within its cell may be regarded as degrees of freedom of subsystem I. Therefore, exclusively substituting equations (4.62) and (4.63) into the equations of motion of either one of the relevant sub-particles allows us to generally express the horizontal and vertical reaction forces for such particles as:

$$\tilde{R}_{x,I}^{\mathbf{m,n}}\left(s\right) = \int_{2-}^{+2\pi} \left(\sum_{h=1}^{2} \varphi_{x;1}^{(h)} A_{1}^{\mathbf{i},(h)} e^{+\frac{\sqrt{2}}{2} i \kappa_{z}^{(h)} \mathbf{n}} + \sum_{h=1}^{2} \varphi_{x;2}^{(h)} A_{2}^{\mathbf{i},(h)} e^{-\frac{\sqrt{2}}{2} i \kappa_{z}^{(h)} \mathbf{n}} \right) e^{-\frac{1}{2} i \kappa_{x} \mathbf{m}} d\kappa_{x}$$

$$(4.66)$$

$$\tilde{R}_{z,l}^{\mathbf{m,n}}\left(s\right) = \int_{-2\pi}^{+2\pi} \left(\sum_{h=1}^{2} \varphi_{z;1}^{(h)} A_{1}^{\mathbf{i},(h)} e^{+\frac{\sqrt{3}}{2} \mathrm{i} \kappa_{z}^{(h)} \mathbf{n}} + \sum_{h=1}^{2} \varphi_{z;2}^{(h)} A_{2}^{\mathbf{i},(h)} e^{-\frac{\sqrt{3}}{2} \mathrm{i} \kappa_{z}^{(h)} \mathbf{n}}\right) e^{-\frac{1}{2} \mathrm{i} \kappa_{x} \mathbf{m}} d\kappa_{x}$$

$$(4.67)$$

Here, the expressions for $\varphi_{x;1}^{(h)}$, $\varphi_{x;2}^{(h)}$, $\varphi_{z;1}^{(h)}$ and $\varphi_{z;2}^{(h)}$, with h=1..2, follow from the substitution of the governing displacements into the expressions for the reaction forces that follow from the corresponding equations of motion and thereby depend on the cell configuration of the sub-particle for which the reaction forces are obtained.

Accordingly, if the particle \mathbf{m} , \mathbf{n} is located in the interior of subsystem II, i.e. for $\mathbf{n} > \mathbf{n}_i$, all particles within its cell may be regarded as degrees of freedom of subsystem II. Substitution of equations (4.64) and (4.65) into the equations of motion of either one of the relevant sub-particles then generally yields the horizontal and vertical reaction forces as:

$$\tilde{R}_{x,H}^{\mathbf{m,n}}\left(s\right) = \int_{-2\pi}^{+2\pi} \left(\sum_{h=1}^{2} \varphi_{x;3}^{(h)} A_{3}^{\mathbf{i},(h)} e^{+\frac{\sqrt{5}}{2} \mathbf{i} \kappa_{z}^{(h)} \mathbf{n}}\right) e^{-\frac{1}{2} \mathbf{i} \kappa_{x} \mathbf{m}} d\kappa_{x}$$

$$(4.68)$$

$$\tilde{R}_{z,II}^{\mathbf{m,n}}\left(s\right) = \int_{-2\pi}^{+2\pi} \left(\sum_{h=1}^{2} \varphi_{z;3}^{(h)} A_{3}^{\mathbf{i},(h)} e^{+\frac{\sqrt{3}}{2} \mathbf{i} \kappa_{z}^{(h)} \mathbf{n}} \right) e^{-\frac{1}{2} \mathbf{i} \kappa_{x} \mathbf{m}} d\kappa_{x}$$

$$(4.69)$$

Here, the expressions for $\varphi_{x;3}^{(h)}$ and $\varphi_{z;3}^{(h)}$, with h=1,2, follow from the shape of the considered cross-section, and thus on the cell configuration of the involved sub-particle.

For the particular case that the particle \mathbf{m} , \mathbf{n} is located exactly at the interface of subsystems I and II, so that $\mathbf{n} = \mathbf{n_i}$, and the interface Γ along which the reaction forces are to be obtained is not horizontal and therefore does not coincide with the interface between the subsystems, the cells of the involved sub-particles consist of degrees of freedom that belong to both subsystems I and II. As an example of this, consider the particle located at the inclined part of the interface Γ depicted in Figure 4.14b for the case that $\mathbf{n} = \mathbf{n_i}$. The reaction forces for this particle are then obtained by substituting equations (4.62) and (4.63) into the equation of motion of particle \mathbf{m} , \mathbf{n} for the degrees of freedom that belong to subsystem I, while substituting equations (4.64) to (4.65) for the degrees of freedom that belong to subsystem II.

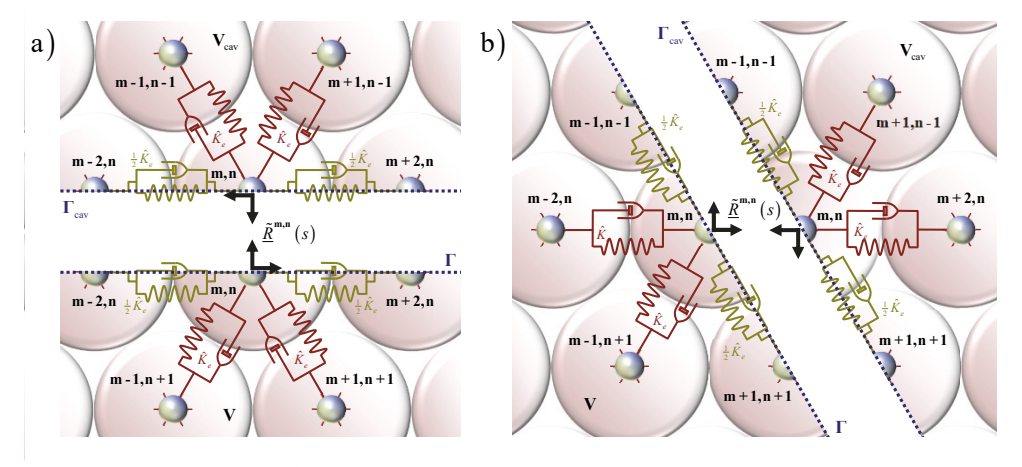


Figure 4.14: Reaction forces at a particle **m,n** located at the interface between the cavity system **V**_{cav} and the discrete particle system **V**: a) horizontal interface b) inclined interface.

This yields the general expressions for the corresponding horizontal and vertical reaction forces as:

$$\tilde{R}_{x,l\cup ll}^{\mathbf{m},\mathbf{n}}\left(s\right) = \int_{-2\pi}^{+2\pi} \left(\sum_{h=1}^{2} \left(\varphi_{x;1}^{(h)} A_{1}^{\mathbf{i},(h)} + \varphi_{x;3}^{(h)} A_{3}^{\mathbf{i},(h)}\right) e^{+\frac{\sqrt{5}}{2} \mathrm{i} \kappa_{z}^{(h)} \mathbf{n}} + \sum_{h=1}^{2} \varphi_{x;2}^{(h)} A_{2}^{\mathbf{i},(h)} e^{-\frac{\sqrt{5}}{2} \mathrm{i} \kappa_{z}^{(h)} \mathbf{n}}\right) e^{-\frac{1}{2} \mathrm{i} \kappa_{x} \mathbf{m}} d\kappa_{x}$$
(4.70)

$$\tilde{R}_{z,l\cup II}^{\mathbf{m,n}}\left(s\right) = \int_{-2\pi}^{+2\pi} \left(\sum_{h=1}^{2} \left(\varphi_{z;l}^{(h)} A_{1}^{\mathbf{i},(h)} + \varphi_{z;3}^{(h)} A_{3}^{\mathbf{i},(h)}\right) e^{+\frac{\sqrt{5}}{2} \mathrm{i} \kappa_{z}^{(h)} \mathbf{n}} + \sum_{h=1}^{2} \varphi_{z;2}^{(h)} A_{2}^{\mathbf{i},(h)} e^{-\frac{\sqrt{5}}{2} \mathrm{i} \kappa_{z}^{(h)} \mathbf{n}}\right) e^{-\frac{1}{2} \mathrm{i} \kappa_{x} \mathbf{m}} d\kappa_{x}$$
(4.71)

Here, note that for a particle \mathbf{m} , \mathbf{n} at the level of the loaded particle \mathbf{i} , i.e. for $\mathbf{n} = \mathbf{n}_i$, which is thus located at the interface between subsystems I and II, and we consider the reaction forces along the horizontal segment of the interface Γ as depicted in Figure 4.14a, all degrees of freedom of the upper half-particle are part of subsystem I, while all degrees of freedom of the lower half-particle belong to subsystem II. Then, for a particle \mathbf{m} , \mathbf{n} which is not the loaded particle \mathbf{i} , i.e. for $\mathbf{m} \neq \mathbf{m}_i$, the reaction forces according to equations (4.66) and (4.67), that are thus valid for the upper half-particle, are equal but opposite to the reaction forces according to equations (4.68) and (4.69), which are then the valid reaction forces for the lower half-particle. This however does not hold for the loaded particle itself, because in that case the applied load must also be accounted for.

Here, note that the general expressions for the corresponding Green's reaction forces are derived in Section 4.4.4, while the specific expressions for all particle configurations that exist along the interface Γ are derived in Appendix F.

4.4.2 Boundary conditions for the half-plane of particles

The expressions for the wave amplitudes $A_1^{\mathbf{i},(h)}$, $A_2^{\mathbf{i},(h)}$ and $A_3^{\mathbf{i},(h)}$ that correspond to the wavenumbers $\kappa_z^{(h)}$ for h=1,2, follow from the boundary conditions for the half-plane of particles with a load applied at a particle \mathbf{i} in the interior of the half-plane of particles.

At the surface of the half-plane of particles there cannot exist any forces, unless there is a load applied to that surface. Thus, when we consider a single load applied at a particle inside the half-plane, the surface of the half-plane is free of reaction forces and the corresponding boundary conditions in the Laplace domain read:

$$\tilde{R}_{x,I}^{\mathbf{m},0}(s) = \tilde{R}_{z,I}^{\mathbf{m},0}(s) = 0$$
 (4.72)

Here, the expressions for the horizontal and vertical reaction forces are respectively found in accordance with equations (4.66) and (4.67), and coincide with the horizontal and vertical equations of motion for a surface particle.

The four remaining boundary conditions are found at the interface between the two subsystems, i.e. at the horizontal level of the loaded particle **i**. To describe these boundary conditions, we split all particles with the vertical nodal coordinate $\mathbf{n} = \mathbf{n_i}$ into two equal-sized half-particles, in accordance with Figure 4.14. Evidently, the displacements of the upper half-particle, which is part of subsystem I, and the lower half-particle, belonging to subsystem II,

must be the same, thus providing us with the following boundary conditions:

$$\tilde{u}_{x,II}^{\mathbf{m},\mathbf{n}_{i}}(s) - \tilde{u}_{x,I}^{\mathbf{m},\mathbf{n}_{i}}(s) = 0 \tag{4.73}$$

$$\tilde{u}_{z,I}^{\mathbf{m},\mathbf{n}_{i}}(s) - \tilde{u}_{z,I}^{\mathbf{m},\mathbf{n}_{i}}(s) = 0 \tag{4.74}$$

Finally, accounting for the point load \underline{P}^{i} at particle **i**, the equilibrium of forces between the upper and lower half-particles with vertical nodal coordinate $\mathbf{n} = \mathbf{n}_{i}$ along the interface of subsystems I and II, yields the following boundary conditions:

$$\tilde{R}_{x,II}^{\mathbf{m},\mathbf{n}_{i}}\left(s\right) - \tilde{R}_{x,I}^{\mathbf{m},\mathbf{n}_{i}}\left(s\right) = P_{x}\delta_{\mathbf{m}_{i}\mathbf{m}} \tag{4.75}$$

$$\tilde{R}_{z,II}^{\mathbf{m},\mathbf{n}_{i}}\left(s\right) - \tilde{R}_{z,I}^{\mathbf{m},\mathbf{n}_{i}}\left(s\right) = P_{z}\delta_{\mathbf{m}_{i}\mathbf{m}} \tag{4.76}$$

Here, P_x and P_z are respectively the horizontal and vertical components of the point load applied at particle \mathbf{i} , and $\delta_{\mathbf{m}_i\mathbf{m}}$ denotes the Kronecker Delta.

Substituting equations (4.66) to (4.69) for the reaction forces in equations (4.72), (4.75) and (4.76), as well as substituting equations (4.62) to (4.65) for the displacements into equations (4.73) and (4.74) yields the system of six algebraic equations that is solved to obtain the unknown wave amplitudes $A_1^{i,(h)}$, $A_2^{i,(h)}$ and $A_3^{i,(h)}$ for h = 1...2. The expressions for the boundary conditions (4.72) to (4.76) in terms of the unknowns $A_1^{i,(h)}$ to $A_3^{i,(h)}$ are derived in Appendix G.1.

For the particular case that particle **i** is located at the surface of the half-plane of particles, the half-plane exclusively consists of subsystem II, yielding a system of only two algebraic equations, that respectively follow from the horizontal and vertical equilibrium of forces at the half-plane surface particles. The corresponding boundary conditions in terms of the unknowns $A_3^{i,(h)}$ for h = 1..2 are derived and given in Appendix G.2.

4.4.3 Green's displacements in the half-plane of particles

The relation between the displacements of a particle \mathbf{j} along the interface Γ due to a two-dimensional load $\underline{P}^{\mathbf{i}}$ at particle \mathbf{i} and the corresponding Green's displacements, previously given by equation (4.35), may be expressed in full matrix notation as:

$$\begin{bmatrix} \tilde{u}_{P,x}^{\mathbf{j},\mathbf{i}}(s) \\ \tilde{u}_{P,z}^{\mathbf{j},\mathbf{i}}(s) \end{bmatrix} = \begin{bmatrix} \tilde{g}_{u,xx}^{\mathbf{j},\mathbf{i}}(s) & \tilde{g}_{u,xz}^{\mathbf{j},\mathbf{i}}(s) \\ \tilde{g}_{y,z}^{\mathbf{j},\mathbf{i}}(s) & \tilde{g}_{u,zz}^{\mathbf{j},\mathbf{i}}(s) \end{bmatrix} \begin{bmatrix} P_{x}^{\mathbf{i}} \\ P_{z}^{\mathbf{i}} \end{bmatrix}$$

$$(4.77)$$

Here, for example $\tilde{g}_{u,xz}^{j,i}(s)$ denotes the horizontal Green's displacement of particle \mathbf{j} along the interface Γ due to a vertical load applied at particle \mathbf{i} along the interface Γ . The other Green's displacements are defined accordingly. Note here that the considered particles are denoted as particles \mathbf{i} and \mathbf{j} along the interface Γ rather than as a particle \mathbf{m} , \mathbf{n} inside the halfplane of particles, because the indices \mathbf{i} and \mathbf{j} together determine the position of the corresponding Green's displacements in the global Green's displacement matrix $\tilde{g}_u(s)$.

Within a discrete particle system, such as the half-plane of particles, a Green's displacement can be straightforwardly defined as the displacement due to a unit point load. For example, if we choose $P_x^i = 1$ and $P_z^i = 0$ in equation (4.77), the Green's displacements $\tilde{g}_{u,xx}^{j,i}(s)$ and $\tilde{g}_{u,zx}^{j,i}(s)$ are equal to the displacements $\tilde{u}_{P,x}^{j,i}(s)$ and $\tilde{u}_{P,z}^{j,i}(s)$. This coincides with the Laplace domain displacements, previously given by equations (4.62) to (4.65), that are obtained by solving the corresponding system of boundary conditions for the case that $P_x = 1$ and $P_z = 0$. Accordingly, if we choose $P_x^i = 0$ and $P_z^i = 1$, the Green's displacements $\tilde{g}_{u,xz}^{j,i}(s)$ and $\tilde{g}_{u,zz}^{j,i}(s)$ are equal to the displacements $\tilde{u}_{P,x}^{j,i}(s)$ and $\tilde{u}_{P,z}^{j,i}(s)$, which coincides with the Laplace domain displacements that are obtained by solving the corresponding system of boundary conditions for $P_x = 0$ and $P_z = 1$.

Let us denote the wave amplitudes resulting from solving the system of boundary conditions for a horizontally applied unit load, i.e. for $P_x = 1$ and $P_z = 0$, as $A_{x;1}^{\mathbf{i},(h)}$ to $A_{x;3}^{\mathbf{i},(h)}$, and accordingly, let us denote the wave amplitudes resulting from solving the system of boundary conditions for a vertical unit load, i.e. for $P_x^{\mathbf{i}} = 0$ and $P_z^{\mathbf{i}} = 1$, as $A_{z;1}^{\mathbf{i},(h)}$ to $A_{z;3}^{\mathbf{i},(h)}$. The Green's displacements for a particle \mathbf{j} in subsystem I, due to unit loads applied at a particle \mathbf{i} , are then respectively found as:

$$\tilde{g}_{u,xx,I}^{\mathbf{j},\mathbf{i}}(s) = \int_{-2\pi}^{+2\pi} \left(\sum_{h=1}^{2} A_{x;1}^{\mathbf{i},(h)} e^{+\frac{\sqrt{5}}{2} i \kappa_{2}^{(h)} \mathbf{n}_{\mathbf{j}}} + \sum_{h=1}^{2} A_{x;2}^{\mathbf{i},(h)} e^{-\frac{\sqrt{5}}{2} i \kappa_{2}^{(h)} \mathbf{n}_{\mathbf{j}}} \right) e^{-\frac{1}{2} i \kappa_{x} \mathbf{m}_{\mathbf{j}}} d\kappa_{x}$$

$$(4.78)$$

$$\tilde{\mathbf{g}}_{u,x,x,l}^{\mathbf{j},\mathbf{i}}\left(s\right) = \int_{-2\pi}^{+2\pi} \left(\sum_{h=1}^{2} D^{(h)} A_{x;1}^{\mathbf{i},(h)} e^{+\frac{\sqrt{5}}{2} \mathrm{i} \kappa_{z}^{(h)} \mathbf{n}_{\mathbf{j}}} - \sum_{h=1}^{2} D^{(h)} A_{x;2}^{\mathbf{i},(h)} e^{-\frac{\sqrt{5}}{2} \mathrm{i} \kappa_{z}^{(h)} \mathbf{n}_{\mathbf{j}}}\right) e^{-\frac{1}{2} \mathrm{i} \kappa_{x} \mathbf{m}_{\mathbf{j}}} d\kappa_{x}$$

$$(4.79)$$

$$\tilde{g}_{u,xz,I}^{\mathbf{j},\mathbf{i}}\left(s\right) = \int_{-2\pi}^{+2\pi} \left(\sum_{h=1}^{2} A_{z;1}^{\mathbf{i},(h)} e^{+\frac{\sqrt{5}}{2} \mathbf{i} \kappa_{z}^{(h)} \mathbf{n}_{\mathbf{j}}} + \sum_{h=1}^{2} A_{z;2}^{\mathbf{i},(h)} e^{-\frac{\sqrt{5}}{2} \mathbf{i} \kappa_{z}^{(h)} \mathbf{n}_{\mathbf{j}}}\right) e^{-\frac{1}{2} \mathbf{i} \kappa_{x} \mathbf{m}_{\mathbf{j}}} d\kappa_{x}$$

$$(4.80)$$

$$\tilde{\mathbf{g}}_{u,zz,I}^{\mathbf{j},\mathbf{i}}\left(s\right) = \int_{-2\pi}^{+2\pi} \left(\sum_{h=1}^{2} D^{(h)} A_{z;1}^{\mathbf{i},(h)} e^{+\frac{\sqrt{2}}{2} i \kappa_{z}^{(h)} \mathbf{n}_{\mathbf{j}}} - \sum_{h=1}^{2} D^{(h)} A_{z;2}^{\mathbf{i},(h)} e^{-\frac{\sqrt{2}}{2} i \kappa_{z}^{(h)} \mathbf{n}_{\mathbf{j}}}\right) e^{-\frac{1}{2} i \kappa_{x} \mathbf{m}_{\mathbf{j}}} d\kappa_{x}$$

$$(4.81)$$

Here, m_j and n_j are respectively the horizontal and vertical nodal coordinates of particle j along the interface Γ .

Furthermore, the Green's displacements for a particle \mathbf{j} located in subsystem II, due to respectively a horizontal and vertical unit load applied at a particle \mathbf{i} , respectively become:

$$\tilde{\mathbf{g}}_{u,xx,H}^{\mathbf{j},\mathbf{i}}\left(s\right) = \int_{-2\pi}^{+2\pi} \left(\sum_{h=1}^{2} A_{x,3}^{\mathbf{i},(h)} e^{+\frac{\sqrt{5}}{2} \mathbf{i} \kappa_{z}^{(h)} \mathbf{n}_{\mathbf{j}}}\right) e^{-\frac{1}{2} \mathbf{i} \kappa_{x} \mathbf{m}_{\mathbf{j}}} d\kappa_{x}$$

$$(4.82)$$

$$\tilde{\mathbf{g}}_{u,zx,H}^{\mathbf{j},\mathbf{i}}\left(s\right) = \int_{-2\pi}^{+2\pi} \left(\sum_{h=1}^{2} D^{(h)} A_{x;3}^{\mathbf{i},(h)} e^{+\frac{\sqrt{5}}{2} \mathbf{i} \kappa_{z}^{(h)} \mathbf{n}_{\mathbf{j}}}\right) e^{-\frac{1}{2} \mathbf{i} \kappa_{x} \mathbf{m}_{\mathbf{j}}} d\kappa_{x}$$

$$(4.83)$$

$$\tilde{g}_{u,xz,II}^{\mathbf{j},\mathbf{i}}\left(s\right) = \int_{-2\pi}^{+2\pi} \left(\sum_{h=1}^{2} A_{z;3}^{\mathbf{i},(h)} e^{+\frac{\sqrt{5}}{2}i\kappa_{z}^{(h)}\mathbf{n}_{\mathbf{j}}}\right) e^{-\frac{1}{2}i\kappa_{x}\mathbf{m}_{\mathbf{j}}} d\kappa_{x}$$

$$(4.84)$$

$$\tilde{g}_{u,zz,II}^{j,i}\left(s\right) = \int_{-2\pi}^{+2\pi} \left(\sum_{h=1}^{2} D^{(h)} A_{z;3}^{i,(h)} e^{+\frac{\sqrt{5}}{2} i \kappa_{z}^{(h)} \mathbf{n}_{j}}\right) e^{-\frac{1}{2} i \kappa_{x} \mathbf{m}_{j}} d\kappa_{x}$$

$$(4.85)$$

For the particular case that particle i is located at the surface of the half-plane of particles, the Green's displacements for a particle j are exclusively described by equations (4.82) to (4.85).

4.4.4 Green's reaction forces in the half-plane of particles

The reaction forces at a particle \mathbf{j} along the boundary Γ of the far-field system \mathbf{V} due to a two-dimensional point load $\underline{P}^{\mathbf{i}}$ applied at a particle \mathbf{i} were previously expressed in terms of the corresponding Green's reaction forces by equation (4.36). In full matrix notation, this relation reads:

$$\begin{bmatrix} \tilde{R}_{P,x}^{\mathbf{j},\mathbf{i}}(s) \\ \tilde{R}_{P,z}^{\mathbf{j},\mathbf{i}}(s) \end{bmatrix} = \begin{bmatrix} \tilde{g}_{R,xx}^{\mathbf{j},\mathbf{i}}(s) & \tilde{g}_{R,xz}^{\mathbf{j},\mathbf{i}}(s) \\ \tilde{g}_{R,zx}^{\mathbf{j},\mathbf{i}}(s) & \tilde{g}_{R,zz}^{\mathbf{j},\mathbf{i}}(s) \end{bmatrix} \begin{bmatrix} P_x^{\mathbf{i}} \\ P_z^{\mathbf{i}} \end{bmatrix}$$

$$(4.86)$$

Here, the location of the particles **i** and **j** along the boundary Γ determine the position of the corresponding Green's reaction force in the global Green's reaction force matrix $\tilde{g}_R(s)$.

In accordance with the Green's displacements, and as testified by equation $\overline{(4.86)}$, the Green's reaction forces can be described in the form of equations (4.66) to (4.71), and are due to either a horizontal or a vertical unit point load. Thus, the Green's reaction forces $\tilde{g}_{R,xx}^{j,i}(s)$ and $\tilde{g}_{R,xx}^{j,i}(s)$ are the Laplace domain reaction forces at particle **j** along the boundary Γ obtained by solving the corresponding system of boundary conditions for $P_x = 1$ and $P_z = 0$. Furthermore, the Green's reaction forces $\tilde{g}_{R,xz}^{j,i}(s)$ and $\tilde{g}_{R,zz}^{j,i}(s)$ are the Laplace domain reaction forces at particle **j** along the boundary Γ that follow from the system of boundary conditions for the case that $P_x^i = 0$ and $P_z^i = 1$.

Noting that the wave amplitudes due to respectively a horizontal and a vertical unit load at a particle **i** along the interface Γ are respectively described as $A_{x,r}^{\mathbf{i},(h)}$ and $A_{z,r}^{\mathbf{i},(h)}$ for r=1...3, depending on whether particle **j** exists in subsystem I or II, the Green's reaction forces at a particle **j** along the interface Γ , with nodal coordinates $\mathbf{m_{i}}, \mathbf{n_{i}}$, may generally be expressed as:

$$\tilde{g}_{R,xx}^{j,i}\left(s\right) = \int_{-2\pi}^{+2\pi} \left(\sum_{r}\sum_{h=1}^{1,3} \varphi_{x;r}^{(h)} A_{x;r}^{i,(h)} e^{+\frac{\sqrt{5}}{2}i\kappa_{z}^{(h)}\mathbf{n}_{j}} + \sum_{h=1}^{2} \varphi_{x;2}^{(h)} A_{x;2}^{i,(h)} e^{-\frac{\sqrt{5}}{2}i\kappa_{z}^{(h)}\mathbf{n}_{j}}\right) e^{-\frac{1}{2}i\kappa_{x}\mathbf{m}_{j}} d\kappa_{x}$$

$$(4.87)$$

$$\tilde{g}_{R,zx}^{j,i}\left(s\right) = \int_{-2\pi}^{+2\pi} \left(\sum_{r}\sum_{h=1}^{1,3} \varphi_{z;r}^{(h)} A_{x;r}^{i,(h)} e^{+\frac{\sqrt{5}}{2}i\kappa_{z}^{(h)}\mathbf{n}_{j}} + \sum_{h=1}^{2} \varphi_{z;2}^{(h)} A_{x;2}^{i,(h)} e^{-\frac{\sqrt{5}}{2}i\kappa_{z}^{(h)}\mathbf{n}_{j}}\right) e^{-\frac{1}{2}i\kappa_{x}\mathbf{m}_{j}} d\kappa_{x}$$

$$(4.88)$$

$$\tilde{g}_{R,xz}^{j,i}\left(s\right) = \int_{-2\pi}^{+2\pi} \left(\sum_{r}^{1,3} \sum_{h=1}^{2} \varphi_{x;r}^{(h)} A_{z;r}^{i,(h)} e^{+\frac{\sqrt{5}}{2} i \kappa_{z}^{(h)} \mathbf{n}_{j}} + \sum_{h=1}^{2} \varphi_{x;2}^{(h)} A_{z;2}^{i,(h)} e^{-\frac{\sqrt{5}}{2} i \kappa_{z}^{(h)} \mathbf{n}_{j}} \right) e^{-\frac{1}{2} i \kappa_{x} \mathbf{m}_{j}} d\kappa_{x}$$

$$(4.89)$$

$$\tilde{g}_{R,zz}^{j,i}\left(s\right) = \int_{-2\pi}^{+2\pi} \left(\sum_{r}^{1,3} \sum_{h=1}^{2} \varphi_{z;r}^{(h)} A_{z;r}^{i,(h)} e^{+\frac{\sqrt{5}}{2}i\kappa_{z}^{(h)}\mathbf{n}_{j}} + \sum_{h=1}^{2} \varphi_{z;2}^{(h)} A_{z;2}^{i,(h)} e^{-\frac{\sqrt{5}}{2}i\kappa_{z}^{(h)}\mathbf{n}_{j}}\right) e^{-\frac{1}{2}i\kappa_{x}\mathbf{m}_{j}} d\kappa_{x}$$

$$(4.90)$$

Here, the expressions for $\varphi_{x;r}^{(h)}$ and $\varphi_{z;r}^{(h)}$, with r = 1..3 and h = 1..2, depend on the shape of boundary Γ of the far-field system \mathbf{V} and on the location of the particle \mathbf{j} at which the Green's reaction forces are considered compared to the location of the loaded particle \mathbf{i} . Here,

furthermore note that the summation over r in equations (4.87) to (4.90) is only applied for r = 1 and r = 3 because they have the same exponents with respect to $\kappa_z^{(h)}$.

As depicted by Figure 4.15, seven different cell configurations exist along the boundary Γ of the discrete particle system V. The resulting expressions for $\varphi_{x;r}^{(h)}$ and $\varphi_{z;r}^{(h)}$ are derived for the seven cell configurations along the interface Γ in respectively Appendices G.3 to G.9.

4.5 An equivalent 1D-response of the half-plane of particles

To verify that the expressions for the displacements and reaction forces of the viscoelastic half-plane of particles are obtained and implemented correctly, we here consider the response of the half-plane of particles to an infinite uniform line-load at its surface and compare it to the response of the semi-infinite viscoelastic cascade. This comparison is valid, because the application of an infinitely-long uniformly-distributed vertical load yields an exclusive vertical response. Ergo, there will be no horizontal response, while the vertical response of the half-plane is the same at any point along the horizontal. That is, if the material properties of the one- and two-dimensional models are properly matched.

In the following, we first obtain the governing equations for the half-plane of particles subjected to an infinitely-long uniformly-distributed load in terms of its Green's functions in Section 4.5.1 and subsequently, in Section 4.5.2, we discuss the matching parameters for the equivalent one- and two-dimensional models. Before comparing the responses of the equivalent one- and two-dimensional models in Section 4.5.5, we will shortly discuss how the Green's displacements and the Green's reaction forces in the semi-infinite viscoelastic cascade follow from the dynamic stiffness relation at its surface in respectively Sections 4.5.3 and 4.5.4.

4.5.1 Governing equations for an infinitely-long uniform load

A two-dimensional solid medium behaves as a one-dimensional solid medium if any occurring waves exclusively propagate in either one of the principal directions and its amplitude is uniform. This means that in one principal direction, the wavenumber is equal to zero, while it is nonzero in the other principal direction. In this case, we aim to compare the response of the half-plane of particles to that of the one-dimensional cascade for a case where both particle systems have the same response. As the one-dimensional cascade can only transmit

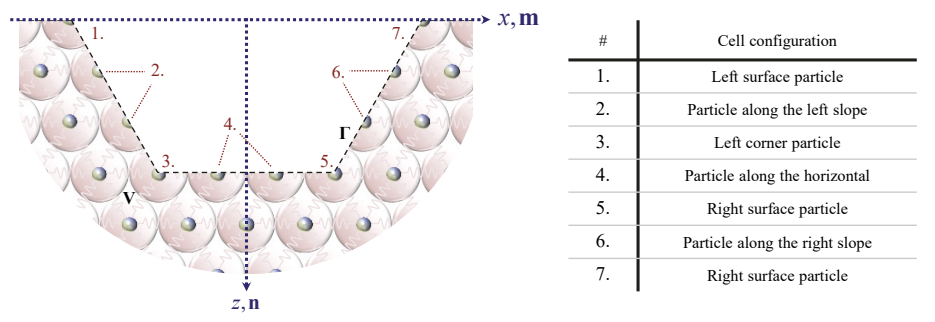


Figure 4.15: The seven different cell configurations for the sub-particles along the boundary Γ .

waves in the longitudinal direction, this means that for the half-plane of particles we must exclusively consider the propagation of compressional waves. Choosing the longitudinal direction for the cascade to coincide with the z-direction in the two-dimensional model, the half-plane of particles will behave in accordance with the one-dimensional cascade when it is subjected to a distributed vertical load that is uniform along its surface. Figure 4.16a and Figure 4.16b respectively show an infinitely-long uniformly-distributed vertical line-load applied to a semi-infinite two-dimensional body V and the corresponding load case for the half-plane of particles, which consists of vertical point loads applied at every single particle at the half-plane surface.

For both load cases depicted in Figure 4.16, there will be no wave propagation in x-direction and the horizontal wavenumber in both systems must be equal to zero. The fact that a zero horizontal wavenumber coincides with the application of the same load at every single surface particle also follows from the integral identity for the Kronecker Delta, given by equation (4.52), which shows that for $\kappa_x = 0$ the Kronecker delta will always be equal to one, independent of the value of the particle coordinate \mathbf{m} . Note here that the direction of wave propagation is independent of the direction of the uniform load; for example applying a uniform dynamic horizontal load at all surface particles yields a shear wave that propagates in z-direction, so that even though all particles will move horizontally, there will be no wave propagation in x-direction.

The one-dimensional response of the viscoelastic half-plane of particles to a uniform load at its surface and the similarity of its behaviour to that of the viscoelastic cascade also becomes evident from considering its dispersion relation. Appendix H.1 regards the dispersion in the half-plane of particles and shows that if we substitute $\kappa_x = 0$ into the expression for the vertical wavenumber, previously given by equation (4.57), we find the following dispersion relations for the one-dimensional vertical response of the half-plane of particles:

$$\cos\frac{\kappa_{z,1}\sqrt{3}}{2} = 1 + \frac{3s^2}{1 + 2\zeta s}, \qquad \cos\frac{\kappa_{z,2}\sqrt{3}}{2} = 1 + \frac{s^2}{1 + 2\zeta s}.$$
 (4.91)

Here, note that the first relation in equation (4.91) describes the dispersion in the half-plane of particles related to the propagation of shear waves in z-direction, while the second relation

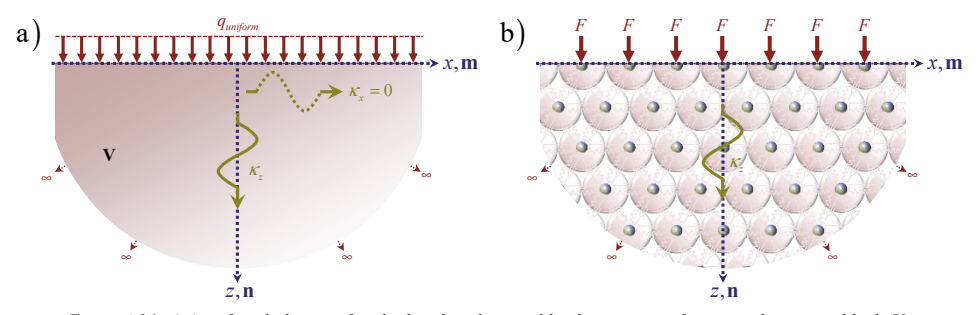


Figure 4.16: a) An infinitely-long uniformly-distributed vertical load on a semi-infinite two-dimensional body V; b) Corresponding uniform vertical load on the half-plane of particles.

in equation (4.91) describes the dispersion in the half-plane of particles related to the propagation of compressional waves in z-direction. The wave types for these dispersion relations can be established by considering that an infinitely-long uniformly-distributed vertical load at the surface of the half-plane of particles yields the propagation of a horizontally uniform compressional wave in z-direction, so that shear waves do not occur. Then, noting that the rheological elements incorporated in the viscoelastic cascade exclusively allow for the propagation of compressional waves in the longitudinal direction, it follows that, when the halfplane of particles is subjected to a uniformly-distributed vertical load at its surface, its dispersive properties must match those of the one-dimensional cascade. Finally, given that the vertical particle spacing in the half-plane is equal to $\frac{1}{2}\sqrt{3}\ell$, while the particle spacing in the cascade is equal to ℓ , it follows that the dispersion relation for the compressional waves in the half-plane, given by the second relation in equation (4.91), matches the dispersion relation for the viscoelastic cascade given by equation (4.14), so that the second dispersion relation in equation (4.91) must be related to the propagation of compressional waves. In the following, we will elaborate on the response of the half-plane of particles subjected to a uniform vertical load at its surface.

The expression for the vertical displacement of any particle in the half-plane due to a load applied at its surface only has to account for waves travelling in positive z-direction. Accounting for the proper behaviour of the half-plane at $z \to \infty$, the vertical displacement of any particle \mathbf{m} , \mathbf{n} in the half-plane of particles due to a vertical load applied at a surface particle \mathbf{i} , with nodal coordinates $\mathbf{m}_{\mathbf{i}}$, $\mathbf{n}_{\mathbf{i}}$, may be obtained using equation (4.65). In the half-plane of particles subjected to a uniform vertical load at its surface, the particle \mathbf{m} , \mathbf{n} will not respond to a load at a single particle, but to the loads applied at all surface particles. The response of particle \mathbf{m} , \mathbf{n} to the uniform vertical load at the half-plane surface may therefore be obtained by summation of its responses due to the vertical loads applied at all surface particles separately. This yields the general expression for the vertical Laplace domain displacement of any particle \mathbf{m} , \mathbf{n} in the half-plane of particles due to the uniform vertical load at its surface as:

$$\tilde{u}_{z}^{\mathbf{m},\mathbf{n}}(s) = \sum_{\mathbf{i}=-\infty}^{+\infty} \int_{-2\pi}^{+2\pi} \left(\sum_{h=1}^{2} D^{(h)} A_{z}^{\mathbf{i},(h)} e^{+\frac{\sqrt{5}}{2} i \kappa_{z}^{(h)} \mathbf{n}} \right) e^{-\frac{1}{2} i \kappa_{x} \mathbf{m}} d\kappa_{x}$$

$$(4.92)$$

Here, $A_z^{\mathbf{i},(h)}$ denotes the wave amplitude due to the vertical point load applied at the surface particle \mathbf{i} with nodal coordinates $\mathbf{m}_{\mathbf{i}}$,0.

Since the application of a uniform vertical load at the surface of the half-plane of particles yields a uniform response of the half-plane in horizontal direction, each horizontal level of **n** will move in unison and all particles with nodal coordinate **n** will have the same vertical response. To describe the response of the half-plane of particles to the uniform surface load, we therefore only need to consider the displacements at a single location of every horizontal level **n**. Therefore, let us now consider the vertical displacements of the particles in the half-plane that exist along the *z*-axis, i.e. any particles with nodal coordinates **0**,**n**. If we denote the Laplace domain displacement of the particles at the *z*-axis due to a load applied at a

surface particle **i** as $\tilde{u}_z^{0,n} \{F^{m_i,0}\}(s)$, we can alternatively write equation (4.92) for any particle with nodal coordinates **0.n** as:

$$\tilde{u}_z^{0,n}\left(s\right) = \sum_{i=-\infty}^{+\infty} \tilde{u}_z^{0,n} \left\{ F^{m_i,0} \right\} \left(s\right) \tag{4.93}$$

Let us consider the particle displacements and applied vertical loads at the surface of the halfplane of particles depicted in Figure 4.17. For the case that the depicted segment of the halfplane of particles is homogeneous, the vertical response of the particle 0,n to the vertical load applied at particle $m_{i},0$ must at any time be exactly equal to the vertical response of particle m_{i},n to the vertical load applied at particle 0,0. That is, if, and only if, the vertical loads applied at particles 0,0 and $m_{i},0$ are equal, which is the case for the uniform vertical load applied at the surface of the half-plane of particles. Thus, we can denote this particular relationship as:

$$\tilde{u}_{z}^{0,n} \left\{ F^{m_{i},0} \right\} (s) = \tilde{u}_{z}^{m_{i},n} \left\{ F^{0,0} \right\} (s) \tag{4.94}$$

Substituting this relation into equation (4.93), then yields the expression for the total vertical Laplace domain displacement of the particle 0,n due to the uniform vertical load as:

$$\tilde{u}_z^{0,\mathbf{n}}(s) = \sum_{i=-\infty}^{+\infty} \tilde{u}_z^{\mathbf{m}_i,\mathbf{n}} \left\{ F^{0,0} \right\} (s) \tag{4.95}$$

Equation (4.95) shows that the vertical response of the particle 0,n to the uniform vertical surface load, i.e. the same vertical load applied at all surface particles, may be obtained as the summation of the vertical responses of all particles at the horizontal level with nodal coordinate n to a single vertical point load applied at particle 0,0, where the magnitude of the point load at particle 0,0 must coincide with the magnitude of the uniform vertical surface load.

Applying the above relations to the general expression for any particle \mathbf{m} , \mathbf{n} in the halfplane of particles, previously given by equation (4.92), the vertical Laplace domain displacement for any particle $\mathbf{0}$, \mathbf{n} at the z-axis and thus for any horizontal level with nodal coordinate \mathbf{n} reads:

$$\tilde{u}_{z}^{0,\mathbf{n}}\left(s\right) = \sum_{i=-\infty}^{+\infty} \int_{-2\pi}^{+2\pi} \left(\sum_{h=1}^{2} D^{(h)} A_{z}^{0,(h)} e^{+\frac{\sqrt{5}}{2}i\kappa_{z}^{(h)}\mathbf{n}} \right) e^{-\frac{1}{2}i\kappa_{x}\mathbf{m}_{i}} d\kappa_{x}$$

$$(4.96)$$

Note here that, although there will be no propagation of waves in horizontal direction in the half-plane of particles subjected to a uniform horizontal load, the response of the half-plane of particles to a single point load applied at the surface particle located at the z-axis will include horizontal wave propagation and the corresponding horizontal wavenumber κ_x is not

equal to zero. In other words, the separate horizontal response of any particle that is not located exactly at the z-axis does have a horizontal displacement. In equation (4.96), the influence of this horizontal response is cancelled out, because the horizontal response to a single point load at the surface particle 0,0 is exactly symmetric with respect to the z-axis. Figure 4.18 shows this symmetry of the horizontal and the vertical displacements in the half-plane of particles due to the single vertical point load applied at particle 0,0. Thus, as long as the response of all particles at the level of the nodal coordinate \mathbf{n} are accounted for symmetrically with respect to the z-axis, i.e. considering an equal number of particles left and right of the z-axis, the resulting response of the considered level of \mathbf{n} will be exclusively vertical. This holds for both even and odd levels of the nodal coordinate \mathbf{n} . Consequently, equation (4.96) correctly describes the uniform vertical response of the half-plane of particles for both even and odd levels of the nodal coordinate \mathbf{n} .

For numerical applications, using equation (4.96) is much more convenient than using equation (4.92). Namely, to obtain the equivalent one-dimensional response of the half-plane according to equation (4.92), we need to first obtain the response of the half-plane of particles to every surface load separately and then apply the summation, while applying equation (4.92) only requires us to consider the response of the half-plane of particles to a single point load and sum the displacements of the particles per horizontal level of the coordinate **n**.

Evidently, for numerical implementation, it is not possible to take the displacements of an infinite number of particles into account. However, the contribution of the response of any particle to the total result of the summation declines rapidly as the distance with the loaded particle increases. Therefore, the number of particles that must be included per horizontal level of the nodal coordinate **n** must be chosen such that the contribution of additional particles is negligible. Practically, this can be done by introducing a certain threshold or simply by trial and error.

Due to the symmetric response of the half-plane of particles subjected to a single point load at the particle 0.0 with respect to the z-axis, the vertical displacements of any two particles that are at an equal distance left and right of the z-axis are exactly the same. Introducing the number of particles that are considered on either side of the z-axis as i_{max} , we obtain the uniform vertical Laplace domain displacement respectively for even and odd levels of the

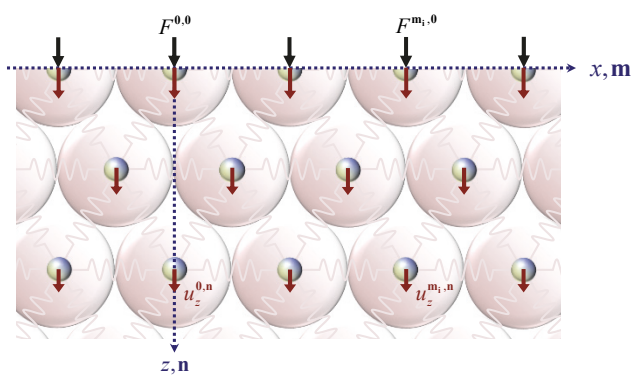


Figure 4.17: Vertical displacements in the half-plane of particles due to the applied vertical surface loads.

nodal coordinate n as:

$$\tilde{u}_{z}^{\mathbf{0},\mathbf{n}_{even}}\left(s\right) = \int_{-2\pi}^{+2\pi} \left(\sum_{h=1}^{2} D^{(h)} A_{z}^{\mathbf{0},(h)} e^{+\frac{\sqrt{5}}{2} i \kappa_{z}^{(h)} \mathbf{n}}\right) d\kappa_{x} + 2 \sum_{i=1}^{i_{\max}} \int_{-2\pi}^{+2\pi} \left(\sum_{h=1}^{2} D^{(h)} A_{z}^{\mathbf{0},(h)} e^{+\frac{\sqrt{5}}{2} i \kappa_{z}^{(h)} \mathbf{n}}\right) e^{-\frac{1}{2} i \kappa_{x} \mathbf{m}_{i}} d\kappa_{x}$$
(4.97)

$$\tilde{u}_{z}^{0,\mathbf{n}_{odd}}\left(s\right) = 2\sum_{i=1}^{i_{\max}} \int_{-2\pi}^{+2\pi} \left(\sum_{h=1}^{2} D^{(h)} A_{z}^{0,(h)} e^{+\frac{\sqrt{5}}{2}i\kappa_{z}^{(h)}\mathbf{n}}\right) e^{-\frac{1}{2}i\kappa_{x}\mathbf{m}_{i}} d\kappa_{x}$$

$$(4.98)$$

For the even levels, $\mathbf{m_i}$ is found from the particle numerator \mathbf{i} as $\mathbf{m_i} = 2\mathbf{i}$, while for the odd levels of \mathbf{n} , $\mathbf{m_i}$ is found from the particle numerator \mathbf{i} as $\mathbf{m_i} = 2\mathbf{i} - 1$. Additionally, for the even levels, the total number of particles considered for that level is equal to $2\mathbf{i_{max}} + 1$, while for the odd levels, the number of particles considered is equal to $2\mathbf{i_{max}}$.

For the reaction forces in the half-plane of particles subjected to a uniform vertical load, a relation can be derived that is similar to equation (4.95). The reaction forces for the equivalent one-dimensional response of the half-plane of particles to a uniform load at its surface read:

$$\tilde{R}_{z}^{\mathbf{0},\mathbf{n}_{even}}\left(s\right) = \int_{-2\pi}^{+2\pi} \left(\sum_{h=1}^{2} \varphi_{z}^{(h)} A_{z}^{\mathbf{0},(h)} e^{\frac{+\sqrt{5}}{2}i\kappa_{z}^{(h)}\mathbf{n}}\right) d\kappa_{x} + 2\sum_{i=1}^{i_{max}} \int_{-2\pi}^{+2\pi} \left(\sum_{h=1}^{2} \varphi_{z}^{(h)} A_{z}^{\mathbf{0},(h)} e^{\frac{+\sqrt{5}}{2}i\kappa_{z}^{(h)}\mathbf{n}}\right) e^{-\frac{1}{2}i\kappa_{x}\mathbf{m}_{i}} d\kappa_{x}$$
(4.99)

$$\tilde{R}_{z}^{\mathbf{0},\mathbf{n}_{odd}}\left(s\right) = 2\sum_{i=1}^{i_{\max}} \int_{-2\pi}^{2\pi} \left(\sum_{h=1}^{2} \varphi_{z}^{(h)} A_{z}^{\mathbf{0},(h)} e^{+\frac{\sqrt{3}}{2} i \kappa_{z}^{(h)} \mathbf{n}}\right) e^{-\frac{1}{2} i \kappa_{x} \mathbf{m}_{i}} d\kappa_{x}$$
(4.100)

As previously discussed for the reaction forces along the boundary Γ of the discrete particle system \mathbf{V} , the expressions for $\varphi_z^{(h)}$ with h=1..2 appearing in equations (4.99) and (4.100) depend on the shape of the interface at which the reaction forces are to be determined and on the location of the particle \mathbf{n} , relative to the loaded particle \mathbf{i} . For the equivalent one-dimensional response of the half-plane of particles, the expressions for $\varphi_z^{(h)}$ with h=1..2 are derived in Appendix G.10.

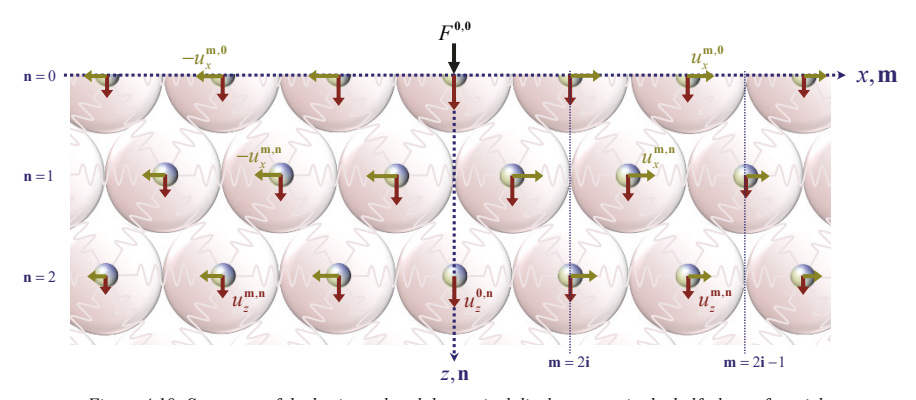


Figure 4.18: Symmetry of the horizontal and the vertical displacements in the half-plane of particles due to the single vertical point load applied at particle 0.0.

4.5.2 Matching the parameters of the 1D and 2D discrete particle systems

To obtain a response of the viscoelastic half-plane of particles to an infinite uniform lineload at its surface that is identical to the response of the viscoelastic cascade to an equivalent point load, the two models must be equivalent and represent the same material. To make sure that the hexagonal viscoelastic half-plane of particles and the viscoelastic cascade correspond, we first match their parameters by comparing their dimensional systems of equations of motion.

The dimensional equations of motion for respectively the horizontal and vertical motion of a particle m,n in the homogeneous hexagonal half-plane of particles are given by equations (4.46) and (4.47). As previously explained, the response of the half-plane of particles to an infinitely-long uniformly-distributed vertical line-load is exclusively vertical and there will be no horizontal response. Consequently, the horizontal displacement of particle \mathbf{m} , \mathbf{n} is equal to zero and equation (4.46) that describes the horizontal motion of the particle m,n is irrelevant. Additionally do note however, that also the horizontal displacement of any particles adjacent to the particle **m**,**n** must be equal to zero, i.e. $u_x^{\mathbf{m},\mathbf{n}} = 0$ for all values of **m** and **n**. Furthermore, the vertical response to the infinitely long uniform line-load is exactly the same for all particles that exist at the same horizontal level of the half-plane of particles, i.e. have the same discrete coordinate n. Regarding the equation of motion for the vertical response of the particle **m,n**, given by equation (4.47), it follows that $u_z^{\mathbf{m-1,n-1}} = u_z^{\mathbf{m+1,n-1}}$ and that $u_z^{\text{m-1,n+1}} = u_z^{\text{m+1,n+1}}$. Denoting the uniform vertical displacement of the particles at the horizontal level with coordinate **n** as $u_z^{n^*}$, accounting for the given displacement relations and including the expression for the operator $\hat{K}_e = K_e + C_e \frac{\partial}{\partial t}$, the equation of vertical motion of the particle m,n due to the infinite uniform distributed line-load becomes:

$$M_{2D}\ddot{u}_{z}^{n^{*}} + \frac{3}{2}C_{e;2D}\left(2\dot{u}_{z}^{n^{*}} - \dot{u}_{z}^{n^{*-1}} - \dot{u}_{z}^{n^{*+1}}\right) + \frac{3}{2}K_{e;2D}\left(2u_{z}^{n^{*}} - u_{z}^{n^{*-1}} - u_{z}^{n^{*+1}}\right) = 0$$

$$(4.101)$$

Here, M_{2D} is the mass of a particle in the interior of the homogeneous half-plane of particles, while $K_{e;2D}$ and $C_{e;2D}$ are respectively the stiffness and damping coefficients of the Kelvin-Voigt elements in the interior of the homogeneous half-plane of particles.

The equation of motion for a particle at the surface of the homogeneous viscoelastic halfplane of particles as it responds to the uniform surface load accordingly follows from equation (4.49) as:

$$\frac{1}{2}M_{2D}\ddot{u}_{z}^{0*} + \frac{3}{2}C_{e;2D}\left(\dot{u}_{z}^{0*} - \dot{u}_{z}^{1*}\right) + \frac{3}{2}K_{e;2D}\left(u_{z}^{0*} - u_{z}^{1*}\right) = F_{2D}\left(t\right)$$

$$(4.102)$$

Here, $F_{2D}(t)$ is the time-dependent load that is separately applied on all the surface particles of the homogeneous viscoelastic half-plane of particles as depicted in Figure 4.19.

The dimensional equation of motion for a particle in the interior of the semi-infinite viscoelastic cascade was previously given by equation (4.1). The corresponding equation of motion for a particle at the surface of the viscoelastic cascade can be derived straightforwardly. Denoting the particles in the viscoelastic cascade using the numerator \mathbf{n} , the

equations of motion for a particle at the surface of the cascade and a particle in the interior of the cascade respectively read:

$$\frac{1}{2}M_{ID}\ddot{u}^{0} + C_{e;ID}\left(\dot{u}^{0} - \dot{u}^{1}\right) + K_{e;ID}\left(u^{0} - u^{1}\right) = F_{ID}\left(t\right) \tag{4.103}$$

$$M_{ID}\ddot{u}^{n} + C_{e;ID} \left(2\dot{u}^{n} - \dot{u}^{n-1} - \dot{u}^{n+1} \right) + K_{e;ID} \left(2u^{n} - u^{n-1} - u^{n+1} \right) = 0$$

$$(4.104)$$

Here, M_{ID} , $K_{e;ID}$ and $C_{e;ID}$ are respectively the particle mass, the stiffness coefficient of the Kelvin-Voigt elements and the damping coefficient of the Kelvin-Voigt elements, all in the interior of the homogeneous cascade. Furthermore, $F_{ID}(t)$ is the time-dependent external load that is applied at the surface particle of the viscoelastic cascade as depicted in Figure 4.19.

Comparing equations (4.103) and (4.104) to respectively equations (4.102) and (4.101), it follows that the parameters of the viscoelastic cascade and the viscoelastic half-plane of particles match when the following relations hold:

$$M_{ID} = M_{2D}, C_{e;ID} = \frac{3}{2} C_{e;2D}, K_{e;ID} = \frac{3}{2} K_{e;2D}, F_{ID}(t) = F_{2D}(t)$$
 (4.105)

Equation (4.105) gives a comparison between the parameters of the viscoelastic cascade and the half-plane of particles for the case that the latter replicates the one-dimensional behaviour. Note here that, by satisfying the relations in equation (4.105), the particle natural frequency of the cascade and the half-plane of particles are also the same. Because the relations between the parameters of the cascade and half-plane of particles with the macromaterial properties are different, we must account for these relations to make sure that both particle systems represent the same material and thereby yield the same response.

To make sure that the relations given by equation (4.105) correspond to matching macromaterial properties, let us start by comparing the spring stiffnesses and the masses in the two equivalent one-dimensional models. The spring stiffnesses and the masses in the homogeneous cascade and the homogeneous hexagonal particle system were previously expressed in terms of the macromaterial properties by respectively equations (3.9) and (3.122). For the geometrical properties of both the homogeneous cascade and the homogeneous hexagonal half-plane of particles, consider Figure 4.19. It is reasonable to assume that the cross-sectional area A of the viscoelastic cascade represents a square and is expressed by its dimensions in x- and y-direction as $A = dx \cdot dy$. Furthermore, we assume that the dimensions of the cascade and the half-plane of particles in the y-direction are the same, i.e. $dy_{1D} = dy_{2D}$. Substituting equations (3.9) and (3.122) into the relations for the stiffness and the mass in equation (4.105), as well as accounting for the given assumptions, it then follows that for the spring stiffnesses and the masses to match in the two models, the following relations must hold:

$$K_{e;ID} = \frac{3}{2} K_{e;2D} \rightarrow dx = \frac{4\sqrt{3}}{5} \ell_{ID}$$
 (4.106)

$$M_{ID} = M_{2D}$$
 $\rightarrow dx \ell_{ID} = \frac{\sqrt{3}}{2} \ell_{2D}^2$ (4.107)

Here, ℓ_{ID} and ℓ_{2D} are the rheological element lengths in respectively the cascade and the half-plane of particles. Note here that while Figure 4.19 gives the spacing between the horizontal levels with coordinate **n** for both the half-plane of particles and the cascade in terms to the element lengths, this does not necessarily mean that the spacing between these horizontal levels is the same for both particle systems. In fact, from combining the relations given in equations (4.106) and (4.107), it follows that to match the parameters of the two systems according to equation (4.105), the lengths of the rheological elements in the cascade and the half-plane of particles must be related as:

$$\ell_{ID} = \sqrt{\frac{5}{8}} \ell_{2D} \tag{4.108}$$

Furthermore, combining equation (4.106) and (4.108), the dimension of the viscoelastic cascade in x-direction may alternatively be expressed as $dx = \sqrt{\frac{6}{5}} \ell_{2D}$.

Next, note that if equations (4.106) and (4.108) are satisfied, and thereby the spring stiffnesses in the two equivalent one-dimensional models are matched according to equation (4.105), also the damping in the two systems must be matched according to equation (4.105). This is because in both systems the stiffness and the damping are related through the damping coefficient ζ_e as $C_e = \zeta_e K_e$ and the damping coefficient ζ_e is a macromaterial property that must be the same for both systems. Ergo, if the stiffnesses in the cascade and the half-plane are properly related, so is the damping.

Thus, if the relations given by equations (4.106) and (4.108) are satisfied, all relations in equation (4.105) are satisfied except for the relation for the applied loading. Clearly, if we employ the dimensional expressions for the equations of motion of both the viscoelastic cascade and the viscoelastic half-plane of particles behaving in an equivalent one-dimensional

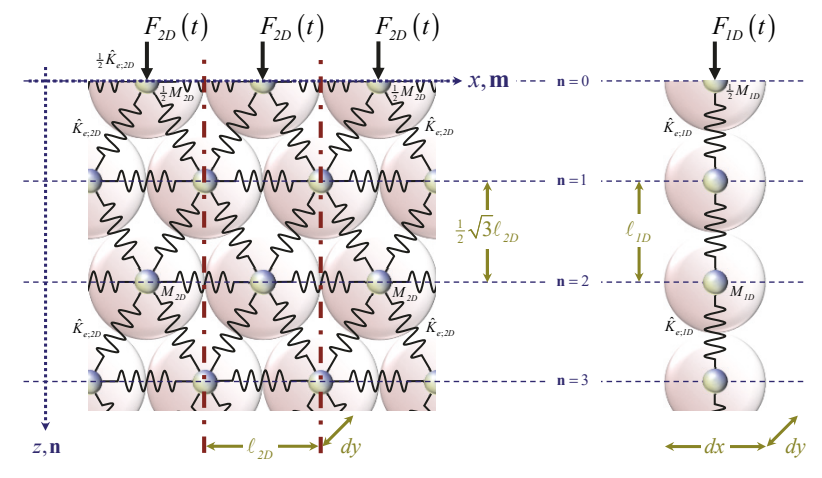


Figure 4.19: Geometry and parameters of the half-plane of particles and the cascade.

manner, while satisfying the given relations, we will obtain the exact same response for both systems to the same load. For the normalized systems however, this is not the case. To illustrate this, let us consider the relations between the dimensionless forces and their dimensional counterparts, here denoted by the subscript dim, in respectively the one- and two-dimensional models. In Appendix B, these relations are obtained as:

$$F_{\text{dl};ID} = \frac{F_{\text{dim};ID}}{2K_{e:ID}\ell_{ID}}, \qquad F_{\text{dl};2D} = \frac{F_{\text{dim};2D}}{3K_{e:2D}\ell_{2D}}$$
(4.109)

Substituting the stiffness relation according to equation (4.105) as well as the relation between the length of the rheological elements in the two systems according to equation (4.108), it follows that if the dimensional force relation according to equation (4.105) is satisfied, the relation between the applied dimensionless forces on the two particle systems reads:

$$F_{\text{dl};ID}\ell_{ID} = F_{\text{dl};2D}\ell_{2D} \rightarrow \sqrt{\frac{5}{8}}F_{\text{dl};ID} = F_{\text{dl};2D}$$
 (4.110)

Consequently, to obtain the same response of the cascade and of the hexagonal half-plane of particles behaving in an equivalent one-dimensional manner by employing the dimensionless equations of motion, the magnitude of the dimensionless load applied to the cascade must be $\sqrt{\frac{5}{8}}$ times larger than the amplitude of the load applied to the half-plane.

Instinctively, it would perhaps seem logical to try to match the dimension of the vertical spacing in the one-dimensional cascade and the half-plane of particles, i.e. choose $\ell_{ID} = \frac{\sqrt{3}}{2} \ell_{2D}$ as depicted in Figure 4.19. However, this will never allow one to properly match the macromaterial properties of the two models, as it is impossible to match their equivalent systems of equations of motion for this relationship. This is due to the differences in the geometry of the one- and two-dimensional models. For a square configuration for the half-plane of particles for example, the vertical geometry of a single column of particles in the half-plane is identical to that of the cascade. Thereby, comparing the cascade with a square configuration for the half-plane of particles emulating the one-dimensional behaviour, we would find that $\ell_{ID} = \ell_{2D} = dx$ and consequently $F_{ID} = F_{2D}$ both for the dimensional and the dimensionless consideration.

4.5.3 Green's displacements of the semi-infinite viscoelastic cascade

The equations of motion for the semi-infinite viscoelastic cascade, with a time-dependent load applied at its tip, were previously obtained as equation (4.103) and (4.104). Rewriting these equations in their dimensionless form using the dimensionless parameters that are introduced in Appendix B.3, as well as applying the Laplace integral transform with respect to time, the equations of motion for the semi-infinite viscoelastic cascade are obtained in the Laplace domain as:

$$\frac{1}{2}s^2\tilde{u}^0 + \frac{1}{2}(1 + 2\zeta s)(\tilde{u}^0 - \tilde{u}^1) = \tilde{F}(s) \tag{4.111}$$

$$s^{2}\tilde{u}^{n} + \frac{1}{2}(1 + 2\zeta s)(2\tilde{u}^{n} - \tilde{u}^{n-1} - \tilde{u}^{n+1}) = 0$$
(4.112)

The solution to equation (4.112) for the Laplace domain displacement of particle $\bf n$ in the interior of the semi-infinite cascade may generally be described as $\tilde{u}^{\bf n}=Ae^{-i\kappa \bf n}$. Here, κ is the dimensionless wavenumber of the propagating wave. The corresponding dispersion relation may be derived from equation (4.112), but was already given by equation (4.14). Note here that, to assure the proper wave decay and account for the proper behaviour of the viscoelastic cascade at infinity, the square root in the expression for the wavenumber is chosen such that its imaginary part is negative. To find the dimensionless wave amplitude A, we substitute the assumed expression for the displacement $\tilde{u}^{\bf n}$ into the force-displacement relation at the surface particle, given by equation (4.111), subsequently rearrange the resulting expression by using Euler's formula and incorporate the aforementioned dispersion relations. This yields the Laplace domain displacement of a particle $\bf n$ in the interior of the semi-infinite cascade as:

$$\tilde{u}^{\mathbf{n}}(s) = \frac{2e^{-i\kappa\mathbf{n}}}{s\sqrt{2 + 4\zeta s + s^2}} \tilde{F}(s) = \tilde{g}_{u}^{\mathbf{n}}(s)\tilde{F}(s) \tag{4.113}$$

Here, $\tilde{g}_{u}^{\mathbf{n}}(s)$ is the Green's displacement that describes the relation between the displacement of any particle \mathbf{n} in the semi-infinite viscoelastic cascade and the loading applied at its tip. For the particular case that $\mathbf{n} = 0$, equation (4.113) describes the force-displacement relation at the tip of the cascade that defines its dynamic compliance in accordance with for example equation (4.32), which describes the dynamic compliance for a two-dimensional system. This is confirmed by comparing equation (4.113) to the dynamic compliance of the semi-infinite viscoelastic rod, previously given by equation (4.20). Thus, we may describe the Green's displacements for any particle \mathbf{n} in the semi-infinite viscoelastic cascade as:

$$\tilde{g}_{u}^{\mathbf{n}}\left(s\right) = \frac{2e^{-i\kappa\mathbf{n}}}{s\sqrt{2+4\zeta s+s^{2}}} = \tilde{\beta}\left(s\right)e^{-i\kappa\mathbf{n}} \tag{4.114}$$

Note here that equation (4.114) describes the Green's displacements in the viscoelastic cascade for the particular case of a load applied at the particle at its tip.

The Green's displacements of any particle \mathbf{n} along the viscoelastic cascade may similarly be derived for a load applied inside the cascade. In accordance with the approach for the viscoelastic half-plane of particles, discussed in Section 4.4.1, let us denote this loaded particle inside the cascade as particle \mathbf{i} , with nodal coordinate $\mathbf{n} = \mathbf{n}_i$. Then, we consider two separate domains of the cascade: one domain between the particle at the tip of the cascade and the loaded particle, where waves propagate in two directions, and the domain beyond the loaded particle where waves propagate towards infinity and thus away from the load. As before, these two domains are respectively denoted as subsystems I and II, the corresponding

displacements may respectively be expressed as:

$$\tilde{u}_I^{\mathbf{n}} = A_I e^{-i\kappa \mathbf{n}} + B_I e^{+i\kappa \mathbf{n}}, \qquad \qquad \tilde{u}_{II}^{\mathbf{n}} = A_{II} e^{-i\kappa \mathbf{n}}. \tag{4.115}$$

The wave amplitudes A_I , B_I and A_{II} are then obtained from the boundary conditions for a load applied at a particle **i** inside the viscoelastic cascade. The first of these boundary conditions follows from considering the force equilibrium of the unloaded particle at the tip of the cascade, while the other two boundary conditions follow from respectively the force equilibrium and the displacement relation at the interface between the two considered domains. This yields the following set of Laplace domain boundary conditions for the viscoelastic cascade with a time-dependent load applied at an interior particle **i**:

$$\frac{1}{2}s^2\tilde{u}_I^0 + \frac{1}{2}(1 + 2\zeta s)(\tilde{u}_I^0 - \tilde{u}_I^1) = 0 \tag{4.116}$$

$$\frac{1}{2}s^{2}\tilde{u}_{I}^{\mathbf{n}_{i}} + \frac{1}{2}(1 + 2\zeta s)(\tilde{u}_{I}^{\mathbf{n}_{i}} - \tilde{u}_{I}^{\mathbf{n}_{i}-1}) + \frac{1}{2}s^{2}\tilde{u}_{II}^{\mathbf{n}_{i}} + \frac{1}{2}(1 + 2\zeta s)(\tilde{u}_{II}^{\mathbf{n}_{i}} - \tilde{u}_{II}^{\mathbf{n}_{i}+1}) = \tilde{F}(s)$$

$$(4.117)$$

$$\tilde{u}_I^{\mathbf{n}_i} = \tilde{u}_I^{\mathbf{n}_i} \tag{4.118}$$

Substituting the displacements given by equation (4.115) into the above set of boundary conditions and solving the resulting system for the wave amplitudes A_I , B_I and A_{II} then yields the expressions for the displacements in the two domains of the cascade. Alternatively, solving the system for the case that $\tilde{F}(s)=1$ yields the wave amplitudes A_I , B_I and A_{II} that correspond to the Green's displacements in the viscoelastic cascade. By incorporating the dispersion relations, previously given by equation (4.14), the Green's displacements of the particles in the viscoelastic cascade with a time-dependent load applied at an interior particle \mathbf{i} , with nodal coordinate $\mathbf{n} = \mathbf{n_i}$, are obtained as:

$$\tilde{g}_{u,I}^{\mathbf{n}}(s) = \tilde{\beta}(s)e^{-i\kappa\mathbf{n}_i}\cos(\kappa\mathbf{n}) \tag{4.119}$$

$$\tilde{g}_{u,H}^{\mathbf{n}}(s) = \tilde{\beta}(s)\cos(\kappa \mathbf{n}_{i})e^{-i\kappa \mathbf{n}}$$
(4.120)

Equations (4.119) and (4.120) respectively describe the Green's displacements in the two domains, or subsystems, of the viscoelastic cascade for the particular case that a load is applied at a particle inside the cascade.

4.5.4 Green's reaction forces in the semi-infinite viscoelastic cascade

Although the so-called reaction forces, which are equivalent to tractions in a continuous medium, are not of importance to derive the dynamic stiffness or dynamic compliance in the viscoelastic cascade, they are required to be able to construct the dynamic compliance matrix along an interface in the half-plane of particles. To verify that the expressions for the reaction forces of the viscoelastic half-plane of particles are obtained and implemented correctly, we here derive the Green's reaction forces in the semi-infinite viscoelastic cascade with the aim to compare them with the Green's reaction forces obtained for the equivalent one-

dimensional response of the half-plane of particles.

The reaction forces in the semi-infinite viscoelastic cascade are determined at its particles, but the reaction forces do not only depend on the location of the particle, but also on the orientation of the interface at which the reaction force is to be determined. Consider for example the interface Γ between the near-field lattice and the half-plane of particles considered in Section 4.4.1; the reaction force at a particle along Γ depends on the orientation of the interface Γ at that particle and a different orientation means a different reaction force. For the comparison between the equivalent one-dimensional response of the half-plane of particles and the response of the viscoelastic cascade, we determine the reaction forces at the particles of both systems along the horizontal level of each particle \mathbf{n} as depicted in Figure 4.19. Consequently, for both the half-plane of particles and the cascade, the reaction force at a particle may be obtained as the force that results from the equation of motion of either the upper or the lower half of that particle. Do note here that the reaction forces of the upper- and lower half-particle only coincide if the considered particle is unloaded. Here, we use the equation of motion of the lower half-particle to determine the reaction forces, because for a surface particle in either discrete particle system, only the lower half of the particles exist.

For any particle **n** in the viscoelastic cascade, the Laplace domain reaction force of that particle at a horizontal interface can straightforwardly be obtained, for example noting that the configuration of the considered half-particle equals the configuration of a surface particle. This yields:

$$\tilde{R}^{\mathbf{n}}\left(s\right) = \frac{1}{2}s^{2}\tilde{u}^{\mathbf{n}} + \frac{1}{2}\left(1 + 2\zeta s\right)\left(\tilde{u}^{\mathbf{n}} - \tilde{u}^{\mathbf{n}+1}\right) \tag{4.121}$$

Denoting that the reaction forces are related to the Green's reaction forces in accordance with, for example, equation (4.36), i.e. $\tilde{R}^{\mathbf{n}}(s) = \tilde{g}_{R}^{\mathbf{n}}(s)\tilde{F}(s)$, and substituting the corresponding equation for the Green's displacement, given by equation (4.113), we obtain an expression for the Green's reaction forces at particle \mathbf{n} of the cascade in terms of the Green's displacements as:

$$\tilde{g}_{R}^{n}(s) = \frac{1}{2}s^{2}\tilde{g}_{u}^{n}(s) + \frac{1}{2}(1 + 2\zeta s)(\tilde{g}_{u}^{n}(s) - \tilde{g}_{u}^{n+1}(s))$$
(4.122)

As the expressions for the Green's displacements depend on the location of the applied load, the same logically follows for the Green's reaction forces. Substituting the Green's displacement according to equation (4.114) into equation (4.122) above and subsequently including the dispersion relations for the cascade according to equation (4.14) yields the Green's reaction forces in the semi-infinite viscoelastic cascade for a load applied at the tip of the cascade as:

$$\tilde{g}_{R}^{n}(s) = \tilde{\chi}(s)\tilde{\beta}(s)e^{-i\kappa n} = e^{-i\kappa n}$$
(4.123)

The expression for the Green's reaction forces in the cascade as described by equation (4.123)

is physically quite trivial, if we consider that the reaction force of the surface particle must be equal to the applied load, i.e. $\tilde{R}^0(s) = \tilde{F}(s)$, and that the reaction forces in the viscoelastic cascade in terms of the applied load must then read $\tilde{R}^n(s) = \tilde{F}(s)e^{-i\kappa n}$.

The expressions for the Green's reaction forces in the cascade for the case that a load is applied at an interior particle i, with nodal coordinate $n = n_i$, are separately derived from equation (4.122) for the domain between the tip of the cascade and the loaded particle, denoted as domain I, and the domain beyond the loaded particle, denoted as domain II. Thus, substituting the Green's displacements according to equations (4.119) and (4.120) into equation (4.122), as well as incorporating the dispersion relations, the Green's reaction forces in the two domains of the semi-infinite viscoelastic cascade may respectively be obtained as:

$$\tilde{g}_{R,I}^{\mathbf{n}}(s) = -e^{-i\kappa\mathbf{n}_{i}} i \sin(\kappa\mathbf{n}) \tag{4.124}$$

$$\tilde{g}_{R,H}^{\mathbf{n}}(s) = \cos(\kappa \mathbf{n}_{i})e^{-i\kappa \mathbf{n}} \tag{4.125}$$

Equation (4.124) correctly shows that for a load applied inside the cascade, i.e. applied at \mathbf{n}_i , the reaction force at the surface of the cascade, i.e. at $\mathbf{n} = \mathbf{0}$, is equal to zero. Additionally, at a loaded particle in the interior of the cascade, the reaction forces of the two half-particles together must be equal to the applied load and the corresponding Green's reaction forces together are equal to one, i.e. $\tilde{g}_{R,I}^{\mathbf{n}_i}(s) - \tilde{g}_{R,I}^{\mathbf{n}_i}(s) = 1$. It can be straightforwardly shown that equations (4.124) and (4.125) satisfy this condition.

4.5.5 Equivalent response of the half-plane of particles and the cascade

To show that the equivalent one-dimensional response of the half-plane of particles matches the response of the cascade, we here consider the response of the two discrete particle systems to a single-sinus pulse load with a dimensionless angular frequency $\Omega=0.5$. If we choose the amplitude of the pulse load for the half-plane of particles as $\bar{F}_{2D}=1.0~\mathrm{MN}$, it follows from the considerations in Section 4.5.2 that, to get a dimensionless response in the cascade that has the same magnitude as the equivalent one-dimensional response in the half-plane of particles, the force applied to the cascade must be chosen as $\bar{F}_{ID}=\sqrt{\frac{5}{8}}\bar{F}_{2D}=0.791~\mathrm{MN}$.

The macromaterial properties are chosen in accordance with the general values given in Section 2.5, which means that the Young's modulus is equal to E=20 MPa and that the mass density is equal to $\rho=2000\,\mathrm{kg/m^3}$. Additionally, the damping ratio is chosen as $\zeta=0.2$ and the third, or y-, dimension of both systems is chosen as $dy=1\,\mathrm{m}$. Again, the spacing of the half-plane of particles is chosen as $\ell_{2D}=0.2\,\mathrm{m}$. It then follows that for the cascade to match the macromaterial properties, the length of the rheological elements in the cascade must be chosen as $\ell_{1D}=\sqrt{\frac{5}{8}}\ell_{2D}=0.158\,\mathrm{m}$ and the x-dimension of the cascade must be chosen as $dx=\sqrt{\frac{6}{5}}\ell_{2D}=0.219\,\mathrm{m}$.

Figure 4.20a and Figure 4.20b respectively show the real and imaginary parts of the Green's displacement for the response of the loaded surface particle in the viscoelastic halfplane of particles for several values of i_{max} , which is the number of particles considered on either side of the z-axis to obtain the equivalent one-dimensional response at the surface of

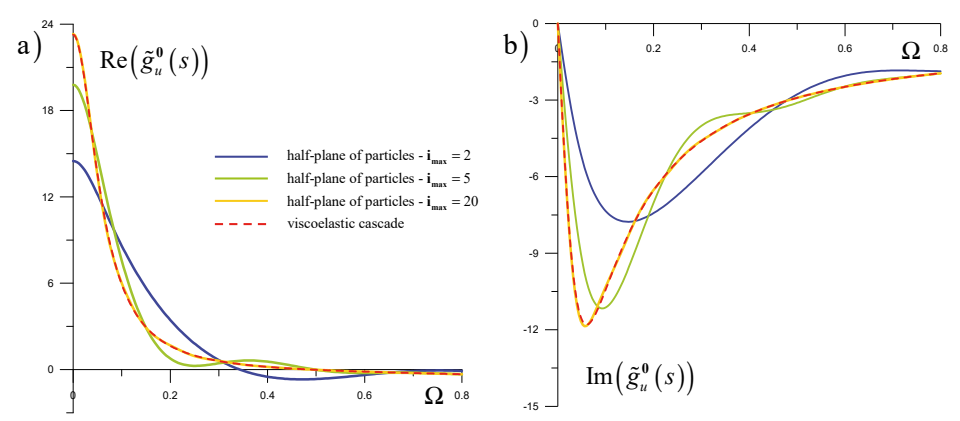


Figure 4.20: Green's displacements for the equivalent one-dimensional response of the loaded surface particle in the viscoelastic half-plane of particles and in the viscoelastic cascade: a) real part; b) imaginary part.

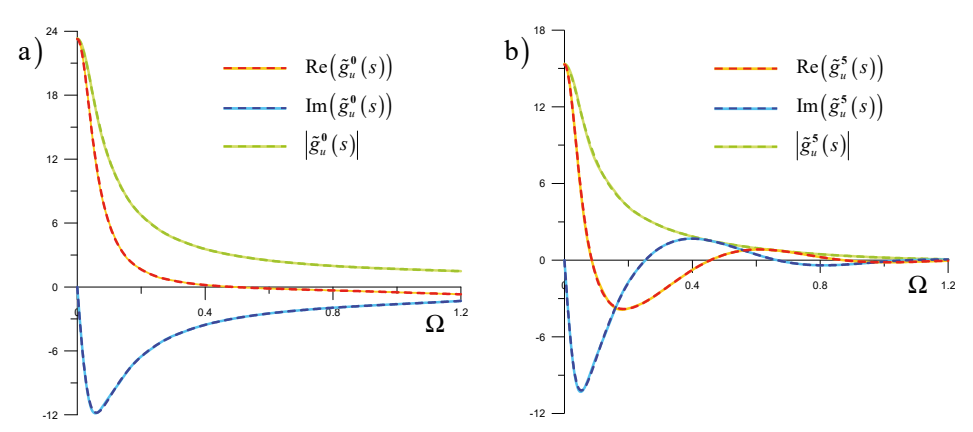


Figure 4.21: Green's displacements for the equivalent one-dimensional response of the half-plane of particles (continuous lines) and for the viscoelastic cascade (dashed lines) for $n_i=0$: a) loaded surface particle, n=0; b) interior particle, n=5.

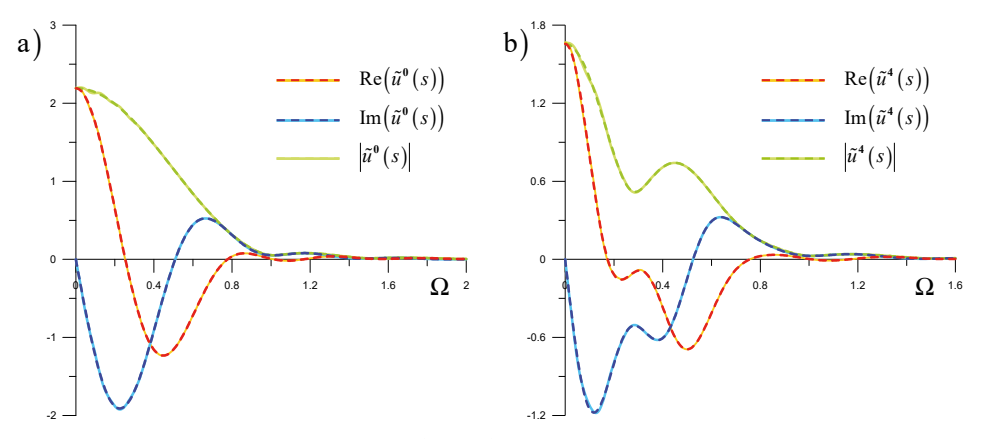


Figure 4.22: Laplace domain displacements in the half-plane of particles (continuous lines) and in the cascade (dashed lines): a) for a loaded particle at the surface, $n_i=n=0$; b) For a loaded particle in the interior, $n_i=n=4$.

the half-plane of particles according to equation (4.97). The continuous blue line gives the Green's displacement for the half-planes' surface particle for $i_{max} = 2$ and the continuous green line gives the Green's displacement for $i_{max} = 5$. As the dashed red line gives the response of the loaded surface particle in the viscoelastic cascade, Figure 4.20 shows that both chosen values for i_{max} are insufficient to properly construct the equivalent one-dimensional behaviour of the half-plane of particles. For increasing values of i_{max} , both the real and imaginary parts of the Green's displacement of the half-planes' surface particle do converge to the Green's displacement of the particle at the tip of the one-dimensional viscoelastic cascade. At a value of i_{max} equal to 20 or higher, for which the corresponding response of the half-plane surface particle in Figure 4.20 is given by the continuous yellow line, the equivalent one-dimensional response of the half-plane of particles matches the behaviour of the viscoelastic cascade in the Laplace domain well.

Figure 4.21 shows a comparison of the real part, the imaginary part and the absolute value of the Green's displacements for two particles in the viscoelastic half-plane, behaving in an equivalent one-dimensional manner, and the viscoelastic cascade, as a function of frequency by substituting $s = i\Omega$. Here, the Green's displacements of the particles in the half-plane are given by continuous lines, while the corresponding Green's displacements of the viscoelastic cascade are given by dashed lines. Figure 4.21a gives the Green's displacement of the surface particle in both systems, which is also the particle at which the load is applied. In accordance with equation (4.114), the Green's displacement of the surface particle, i.e. the particle for which $\mathbf{n} = 0$, matches the dynamic compliance of the viscoelastic cascade, previously depicted in Figure 4.3b. From comparing Figure 4.21a with Figure 4.3b, it is evident that the Green's displacements of the surface particle in both systems indeed match the dynamic compliance. Whereas Figure 4.21a shows the Green's displacements for a surface particle and thus for an even level of the nodal coordinate \mathbf{n} , Figure 4.21b shows the corresponding Green's displacements for an interior particle, at an odd level of the nodal coordinate \mathbf{n} , in this case $\mathbf{n} = 5$, which for the half-plane of particles follows from equation (4.98).

When the Green's displacements of the two systems match and we apply the same load in both systems, evidently the Laplace domain displacements of both systems must also coincide. This is confirmed by Figure 4.22a that shows the Laplace domain displacements of the loaded surface particle for both the viscoelastic half-plane of particles, given by the continuous lines, and the viscoelastic cascade, given by the dashed lines. Additionally, Figure 4.22b shows the Laplace domain displacements of the loaded particle for the case that the loaded particle is located in the interior of respectively the half-plane of particles and the viscoelastic cascade, in this case $\mathbf{n}_i = 4$.

Then, applying the inverse Laplace transform to the obtained Laplace domain displacements may be expected to yield corresponding time domain displacements for both the halfplane of particles and the viscoelastic cascade. Figure 4.23a shows the time domain response of the two equivalent one- and two-dimensional models for a load applied at the surface of the half-plane, i.e. the tip of the cascade. Here, the continuous yellow and light blue lines give the time domain displacement in the half-plane of respectively the loaded surface particle, i.e. at $\mathbf{n}_i = \mathbf{n} = 0$, and of the interior particle at $\mathbf{n} = 5$, both for $\mathbf{i}_{max} = 20$. Furthermore,

the dashed yellow and light blue lines give the corresponding time domain displacements for $i_{max}=10$, while the dashed red and blue lines respectively give the corresponding displacements for the viscoelastic cascade. Additionally, Figure 4.23b again shows the time domain response of the two equivalent one- and two-dimensional models, but now for a load applied at the horizontal level $n_i=4$. Here, the continuous yellow and dashed red lines again give the time domain responses of the loaded particle in the half-plane and the cascade respectively, while the continuous light blue line and dashed blue line now give the time domain responses of the particle located at the surface of the half-plane and at the tip of the cascade respectively.

Although we previously found that in the Laplace domain, the equivalent one-dimensional response of the half-plane of particles closely resembles the Laplace domain response of the viscoelastic cascade for $i_{max} = 20$, Figure 4.23 shows that in the time domain, the responses of the two systems correspond only for a limited duration. Figure 4.23a additionally shows that the duration at which the equivalent one-dimensional response of the halfplane of particles corresponds with the response of the viscoelastic cascade increases with the number of particles per horizontal level, i.e. i_{max} , that are accounted for when determining the equivalent one-dimensional response of the half-plane of particles. From the displacement response in Figure 4.23a for both $i_{max} = 10$ and $i_{max} = 20$ and in Figure 4.23b only for $i_{max} = 20$, it appears that the particles in the half-plane of particles are at some point in time subjected to a secondary wave. The time at which this wave appears in the response depends on the value of imax and for both considered values of imax this wave arrives well after the incident wave due to the applied pulse load. The appearance of this secondary wave can be explained by considering the relation described by equation (4.94); this relation shows that the obtained equivalent one-dimensional response of the half-plane of particles can be alternatively considered as the response of the particles at the z-axis to the uniform vertical loading over the horizontal domain $\mathbf{m}_i = -2\mathbf{i}_{max} \dots + 2\mathbf{i}_{max}$. Both edges of the horizontal domain defined by the value of imax induce waves in the half-plane of particles that propagate in both the positive and negative direction of the x-axis. As the equivalent one-dimensional response

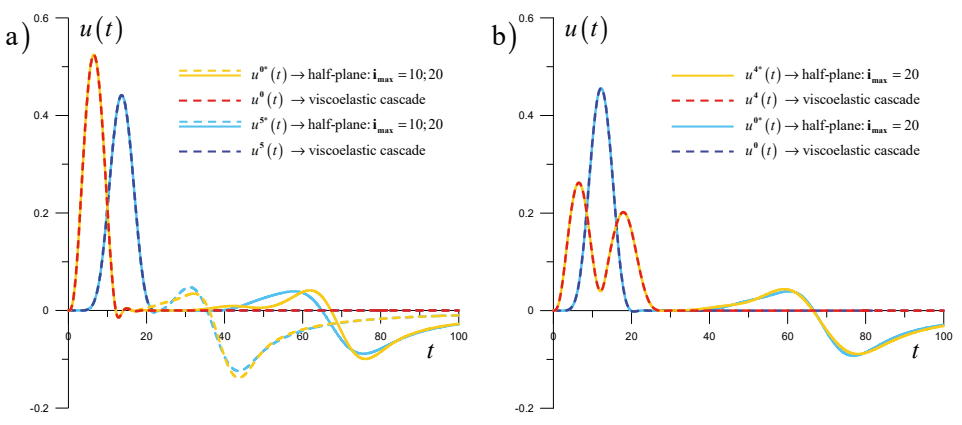


Figure 4.23: a) Time domain displacements of two particles in the half-plane (for 2 values of imax) and in the cascade; b) Time domain displacements of the loaded and the surface particle in the half-plane and in the cascade.

of the half-plane of particles is determined exactly at the z-axis, and both edges of the applied loading are located at the same distance of the z-axis, the waves induced at the two edges arrive at the z-axis simultaneously, thereby explaining why only a single secondary wave appears in the equivalent one-dimensional response of the half-plane of particles.

Although the edges of the applied loading in the half-plane of particles will induce both shear and compressional waves, the resulting waves are mainly characterized as shear waves. Not accounting for the damping in the half-plane, the dimensionless time at which the shear waves, induced by the edges of the applied loading, arrive at the z-axis can straightforwardly be derived from the chosen properties of the half-plane as $t_{arr} = \mathbf{i}_{max} \sqrt{8}$. For $\mathbf{i}_{max} = 10$ and $\mathbf{i}_{max} = 20$, the dimensionless arrival times are therefore respectively obtained as $t_{arr} = 28.3$ and $t_{arr} = 56.6$. These values match well with the dimensionless arrival times observed for these waves in the equivalent one-dimensional response of the half-plane that are depicted in Figure 4.23.

The correspondence between the equivalent one-dimensional time domain response of the half-plane of particles with that of the cascade can be improved by simply increasing the value of i_{max} . As the results presented here already show that the equivalent one-dimensional response of the half-plane of particles matches the response of the cascade well, this is not further investigated.

Comparison of the Green's reaction forces in the half-plane and the cascade

Figure 4.24 gives the corresponding real part, imaginary part and absolute value of the Green's reaction forces at two different particles as a function of frequency for the equivalent one-dimensional behaviour of the half-plane of particles and for the semi-infinite viscoelastic cascade by using $s = i\Omega$. The Green's reaction forces depicted here, are due to a load applied at the horizontal level $\mathbf{n}_i = 4$. Figure 4.24a thus gives the Green's reaction forces at a particle located in subsystem I, i.e. in the domain between the loaded particle and its surface or tip, in this case for $\mathbf{n} = 1$, while Figure 4.24b gives the Green's reaction forces at a particle located in subsystem II, i.e. in the domain beyond the loaded particle, in this case for $\mathbf{n} = 8$. Here, the continuous lines give the equivalent one-dimensional Green's reaction forces for the half-plane of particles, which are respectively obtained by means of equations (4.99) and (4.100) for $i_{\text{max}} = 20$. The expressions for $\varphi_z^{(h)}$ appearing in equations (4.99) and (4.100) are derived in Appendix G.10 for both subsystems. Furthermore, the dashed lines give the Green's reaction forces that are obtained for the viscoelastic cascade. Here, the Green's reaction force $\tilde{g}_{R}^{1}(s)$, i.e. for particle $\mathbf{n}=1$ in subsystem I of the cascade, follows from equation (4.124), while the Green's reaction force $\tilde{g}_{R}^{8}(s)$, i.e for $\mathbf{n} = 8$ in subsystem II of the cascade, follows from equation (4.125).

The Green's reaction forces at the surface of the half-plane, or at the tip of the cascade, are deliberately not shown here because the reaction forces at both the unloaded surface of the half-plane and at the unloaded tip of the cascade must be equal to zero at all times. For the cascade, this follows directly from equation (4.124), while for the half-plane of particles with $i_{max} = 20$, the reaction forces obtained incorporate some small numerical errors that are negligible. Additionally, also the reaction forces at the interior loaded particle, i.e. at

 $\mathbf{n_i} = \mathbf{n} = \mathbf{4}$ are not shown here because at the applied load, the resulting reaction forces of the half-particles in the two subsystems must satisfy equations (4.75) and (4.76). It turns out that in this case, the magnitude of the reaction forces in the half-particles in respectively subsystem I and II are both half the magnitude of the applied load, which only shows that the applied load is evenly divided over the two half-particles.

As the Green's reaction forces for the equivalent one-dimensional response of the halfplane of particles match the corresponding Green's reaction forces for the viscoelastic cascade, there is not much value in further elaborating on the corresponding reaction forces in either the Laplace or the time domain. Do note however that the time domain reaction forces in the half-plane of particles will again show the occurrence of the shear wave due to the edges of the applied loading that was previously observed for the time domain displacements depicted in Figure 4.23.

Figure 4.20 to Figure 4.24 verify that the approach to obtain an equivalent one-dimensional response of the half-plane of particles is valid for the given relations between the properties of the one- and two-dimensional particle systems, and that the routines to obtain the Green's displacements and the Green's reaction forces in the half-plane of particles are implemented correctly.

4.6 The half-plane of particles versus the continuum

In this section, we compare the dynamic behaviour of the half-plane of particles with that of the continuous layer by considering their dispersive properties and their directionality. Here, we consider a continuous layer, i.e. a two-dimensional continuum with a fixed bottom, and not a continuous half-plane, because the continuous half-plane is known to move as a whole under the application of a vertical load. The difference between the geometry of the discrete particle system and the continuum does not influence the comparison between the dispersive properties of their body waves, but wave reflections from the fixed bottom of the layer do cause the response of the layer to be different than that of the half-plane of particles.

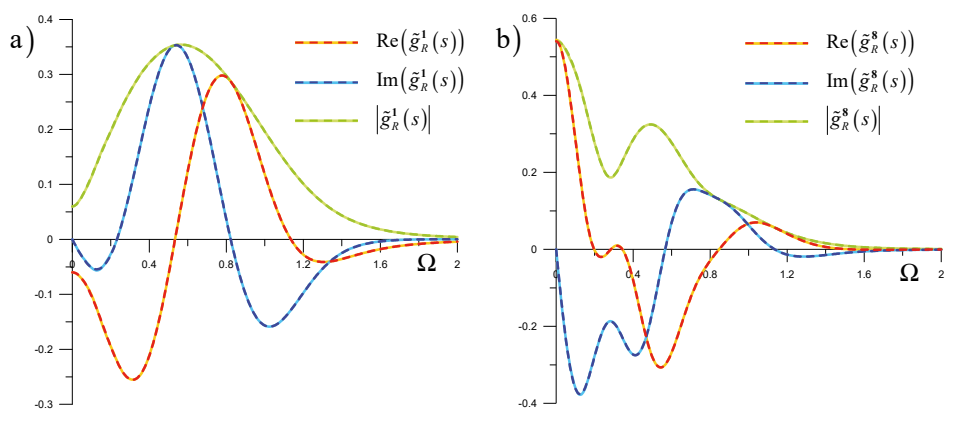


Figure 4.24: Green's reaction forces in the half-plane of particles (continuous lines) and in the viscoelastic cascade (dashed lines) for n_i =4: a) interior particle in domain I, n=1; b) interior particle in domain II, n=8.

4.6.1 Wave dispersion in the half-plane of particles and in the continuum

To compare the dispersive properties of the half-plane of particles and the continuum, let us first regard the dispersion in both media along the principal axes, i.e. in x- and z-directions. For any two-dimensional solid medium, the dispersion relation for a wave propagating in x-direction may be obtained from its two-dimensional dispersion relation by substituting $\kappa_z = 0$. Similarly, the dispersion relation for a wave propagating in z-direction is obtained by substituting $\kappa_x = 0$. The corresponding dispersion relations have been derived accordingly for the half-plane of particles with a hexagonal configuration in Appendix H.1 and for the continuous layer in Appendix H.2.

In the hexagonal half-plane of particles, the dispersion relations for the propagation of shear and compressional waves in z-direction respectively follow from equation (4.56) as:

$$\cos\frac{\kappa_{z,s}\sqrt{3}}{2} = 1 + \frac{3s^2}{1 + 2\zeta s}, \qquad \cos\frac{\kappa_{z,p}\sqrt{3}}{2} = 1 + \frac{s^2}{1 + 2\zeta s}.$$
 (4.126)

Note that these equations were previously given by equation (4.91) for the equivalent onedimensional response of the half-plane of particles for waves propagating in z-direction.

The corresponding dispersion relations for the propagation of shear and compressional waves in x-direction are respectively obtained as:

$$\cos\frac{\kappa_{x,S}}{2} = 1 + \frac{s^2}{1 + 2\zeta s}, \qquad \cos\frac{\kappa_{x,P}}{2} = -\frac{1}{8} \pm \frac{9}{8} \sqrt{1 + \frac{48}{81} \frac{s^2}{1 + 2\zeta s}}.$$
 (4.127)

As explained in Appendix H.1, the expression for the propagation of compressional waves in x-direction consists of two solutions that correspond to two different segments of the dispersion relation within the first Brillouin zone. Furthermore note that, even though the right-hand sides of the second dispersion relation in equation (4.126) and the first dispersion relation in equation (4.127) are identical, they relate to the propagation of waves in different directions, and given the fact that their left-hand sides are different as well, they also relate to different wavenumbers.

For the continuous layer, as shown by the derivation in Appendix H.2, the dispersion relations for the shear and compressional waves in the continuum are decoupled and are independent from the direction of wave propagation. The dispersion relations for the propagation of shear and compressional waves in the continuum are respectively obtained as:

$$\kappa_S = \pm is \sqrt{\frac{8}{1 + 2\zeta s}}, \qquad \kappa_P = \pm \frac{is}{\sqrt{3}} \sqrt{\frac{8}{1 + 2\zeta s}}.$$
 (4.128)

Figure 4.25 shows the dispersion curves for wave propagation in x- and z-directions in both the hexagonal half-plane of particles (HPoP) and in the continuous layer (Cont). These

dispersion curves are obtained as frequency-wavenumber relations by substituting $s = i\Omega$ into equations (4.126) to (4.128). Here, the dispersion curves are given for the particular case that there is no damping present. By including damping, the dispersion relations become complex-valued, but essentially the dispersion characteristics do not change significantly by including damping and therefore, the corresponding complex-valued dispersion relations are not investigated here. While Figure 4.25a gives the dispersion curves for the propagation of shear waves in x- and z-direction, Figure 4.25b gives the dispersion curves for the propagation of compressional waves in x- and z-directions. Since the dispersion curves are symmetric in the wavenumber and frequency axes, the dispersion curves are given here for positive values of wavenumber and frequency only.

Figure 4.25 shows that in the long-wave limit, and for waves propagating in both x- and z-directions, the dispersive properties of the hexagonal half-plane of particles match those of the continuum well. The correspondence between the two models can be considered to be good on the wavenumber domain $\kappa_x = \kappa_z = \left[0, \frac{1}{2}\pi\right]$, so that, within this domain, the phase velocities of the shear and compressional waves for both models match well in both directions. Figure 4.25 also clearly illustrates the differences in dispersive properties between the continuum and the hexagonal half-plane of particles for larger wavenumbers. For zero damping, the continuum has a linear dispersion relation, i.e. is non-dispersive, while the corresponding dispersion relations for the hexagonal half-plane of particles are periodic for increasing wavenumbers. This periodicity is due to the sinusoidal character of the dispersion relation. For waves propagating in x-direction, the periodic domain is found as $\kappa_x = \left[-2\pi + 4\pi n, 2\pi + 4\pi n\right]$, where n is an integer. Accordingly, for waves propagating in z-direction, the periodic domain is found as $\kappa_z = \left[-\frac{2}{\sqrt{3}}\pi + \frac{4}{\sqrt{3}}\pi n, \frac{2}{\sqrt{5}}\pi + \frac{4}{\sqrt{3}}\pi n\right]$. The repeating zones in the dispersion relation correspond to the so-called Brillouin zones of the lattice [Brillouin, 1953] and are typical for the dynamic response of discrete particle systems.

There are examples in literature stating that only the first Brillouin zone, corresponding to the given periodic domains for n = 0, should be considered, because the incorporation of higher Brillouin zones results in a non-unique relation between the frequency and the wave number [Suiker et al., 2001b]. This implies that within the zone of the dispersion curve that corresponds to a single Brillouin zone, the frequency-wavenumber relation is unique. As

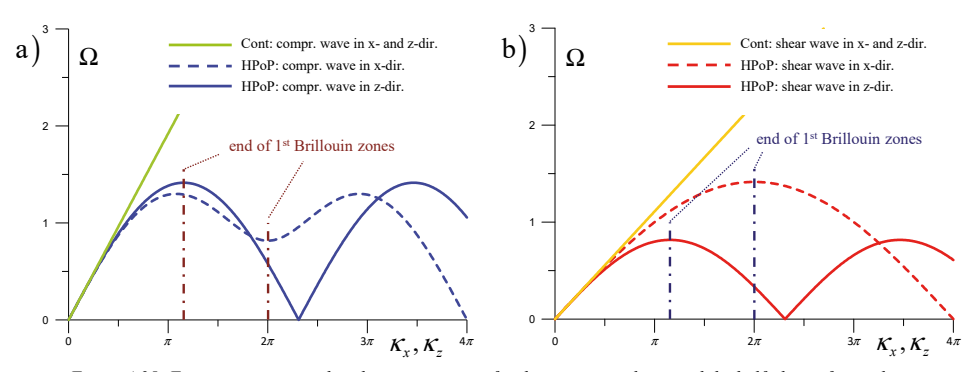


Figure 4.25: Frequency-wavenumber dispersion curves for the continuous layer and the half-plane of particles:
a) shear waves; b) compressional waves.

shown by Figure 4.25, this statement holds for the dispersion curves that regard the propagation of shear waves in x- and z-directions and the propagation of compressional waves in zdirection, but it does not hold for the propagation of compressional waves in x-direction. The dispersion curve for the horizontal propagation of the compressional wave in Figure 4.25a shows that within the domain of the first Brillouin zone, i.e. on the domain $\kappa_x = [0, 2\pi]$, two different values for the horizontal wavenumber correspond to one and the same frequency. At the frequency range $\Omega = \left| \sqrt{\frac{2}{3}} \approx 0.8165, \sqrt{\frac{81}{48}} \approx 1.2290 \right|$, the frequency-wavenumber dispersion relation is ambiguous. The fact that this frequency-wavenumber is ambiguous within the first Brillouin zone for the propagation of compressional waves in x-direction, but is unique for the propagation of compressional waves in z-direction, shows that the dispersion relations are distinctly dependent on the direction of wave propagation. We should therefore regard the Brillouin zones to fully characterize the frequency-wavenumber relation for the corresponding cells of the lattice, rather than regard the Brillouin-zones to describe a unique frequency-wavenumber relation. The reason that generally only the first Brillouin zone is considered is because the dispersive properties of the periodic discrete lattice are fully characterized by its behaviour in a single, and thus in the first, Brillouin zone.

Another consequence of the sinusoidal character of the dispersion relations in the halfplane of particles is that the frequency range at which waves can propagate through the lattice is limited; while the continuum allows for wave propagation at all frequencies, the hexagonal half-plane of particles acts as a low-pass filter that transmits only relatively low frequencies. Here, the shear wave in x-direction has a frequency range $\Omega_{x,S} = \left[0,\sqrt{2}\right]$, while the shear wave in z-direction has a frequency range $\Omega_{x,P} = \left[0,\sqrt{\frac{2}{3}}\right]$. Furthermore, the compressional wave in x-direction has a frequency range $\Omega_{x,P} = \left[0,\sqrt{\frac{2}{3}}\right]$ with a local minimum $\Omega = \sqrt{\frac{2}{3}} \approx 0.8165$. The compressional wave in z-direction has a frequency range $\Omega_{z,P} = \left[0,\sqrt{2}\right]$. At higher frequencies, i.e. at frequencies outside the given ranges for wave propagation, the frequency-wavenumber relation becomes complex-valued. At these frequencies, so-called evanescent waves exist, which do not propagate.

Directionality of wave propagation

The above explanations and deliberations clearly identify that the dispersion within the hexagonal half-plane of particles is distinctly different when considering waves propagating in different directions. For the continuum on the other hand, the dispersion characteristics are independent from the direction of wave propagation. The fact that the dispersive characteristics for the hexagonal half-plane are direction-dependent can be attributed to the fact that its geometry is distinctly different in, for example, *x*- and *z*-directions. The dependency of the dispersion characteristics on the direction of wave propagation is illustrated by Figure 4.26.

Figure 4.26a shows the directionality of the shear waves in both the hexagonal half-plane and the continuous layer by including the dispersion curves in the wavenumber plane for several dimensionless frequencies. Accordingly, Figure 4.26b shows the directionality of the compressional waves in the hexagonal half-plane and the continuum. Here, note that the dispersion curves in the wavenumber plane are symmetric in both the horizontal and the vertical wavenumber axes, so that the first quadrant of the wavenumber plane includes the

information for wave propagation in all directions. Here, note that the dispersion curves in Figure 4.26 have been obtained by solving equation (4.57) for the wavenumbers $\kappa_z^{(1)}$ and $\kappa_z^{(2)}$, and subsequently matching the resulting curves with the dispersion relations along the principal axes according to equations (4.126) and (4.127).

Figure 4.26 shows that, for smaller frequencies and thus for large wavelengths, the dispersion in the hexagonal half-plane corresponds well with the dispersion in the continuous layer. Because of its isotropy, the dispersion curves for the continuum in the wavenumber plane are circular. For small frequencies, the dispersion curves for the hexagonal half-plane in the wavenumber plane are by approximation circular as well and therefore, the hexagonal half-plane by approximation behaves isotropically as well. For higher frequencies and thus for smaller wavelengths, the discrepancy between the hexagonal half-plane and the continuum increases rapidly and the hexagonal half-plane is distinctly anisotropic. Note here that for the shear waves in the hexagonal half-plane, depicted by the red lines in Figure 4.26a, the orientations of the rheological elements correspond to the smallest magnitude of the wavenumber, while the largest magnitudes of the wavenumber are found in between any two rheological element orientations. For the compressional waves in the hexagonal half-plane however, depicted by the blue line in Figure 4.26b, the orientations of its rheological elements do correspond to the largest magnitudes of the wavenumber in the dispersion curves. The deviation in the magnitude of the wavenumber appears to be most pronounced for shear waves.

In addition to the anisotropy, it is also clear that for higher frequencies and smaller wavelengths, the wavenumbers in the hexagonal lattice are larger than those for the continuum. By increasing the frequency and by thus reducing the wavelength, the difference between the value of the wavenumbers in the two models increase, as we have already observed in Figure 4.25. The differences in the directionality of the dispersion relations for the hexagonal halfplane and the continuum for high frequencies is thereby not only due to the difference in geometry of the hexagonal half-plane in different directions, i.e. due to the anisotropic aspects, but also due to the differences in the material parameters of the two models.

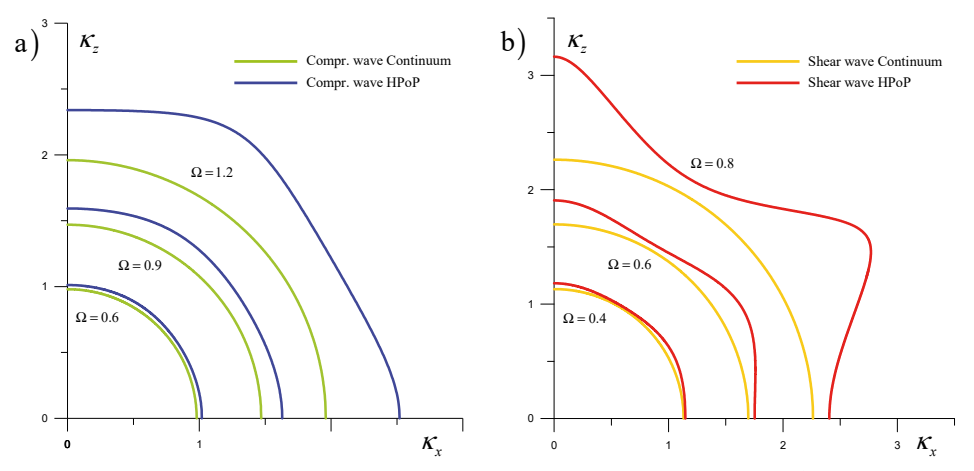


Figure 4.26: Directionality of wave propagation in the continuous layer and the half-plane of particles for several frequencies: a) shear waves; b) compressional waves.

4.6.2 Direction-dependent polarization of body waves

As opposed to the two-dimensional continuum, the shear and compressional waves in the discrete lattice are coupled and cannot be isolated in the dispersion relation (4.56). Thus, as the particles in the discrete lattice move in both x- and z-directions simultaneously, the motion in either direction may contribute to the propagation of both shear and compressional waves at the same time. As a result, the waves propagating in a given direction are not purely shear or compressional. Instead, they may be predominantly shear, predominantly compressional or even equally shear and compressional. In this section, we illustrate the differences in wave propagation properties for the discrete half-plane of particles and the continuous layer by considering the motion, at a certain particle in the lattice or at a certain point in the continuum, that is associated with the propagation of shear and compressional waves respectively, depending on the direction of wave propagation in either medium. Moreover, this section shows that for certain specific directions of wave propagation and for some magnitudes of the wavenumber, the shear and compressional waves can be isolated, but only for a few specific cases.

To determine the contributions of the shear and the compressional waves in any given direction of propagation, we consider the expression for $D^{(h)}$, previously given by equation (4.61), which describes the ratio between the vertical and horizontal amplitudes of the propagating waves, respectively given by $B^{(h)}$ and $A^{(h)}$, where h corresponds to the propagation of either the shear or the compressional wave. Therefore, the value of $D^{(h)}$ describes the direction of the particle motion associated with respectively the shear and the compressional waves and thereby gives us information about the direction-dependent polarization of the body waves. Based on the equations derived in Section 4.4 however, we do not know to which type of wave each value for h corresponds.

To determine $D^{(h)}$ for the shear and compressional waves respectively, first note that equation (4.61) expresses $D^{(h)}$ in terms of the Laplace parameter s, as well as in terms of the horizontal and vertical wavenumbers κ_x and κ_z . To consider the direction-dependent polarization of the wave propagation, we require the amplitude ratio $D^{(h)}$ in terms of the horizontal and vertical wavenumbers exclusively. Evidently, the Laplace parameter and the horizontal and vertical wavenumbers are related through the dispersion relation (4.56). Thus, solving the dispersion relation for the Laplace parameter s and substituting this solution into equation (4.61) allows us to express $D^{(h)}$ exclusively in terms of the horizontal and vertical wavenumbers. Solving the dispersion relation (4.56) for s, principally yields four solutions for s. More conveniently however, we can solve the dispersion relation (4.56) for the common term $1+s^2/(1+2\zeta s)$. This yields:

$$\left(1 + \frac{s^2}{1 + 2\zeta s}\right)_{1,2} = \frac{1}{3} \left(\cos \kappa_x + 2\cos \frac{\kappa_x}{2}\cos \frac{\kappa_z\sqrt{3}}{2}\right) \\
\pm \frac{1}{3} \sqrt{\cos \kappa_x} \left(\cos \kappa_x + \cos \kappa_z\sqrt{3} - 2\cos \frac{\kappa_x}{2}\cos \frac{\kappa_z\sqrt{3}}{2}\right) + 2 - \cos^2 \frac{\kappa_z\sqrt{3}}{2}} \tag{4.129}$$

Substituting the above into equation (4.61), yields the amplitude ratio $D^{(h)}$, with h = 1...2,

exclusively in terms of the horizontal and vertical wavenumbers. As such, the resulting expressions for $D^{(h)}$ are independent of the damping ratio ζ , which shows that the damping does not influence the direction-dependent polarization of the shear and compressional waves. As an alternative, we can therefore also choose to solve the dispersion relation (4.56) for s for the case that the damping is zero, i.e. $\zeta = 0$. This still yields four solutions for s, but since s remains in the dispersion relation as s^2 , we find two positive solutions for s, let's say s_1 and s_2 , and two negative solutions that are equal in magnitude to s_1 and s_2 respectively. Substituting these solutions for s into equation (4.61) for the case that $\zeta = 0$, then again yields the two expressions for $D^{(h)}$ with h = 1...2.

To consider the polarization of the shear and compressional waves in all directions, we choose to express $D^{(h)}$ in polar coordinates by introducing:

$$\kappa_x = \kappa_r \cos \theta, \qquad \kappa_z = \kappa_r \sin \theta.$$
(4.130)

Here, κ_r is the magnitude of the wavenumber and θ gives the direction of wave propagation, so that the case $\theta = 0$ corresponds to wave propagation in x-direction, ergo $\kappa_z = 0$, and the case $\theta = \frac{\pi}{2}$ corresponds to wave propagation in z-direction, ergo $\kappa_x = 0$.

To determine which of the expressions for $D^{(h)}$ is specifically related to either the shear or the compressional waves, let us consider the zero damping solutions for s in the long-wave limit, i.e. for $\kappa_r \to 0$, obtained by solving the dispersion relation in terms of κ_r and θ . Using a series expansion at $\kappa_r = 0$ then yields the four solutions for the Laplace parameter s, as:

$$s^{(1)} = \pm i \kappa_r \sqrt{\frac{1}{8}}, \qquad s^{(2)} = \pm i \kappa_r \sqrt{\frac{3}{8}}.$$
 (4.131)

Since the phase speed of either wave corresponds to the Laplace parameter-wavenumber ratio, it follows that $c^{(2)} = c^{(1)}\sqrt{3}$. Noting that the shear and compressional wave velocities in the two-dimensional continuum are known to be related as $c_P = c_S\sqrt{3}$, and that this must also be the case for the lattice in the long wave limit, it follows that $s^{(1)}$ in equation (4.131) must be related to the shear wave, i.e. $s^{(1)} = s_S$, and that $s^{(2)}$ in equation (4.131) is related to the compressional wave, i.e. $s^{(2)} = s_P$. Since the positive and negative values for $s^{(1)}$ in equation (4.131) both yield the same expression for $D^{(h)}$, we find $D^{(1)} = D^{(h)} \left(s = s^{(1)} \right)$ as the relation for the shear wave. Accordingly, the positive and negative values for $s^{(2)}$ in equation (4.131) both yield the same expression for $D^{(h)}$ and thus, we find $D^{(2)} = D^{(h)} \left(s = s^{(2)} \right)$ as the relation for the compressional wave.

Figure 4.27 gives the resulting values for the amplitude ratios $D^{(1)}$ and $D^{(2)}$, and thereby shows the polarization of respectively the shear and compressional waves in the hexagonal half-plane, as a function of the angle θ , which describes the direction of wave propagation with respect to the *x*-axis. Here, Figure 4.27a gives the polarization in the long-wave limit, i.e. for $\kappa_r \to 0$, while Figure 4.27b shows the polarization for an arbitrary non-zero value of the wavenumber magnitude, here $\kappa_r = 5$. In both figures, the continuous red line gives the value for $D^{(1)}$, related to the shear wave, while the continuous blue line gives the value for

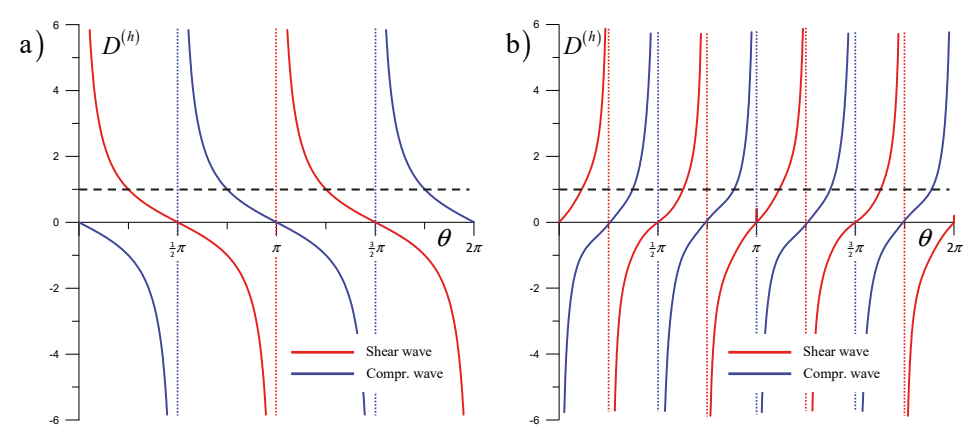


Figure 4.27: Amplitude ratios of the shear and compressional waves depending on the direction of wave propagation in the hexagonal half-plane: a) in the long-wave limit, i.e. for $\kappa_r \to 0$; b) for $\kappa_r = 5$.

 $D^{(2)}$, related to the compressional wave.

Note here that the resulting values for $D^{(h)}$ in the long-wave limit depicted in Figure 4.27a are not obtained straightforwardly by substituting $\kappa_r = 0$, as $D^{(1)}$ and $D^{(2)}$ are undefined for $\kappa_r = 0$ while both their numerators and denominators are equal to zero for this wavenumber. Additionally, applying l'Hôpital's rule does not suffice, as the derivatives of both numerator and denominator with respect to the wavenumber κ_r are also equal to zero at $\kappa_r = 0$. Instead, the results for the long-wave limit are obtained using a series expansion around $\kappa_r = 0$. This yields $D^{(1)}$ and $D^{(2)}$ as a function of the direction of wave propagation in the long-wave limit as:

$$D^{(1)}(\kappa_r \to 0) = \frac{\cos \theta}{\sin \theta}, \qquad D^{(2)}(\kappa_r \to 0) = -\frac{\sin \theta}{\cos \theta}. \tag{4.132}$$

Note here that the results for the long-wave limit are easily verified by comparison with the results obtained from substituting a small but non-zero value for the wavenumber κ_r into the original expressions for $D^{(1)}$ and $D^{(2)}$.

To interpret the results depicted in Figure 4.27, consider that $D^{(h)}$ describes the direction of the particle motion associated with the propagation of the shear and compressional waves for h=1 and h=2 respectively, as a ratio between the vertical and horizontal amplitudes. Consequently, the following typical values for $D^{(h)}$ are identified:

 $D^{(h)} = 0$: the wave amplitude in z-direction is equal to zero, while the wave amplitude in x-direction is non-zero. Therefore, the particle motion associated with the propagation of the corresponding wave is exclusively horizontal.

 $D^{(h)} = \pm \infty$: the wave amplitude in x-direction is equal to zero, while the wave amplitude in z-direction is not, so that the particle motion associated with the propagation of the corresponding wave is exclusively vertical.

 $D^{(h)} = \pm 1$: the horizontal and vertical wave amplitudes are equal in magnitude. The value $D^{(h)} = +1$ is given in Figure 4.27 by the dashed black line.

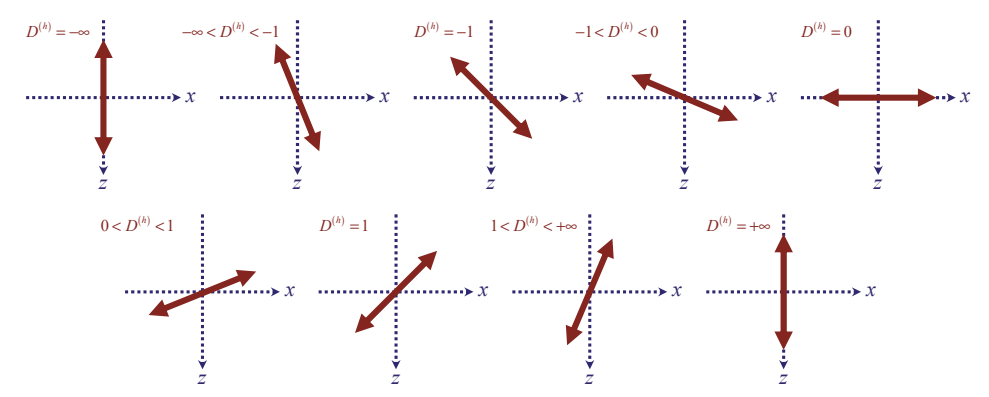


Figure 4.28: Direction of the particle motion in the half-plane of particles depending on the amplitude ratio.

The particle motions that correspond to these typical values for $D^{(h)}$ are depicted in Figure 4.28.

Accounting for the particle motion in the hexagonal half-plane as it depends on the value of $D^{(h)}$ according to Figure 4.28 and noting that the amplitude ratios in the long-wave limit, given by Figure 4.27a, match the amplitude ratios for the continuum, the results given by Figure 4.27a make perfect sense. As an example, let us first consider the wave propagation in x-direction, i.e. for $\theta = 0$. For the shear wave, we find $D^{(1)} = \pm \infty$, which corresponds to a vertical particle motion that is thus normal to the direction of wave propagation. For the compressional wave, we find $D^{(2)} = 0$ corresponding to a horizontal particle motion, thus in the direction of wave propagation. Accordingly, for the wave propagation in z-direction, i.e. for $\theta = \frac{\pi}{2}$, we find $D^{(1)} = 0$ and $D^{(2)} = \pm \infty$. Thus, for the shear wave propagating in z-direction the particle motion is horizontal, while for the compressional wave propagating in zdirection the particle motion is vertical. These particle motions correspond to what is commonly expected for the propagation of shear and compressional waves in the continuum. Here, note that it can straightforwardly be derived from the expressions for the horizontal and vertical displacements of the continuum in the Laplace-wavenumber domain that the amplitude ratios for the continuum are independent from the wavenumber magnitude. Consequently, the magnitude of the wavenumber has no influence on the direction-dependent polarization of the shear and compressional waves, so that Figure 4.27a is valid for the continuum for any magnitude of the wavenumber. Introducing the polar representation by substitution of equation (4.130) then shows that the expressions for $D^{(1)}$ and $D^{(2)}$ for the continuum coincide with those obtained for the hexagonal half-plane of particles in the longwave limit, as given by equation (4.132).

As illustrated by Figure 4.27b, which shows the results for a wavenumber magnitude $\kappa_r = 5$, changing the wavenumber magnitude significantly changes the direction-dependent polarization of the shear and compressional waves. For example, if we again consider the wave propagation in x-direction, i.e. for $\theta = 0$, we now find that $D^{(1)} = 0$ and $D^{(2)} = \pm \infty$; this means that for $\kappa_r = 5$ the shear wave propagating in x-direction is now associated with a horizontal particle motion, while the propagation of the compressional wave in x-direction

is now associated with a vertical particle motion. For the wave propagation in z-direction, i.e. for $\theta = \frac{\pi}{2}$, however, we still find that $D^{(1)} = 0$ and $D^{(2)} = \pm \infty$, which corresponds to the results found for the long-wave limit, i.e. for $\kappa_r \to 0$. Clearly, the predominance of the shear and compressional waves in a certain direction depends on the magnitude of the wavenumber.

The dependency of the shear and compressional wave amplitude ratios on the wavenumber magnitude is given in Figure 4.29, where Figure 4.29a and Figure 4.29b by approximation consider the wave propagation in x- and z-direction respectively. Since $D^{(h)}$ is undefined at both $\theta=0$ and $\theta=\frac{\pi}{2}$, Figure 4.29a gives $D^{(1)}$ and $D^{(2)}$ as a function of the wavenumber magnitude for $\theta=0.01$, while Figure 4.29b gives the wavenumber dependence of $D^{(1)}$ and $D^{(2)}$ for $\theta=\frac{\pi}{2}+0.01$.

Figure 4.29a shows that for small magnitudes of the wavenumber, $D^{(1)}$ mostly has a large nonzero value, i.e. $D^{(1)} >> 0$, which means that the propagation of the shear wave in x-direction for these wavenumbers is predominantly associated with a vertical particle motion. At these wavenumbers, $D^{(2)}$ is found to be equal to zero, which means that the propagation of the compressional wave in x-direction for these wavenumbers is associated with a horizontal particle motion only.

At a wavenumber magnitude $\kappa_r = \frac{4}{3}\pi$, which is exactly the wavenumber for which both the shear and the compressional wave propagating in x-direction correspond to the same frequency, the directionality switches. Figure 4.29a thus shows that for the wavenumber domain $\kappa_r = \left\langle \frac{4}{3}\pi, \frac{8}{3}\pi \right\rangle$, which includes the value $\kappa_r = 5$ for which the amplitude ratios are given in Figure 4.27b, the value for $D^{(1)}$ is now equal to zero, while the value of $D^{(2)}$ is nonzero, its magnitude is mostly rather large and becomes infinite for $\kappa_r = 2\pi$. Consequently, for this wavenumber domain, the propagation of the shear wave in x-direction is associated with a horizontal particle motion only, while the propagation of the compressional wave in x-direction for these wavenumbers is also predominantly associated with a horizontal particle motion. For the wavenumber domain $\kappa_r = \left\langle \frac{8}{3}\pi, 2\pi \right\rangle$, the directionality of the particle motion coincides with that of the wavenumber domain $\kappa_r = \left\langle 0, \frac{4}{3}\pi \right\rangle$, except that $D^{(1)}$ is negative on this domain. For increasing magnitudes of the wavenumber, the switching of the

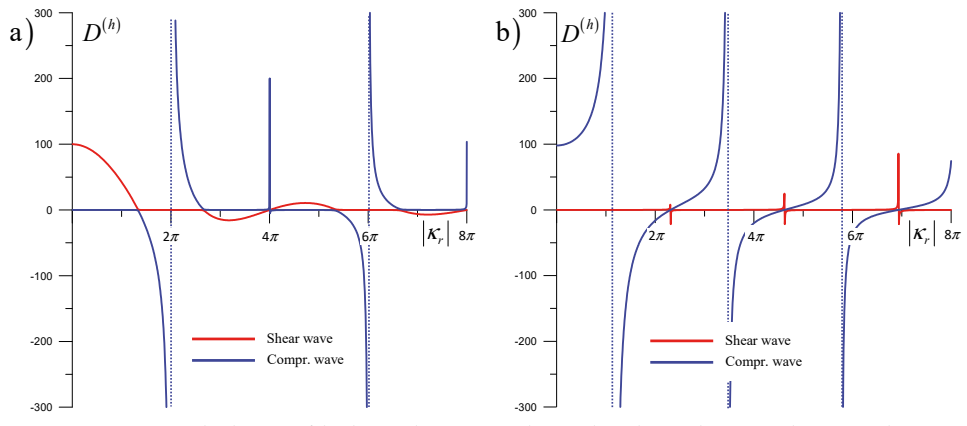


Figure 4.29: Amplitude ratios of the shear and compressional waves depending on the wavenumber magnitude: a) wave propagation in x-direction, i.e. $\theta \cong 0$; b) wave propagation in z-direction, i.e. $\theta \cong \frac{\pi}{2}$.

directionality of the particle motion associated with the wave propagation of the shear and compressional waves in x-direction repeats itself every 4π . This is in accordance with the Brillouin zones for waves propagating in the lattice in x-direction. The peaks at $\kappa_r = 4\pi j$, with j an integer, are associated with a zero frequency in the dispersion relation, so that at these wavenumbers, the phase speed of waves propagating through the hexagonal half-plane in x-direction is equal to zero.

For the propagation in z-direction, depicted in Figure 4.29b, it follows that for all wavenumbers the shear waves are associated with horizontal particle motion only, while the compressional waves are also predominantly associated with vertical particle motion. Only for wavenumbers $\kappa_r = \frac{4}{\sqrt{3}}\pi j$ with j an integer, the values for both $D^{(1)}$ and $D^{(2)}$ are undefined as these are the wavenumbers at which the phase speed of waves propagating in z-direction are equal to zero. For the wave propagation of shear and compressional waves in z-direction, the directionality of the particle motion repeats itself every $\frac{4}{\sqrt{3}}\pi$, in accordance with the corresponding Brillouin zones for the lattice.

The differences in wavenumber dependency for the propagation of shear and compressional waves in respectively x- and z-direction as depicted in Figure 4.29, can be attributed to the different geometry of the hexagonal half-plane in x- and z-directions. For a square lattice geometry, which has the same geometry in x- and z-directions, the wavenumber dependency for wave propagation in x- and z-directions are likely to be the same. Yet, choosing any other direction of wave propagation, will again change the wavenumber dependency, while only for the continuum, this dependency is direction independent. The fact that the wavenumber dependency for the propagation of shear and compressional waves is direction dependent, is thus a property of discrete particle systems. Additionally including different rheological elements, for example introducing shear elements, rather than only using axial elements, will also influence this behaviour.

4.7 The two-dimensional fully discrete BKV system

In this section, we discuss the two-dimensional fully discrete BKV system that is depicted in Figure 4.30 and is comprised of a hexagonal BKV lattice in the near field and a viscoelastic half-plane of particles in the far field. As before, there is an external time-dependent load applied at the particle with nodal coordinates $\mathbf{0}$,0 at the origin of the system. Each particle with nodal coordinates \mathbf{m} , \mathbf{n} inside the hexagonal BKV lattice has a mass $M^{\mathbf{m},\mathbf{n}}$ and the lattice has a distance ℓ . Principally, the parameters of the hexagonal BKV lattice in the near field may be varied such that it is described as an irregular lattice. For the hexagonal BKV lattice this means that only the average distance between adjacent particles initially equals ℓ , while for a regular lattice, such as depicted in Figure 4.30, the initial distance between any two adjacent particles always equals ℓ . For each BKV element between a particle \mathbf{m} , \mathbf{n} and an adjacent particle \mathbf{m} , \mathbf{n} , the Kelvin-Voigt element has a stiffness coefficient $K_{e;j}^{\mathbf{m},\mathbf{n}}$ and a critical friction force $F_{c;j}^{\mathbf{m},\mathbf{n}}$, while the Bingham element has a damping coefficient $C_{f;j}^{\mathbf{m},\mathbf{n}}$ and a critical friction force $F_{c;j}^{\mathbf{m},\mathbf{n}}$.

At its boundary the hexagonal BKV lattice is connected to a viscoelastic half-plane of particles. The location of the interface Γ between the lattice and the half-plane is chosen at

such a distance from the origin that nonlinearities due to the applied loading only occur in the vicinity of the load and never reach the interface. Here, the distance between the origin of the near-field lattice, i.e. the loaded particle, and any particle at the interface Γ is bridged by N rheological elements, where N equals the nodal coordinate of the horizontal segment of the interface. As a result, the number of particles in the hexagonal BKV lattice are found in terms of N as $\frac{N+1}{2}(3N+2)$ and the number of rheological elements in the lattice is found as $\frac{N}{2}(9N+5)$.

To eliminate any unwanted wave reflections from the interface Γ between the lattice and the half-plane, the geometry of the cells in the interior of the half-plane matches the geometry of the cells in the interior of the BKV lattice and the material parameters of the half-plane are matched with the linear material parameters of the BKV lattice. The half-plane of particles is described as a regular lattice, so that the initial distance between any two adjacent particles in the half-plane is equal to the distance ℓ . Additionally, since nonlinearities do not have to be accounted for in the half-plane of particles, the interaction between its adjacent particles is described by Kelvin-Voigt elements with a constant stiffness coefficient K_e and a constant damping coefficient Ce. Furthermore, since nonlinearities do not reach the interface, the Bingham segments of the BKV elements that are connected to the interface are not activated and these elements behave as Kelvin-Voigt elements, and their stiffness and damping respectively match the stiffness and damping of the Kelvin-Voigt elements in the far-field domain. Note here that as long as the material parameters of the hexagonal lattice and the discrete farfield match, the material parameters of the two-dimensional fully discrete system do not necessarily have to be related to macromaterial properties, such as density and Young's modulus. Nevertheless, to enable a comparison between the fully discrete and the discrete-continuous

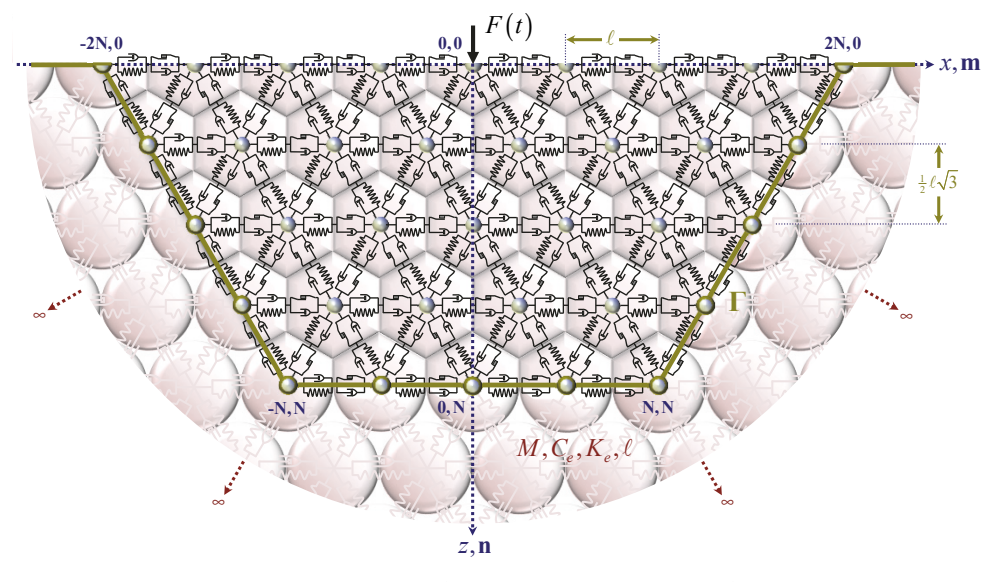


Figure 4.30: The two-dimensional fully discrete BKV system consisting of a hexagonal BKV lattice and a viscoelastic half-plane of particles

systems, the same macromaterial properties are adopted for both systems and the parameters of the fully discrete system may be derived in accordance with those derived for the discrete-continuous system.

In the following, we will first regard the interface Γ and the associated properties of the two-dimensional fully discrete system in further detail and discuss the corresponding differences with the two-dimensional discrete-continuous system. Then, in Section 4.7.2, the governing equations are given for the particles at the interface Γ in both the Laplace and the time domains that include the interaction with the half-plane of particles employing the boundary formulation presented in Section 4.3. The governing system of equations for the two-dimensional fully discrete system is completed by including the governing equations for the particles in the interior and at the surface of the hexagonal BKV-lattice in Section 4.7.3. Subsequently, Section 4.7.4 regards the viscoelastic response of the two-dimensional fully discrete BKV system in comparison to the response of the full viscoelastic half-plane of particle. Finally, in Section 4.7.5, the nonlinear response of the two-dimensional fully discrete BKV system is presented and the performance of the viscoelastic half-plane of particles as a boundary to the hexagonal BKV-lattice is discussed.

4.7.1 Interface properties of the fully discrete system

In Figure 4.30, the interface Γ between the near and the far field of the two-dimensional fully discrete system is given by a straight line between the corner points of the hexagonally shaped BKV lattice in the near field. The chosen shape of the interface may seem evident, but this shape is possible for the fully discrete system only because the reaction forces along the interface exist at the boundary particles as point loads. Thereby, the interaction between the BKV lattice and the half-plane of particles exclusively exists at the boundary particles. Nevertheless, the chosen shape of the interface is not arbitrary as it directly determines the configuration of the boundary cells.

Note here that, in comparison, for the two-dimensional discrete-continuous system, previously depicted in Figure 3.22, choosing the interface Γ to be straight between the boundary particles is not a valid option. This is because in the discrete-continuous system, the reaction force at any of the lattice boundary particles must match the resultant of the tractions along the continuum boundary obtained by integrating the tractions over a representative domain of the interface Γ . To determine the corresponding Green's functions of the continuum, and thereby the response of the continuum to its interaction with the near-field lattice, the shape of the interface Γ is required to be horizontal in the region of each boundary particle. Adjusting the shape of the interface Γ accordingly results in the interface Γ for the discrete-continuous system depicted in Figure 3.22. The fact that constructing an artificial shape of the interface is not a necessity for the fully discrete system is a clear advantage over the discrete-continuous system.

Accounting for the shape of the interface Γ , Figure 4.31 depicts the area that the cells of each particle represent within the hexagonal BKV-lattice. Assuming this lattice to be regular and homogeneous, the depicted hexagon can be considered as the elementary unit of the lattice, where the area of the unit hexagon straightforwardly follows from the distance ℓ . For

the particles in the interior of the particle half-plane, the area of the corresponding cells match the unit hexagon and their mass is denoted as the unit mass M. Based on the area that the cells of the other particles represent their relative or dimensionless masses can straightforwardly be determined. The masses of the particles along the interface Γ thus vary depending on the location along the interface. For all cell types, the dimensionless particle mass is given in the table accompanying Figure 4.31. Here, note that only for the particles at the corners of the interface, respectively denoted as particles iv and v, the masses in the fully discrete system differ from those in the discrete-continuous system.

In addition to the masses of the boundary particles, also the rheological elements at the interface Γ that are situated in between adjacent boundary particles, differ from those inside the half-plane. By choosing the interface Γ as a straight line between the boundary particles, the inner boundary cells effectively correspond to half an inner cell. As previously explained in Section 2.4.1 and corresponding to the surface elements, the rheological elements at the interface have half the stiffness and half the damping of the rheological elements in the interior of the lattice.

Note here that, in line with the approach for the one-dimensional fully discrete system discussed in Section 4.1.1, the position and the shape of the interface Γ may be freely chosen as long as the fully discrete system is homogeneous in the vicinity of the interface. Changing the path of the interface Γ compared to the configuration depicted in Figure 4.31 however, changes the representative area of the corresponding cells and thereby changes the mass of the boundary particles. Nevertheless, the cumulative mass of an boundary particle and the corresponding sub-particle at the boundary of the half-plane must together always equal the unit mass M. Furthermore, changing the path or location of the interface also changes the

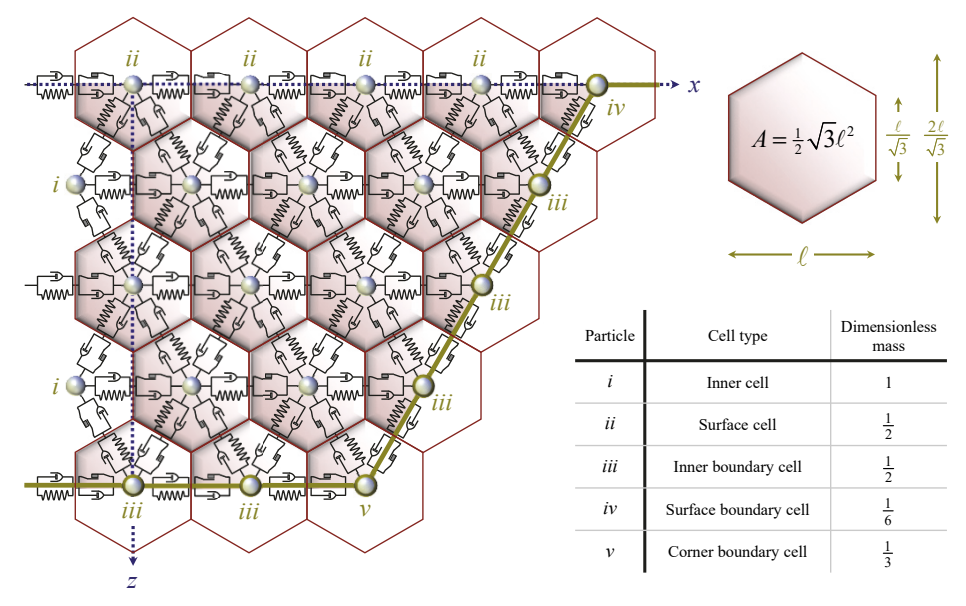


Figure 4.31: Representative area of the cells and the corresponding mass of the particles in the hexagonal BKV lattice.

material parameters of some of the rheological elements in the cells of the boundary particles. This is again in correspondence with the one-dimensional fully discrete system discussed in Section 4.1.1. It is however emphasized here that choosing a different configuration for the interface does not only change the equations of motion of the boundary particles in the hexagonal BKV lattice, but it also changes the expressions for the Green's reactions forces in the half-plane of particles that were previously derived in Section 4.4.4. In this thesis, the possible different configurations for the interface Γ are not further investigated and the configuration of the interface according to Figure 4.31 is adopted.

4.7.2 System of boundary integral equations

While the force-displacement relations at the interface Γ , i.e. the dynamic stiffness and compliance matrices, are derived in Section 4.3, this section presents the governing equations for the boundary particles that include the interaction with the viscoelastic half-plane of particles.

In correspondence with the one-dimensional fully discrete system, we normalize the interface equation by introducing the following dimensionless parameters for time, displacement and mass:

$$t = t_{\text{dim}} \omega_0, \quad u^{\mathbf{m},\mathbf{n}} = \frac{u_{\text{dim}}^{\mathbf{m},\mathbf{n}}}{\ell}, \quad M^{\mathbf{m},\mathbf{n}} = \frac{M_{\text{dim}}^{\mathbf{m},\mathbf{n}}}{M}.$$

Here, the subscript 'dim' denotes the dimensional parameters and ω_0 is the particle frequency of both the regular hexagonal BKV lattice and the half-plane of particles. Furthermore, the damping is normalized using the damping ratio $\zeta = C_e/C_{crit}$, where C_{crit} is the critical particle damping. The particle frequency and critical particle damping are derived for the hexagonal lattice in Appendix B.4 and obtained as $\omega_0 = \sqrt{3K_e/M}$ and as $C_{crit} = \frac{2}{3}M\omega_0$ respectively. As explained in Appendix B.3, introducing these dimensionless parameters yields the following relations between respectively the dimensionless damping, stiffness and force, and their dimensional counterparts as:

$$C_{e;j}^{\mathbf{m},\mathbf{n}} = \frac{C_{e;j,\text{dim}}^{\mathbf{m},\mathbf{n}}}{\frac{3}{2}\,C_{crit}}, \quad K_{e;j}^{\mathbf{m},\mathbf{n}} = \frac{K_{e;j,\text{dim}}^{\mathbf{m},\mathbf{n}}}{M\,\omega_0^2} = \frac{K_{e;j,\text{dim}}^{\mathbf{m},\mathbf{n}}}{3\,K_e}, \quad F^{\mathbf{m},\mathbf{n}} = \frac{F_{\text{dim}}^{\mathbf{m},\mathbf{n}}}{M\,\omega_0^2\ell} = \frac{F_{\text{dim}}^{\mathbf{m},\mathbf{n}}}{3\,K_e\ell}.$$

Here, the numerator j refers to the BKV element between the particle \mathbf{m}_{i} , \mathbf{n}_{i} and an adjacent particle \mathbf{m}_{i} , \mathbf{n}_{j} .

To account for the response of the viscoelastic half-plane of particles as the far-field domain for the hexagonal BKV lattice, the corresponding force-displacement relation at the interface Γ must be incorporated in the equations of motion for the boundary particles. Even though the properties of the far-field domain determine the dynamic stiffness relation at the boundary, the expression for the equations of motion of the boundary particles remains the same and is thereby identical to system of interface equations derived and presented for the two-dimensional discrete-continuous system in Section 3.6.2. Accordingly, the Laplace

domain system of equations for the boundary reads:

$$\underline{\tilde{u}}_{lnt} + \underline{\tilde{\beta}}(s) \left(\underline{\underline{M}}_{lnt} s^2 \underline{\tilde{u}}_{lnt} + \left(\underline{\underline{C}}_{lnt} s + \underline{\underline{K}}_{lnt}\right) \underline{\tilde{u}}\right) = 0 \tag{4.133}$$

Here, $\tilde{\beta}(s)$ is the dynamic compliance matrix according to equation (4.44) and $\underline{\underline{M}}_{lnt}$, $\underline{\underline{C}}_{lnt}$ and $\underline{\underline{K}}_{lnt}^{\underline{\underline{m}}}$ are respectively the mass, damping and stiffness matrices for the particles along the interface. Furthermore, the vector $\underline{\tilde{u}}_{lnt}$ contains only the Laplace domain displacements of the boundary particles, while the vector $\underline{\tilde{u}}$ also includes the Laplace domain displacements of all particles that are adjacent to the boundary particles.

As derived in Section 3.6.2, successively applying the inverse Laplace transform to equation (4.133), differentiating the resulting time domain equation using Leibniz' rule for differentiation of integrals and applying the linearization for large elongations according to Appendix A.2, the governing system of interface equations for the two-dimensional fully discrete system is expressed in the time domain as:

$$\underline{\dot{u}}_{Int} + \underbrace{\beta}_{=}(0)\underline{F}_{Int}(t) + \int_{0}^{t} \underline{\dot{\beta}}(t-\tau)\underline{F}_{Int}(\tau)d\tau = 0 \tag{4.134}$$

Here, $\beta(0)$ is the time domain dynamic compliance matrix at t = 0 and $\dot{\beta}(t)$ is the time domain admittance matrix time, which may either be obtained as the time derivative of the time domain dynamic compliance matrix or by applying the inverse Laplace transform to the corresponding Laplace domain force-velocity relation. Furthermore, $\underline{F}_{lnt}(t)$ contains the forces that are applied by the boundary particles to the far-field domain and reads:

$$\underline{F}_{lnt}(t) = \underline{M}_{lnt}\underline{\ddot{u}}_{lnt} + \underline{C}_{lnt}\underline{\dot{u}} + \underline{K}_{lnt}\underline{u} + \underline{F}_{\varepsilon,lnt}$$

$$\tag{4.135}$$

In correspondence with the expression for the time domain dynamic compliance obtained for the viscoelastic cascade in Section 4.1.3, all terms in the dynamic compliance matrix $\beta(t)$ go to zero for $t \downarrow 0$. As a consequence, the accelerations of the boundary particles \overline{at} the current time step are only present in equation (4.134) inside the convolution integral and their contribution thereby depends on the size of the time step used to evaluate the convolution integral. As explained in Section 4.2.3, the resulting boundary formulation is numerically unstable and therefore, we differentiate the boundary formulation a second time to obtain a nonzero acceleration term outside the convolution integral. Using Leibniz' rule for differentiation of integrals to apply this time differentiation to equation (4.134), yields the equation of motion for the boundary particles at the lattice boundary as:

$$\underline{\ddot{u}}_{lnt} + \underline{\dot{\beta}}(0)\underline{F}_{lnt}(t) + \int_{0}^{t} \underline{\ddot{\beta}}(t-\tau)\underline{F}_{lnt}(\tau)d\tau = 0$$
(4.136)

Here, $\dot{\beta}(0)$ is the time domain admittance matrix at t=0 and $\ddot{\beta}(t)$ is the time derivative of the time domain admittance matrix, or the second time derivative of the time domain dynamic compliance matrix. Due to applying the time differentiation a second time and noting that the diagonal terms of $\dot{\beta}(0)$ are nonzero, the boundary integral equation (4.136) now includes, not one, but two acceleration terms that are independent of the convolution integral, and thereby equation (4.136) is numerically robust. Here, note that the manipulation of the boundary integral equation to properly isolate the contribution of the acceleration is required only because we described the Laplace domain interface relation, given by equation (4.133), in terms of the dynamic compliance matrix. After all, if we would have used the dynamic stiffness instead, the interaction force vector $\underline{F}_{Int}(t)$, as well as the acceleration term it contains, would not be in the convolution integral. Nevertheless, due to the increase of the dynamic stiffness with frequency, this is not an option.

By applying the linearization for large elongations, the total elongation of the BKV elements in the lattice at a time t is described in terms of the particle displacements during the current time step dt, included in the displacement vector \underline{u} , and the elongations of the involved BKV elements at time t-dt. The forces in the springs of the involved BKV elements that follow from these elongations at time t-dt are given by the vector $\underline{F}_{\varepsilon,lnt}$. Note here that even though the BKV elements in the boundary cells may be considered to behave viscoelastically and therefore the elongations of these elements will be small compared to the elongations closer to the load source, we include the linearization for large elongations in the system of interface equations to make sure that the governing system of equations for the two-dimensional fully discrete system is uniform throughout.

Equation (4.136) gives the general system of equations of motion for the boundary particles of the hexagonal BKV lattice. Inserting the time domain dynamic compliance matrix for the viscoelastic half-plane of particles obtained by applying the inverse Laplace transform to the Laplace domain dynamic compliance matrix given by equation (4.44) completes the interface relations for the two-dimensional fully discrete system.

4.7.3 Equations of motion for interior and surface particles

This section presents the governing equations of motion for the interior and surface particles of the hexagonal BKV lattice. Together with the governing equations of motion for the boundary particles derived in the previous section, these equations complete the governing system of equations of motion for the two-dimensional fully discrete system.

The equations of motion for stick and slip presented in respectively Sections 2.4.3 and 2.4.4 are derived for the particular case that the BKV elements of the considered inner cell are either all in stick, or all in slip. These equations of motion do not serve to properly describe the behaviour of the particles inside the hexagonal BKV lattice because the different BKV elements in a cell may simultaneously be in different motion states. Additionally, the motion states of all BKV elements in the lattice, that is if they are not part of a boundary cell, may change and vary individually depending on whether and when any of the state-transition thresholds, given in Section 2.4.6, are met. Consequently, for every state-transition that occurs, the equations of motion for the hexagonal BKV lattice must be updated. In the

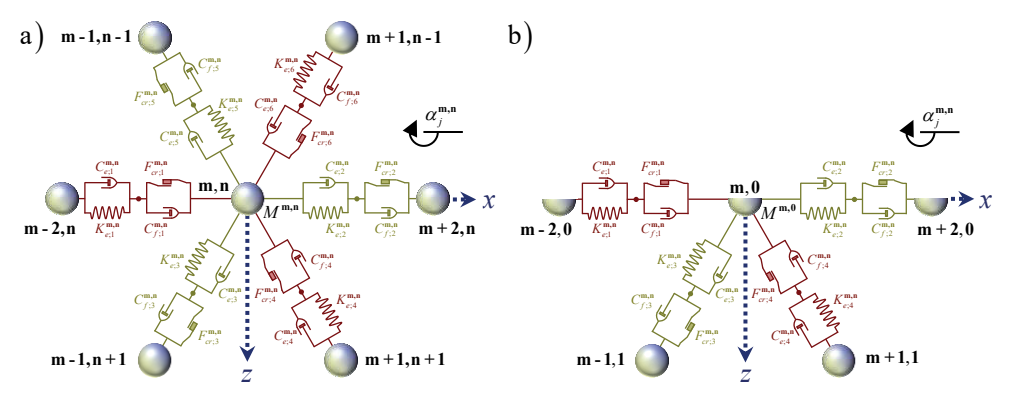


Figure 4.32: Cell configurations in the hexagonal BKV lattice: a) Inner cell; b) Surface cell.

following, we present a full description of the governing system of equations of motion for the interior and surface particles of the hexagonal BKV lattice that accounts for any combination of motion states throughout the lattice at any given time. Next to accounting for stick and slip in the governing system of equations of motion, also the occurrence of lock, previously discussed in Section 2.4.5, is taken into account.

Figure 4.32a and Figure 4.32b depict the cell configurations for a particle **m,n** respectively in the interior and at the surface of the hexagonal BKV lattice. Note here that within each cell the BKV elements have two different orientations. The BKV elements with the Kelvin-Voigt element directly connected to the particle **m,n** are depicted in green, while the BKV elements with the Bingham element directly connected to the particle **m,n** are depicted in dark red. Accounting for the two different orientations, as well as accounting for the variation in motion states, the general governing equations of motion for any free particle, that thus either exists in the interior or at the surface of the hexagonal BKV lattice, read:

$$M^{\mathbf{m},\mathbf{n}} \ddot{u}_{x}^{\mathbf{m},\mathbf{n}} - \sum_{j \in j_{Kl'}^{\mathbf{m},\mathbf{n}}} \left(C_{e;j}^{\mathbf{m},\mathbf{n}} \dot{e}_{state;j}^{\mathbf{m},\mathbf{n}} + K_{e;j}^{\mathbf{m},\mathbf{n}} e_{state;j}^{\mathbf{m},\mathbf{n}} \right) \cos \alpha_{j}^{\mathbf{m},\mathbf{n}} - \sum_{j \in j_{lock}^{\mathbf{m},\mathbf{n}}} F_{lock;j}^{\mathbf{m},\mathbf{n}} \cos \alpha_{j}^{\mathbf{m},\mathbf{n}} - \sum_{j \in j_{lock}^{\mathbf{m},\mathbf{n}}} F_{lock;j}^{\mathbf{m},\mathbf{n}} \cos \alpha_{j}^{\mathbf{m},\mathbf{n}} = 0$$

$$M^{\mathbf{m},\mathbf{n}} \vdots m,\mathbf{n} = \sum_{j \in j_{lock}^{\mathbf{m},\mathbf{n}}} \left(C_{lock}^{\mathbf{m},\mathbf{n}} \dot{e}_{j}^{\mathbf{m},\mathbf{n}} + K_{lock}^{\mathbf{m},\mathbf{n}} e_{j}^{\mathbf{m},\mathbf{n}} \right) \sin \alpha_{j}^{\mathbf{m},\mathbf{n}}$$

$$(4.137)$$

$$M^{\mathbf{m},\mathbf{n}} \ddot{u}_{z}^{\mathbf{m},\mathbf{n}} - \sum_{j \in j_{KV}^{\mathbf{m},\mathbf{n}}} \left(C_{e;j}^{\mathbf{m},\mathbf{n}} \dot{e}_{state;j}^{\mathbf{m},\mathbf{n}} + K_{e;j}^{\mathbf{m},\mathbf{n}} e_{state;j}^{\mathbf{m},\mathbf{n}} \right) \sin \alpha_{j}^{\mathbf{m},\mathbf{n}} - \sum_{j \in j_{lock}^{\mathbf{m},\mathbf{n}}} F_{lock;j}^{\mathbf{m},\mathbf{n}} \cos \alpha_{j}^{\mathbf{m},\mathbf{n}} = 0$$

$$(4.138)$$

Here, $j_{KV}^{\mathbf{m,n}}$ and $j_{B}^{\mathbf{m,n}}$ denote the set of BKV elements in the cell that respectively have the Kelvin-Voigt element or the Bingham element directly connected to the particle $\mathbf{m,n}$, while $j_{lock}^{\mathbf{m,n}}$ denotes the set of elements in the cell that are in lock-state. Furthermore, $K_{e;j}^{\mathbf{m,n}}$ and $C_{e;j}^{\mathbf{m,n}}$ are respectively the stiffness and damping in the corresponding Kelvin-Voigt elements. The elongation $e_{state;j}^{\mathbf{m,n}}$, the elongation rate $\dot{e}_{state;j}^{\mathbf{m,n}}$ and the force $F_{state;j}^{\mathbf{m,n}}$ all follow from the motion state of the considered BKV element. Note here that for an element in stick or in slip,

and that is therefore not in lock, the force $F_{lock;i}^{m,n}$ does not have to be considered.

Expressions for Stick

If a BKV element between particles \mathbf{m} , \mathbf{n} and \mathbf{m}_{i} , \mathbf{n}_{i} is in stick-state, we find:

$$e_{state;j}^{\mathbf{m,n}} = e_{j}^{\mathbf{m,n}} - \varepsilon_{B;j}^{\mathbf{m,n}}, \qquad F_{state;j}^{\mathbf{m,n}} = C_{e;j}^{\mathbf{m,n}} \dot{e}_{state;j}^{\mathbf{m,n}} + K_{e;j}^{\mathbf{m,n}} e_{state;j}^{\mathbf{m,n}}.$$

Note here that the expression for $e_{state;j}^{\mathbf{m,n}}$ is also incorporated in the expression for $F_{state;j}^{\mathbf{m,n}}$.

Expressions for Slip

If the BKV element between particles \mathbf{m} , \mathbf{n} and $\mathbf{m}_{\mathbf{j}}$, $\mathbf{n}_{\mathbf{j}}$ is in slip-state, we find the elongation of the considered element and the force at the particle \mathbf{m} , \mathbf{n} as:

$$e_{\textit{state};j}^{\mathbf{m,n}} = e_{\textit{KV};j}^{\mathbf{m,n}}, \qquad F_{\textit{state};j}^{\mathbf{m,n}} = C_{f;j}^{\mathbf{m,n}} \dot{e}_{B;j}^{\mathbf{m,n}} + F_{cr;j}^{\mathbf{m,n}} \operatorname{sgn} F_{B:\textit{slip};j}^{\mathbf{m,n}}.$$

For any BKV element that is in slip-state, the equation of motion for the slip-node intermediate particles \mathbf{m} , \mathbf{n} and \mathbf{m}_i , \mathbf{n}_i must be added to the system of equations of motion. The corresponding equation of motion, previously given in its dimensional form by equation (2.38), reads:

$$C_{e;j}^{\mathbf{m,n}} \dot{\mathbf{c}}_{KV;j}^{\mathbf{m,n}} + K_{e;j}^{\mathbf{m,n}} e_{KV;j}^{\mathbf{m,n}} - C_{f;j}^{\mathbf{m,n}} \dot{\mathbf{c}}_{B;j}^{\mathbf{m,n}} - F_{cr;j}^{\mathbf{m,n}} \operatorname{sgn} F_{B:slip;j}^{\mathbf{m,n}} = 0$$

$$(4.139)$$

Here, $C_{f;j}^{\mathbf{m,n}}$ and $F_{cr;j}^{\mathbf{m,n}}$ are respectively the dimensionless damping and critical friction force of the Bingham element. They are found in terms of their dimensional counterparts as:

$$C_{f;j}^{\mathbf{m,n}} = \frac{C_{f;j,\text{dim}}^{\mathbf{m,n}}}{\frac{3}{2}C_{crit}}, \qquad F_{cr;j}^{\mathbf{m,n}} = \frac{F_{cr;j,\text{dim}}^{\mathbf{m,n}}}{3K_{c}\ell}.$$

Expressions for Lock

If a BKV element between particles \mathbf{m} , \mathbf{n} and $\mathbf{m}_{\mathbf{j}}$, $\mathbf{n}_{\mathbf{j}}$ is in lock-state, we find:

$$e_{\textit{state};j}^{\mathbf{m},\mathbf{n}} = e_{j}^{\mathbf{m},\mathbf{n}} - \varepsilon_{B;j}^{\mathbf{m},\mathbf{n}}, \qquad F_{\textit{state};j}^{\mathbf{m},\mathbf{n}} = C_{e;j}^{\mathbf{m},\mathbf{n}} \dot{e}_{\textit{state};j}^{\mathbf{m},\mathbf{n}} + K_{e;j}^{\mathbf{m},\mathbf{n}} e_{\textit{state};j}^{\mathbf{m},\mathbf{n}} \qquad F_{\textit{lock};j}^{\mathbf{m},\mathbf{n}} = K_{\textit{lock};j}^{\mathbf{m},\mathbf{n}} + \Delta D_{0;j}^{\mathbf{m},\mathbf{n}} \Big).$$

Here, the first two terms coincide with the expressions for stick, so that accordingly the expression for $e^{\mathbf{m},\mathbf{n}}_{state;j}$ must be incorporated in the expression for $F^{\mathbf{m},\mathbf{n}}_{state;j}$. In the third term, $K^{\mathbf{m},\mathbf{n}}_{lock;j}$ is the stiffness of the additional spring that is placed parallel to the BKV element to significantly reduce the relative motion between the particles \mathbf{m},\mathbf{n} and $\mathbf{m}_{\mathbf{j}},\mathbf{n}_{\mathbf{j}}$. The stiffness of this additional spring is chosen to be a factor φ_{lock} larger than the stiffness of the spring in the BKV element, i.e. $K^{\mathbf{m},\mathbf{n}}_{lock;j} = \varphi_{lock}K^{\mathbf{m},\mathbf{n}}_{e;j}$. Instinctively, it would seem logical to choose a rather large value for this stiffness-factor to fully impede the relative motion between the two

particles involved. Choosing the value for φ_{lock} too large however, will lead to ill-conditioned matrices in the system of differential equations and is therefore not favourable, while choosing a value $\varphi_{lock} = 5$ is more than sufficient to significantly reduce the relative motion between the particles \mathbf{m} , \mathbf{n} and \mathbf{m}_{i} , \mathbf{n}_{i} , and to obtain the intended effect. Furthermore, $\Delta D_{0;j}^{\mathbf{m},\mathbf{n}}$ is the length reduction of the BKV element at which lock occurs. The value for $\Delta D_{0;j}^{\mathbf{m},\mathbf{n}}$ may be obtained as the difference between the initial distance $D_{0;j}^{\mathbf{m},\mathbf{n}}$ between the particles \mathbf{m} , \mathbf{n} and \mathbf{m}_{j} , \mathbf{n}_{j} and the threshold distance $D_{\min;j}^{\mathbf{m},\mathbf{n}}$ at which lock occurs in the considered element.

Independent of the motion states and accounting for the linearization for large elongations according to Appendix A.2, the system of equations of motion for all free particles in the hexagonal lattice, being all particles not located at the lattice boundary, can be expressed in matrix format as:

$$\underline{\underline{M}}_{free} \underline{\ddot{u}}_{free} + \underline{\underline{C}}_{free} \underline{\dot{u}} + \underline{\underline{K}}_{free} \underline{u} + \underline{F}_{\varepsilon, free} + \underline{F}_{cr, free} = \underline{F}_{ext}$$
(4.140)

Here, $\underline{\underline{M}}_{free}$, $\underline{\underline{C}}_{free}$ and $\underline{\underline{K}}_{free}$ are respectively the mass, damping and stiffness matrices exclusively for all free particles in the hexagonal lattice. Here, the matrix $\underline{\underline{C}}_{free}$ contains the damping of both the Bingham and the Kelvin-Voigt elements in the lattice. Additionally, the vector $\underline{F}_{\varepsilon,free}$ contains the contributions of the elongations $\varepsilon_j^{\text{m,n}}$ of all BKV elements at time t-dt to the system of equations of motion, which follow from the applied linearization for large elongations, while the vector $\underline{F}_{cr,free}$ contains all terms related to the critical friction force of the Bingham elements. Finally, the vector \underline{F}_{ext} contains any forces that are externally applied to the hexagonal lattice.

Equations (4.136) and (4.140) together give the complete governing system of equations of motion for the two-dimensional fully discrete system.

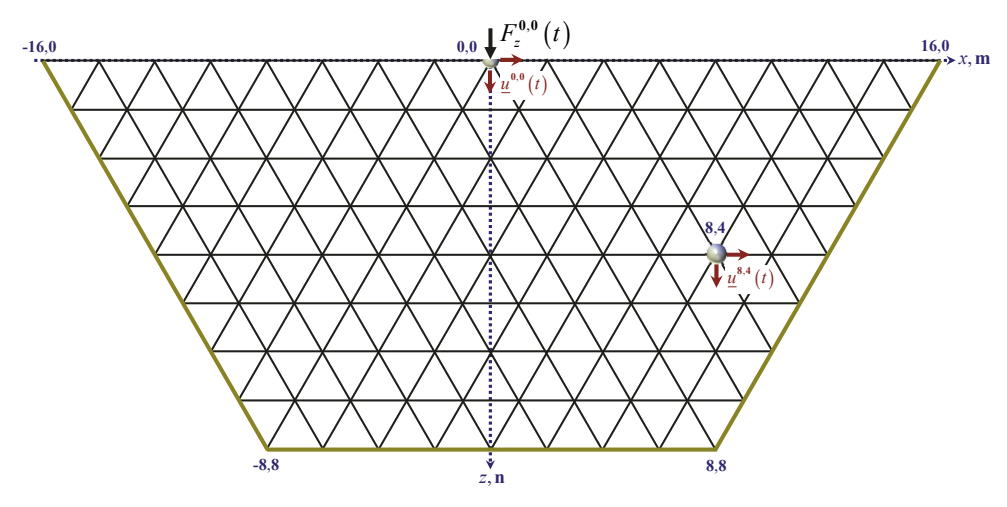


Figure 4.33: Mesh of the hexagonal lattice with dimension N equal to 8.

4.7.4 Linear response of the fully discrete BKV system

This section presents and discusses the response of the fully discrete BKV system for the case that the occurrence of nonlinear phenomena is not allowed for in the near-field domain and its response is exclusively viscoelastic. Using a boundary formulation derived from a far-field that is modelled as a viscoelastic half-plane of particles, the resulting system represents a homogeneous medium and its response is completely viscoelastic. To show that the equations of motion for the system are well formulated and the approach used is valid, the viscoelastic response of the fully discrete BKV system is compared to the response of the viscoelastic half-plane of particles, which should be expected to match exactly.

The hexagonal BKV-lattice considered here has a dimension N equal to 8 and is depicted in Figure 4.33. This regular lattice consists of 117 particles and 308 Kelvin-Voigt elements as we here consider the viscoelastic response exclusively. The interparticle distance in the lattice is chosen as $\ell=0.2$ m and the third dimension is arbitrarily chosen as dy=1 m. Based on the macromaterial properties used throughout this thesis, the mass of the particles in the hexagonal lattice is found as M=69.28 kg and the stiffness of the springs in the lattice is found as $K_e=18.48$ MN/m. This yields the particle frequency of the hexagonal lattice as $\omega_0=\sqrt{3K_e/M}=894,4$ rad/s and its critical damping as $C_{crit}=\frac{2}{3}M\omega_0=41.31$ kNs/m. Furthermore, the damping ratio is chosen as $\zeta=0.2$, so that the dashpots in the hexagonal lattice have a damping coefficient $C_e=8.26$ kNs/m.

In this section, we consider the response of the viscoelastic discrete systems to a vertical single-sinus pulse load $F_z(t)$ applied at particle ${\bf 0},{\bf 0}$, located at the origin of the lattice. Figure 4.34a gives the frequency dependency of the real part, the imaginary part and the absolute value of the single-sinus pulse load in the Laplace domain for an amplitude $\bar{F}=0.1$ MN and a dimensionless angular frequency $\Omega_F=0.5$ for $s=i\Omega$. This load yields the vertical Laplace domain displacement response of particle ${\bf 0},{\bf 0}$ that is depicted in Figure 4.34b for both the fully discrete BKV system and the half-plane of particles. Even though the frequency domain dependency of the applied load at particle ${\bf 0},{\bf 0}$ in Figure 4.34a and the corresponding response in Figure 4.34b are given for different frequency ranges, it is clear from comparing

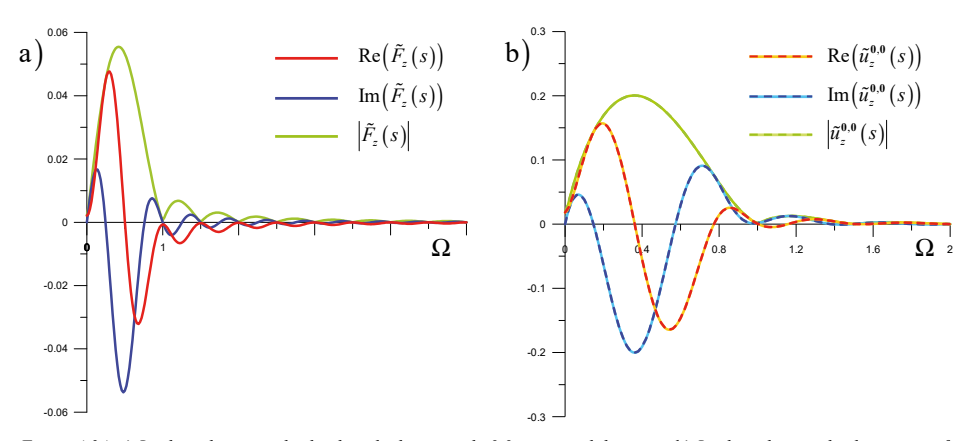


Figure 4.34: a) Laplace domain pulse load applied at particle 0.0 in vertical direction; b) Laplace domain displacements of particle 0.0 in the half-plane of particles (continuous lines) and the fully discrete BKV system (dashed lines).

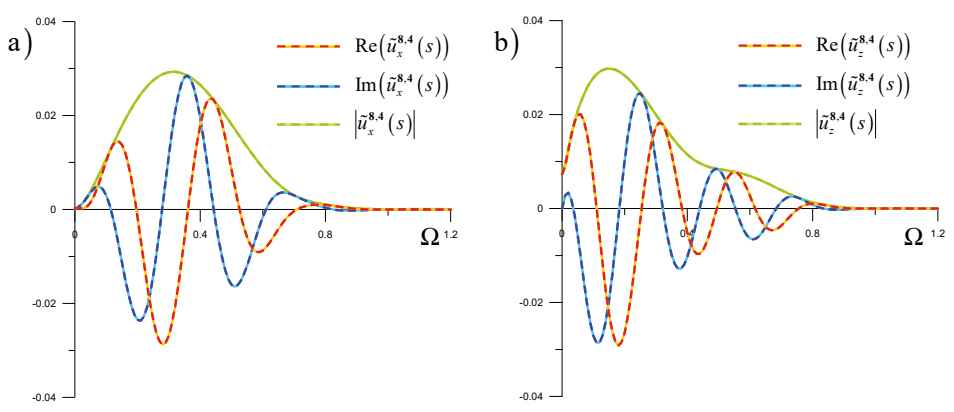


Figure 4.35: Laplace domain displacements of particle 8.4 in the half-plane of particles (continuous lines) and the fully discrete BKV system (dashed lines): a) horizontal displacements; b) vertical displacements.

the two graphs that the shapes of the real and imaginary parts of the Laplace domain displacements are similar to the shapes of the real and imaginary parts of the Laplace domain loading.

Figure 4.35a and Figure 4.35b respectively give the horizontal and vertical Laplace domain displacements of particle 8,4 for both the fully discrete BKV system and the half-plane of particles. Here, note that the location of particle 8,4 is given in Figure 4.33. The continuous lines in Figure 4.34b and Figure 4.35 give the real part, the imaginary part and the absolute value of the vertical Laplace domain displacements of respectively particle 0.0 and particle 8,4 in the half-plane of particles, which are obtained directly from the Green's displacements of the particles in the half-plane of particles. Furthermore, the dashed lines in Figure 4.34b and Figure 4.35 give the corresponding Laplace domain displacements for the particles in the fully discrete BKV system. These displacements have been obtained by solving the algebraic system of Laplace domain equations of motion for the hexagonal lattice that incorporates the dynamic compliance of the discrete far-field domain in its boundary formulation. From the comparison of the Laplace domain displacements presented by Figure 4.34b and Figure 4.35, it is evident that both models yield the exact same displacement response in the Laplace domain. This confirms that, at least for the Laplace domain, the implemented fully discrete BKV system incorporates the response of the far-field domain, modelled as a viscoelastic half-plane of particles, correctly.

The time domain displacement response of particle **0,0** is depicted in Figure 4.36. Here, Figure 4.36a gives the overall vertical displacement response for both the half-plane of particles (HPoP) and the fully discrete BKV system (BKV), while Figure 4.36b gives a close-up at a 40 times smaller scale to provide a more detailed comparison of the response for different approaches used. The continuous light blue line and the dashed blue line in Figure 4.36 give the displacements of the loaded particle in respectively the half-plane of particles and the fully discrete BKV system, which are both obtained by applying the inverse Laplace transform to the Laplace domain displacements previously presented in Figure 4.34. For the fully discrete BKV system this means that the time domain displacements originate from first

solving the algebraic system of equations of motion in the Laplace domain and then applying the inverse Laplace transform. This approach is here referred to as the frequency domain solution, or the FD-solution. Since the Laplace domain displacements for the fully discrete BKV system and the half-plane of particles were previously shown by Figure 4.34b to match closely, evidently the displacement responses that are obtained for the fully discrete BKV system and the half-plane of particles using the FD-solution must also closely match. This is verified by comparison of the continuous light blue line and the dashed blue line in Figure 4.36.

The dashed red line in Figure 4.36 gives the displacement response of the fully discrete BKV system that is obtained by numerically solving the system of ordinary differential equations (ODEs) directly in the time domain using the Runge-Kutta method. Here, the system of ODEs used includes the boundary formulation according to equation (4.136). We refer to this approach as the time domain solution, or the TD-solution. From Figure 4.36a, it is clear that the displacement response resulting from the TD-solution matches the corresponding response for the FD-solution well and any differences are not visible at the scale of this figure. Nevertheless, as explained in Section 4.2.3, the numerical evaluation of the convolution integral that is incorporated in the boundary formulation in combination with the application of the Runge-Kutta method yields a small numerical error in the boundary formulation, which in turn causes small reflections from any incident waves arriving at the boundary. This small numerical error is visible in Figure 4.36b. While even at the scale of this close-up the responses of the half-plane of particles and for the FD-solution of the fully discrete BKV system still match exactly, the response obtained using the TD-solution slightly deviates from those obtained using the FD-solution. Close examination of the results show that this deviation is indeed due to a reflected incident wave and its magnitude depends on the time intervals used to evaluate the convolution integral and the time step used for the Runge-Kutta scheme.

The additional continuous dark yellow line that is included in Figure 4.36b gives the displacement response of the fully discrete BKV system that follows from the TD-solution using the linearization for large elongations, while the response given by the dashed red line follows

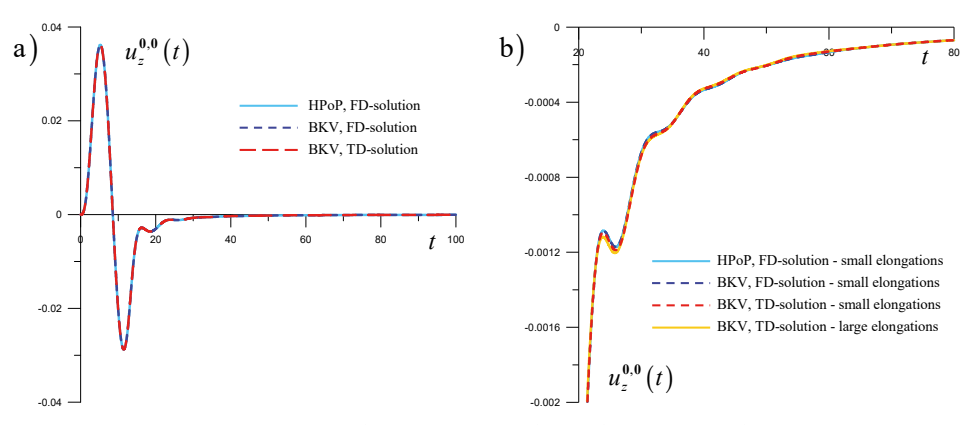


Figure 4.36: Time domain displacements of particle **0.0** in the half-plane of particles and the fully discrete BKV system.

a) Vertical displacement response; b) Close-up of the response.

from applying the TD-solution using the linearization for small elongations. Note here that, as explained in Section 2.4.2, the linearization for large elongations solves the system of ODEs and obtains the lattice response at every time step by considering the positioning of the particles and elements in the lattice at the previous time step, while the linearization for small elongations obtains the lattice response relative to the initial positioning of its particles and elements, and is thus in correspondence with the FD-solution. Figure 4.36b shows that the response obtained using the linearization for large elongations is very close to the response obtained using the linearization for small strains, so that the response of the lattice to a single-sinus pulse load with an amplitude $\bar{F} = 0.1 \, \text{MN}$ is valid for the linearization for small elongations.

Figure 4.37a and Figure 4.37b respectively depict the horizontal and vertical displacement response of particle 8,4 for both the half-plane of particles and the fully discrete BKV system, and for the different solution methods considered. As before, the continuous light blue line and the dashed blue line respectively give the response of the half-plane of particles and the fully discrete BKV system for the FD-solution, while the dashed red line and the continuous yellow line give the response of the fully discrete BKV system for the TD-solution respectively using the linearizations for small and large elongations. Here, note that the amplitudes of the displacement response of particle 8,4 are approximately ten times smaller than the displacement response of the loaded particle, i.e. particle 0.0. This decline in amplitude is attributed to both the viscous damping present in the Kelvin-Voigt elements and the geometric damping that exists in any two-dimensional medium. At the scale of these graphs, the responses obtained for the FD-solutions are not visible because they match the responses obtained for the TD-solutions well. Moreover, even at the scale of Figure 4.36b, the differences between the responses obtained by the FD-solutions and the TD-solutions would hardly be visible. For both the linearizations, Figure 4.38 therefore gives the difference between the time domain response and the frequency domain response. The continuous red lines in Figure 4.38 give the difference between the displacement responses of the fully discrete BKV system obtained using the FD-solution and the corresponding TD-solution for small elongations,

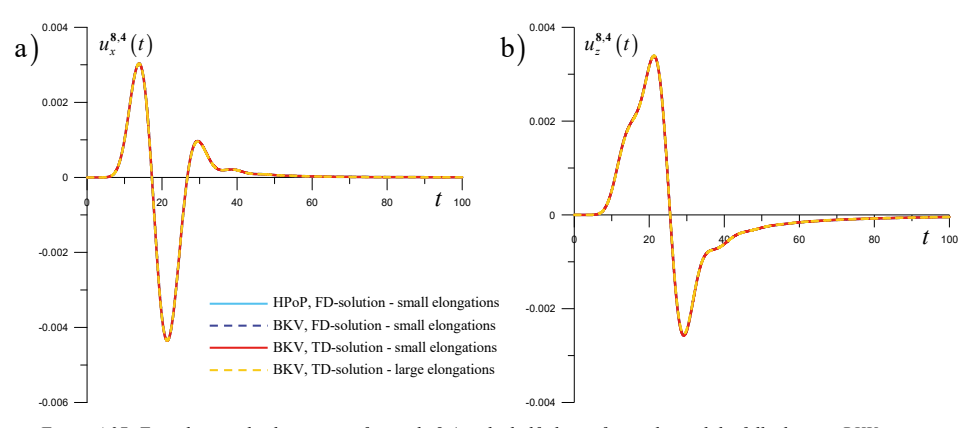


Figure 4.37: Time domain displacements of particle 8.4 in the half-plane of particles and the fully discrete BKV system.

a) Horizontal displacement; b) Vertical displacement.

while the continuous blue lines give the difference between the responses obtained using the FD-solution and the corresponding TD-solution for large elongations. Specifically, Figure 4.38a gives the differences in vertical displacement response for the loaded particle, i.e. particle **0,0**, while Figure 4.38b gives the differences in vertical displacement response for particle **8.4**.

For both particles, any differences between the vertical displacement responses for the FD-solution and that of the TD-solution for small elongations, given in Figure 4.38 by the red lines, must be due to numerical errors, because the two solutions are two different approaches to finding the response of the same medium. For both particles, the numerical error in the displacement response is most pronounced during the incident wave, although relative to the amplitude of the incident wave, which is by approximation 100 times larger, these numerical errors are still quite small. After the incident wave has passed, the numerical error that remains must be exclusively due to reflections from the boundary in the TD-solution, and since the response obtained using the FD-solution has no reflections at all, this numerical error is of much more concern. From comparing the reflections in Figure 4.38a and Figure 4.38b, we can observe that the magnitude of the reflected wave is significantly larger in the displacement response of particle 0,0 than in the displacement response of particle 8,4. Because of the presence of viscous damping however, the amplitude of the reflected wave in the response of particle 0.0 should be expected to be smaller than for the response for particle 8,4. The fact that the amplitude of the reflected wave is more pronounced for particle 0,0 can be attributed to the position of this particle at the origin of the lattice. As the distance from the origin to any particle at the boundary of the lattice is equal, all reflections from these boundary particles will arrive back at the origin, i.e. at particle 0.0, at the same time. The reflected wave due to the numerical error in the boundary formulation is thereby greatly amplified at particle 0,0, and less significant for the displacement response of any other particles in the lattice.

Furthermore, Figure 4.38 shows that the differences of the TD-solution with the response for the FD-solution are much larger for large elongations than for small elongations, and that

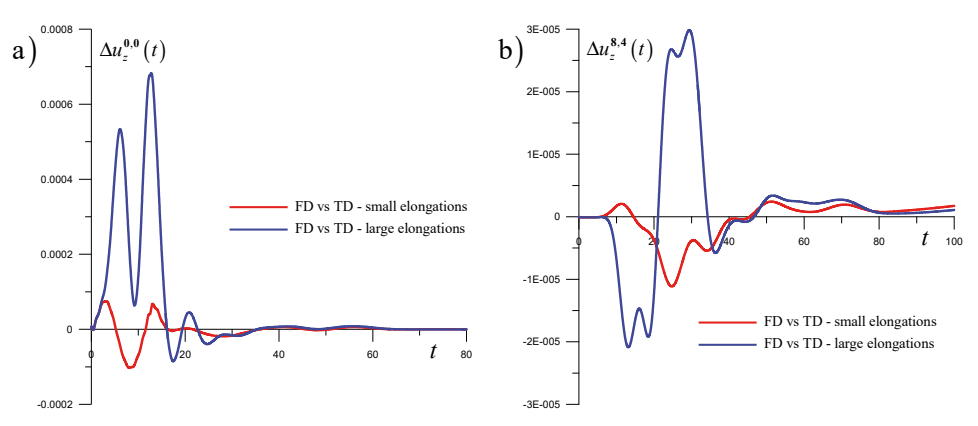


Figure 4.38: Differences in displacement response of the time domain solutions versus the frequency domain solutions:
a) vertical displacement of particle 0,0; b) vertical displacement of particle 8,4.

these differences mainly occur during the incident wave. This is because the TD-solution for large elongations accounts for the change in geometry of the lattice due to its own response, and thereby gives a different representation of the fully discrete BKV system than the FD-solution and the TD-solution for small elongations. The fact that the differences for the TD solution for large elongations are largest during the incident wave is a logical consequence of the properties of the corresponding medium. Because the lattice accounts for the changing angles in its system of equations, the corresponding displacements response may be expected to be amplified. Consequently, while the current load case and its response are still valid for small elongations, increasing the amplitude of the load, and thereby the amplitude of the response, will show a significant increase in these differences and require us to account for large elongations.

As an example of this, Figure 4.39 presents the vertical displacement response of particle 0,0 for a single-sinus pulse load with an amplitude $\overline{F}=1.0$ MN and the same load frequency as before. Figure 4.39a gives the overall vertical displacement response for the fully discrete BKV system, while Figure 4.39b gives a close-up of this response at a 15 times smaller scale. While the response resulting from the TD-solution for small elongations is not distinguishable from the response obtained for the FD-solution at the scale of Figure 4.39a and the corresponding numerical error is barely visible at the scale of Figure 4.39b, the TD-solution for large elongations yields a response that is significantly different from the response obtained using the FD-solution.

Here, note that the Green's functions for the displacements and the reaction forces in the half-plane of particles, used to construct the dynamic compliance matrix according to equation (4.44) and the boundary integral equation according to equation (4.136), have been derived using the linearization for small elongations and does not account for any geometrical nonlinearities. Thereby, the resulting boundary formulation is expected to yield a perfectly nonreflective boundary only when the particle displacements, and thus the elongations of the rheological elements, at the boundary of the near-field lattice are also small. Since the model for the near-field lattice allows for large elongations and accounts for geometrical

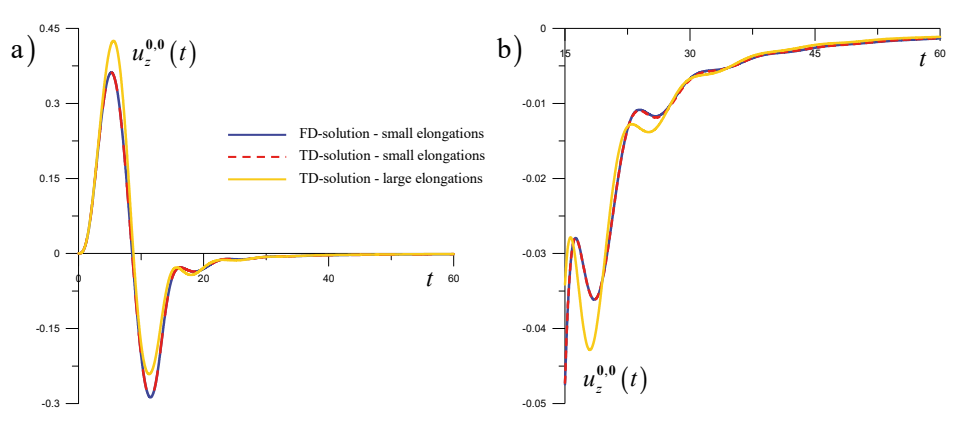


Figure 4.39: Time domain displacements of particle 0.0 in the half-plane of particles and the fully discrete BKV system for a load amplitude of 1.0 MN. a) Overall displacement response; b) Fragment of the response.

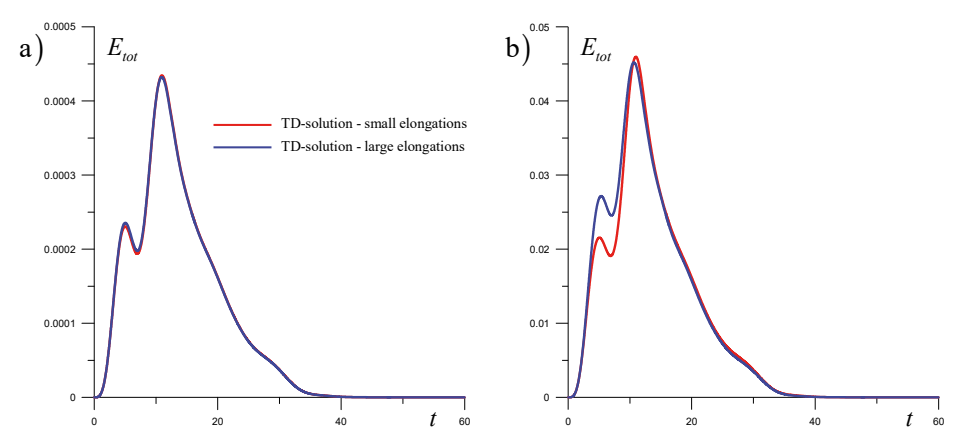


Figure 4.40: Total energy present in the near-field lattice comparing the models that allow for small and large elongations:
a) for a load amplitude of 0.1 MN; b) for a load amplitude of 1.0 MN.

nonlinearities, it is of interest to investigate the magnitude of the displacements and the elongations in the near-field lattice.

To address this, Figure 4.40 compares the total energy, $E_{\rm tot}$, present in the near-field lattice of the fully discrete BKV system as a function of time for the TD-solutions for small and large elongations, respectively given by the continuous red and blue lines. Here, Figure 4.40a gives the total energy in the near-field lattice as a function of time for a single-sinus pulse load applied at particle **0.0** with a load amplitude of 0.1 MN, while Figure 4.40b gives the corresponding results for a load amplitude of 1.0 MN. Because the elongations that occur in the near-field lattice due to a load amplitude of 0.1 MN can be considered to be small, the responses of both TD-solutions correspond well and therefore, the total energy in the near-field over time presented in Figure 4.40a for both TD-solutions also correspond well. For a load amplitude of 1.0 MN however, Figure 4.39 shows that the TD-solutions for small and large elongations are different, and as a consequence, the total energy present in the near-field lattice as a function of time, as presented in Figure 4.40b, is also different for both TD-solutions.

Figure 4.40 thus demonstrates that, even when physical nonlinearities, such as stick-to-slip transitions, do not occur or are not accounted for in the near field lattice, the geometrical nonlinearities, associated with the changing angles of the lattice elements, may significantly influence the response of the BKV lattice depending on the magnitude of the applied loading. Despite the differences in the models applied for both TD-solutions however, the decay of the total energy over time is similar, implying that the boundary formulation that models the far-field domain as a half-plane of particles also performs well when we account for the geometrical nonlinearities in the near field lattice.

4.7.5 Nonlinear response of the fully discrete BKV system

To demonstrate that the boundary formulation that is obtained using the methodology presented in Section 4.3 also properly accounts for the behaviour of the far-field domain when physical nonlinearities occur in the near field, this section regards the nonlinear response of

the fully discrete BKV system to an externally applied time-dependent load. In this section, we will show that, even for a nonlinear response of the near-field lattice, the waves properly propagate through the boundary, and that the boundary formulation that accounts for the far-field domain by modelling it as a semi-infinite half-plane of particles yields a non-reflective boundary for the near-field BKV lattice.

In Section 4.7.4, we have shown that the proposed methodology works for small elongations by comparing the viscoelastic time domain response of the fully discrete BKV system obtained using a time domain solution, i.e. by solving the time domain system of ODEs, with the response obtained using a frequency domain solution, in this case by solving the system of equations of motion algebraically in the Laplace domain. For the nonlinear response of the fully discrete system however, this frequency domain approach is not available. Although, based on the findings presented in Chapter 5, it is principally possible to obtain the nonlinear response of a two-dimensional system by repeatedly solving its algebraic system of equations in the frequency domain, we have not implemented this mixed time-frequency domain method for the two-dimensional systems as a part of this thesis. In this section, we will instead use the time domain approach to compare the nonlinear time domain response of two matching fully discrete BKV systems, for which the near-field BKV lattice has different dimensions and thereby, the boundary of the two BKV systems is located at a different distance from the origin and the load. Then, if the responses are the same for both BKV systems, the boundary must be non-reflective for both and the behaviour of the far-field domain is correctly incorporated in the boundary formulation. After all, due to the different distances of their boundaries from the origin, any wave reflections would cause the two BKV systems to respond differently.

The matching configurations of the two fully discrete BKV systems are depicted in Figure 4.41. Here, we consider one system where the BKV lattice has dimension N equal to 8 and one system where the BKV lattice has a dimension N equal to 12. The BKV lattice with

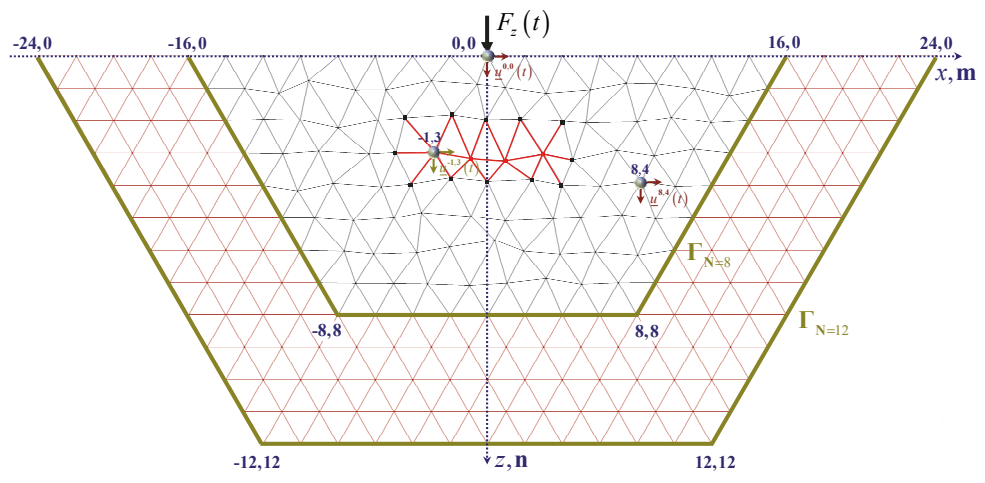


Figure 4.41: Matching BKV lattices with respectively dimension N equal to 8 and N equal to 12, with a cluster of weak BKV elements and the locations of particles with nodal coordinates 0,0,-1,3 and 8,4.

N=8 consists of 117 particles and 308 BKV elements. Its geometry is randomized and depicted in Figure 4.41 representing its BKV elements by black lines. Here, note that the particle coordinates are randomized using a Gauss distribution with a mean that is equal to the interparticle distance chosen as $\ell=0.2$ m, and a standard deviation $\frac{1}{6}\ell$. The BKV lattice with N=12 consists of 247 particles and is depicted in Figure 4.41 representing its 678 BKV elements by dark red lines. Here, note that on the domain of the BKV lattice with N=8, the geometry of both lattices match and therefore the geometry of the lattice with N=12 is not visible for that domain in Figure 4.41. To make sure that the geometry of both fully discrete systems match, the remainder of the lattice with N=12 has deliberately not been randomized, because for the system with dimension N=8 the particles at this domain lie within the half-plane of particles that has a regular geometry.

To match the material properties of the lattice to the macromaterial properties presented in Section 2.5 and used throughout this thesis, the third dimension of the space that each particle represents is arbitrarily chosen as $dy=1\,\mathrm{m}$. As a consequence, the particles in the interior of the lattice have a mass $M=69.28\,\mathrm{kg}$ and the stiffness of the springs in the lattice is found as $K_e=18.48\,\mathrm{MN/m}$. The corresponding particle natural frequency and critical damping in the lattice are respectively found as $\omega_0=\sqrt{3K_e/M}=894,4\,\mathrm{rad/s}$ and $C_{crit}=\frac{2}{3}\,M\,\omega_0=41.31\,\mathrm{kNs/m}$. Then, choosing a damping ratio $\zeta=0.2$, the dashpots in the lattice have a damping coefficient $C_e=C_f=8.262\,\mathrm{kNs/m}$.

To induce stick-slip behaviour in the BKV lattice, the critical friction force of the dry friction elements in the BKV lattice is chosen relative to the amplitude of the applied load as $F_{cr} = 0.4\overline{F}$, while the threshold distance for lock is set as $D_{min} = 0.9D_{init}$. To enhance the possibility that nonlinear phenomena occur, the BKV lattice incorporates a cluster of weak BKV elements, depicted in Figure 4.41 by the red lines, that are five times weaker than the regular elements in the lattice, given in Figure 4.41 by the black lines. Consequently, the springs in the weak cluster of the lattice have a stiffness $K_e^{weak} = 3.695$ MN/m and a damping coefficient $C_e^{weak} = C_f^{weak} = 1.652$ kNs/m. Furthermore, the critical friction force of the weak BKV elements is chosen as $F_{cr}^{weak} = 0.2F_{cr} = 0.08\overline{F}$.

Figure 4.42, Figure 4.43 and Figure 4.44 give the time domain displacement responses of the three particles for which the locations are depicted in Figure 4.41, i.e. for the particles with nodal coordinates 0,0, -1,3 and 8,4 respectively. In each figure, the displacement responses of the corresponding particles are compared for the two BKV lattices and for two different load amplitudes of a vertical single-sinus pulse load applied at the origin of the lattice, i.e. at particle 0,0. Here, the applied pulse load has a dimensionless angular frequency $\Omega_F = 0.5$. The continuous blue line in these figures gives the displacement response for the lattice with dimension N = 8 and a load amplitude $\overline{F} = 1.0$ MN, while the dashed light-blue line gives the corresponding displacement response for the lattice with dimension N = 12 and the same load amplitude. Accordingly, the continuous red and the dashed dark-yellow line respectively give the displacement response for the lattices with dimension N = 8 and dimension N = 12, both for a load amplitude $\overline{F} = 2.0$ MN.

First and foremost, from evaluating the displacement responses in Figure 4.42 to Figure 4.44, we observe that, at the scale of the depicted graphs, the response of the lattices with

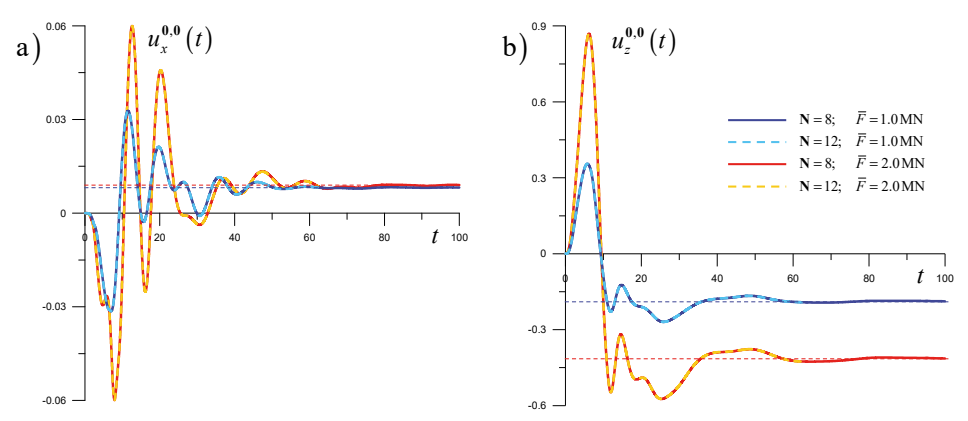


Figure 4.42: Time domain response of the lattices with dimension N=8 and N=12 for two different load amplitudes: a) horizontal displacements of particle 0.0; b) vertical displacements of particle 0.0.

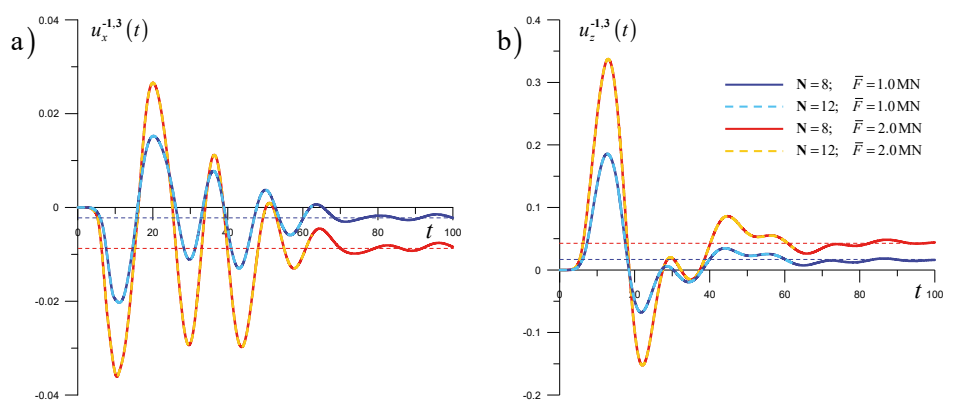


Figure 4.43: Time domain response of the lattices with dimension N=8 and N=12 for two different load amplitudes: a) horizontal displacements of particle -1,3; b) vertical displacements of particle -1,3.

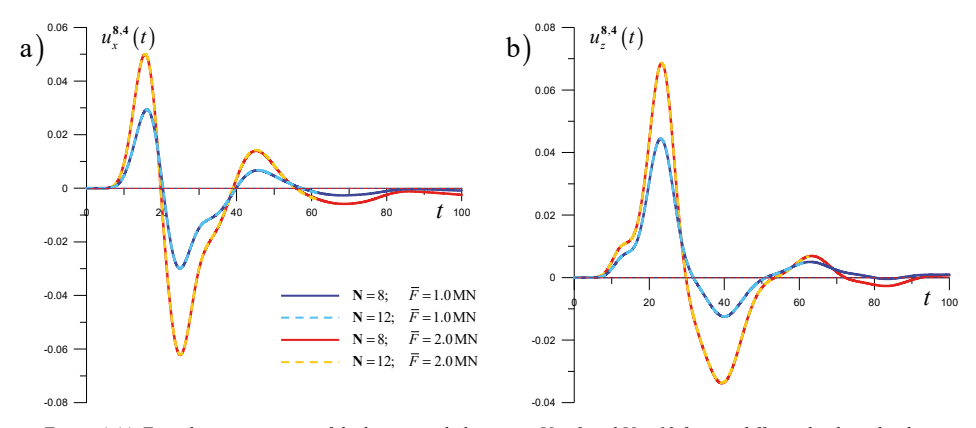


Figure 4.44: Time domain response of the lattices with dimension N=8 and N=12 for two different load amplitudes: a) horizontal displacements of particle 8,4; b) vertical displacements of particle 8,4.

dimensions N = 8 and N = 12 match exactly for both load amplitudes considered. Here, wave reflections exist and that their amplitudes are roughly proportional to the load specifically note that the response of the lattice with dimension N = 12 in all figures is depicted only up to dimensionless time t = 62.3. The reason for this is that, despite the implementation using sparse matrices, the large amount of degrees of freedom in the lattice with dimension N = 12 combined with the presence of the convolution integral in the boundary equation and the small time step required to obtain an accurate time domain response, the computer on which we ran the calculations ran out of virtual memory and caused the calculations to stop at the given time moment. From the matching responses, we can nevertheless conclude that for both lattices, the boundary formulation as obtained using the methodology presented in Section 4.3 is non-reflective and thereby correctly represents the far-field behaviour of the fully discrete BKV system. That is, at the scale of the graphs depicted. From the results discussed in Sections 4.2.3 and 4.7.4 however, we know that using the time domain approach, and thereby numerically evaluating the convolution integral, yields a small numerical error in the boundary formulation. In turn, this causes the boundary to not be completely nonreflective and return small reflections due to any incident waves arriving at the boundary. Due to the boundaries of the two lattices with dimensions N = 8 and N = 12 being located at different distances from the origin, these reflections occur at different moments in time and should therefore be visible by comparing the displacement response of any particle for both lattices.

To illustrate this, Figure 4.45a and Figure 4.45b give the differences in the horizontal and vertical displacement response of particle **8,4** due to these wave reflections, respectively. Here, the continuous blue line gives the difference in displacement response of particle **8,4** between the two lattices for a load amplitude $\bar{F} = 1.0 \, \mathrm{MN}$, while the continuous red line gives the corresponding difference for a load amplitude $\bar{F} = 2.0 \, \mathrm{MN}$. Figure 4.45 clearly shows that the aforementioned amplitude. Additionally, from comparing the range of the differences in displacement responses for the two lattices with the original displacement

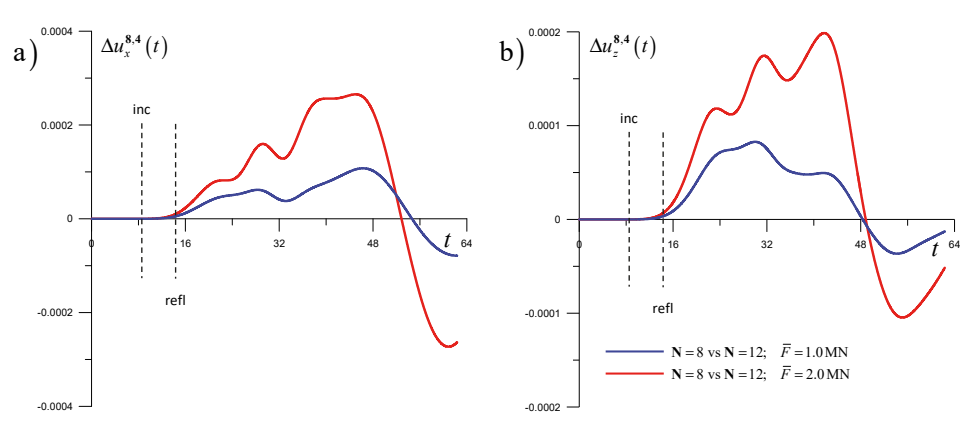


Figure 4.45: Differences in responses for the lattice with dimension N = 8 versus the lattice with dimension N = 12.

a) Horizontal displacement of particle 8.4; b) Vertical displacement of particle 8.4.

response, we find that the amplitudes of the reflected waves are roughly 200 to 300 times smaller than the amplitude of the incident wave.

Next to showing that the displacement responses for the two lattices match well, the displacement responses depicted in Figure 4.42 and Figure 4.43 show clear evidence of nonlinear behaviour. The dashed blue and red lines in these figures give the final displacements of the considered particle for the corresponding direction and the two load amplitudes considered, when all energy due to the applied load has been dissipated by and from the near-field lattice. Comparing these permanent displacements for the different particles, it is clear that the deformation is most severe for the loaded particle, i.e. for particle 0,0, in vertical direction and that the deformation quickly reduces as the distance from the origin of the lattice increases. This is also clearly visible in Figure 4.46, as it shows the positioning of all particles and elements in the two lattices at the end of the performed simulations compared to their initial positioning, given by the grey-lined mesh. In total, there were 18 BKV elements in the lattices that experienced one or multiple nonlinear events. These elements are depicted in Figure 4.46 by the blue lines. All these BKV elements are either close, or directly connected, to the loaded particle, or are part of the cluster of weak elements in the interior of the lattice. In total, 50 nonlinear events occurred during the simulation. Of these, there were 19 transition into lock, 19 lock-to-stick transitions, 6 stick-to-slip transitions and 6 slip-to-stick transitions. Since the lock-state only occurs in compression and not in tension, and lock occurs at a relatively large ratio of the initial distance between the particles, the motion of the particles in positive z-direction is impeded, while the motion of these particles in negative z-direction is not. As a result of this, the final permanent deformation of particle 0,0 is directed upwards in Figure 4.46, but has a negative value in Figure 4.42b.

The fact that the permanent deformation in vertical direction of particle **0,0** is far more severe than the deformation in horizontal direction is a logical consequence of the external dynamic load having been applied vertically. Here, note that the horizontal displacement

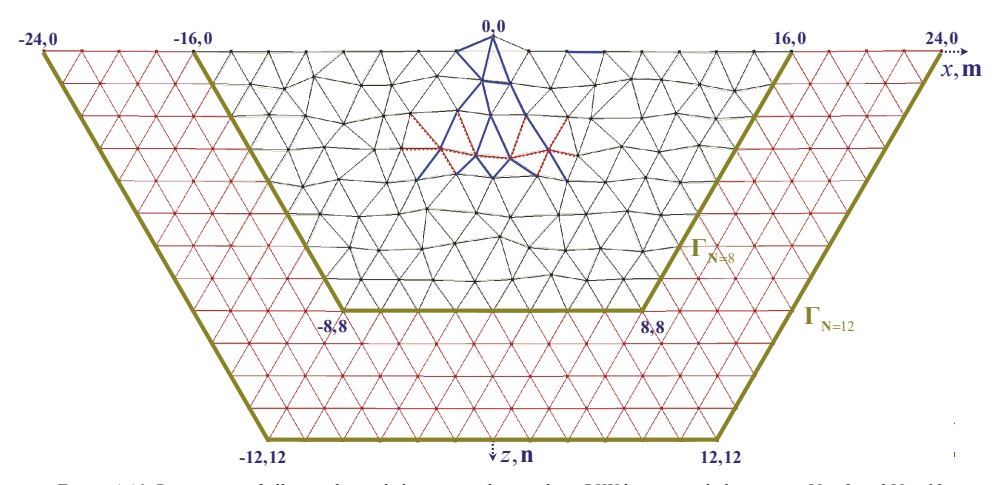


Figure 4.46: Positioning of all particles and elements in the matching BKV lattices with dimensions N=8 and N=12 at the end of the simulations performed.

response of the vertically loaded particle, i.e. particle **0,0**, depicted in Figure 4.42a is nonzero only because the geometry has been randomized and is therefore no longer symmetric in the *z*-axis. Additionally, Figure 4.42b shows that the permanent deformation in vertical direction is proportional to the amplitude of the applied load. For the vertical response under the applied vertical load, this makes sense.

Also for the vertical displacement response of particle -1.3, depicted in Figure 4.43b, we observe a similar proportionality with respect to the applied loading. Because particle -1,3 is located relatively close to the z-axis, and quite a bit closer to the origin of the lattice than particle 8,4, we observe that the displacement response in vertical direction is much more significant than the displacement response in horizontal direction. Furthermore, the horizontal displacement response of particle -1,3, depicted in Figure 4.43a, shows a striking oscillatory motion, which is likely present because this particle is located within the cluster of weak elements of the lattice. This can be explained by considering that at any interface at which material properties suddenly change, incident waves will, depending on the orientation of the interface, partially reflect and partially scatter. Accordingly, reflections and wave dispersions may originate from the occurrence of nonlinear events, such as the transitions to slip or lock, which actually correspond to a change in properties of the lattice. In this case, when the incident wave due to the applied loading reaches the weak cluster of elements, it will partially reflect back to the lattice surface and partially transmit into the weak domain. Then, the wave energy that is transmitted into the weak domain, in turn partially reflects from the edges of the weak domain and partially reflects due to the occurrence of nonlinear events within the weak domain. As a result, the oscillatory motion present in the horizontal displacement response of particle -1.3 also influences the horizontal displacement response of particle 0.0, depicted in Figure 4.42a, which shows a similar oscillatory motion. Nevertheless, note here that this oscillatory motion is also present in the vertical displacement responses of particles 0,0 and -1,3, but is not equally apparent because their magnitude is significantly smaller than the amplitude of the direct vertical response to the applied pulse load.

For particle **8,4**, which is located at a larger distance from both the loaded particle and the z-axis and outside the domain of weak elements, the presence of damping causes these highly oscillatory motions to no longer be present. Additionally, we observe that due to its positioning, the horizontal and vertical displacement responses of particle **8,4**, respectively depicted in Figure 4.44a and Figure 4.44b, have similar magnitudes.

Finally, Figure 4.47 shows how the total energy present in the two BKV-lattices changes over time and eventually disappears from both lattices. Here, Figure 4.47a compares the total energy over time in the two lattices with dimensions N=8 and N=12 for the applied pulse load with a load amplitude of 1.0 MN, while Figure 4.47a makes the same comparison, but now for the load with an amplitude of 2.0 MN. The continuous lines in Figure 4.47 both give the total energy in the BKV lattice with dimension N=8, while the dashed lines correspond to the total energy in the BKV lattice with dimension N=12.

For both load cases, we see that up to dimensionless time $t \cong 16$ the total energy over time is approximately equal for both lattices. This corresponds with the moment in time at which the front of the incident wave due to the applied pulse load can be observed to reach

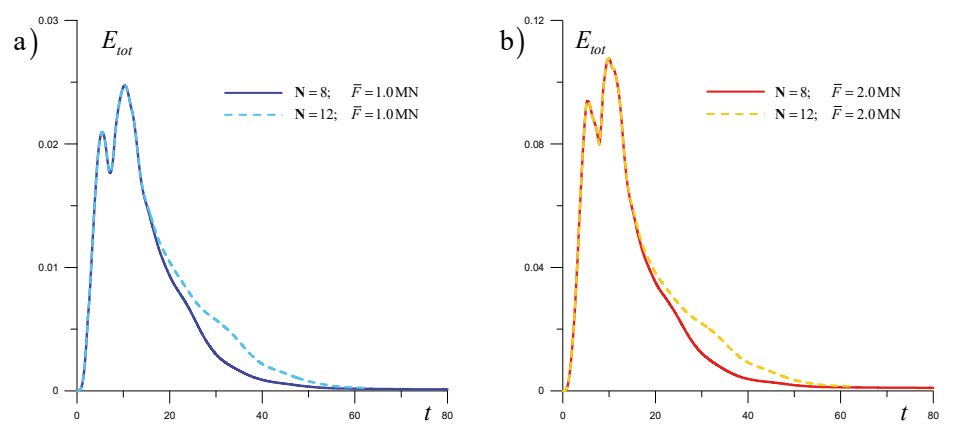


Figure 4.47: Total energy present in the lattice during its response comparing the lattices with dimension N = 8 and N = 12:
a) for a load amplitude of 1.0 MN; b) for a load amplitude of 2.0 MN.

the boundary of the BKV lattice with dimension N = 8 and is transmitted into the corresponding far-field domain. At this time however, the front of the incident wave has not yet perceivably reached the boundary of the BKV lattice with dimension N = 12 and, as a consequence, the total energy present inside is no longer the same for both lattices. Here, note that the maximum of the total energy in both lattices coincides with the moment at which the single-sinus pulse load has been fully applied, and from that moment onwards, the total energy in the system declines due to viscous damping and the occurrence of nonlinear events, although most of the nonlinear events occur during the application period of the load. This can be confirmed by comparing the total energy over time that is present for the nonlinear response of the BKV lattices for a load amplitude of 1.0 MN depicted in Figure 4.47a with the total energy over time present for the viscoelastic response depicted in Figure 4.40. While the applied loading is exactly the same in both cases, the shape of the total energy during the application of the load is quite different and the magnitude of the total energy in the system is much lower for the nonlinear response. As all other properties of the two lattices are exactly the same, the difference in total energy during the application of the load can only be due to the occurrence of nonlinear events. By comparing Figure 4.47a and Figure 4.40, it follows that it takes significantly longer for all the energy to dissipate from the lattice in which nonlinear events occur, as compared to the lattice that responds viscoelastically. This can be explained by considering the fact that, as mentioned above, both the presence of the cluster of weak elements and the occurrence of nonlinear events cause wave reflections within the BKV lattice. In many cases, these reflected waves will first travel back to the lattice surface and thereby will take a lot longer to finally arrive at the boundary, before their energy is transmitted into the far-field domain and removed from the BKV lattice. Nevertheless, for both load amplitudes, Figure 4.47 shows that the total energy eventually fully dissipates from both BKV lattices.

From the findings in this section, we conclude that the boundary formulation as obtained using the methodology presented in Section 4.3 is not only valid for small elongations, i.e. when both physical and geometrical nonlinearities do not occur or are not accounted for in

the near field lattice as proven in section 4.7.4, but is also valid when large elongations occur and both physical and geometrical nonlinearities are accounted for. That is, as long as the boundary is sufficiently far away from the load so that both physical and geometrical nonlinearities do not reach the boundary.

5

A mixed time-frequency domain approach for 1D systems

The BKV lattice models considered in this thesis are non-smooth dynamical systems [Kunze, 2000] whose dynamic properties may change at any given moment in time, but where the change in behaviour is always instant. This means that, whenever a nonlinear event occurs, the motion state of the corresponding rheological element changes instantly, while both before and after the nonlinear event the lattice response is linear. The non-smooth dynamic response of a BKV lattice is thereby piecewise linear and, for the time period in which the response remains linear, the corresponding system of equations of motion can be solved algebraically in the frequency domain. For each piecewise-linear time period however, the system of equations of motion must be evaluated for a new set of nonzero initial conditions. To obtain the algebraic system of equations of motion in the frequency domain, we therefore apply the Laplace integral transform that is able to account for nonzero initial conditions.

The approach discussed in this chapter can be considered as a mixed time-frequency domain method in the sense that the properties of the lattice change over time due to the occurrence of nonlinearities, while during each piecewise-linear time period, the response of the lattice is determined by solving its algebraic system of equations of motion in the frequency or Laplace domain. This approach may seem somewhat laborious, or even superfluous, for one-dimensional systems, because the non-smooth response of these lattices can be straightforwardly and efficiently modelled using time domain approaches. Nevertheless, as for example illustrated by Figure 4.7, for one-dimensional systems that incorporate boundary formulations there is an advantage of using frequency domain methods over time domain methods. Additionally, due to the longer calculation times that are generally required to obtain the response of two- and three-dimensional media, the mixed time-frequency method, or in short MTFD-method, shows the potential to be particularly effective to model the non-smooth response of two- and three-dimensional models that incorporate boundary formulations. For the sake of simplicity and clarification however, the concept of the MTFD-method is here introduced on the basis of one-dimensional systems only.

5.1 Methodology of the mixed time-frequency domain approach

Let us consider an arbitrary BKV lattice in which instant nonlinear events may occur due to an externally applied load. Assuming that, prior to time t=0, the lattice is at rest and has zero initial conditions, the initial response of the lattice may be expected to be linear and thus without occurrences of nonlinear events in its response. To obtain the response of the lattice for the time period during which it responds linearly, i.e. until the occurrence of the first nonlinear event, we solve its system of equations of motion algebraically in the Laplace domain for all its degrees of freedom. We then obtain the time domain response of all degrees of freedom in the lattice by applying the inverse Laplace transform. This method to obtain the response in the time domain remains valid for as long as the lattice continues to behave in a linear manner.

Now, suppose that at a given time $t = t_0$, a nonlinear event occurs in the BKV lattice, i.e. the motion state of one of its rheological elements changes instantly. After the occurrence of this nonlinear event, i.e. for $t > t_0$, the response of the lattice is again linear until the next nonlinear event occurs. To properly consider the new situation for the lattice that starts at $t = t_0$ in both the time and the Laplace domains, we reset the time parameter t. The time domain response of the lattice after the first nonlinear event is then obtained by algebraically solving its system of equations of motion in the Laplace domain, but now with nonzero initial conditions and possibly accounting for different motion states in its rheological elements, and subsequently applying the inverse Laplace transform at every time step until the next nonlinear event occurs. This procedure is repeated every time a nonlinear event occurs.

The resulting approach is here referred to as the mixed time-frequency domain method, or in short the MTFD-method, and has been visualized in Figure 5.1. Starting with a zero initial displacement at t = 0 in the first period of linear response, the occurrence of a nonlinear event at $t = t_0$ resets the time parameter t. This new time parameter then remains valid until another nonlinear event occurs. Every time a nonlinear event occurs and thus every time the time parameter t is reset, the response of the lattice prior to that time moment is included in the new time period by incorporating the nonzero initial conditions at t = 0 for that time period.

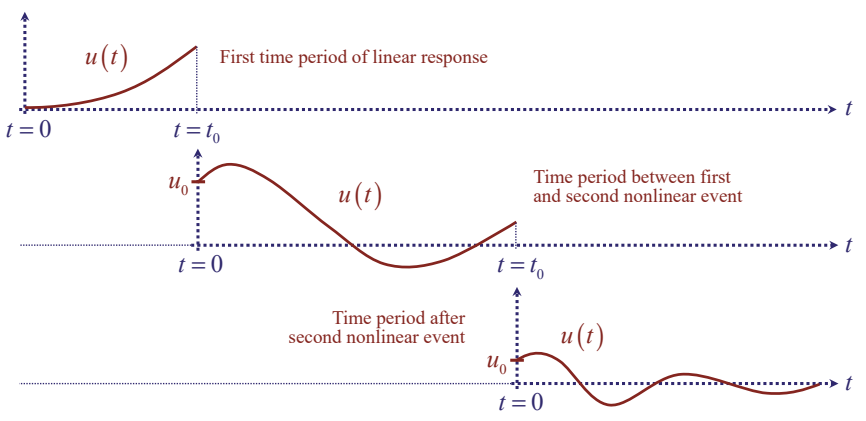


Figure 5.1: Procedure of resetting the time parameter every time a nonlinear event occurs.

In the following, we will first exemplify the MTFD-method by considering a discrete-continuous system consisting of a one-dimensional Hooke lattice in the near field and a linear-elastic rod in the far field in Section 5.2. Although this linear-elastic system does not allow for nonlinear events to occur, its system of equations of motion can be solved directly in both the Laplace and the time domains, so that application of the MTFD-method can be verified. Section 5.2 furthermore shows that incorporating nonzero initial conditions poses additional challenges when numerically evaluating the inverse Laplace transform to obtain the time domain response of the lattice. To address these challenges, an alternative approach is presented in Section 5.2.3, which greatly improves the performance of the numerical evaluation of the inverse Laplace transform. In Section 5.3, we apply the MTFD-method to a discrete-continuous system that consists of a one-dimensional BKV lattice in the near field and a viscoelastic rod in the far field. Thereby, we showcase the MTFD-method for a system that allows for the occurrence of nonlinear events and thus has a non-smooth response. This chapter is concluded by a discussion of the advantages and disadvantages of the MTFD-method.

5.2 The MTFD-method applied to 1D discrete-continuous systems

To demonstrate the mixed time-frequency domain method, or MTFD-method, we here apply it to a one-dimensional discrete-continuous Hooke system which is the most elementary of one-dimensional systems. Thereby, it gives a good insight into the method and allows us to clarify all issues that must be accounted for when applying the MTFD-method.

In Section 5.2.1, we first derive the equation of motion for the particle at the interface between the one-dimensional Hooke lattice and the linear-elastic rod that accounts for nonzero initial conditions (ICs). Next, Section 5.2.2 presents the governing system of equations of motion for the one-dimensional discrete-continuous Hooke system that is valid for the MTFD-method. Here, Section 5.2.1 and Section 5.2.2 both regard the equations of motion for the discrete-continuous Hooke system in the Laplace domain. Subsequently, Section 5.2.3 discusses the influence of the nonzero initial conditions on applying the inverse Laplace integral transform used to obtain the time domain response of the lattice. Additionally, this section shows that truncation of the semi-infinite domain, required to numerically apply the inverse Laplace transform, causes errors in the time domain response, especially near the nonzero initial conditions. Therefore, at the end of Section 5.2.3 an alternative formulation for the inverse Laplace transform is presented that greatly improves the behaviour of the time domain response. The results of applying the MTFD-method to the discrete-continuous Hooke system are presented in Section 5.2.4.

5.2.1 Boundary formulation in the Laplace domain for nonzero ICs

Let us consider the discrete-continuous Hooke system depicted in Figure 5.2 that consists of a one-dimensional Hooke lattice, i.e. a cascade of masses and springs, and the semi-infinite linear-elastic rod with a density ρ , Young's modulus E and a cross-section area A, which was previously regarded for zero initial conditions in Appendix D.1. In the time domain, the behaviour of the linear-elastic rod in interaction with the Hooke lattice is described by the

following set of equations:

$$\ddot{u}(x,t) - \frac{1}{2}u''(x,t) = 0 \tag{5.1}$$

$$M^{N}\ddot{u}^{N} + K_{e}^{N-1,N} e^{N-1,N} = \frac{1}{2} u'(x_{lnt}, t)$$
(5.2)

$$u^{N} = u(x_{lnt}, t) \tag{5.3}$$

Here, equation (5.1) gives the dimensionless wave equation for the linear-elastic rod on the domain $x > x_{lnt}$, and equations (5.2) and (5.3) respectively describe the force equilibrium and the displacement continuity at the interface between the Hooke lattice and the linear-elastic rod.

When the system has zero initial conditions, it may be solved straightforwardly using the approach discussed in Appendix D.1. However, applying the Laplace transform with respect to time taking into account nonzero initial conditions, as derived in Appendix J.1, yields equations (5.1) to (5.3) in the Laplace domain as:

$$s^{2}\tilde{u}(x,s) - \frac{1}{2}\tilde{u}''(x,s) = su_{0}(x) + v_{0}(x)$$
(5.4)

$$M^{N}s^{2}\tilde{u}^{N} - M^{N}\left(su_{0}^{N} + v_{0}^{N}\right) + K_{e}^{N-1,N}\tilde{e}^{N-1,N} = \frac{1}{2}\tilde{u}'(x_{Int},s)$$
(5.5)

$$\tilde{u}^{N} = \tilde{u}(x_{lnt}, s) \tag{5.6}$$

Here, $u_0(x)$ and $v_0(x)$ are respectively the initial displacement and initial velocity along the linear-elastic rod. Accordingly, u_0^N and v_0^N denote the initial displacement and initial velocity of the boundary particle **N**. Note here that by extension of the displacement continuity, previously given by equation (5.3), both the initial displacement and the initial velocity of the boundary particle **N** and the tip of the rod must coincide, i.e. $u_0^N = u_0(x_{lnt})$ and $v_0^N = v_0(x_{lnt})$.

Accounting for the proper behaviour of the linear-elastic rod for $x \to \infty$ and noting that Re(s) > 0, the general solution to equation (5.4) reads:

$$\tilde{u}(x,s) = Ae^{-s\sqrt{2}x} + \tilde{u}_p(x,s) \tag{5.7}$$

The first term on the right-hand side of equation (5.7) is the solution to the homogeneous version of equation (5.4), where the amplitude A may be derived by considering the

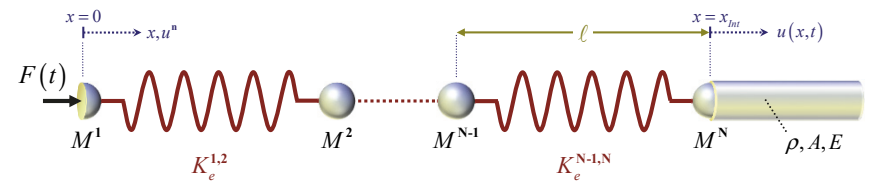


Figure 5.2: The one-dimensional semi-infinite discrete-continuous Hooke system.

displacement relation at the interface. Furthermore, $\tilde{u}_p(x,s)$ denotes its, yet unknown, particular solution due to the initial conditions $u_0(x)$ and $v_0(x)$ given on the right-hand side of equation (5.4). For zero initial conditions, equation (5.4) reduces to the corresponding homogeneous equation, which emphasizes that the particular solution exists exclusively due to the presence of nonzero initial conditions.

Applying the differentiation to space to equation (5.7) and rearranging the resulting expression to isolate the Laplace domain displacement of the linear-elastic rod allows us to express its spatial derivative as:

$$\tilde{u}'(x,s) = -s\sqrt{2}\tilde{u}(x,s) + s\sqrt{2}\tilde{u}_p(x,s) + \tilde{u}'_p(x,s)$$

$$(5.8)$$

Substituting equation (5.8) into equation (5.5), as well as taking equation (5.6) into account, the Laplace domain equation of motion for the boundary particle **N**, describing the interaction between the one-dimensional Hooke lattice and the linear-elastic rod, becomes:

$$M^{N}s^{2}\tilde{u}^{N} + K_{e}^{N-1,N}\tilde{e}^{N-1,N} + \frac{1}{2}s\sqrt{2}\tilde{u}^{N} = M^{N}\left(su_{0}^{N} + v_{0}^{N}\right) + \frac{1}{2}s\sqrt{2}\tilde{u}_{p}\left(x_{Int}, s\right) + \frac{1}{2}\tilde{u}'_{p}\left(x_{Int}, s\right)$$
(5.9)

Here note that all terms related to the initial conditions are given at the right-hand side of equation (5.9). Consequently, for the particular case that the initial conditions are equal to zero, the right-hand side of equation (5.9) is equal to zero, so that this equation exactly matches the interface equation for zero initial conditions previously derived for the discrete-continuous Hooke system in Appendix D.1.

A Green's function approach to obtain the response of the rod

To find the particular solution to the equation of motion of the linear-elastic rod, given by equation (5.4), we use a Green's function approach and express equation (5.4) as:

$$s^{2}\tilde{u}(x,s) - \frac{1}{2}\tilde{u}''(x,s) = \tilde{f}(x,s) = \int_{x_{lm}}^{+\infty} \tilde{f}(\xi,s)\delta(x-\xi)d\xi$$

$$(5.10)$$

Here, the variable of integration ξ gives a coordinate along the linear-elastic rod so that the integration is applied over the domain $\xi = x_{lm} ... + \infty$. Furthermore, the expression for the function of ξ in the integral reads $\tilde{f}(\xi,s) = su_0(\xi) + v_0(\xi)$ and $\delta(...)$ is the Dirac delta function. A particular solution to the equation of motion for the semi-infinite linear-elastic rod, given by equation (5.10), can then be found as:

$$\tilde{u}_{p}(x,s) = \int_{x_{lu}}^{\infty} \tilde{f}(\xi,s) \,\tilde{g}_{u}(x-\xi,s) \,d\xi \tag{5.11}$$

Here, $\tilde{g}_u(x-\xi,s)$ denotes the Green's displacement of the linear-elastic rod, found as the solution to equation (5.10) for the case that $\tilde{f}(x,s) = \delta(x-\xi)$. In Appendix I.3, it is derived

that, by applying the Fourier transform with respect to space, the corresponding Green's displacement in the Laplace-wavenumber domain is found as:

$$\tilde{\tilde{g}}_{u}(k,s) = \frac{2}{2s^{2} + k^{2}}$$
(5.12)

Subsequently, applying the inverse Fourier transform to equation (5.12) yields the dimensionless Green's displacement of the linear-elastic rod in the Laplace domain. The resulting integral transform is evaluated using contour integration by means of the residue theorem. When $x - \xi > 0$, the contour is chosen over the upper half of the complex k-plane to assure that the contribution of the infinite semi-circle that closes the contour is zero. Within this half of the complex k-plane the only pole, or singularity, is found as $k_1^{\times} = +is\sqrt{2}$. Accordingly, when $x - \xi < 0$, the contour is chosen over the lower half of the complex k-plane where we find a single pole at the wavenumber $k_2^{\times} = -is\sqrt{2}$. As shown by Appendix I.3, the Green's displacement of the linear-elastic rod in the Laplace domain is thus found as:

$$\tilde{g}_u\left(x-\xi,s\right) = \frac{1}{s\sqrt{2}}e^{-s\sqrt{2}|x-\xi|} \tag{5.13}$$

Substituting equation (5.13) into equation (5.11), and using Leibniz' integral rule for differentiation of integrals [Abramowitz and Stegun, 1972; Woods, 1926], we respectively find the particular solution to the equation of motion for the semi-infinite linear-elastic rod and its spatial derivative as:

$$\tilde{u}_{p}(x,s) = \frac{1}{s\sqrt{2}} \int_{x_{hit}}^{x} \tilde{f}(\xi,s) e^{-s\sqrt{2}(x-\xi)} d\xi + \frac{1}{s\sqrt{2}} \int_{x}^{+\infty} \tilde{f}(\xi,s) e^{-s\sqrt{2}(\xi-x)} d\xi$$
(5.14)

$$\tilde{u}_{p}'(x,s) = -\int_{x_{ht}}^{x} \tilde{f}(\xi,s)e^{-s\sqrt{2}(x-\xi)}d\xi + \int_{x}^{+\infty} \tilde{f}(\xi,s)e^{-s\sqrt{2}(\xi-x)}d\xi$$
(5.15)

Substituting equations (5.14) and (5.15) into equation (5.9), as well as including the expression for $\tilde{f}(\xi,s)$, the Laplace domain equation of motion for the boundary particle N reads:

$$M^{N} s^{2} \tilde{u}^{N} + K_{e}^{N-1,N} \tilde{e}^{N-1,N} + \frac{1}{2} s \sqrt{2} \tilde{u}^{N} = M^{N} \left(s u_{0}^{N} + v_{0}^{N} \right) + f_{0} \left(s \right)$$
(5.16)

Here, the expression for $\tilde{f}_0(s)$ is found as:

$$f_0(s) = \int_{x_{Int}}^{+\infty} e^{-s\sqrt{2}(\xi - x_{Int})} \left(su_0(\xi) + v_0(\xi) \right) d\xi$$

$$(5.17)$$

This expression signifies the contribution of the rod's initial conditions to the interface

equation and therefore equation (5.16) does not yet describe the Laplace domain equation of motion for the boundary particle **N** exclusively in terms of the one-dimensional Hooke lattice, which would be the case when zero initial conditions are considered. In the following, we further analyse the integral expression given by equation (5.17).

Analysis of the remaining integral expression

Let us suppose that the Laplace domain equation of motion given by equation (5.16) is valid for a time period that, due to the occurrence of an instant nonlinear event, is reinitiated at $t = t_0$. For that time period, the initial displacement and velocity along the linear-elastic rod, denoted in equation (5.17) as $u_0(\xi)$ and $v_0(\xi)$, then correspond to the displacement and the velocity along the linear-elastic rod at time t_0 of the previous time period. Since we only consider loads that are applied at the tip of the one-dimensional system, i.e. at particle 1, the response of the rod follows from its interaction with the lattice and, in accordance with Huygens' principle [Huygens, 1690], the lattice-rod interface may be considered as a source for the response along the rod. Then, to express the displacements and velocities along the linear-elastic rod at any time t, and thus also at time t_0 , we must account for the full response history of the boundary particle N.

When we consider time globally, so in terms of its original time parameter that has not been reset, and thus with zero initial conditions, the corresponding equation of motion for the linear-elastic rod in the Laplace domain is a homogeneous equation. Accounting for the proper behaviour of the rod at $\xi \to \infty$, the Laplace domain displacement along the linear-elastic rod is then found as $\tilde{u}(\xi,s) = Ae^{-s\sqrt{2}\xi}$. Here, the expression for A follows from the displacement relation at the lattice-continuum interface, given by equation (5.6), as $A = \tilde{u}^N e^{+s\sqrt{2}x_{lnt}}$, thereby establishing the relation between the Laplace domain displacement $\tilde{u}(\xi,s)$ along the rod and the Laplace domain displacement \tilde{u}^N at the boundary particle. Additionally noting that $\tilde{v}(\xi,s) = s\tilde{u}(\xi,s)$ and therefore $\tilde{v}^N = s\tilde{u}^N$, we find the relations between respectively the displacement and velocity along the linear-elastic rod in terms of the displacement and velocity of the boundary particle N as:

$$\tilde{u}(\xi, s) = \tilde{u}^{N} e^{-s\sqrt{2}(\xi - x_{lnt})}$$
(5.18)

$$\tilde{v}(\xi, s) = \tilde{v}^{N} e^{-s\sqrt{2}(\xi - x_{lnt})}$$
(5.19)

Applying the inverse Laplace transform to equations (5.18) and (5.19), and noting that the initial conditions $u_0(\xi)$ and $v_0(\xi)$ occur at time $t = t_0$, yield the initial conditions along the linear-elastic rod in terms of the displacement and velocity of the boundary particle **N** as:

$$u_{0}(\xi) = u^{N} \left(t_{0} - \sqrt{2} \left(\xi - x_{lnt} \right) \right) H \left(t_{0} - \sqrt{2} \left(\xi - x_{lnt} \right) \right)$$
(5.20)

$$v_0\left(\xi\right) = v^{N}\left(t_0 - \sqrt{2}\left(\xi - x_{lnt}\right)\right) H\left(t_0 - \sqrt{2}\left(\xi - x_{lnt}\right)\right)$$

$$(5.21)$$

Here, H(...) denotes the Heaviside function. Furthermore, note that equations (5.20) and

(5.21) are dimensionless expressions for the initial conditions $u_0(\xi)$ and $v_0(\xi)$ along the linear-elastic rod expressed in terms of respectively the displacement and velocity of the boundary particle **N** as a function of both time and space, and that the relation between time t and the position ξ along the linear-elastic rod is described by the wave velocity in the rod.

Due to the Heaviside function in both equations (5.20) and (5.21), it follows that the initial conditions $u_0(\xi)$ and $v_0(\xi)$ are nonzero only in the segment $\xi < x_{lnt} + t_0/\sqrt{2}$. Substituting equations (5.20) and (5.21) into equation (5.17), the expression for $f_0(s)$ thus becomes:

$$\tilde{f}_{0}(s) = \int_{x_{Int}+t_{0}/\sqrt{2}}^{x_{Int}+t_{0}/\sqrt{2}} e^{-s\sqrt{2}(\xi-x_{Int})} \left(su^{N} \left(t_{0} - \sqrt{2} \left(\xi - x_{Int} \right) \right) + v^{N} \left(t_{0} - \sqrt{2} \left(\xi - x_{Int} \right) \right) \right) d\xi$$
 (5.22)

Finally, replacing the variable of integration ξ in equation (5.22) by a variable of integration τ , where $\tau = \sqrt{2} (\xi - x_{lnt})$, yields the expression for $\tilde{f}_0(s)$ as:

$$\tilde{f}_0(s) = \frac{1}{2} \sqrt{2} \int_0^{t_0} e^{-s\tau} \left(su^{\mathbf{N}} \left(t_0 - \tau \right) + v^{\mathbf{N}} \left(t_0 - \tau \right) \right) d\tau \tag{5.23}$$

The expression for $\tilde{f}_0(s)$ according to equation (5.23) is a convolution integral over the time domain $\tau = 0...t_0$. Here, $\tau = 0$ is the absolute starting point in the time domain, i.e. the time at which the complete lattice was at rest before any loading is applied, while $\tau = t_0$ is the last time moment at which new initial conditions were considered for the lattice. Here, note that Appendix J.7 gives an alternative derivation to obtain equation (5.23) from equation (5.17).

Equation (5.23) no longer contains any initial displacements or initial velocities of the linear-elastic rod. Instead, the expression for $f_0(s)$ now exclusively consists of terms related to the boundary particle **N** and thereby accounts for the response of the linear-elastic rod in terms of the motion at the lattice-rod interface. Having derived the equation of motion for the boundary particle **N** that includes the boundary formulation for the linear-elastic rod, let us consider the full system of equations of motion for the one-dimensional discrete-continuous Hooke system, depicted in Figure 5.2, accounting for nonzero initial conditions.

5.2.2 Governing equations for the discrete-continuous Hooke system

Applying the Laplace transform to the equations of motion for particles $\mathbf{n} = 1...\mathbf{N-1}$ in the one-dimensional Hooke lattice, given in Appendix D.1 for zero initial conditions, accounting for nonzero initial conditions, as well as including the Laplace domain interface equation, previously given by equation (5.16), the governing system of equations of motion for the one-dimensional discrete-continuous Hooke system with nonzero initial conditions is found in the Laplace domain as:

$$M^{1}s^{2}\tilde{u}^{1} - K_{e}^{1,2}\tilde{e}^{1,2} = \tilde{F}(s) + M^{1}(su_{0}^{1} + v_{0}^{1})$$

$$(5.24)$$

$$M^{n} s^{2} \tilde{u}^{n} + K_{e}^{n-1,n} \tilde{e}^{n-1,n} - K_{e}^{n,n+1} \tilde{e}^{n,n+1} = M^{n} \left(s u_{0}^{n} + v_{0}^{n} \right)$$
(5.25)

$$M^{N} s^{2} \tilde{u}^{N} + K_{e}^{N-1,N} \tilde{e}^{N-1,N} + \frac{1}{2} s \sqrt{2} \tilde{u}^{N} = M^{N} \left(s u_{0}^{N} + v_{0}^{N} \right) + f_{0} \left(s \right)$$
(5.26)

Here, u_0^n and v_0^n are respectively the initial displacement and initial velocity of the particles in the one-dimensional Hooke lattice for $\mathbf{n} = 1...\mathbf{N}$, and $f_0(s)$ is given by equation (5.23). In equation (5.24), $\tilde{F}(s)$ is the Laplace domain expression for the external force applied at particle 1. In general, the transformation of a time-dependent load to the Laplace domain is rather straightforward. Nevertheless, care should be taken that the Laplace domain expression for the applied load is used that corresponds to the correct time period, i.e. the time period for which new initial conditions are introduced at time t_0 .

To clarify this, let us here consider the pulse load F(t) with a single sinus period T_F , which is depicted in Figure 5.3 for two different cases: in the top graph, the pulse load is considered in time globally and thus for zero initial conditions with the sinus period T_F fully included, while the bottom graph shows a time period for which the time parameter t has been reset at time t_0 , where t_0 is chosen as $0 < t_0 < T_F$, and that has nonzero initial conditions. In the time period that starts at time t_0 , the loading that is applied prior to time t_0 is included in the lattice response by the nonzero initial conditions and the time-dependent load should therefore be considered to start at time t_0 . As a function of global time, and thus with zero initial conditions, the expression for the part of the load period that starts at time t_0 then becomes:

$$F(t) = \overline{F}\sin(\Omega t)H(T_F - t)H(t - t_0)$$
(5.27)

Here, \overline{F} is the amplitude and Ω is the dimensionless angular frequency of the pulse load. Note here that for the case that $t_0 \leq 0$, equation (5.27) reduces to the time domain expression for the full single-sinus pulse load, while for the case that $t_0 \geq T_F$, the load is equal to zero.

For the time period that starts at time t_0 , we must describe the applied loading to start at t = 0. The expression for the applied load in this time period can then be obtained from equation (5.27), by replacing the time t by the time $t + t_0$. In the time period for which the time parameter t has been reset at time t_0 , the expression for the load thus becomes:

$$F(t) = \overline{F}\sin(\Omega(t+t_0))H(T_F - (t+t_0))H(t)$$
(5.28)

Evaluating the Laplace transform to equation (5.28) analytically yields the expression for the sinus pulse load in the Laplace domain as:

$$\tilde{F}(s) = \overline{F} \frac{s \sin \Omega t_0 + \Omega \cos \Omega t_0 - \Omega e^{-s(T_F - t_0)}}{s^2 + \Omega^2} H(T_F - t_0)$$
(5.29)

Here, the Heaviside function is included to make sure that the expression for the applied load in the Laplace domain is equal to zero for $t_0 \ge T_F$.

In the example considered here, the applied load was chosen as a single sinus pulse load. A more elaborate derivation of the Laplace domain expression for this pulse load is given in Appendix J.5. In this appendix, additionally the corresponding Laplace domain expressions are derived for a continuous harmonic load and a half sinus pulse with a carrier frequency.

With the Laplace domain expression for the external force $\tilde{F}(s)$ known, equations (5.24) to (5.26) describe the full algebraic system of equations of motion for the one-dimensional discrete-continuous Hooke system. Solving this algebraic system yields the Laplace domain displacements \tilde{u}^n for all particles n = 1...N in the discrete-continuous Hooke system.

5.2.3 Transformation to the time domain accounting for nonzero ICs

For all particles, the time domain displacements u^n are obtained from the Laplace domain displacements \tilde{u}^n by applying and numerically evaluating the inverse Laplace transform. To numerically evaluate the inverse Laplace transform, its semi-infinite integral domain is truncated. Appendix J.2 shows how a time domain expression may be obtained by applying the inverse Laplace transform to a Laplace domain expression in terms of frequency ω rather than in terms of the complex-valued Laplace parameter s. Truncating the semi-infinite domain of the inverse Laplace transform at a frequency ω_{tr} , thus yields the time domain displacements u^n of a particle \mathbf{n} from the Laplace domain displacements \tilde{u}^n as:

$$u^{\mathbf{n}} = \frac{e^{\sigma t}}{\pi} \int_{0}^{\omega_{r}} \operatorname{Re}\left\{\tilde{u}^{\mathbf{n}} e^{i\omega t}\right\} d\omega \tag{5.30}$$

Applying the inverse Laplace transform in accordance with equation (5.30) is only valid if its integrand is integrable and has decayed sufficiently within the truncated integral domain, so that the part of the integral that is not included, i.e. the integral over the domain $\omega = \omega_{tr} \dots \infty$, is negligible.

Let us consider this for the Laplace domain displacement \tilde{u}^n of a particle **n** in the interior of the discrete-continuous Hooke system. Assuming that the lattice is homogeneous, the particle **n** has a mass M and all Hooke elements have a stiffness K_e , so that the dimensionless

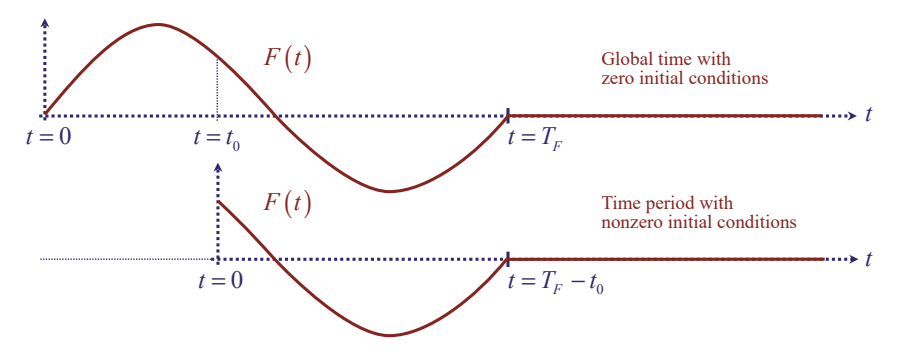


Figure 5.3: A single-sinus pulse load in global time with zero initial conditions and for a new time period with nonzero initial conditions.

mass and stiffnesses are respectively found as $M^n = 1$ and $K_e^{n-1,n} = K_e^{n,n+1} = \frac{1}{2}$. The Laplace domain displacement \tilde{u}^n of a particle **n** can then be obtained from equation (5.25) as:

$$\tilde{u}^{\mathbf{n}} = \frac{su_0^{\mathbf{n}} + v_0^{\mathbf{n}}}{s^2 + 1} + \frac{\tilde{u}^{\mathbf{n}-1} + \tilde{u}^{\mathbf{n}+1}}{2(s^2 + 1)}$$
(5.31)

For any particle **n** in the interior of the lattice, the decay of its Laplace domain displacements for $\omega \to \infty$ must be similar. Thus, if the Laplace domain displacement \tilde{u}^n tends to zero for $\omega \to \infty$, the second term on the right-hand side of equation (5.31) must always tend to zero as well. Considering the first term on the right-hand side of equation (5.31) then shows that the Laplace domain displacement \tilde{u}^n decays with a rate ω^{-1} for $\omega \to \infty$.

Laplace domain velocity and acceleration for nonzero initial conditions

The corresponding velocities and the accelerations of particle $\bf n$ may either be obtained from time differentiation, i.e. by taking the first and second time derivatives of equation (5.30) respectively, or by evaluation of the Laplace transforms of the velocities and accelerations. In this case, obtaining the velocity and acceleration by time differentiation of equation (5.30) is only allowed for zero initial conditions, because for nonzero initial conditions its integral is not convergent. This is illustrated by Figure 5.4a and Figure 5.4b that give the absolute values of the corresponding Laplace domain expressions for a one-mass-spring system, which according to Appendix J.4 are respectively found as $s\tilde{u}^n$ and $s^2\tilde{u}^n$, for respectively zero and nonzero initial conditions. Here, Figure 5.4b shows that the magnitudes of both these expressions do not tend to zero for $\omega \to \infty$ for nonzero initial conditions.

Instead, we derive the Laplace domain expressions for the velocity and acceleration of a particle **n** by evaluating the Laplace transforms of the corresponding time domain expressions. Appendix J.1 shows that evaluating the Laplace transforms of the velocity and acceleration, respectively yields the expressions for the Laplace domain velocity and acceleration as $\tilde{v}^n = s\tilde{u}^n - u_0^n$ and $\tilde{a}^n = s^2\tilde{u}^n - su_0^n - v_0^n$.

Substituting equation (5.31) into the expressions for the Laplace domain velocity and acceleration that include the initial conditions, we respectively find:

$$\tilde{v}^{n} = s\tilde{u}^{n} - u_{0}^{n} = \frac{-u_{0}^{n} + sv_{0}^{n}}{s^{2} + 1} + \frac{s\left(\tilde{u}^{n-1} + \tilde{u}^{n+1}\right)}{2\left(s^{2} + 1\right)}$$
(5.32)

$$\tilde{a}^{\mathbf{n}} = s^{2}\tilde{u}^{\mathbf{n}} - su_{0}^{\mathbf{n}} - v_{0}^{\mathbf{n}} = \frac{-su_{0}^{\mathbf{n}} - v_{0}^{\mathbf{n}}}{s^{2} + 1} + \frac{s^{2}\left(\tilde{u}^{\mathbf{n}-1} + \tilde{u}^{\mathbf{n}+1}\right)}{2\left(s^{2} + 1\right)}$$
(5.33)

From equations (5.32) and (5.33) it follows that, if we account for the initial conditions in the Laplace domain expressions for the velocity and acceleration of a particle \mathbf{n} , both the Laplace domain velocity and acceleration tend to zero for $\omega \to \infty$ and have a decay rate that is similar to that of the Laplace domain displacement obtained in equation (5.31).

The expression for the Laplace domain displacement \tilde{u}^1 of particle 1 contains an additional term that is related to the applied load, denoted in the Laplace domain as $\tilde{F}(s)$. From equation (5.29) it can be straightforwardly determined that, for any time t_0 , the magnitude of the Laplace domain expression for the single sinus pulse load decays with a rate of at least ω^{-1} for $\omega \to \infty$. Accordingly, the expression for the Laplace domain displacement of particle N located at the interface between the lattice and the rod, i.e. \tilde{u}^N , contains an additional term related to the expression for $\tilde{f}_0(s)$. From incorporating $\tilde{f}_0(s)$ into the expression for the displacement of particle N, it cannot be unambiguously determined whether the corresponding term in the displacement \tilde{u}^N will tend to zero for $\omega \to \infty$. Nevertheless, as $\tilde{f}_0(s)$ describes the contribution of the rod's initial conditions at time t_0 in terms of the displacement of particle N prior to time t_0 , its decay for $\omega \to \infty$ is expected to be similar to the decay of the Laplace domain displacement of any other particle in the lattice. The fact that the term related to $\tilde{f}_0(s)$ in the Laplace domain displacement \tilde{u}^N indeed tends to zero for $\omega \to \infty$ for either particle in the interior of the lattice has numerically been verified.

Erroneous response at and shortly after reinitiation of the time parameter

Since the magnitude of each of the obtained Laplace domain expressions for the displacement, velocity and acceleration of a particle \mathbf{n} , given by equations (5.31) to (5.33), tend to zero for $\omega \to \infty$, the displacement, velocity and acceleration of a particle \mathbf{n} in the interior of the lattice may respectively be obtained in the time domain by analytically evaluating their inverse Laplace transforms. Nevertheless, when these inverse Laplace transforms are evaluated numerically, and their semi-infinite integral domains are truncated, they do not yield the proper time domain response.

To illustrate this, let us consider the time domain expression for the displacement $u^{\mathbf{n}}$ of a particle \mathbf{n} in the interior of the lattice, given by equation (5.30), which follows from applying the inverse Laplace transform. Appendix J.3 shows that by employing the causality principle, the integrand of the inverse Laplace transform, in equation (5.30) given as $\operatorname{Re}\left\{\tilde{u}^{\mathbf{n}}e^{i\omega t}\right\}$, may alternatively be described as either $2\operatorname{Re}\left\{\tilde{u}^{\mathbf{n}}\right\}\cos\omega t$ or $-2\operatorname{Im}\left\{\tilde{u}^{\mathbf{n}}\right\}\sin\omega t$. These integrands can only yield the exact same and correct time domain displacement when the full semi-

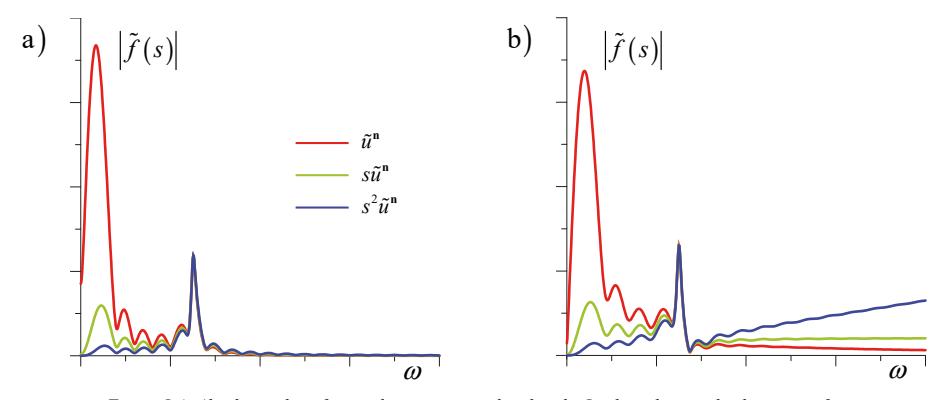


Figure 5.4: Absolute value of several expressions related to the Laplace domain displacement of a one-mass-spring system, with: a) Zero initial conditions; b) Nonzero initial conditions.

infinite domain of the inverse Laplace transform is taken into account. Therefore, let us compare the time domain displacements that result from numerically applying the inverse Laplace transform to each of these integrands. As an alternative to equation (5.30), applying the truncation of the semi-infinite domain of the inverse Laplace transform at frequency ω_{tr} , the time domain displacement $u^{\mathbf{n}}$ of a particle \mathbf{n} may be obtained from the Laplace domain displacements $\tilde{u}^{\mathbf{n}}$ as either one of:

$$u^{\mathbf{n}} = \frac{2e^{\sigma t}}{\pi} \int_{0}^{\omega_{\mathbf{n}}} \operatorname{Re}\left\{\tilde{u}^{\mathbf{n}}\right\} \cos \omega t d\omega \tag{5.34}$$

$$= \frac{-2e^{\sigma t}}{\pi} \int_{0}^{\omega_{\text{tr}}} \text{Im} \left\{ \tilde{u}^{\text{n}} \right\} \sin \omega t d\omega \tag{5.35}$$

Figure 5.5 shows the different instances of the time domain displacement of the mass in a one-mass-spring system due to an applied single sinus pulse load, obtained by respectively employing the inverse Laplace transform according to equations (5.30), (5.34) and (5.35). To enforce the necessity to take nonzero initial conditions into account, the time domain simulation was manually reinitiated at respectively time t_0 , t_1 and t_2 . Here, Figure 5.5a shows the displacements as a function of the global time parameter t, while Figure 5.5b shows the displacements in the time period for which the time parameter t has been reset at time t_0 . In both figures, the dashed black line shows the exact solution.

Figure 5.5a clearly shows that, each time the time variable is reset and new nonzero initial conditions are taken into account, numerically applying the inverse Laplace transform with a finite domain of integration yields an error in the displacement near the reinitiation point. The error for the different instances of the inverse Laplace transform according to respectively equations (5.30), (5.34) and (5.35) are clearly visible in Figure 5.5b. The displacement obtained by applying the inverse Laplace transform according to equation (5.35) is given by the red line and has the largest error. This large error can be explained by considering that, for a finite domain of integration and thus independent of the truncation frequency ω_{tr} , the term $\sin \omega t$ in equation (5.35) will always be equal to zero for t=0. Consequently, noting that $\text{Im}\left\{\tilde{u}^{\mathbf{n}}\right\}$ is finite for all frequencies within the integral domain, the numerical integration over a finite integral domain according to equation (5.35) will also always be equal to zero for time t=0 and can never yield a nonzero result. Thereby, the identity of the inverse Laplace transform according to equation (5.35) is invalid for nonzero initial conditions.

Although Figure 5.5b clearly shows that applying the inverse Laplace transform according to equation (5.34), given by the blue line, yields a relatively accurate displacement, a certain error remains. Taking the time derivative of equation (5.34), it can be straightforwardly derived that the initial velocity is related to the corresponding initial displacement as $\dot{u}_0 = \sigma u_0$. Now, generally the Laplace parameter σ is chosen as a small real positive value and is included only to make sure that the inverse Laplace transform over its integrand is in the region of convergence. In the limit of the Laplace parameter σ going to zero, it follows that \dot{u}_0 must tend to zero, and thereby does not coincide with the initial velocity at t = 0. As

a result, the initial slope of the displacement of the one-mass-spring system, obtained by applying the inverse Laplace equation using equation (5.34), is significantly smaller than the slope of the exact solution. Nevertheless, its error is significantly smaller than the error obtained by using equation (5.35).

The green lines in Figure 5.5 show the resulting displacement of the one-mass-spring system obtained by applying the inverse Laplace transform according to equation (5.30). By expanding the integrand of equation (5.30) using Euler's formula, it can be straightforwardly shown that the resulting displacement must be the exact average of the displacements obtained by employing equations (5.34) and (5.35). The oscillation of the obtained displacements around the exact displacement as a function of time is a logical consequence of the error at the time of reinitiation. Note here that the behaviour of the corresponding velocities and accelerations of a particle **n** in the lattice, for which the expressions are given in Appendix J.4, is even worse. This is testified by Appendix J.6, which considers the application of the MTFD-method to the one-mass-spring system, and thereby includes all derivations for the example of the one-mass-spring system discussed here.

If we analytically evaluate the inverse Laplace transforms according to equations (5.30), (5.34) and (5.35) for a semi-infinite integral domain, i.e. for $\omega_{tr} = \infty$, each would yield the exact same and correct time domain displacements. Figure 5.5 however shows that numerically evaluating these inverse Laplace transforms for a finite domain of integration yields unsatisfactory results for nonzero initial conditions. In the following, we will introduce a formulation for the inverse Laplace transform that greatly improves the performance for a finite integration domain and is generally applicable for nonzero initial conditions.

Improved formulation for the inverse Laplace transform accounting for nonzero ICs

To improve the results for the numerical evaluation of the inverse Laplace transform when using a truncated, and thus finite, domain of integration for a lattice that, in the time domain, has nonzero initial conditions, we extract the contribution of the initial conditions from the corresponding Laplace domain expression and separately include their contribution in the time domain. As a consequence, the remaining Laplace domain expression, henceforth

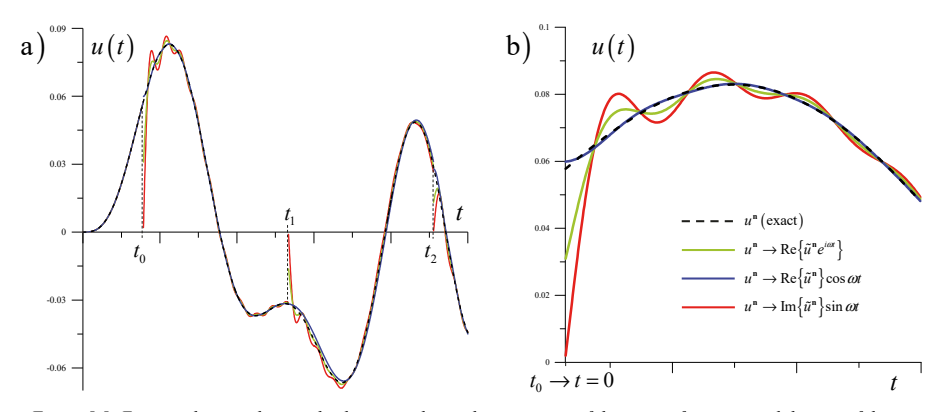


Figure 5.5: Error in the time domain displacement due to the truncation of the semi-infinite integral domain of the inverse Laplace transform: a) As a function of global time; b) In the time period that is reset at to.

denoted as the improved Laplace domain expression, can be considered as a Laplace domain expression for a lattice with zero initial conditions. To clarify this, let us consider an arbitrary Laplace domain relation \tilde{f} that is valid for a lattice with a nonzero initial condition f_0 in the time domain. Extracting the contribution of the nonzero initial condition f_0 then yields the corresponding time domain relation as:

$$f(t) = \mathcal{L}^{-1}\left\{\tilde{f}\right\} = \mathcal{L}^{-1}\left\{\tilde{f} - \frac{f_0}{s}\right\} + \mathcal{L}^{-1}\left\{\frac{f_0}{s}\right\} = \mathcal{L}^{-1}\left\{\tilde{f}_{imp}\right\} + f_0H(t)$$
(5.36)

Here, \tilde{f}_{imp} is the so-called improved Laplace domain relation that corresponds to a time domain relation with zero initial conditions. Consequently, numerically evaluating the inverse Laplace transform of the improved Laplace domain relation \tilde{f}_{imp} over a finite integral domain should not result in any erroneous behaviour in the time domain response after reinitiation of the time variable and the introduction of new nonzero initial conditions.

To obtain an improved expression for the Laplace domain displacement of a particle \mathbf{n} in the interior of the discrete-continuous Hooke system, we do not only extract the contribution of the initial displacement, but we also extract the contributions of the initial velocity and the initial acceleration from the Laplace domain displacement. Similarly, next to extracting the contribution of the initial velocity from the expression for the Laplace domain velocity, we additionally extract the contribution of the initial acceleration. Thus, the improved Laplace domain expressions for the displacement, velocity and acceleration of a particle \mathbf{n} respectively read:

$$\tilde{u}_{imp}^{n} = \tilde{u}^{n} - \frac{u_{0}^{n}}{s} - \frac{v_{0}^{n}}{s^{2}} - \frac{a_{0}^{n}}{s^{3}}$$
(5.37)

$$\tilde{v}_{imp}^{n} = \tilde{v}^{n} - \frac{v_{0}^{n}}{s} - \frac{a_{0}^{n}}{s^{2}}$$
 (5.38)

$$\tilde{a}_{imp}^{\mathbf{n}} = \tilde{a}^{\mathbf{n}} - \frac{a_0^{\mathbf{n}}}{s} \tag{5.39}$$

Taking into account that the Laplace domain velocity and acceleration are respectively obtained as $\tilde{v}^{\mathbf{n}} = s \tilde{u}^{\mathbf{n}} - u_0^{\mathbf{n}}$ and $\tilde{a}^{\mathbf{n}} = s^2 \tilde{u}^{\mathbf{n}} - s u_0^{\mathbf{n}} - v_0^{\mathbf{n}}$, we may express the improved Laplace domain expressions for the velocity and acceleration as $\tilde{v}_{imp}^{\mathbf{n}} = s \tilde{u}_{imp}^{\mathbf{n}}$ and $\tilde{a}_{imp}^{\mathbf{n}} = s^2 \tilde{u}_{imp}^{\mathbf{n}}$ respectively. Applying the inverse Laplace transform then yields the time domain displacement, velocity and acceleration of particle \mathbf{n} in the discrete-continuous Hooke system for $t \ge 0$ as:

$$u^{\mathbf{n}} = \frac{e^{\sigma t}}{\pi} \int_{0}^{+\infty} \text{Re} \left\{ \tilde{u}_{imp}^{\mathbf{n}} e^{i\omega t} \right\} d\omega + u_{0}^{\mathbf{n}} + v_{0}^{\mathbf{n}} t + \frac{1}{2} a_{0}^{\mathbf{n}} t^{2}$$
(5.40)

$$\dot{u}^{\mathbf{n}} = \frac{e^{\sigma t}}{\pi} \int_{0}^{+\infty} \operatorname{Re}\left\{s\tilde{u}_{imp}^{\mathbf{n}} e^{i\omega t}\right\} d\omega + v_{0}^{\mathbf{n}} + a_{0}^{\mathbf{n}} t \tag{5.41}$$

$$\ddot{u}^{\mathbf{n}} = \frac{e^{\sigma t}}{\pi} \int_{0}^{+\infty} \operatorname{Re}\left\{s^{2} \tilde{u}_{imp}^{\mathbf{n}} e^{i\omega t}\right\} d\omega + a_{0}^{\mathbf{n}}$$
(5.42)

The expressions for the velocity and the acceleration according to equations (5.41) and (5.42) may alternatively be obtained by direct time differentiation of equation (5.40).

Substituting the Laplace domain displacement \tilde{u}^n , given by equation (5.31), into equation (5.37) yields the improved Laplace domain expression for the displacement as:

$$\tilde{u}_{imp}^{\mathbf{n}} = -\frac{su_0^{\mathbf{n}} + v_0^{\mathbf{n}}}{s^2 \left(s^2 + 1\right)} - \frac{a_0^{\mathbf{n}}}{s^3} + \frac{\tilde{u}^{\mathbf{n}-1} + \tilde{u}^{\mathbf{n}+1}}{2\left(s^2 + 1\right)}$$
(5.43)

The improved Laplace domain displacement according to equation (5.43) decays with a rate ω^{-3} for $\omega \to \infty$. Consequently, the improved Laplace domain velocity and acceleration respectively decay with a rate ω^{-2} and ω^{-1} for $\omega \to \infty$. Evidently, comparing equation (5.43) with equation (5.31) shows that the improved Laplace domain expressions decay and tend to zero for $\omega \to \infty$ with a rate ω^2 faster than the original Laplace domain expressions.

Alternate time domain expressions following from the causality principle

By employing the causality principle, as demonstrated in Appendix J.3, we may, as an alternative to equation (5.40), obtain the time domain displacement of a particle \mathbf{n} in the discrete-continuous Hooke system for $t \ge 0$ as either one of:

$$u^{\mathbf{n}} = \frac{2e^{\sigma t}}{\pi} \int_{0}^{+\infty} \text{Re}\{\tilde{u}_{imp}^{\mathbf{n}}\}\cos\omega t d\omega + u_{0}^{\mathbf{n}} + v_{0}^{\mathbf{n}}t + \frac{1}{2}a_{0}^{\mathbf{n}}t^{2}$$
 (5.44)

$$= \frac{-2e^{\sigma t}}{\pi} \int_{0}^{+\infty} \text{Im} \left\{ \tilde{u}_{imp}^{\mathbf{n}} \right\} \sin \omega t d\omega + u_{0}^{\mathbf{n}} + v_{0}^{\mathbf{n}} t + \frac{1}{2} a_{0}^{\mathbf{n}} t^{2}$$
 (5.45)

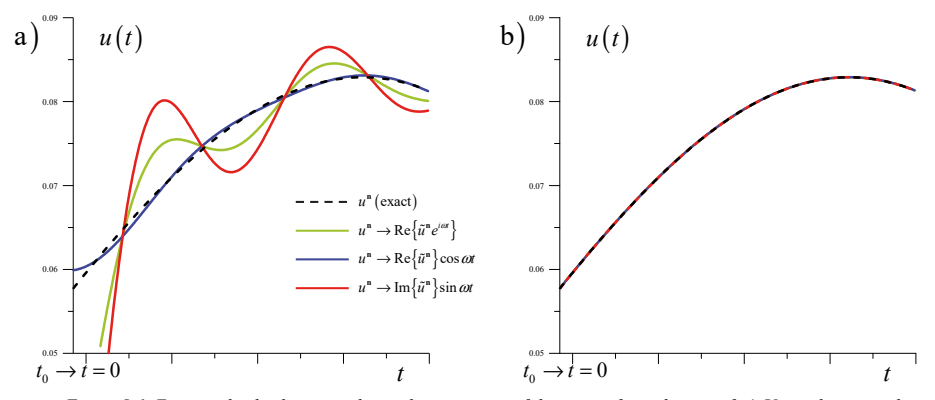


Figure 5.6: Error in the displacement due to the truncation of the semi-infinite domain of: a) Using the original expression; and b) Using the improved expression for the inverse Laplace transform.

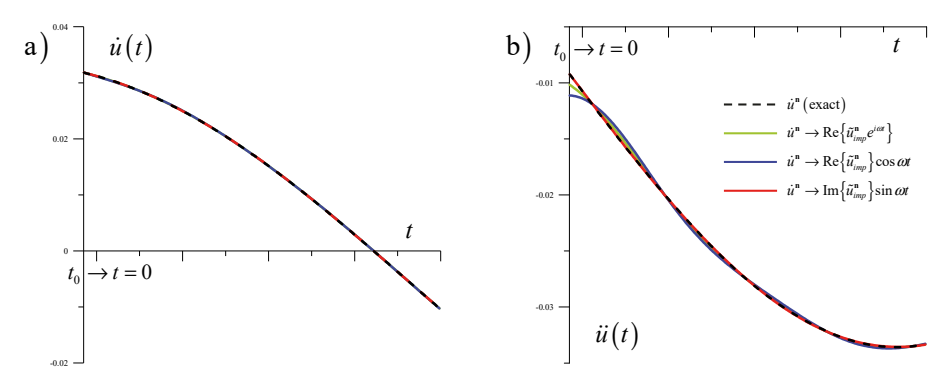


Figure 5.7: a) Velocity; and b) Acceleration of the one-mass-spring system obtained using the improved expressions for the inverse Laplace transform accounting for nonzero initial conditions.

Corresponding alternative expressions for the velocity and acceleration of a particle \mathbf{n} in the discrete-continuous Hooke system may be obtained from equations (5.44) and (5.45) by differentiation to time. The resulting expressions are given in Appendix J.4.

To illustrate the improvements of the time domain displacements resulting from numerically applying the inverse Laplace transform according to respectively equations (5.40), (5.44) and (5.45) compared to numerically applying the inverse Laplace transform according to the original expression, we here once again consider the one-mass-spring system. Figure 5.6a is a close-up of Figure 5.5b and thus shows the displacements that were previously obtained by numerically applying the inverse Laplace transform according to respectively equations (5.30), (5.34) and (5.35) right after the lattice was reinitiated at time t_0 . For the same time segment, Figure 5.6b shows the displacements obtained by applying the inverse Laplace transform according to respectively equations (5.40), (5.44) and (5.45).

According to Figure 5.6b equations (5.40), (5.44) and (5.45) each yield practically the same time domain displacement as the exact displacement, again given by the dashed black line. Comparing Figure 5.6a and Figure 5.6b it is apparent that, for the example of the one-mass-spring system, the behaviour near the nonzero initial conditions has significantly improved by numerically applying the inverse Laplace transform according to equations (5.40), (5.44) and (5.45). The improvement is even more striking when noting that the displacements of Figure 5.6a were obtained using a numerical integration scheme with a four times finer mesh than the numerical scheme used to acquire the displacements of Figure 5.6b.

Figure 5.7a and Figure 5.7b respectively show the velocities and accelerations of the one-mass-spring system resulting from respectively applying the inverse Laplace transform according to equations (5.41) and (5.42), as well as the velocities and accelerations that follow from applying the inverse Laplace transforms that are obtained by respectively differentiating equations (5.44) and (5.45) to time once and twice. From Figure 5.7a it is evident that, just like the displacements, the obtained velocities of the one-mass-spring system are in correspondence with the exact solution. Although significantly improved, Figure 5.7b clearly shows that, using the improved formulation for the inverse Laplace transform, the accelerations of the one-mass-spring system resulting from equations (5.40) and (5.44) still have a small deviation from the exact solution at and shortly after resetting the time parameter, i.e.

at and shortly after time t_0 . The error of the accelerations at the reinitiation point is much more pronounced than the error of either the displacement or velocity because the decay of the improved Laplace domain acceleration for $\omega \to \infty$ is much slower than the decay of the corresponding relations for the displacement and velocity. When numerically evaluating the inverse Laplace transform of the accelerations, using a smaller frequency interval, as well as increasing the truncation frequency ω_{tr} will both reduce the absolute error.

5.2.4 Response of the 1D Hooke system using the MTFD-method

The parameters of the one-dimensional discrete-continuous Hooke system, depicted in Figure 5.2, are here chosen in accordance with the parameters of the one-dimensional discrete-continuous BKV system for which the response is depicted in Figure 3.5 in Section 3.2.5. The one-dimensional discrete-continuous Hooke system thus has a Young's modulus E=20 MPa, a mass density $\rho=2000$ kg/m³ and a cross-section area $A=dy\cdot dz=1$ m². The featured one-dimensional Hooke lattice consists of 80 particles at an interparticle distance of $\ell=0.2$ m, and the mass of its particles and the stiffness of its elements respectively follow from the general properties as M=400 kg and $K_e=100$ MN/m. Consequently, the particle frequency of the homogeneous Hooke lattice is found as $\omega_0=707.1$ rad/s.

Figure 5.8 shows the longitudinal displacements along the one-dimensional discrete-continuous Hooke system at eight consecutive time moments that are due to a single-sinus pulse load applied to particle 1. In its dimensionless form, the pulse load is expressed as:

$$F(t) = \overline{F}\sin(\Omega t)H(T_F - t)H(t)$$

In this case, the amplitude and angular frequency of the sinus in the pulse load are respectively chosen as $\overline{F}=1\,\mathrm{MN}$ and $\omega_F=80\,\mathrm{rad/s}$. The given load frequency ω_F corresponds to a dimensionless frequency of the sinus in the applied single-sinus pulse load of $\Omega_F=0.113$. The period T_F of the applied pulse consists of exactly 200 time steps and the total time simulation consists of a 1000 time steps.

The continuous red line in Figure 5.8 gives the displacement that results from applying the MTFD-method, where the time parameter was reinitiated every 100 time steps, while the dashed blue line gives the displacements resulting from the frequency domain solution. Note here that, without reinitiation of the time parameter, the MTFD-method and the frequency domain solution would be exactly the same. At each reinitiation, the error of the acceleration, as portrayed by Figure 5.7b for the one-mass-spring system, also occurs for the discrete-continuous Hooke system. Under the loads applied here however, the magnitude of this error is only slightly larger than the precision of the numerical model. Consequently, only in the vicinity of each reinitiation point, the time domain response of the MTFD-method and frequency domain solution are slightly different, while Figure 5.8 verifies that these differences are negligible on the depicted scale.

In Figure 5.8, the continuous green line shows the displacement resulting from applying a Runge-Kutta scheme to solve the system directly in the time domain, here denoted as the time domain solution. The displacement obtained by the time domain solution is slightly

shifted rightward compared to the displacements found by the MTFD-method and the frequency domain solution, but as the continuous green line, which is behind the continuous red and dashed blue lines, is hardly visible in Figure 5.8, the differences are very small.

To compare the calculation time spent by respectively the MTFD-method, the frequency domain solution and the time domain solution, we consider the average of ten runs for each corresponding numerical model. The purpose of this is to minimize the influence on the calculation time of other computer processes running in the background, while running each of the numerical models. Here, we consider the calculation time as the time spent on actually solving the equations and for example time spent on data traffic and output are not included. For the MTFD-method and the frequency domain solution this involves solving the algebraic system of equations in the frequency domain and applying the inverse Laplace transform to obtain the time domain displacements for every time step. For the time domain solution the calculation time solely consists of applying the Runge-Kutta scheme to obtain the time domain displacement for every time step directly.

For each method of solution, Table 5.1 gives the range as well as the average of the calculation times that were found for the ten runs and thereby gives a good impression of the numerical effort that each of the numerical models require. The frequency domain solution on average takes approximately 1.75 seconds of calculation time during the numerical simulation. This is logically the least amount of required calculation time as it only needs to solve the algebraic system of equations in the frequency domain once and for zero initial conditions. Performing the numerical simulation using the MTFD-method on average requires approximately 2.85 seconds of calculation time. Thus, reinitiating the time parameter every 100 time steps and consequently solving the algebraic system of equations in the frequency domain another nine times for nonzero initial conditions requires a little over a second additional calculation time. At an average of approximately 5.27 seconds of required calculation time, the time domain solution is significantly slower. Linearly extrapolating the required

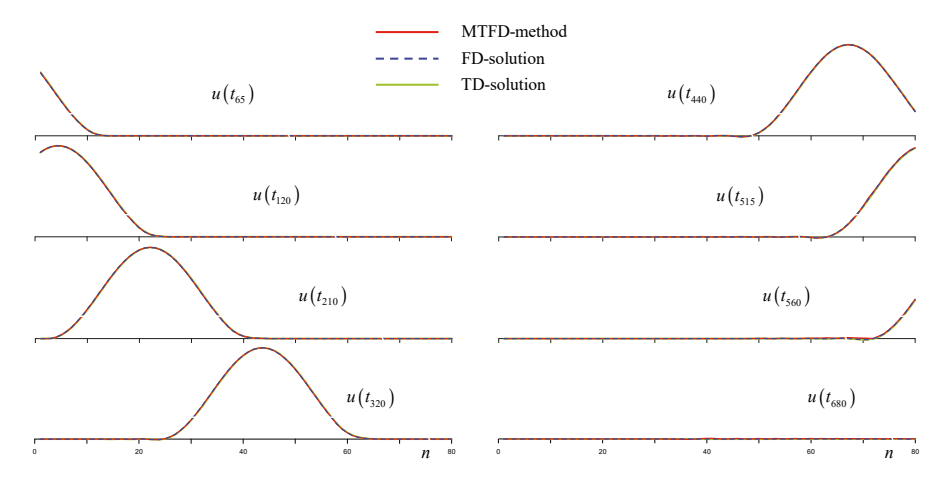


Figure 5.8: Longitudinal displacement along the one-dimensional discrete-continuous linear-elastic Hooke system at successive time moments due to a single-sinus pulse load applied at the first particle.

Table 5.1: Minimum, average and maximum calculation times for ten separate runs of the MTFD-method, frequency domain and time domain solutions.

	MTFD-method	FD-solution	TD-solution
Min	2,434 s	1,607 s	5,087 s
Average	2,847 s	1,747 s	5,271 s
Max	3,370 s	1,856 s	5,477 s

calculation time for the MTFD-method as a function of the amount of time-parameter-reinitiations, it follows that at roughly 32 reinitiations of the time parameter, the MTFD-method and the time domain solution will require the same amount of calculation time.

Since the MTFD-method is here manually applied to the rather simplistic discrete-continuous Hooke system, it does not actually yield any computational profit, after all, the Hooke system may always be evaluated using the frequency domain solution. Nevertheless, once we consider the nonlinear behaviour of for example the BKV system, the frequency domain solution is no longer valid to determine the overall response of the system. Additionally, taking into account that a time domain solution requires more calculation time when nonlinear events are accounted for, the real potential of the MTFD-method is found in its application to a lattice that allows for nonlinear phenomena. In the following section, we will therefore apply the MTFD-method to a discrete-continuous BKV system. Compared to the discrete-continuous Hooke system, the discrete-continuous BKV system does not only pose additional challenges by allowing for nonlinear events, but also by incorporating viscous damping.

5.3 The MTFD-method applied to a discrete-continuous BKV system

In Section 5.2, the mixed time-frequency domain, or MTFD-, method was applied to a one-dimensional discrete-continuous Hooke system to demonstrate how the method works and to emphasize several issues that must be accounted for when applying this method. As the MTFD-method is particularly developed for media that incorporate nonlinear effects, ergo non-smooth dynamic systems, its application to the Hooke system is superfluous. In this section, we will therefore apply the MTFD-method to the discrete-continuous BKV system that consists of a one-dimensional BKV-lattice in the near field and a viscoelastic rod in the far field, as previously depicted in Figure 3.2. Note here that, although the BKV-lattice allows for the non-smooth dynamic response to an externally applied load, nonlinear phenomena are only allowed within the domain of the BKV-lattice and should not reach the interface with the viscoelastic rod. After all, the interface with the viscoelastic rod is chosen at such a distance from the load that the system response at this interface is linear.

In Section 5.3.1, we will first derive the equation of motion for the interface between the BKV-lattice and the viscoelastic rod specifically accounting for nonzero initial conditions (ICs). Subsequently, in Section 5.3.2, we state the governing system of equations of motion for the discrete-continuous BKV system accounting for nonzero initial conditions in the Laplace domain. Then, in Section 5.3.3, we will present the response of the discrete-continuous to an external load source as obtained by numerical implementation of the MTFD-method,

and verify the method by comparing its results to the corresponding response obtained by using a direct time domain approach. Finally, the advantages and disadvantages of the MTFD-method are discussed in Section 5.3.4.

5.3.1 Boundary formulation for the BKV system with nonzero ICs

The behaviour of the viscoelastic rod in interaction with the one-dimensional BKV lattice was previously described in the time domain by equations (3.11) to (3.13). Applying the Laplace transform with respect to time as derived in Appendix J.1, and thereby accounting for nonzero initial conditions, yields equations (3.11) to (3.13) in the Laplace domain as:

$$s^{2}\tilde{u}(x,s) - \frac{1}{2}(1 + 2\zeta s)\tilde{u}''(x,s) = su_{0}(x) + v_{0}(x) - \zeta u_{0}''(x)$$
(5.46)

$$M^{N}s^{2}\tilde{u}^{N} + \left(C_{e}^{N-1,N}s + K_{e}^{N-1,N}\right)\tilde{e}^{N-1,N} - M^{N}\left(su_{0}^{N} + v_{0}^{N}\right) - C_{e}^{N-1,N}e_{0}^{N-1,N} = \frac{1}{2}\left(1 + 2\zeta s\right)\tilde{u}'(x_{Int},s) - \zeta u_{0}'(x_{Int})$$
(5.47)

$$\tilde{u}^{N} = \tilde{u}(x_{lnt}, s) \tag{5.48}$$

Here, $u_0(x)$, $v_0(x)$, u_0^N and v_0^N are the initial displacements and initial velocities along the viscoelastic rod and of the boundary particle **N** in the time domain respectively. Whereas equations (5.47) and (5.48) are respectively the force and displacement relations at the discrete-continuous interface, equation (5.46) gives the equation of motion of the viscoelastic rod and is valid only for $x > x_{Int}$.

Introducing $s_{\zeta} = s/\sqrt{1+2\zeta s}$ and choosing the featured square root such that the real part of s_{ζ} is positive, i.e. Re $(s_{\zeta}) > 0$, the general solution to equation (5.46) that accounts for the proper behaviour of the viscoelastic rod for $x \to \infty$ reads:

$$\tilde{u}(x,s) = Ae^{-s\zeta\sqrt{2}x} + \tilde{u}_p(x,s)$$
(5.49)

The first term on the right-hand side of equation (5.49) is the solution to the homogeneous version of equation (5.46), previously given as equation (3.14), where the amplitude A may be derived by considering the displacement relation at $x = x_{lnt}$ and, comparing its expression to the dispersion relations given in Appendix E.1, s_{ζ} can be considered as a complex-valued wavenumber. Furthermore, $\tilde{u}_{p}(x,s)$ denotes the particular solution to equation (5.46), which exclusively exists for nonzero initial conditions for the rod.

In accordance with the approach used for the discrete-continuous Hooke system, applying the differentiation to space to equation (5.49) and isolating the Laplace domain displacement of the viscoelastic rod, we may express its spatial derivative as:

$$\tilde{u}'(x,s) = -s_{\zeta}\sqrt{2}\tilde{u}(x,s) + s_{\zeta}\sqrt{2}\tilde{u}_{p}(x,s) + \tilde{u}'_{p}(x,s)$$

$$(5.50)$$

Substituting equation (5.50) into equation (5.47), accounting for equation (5.48), and

collecting all nonzero initial conditions on its right-hand side, we find the Laplace domain interface equation as:

$$M^{N}s^{2}\tilde{u}^{N} + \left(C_{e}^{N-1,N}s + K_{e}^{N-1,N}\right)\tilde{e}^{N-1,N} + \tilde{\chi}(s)\tilde{u}^{N} = M^{N}\left(su_{0}^{N} + v_{0}^{N}\right) + C_{e}^{N-1,N}e_{0}^{N-1,N} + \tilde{f}_{0}(s) \quad (5.51)$$

Here, the dynamic stiffness of the viscoelastic rod is equal to the dynamic stiffness previously found for the lattice with zero initial conditions and reads $\tilde{\chi}(s) = \frac{1}{2}s\sqrt{2+4\zeta s}$. Furthermore, the expression for $\tilde{f}_0(s)$ reads:

$$\tilde{f}_{0}(s) = \frac{1}{2} (1 + 2\zeta s) \left\{ s_{\zeta} \sqrt{2} \tilde{u}_{p}(x_{Int}, s) + \tilde{u}'_{p}(x_{Int}, s) \right\} - \zeta u'_{0}(x_{Int})$$
(5.52)

For the case of zero initial conditions, the right-hand side of equation (5.51) is equal to zero, so that equation (5.51) exactly matches the corresponding interface equation for zero initial conditions previously derived as equation (3.20).

Obtaining the particular solution

In correspondence with the derivation of the particular solution for the linear-elastic rod, we use a Green's function approach to find the particular solution to the equation of motion of the viscoelastic rod. To do this, we express equation (5.46) as:

$$s_{\xi}^{2}\tilde{u}(x,s) - \frac{1}{2}\tilde{u}''(x,s) = \tilde{f}(x,s) = \int_{x_{lm}}^{+\infty} \tilde{f}(\xi,s)\delta(x-\xi)d\xi$$

$$(5.53)$$

Here, the variable of integration ξ gives a coordinate along the linear-elastic rod, so that the integration is applied over the domain $\xi = x_{lnt} \dots \infty$. The expression for $\tilde{f}(\xi, s)$ is found as:

$$\tilde{f}(\xi,s) = \frac{su_0(\xi) + v_0(\xi) - \zeta u_0''(\xi)}{1 + 2\zeta s}$$

To obtain the particular solution to the equation of motion for the semi-infinite viscoelastic rod, given by equation (5.53), we may apply the same Green's function approach as previously used for the discrete-continuous Hooke system in Section 5.2.1. In fact, as shown in Appendix I.4, the particular solution for the viscoelastic rod may be obtained directly from the particular solution for the linear-elastic rod by substituting $s = s_{\zeta}$. The particular solution to the equation of motion for the semi-infinite viscoelastic rod is thus found as:

$$\tilde{u}_{p}(x,s) = \frac{1}{s_{\zeta}\sqrt{2}} \int_{x_{lm}}^{x} \tilde{f}(\xi,s) e^{-s_{\zeta}\sqrt{2}(x-\xi)} d\xi + \frac{1}{s_{\zeta}\sqrt{2}} \int_{x}^{+\infty} \tilde{f}(\xi,s) e^{-s_{\zeta}\sqrt{2}(\xi-x)} d\xi$$
(5.54)

Substituting the particular solution, given by equation (5.54), and its spatial derivative,

obtained by applying Leibniz' rule for differentiation of integrals, into equation (5.52) as well as taking into account the expression for $\tilde{f}(\xi,s)$, the expression for $\tilde{f}_0(s)$ becomes:

$$\tilde{f}_{0}(s) = -\zeta u'_{0}(x_{Int}) + \int_{x_{Int}}^{+\infty} e^{-s_{\zeta}\sqrt{2}(\xi - x_{Int})} \left(su_{0}(\xi) + v_{0}(\xi) - \zeta u''_{0}(\xi) \right) d\xi$$
(5.55)

Applying integration by parts to the part of the integrand that is related to $u_0''(\xi)$ yields:

$$\int_{x_{lnt}}^{+\infty} u_0''(\xi) e^{-s_{\zeta}\sqrt{2}(\xi - x_{lnt})} d\xi = -u_0'(x_{lnt}) - s_{\zeta}\sqrt{2}u_0(x_{lnt}) + 2s_{\zeta}^2 \int_{x_{lnt}}^{+\infty} u_0(\xi) e^{-s_{\zeta}\sqrt{2}(\xi - x_{lnt})} d\xi$$
 (5.56)

Substituting equation (5.56) into equation (5.55) and noting that the initial displacement of the rod's tip is equal to the initial displacement of the boundary particle, i.e. $u_0(x_{Int}) = u_0^N$, allows us to rearrange the expression for $\tilde{f}_0(s)$ as:

$$\tilde{f}_{0}\left(s\right) = \zeta s_{\zeta} \sqrt{2} u_{0}^{N} + \int_{x_{loc}}^{+\infty} e^{-s_{\zeta} \sqrt{2} \left(\xi - x_{loc}\right)} \left(\frac{s_{\zeta}^{2}}{s} u_{0}\left(\xi\right) + v_{0}\left(\xi\right)\right) d\xi \tag{5.57}$$

The integral in equation (5.57) describes the contribution of the rod's initial conditions to the interface equation. In the current form, the expression for $\tilde{f}_0(s)$ does not yet describe the Laplace domain interface equation exclusively in terms of the one-dimensional BKV-lattice, which would be true if zero initial conditions were considered. In the following, we will show how the explicit dependency on the motion of the viscoelastic rod can be removed from the interface equation by further analysing the expression for $\tilde{f}_0(s)$ given by equation (5.57).

Analysis of the remaining integral expression

Following Huygens' principle, the response of the lattice-rod interface can be considered as the input for the response of the viscoelastic rod. Therefore, the displacement and velocity of the viscoelastic rod can always be expressed in terms of the displacement and velocity of the boundary particle **N**, by accounting for the full response history of this particle.

To this purpose, we note that the initial displacement $u_0(\xi)$ and the initial velocity $v_0(\xi)$ along the rod for a new time period respectively correspond to the displacement and the velocity along the viscoelastic rod at time t_0 in terms of global time. We then express the displacement and the velocity at time t_0 , given in the integral of equation (5.57), as the inverse Laplace transform of the corresponding Laplace domain expressions. This yields equation (5.57) as:

$$\tilde{f}_{0}\left(s\right) = \zeta s_{\zeta} \sqrt{2} u_{0}^{\mathbf{N}} + \int_{s_{Int}}^{+\infty} e^{-s_{\zeta} \sqrt{2}(\xi - x_{Int})} \left(\frac{s_{\zeta}^{2}}{s} \mathcal{L}_{\hat{s}}^{-1} \left\{ \tilde{u}\left(\xi, \hat{s}\right) \right\} + \mathcal{L}_{\hat{s}}^{-1} \left\{ \tilde{v}\left(\xi, \hat{s}\right) \right\} \right) d\xi$$

$$(5.58)$$

Here, \hat{s} is the complex-valued Laplace parameter that corresponds to the application of the inverse Laplace transform with respect to time t_0 , which is denoted as such to distinguish it from the Laplace parameter s already appearing in equations (5.57) and (5.58). The corresponding inverse Laplace transform is defined as:

$$\mathcal{L}_{\hat{s}}^{-1}\left\{\tilde{f}\left(\xi,\hat{s}\right)\right\} = \frac{1}{2\pi i} \lim_{\alpha \to \infty} \int_{\sigma-i\alpha}^{\sigma+i\alpha} \tilde{f}\left(\xi,\hat{s}\right) e^{\hat{s}t_0} d\hat{s}$$

$$(5.59)$$

For the inverse Laplace transforms in equation (5.58), we consider the response of the viscoelastic rod at time t_0 in time globally, so in terms of its original time parameter that has not been reset, and thus for zero initial conditions. To obtain these inverse transforms, we may therefore disregard the particular solution that was previously included in for example equation (5.49). Accounting for the proper behaviour of the rod at $\xi \to \infty$, the Laplace domain displacement along the viscoelastic rod is then found as $\tilde{u}(\xi,\hat{s}) = Ae^{-\hat{s}_{\xi}\sqrt{2}\xi}$, where $\hat{s}_{\zeta} = \hat{s}/\sqrt{1+2\zeta\hat{s}}$. Taking the displacement relation at the lattice-continuum interface into account, given by equation (5.48), and noting that $\tilde{v}(\xi,\hat{s}) = \hat{s}\tilde{u}(\xi,\hat{s})$ and therefore $\tilde{v}^N(\hat{s}) = \hat{s}\tilde{u}^N(\hat{s})$, the Laplace domain displacement and velocity along the viscoelastic rod for zero initial conditions respectively follow from equation (5.49) as:

$$\tilde{u}\left(\xi,\hat{s}\right) = \tilde{u}^{N}\left(\hat{s}\right)e^{-\hat{s}_{\zeta}\sqrt{2}\left(\xi - x_{lnt}\right)}$$
(5.60)

$$\tilde{v}(\xi,\hat{s}) = \tilde{v}^{N}(\hat{s})e^{-\hat{s}_{\zeta}\sqrt{2}(\xi-x_{lnt})}$$
(5.61)

In these expressions, the Laplace parameter \hat{s} has been included as an argument to emphasize that the given displacements and velocities depend on \hat{s} rather than on s.

Substituting the Laplace domain displacement and velocity of the viscoelastic rod, i.e. equations (5.60) and (5.61), into equation (5.58), changing the order of integration and analytically solving the remaining integral over the semi-infinite domain of the viscoelastic rod, then yields:

$$\tilde{f}_{0}\left(s\right) = \zeta s_{\zeta} \sqrt{2} u_{0}^{\mathbf{N}} + \frac{1}{\sqrt{2}} \mathcal{L}_{\hat{s}}^{-1} \left\{ \frac{1}{\hat{s}_{\zeta} + s_{\zeta}} \left(\frac{s_{\zeta}^{2}}{s} \tilde{u}^{\mathbf{N}} \left(\hat{s} \right) + \tilde{v}^{\mathbf{N}} \left(\hat{s} \right) \right) \right\}$$

$$(5.62)$$

As the displacement and velocity of the boundary particle in equation (5.62) are both related to the Laplace parameter \hat{s} , the inverse Laplace transforms with respect to this Laplace parameter may be obtained as the convolution of its separate components. Consequently, equation (5.62) becomes:

$$\tilde{f}_{0}(s) = \zeta s_{\zeta} \sqrt{2} u_{0}^{N} + \frac{1}{\sqrt{2}} \int_{0}^{t_{0}} \mathcal{L}_{\hat{s}}^{-1} \left\{ \frac{1}{\hat{s}_{\zeta} + s_{\zeta}} \right\} (\tau) \left\{ \frac{s_{\zeta}^{2}}{s} u^{N} (t_{0} - \tau) + v^{N} (t_{0} - \tau) \right\} d\tau$$
(5.63)

The remaining integral in the expression for $f_0(s)$ in equation (5.69) is a convolution integral over the time period $\tau = 0...t_0$. Here, $\tau = 0$ is the absolute starting point in time, i.e. the time at which the complete system was at rest before any loading is applied and thus has zero initial conditions, while $\tau = t_0$ is the last time moment at which the time parameter was reset and new nonzero initial conditions were introduced.

The inverse Laplace transform in the convolution integral of equation (5.63) cannot be solved analytically and with a decay rate $\hat{\omega}^{-\frac{1}{2}}$ for $\hat{\omega} \to \infty$, its argument does not tend to zero fast enough to evaluate it numerically. Alternatively, we could substitute $\tilde{v}^N(\hat{s}) = \hat{s}\tilde{u}^N(\hat{s})$ into equation (5.62) and solve the remaining inverse Laplace transform for $\tilde{u}^N(\hat{s})$, but this will only reduce the decay rate of its argument for $\hat{\omega} \to \infty$ by an order $\hat{\omega}$. Instead, we both multiply and divide the argument of the inverse Laplace transform in equation (5.62) by \hat{s} and rearrange the resulting Laplace domain expression. Substituting $\hat{s}\tilde{u}^N(\hat{s}) = \tilde{v}^N(\hat{s})$ and $\hat{s}\tilde{v}^N(\hat{s}) = \tilde{a}^N(\hat{s})$ then yields:

$$\tilde{f}_{0}\left(s\right) = \zeta s_{\zeta} \sqrt{2} u_{0}^{N} + \int_{0}^{t_{0}} \mathcal{L}_{\hat{s}}^{-1} \left\{ \frac{1}{\hat{s}\sqrt{2}\left(\hat{s}_{\zeta} + s_{\zeta}\right)} \right\} \left(\tau\right) \left\{ \frac{s_{\zeta}^{2}}{s} v^{N}\left(t_{0} - \tau\right) + a^{N}\left(t_{0} - \tau\right) \right\} d\tau \tag{5.64}$$

Compared to equation (5.63), the decay rate of the inverse Laplace transform for $\hat{\omega} \to \infty$ remaining in equation (5.64) now has increased by an order $\hat{\omega}$ and thereby decays sufficiently fast to numerically evaluate the inverse Laplace transform for a finite integral domain.

Solution to the remaining inverse Laplace transform

To evaluate the inverse Laplace transform that remains in equation (5.64), we denote its argument, i.e. the corresponding Laplace domain expression, as $\tilde{f}(\hat{s})$. Substituting the expressions for s_{ζ} and \hat{s}_{ζ} , we rearrange the Laplace domain expression for $\tilde{f}(\hat{s})$ as:

$$\tilde{f}(\hat{s}) = \frac{s\sqrt{2+4\zeta s} \left(1+2\zeta \hat{s}\right)}{\hat{s}\left(s^2 \left(2+4\zeta \hat{s}\right) - \hat{s}^2 \left(2+4\zeta s\right)\right)} - \frac{\left(1+2\zeta s\right)\sqrt{2+4\zeta \hat{s}}}{s^2 \left(2+4\zeta \hat{s}\right) - \hat{s}^2 \left(2+4\zeta s\right)}$$
(5.65)

Here, note that, as before, the featured square roots are chosen such that their real parts are positive, so that $Re(s_{\zeta}) > 0$ and the general solution for the displacement in the rod, given by equation (5.49), satisfies the infinity condition.

Now, the first term on the right-hand side of equation (5.65), henceforth denoted as $\tilde{f}_1(\hat{s})$, is a polynomial function with regard to \hat{s} . Consequently, its inverse Laplace transform with respect to \hat{s} can be obtained analytically and reads:

$$\mathcal{L}_{s}^{-1}\left\{\tilde{f}_{1}\left(\hat{s}\right)\right\} = \frac{\sqrt{2+4\zeta s}}{4s\left(1+\zeta s\right)} \left(2\left(1+\zeta s\right) - e^{\frac{-s\tau}{1+2\zeta s}} - e^{s\tau}\left(1+2\zeta s\right)\right)$$
(5.66)

The inverse Laplace transform of the second term on the right-hand side of equation (5.65),

henceforth denoted as $\tilde{f}_2(\hat{s})$, cannot be obtained accordingly. Instead, we evaluate its inverse Laplace transform with respect to \hat{s} using contour integration by means of the residue theorem. The application of the contour integration to obtain the inverse Laplace transform of $\tilde{f}_2(\hat{s})$ is extensively discussed in Appendix I.5. Note here that the contour integration is performed to obtain an inverse Laplace transform and thus corresponds to a line integral running parallel to the imaginary axis, while previously contour integration was applied to determine the inverse Fourier transform and therefore considered an integral along the real axis. Particular about applying the contour integration to $\tilde{f}_2(\hat{s})$ in comparison with for example performing the contour integration to obtain equation (5.66), is that, next to the existence of poles at respectively $\hat{s}_1^\times = -s/(1+2\zeta s)$ and $\hat{s}_2^\times = s$, additionally there is a branch point at $\hat{s}^\bullet = -1/(2\zeta)$, and therefore a branch cut is applied along the real axis for $\hat{s} = -\infty \dots -1/(2\zeta)$. Ultimately, the inverse Laplace transform of $\tilde{f}_2(\hat{s})$ is found as:

$$\mathcal{L}_{\hat{s}}^{-1}\left\{\tilde{f}_{2}\left(\hat{s}\right)\right\} = \frac{\sqrt{2+4\zeta s}}{4s\left(1+\zeta s\right)} \left(e^{\frac{-s\tau}{1+2\zeta s}} - e^{s\tau}\left(1+2\zeta s\right)\right) - \frac{1}{\pi} \int_{-\infty}^{-\frac{1}{2\zeta}} \frac{e^{\hat{s}\tau}\left(1+2\zeta s\right)\sqrt{-2-4\zeta \hat{s}}}{s^{2}\left(2+4\zeta \hat{s}\right) - \hat{s}^{2}\left(2+4\zeta s\right)} d\hat{s} \quad (5.67)$$

Here, note that the square root in the numerator of the integrand in equation (5.67) has been rewritten using $\sqrt{2+4\zeta\hat{s}}=\pm i\sqrt{-2-4\zeta\hat{s}}$ to assure that the square root is always real on the considered domain of the contour integral. Thereby, the remaining integral is an integral over the real axis of \hat{s} that decays sufficiently fast for $\hat{\omega}\to -\infty$ that thus can be evaluated numerically. Subtracting equation (5.67) from equation (5.66) then finally yields the inverse Laplace transform of $\tilde{f}(\hat{s})$, denoted as the convolution term $f(\tau)$, in terms of the time domain operator τ , as:

$$f(\tau) = \frac{\sqrt{2 + 4\zeta s}}{2s(1 + \zeta s)} \left(1 + \zeta s - e^{\frac{-s\tau}{1 + 2\zeta s}} \right) - \frac{1}{\pi} \int_{-\infty}^{\frac{1}{2\zeta}} \frac{e^{s\tau} (1 + 2\zeta s) \sqrt{-2 - 4\zeta \hat{s}}}{s^2 (2 + 4\zeta \hat{s}) - \hat{s}^2 (2 + 4\zeta s)} d\hat{s}$$
 (5.68)

And thus, the final expression for $f_0(s)$ becomes:

$$\tilde{f}_0(s) = \zeta s_\zeta \sqrt{2} u_0^{\mathbf{N}} + \int_0^{t_0} f(\tau) \left\{ \frac{s_\zeta^2}{s} v^{\mathbf{N}} (t_0 - \tau) + a^{\mathbf{N}} (t_0 - \tau) \right\} d\tau \tag{5.69}$$

The expression given by equation (5.69) now exclusively consists of terms related to the boundary particle N. Note that the approach applied here is different from the approach applied to obtain equation (5.23) for the linear-elastic rod in Section 5.2.1. Appendix J.7 however shows that applying the derivation above to the problem for the linear-elastic rod also leads to equation (5.23). Alternatively, for zero damping s_{ζ} and \hat{s}_{ζ} are respectively replaced by $s\sqrt{2}$ and $\hat{s}\sqrt{2}$, and the remaining inverse Laplace transform can be evaluated straightforwardly, so that equation (5.63) reduces to the expression for the linear-elastic rod, previously given by equation (5.23).

5.3.2 Governing Laplace domain equations for the 1D BKV-lattice

The governing system of equations of motion for the one-dimensional discrete-continuous BKV system, depicted in Figure 5.9, is previously given in Section 3.2.4. Because the system in Section 3.2.4 is given in the time domain, it holds for both zero and nonzero initial conditions. For the application of the MTFD-method, we here give the corresponding Laplace domain system of equations that accounts for nonzero initial conditions and for the different motion states according to which any BKV-element may behave.

Applying the Laplace integral transform to the time domain system of equations of motion, previously given in Section 3.2.4, accounting for nonzero initial conditions yields the dimensionless equations of motion for particles n = 1...N-1 as:

$$M^{1}s^{2}\tilde{u}^{1} - \left(C_{e}^{1,2}s + K_{e}^{1,2}\right)\tilde{e}_{state}^{1,2} - \tilde{F}_{lock}^{1,2} = \tilde{F}\left(s\right) + M^{1}\left(su_{0}^{1} + v_{0}^{1}\right) - C_{e}^{1,2}e_{state;0}^{1,2} - s^{-1}K_{e}^{1,2}\varepsilon_{state}^{1,2}$$
 (5.70)

$$M^{\mathbf{n}} s^{2} \tilde{u}^{\mathbf{n}} + \tilde{F}_{state}^{\mathbf{n}-\mathbf{1},\mathbf{n}} + \tilde{F}_{lock}^{\mathbf{n}-\mathbf{1},\mathbf{n}} - \left(C_{e}^{\mathbf{n},\mathbf{n}+\mathbf{1}} s + K_{e}^{\mathbf{n},\mathbf{n}+\mathbf{1}}\right) \tilde{e}_{state}^{\mathbf{n},\mathbf{n}+\mathbf{1}} - \tilde{F}_{lock}^{\mathbf{n},\mathbf{n}+\mathbf{1}} = M^{\mathbf{n}} \left(s u_{0}^{\mathbf{n}} + v_{0}^{\mathbf{n}}\right) - C_{e}^{\mathbf{n},\mathbf{n}+\mathbf{1}} e_{state}^{\mathbf{n},\mathbf{n}+\mathbf{1}} - s^{-1} K_{e}^{\mathbf{n},\mathbf{n}+\mathbf{1}} \varepsilon_{state}^{\mathbf{n},\mathbf{n}+\mathbf{1}}$$

$$(5.71)$$

Note here that the Laplace domain expression for the load applied at particle 1, denoted as $\tilde{F}(s)$, must be adapted such that it is valid for the time period reinitiated at time t_0 . For a single sinus pulse load, the corresponding expression for $\tilde{F}(s)$ is previously given by equation (5.29). Appendix J.5 gives the derivation of the expression for $\tilde{F}(s)$ that is valid for the time period reinitiated at time t_0 , for respectively the single sinus pulse load, a continuous harmonic load and a half sinus pulse with a carrier frequency.

In equations (5.70) and (5.71), $\tilde{e}_{state}^{\mathbf{n},\mathbf{n}+1}$ denotes the total elongation of the rheological element between particles \mathbf{n} and $\mathbf{n}+1$, while $e_{state;0}^{\mathbf{n},\mathbf{n}+1}$ denotes the corresponding elongation at time t_0 . Furthermore, $\varepsilon_{state}^{\mathbf{n},\mathbf{n}+1}$ is included to account for the constant elongation of the Bingham element during stick, while $\tilde{F}_{state}^{\mathbf{n}-1,\mathbf{n}}$ is the Laplace domain expression for the force in the rheological element between particles $\mathbf{n}-\mathbf{1}$ and \mathbf{n} . Finally, $\tilde{F}_{lock}^{\mathbf{n}-1,\mathbf{n}}$ and $\tilde{F}_{lock}^{\mathbf{n},\mathbf{n}+1}$ give the forces in the parallel springs that are activated when the corresponding BKV elements lock.

For the case that the BKV element between particles **n** and **n+1** is in stick-state, we find:

$$\begin{split} \tilde{F}_{state}^{\mathbf{n},\mathbf{n}+1} &= \left(C_e^{\mathbf{n},\mathbf{n}+1} s + K_e^{\mathbf{n},\mathbf{n}+1} \right) \tilde{e}^{\mathbf{n},\mathbf{n}+1} - C_e^{\mathbf{n},\mathbf{n}+1} e_0^{\mathbf{n},\mathbf{n}+1} - s^{-1} K_e^{\mathbf{n},\mathbf{n}+1} e_{B;0}^{\mathbf{n},\mathbf{n}+1}, \qquad \qquad \tilde{e}_{state}^{\mathbf{n},\mathbf{n}+1} &= \tilde{e}^{\mathbf{n},\mathbf{n}+1}, \\ e_{state;0}^{\mathbf{n},\mathbf{n}+1} &= e_0^{\mathbf{n},\mathbf{n}+1} &= e_{B;0}^{\mathbf{n},\mathbf{n}+1}, \qquad \qquad \tilde{F}_{lock}^{\mathbf{n},\mathbf{n}+1} &= 0. \end{split}$$

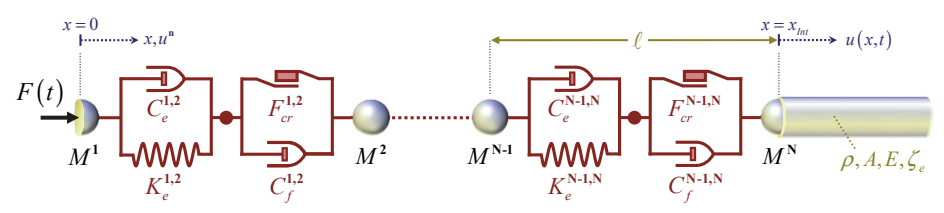


Figure 5.9: The one-dimensional semi-infinite discrete-continuous BKV system.

While for the case that the BKV element between particles n and n+1 is in slip-state, we find:

$$\begin{split} \tilde{F}_{state}^{\mathbf{n},\mathbf{n}+1} &= C_f^{\mathbf{n},\mathbf{n}+1} s \tilde{e}_B^{\mathbf{n},\mathbf{n}+1} - C_f^{\mathbf{n},\mathbf{n}+1} e_{B;0}^{\mathbf{n},\mathbf{n}+1} + s^{-1} F_{cr}^{\mathbf{n},\mathbf{n}+1} \operatorname{sgn} F_{B;slip}^{\mathbf{n},\mathbf{n}+1}, & \tilde{e}_{state}^{\mathbf{n},\mathbf{n}+1} &= \tilde{e}_{KV}^{\mathbf{n},\mathbf{n}+1}, \\ e_{state;0}^{\mathbf{n},\mathbf{n}+1} &= e_{KV;0}^{\mathbf{n},\mathbf{n}+1}, & \tilde{e}_{state}^{\mathbf{n},\mathbf{n}+1} &= 0, & \tilde{F}_{lock}^{\mathbf{n},\mathbf{n}+1} &= 0. \end{split}$$

In the expressions given above, the subscripts KV and B respectively refer to the Kelvin-Voigt and Bingham elements that together comprise the BKV element. For any BKV element between particles **n** and **n+1** that is in slip-state, the following equation of motion for the slip-node intermediate particles **n** and **n+1** is added to the system of equations of motion:

$$\left(C_{e}^{\mathbf{n},\mathbf{n}+1}s+K_{e}^{\mathbf{n},\mathbf{n}+1}\right)\tilde{e}_{KV}^{\mathbf{n},\mathbf{n}+1}-C_{f}^{\mathbf{n},\mathbf{n}+1}s\tilde{e}_{B}^{\mathbf{n},\mathbf{n}+1}-s^{-1}F_{cr}^{\mathbf{n},\mathbf{n}+1}\operatorname{sgn}F_{B:slip}^{\mathbf{n},\mathbf{n}+1}=C_{e}^{\mathbf{n},\mathbf{n}+1}e_{KV;0}^{\mathbf{n},\mathbf{n}+1}-C_{f}^{\mathbf{n},\mathbf{n}+1}e_{B;0}^{\mathbf{n},\mathbf{n}+1}$$
(5.72)

Finally, for the case that the BKV-element between particles **n** and **n+1** is in lock-state, we find:

$$\begin{split} \tilde{F}_{\textit{state}}^{\,\mathbf{n},\mathbf{n}+1} &= \left(C_e^{\,\mathbf{n},\mathbf{n}+1} s + K_e^{\,\mathbf{n},\mathbf{n}+1} \right) \tilde{e}^{\,\mathbf{n},\mathbf{n}+1} - C_e^{\,\mathbf{n},\mathbf{n}+1} e_0^{\,\mathbf{n},\mathbf{n}+1} - s^{-1} K_e^{\,\mathbf{n},\mathbf{n}+1} e_{B;0}^{\,\mathbf{n},\mathbf{n}+1} \,, \qquad \qquad \tilde{e}_{\textit{state}}^{\,\mathbf{n},\mathbf{n}+1} &= \tilde{e}^{\,\mathbf{n},\mathbf{n}+1} \,, \\ e_{\textit{state};0}^{\,\mathbf{n},\mathbf{n}+1} &= e_0^{\,\mathbf{n},\mathbf{n}+1} \,, \qquad \qquad \tilde{F}_{\textit{lock}}^{\,\mathbf{n},\mathbf{n}+1} &= K_{\textit{lock}}^{\,\mathbf{n},\mathbf{n}+1} \left(\tilde{e}^{\,\mathbf{n},\mathbf{n}+1} + s^{-1} \Delta D_0^{\,\mathbf{n},\mathbf{n}+1} \right) . \end{split}$$

When applying the MTFD-method, the state-transitions can straightforwardly be monitored in the time domain according to the rules discussed in Section 2.3.5. Here, note that all possible state-transitions are instant nonlinear events, and that the resulting system of equations of motion is linear for the duration of each motion state.

Finally, note that the equation of motion for the boundary particle **N** is previously given as the interface equation (5.51), where the expression for $f_0(s)$ in equation (5.51) is given by equation (5.69). Here, note that the equation of motion for the boundary particle **N** is not subject to different motion states.

Equations (5.70) to (5.72), together with equation (5.51), describe the full dimensionless system of equations of motion for the one-dimensional discrete-continuous BKV system in the Laplace domain accounting for nonzero initial conditions and for different motion states that is thereby applicable to the MTFD-method. Solving the algebraic system of equations of motion in the Laplace domain then yields the Laplace domain displacements of all particles in the BKV system. To obtain the response of the discrete-continuous BKV system in the time domain, we employ the improved formulations for the inverse Laplace transform given by equations (5.40) to (5.42).

5.3.3 Response of the 1D BKV system using the MTFD-method

In this section, both a linear and a nonlinear response of the discrete-continuous BKV system to an applied single sinus pulse load are presented and discussed. Subsequently, we discuss the calculation times that were required for the different solution methods to obtain the linear and nonlinear responses of the BKV system.

Linear response of the discrete-continuous BKV system to a single sinus pulse load

To verify the MTFD-method, and its application to the discrete-continuous BKV system, depicted in Figure 5.9, we have first simulated the longitudinal response to a unit single sinus pulse load where the properties of the BKV system are chosen such that its response is exclusively linear. The purpose of performing this simulation is to verify that the viscous damping of the BKV system is correctly incorporated in the equations of motion for both the lattice and the lattice-rod interface. The resulting longitudinal response is depicted in Figure 5.10 for eight consecutive time moments.

The parameters that are used here to obtain the response of the discrete-continuous BKV system by means of the MTFD-method match those previously used in Section 3.2.5 to obtain Figure 3.5, as well as those used in Section 5.2.4 to obtain Figure 5.8. Consequently the Young's modulus, density and damping ratio of the discrete-continuous BKV system are chosen as E = 20 MPa, $\rho = 2000 \text{ kg/m}^3$ and $\zeta = 0.75$ respectively. As before, the viscoelastic rod has a cross-section area of $A = 1 m^2$, while the one-dimensional BKV lattice consists of 80 particles at an interparticle distance of $\ell = 0.2$ m. The mass, damping and stiffness in the lattice elements then follow from equation (3.9) as M = 400 kg, $C_e = 212.1 \text{ kNs/m}$ and $K_e = 100 \text{ MN/m}$. Consequently, the particle frequency in the BKV-lattice is found as $\omega_0 = 707.1 \text{ rad/s}$. The amplitude and angular frequency of the single sinus pulse load are respectively chosen as $\bar{F} = 1 \,\text{MN}$ and $\omega_F = 80 \,\text{rad/s}$. The duration of the applied single sinus pulse is set to exactly 200 time steps and the total time simulation lasts a 1000 time steps. For the MTFD-method and the frequency domain solution, the time domain displacements are obtained from the frequency domain displacements numerically. To this purpose, the semi-infinite domain of the inverse Laplace transform is truncated at $\omega_r = 1200 \text{ rad/s}$ and discretized using 300 frequency steps.

To assure the linear viscoelastic behaviour of the discrete-continuous BKV system, the critical friction force of the featured Bingham elements is chosen larger than the amplitude

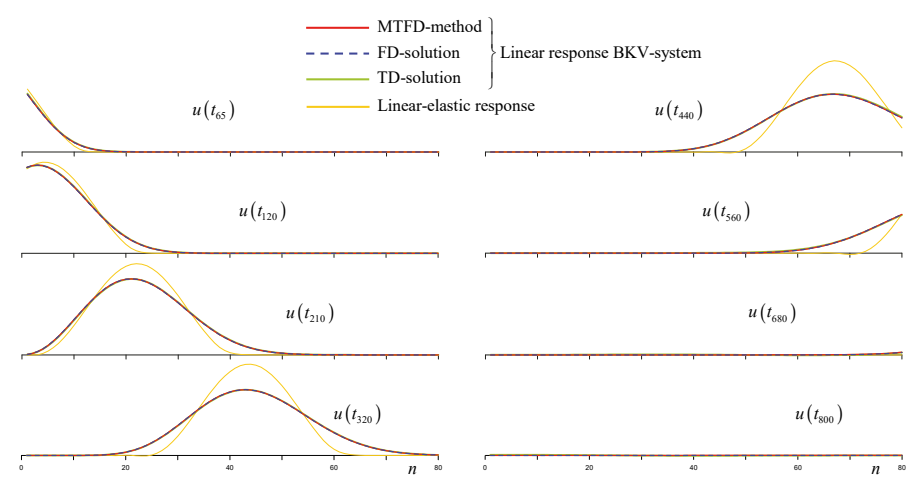


Figure 5.10: Displacement along the one-dimensional discrete-continuous BKV system, with properties that yield a linear response, at consecutive time moments due to a single sinus pulse load.

of the single sinus pulse load, i.e. $F_{cr}^{n,n+1} > \overline{F}$. As a consequence the Bingham elements will not be activated and the discrete-continuous BKV system acts as a purely viscoelastic system composed of a one-dimensional Kelvin-Voigt lattice and a viscoelastic rod.

In Figure 5.10, the displacements along the discrete-continuous BKV system that result from applying the MTFD-method are given by the continuous red line, while the dashed blue line gives the longitudinal displacements that result from the frequency domain solution. The only difference between the two simulations is that for the MTFD-method, the time parameter was reinitiated every 100 time steps, where at every reinitiation, the algebraic system of Laplace domain equations of motion is solved anew for a corresponding set of nonzero initial conditions. Additionally, the continuous green line in Figure 5.10 gives the displacements along the BKV system obtained by solving the system of differential equations directly in the time domain using a Runge-Kutta scheme. Note here that the linear response of the BKV system obtained through the time domain solution was previously given in Figure 3.5 by the dashed blue line. As a reference, the yellow line in Figure 5.10 portrays the purely linear-elastic response of the discrete-continuous Hooke system, previously depicted in Figure 5.8.

Comparing the longitudinal displacements along the BKV system obtained by applying the MTFD-method with the responses of the BKV system obtained by both the frequency and time domain solutions, it is evident that the viscous damping has correctly been incorporated into the governing system of Laplace domain equations of motion that accounts for nonzero initial conditions and thereby allows for the application of the MTFD-method.

Although, on the scale of Figure 5.10, the difference between the three obtained viscoelastic responses of the one-dimensional discrete-continuous BKV system appear to be negligible, the differences between the three solution methods become apparent if we consider the reflection of the corresponding incident wave at the lattice-rod interface depicted in Figure 5.11a for four consecutive moments in time. The scale of the response given by Figure 5.11a is approximately 100 times smaller than the scale of the response depicted in Figure 5.10.

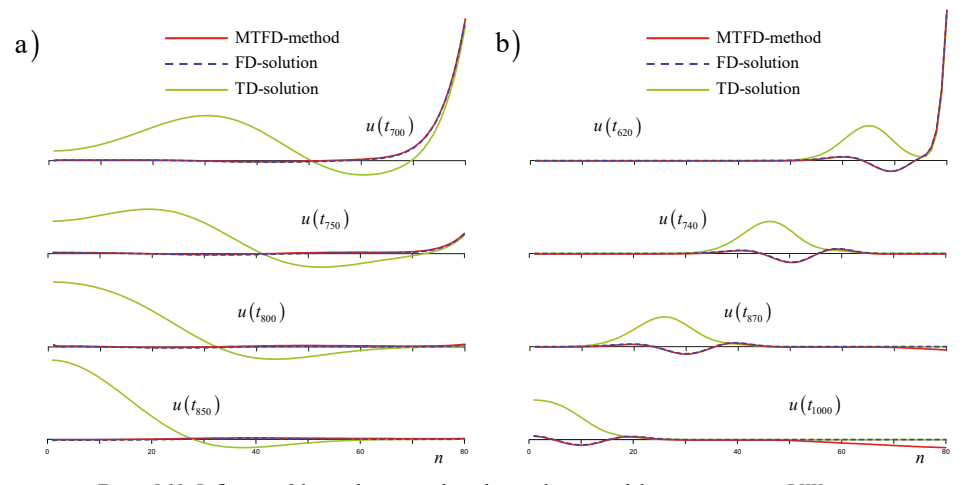


Figure 5.11: Reflection of the incident wave along the one-dimensional discrete-continuous BKV system at consecutive time moments: a) $\zeta = 0.75$ and $\Omega = 0.16$; b) $\zeta = 0.1$ and $\Omega = 0.5$.

Additionally, Figure 5.11b shows the reflection of the incident wave at the lattice-rod interface of the linearly behaving one-dimensional discrete-continuous BKV system that corresponds to the reflection previously depicted in Figure 4.7a and Figure 4.7b for respectively the time domain and frequency domain solutions. Note here that the parameters for the responses in Figure 5.11a and Figure 5.11b are identical except for the damping ratio of the considered system and the angular frequency of the applied single-sinus pulse load. For the response depicted by Figure 5.11a the damping ratio and the dimensionless frequency are respectively $\zeta = 0.75$ and $\Omega = 0.16$, while the response depicted by Figure 5.11b is obtained for a damping ratio $\zeta = 0.1$ and a dimensionless frequency $\Omega = 0.5$.

As expected, Figure 5.11a and Figure 5.11b both show that the responses obtained by the frequency domain solution and the MTFD-method, respectively given by the dashed blue line and the continuous red line, yield a much smaller reflection than the response obtained by the time domain method, which is given by the continuous green line.

If properly implemented, we would expect the MTFD-method to yield exactly the same response, and thus the same reflections, as the frequency domain solution. Nevertheless as shown by the last two graphs in Figure 5.11b, i.e. the displacements along the Kelvin-Voigt lattice at t₈₇₀ and t₁₀₀₀, the response obtained by respectively the MTFD-method and the frequency domain solution start to deviate. The difference is most pronounced near the latticerod interface, and is caused by a numerical error in the expression for $\tilde{f}_0(s)$ that appears in the equation of motion of the boundary particle N, given by equation (5.51). According to equation (5.69), the expression for $f_0(s)$ contains the convolution of a term $f(\tau)$ and the response of the boundary particle N over the global time period $\tau = 0...t_0$. As the expression for $f(\tau)$, as given by equation (5.68), contains an integral with a semi-infinite domain that must be evaluated numerically and is thus truncated, its result is not without a small numerical error. Consequently, every time the system is reinitiated and the domain of the convolution integral increases, the contribution of the numerical error in the expression for $f(\tau)$ to the total error in the numerically applied convolution integral accumulates, causing a reduction in the accuracy of the expression for $\tilde{f}_0(s)$. Eventually, this leads to a significant error in the expression for $f_0(s)$ and therefore in a significant error in the displacement of the boundary particle N. The resulting nonzero displacement of the boundary particle N can be considered as an input of energy into the one-dimensional lattice, to which the lattice will respond. This does not only explain why this error originates from the lattice-rod interface, it also explains its influence on the lattice response at later time steps. The magnitude of this error is proportional to the chosen time step of the simulation and can thus be reduced by choosing a smaller time step.

Nonlinear response of the BKV system to a single-sinus pulse load

Figure 5.12 again shows the longitudinal response of the discrete-continuous BKV-lattice to the unit single-sinus pulse load, but now its properties are chosen to accommodate the occurrence of nonlinear events. The chosen properties of the discrete-continuous BKV system and the applied single-sinus pulse load are the same as for the linear response, except for the critical friction force of the Bingham elements, which is now chosen as 80% of the amplitude

of the sinus pulse, i.e. $F_{cr} = 0.8 \overline{F}$, thereby allowing for the activation of the featured Bingham elements. The damping of the Bingham elements is chosen equal to that of the Kelvin-Voigt elements, i.e. $C_f = C_e$. In addition to the change of the overall critical friction force, the BKV elements between particles $\mathbf{n} = 20...40$ are chosen weaker than the other elements; these particles are chosen to have a critical friction force equal to 40% of the amplitude of the single sinus pulse, i.e. $F_{cr}^{\mathbf{n},\mathbf{n}+1} = 0.4\overline{F}$, while the damping of the Bingham and the Kelvin-Voigt elements between particles $\mathbf{n} = 20...40$ is reduced by 20%, so that for these elements $C_e^{\mathbf{n},\mathbf{n}+1} = C_f^{\mathbf{n},\mathbf{n}+1} = 169.7 \text{ kNs/m}$.

The resulting nonlinear response of the discrete-continuous BKV system is depicted in Figure 5.12. Here, the continuous red line again gives the displacement response of the discrete-continuous BKV system obtained by applying the MTFD-method, while the dashed blue line now gives the displacements obtained from applying the direct time domain solution, which was previously depicted for the same set of consecutive time moments in Figure 3.5. Note here that, due to the occurring nonlinear events, the nonlinear response of the discrete-continuous BKV system can no longer be obtained by a frequency domain solution. As a reference, the green line in Figure 5.12 gives the purely viscoelastic response of the discrete-continuous BKV system. Again the differences between the responses that follow from respectively applying the MTFD-method and the direct time domain solution are negligible. Consequently, Figure 5.12 verifies that the MTFD-method has been applied correctly and may indeed be used to obtain the response of non-smooth dynamical systems.

Comparison of calculation times required by the difference solution methods

For both the linear and nonlinear responses of the discrete-continuous BKV system, Table 5.2 gives an overview of the calculation times required by respectively applying the MTFD-

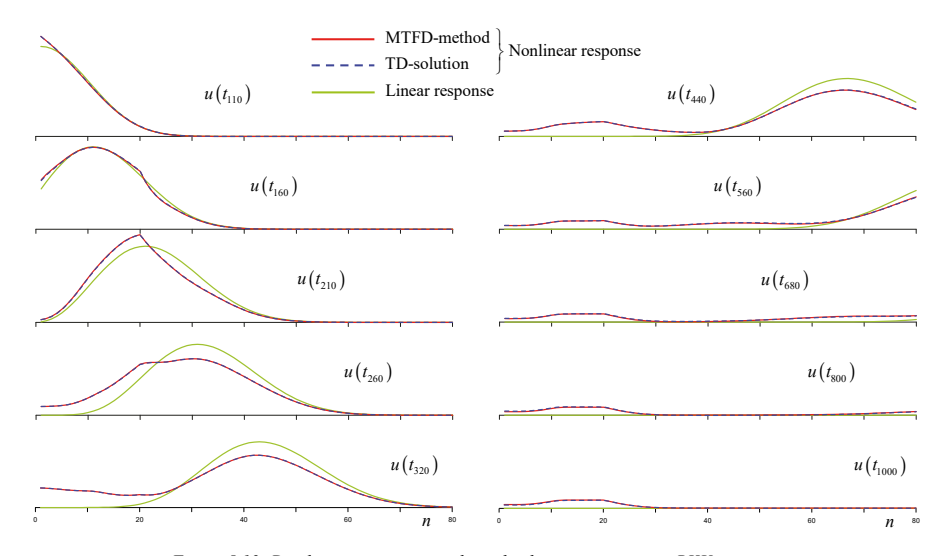


Figure 5.12: Displacement response along the discrete-continuous BKV system to a single sinus pulse load at consecutive time moments.

method, the frequency domain solution and the time domain solution. To minimize the influence on the calculation time of other computer processes running in the background, we have applied ten simulations for each numerical model; the minimum, average and maximum calculation time required are given in Table 5.2 for each solution method. For the MTFD-method and the frequency domain solution the calculation time involves the time spent on solving the algebraic system of equations in the frequency domain as well as applying the inverse Laplace transform to obtain the time domain displacements at every time step. For the time domain solution, the calculation time solely consists of applying the Runge-Kutta scheme to obtain the time domain displacement for every time step directly. For example, the time spent on data trafficking and writing output are not included.

For the linear response of the discrete-continuous BKV system, i.e. without nonlinear events, Table 5.2 shows that, at an average of approximately 1.74 seconds of required calculation time, the frequency domain solution requires the smallest computational effort. This is according to expectation, as for the frequency domain solution the algebraic system of equations of motion in the frequency domain is solved only once for zero initial conditions. In the numerical simulation using the MTFD-method, the time parameter was manually reinitiated every 100 time steps, so that, in addition to the frequency domain solution, the algebraic system of equations in the frequency domain was solved nine times for nonzero initial conditions. Consequently, using the MTFD-method, this simulation required on average 0.9 seconds of additional calculation time compared to the frequency domain solution. For the linear response, the largest computational effort was required for the time domain solution. Assuming that additional time domain reinitiations linearly increase the required calculation time for the MTFD-method, it follows that at roughly 32 reinitiations, the MTFD-method and the time domain solution will require similar computational effort.

Comparing the required calculation times for the viscoelastic response in Table 5.2 with the corresponding calculation times required for the linear-elastic response given in Table 5.1, we find that the computational effort for the frequency domain solution is similar for both models, while for both the MTFD-method and the time domain solution determining the viscoelastic response requires less computational effort than the linear-elastic response. For the MTFD-method this is due to a faster decay rate of the improved Laplace domain displacements within the finite domain of integration, while for the time domain solution this is due to a smaller amount of iteration steps required. Do note however that the error of the time domain solution is slightly larger for the viscoelastic response than the error for the linear-elastic response. Furthermore note that the differences between the simulations for the viscoelastic and linear-elastic responses are generally very small, and that computational efforts for the viscoelastic and linear-elastic responses are of the same order of magnitude.

Once the response of the discrete-continuous BKV system includes nonlinearities, the frequency domain solution is no longer valid and therefore the corresponding calculation times are not included in Table 5.2. Comparing the resulting calculation times for the nonlinear response of the discrete-continuous BKV system depicted in Figure 5.12, it is evident that the MTFD-method now requires significantly more computational effort than the time domain solution. In fact, for the time domain solution, the required calculation time for the

simulation of the nonlinear response is only slightly larger than the time required for the linear response, while for the MTFD-method this difference is much more significant.

In the nonlinear response, a total of 108 nonlinear events occurred, but as some of the nonlinear events occurred at the same time step, this yielded 101 time domain-reinitiations in the simulation employing the MTFD-method. For the linear response, we already derived that the MTFD-method and time domain solution would require similar computational effort when the MTFD-method is employed with 32 time domain-reinitiations. It is therefore clear that at 101 time domain-reinitiations, the MTFD-method indeed becomes slower than the time domain solution. In fact, for the linear response, it was found that every time domain-reinitiation required approximately 0.1 second of additional calculation time for the MTFD-method compared to the frequency domain solution, which coincides with the nonlinear response in approximate sense. This can be illustrated by considering that, if we would apply 101 time domain-reinitiations in the linear response, the MTFD-method would require approximately 11.8 seconds of calculation time, which is in the same order of magnitude as the required computational effort by employing the MTFD-method for the nonlinear response.

Although the additional computation effort required by the MTFD-method can be explained, these results are somewhat disappointing. After all, as the system of equations of motion becomes larger when the motion of slip-nodes must be accounted for, the influence of the nonlinear events on the required calculation time for the time domain solution were expected to be more significant. However, per time step only very few BKV-elements are in slip-state simultaneously, so that in the nonlinear response, the amount of additional degrees of freedom that has to be taken into account by the time domain solution is limited. Consequently, the increase in calculation time is also limited. When multiple nonlinear events occur simultaneously, it is expected that the advantage of the time domain solution compared to employing the MTFD-method is reduced.

Nevertheless, as the MTFD-method is a non-iterative method, it is more exact than the time domain solution, of which the error slightly increases with every occurrence of a non-linear event. In fact, due to the small, but existing, differences in displacement response between the results from the MTFD-method and the time domain solution, the nonlinear events

Table 5.2: Minimum, average and maximum calculation times for ten separate runs of the MTFD-method, frequency- and time domain solutions, for respectively the linear and nonlinear response of the discrete-continuous BKV system.

		MTFD-method	FD-solution	TD-solution
Linear Response	Min	2,371 s	1,591 s	4,680 s
	Average	2,641 s	1,741 s	4,934 s
	Max	2,870 s	1,950 s	5,132 s
Nonlinear Response: 108 nonlinear events	Min	11,700 s	-	4,898 s
	Average	12,833 s	-	5,111 s
	Max	13,541 s	-	5,335 s

in both simulations do not occur at exactly the same time steps. Especially in more complex, or multi-dimensional, models this effect may quickly accumulate and lead to more significant errors. Furthermore, it should also be taken into account that for the time domain solution the highly optimized Fortran-library RK-suite [Brankin and Gladwell, 1997] is used, while the code for the MTFD-method has been developed as part of this research and is prone to further optimalisation.

5.3.4 Advantages and disadvantages of the MTFD-method

It is important to emphasize that the mixed time-frequency domain method does not only allow one to model non-smooth dynamical processes taking advantage of the algebraic system of equations of motion that is obtained when solving dynamic problems in the frequency domain; the mixed time-frequency domain method also improves the general applicability of the regular frequency domain solutions due to regularly reinitiating its time parameter, as discussed in the following.

To explain this, let us consider that, after the algebraic system of equations is solved to obtain the frequency or Laplace domain response, we generally have to numerically apply the inverse integral Laplace transform to obtain the corresponding response in the time domain. The expression for the inverse Laplace transform, as used in both the frequency domain solution and the MTFD-method, is expressed in terms of frequency as:

$$f(t) = \mathcal{L}^{-1}\left\{\tilde{f}(s)\right\} = \frac{e^{\sigma t}}{\pi} \int_{0}^{+\infty} \operatorname{Re}\left\{\tilde{f}(s)e^{i\omega t}\right\} d\omega \tag{5.73}$$

Here note that the integrand of the inverse Laplace transform includes an exponent $e^{i\omega t}$. Consequently, for large values of the time variable t, this integrand becomes highly oscillatory, which dramatically reduces the precision of any applied numerical integration scheme or requires more sophisticated quadrature schemes. Do note that there are quadrature schemes available for highly oscillatory functions that are numerically efficient [Iserles et al., 2006], but not having to apply these sophisticated schemes at all is more efficient still. Alternatively, the step size of the frequency must be dramatically reduced to maintain some level of accuracy.

Next to the highly oscillatory integrand, there is another issue that occurs for large values of the time variable t. This issue is particular for the Laplace integral transform and is due to the exponent $e^{\sigma t}$. Here, σ is the small positive real value of the complex-valued Laplace parameter that is commonly defined as $s = i\omega + \sigma$. Because σ is real and positive, the value of the exponent $e^{\sigma t}$ will become tremendous for large values of the time variable t, even though σ itself is small. Consequently, as long as the result of the integral in equation (5.73) is nonzero, which it always will be for large values of t due to the degradation of the quadrature scheme, the exponent $e^{\sigma t}$ will eventually blow up any numerical error in the integral and cause severe numerical inaccuracy in the considered time domain response. Figure 5.13a clearly shows the occurrence of this numerical inaccuracy for the frequency domain solution of the one-dimensional discrete-continuous Kelvin-Voigt system. This figure depicts the

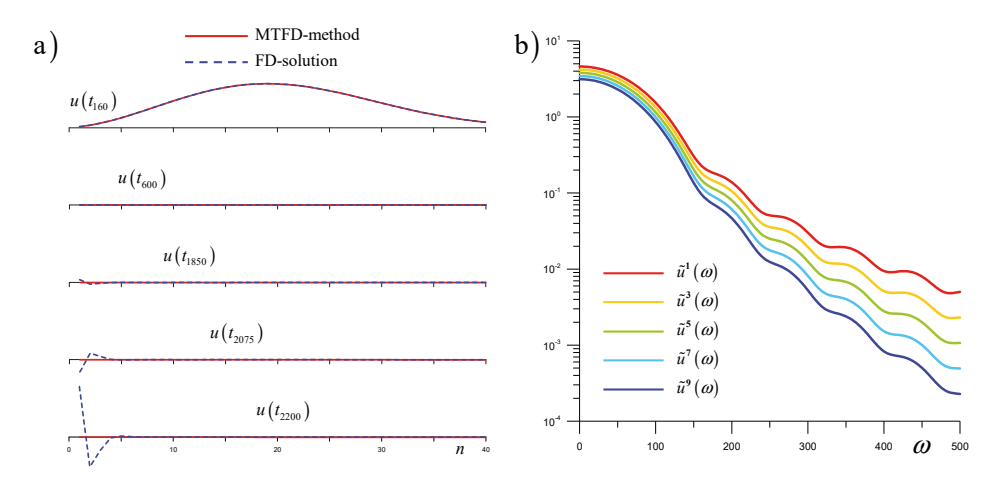


Figure 5.13: a) Response of the discrete-continuous Kelvin-Voigt system for large values of the time variable t; b) Laplace domain displacements of several particles at and near the tip of the Kelvin-Voigt system.

response of the first half of the discrete-continuous Kelvin-Voigt system for five consecutive time moments for both the frequency domain solution and the MTFD-method, respectively given by the dashed blue and continuous red lines. Here, the first time moment at t_{100} shows the magnitude of the incident wave induced by the single sinus pulse load, after which the second time moment shows that the incident wave has propagated beyond the depicted domain of the lattice. The next three time moments show how the numerical inaccuracy originates from the tip, slowly increases in magnitude and propagates into the one-dimensional lattice even though the incident wave has travelled far past the lattice-rod interface and only the much smaller reflected waves remain. The MTFD-method was here employed by reinitiating the time parameter at respectively t_{500} and t_{1000} , which is clearly sufficient to prevent the occurrence of the numerical inaccuracy.

Note here that the numerical inaccuracy first shows at the tip of the Kelvin-Voigt system because the Laplace domain displacement of particle 1 at the tip has the slowest decay rate for $\omega \to \infty$. This is confirmed by Figure 5.13b that depicts the Laplace domain displacements of several particles at and near the tip of the system. Because the inverse Laplace transform is applied numerically over a finite domain of the frequency, the slower decay rate of the Laplace domain displacement of this particle at the tip of the system yields the largest numerical error. Although the numerical error of the inverse Laplace transform is marginal, the multiplication with the exponent $e^{\sigma t}$ and, more significantly, the degradation of the quadrature scheme magnify the error for large values of the time variable t until eventually it is of the same order of magnitude as the original incident wave. Evidently, the time at which this numerical inaccuracy occurs is dependent on the chosen values for σ . So, for example, choosing $\sigma = 0$ will remove the magnification of the numerical error due to multiplication with the exponent $e^{\sigma t}$. Doing so however, increases the sharpness of the peaks, and thus the degradation of the quadrature scheme, in the vicinity of the poles in the Laplace domain. As a consequence choosing $\sigma = 0$ only slightly delays the occurrence of the numerical inaccuracy.

Despite the availability of several options to increase the value of the time parameter t at which the numerically applied inverse Laplace transform is still accurate, eventually this accuracy will always be lost. Since the MTFD-method allows for the regular reinitiation of the time parameter, this method allows you to keep the value of the time parameter t small, for which the application of the inverse Laplace transform is numerically more efficient and its results are more accurate. Hence, even for linear dynamical processes, application of the MTFD-method with periodic reinitiations of the time parameter allows for much longer time simulations than using the regular frequency domain solution method.

6 Conclusions and Recommendations

As explained in the introduction, this thesis aims to efficiently model a medium that exhibits non-smooth behaviour in the vicinity of a dynamic load, by replacing the domain of the medium that responds linearly, i.e. the far-field domain, and representing it by a boundary formulation at the limits of the near-field domain. Thereby, the main objective to this thesis is:

To develop a methodology capable of efficiently describing the nonlinear time domain response of a medium in the near field, while properly accounting for its response in the far field.

This chapter discusses to what extent this objective has been achieved, summarizes the most relevant findings and provides recommendations for further research. First, Section 6.1 discusses conclusions and recommendations regarding the ability and the performance of the presented discrete lattices to model non-smooth phenomena in the vicinity of an externally applied dynamic load. Subsequently, findings with respect to using boundary formulations to account for the linearly behaving far-field domain are extensively regarded in Section 6.2. This section generally discusses the application of boundary formulations in both one-dimensional and two-dimensional systems, as well as the performance of using either a continuum or a discrete far-field domain, which in combination with the discrete lattice in the near-field are respectively referred to as the discrete-continuous and fully discrete approaches. Sections 6.2.1 and 6.2.2 specifically discuss the conclusions and recommendations that regard the twodimensional discrete-continuous and two-dimensional fully discrete systems respectively. Finally, Section 6.3 discusses findings with regard to applying the proposed methodology in both the frequency and the time domains, as well as the application of the so-called mixed time-frequency domain method. Both Sections 6.2 and 6.3 include conclusions with regard to the numerical implementation and the resulting limitations of the modelling, as well as recommendations to extend and improve the applicability of the applied methodology.

6.1 Discrete lattice models for non-smooth dynamic phenomena

The one-dimensional and two-dimensional discrete lattice models, presented in Chapter 2 of this thesis, are well able to capture non-smooth dynamic phenomena that may occur in the vicinity of a load source as convincingly shown by the response of the hexagonal BKV lattice presented and discussed in Section 2.6.

Both the one-dimensional and two-dimensional lattice models incorporate stick-slip behaviour based on Coulomb friction, and collisions between particles by temporarily 'locking' the interaction between these particles. It is important to emphasize that these discrete lattice models were not specifically aimed at mimicking real-life material behaviour. Instead, stick, slip and lock were incorporated in the lattice as motion states with the sole aim of showing that the methodology to determine boundary integral formulations to account for the far-field domain could be applied to systems that allow for both linear and non-smooth behaviour in the near field. Chapter 2 shows that, because of the intrinsic discrete nature of nonlinear and non-smooth phenomena in material behaviour, it is fairly straightforward to properly account for these effects and to do so efficiently. In fact, while here only stick-slip and lock were incorporated, other nonlinear material behaviour such as fracture could have easily been included, for example by deleting rheological elements that are extended beyond a certain threshold, or to include the interaction between particles that are initially far apart from each other, by adding new rheological elements. To improve its performance to mimic real-life behaviour, it is generally recommended to update the lattice models to specifically account for these desired phenomena and validate the models using measurements of real-life cases.

While the workings of the discussed non-smooth phenomena and the transitions between stick, slip and lock are the same for lattice models in either dimension, there are several properties that should be specifically accounted for when considering lattices in two or more dimensions. The most notable here is that in two-dimensional lattices, rheological elements rotate and that the expressions for the elongations of these elements must therefore not only be linearized to be able to obtain the corresponding system of equations of motion as a set of linear ordinary differential equations, but the lattice geometry must also be updated over time when the corresponding deformations become large. In this thesis, linearizations are applied for both small and large elongations, where the geometry is generally assumed constant when small elongations are considered, while the geometry is generally updated over time when large elongations are considered. As shown in Section 2.6, the chosen linearization very much influences the response and behaviour of the lattice. While both linearizations yield the same results for loads that yield small deformations, the differences between the two linearizations become apparent as loads and the resulting deformations increase. Since the rotation of rheological elements in the lattice is a property of the modelling approach and not necessarily a property of the modelled medium, the aforementioned validation, by comparing model results to real-life or test results, will have to show to what extent either linearization is best capable of mimicking real-life material behaviour. For now, it is therefore best to regard the linearizations for small and large elongations as two different modelling approaches, rather than stating that the linearization for large elongations is by definition better than the linearization for small elongations.

Recommendations to improve discrete lattice modelling

Next to incorporating any of the additional non-smooth properties proposed above, other adaptations can be proposed to increase the potential and flexibility of using discrete lattice models. For example, choosing to incorporate gravity, as self-weight has not been accounted for in the lattice models presented in this thesis, or choosing to change the lattice configuration altogether, for example by modelling the lattice using a square instead of a hexagonal geometry. Otherwise maintaining the hexagonal configuration, the macromaterial behaviour of a medium may be adapted by describing the interactions between the particles differently. For example, although the hexagonal lattice by itself is anisotropic, incorporating additional rheological elements, as for example done for the so-called extended hexagonal lattice [Askes and Metrikine, 2004], allows hexagonal lattices to be used to model isotropy. Additionally, instead of only considering interactions between particles in longitudinal direction, also transverse and rotational interactions can be introduced. In fact, it would academically be very interesting to determine how such adaptations of the discrete lattice modelling would affect the formulation of the boundary integral equations according to the methodology presented in this thesis.

6.2 Boundary integral formulations to account for the far-field domain

This thesis presents a methodology that successfully describes the nonlinear response in the vicinity of an applied dynamic load by means of a discrete lattice while properly accounting for the linear response of the far-field domain by using boundary integral formulations. This methodology was successfully applied for both semi-infinite and finite one-dimensional continuous far-fields, as demonstrated in Sections 3.2.5 and 3.4 respectively, as well as for semi-infinite one-dimensional discrete far-fields, as demonstrated in Section 4.1.5. Furthermore, the nonlinear response of a two-dimensional fully discrete BKV system was successfully obtained in Section 4.7.5. Thereby, this thesis presents the first derivation of a boundary integral formulation for a far-field domain described as a semi-infinite system of discrete particles and its successful application to a nonlinear discrete lattice in the near-field. Based on the findings in this thesis, it is reasonable to assume that a boundary formulation for a corresponding finite discrete far-field can straightforwardly be obtained by deriving the required Green's functions for the relevant boundary conditions.

Analytically, both the one-dimensional and two-dimensional semi-infinite fully discrete systems are non-reflective for all frequencies, as discussed in Sections 4.2 and 4.7 respectively. The corresponding discrete-continuous systems however are only non-reflective in the long-wave limit and the magnitude of the wave reflection has therefore been extensively discussed in Section 3.3.2, specifically for one-dimensional continuous far-field models. As shown by the analysis of the reflection coefficient in this section, the reflections from the one-dimensional continuous far-field are a consequence of their dispersive properties being different from those of the near-field lattice, and a continuous far-field can thereby never yield the non-reflectiveness of a discrete far-field. As discussed in Section 3.6.3, in two-dimensional discrete-continuous systems, this non-reflectiveness is further degraded due to the geometrical mismatch at the lattice-continuum interface.

Numerical implementation of boundary formulations

Even though the non-reflectiveness of the fully discrete systems has been demonstrated by numerically solving the corresponding system of equations of motion in the frequency domain, the level of non-reflectiveness for the semi-infinite fully discrete systems when the corresponding system of ordinary differential equations is solved in the time domain is determined by the quality of the numerical implementation. In fact, as shown in Section 4.2.3, depending on the modelling approach and load parameters used, it is possible that the reflections from the boundary in a discrete-continuous system are smaller than the corresponding reflections in fully discrete systems. This is remarkable, because the reflections in the discrete-continuous system logically result from the difference in properties between the lattice and the continuous far-field domain, while the reflections in both one-dimensional and two-dimensional fully discrete systems are exclusively due to numerical errors in the implementation of the boundary integral equations.

While these numerical errors are mainly due to the numerical evaluation of the convolution integral present in the boundary formulation, and the error is thereby proportional to the area under the convolution integral, there are several pointers available to minimize these errors. First and foremost, as any time domain system of ordinary differential equations is typically solved for the highest time derivative present, it is vital to obtain acceleration terms in the boundary integral equation that do not exclusively follow from the convolution integral, so that its contribution is independent from the size of the time step used. Thereby, the performance of the boundary integral equation can be improved by reducing the time step and by using a higher-order numerical integration scheme for the convolution integral.

In this thesis, the suggested form of the boundary integral equation has been obtained by first applying the inverse Laplace transform to the force-displacement relation in the Laplace domain, and subsequently applying time differentiation to the resulting time domain equations. The same boundary integral equation can however also be obtained directly from applying the inverse Laplace transform to the force-acceleration relation in the Laplace domain, or alternatively starting from the corresponding force-velocity relation. Nevertheless, the fact that the boundary integral equation must be manipulated in order to obtain a proper contribution of the acceleration terms is triggered by the numerical application of the inverse Laplace transform. As explained in Section 3.1, to obtain an accurate time domain expression for the interface relation, the inverse Laplace transform is applied to the dynamic compliance relation rather than to the dynamic stiffness relation. The main reason for this is that to apply the inverse Laplace transform numerically, its semi-infinite domain of integration must be truncated and the magnitude of the corresponding Laplace domain expression must decrease sufficiently fast for increasing frequencies. Since the dynamic stiffness increases with frequency, its inverse relation known as the dynamic compliance is used instead. However, as a result of using the dynamic compliance relation, the acceleration terms in the boundary integral equation are present in the convolution integral, while starting from the dynamic stiffness relation, these acceleration terms would be outside the convolution integral and additional manipulation of the interface equation would not have been required. Finally, as discussed in Section 5.2.3, the truncation of the semi-infinite domain of the inverse Laplace integral transform, which is required to obtain the dynamic compliance numerically in the time domain, yields different results for different identities of the inverse Laplace transform. The chosen identity, i.e. the chosen expression for its integrand, thereby significantly influences the performance of the numerical evaluation.

Despite taking all of the above considerations into account, as well as using sparse matrices in the implementation, Section 4.7.5 shows that the number of degrees of freedom that the current implementation can handle is still fairly limited and further improvements to the numerical implementation should be made to make it more robust and make it more widely applicable. The main recommendation is thereby to improve the data management in the current implementation and thereby reduce the requirements with regard to (virtual) memory. This would not only allow for a larger number of degrees of freedom, but would also allow for more and thus smaller time steps. Another recommendation is to look for improvements of or alternatives for the Runge-Kutta method, with the aim to improve the numerical approximation of the solution to the system of ordinary differential equations in the time domain. Finally, the numerical performance can also be improved by redesigning the numerical implementation to make it fit for parallel and/or concurrent computing.

6.2.1 Two-dimensional discrete-continuous systems

In the introduction of this thesis, it was stated that, despite their different properties, it is worth deriving a boundary formulation for the near-field lattice by modelling the far-field domain as a continuum. As argued in Section 1.3, applications of boundary formulations that account for the far-field domain by modelling it using semi-infinite continuum models are abundantly available in literature, while the corresponding literature that treats unbounded discrete models to represent the far-field domain is very limited, if not absent. This has led to the expectation that deriving and implementing a boundary formulation that models the far-field domain as a continuum would be relatively easy. This thesis however shows that when the near-field is modelled as a hexagonal lattice, this is not necessarily the case.

Despite considerable efforts, the implementation of a numerical model that uses the methodology presented in Section 3.5 to obtain a boundary formulation that accounts for the far-field domain by modelling it as a two-dimensional continuum was unsuccessful. This is mainly because, specifically in two dimensions, using a continuum as a far-field domain for a discrete near-field domain has several clear disadvantages over using a far-field domain that matches the discrete properties of the near-field. First of all, note that any forces applied by the lattice to the continuum are point loads and that the application of point loads to a continuum yields singular displacements under these point loads. To circumvent this issue, shape functions were introduced that convert the point loads at the lattice-continuum interface to equivalent distributed loads. To satisfy the boundary conditions used to derive the Green's functions for the continuum, the resulting distributed loads had to be restricted to the horizontal segments of the discrete-continuous interface and therefore, narrow shape functions were used that quickly decay in horizontal direction. The shape of these load distributions however significantly increased the required size of the contour and the number of poles required to obtain the corresponding Green's functions using the contour integration. Not

only did this increase computation time, but it additionally caused degradation of the discrete-continuous interface relations, because the accuracy of the poles decreases with increasing distance to the origin of the complex *k*-plane. Next to the difficulties encountered to properly describe the dynamic interaction at the discrete-continuous interface, there are some concerns related to modelling the continuous far-field domain as a layer with a fixed bottom, which was used instead of a continuous half-plane because the dynamic compliance of the half-plane is infinitely large at zero frequency. Despite the geometrical damping, this fixed bottom will always result in reflected waves that travel back into the near-field lattice. If the aim is to model finite media, this does not necessarily yield any issues, but for semi-infinite media, for which the far-field domain is supposed to be non-reflective, this is a problem, and clearly limits the applicability of using a continuum as a far-field domain.

As explained in Section 3.6.3 however, it is still considered to be feasible to model the far-field domain as a continuum and thereby obtain a valid boundary formulation for any lattice that is by approximation non-reflective in the long-wave limit. To do so, it is recommended to first determine the displacement and traction fields along the interface of a fully continuous system and then use these to derive shape functions that approximate a more realistic traction field along the boundary of the far-field domain. Despite these and other possible improvements discussed in Section 3.6.3, it remains evident that a boundary formulation for the hexagonal lattice that models the far-field domain as a continuum will never yield the same performance as a boundary formulation for a matching discrete far-field domain.

6.2.2 Two-dimensional fully discrete systems

The latter conclusion of the previous section supports the claim made in Section 1.3 that to achieve a perfect boundary formulation such that there are no unwanted wave reflections at the boundary, the far-field domain should at least match the discrete properties of the near-field domain. At this point, this statement can be extended and completed by listing the components that are required to achieve a perfect boundary formulation. First, note that both the macromaterial and the dispersive properties of the far-field domain must match those of the near-field domain. Additionally, in the region of the interface between the near-field and the far-field domain, the material properties of both models must match. Because the far-field domain is both linear and assumes small elongations, this practically means that any nonlinear phenomena that occur in the near-field domain may not reach the interface with the far-field domain. Last but not least, the geometrical properties of the near-field and the far-field domain must match at their interface.

In Section 4.4, the Green's functions for the displacements and the reaction forces of the discrete half-plane of particles with a matching hexagonal geometry were successfully derived, thereby meeting all the property-requirements listed above and serving as a perfect boundary formulation for the nonlinear hexagonal lattice. To verify that the discrete half-plane of particles gives the proper response, the equivalent one-dimensional response of the half-plane of particles, obtained by applying an infinitely-long uniformly-distributed load at its surface, has been compared to the corresponding response obtained for the one-dimensional cascade in Section 4.5. Even though the edges of the 'infinitely-long' loading applied

at the surface induced some wave propagation in horizontal direction, both displacements and reaction forces were found to match well in both discrete particle systems. Here, note that the domain of the applied surface load was finite simply because it was not possible to consider infinitely many particles in the direct numerical simulation. To avoid the resulting horizontal wave propagation in the half-plane of particles and thereby improve the correspondence of its response with that of the cascade, boundary formulations can be used at the edges of the load.

Here note that by modelling the discrete far-field domain as a semi-infinite half-plane, the boundary formulation is completely non-reflective by design. Alternatively, the discrete far-field domain may also be modelled to have a finite domain, for example by introducing a fixed bottom, that would result in reflected waves entering the near-field domain. Thereby, the methodology presented in this thesis is more widely applicable than approaches solely aimed at suppressing wave reflections and introducing silent boundaries. Nevertheless, to extend the field of application, it is recommended to investigate how the corresponding Green's functions can be derived for a discrete far-field that is finite in both *x*- and *z*-direction, rather than only in *z*-direction.

In Section 4.6, the wave propagation properties of the hexagonal half-plane of particles were analysed to show that, as opposed to the two-dimensional continuum, the wave propagation properties of both shear and compressional waves in the hexagonal half-plane of particles are distinctly direction-dependent. The anisotropy of the hexagonal particle system is attributed to its geometry, which is quite different in, for example, *x*- and *z*-directions, and becomes more distinct for higher frequencies. Due to this anisotropy, the shear and compressional waves in the hexagonal particle system are coupled and cannot be isolated in the dispersion relation. As a consequence, the particle motion in most directions contributes to the propagation of both shear and compressional waves at the same time, while only for certain specific directions of wave propagation and for certain specific magnitudes of the wavenumber, the corresponding particle motion exclusively contributes to either shear or compressional waves.

As explained in Section 2.4.2, the system of equations of motion was linearized and the geometrical nonlinearity was accounted for to allow for large elongations that will undeniably occur when accounting for nonlinear phenomena in the near-field lattice. The boundary formulation at the interface with the far-field domain however, has been determined in the Laplace domain, and its representation in the time domain is therefore by default valid only for small elongations and does not take the geometrical nonlinearity into account. The two load cases considered in Section 4.7.5 show that despite the different modelling approaches, the corresponding boundary formulation performs well, even when large elongations occur in the near field. The reason for this is that due to the distance of the load source to the lattice boundary, in combination with the energy dissipation due to the geometrical damping, the viscous damping and the occurrence of nonlinear events in the vicinity of the load, the elongations that occur in the elements at the boundary of the near-field lattice are small and the corresponding geometrical nonlinearities are negligible. This assures that the fully discrete BKV system is homogeneous in the region of the interface.

The shape of the interface between the near-field and far-field systems

As explained in Section 4.7.1, the shape of the near-field boundary was chosen as the shortest path that connects all boundary particles, where all boundary particles are located at the same distance to the loaded particle at the origin of the near-field lattice. Choosing a boundary that directly connects the discrete particles and disregards the orientation of the interface at these particles is only allowed because the reaction forces along the interface exist only at the boundary particles as point loads. After all, for the discrete-continuous system the corresponding tractions exist along the whole boundary and thereby impose additional restrictions to its shape. Alternatively however, as discussed in Section 4.1.1 and shown in Figure 4.2 for the corresponding one-dimensional systems, it is also possible to choose the boundary exactly in between the particles, so that it coincides with the edges of the representative area that each particle represents. As such, all particles in the near-field lattice would have the same mass, but then the properties of the elements at this boundary would have to be adapted to let the near-field lattice interact homogeneously with the discrete far-field domain. While this limits the number of degrees of freedom involved in the interaction per interface node, and thereby simplifies the derivation of the corresponding Green's reaction forces, this approximately doubles the number of interface nodes that need to be accounted for in the corresponding boundary formulation. Choosing the boundary nodes in between the particles thus significantly increases the dimension of the dynamic compliance matrix, and thereby limits the numerical performance of the fully discrete system. To minimize the size of the dynamic compliance matrix, and thus optimize the total number of degrees of freedom that the implementation for the fully discrete system can handle, it is therefore recommended to choose the path of the lattice boundary by connecting particles. Here, note that this path between particles principally can be chosen at random, but that again for numerical reasons, it is wise to choose this boundary as short as possible.

6.3 The time domain versus the frequency domain

Comparing the linear responses that were obtained for the near-field lattice by either solving its system of equations of motion algebraically in the frequency domain, or by solving the corresponding system of ordinary differential equations in the time domain, it is evident that the frequency domain solution always yields the best results. This is mainly because an algebraic solution is always far more accurate than numerically solving a system of ordinary differential equations, while transforming the resulting displacements or the corresponding system of equations from the frequency to the time domain hardly influences this accuracy. As already concluded in Section 6.1, specifically for systems that include a boundary formulation, solving the system of ordinary differential equations poses additional numerical difficulties due to the presence of the convolution integral. Therefore, one should principally always attempt to solve any system of equations of motion in the frequency domain and invert only the resulting frequency domain response to the time domain. While the common understanding is that any model that accounts for nonlinear phenomena must be evaluated in the time domain, by showcasing the mixed time-frequency domain method for the one-dimensional discrete-continuous BKV system in Section 5.3, this thesis has demonstrated that even

when regarding the nonlinear response near a load source, the corresponding system of equations of motion can be solved in the frequency domain.

Application of the mixed time-frequency domain method

The mixed time-frequency domain, or MTFD, method is a non-iterative method that can be applied to simulate the non-smooth dynamic response of particle systems by solving the corresponding algebraic system of equations of motion in the frequency domain for nonzero initial conditions after each occurrence of a nonlinear event. Subsequently, the inverse Laplace integral transform is used to obtain the corresponding time domain response. Here, the use of the Laplace transform is preferred over using the Fourier transform, because the Laplace integral domain is by definition one-sided and thereby is able to account for initial conditions. Alternatively however, a one-sided Fourier integral transform could also be successfully applied. Nevertheless, as discussed and explained in Section 5.2.3, it is here important to emphasize that when numerically applying the inverse Laplace transform, the truncation of its semi-infinite domain of integration yields significant erroneous behaviour of the time domain relations near the nonzero initial conditions. To repair this, an improved formulation of the inverse Laplace transform was introduced that extracts the contribution of the nonzero initial conditions from its Laplace domain expression and separately includes their analytically known contribution in the time domain. As demonstrated in Section 5.2.3, this approach greatly improves the performance of the integral transform when nonzero initial conditions have to be accounted for.

In principal, the MTFD-method may only be applied to non-smooth dynamical systems that exclusively feature instant nonlinear events, meaning that the nonlinearities change the systems behaviour instantly, but in between these nonlinear events the considered system behaves in a linear manner. Nonetheless, by reinitiating the time parameter t at every single time step, the MTFD-method may also be used to model the dynamic response of systems that involve gradual, or smooth, nonlinear properties. In this case, any occurring smooth nonlinear events are discretized by the time stepping scheme and therefore, the influence of this discretisation on the proper dynamic response must be investigated. For example, the size of the time step may have to be adapted to make sure that the incorporated nonlinear effects are accounted for correctly. In any case, in its current implementation, the computational effort required by the MTFD-method is highly dependent on the number of required time domain reinitiations. Consequently, applying the MTFD-method with reinitiations at every single time step for the duration of a gradual nonlinear event may dramatically increase the required computational effort and is therefore currently not advised. It is nevertheless recommended to investigate ways to further optimize the numerical implementation of the MTFD-method with the aim to reduce the required computational effort.

Even though Chapter 5 only considers the application of the MTFD-method to one-dimensional discrete-continuous systems, the MTFD-method may straightforwardly be applied to the one-dimensional fully discrete BKV system in similar fashion. Applying the MTFD-method for the two-dimensional fully discrete systems presented in this thesis, will increase the complexity of the equations of motion of the boundary particles, which could potentially

increase the numerical problems involved with the evaluation of the boundary integral equation in the time domain. Fortunately however, when applying the MTFD-method and thereby solving the system of equations of motion algebraically in the frequency domain, the numerical evaluation of the convolution integral is not required. Additionally, for systems with increasing numbers of degrees-of-freedom, the advantage of numerically solving a system of algebraic equations over numerically solving a system of differential equations increases as well. Consequently, for two- and three-dimensional systems, the performance of the MTFD-method is expected to improve significantly compared to the performance of the time domain solution. Even so, the application of the MTFD-method to fully discrete systems, whether one-, two- or three-dimensional, has not been further considered in this thesis.

Finally, it is here important to emphasize that the MTFD method is not solely of use when considering the non-smooth dynamic response of discrete systems, but can also be used to address numerical issues due to the highly oscillatory behaviour that comes with large values of time, for example when considering the viscoelastic response of a medium. Using the MTFD-method to reset time at regular intervals, the value of time can be kept small, which allows the simulation time of any numerical simulation to be extended greatly.

List of references

- Abramowitz, M., & Stegun, I.A. (1972). Handbook of Mathematical Functions with Formulas, Graphs, and Mathematical Tables, 9th printing. New York: Dover.
- Achenbach, J.D. (1973). Wave propagation in elastic solids. Amsterdam: Elsevier Science Publishers.
- Achenbach, J.D. (2004). Reciprocity in Elastodynamics. Cambridge: Cambridge University Press.
- Ahlfors, L.V. (1966). Complex analysis: An introduction of the theory of analytic functions of one complex variable (2nd ed.). New York: McGraw-Hill.
- Andreaus, U., & Casini, P. (2001). *Dynamics of friction oscillators excited by a moving base and/or driving force*. J. of Sound and Vibration, 245, p. 685-699.
- Askes, H., & Aifantis, E.C. (2011). Gradient elasticity in statics and dynamics: An overview of formulations, length scale identification procedures, finite element implementations and new results. Int. J. of Solids and Structures, 48(13), p. 1962-1990. doi: 10.1016/j.ijsolstr.2011.03.006
- Askes, H., & Metrikine, A.V. (2002). One-dimensional dynamically consistent gradient elasticity models derived from a discrete microstructure: Part 2: Static and dynamic response. European J. of Mechanics A/Solids, 21(4), p. 573-588. doi: 10.1016/S0997-7538(02)01217-2
- Askes, H., & Metrikine, A.V. (2004). Higher-order continua derived from discrete media: continualisation aspects and boundary conditions. Int. J. of Solids and Structures, 42, p. 187-202.
- Banaugh, R.P., & Goldsmith, W. (1963). *Diffraction of steady elastic waves by surfaces of arbitrary shape*. J. of Applied Mechanics, 30, p. 589-597.
- Banerjee, P.K., & Butterfield, R. (1981). *The boundary element methods in engineering science*. London: McGraw-Hill.
- Bavinck, H., & Dieterman, H.A. (2000). Closed-form dynamic response of damped mass-spring cascades. J. of computational and applied mathematics, 114(2), p. 291-303.
- Bavinck, H., Dieterman, H.A., & Stieltjes, J.E.D. (1994). Pulse-responses of discrete semi-infinite and finite one-dimensional media: TU Delft, fac. TWI.
- Bažant, Z.P., Tabbara, M.R., Kazemi, M.T., & Pijaudier-Cabot, G. (1990). Random Particle Model for Fracture of Aggregate or Fiber Composites. J. of eng. mechanics, 116(8), p. 1686-1705. doi: 10.1061/(ASCE)0733-9399(1990)116:8(1686)
- Bérenger, J.P. (1994). A Perfectly Matched Layer for the Absorption of Electromagnetic Waves J. of Computational Physics, 114(2), p. 185-200.
- Beskos, D.E. (1987). Boundary Element Methods in Dynamic Analysis. Applied Mechanics Reviews, 40(1), p. 1-23. doi: 10.1115/1.3149529
- Beskos, D.E. (1997). Boundary Element Methods in Dynamic Analysis: Part II (1986-1996). Applied Mechanics Reviews, 50(3), p. 149-197. doi: 10.1115/1.3101695
- Bićanić, N. (2004). Discrete Element Methods Encyclopedia of Computational Mechanics.
- Bingham, E.C. (1922). Fluidity and Plasticity. New York: McGraw-Hill.
- Bolander, J.E., Eliáš, J., Cusatis, G., & Nagai, K. (2021). Discrete mechanical models of concrete fracture. Eng. Fracture Mechanics, 257, p. 108030. doi: 10.1016/j.engfracmech.2021.108030
- Bolander, J.E., Shiraishi, T., & Isogawa, Y. (1996). An adaptive procedure for fracture simulation in extensive lattice networks. Eng. Fracture Mechanics, 54(3), p. 325-334. doi: 10.1016/0013-7944(95)00200-6

- Boon, C.W., Houlsby, G.T., & Utili, S. (2012). A new algorithm for contact detection between convex polygonal and polyhedral particles in the discrete element method. Computers and Geotechnics, 44, p. 73-82. doi: 10.1016/j.compgeo.2012.03.012
- Brankin, R.W., & Gladwell, I. (1997). Algorithm 771: rksuite_90: Fortran 90 software for ordinary differential equaition initial-value problems. ACM Transactions on Mathematical Software (TOMS), 23(3), p. 402-415.
- Brillouin, L. (1953). Wave propagation in periodic structures: electric filters and crystal lattices (2nd Edition ed.). New York, NY: Dover.
- Cai, W., de Koning, M., Bulatov, V.V., & Yip, S. (2000). *Minimizing boundary reflections in coupled-domain simulations*. Physical Review Letters, 85(15), p. 3213-3216.
- Carpio, A., & Tapiador, B. (2010). *Nonreflecting boundary conditions for discrete waves*. J. of Computational Physics, 229(5), p. 1879-1896.
- Cheng, G., & Zu, J.W. (2004). *Dynamics of a dry friction oscillator under two-frequency excitations*. J. of Sound and Vibration, 275, p. 591-603.
- Clouteau, D., Cottereau, R., & Lombaert, G. (2013). Dynamics of structures coupled with elastic media - A review of numerical models and methods. J. of Sound and Vibration, 332, p. 2415-2436
- Coda, H.B., Venturini, W.S., & Aliabadi, M.H. (1999). A general 3D BEM/FEM coupling applied to elastodynamic continua/frame structures interaction analysis. Int. J. for numerical methods in eng., 46, p. 695-712.
- Cosserat, E.M.P., & Cosserat, F. (1909). Théorie des corps déformables: A.Hermann et fils.
- Coulier, P. (2014). *The numerical solution of large scale dynamic soil-structure interaction problems*. (PhD), KU Leuven, Leuven, Belgium
- Coulomb, C.A. (1821). Théorie des machines simples, en ayant égard au frottement de leurs parties et à la roideur des cordages *Mémoires des mathématique et de physique présentés à l'Académie des Sciences*. Paris: Bachelier Libraire, Quai des Augustins.
- Cundall, P.A. (1971). A computer model for simulating progressive large scale movements in blocky rock systems. Proceedings of the Int. symposium on rock fracture Nancy, France.
- Cusatis, G., Mencarelli, A., Pelessone, D., & Baylot, J. (2011a). *Lattice Discrete Particle Model* (*LDPM*) for failure behavior of concrete. *II: Calibration and validation*. Cement and Concrete Composites, 33(9), p. 891-905. doi: https://doi.org/10.1016/j.cemconcomp.2011.02.010
- Cusatis, G., Pelessone, D., & Mencarelli, A. (2011b). *Lattice Discrete Particle Model (LDPM) for failure behavior of concrete. I: Theory.* Cement and Concrete Composites, 33(9), p. 881-890. doi: 10.1016/j.cemconcomp.2011.02.011
- D'Alembert, J. (1747). Recherches sur la courbe que forme une corde tenduë mise en vibration *Histoire de l'academie royale des sciences et belles lettres* (Vol. 3, pp. 214-219). Berlin.
- de Hoop, A.T. (1966). An elastodynamic reciprocity theorem for linear, viscoelastic media. Applied Scientific Research, 16(1), p. 39-45.
- de Oliveira Barbosa, J.M., Fărăgău, A.B., & van Dalen, K.N. (2021). *A lattice model for transition zones in ballasted railway tracks*. J. of Sound and Vibration, 494, p. 115840. doi: 10.1016/j.jsv.2020.115840
- de Oliveira Barbosa, J.M., Fărăgău, A.B., van Dalen, K.N., & Steenbergen, M.J.M.M. (2022). Modelling ballast via a non-linear lattice to assess its compaction behaviour at railway transition zones. J. of Sound and Vibration, 530, p. 116942. doi: https://doi.org/10.1016/j.jsv.2022.116942

- Delaplace, A., Pijaudier-Cabot, G., & Roux, S. (1996). *Progressive damage in discrete models and consequences on continuum modelling*. J. of the Mechanics and Physics of Solids, 44(1), p. 99-136. doi: 10.1016/0022-5096(95)00062-3
- Dieterman, H.A., & Metrikine, A.V. (1997). *Eigenfrequencies and Simplified models of semi-infinite cascades with variable boundary mass*. Short communications on Mathematical Mechanics, 77(3), p. 232-235.
- Dieterman, H.A., Stieltjes, J.E.D., & Bavinck, H. (1995). Structural differences in wave propagation in discrete and continuous systems. Archive of Applied Mechanics, 66(1), p. 100-110. doi: 10.1007/BF00786693
- Dominguez, J. (1993). *Boundary elements in dynamics*. London: Computational mechanics publications.
- Dorival, O., Metrikine, A.V., & Simone, A. (2008). *A lattice model to simulate ice-structure interaction*. Proceedings of the ASME 27th Int. conference on offshore mechanics and arctic eng. (OMAE), Estoril, Portugal.
- Fakhimi, A. (2009). *A hybrid discrete–finite element model for numerical simulation of geomaterials*. Computers and Geotechnics, 36(3), p. 386-395. doi: 10.1016/j.compgeo.2008.05.004
- Frangi, A., & Novati, G. (1999). On the numerical stability of time-domain elastodynamic analyses by BEM. Computational methods in applied mechanics and eng., 173, p. 403-417.
- Friedman, M.B., & Shaw, R.P. (1962). Diffraction of pulses by cylindrical obstacles of arbitrary cross-section. J. of Applied Mechanics, 29, p. 40-46.
- Goldstein, H., Poole, C., & Safko, J. (2002). *Classical Mechanics* (3rd edition ed.). San Fransisco: Addison-Wesley Publishing Company Inc.
- Haverkamp, B.C. (2008). *Ice-induced vibrations on gravity based structures*. (M.Sc.), Delft University of Technology, Delft.
- Hendrikse, H., & Nord, T.S. (2019). Dynamic response of an offshore structure interacting with an ice floe failing in crushing. Marine Structures, 65, p. 271-290. doi: 10.1016/j.marstruc.2019.01.012
- Herrmann, H.J., Hansen, A., & Roux, S. (1989). Fracture of disordered, elastic lattices in two dimensions. Physics Revisions B, 39, p. 637-648.
- Herrmann, H.J., & Roux, S. (1990). *Statistical models for the fracture of disordered media*. Amsterdam: North-Holland.
- Hooke, R. (1678). Lectures de Potentia Restitutiva. London.
- Hrennikoff, A.P. (1940). *Plane stress and bending of plates by method of articulated framework.* (PhD), Massachusetts Institute of Technology, Cambridge.
- Hrennikoff, A.P. (1941). Solution of problems of elasticity by the framework method. J. of Applied Mechanics, 8, p. 169-175.
- Huygens, C. (1690). Traité de la Lumière. Leiden: Pierre vander Aa.
- Hwang, Y.K., Bolander, J.E., & Lim, Y.M. (2016). Simulation of concrete tensile failure under high loading rates using three-dimensional irregular lattice models. Mechanics of Materials, 101, p. 136-146. doi: https://doi.org/10.1016/j.mechmat.2016.08.002
- Iserles, A., Nørsett, S.P., & Olver, S. (2006). Highly Oscillatory Quadrature: The Story so Far. In A.B.d. Castro, D. Gómez, P. Quintela & P. Salgado (Eds.), *Numerical Mathematics and Advanced Applications* (pp. 97-118): Springer Berlin Heidelberg.
- Kaewunruen, S., & Remennikov, A.M. (2016). Current state of practice in railway track vibration isolation: an Australian overview. Australian J. of Civil Eng., 14, p. 63-71. doi: 10.1080/14488353.2015.1116364

- Kafashan, J., Wiącek, J., Abd Rahman, N., & Gan, J. (2019). *Two-dimensional particle shapes modelling for DEM simulations in engineering: a review*. Granular Matter, 21(3), p. 80. doi: 10.1007/s10035-019-0935-1
- Kale, S., & Ostoja-Starzewski, M. (2022). Lattice and particle modeling of damage phenomena Handbook of Damage Mechanics: Nano to Macro Scale for Materials and Structures (pp. 1143-1179): Springer.
- Karpov, E.G., Wagner, G.J., & Liu, W.K. (2005). A Greens function approach to deriving non-reflecting boundary conditions. Int. J. for numerical methods in eng., 62, p. 1250-1262.
- Katsura, S., Morita, T., Inawashiro, S., Horiguchi, T., & Abe, Y. (1971). *Lattice Green's Function*. *Introduction*. J. of Mathematical Physics, 12(5), p. 892-895. doi: 10.1063/1.1665662
- Kausel, E., & de Oliveira Barbosa, J.M. (2012). *PMLs: A direct approach*. Int. J. for numerical methods in eng., 90, p. 343-352. doi: 10.1002/nme.3322
- Kausel, E., & Roësset, J.M. (1981). *Stiffness matrices for layered soils*. Bulletin of the Seismological Society of America, 71, p. 1743-1761.
- Kézdi, Á. (1974). *Handbook of Soil Mechanics: Soil Physics* (Vol. 1). Amsterdam: Elsevier Scientific Publishing Company.
- Kim, K., & Lim, Y.M. (2011). Simulation of rate dependent fracture in concrete using an irregular lattice model. Cement and Concrete Composites, 33(9), p. 949-955. doi: 10.1016/j.cemconcomp.2011.01.002
- Kirkup, S. (2019). *The Boundary Element Method in Acoustics: A Survey*. Applied Sciences, 9(8), p. 1642.
- Krantz, S.G. (1999). The Argument Principle *Handbook of Complex Variables* (pp. 69-78): Birkhäuser Boston.
- Kunze, M. (2000). Non-Smooth Dynamical Systems: Springer Berlin Heidelberg.
- Lagrange, J.-L.d. (1759). *Recherches sur la nature et la propagation du son*. Miscellanea Taurinensia, 1, p. 39-148.
- Lanczos, C. (1966). The Variational Principles of Mechanics (3rd edition ed.). Toronto: University of Toronto Press.
- Landau, L.D., & Lifshitz, E.M. (1976). Mechanics. Oxford: Pargamon.
- Maradudin, A.A., Montroll, E.M., Weiss, G.H., & Ipatova, I.P. (1971). Theory of Lattice Dynamics in the Harmonic Approximation *Solid State Physics* (Second Edition ed.). New York and London: Academic Press.
- Martin, P.A. (2006). Discrete scattering theory: Green's function for a square lattice. Wave Motion, 43(7), p. 619-629. doi: 10.1016/j.wavemoti.2006.05.006
- McHenry, D. (1942). The Numerical Solution of Two-Dimensional Problems in Elasticity by a Lattice Analogy (Vol. Technical Memorandum No. 624): U.S. Bureau of Reclamation.
- McHenry, D. (1943). A lattice analogy for the solution of stress problems. J. of the institution of civil engineers, 21(2), p. 59-82.
- Metrikine, A.V., & Askes, H. (2002). One-dimensional dynamically consistent gradient elasticity models derived from a discrete microstructure: Part 1: Generic formulation. European J. of Mechanics A/Solids, 21(4), p. 555-572. doi: 10.1016/S0997-7538(02)01218-4
- Metrikine, A.V., & Askes, H. (2006). *An isotropic dynamically consistent gradient elasticity model derived from a 2D lattice*. Philosophical Magazine, 86(21-22), p. 3259-3286.
- Metrikine, A.V., Kudarova, A.M., Hoving, J.S., & van Vliet, R. (2014). On the minimization of wave reflection at the interface of a discrete system and a dispersively-similar continuum. J. of Sound and Vibration, p. in press.

- Mühlhaus, H.B., & Oka, F. (1996). Dispersion and wave propagation in discrete and continuous models for granular materials. Int. J. of Solids and Structures, 33(19), p. 2841-2858. doi: https://doi.org/10.1016/0020-7683(95)00178-6
- Nelder, J.A., & Mead, R. (1965). A Simplex Method for Function Minimization. The Computer J., 7(4), p. 308-313. doi: 10.1093/comjnl/7.4.308
- Nikolić, M., Karavelić, E., Ibrahimbegovic, A., & Miščević, P. (2018). *Lattice Element Models and Their Peculiarities*. Archives of Computational Methods in Eng., 25(3), p. 753-784. doi: 10.1007/s11831-017-9210-y
- Ostoja-Starzewski, M. (2002). *Lattice models in micromechanics*. Applied Mechanics Reviews, 55(1), p. 35-60.
- Ostoja-Starzewski, M., Sheng, P.Y., & Alzebdeh, K. (1996). Spring network models in elasticity and fracture of composites and polycrystals. Computational Materials Science, 7(1), p. 82-93. doi: 10.1016/S0927-0256(96)00064-X
- Pan, Y., Prado, A., Porras, R., Hafez, O.M., & Bolander, J.E. (2017). Lattice Modeling of Early-Age Behavior of Structural Concrete. *Materials*, 10(3). doi:10.3390/ma10030231
- Pan, Z., Ma, R., Wang, D., & Chen, A. (2018). A review of lattice type model in fracture mechanics: theory, applications, and perspectives. Eng. Fracture Mechanics, 190, p. 382-409. doi: 10.1016/j.engfracmech.2017.12.037
- Pavlatos, G.D., & Beskos, D.E. (1994). *Dynamic elastoplastic analysis by BEM/FEM*. Eng. analysis with boundary elements, 14, p. 51-63.
- Peirce, A., & Siebrits, E. (1997). Stability analysis and design of time-stepping schemes for general elastodynamic boundary element models. Int. J. for numerical methods in eng., 40, p. 319-342.
- Pinto, F., & Prato, C.A. (2006). *Three-dimensional indirect Boundary Element Method formulation* for dynamic analysis of frames buried in semi-infinite elastic media. J. of eng. mechanics, 132(9), p. 967-978. doi: 10.1061/0733-9399
- Popp, K., Hinrichs, N., & Oestreich, M. (1996). Analysis of a self-excited friction oscillator with external excitation. Series on Stability, Vibration and Control of Systems Series B, 7, p. 1-35.
- Prandtl, L. (1904). Über Flüssigkeitsbewegung bei sehr kleiner Reibung. Heidelberg: Verh. III. Intern. Math. Kongr.
- Press, W.H., Flannery, B.P., Teukolsky, S.A., & Vetterling, W.T. (1989). *Numerical Recipes in Pascal: The Art of Scientific Computing* (First Edition ed. Vol. 1). Cambridge, England: Cambridge University Press.
- Radjai, F., & Dubois, F. (Eds.). (2011). Discrete Numerical Modeling of Granular Materials: Wiley-ISTE.
- Ricci, L., Nguyen, V.-H., Sab, K., Duhamel, D., & Schmitt, L. (2005). *Dynamic behaviour of ballasted railway tracks: A discrete/continuous approach*. Computers & Structures, 83(28-30), p. 2282-2292.
- Rizzo, F.J. (1967). An integral equation approach to boundary value problems of classical elastostatics. Quarterly of Applied Mathematics, 25, p. 83-95.
- Roux, S., & Guyon, E. (1985). *Mechanical percolation: a small beam lattice study*. J. Physique Lett., 46(21), p. 999-1004.
- Sahimi, M., & Goddard, J.D. (1986). Elastic percolation models for cohesive mechanical failure in heterogeneous systems. Physical Review B, 33(11), p. 7848-7851. doi: 10.1103/PhysRevB.33.7848

- Schlangen, E., & Garboczi, E.J. (1997). Fracture simulations of concrete using lattice models: Computational aspects. Eng. Fracture Mechanics, 57(2), p. 319-332. doi: 10.1016/S0013-7944(97)00010-6
- Schlangen, E., & van Mier, J.G.M. (1992). Simple lattice model for numerical simulation of fracture of concrete materials and structures. Materials and Structures 25, p. 534-542.
- Suiker, A.S.J., Metrikine, A.V., & de Borst, R. (2001a). *Comparison of wave propagation characteristics of the Cosserat continuum model and corresponding discrete lattice models*. Int. J. of Solids and Structures, 38, p. 1563-1583.
- Suiker, A.S.J., Metrikine, A.V., & de Borst, R. (2001b). *Dynamic behaviour of a layer of discrete* particles, part 1: Analysis of body waves and eigenmodes. J. of Sound and Vibration 240, p. 1-18.
- Suiker, A.S.J., Metrikine, A.V., & de Borst, R. (2001c). *Dynamic behaviour of a layer of discrete particles, part 2: Response to a uniformly moving, harmonically vibrating load*. J. of Sound and Vibration 240, p. 19-39.
- Thomson, W., & Tait, P.G. (1867). Treatise on Natural Philosophy: Cambridge University Press. Tipler, P. (1998). *Physics for Scientists and Engineers* (4th ed. Vol. 1): W.H. Freeman.
- van Vliet, R., & Metrikine, A.V. (2018). *Derivation and verification of a lattice model for bending vibration of a plate*. ZAMM J. of Applied Mathematics and Mechanics / Zeitschrift für Angewandte Mathematik und Mechanik, 98(3), p. 367-387. doi: 10.1002/zamm.201700024
- Voigt, W. (1887). Ueber das Doppler'sche Princip Nachrichten von der Königliche Gesellschaft der Wissenschaften, No. 2.
- von Estorff, O., & Firuziaan, M. (2000). Coupled BEM/FEM approach for nonlinear soil/structure interaction. Eng. analysis with boundary elements, 24, p. 715-725.
- Wang, G., Al-Ostaz, A., Cheng, A.H.D., & Mantena, P.R. (2009). Hybrid lattice particle modeling of wave propagation induced fracture of solids. Computer methods in applied mechanics and eng., 199(1), p. 197-209. doi: 10.1016/j.cma.2009.10.002
- Williams, J.W.J. (1964). *Algorithms*. Communications of the ACM, 7(6), p. 347-348. doi: 10.1145/512274.512284
- Wolf, J.P. (1985). *Dynamic Soil-Structure Interaction*. Englewood Cliffs, New Jersey, United States of America: Prentice-Hall.
- Wolf, J.P., & Darbre, G.R. (1984a). *Dynamic-stiffness matrix of soil by the boundary-element method: conceptual aspects*. J. of Earthquake eng. and structural dynamics, 12, p. 385-400.
- Wolf, J.P., & Darbre, G.R. (1984b). *Dynamic-stiffness matrix of soil by the boundary-element method: embedded foundation*. J. of Earthquake eng. and structural dynamics, 12, p. 401-416.
- Woods, F.S. (1926). Differentiation of a Definite Integral Advanced Calculus: A Course Arranged with Special Reference to the Needs of Students of Applied Mathematics. pp. 141-144. Boston, MA: Ginn.
- Zhao, S.-F., & Zhao, G.-F. (2012). *Implementation of a high order lattice spring model for elasticity*. Int. J. of Solids and Structures, 49(18), p. 2568-2581. doi: 10.1016/j.ijsolstr.2012.05.015
- Ziman, J.M. (1979). *Models of disorder: the theoretical physics of homogeneously disordered systems*: Cambridge University Press.

Appendices

Α	Linearization of elongations in rheological elements	277
A.1	Linearization for small elongations	277
A.2	Linearization for large elongations	279
A.3	A higher-order approach for large elongations	280
В	Normalisation and dimensionless parameters	282
B.1	Normalisation in one-dimensional discrete-continuous systems	282
B.2	Normalisation in two-dimensional discrete-continuous systems	284
B.3	Normalisation in 1D and 2D fully discrete systems	285
B.4	Particle natural frequency and critical particle damping	287
С	Parameters of one- and two-dimensional lattices	293
C.1	Derivation of material parameters for the hexagonal lattice	293
C.2	Lock in the one-dimensional BKV lattice by means of a rigid bar	
C.3	Lock in the hexagonal BKV lattice by means of a rigid bar	
D	One-dimensional systems in the time domain	304
D.1	The one-dimensional discrete-continuous Hooke system	304
D.2	The elastically supported 1D discrete-continuous Hooke system	
D.3	The one-dimensional fully discrete Hooke system	
D.4	The 1D fully discrete Hooke system - alternate interface	315
D.5	The elastically supported 1D discrete-continuous KV-system	317
E	Wave propagation in one-dimensional systems	322
E.1	Dispersion in linear-elastic and viscoelastic rods	322
E.2	Dispersion in one-dimensional linear-elastic particle systems	
E.3	Dispersion in one-dimensional viscoelastic particle systems	
E.4	Reflection coefficients for discrete-continuous Hooke systems	
E.5	Reflection coefficients for discrete-continuous KV systems	
F	The dynamic compliance of the continuous layer	336
F.1	Properties of the lumping matrix	336
F.2	Properties of the flexibility matrix	
F.3	Displacements and stresses in the Laplace-wavenumber domain	
F.4	Green's functions for a load inside the continuous layer	
F.5	Green's functions for a load at the surface of the continuum	347

G	The dynamic compliance of the half-plane of particles	350
G.1	Boundary conditions for a load inside the half-plane of particles	350
G.2	Boundary conditions for a load at the half-plane surface	355
G.3	Green's reaction forces at the left surface particle	356
G.4	Green's reaction forces at a particle along the left slope	358
G.5	Green's reaction forces at the left corner particle	361
G.6	Green's reaction forces at a particle along the horizontal domain	362
G.7	Green's reaction forces at the right corner particle	363
G.8	Green's reaction forces at a particle along the right slope	365
G.9	Green's reaction forces at the right surface particle	367
G.10	Equivalent 1D Green's reaction forces in the half-plane of particles	368
Н	Wave propagation in two-dimensional systems	370
H.1	Dispersion in the half-plane of particles	370
H.2	Dispersion in the continuous layer	372
I	Contour integration and the residue theorem	374
I.1	Contour integration to evaluate the inverse Fourier transform	374
I.2	Algorithm to find the roots of a function in the complex plane	
I.3	Green's functions of the linear-elastic rod	378
I.4	Green's functions of the viscoelastic rod	381
I.5	Convolution term in the Green's function for the viscoelastic rod	382
J	The Laplace transform and nonzero initial conditions	387
J.1	Identities of the Laplace transform	387
J.2	The inverse Laplace transform in terms of frequency	
J.3	The causality principle and the Laplace transform	
J.4	Identities of the inverse Laplace transform	
J.5	Laplace domain expressions for applied loads	
J.6	The MTFD-method applied to a one-mass-spring-system	
J 7	Alternative derivation of the convolution for the linear-elastic rod	

A Linearization of elongations in rheological elements

To describe the system of equations of motion for a two-dimensional lattice as a system of linear ordinary differential equations, the expressions for the elongations of its rheological elements must be linearized. The way these elongations are linearized depends on the magnitude and the definition of the involved particle displacements. This appendix gives an overview of several linearizations that apply to different magnitudes of the elongation.

A.1 Linearization for small elongations

Figure A.1a shows the displacement of a particle $\mathbf{m_{j}}, \mathbf{n_{j}}$ relative to the position of a particle $\mathbf{m,n}$ in two-dimensional space. Here, the interaction between particles $\mathbf{m,n}$ and $\mathbf{m_{j}}, \mathbf{n_{j}}$ is described by a linear spring. The spring between particles $\mathbf{m,n}$ and $\mathbf{m_{j}}, \mathbf{n_{j}}$ initially has a length $\ell_{j}^{\mathbf{m,n}}$ and an angle $\alpha_{j}^{\mathbf{m,n}}$ with respect to the *x*-axis. Following the geometry depicted in Figure A.1a, we can express the elongation of the spring between particles $\mathbf{m,n}$ and $\mathbf{m_{j}}, \mathbf{n_{j}}$ as:

$$e_j^{\mathbf{m},\mathbf{n}} = \sqrt{\left(\ell_{x,j}^{\mathbf{m},\mathbf{n}} + e_{x,j}^{\mathbf{m},\mathbf{n}}\right)^2 + \left(\ell_{z,j}^{\mathbf{m},\mathbf{n}} + e_{z,j}^{\mathbf{m},\mathbf{n}}\right)^2} - \ell_j^{\mathbf{m},\mathbf{n}}$$
(A.1)

As the particles \mathbf{m} , \mathbf{n} and $\mathbf{m_j}$, $\mathbf{n_j}$ move relative to each other, both the elongation and the angle of the spring change continuously. Although the horizontal and vertical components of the initial spring length, respectively denoted as $\ell_{x;j}^{\mathbf{m},\mathbf{n}}$ and $\ell_{z;j}^{\mathbf{m},\mathbf{n}}$, can be described in terms of the length $\ell_j^{\mathbf{m},\mathbf{n}}$ through the angle $\alpha_j^{\mathbf{m},\mathbf{n}}$, the horizontal and vertical components of the elongation, respectively denoted as $e_{x;j}^{\mathbf{m},\mathbf{n}}$ and $e_{z;j}^{\mathbf{m},\mathbf{n}}$, cannot. Then, using trigonometry to express the horizontal and vertical length components, as well as taking the spring length out from under the square root, the elongation of the spring between particles \mathbf{m} , \mathbf{n} and \mathbf{m}_j , \mathbf{n}_j becomes:

$$e_{j}^{\mathbf{m},\mathbf{n}} = \ell_{j}^{\mathbf{m},\mathbf{n}} \sqrt{1 + \frac{2}{\ell_{j}^{\mathbf{m},\mathbf{n}}} \left(e_{x;j}^{\mathbf{m},\mathbf{n}} \cos \alpha_{j}^{\mathbf{m},\mathbf{n}} + e_{z;j}^{\mathbf{m},\mathbf{n}} \sin \alpha_{j}^{\mathbf{m},\mathbf{n}} \right) + \left(\frac{e_{x;j}^{\mathbf{m},\mathbf{n}}}{\ell_{j}^{\mathbf{m},\mathbf{n}}} \right)^{2} + \left(\frac{e_{z;j}^{\mathbf{m},\mathbf{n}}}{\ell_{j}^{\mathbf{m},\mathbf{n}}} \right)^{2} - \ell_{j}^{\mathbf{m},\mathbf{n}}$$
(A.2)

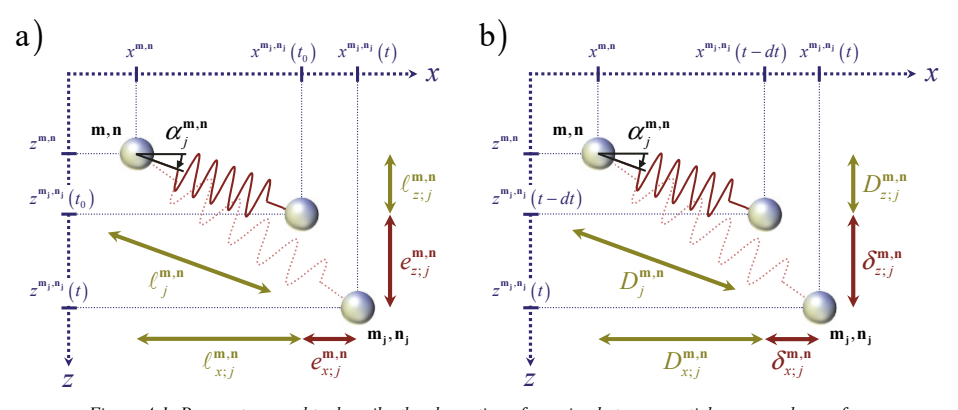


Figure A.1: Parameters used to describe the elongation of a spring between particles m,n and m_j,n_j for:
a) small elongations; b) large elongations.

For small strains, we linearize the expression for the elongation of the spring between particles \mathbf{m} , \mathbf{n} and $\mathbf{m_j}$, $\mathbf{n_j}$ by comparing it to the initial spring length. Provided that the horizontal and vertical components of the elongation are significantly smaller than the initial spring length, it follows that the quadratic terms under the square root are negligible. Additionally, the second term under the square root must be significantly smaller than one. To approximate the elongation, we can take the Taylor series of the square root in equation (A.2) and only take the linear terms into account so that $\sqrt{1+a} = 1 + \frac{a}{2}$. Rearranging the remainder of equation (A.2) then yields the elongation as:

$$e_j^{\mathbf{m},\mathbf{n}} = e_{x;j}^{\mathbf{m},\mathbf{n}} \cos \alpha_j^{\mathbf{m},\mathbf{n}} + e_{z;j}^{\mathbf{m},\mathbf{n}} \sin \alpha_j^{\mathbf{m},\mathbf{n}}$$
(A.3)

Note here that the higher-order terms of the involved Taylor series are neglected because they are related to, or are of the same order as, the quadratic terms previously neglected.

The horizontal and vertical displacement of a particle \mathbf{m} , \mathbf{n} are defined as the total distance that the particle has travelled in respectively horizontal and vertical direction at time t compared to its initial position at time t_0 . The horizontal and vertical displacements of a particle \mathbf{m} , \mathbf{n} may thus respectively be expressed as:

$$u_x^{\mathbf{m},\mathbf{n}} = x^{\mathbf{m},\mathbf{n}}(t) - x^{\mathbf{m},\mathbf{n}}(t_0) \tag{A.4}$$

$$u_z^{\mathbf{m},\mathbf{n}} = z^{\mathbf{m},\mathbf{n}} \left(t \right) - z^{\mathbf{m},\mathbf{n}} \left(t_0 \right) \tag{A.5}$$

The displacements $u_x^{\mathbf{m_j},\mathbf{n_j}}$ and $u_z^{\mathbf{m_j},\mathbf{n_j}}$ of particle $\mathbf{m_j},\mathbf{n_j}$ may be described accordingly. Consequently, the horizontal and vertical components of the elongation may be expressed as:

$$e_{x,j}^{\mathbf{m},\mathbf{n}} = x^{\mathbf{m}_{j},\mathbf{n}_{j}}(t) - x^{\mathbf{m},\mathbf{n}}(t) - \ell_{x,j}^{\mathbf{m},\mathbf{n}} = u_{x}^{\mathbf{m}_{j},\mathbf{n}_{j}} - u_{x}^{\mathbf{m},\mathbf{n}}$$
(A.6)

$$e_{z;j}^{\mathbf{m},\mathbf{n}} = z^{\mathbf{m}_{j},\mathbf{n}_{j}}(t) - z^{\mathbf{m},\mathbf{n}}(t) - \ell_{z;j}^{\mathbf{m},\mathbf{n}} = u_{z}^{\mathbf{m}_{j},\mathbf{n}_{j}} - u_{z}^{\mathbf{m},\mathbf{n}}$$
(A.7)

Substituting equations (A.6) and (A.7) into equation (A.3), the elongation of the spring between particles \mathbf{m} , \mathbf{n} and $\mathbf{m}_{\mathbf{i}}$, $\mathbf{n}_{\mathbf{j}}$ becomes:

$$e_j^{\mathbf{m},\mathbf{n}} = \left(u_x^{\mathbf{m}_j,\mathbf{n}_j} - u_x^{\mathbf{m},\mathbf{n}}\right)\cos\alpha_j^{\mathbf{m},\mathbf{n}} + \left(u_z^{\mathbf{m}_j,\mathbf{n}_j} - u_z^{\mathbf{m},\mathbf{n}}\right)\sin\alpha_j^{\mathbf{m},\mathbf{n}}$$
(A.8)

Let us emphasize here that the elongation of the spring between particles \mathbf{m} , \mathbf{n} and \mathbf{m}_j , \mathbf{n}_j may only be approximated by equation (A.8) when the elongation is small compared to the initial spring length. In many cases and especially when considering nonlinear behaviour, we can not assume that the displacements and elongations in a lattice are small. In Appendix A.2, we will therefore consider a linearization that is appropriate for large elongations.

For one-dimensional lattices, or cascades, the angle of all rheological elements is the same and does not change. Consequently, the expression for the elongation of a rheological element between two adjacent particles $\bf n$ and $\bf n+1$ is independent from its angle and may be

derived directly and without making any assumptions from equation (A.1) as:

$$e^{n,n+1} = u^{n+1} - u^n (A.9)$$

Due to the straightforward expression for the elongation given by equation (A.9), one-dimensional lattice models do not require linearization.

A.2 Linearization for large elongations

To allow for large elongations, i.e. elongations that are of the same order as the initial length, we linearize the expression for the elongation of the spring between particles \mathbf{m} , \mathbf{n} and $\mathbf{m}_{\mathbf{j}}$, $\mathbf{n}_{\mathbf{j}}$ about its current state, rather than about its original state. To do so, we alter the definition for the displacements of the particles in the lattice; instead of describing the particle displacement relative to its initial position, we now define the particle displacement as the distance between its position at time t compared to its previous position at the time t-dt. The horizontal and vertical displacement of a particle \mathbf{m} , \mathbf{n} may thus respectively be expressed as:

$$u_x^{m,n} = x^{m,n}(t) - x^{m,n}(t - dt)$$
(A.10)

$$u_z^{m,n} = z^{m,n}(t) - z^{m,n}(t - dt)$$
(A.11)

Here, $x^{\mathbf{m},\mathbf{n}}(t)$ and $z^{\mathbf{m},\mathbf{n}}(t)$ respectively denote the horizontal and vertical coordinates of particle \mathbf{m},\mathbf{n} at time t. The displacements $u_x^{\mathbf{m}_j,\mathbf{n}_j}$ and $u_z^{\mathbf{m}_j,\mathbf{n}_j}$ of particle $\mathbf{m}_j,\mathbf{n}_j$ are derived accordingly. The corresponding displacement of a particle $\mathbf{m}_j,\mathbf{n}_j$ relative to the position of a particle \mathbf{m},\mathbf{n} in two-dimensional space is depicted in Figure A.1b. Here, $D_j^{\mathbf{m},\mathbf{n}}$ is the distance between particles \mathbf{m},\mathbf{n} and $\mathbf{m}_j,\mathbf{n}_j$ at time t-dt and $\alpha_j^{\mathbf{m},\mathbf{n}}$ now denotes the angle of the spring with respect to the x-axis at time t-dt. Following the geometry depicted in Figure A.1b, we can then express the elongation $e_j^{\mathbf{m},\mathbf{n}}$ of the spring between particles \mathbf{m},\mathbf{n} and $\mathbf{m}_j,\mathbf{n}_j$ as:

$$e_j^{\mathbf{m},\mathbf{n}} = \sqrt{\left(D_{x;j}^{\mathbf{m},\mathbf{n}} + \delta_{x;j}^{\mathbf{m},\mathbf{n}}\right)^2 + \left(D_{z;j}^{\mathbf{m},\mathbf{n}} + \delta_{z;j}^{\mathbf{m},\mathbf{n}}\right)^2} - \ell_j^{\mathbf{m},\mathbf{n}}$$
(A.12)

Here, $D_{x;j}^{\mathbf{m},\mathbf{n}}$ and $D_{z;j}^{\mathbf{m},\mathbf{n}}$ respectively denote the horizontal and vertical distance between particles \mathbf{m} , \mathbf{n} and \mathbf{m}_j , \mathbf{n}_j at time t-dt and $\ell_j^{\mathbf{m},\mathbf{n}}$ is the initial length of the spring at time t_0 . Furthermore, $\delta_{x;j}^{\mathbf{m},\mathbf{n}}$ and $\delta_{z;j}^{\mathbf{m},\mathbf{n}}$ respectively denote the change in horizontal and vertical distance between the particles during the current time step dt.

Expressing $D_{x:j}^{\mathbf{m},\mathbf{n}}$ and $D_{z:j}^{\mathbf{m},\mathbf{n}}$ in terms of the distance $D_j^{\mathbf{m},\mathbf{n}}$ using the angle $\alpha_j^{\mathbf{m},\mathbf{n}}$, as well as taking $D_j^{\mathbf{m},\mathbf{n}}$ out from under the square root, the elongation of the spring between particles \mathbf{m},\mathbf{n} and $\mathbf{m}_{\mathbf{j}},\mathbf{n}_{\mathbf{j}}$ follows from equation (A.12) as:

$$e_{j}^{\mathbf{m},\mathbf{n}} = D_{j}^{\mathbf{m},\mathbf{n}} \sqrt{1 + \frac{2}{D_{j}^{\mathbf{m},\mathbf{n}}} \left(\delta_{x;j}^{\mathbf{m},\mathbf{n}} \cos \alpha_{j}^{\mathbf{m},\mathbf{n}} + \delta_{z;j}^{\mathbf{m},\mathbf{n}} \sin \alpha_{j}^{\mathbf{m},\mathbf{n}} \right) + \left(\frac{\delta_{x;j}^{\mathbf{m},\mathbf{n}}}{D_{j}^{\mathbf{m},\mathbf{n}}} \right)^{2} + \left(\frac{\delta_{z;j}^{\mathbf{m},\mathbf{n}}}{D_{j}^{\mathbf{m},\mathbf{n}}} \right)^{2} - \ell_{j}^{\mathbf{m},\mathbf{n}}$$
(A.13)

According to the definition given by equations (A.10) and (A.11), we describe the displacements of a particle as the distance travelled by that particle during the current time step dt. Consequently, the change in respectively the horizontal and vertical distance between the particles during the current time step can then be described in terms of the particle displacements as:

$$\delta_{x;j}^{m,n} = x^{m_j,n_j}(t) - x^{m,n}(t) - D_{x;j}^{m,n} = u_x^{m_j,n_j} - u_x^{m,n}$$
(A.14)

$$\delta_{z;j}^{\mathbf{m},\mathbf{n}} = z^{\mathbf{m}_{j},\mathbf{n}_{j}} (t) - z^{\mathbf{m},\mathbf{n}} (t) - D_{z;j}^{\mathbf{m},\mathbf{n}} = u_{z}^{\mathbf{m}_{j},\mathbf{n}_{j}} - u_{z}^{\mathbf{m},\mathbf{n}}$$
(A.15)

As $\delta_{x,j}^{m,n}$ and $\delta_{z,j}^{m,n}$ only describe the change in the horizontal and vertical distance between particles \mathbf{m} , \mathbf{n} and \mathbf{m}_{j} , \mathbf{n}_{j} during the current time step dt, their magnitudes are small compared to the interparticle distance $D_{j}^{m,n}$ at time t-dt. That is, if the time step dt is chosen sufficiently small. Consequently, the quadratic terms under the square root are negligible and the second term under the square root is significantly smaller than one, allowing us to approximate the elongation using a truncated Taylor approximation, so that $\sqrt{1+a} = 1 + \frac{a}{2}$. Thus, here we only take the linear terms of the involved Taylor series into account and neglect the higher-order terms because they are related to, or are of the same order as, the quadratic terms previously neglected. This yields the elongation of the spring between particles \mathbf{m} , \mathbf{n} and \mathbf{m}_{j} , \mathbf{n}_{j} as:

$$e_j^{\mathbf{m},\mathbf{n}} = \left(u_x^{\mathbf{m}_j,\mathbf{n}_j} - u_x^{\mathbf{m},\mathbf{n}}\right)\cos\alpha_j^{\mathbf{m},\mathbf{n}} + \left(u_z^{\mathbf{m}_j,\mathbf{n}_j} - u_z^{\mathbf{m},\mathbf{n}}\right)\sin\alpha_j^{\mathbf{m},\mathbf{n}} + \varepsilon_j^{\mathbf{m},\mathbf{n}} \tag{A.16}$$

Here, $\varepsilon_j^{\mathbf{m},\mathbf{n}}$ is the elongation of the spring between particles \mathbf{m},\mathbf{n} and $\mathbf{m}_j,\mathbf{n}_j$ at time t-dt that during the current time step is a constant and can be obtained as $\varepsilon_j^{\mathbf{m},\mathbf{n}} = D_j^{\mathbf{m},\mathbf{n}} - \ell_j^{\mathbf{m},\mathbf{n}}$. Expressing the elongation $e_j^{\mathbf{m},\mathbf{n}}$ according to equation (A.16) allows for significantly larger deformations in the lattice than equation (A.8), which is valid for small deformations.

For the one-dimensional case, the angle of all rheological elements is constant and equal to zero at all times and the expression for the corresponding elongation between two adjacent particles **n** and **n+1**, follows from equation (A.12) without any assumptions or linearization as:

$$e^{n,n+1} = u^{n+1} - u^n + \varepsilon^{n,n+1} \tag{A.17}$$

Here, $\varepsilon^{\mathbf{n},\mathbf{n}+1}$ is the elongation of the rheological element between particles \mathbf{n} and $\mathbf{n}+1$ at time t-dt, which may be obtained as $\varepsilon^{\mathbf{n},\mathbf{n}+1} = D^{\mathbf{n},\mathbf{n}+1} - \ell^{\mathbf{n},\mathbf{n}+1}$.

A.3 A higher-order approach for large elongations

In the preceding section, we have linearized the expression for the elongation according to equation (A.13) by assuming that the quadratic terms under the square root are negligible and using a truncated Taylor approximation. By maintaining the quadratic terms under the square root in equation (A.13) before applying the Taylor approximation, a more accurate expression for the elongation can be obtained. To be consistent with taking the quadratic terms in

equation (A.13) into account, we approximate the elongation by taking the Taylor series up to its second order term, so that $\sqrt{1+a} = 1 + \frac{1}{2}a - \frac{1}{8}a^2$. This yields the elongation of the spring between particles \mathbf{m} , \mathbf{n} and \mathbf{m}_i , \mathbf{n}_i as:

$$e_{j}^{\mathbf{m,n}} = \delta_{x;j}^{\mathbf{m,n}} \cos \alpha_{j}^{\mathbf{m,n}} + \delta_{z;j}^{\mathbf{m,n}} \sin \alpha_{j}^{\mathbf{m,n}} + \varepsilon_{j}^{\mathbf{m,n}} +$$

Here, $\varepsilon_j^{\mathbf{m},\mathbf{n}}$ is again the elongation of the spring between particles \mathbf{m},\mathbf{n} and $\mathbf{m}_i,\mathbf{n}_i$ at time t-dt that is constant during the current time step dt, and can be obtained as $\varepsilon_j^{\mathbf{m},\mathbf{n}} = D_j^{\mathbf{m},\mathbf{n}} - \ell_j^{\mathbf{m},\mathbf{n}}$.

Since $\delta_{x;j}^{\mathbf{m},\mathbf{n}}$ and $\delta_{z;j}^{\mathbf{m},\mathbf{n}}$ describe the change in the horizontal and vertical distance between particles \mathbf{m},\mathbf{n} and $\mathbf{m}_j,\mathbf{n}_j$ only during the current time step, and assuming that the time step dt is chosen sufficiently small, their magnitudes are significantly smaller than the interparticle distance $D_j^{\mathbf{m},\mathbf{n}}$ at time t-dt. In this case, we can safely neglect the last two terms as they include a division by the interparticle distance $D_j^{\mathbf{m},\mathbf{n}}$ with an order of two or higher. Thus, equation (A.18) reduces to:

$$e_{j}^{\mathbf{m},\mathbf{n}} = \left(u_{x}^{\mathbf{m}_{j},\mathbf{n}_{j}} - u_{x}^{\mathbf{m},\mathbf{n}}\right) \cos \alpha_{j}^{\mathbf{m},\mathbf{n}} + \left(u_{z}^{\mathbf{m}_{j},\mathbf{n}_{j}} - u_{z}^{\mathbf{m},\mathbf{n}}\right) \sin \alpha_{j}^{\mathbf{m},\mathbf{n}} + \varepsilon_{j}^{\mathbf{m},\mathbf{n}} + \frac{1}{2D_{j}^{\mathbf{m},\mathbf{n}}} \left(\left(\delta_{x,j}^{\mathbf{m},\mathbf{n}}\right)^{2} \left(1 - \cos^{2}\alpha_{j}^{\mathbf{m},\mathbf{n}}\right) - 2\delta_{x,j}^{\mathbf{m},\mathbf{n}}\delta_{z,j}^{\mathbf{m},\mathbf{n}} \sin \alpha_{j}^{\mathbf{m},\mathbf{n}} \cos \alpha_{j}^{\mathbf{m},\mathbf{n}} + \left(\delta_{z,j}^{\mathbf{m},\mathbf{n}}\right)^{2} \left(1 - \sin^{2}\alpha_{j}^{\mathbf{m},\mathbf{n}}\right)\right)$$
(A.19)

Compared to the linearized expression for large elongations, previously given by equation (A.16), equation (A.19) includes a second-order term with respect to $\delta_{x;j}^{\mathbf{m},\mathbf{n}}$ and $\delta_{z;j}^{\mathbf{m},\mathbf{n}}$. Note here that for the additional term, equations (A.14) and (A.15) have not been substituted as this would yield the system of equations of motion as a system of nonlinear differential equations. Instead, we assume that the change in horizontal and vertical distance between particles \mathbf{m},\mathbf{n} and $\mathbf{m}_{\mathbf{j}},\mathbf{n}_{\mathbf{j}}$ during the current time step dt is equal to the corresponding distance changes during the prior time step. Since the values for $\delta_{x;j}^{\mathbf{m},\mathbf{n}}$ and $\delta_{z;j}^{\mathbf{m},\mathbf{n}}$ during the time step prior to the current time step are constants during the current time step, this reduces the whole last term in equation (A.19) to a constant. The additional error made by this assumption is an order of magnitude smaller than the error made by completely neglecting the last term, as the error is not directly related to $\delta_{x;j}^{\mathbf{m},\mathbf{n}}$ and $\delta_{z;j}^{\mathbf{m},\mathbf{n}}$, but to their time derivatives.

B Normalisation and dimensionless parameters

B.1 Normalisation in one-dimensional discrete-continuous systems

To discuss the normalisation in one-dimensional discrete-continuous systems, let us consider the system that is comprised of a one-dimensional Kelvin-Voigt lattice and the viscoelastic rod. According to Section 3.2.1, the material parameters of the lattice match the material properties of the continuum for the following relations:

$$M = \rho A \ell, \quad C_e = \zeta_e \frac{EA}{\ell}, \quad K_e = \frac{EA}{\ell}.$$
 (B.1)

Here, M is the mass of a particle in the interior of the one-dimensional Kelvin-Voigt lattice, while C_e and K_e are the corresponding damping and stiffness of the Kelvin-Voigt elements in the interior of the lattice. Furthermore, ρ , A, E, ζ_e and ℓ respectively denote the density, cross-sectional area, Young's modulus, damping of the viscoelastic rod and the distance between two adjacent particles.

To normalize the system, we introduce the following dimensionless parameters:

$$t = t_{\text{dim}} \omega_0, \quad u^{\text{n}} = \frac{u_{\text{dim}}^{\text{n}}}{\ell}, \quad M^{\text{n}} = \frac{M_{\text{dim}}^{\text{n}}}{\rho A \ell}.$$
 (B.2)

Here, ω_0 is the particle frequency, i.e. the natural frequency of a particle in the homogeneous lattice for the particular case that the motion of all adjacent particles is impeded. In the relations given by equation (B.2), the subscript dim is used to denote dimensional variables, and to distinguish them from their corresponding dimensionless forms.

From the dimensionless parameters given by equation (B.2), we can derive corresponding dimensionless parameters for the damping and the stiffness of the Kelvin-Voigt elements, as well as for any applied external force. To derive these dimensionless parameters, consider the system of equations of motion for the Kelvin-Voigt lattice, where the surface particle is loaded by a time-dependent force in its dimensional form:

$$M_{\text{dim}}^{0} \ddot{u}_{\text{dim}}^{0} + C_{e,\text{dim}}^{0,1} \left(\dot{u}_{\text{dim}}^{0} - \dot{u}_{\text{dim}}^{1} \right) + K_{e,\text{dim}}^{0,1} \left(u_{\text{dim}}^{0} - u_{\text{dim}}^{1} \right) = F_{\text{dim}}^{0} \left(t \right)$$
(B.3)

$$M_{\dim}^{\mathbf{n}} \ddot{u}_{\dim}^{\mathbf{n}} + C_{e,\dim}^{\mathbf{n},\mathbf{n}+1} \left(2\dot{u}_{\dim}^{\mathbf{n}} - \dot{u}_{\dim}^{\mathbf{n}-1} - \dot{u}_{\dim}^{\mathbf{n}+1} \right) + K_{e,\dim}^{\mathbf{n},\mathbf{n}+1} \left(2u_{\dim}^{\mathbf{n}} - u_{\dim}^{\mathbf{n}-1} - u_{\dim}^{\mathbf{n}+1} \right) = 0 \tag{B.4}$$

Replacing the variables for time and space in equations (B.3) and (B.4) by the dimensionless parameters for time and space according to the relations given by equation (B.2), we find:

$$M_{\dim}^{0} \omega_{0}^{2} \ell \ddot{u}^{0} + C_{e,\dim}^{0,1} \omega_{0} \ell \left(\dot{u}^{0} - \dot{u}^{1} \right) + K_{e,\dim}^{0,1} \ell \left(u^{0} - u^{1} \right) = F_{\dim}^{0} \left(t \right)$$
(B.5)

$$M_{\dim}^{\mathbf{n}} \omega_0^2 \ell \ddot{u}^{\mathbf{n}} + C_{e,\dim}^{\mathbf{n},\mathbf{n}+1} \omega_0 \ell \left(2\dot{u}^{\mathbf{n}} - \dot{u}^{\mathbf{n}-1} - \dot{u}^{\mathbf{n}+1} \right) + K_{e,\dim}^{\mathbf{n},\mathbf{n}+1} \ell \left(2u^{\mathbf{n}} - u^{\mathbf{n}-1} - u^{\mathbf{n}+1} \right) = 0$$
 (B.6)

Then, dividing equations (B.5) and (B.6) by $\rho A\omega_0^2 \ell^2$ respectively yields:

$$\frac{M_{\text{dim}}^{0}}{\rho A \ell} \ddot{u}^{0} + \frac{C_{e,\text{dim}}^{0,1}}{\rho A \omega_{0} \ell} (\dot{u}^{0} - \dot{u}^{1}) + \frac{K_{e,\text{dim}}^{0,1}}{\rho A \omega_{0}^{2} \ell} (u^{0} - u^{1}) = \frac{F_{\text{dim}}^{0}(t)}{\rho A \omega_{0}^{2} \ell^{2}}$$
(B.7)

$$\frac{M_{\text{dim}}^{n}}{\rho A \ell} \ddot{u}^{n} + \frac{C_{e,\text{dim}}^{n,n+1}}{\rho A \omega_{0} \ell} \left(2\dot{u}^{n} - \dot{u}^{n-1} - \dot{u}^{n+1} \right) + \frac{K_{e,\text{dim}}^{n,n+1}}{\rho A \omega_{0}^{2} \ell} \left(2u^{n} - u^{n-1} - u^{n+1} \right) = 0$$
(B.8)

The multiplicator of the dimensionless acceleration \ddot{u}^n now equals the normalized or dimensionless mass previously given in equation (B.2).

Noting that the particle frequency and the critical particle damping of the one-dimensional lattice are respectively found as $\omega_0 = \sqrt{2K_e/M}$ and $C_{crit} = M\omega_0$ and inserting the relations given by equation (B.1), it follows that $\rho A\omega_0 \ell = C_{crit}$ and $\rho A\omega_0^2 \ell^2 = 2EA$. Substituting these relations into equations (B.7) and (B.8), the dimensionless system of equations may now be written as:

$$M^{0}\ddot{u}^{0} + C_{e}^{0,1}(\dot{u}^{0} - \dot{u}^{1}) + K_{e}^{0,1}(u^{0} - u^{1}) = F^{0}(t)$$
(B.9)

$$M^{n}\ddot{u}^{n} + C_{e}^{n,n+1} \left(2\dot{u}^{n} - \dot{u}^{n-1} - \dot{u}^{n+1} \right) + K_{e}^{n,n+1} \left(2u^{n} - u^{n-1} - u^{n+1} \right) = 0$$
(B.10)

Here, the dimensionless parameters for respectively the damping and the stiffness of the Kelvin-Voigt elements in the one-dimensional lattice, as well as the expression for the applied dimensionless force, are described as:

$$C_e^{\mathbf{n},\mathbf{n}+1} = \frac{C_{e;\text{dim}}^{\mathbf{n},\mathbf{n}+1}}{C_{e;\text{dim}}}, \quad K_e^{\mathbf{n},\mathbf{n}+1} = \frac{K_{e;\text{dim}}^{\mathbf{n},\mathbf{n}+1}\ell}{2EA} = \frac{K_{e;\text{dim}}^{\mathbf{n},\mathbf{n}+1}}{2K_o}, \quad F^{\mathbf{n}} = \frac{F_{\text{dim}}^{\mathbf{n}}}{2EA} = \frac{F_{\text{dim}}^{\mathbf{n}}}{2K_o\ell}.$$
(B.11)

In equation (B.1), the damping C_e of a Kelvin-Voigt element in the homogeneous one-dimensional lattice is found by multiplication of the stiffness K_e with the dimensional damping coefficient ζ_e . In its dimensionless form, the damping is commonly described by means of the so-called damping ratio as $\zeta = C_e/C_{crit}$. Incorporating the dimensional relation for the damping C_e from equation (B.1), as well as substituting the expression for the critical particle damping, the relation between the damping ratio and the dimensional damping coefficient is obtained as:

$$\zeta = \frac{C_e}{C_{crit}} = \frac{\zeta_e K_e}{M \omega_0} = \frac{1}{2} \zeta_e \omega_0 \tag{B.12}$$

Note here that, for a homogeneous lattice, the expressions given by equations (B.2) and (B.11), yield the dimensionless mass, damping and stiffness as $M^n = 1$, $C_e^{n,n+1} = \zeta$ and $K_e^{n,n+1} = \frac{1}{2}$ respectively.

B.2 Normalisation in two-dimensional discrete-continuous systems

To discuss the normalisation in two-dimensional discrete-continuous systems, we consider the discrete-continuous system that is comprised of the hexagonal Kelvin-Voigt lattice and the viscoelastic continuous layer. As derived in Section 3.6.1, the material parameters of the lattice coincide with the material properties of the continuum for the following relations:

$$M = \frac{\sqrt{3}}{2} \rho \ell^2 dy, \quad C_e = \frac{8}{5\sqrt{3}} \zeta_e E dy, \quad K_e = \frac{8}{5\sqrt{3}} E dy$$
 (B.13)

Here, M is the mass of a particle in the interior of the hexagonal Kelvin-Voigt lattice, while C_e and K_e respectively denote the damping and the stiffness of the Kelvin-Voigt elements in the lattice. Furthermore, ℓ denotes the unit particle distance in the lattice, while ρ , E, ζ_e and dy respectively denote the density, Young's modulus, damping coefficient and unit width or third dimension of the continuous layer.

To normalize the two-dimensional system, the following dimensionless parameters for time, space and mass are introduced:

$$t = t_{\text{dim}} \omega_0, \quad u^{m,n} = \frac{u_{\text{dim}}^{m,n}}{\ell}, \quad M^{m,n} = \frac{M_{\text{dim}}^{m,n}}{\frac{\sqrt{3}}{2} \rho \ell^2 dy}.$$
 (B.14)

Here, ω_0 is the particle frequency in the hexagonal lattice, i.e. the natural frequency of a particle in the lattice when the motion of all adjacent particles is impeded, and the subscript dim is used to denote dimensional variables, as opposed to their dimensionless counterparts.

To derive dimensionless parameters for the damping and stiffness of the Kelvin-Voigt elements, as well as for any applied external force, we consider the dimensional system of equations of motion for the hexagonal Kelvin-Voigt lattice with a load applied at its surface:

$$M_{\dim}^{\mathbf{m},0} \ddot{u}_{\dim}^{\mathbf{m},0} + \sum_{j} C_{e;j,\dim}^{\mathbf{m},0} f\left(\dot{u}_{\dim}^{\mathbf{m},0}\right) + \sum_{j} K_{e;j,\dim}^{\mathbf{m},0} f\left(u_{\dim}^{\mathbf{m},0}\right) = F_{\dim}^{\mathbf{m},0}(t)$$
(B.15)

$$M_{\dim}^{\mathbf{m},\mathbf{n}} \dot{u}_{\dim}^{\mathbf{m},\mathbf{n}} + \sum_{j} C_{e;j,\dim}^{\mathbf{m},\mathbf{n}} f(\dot{u}_{\dim}^{\mathbf{m},\mathbf{n}}) + \sum_{j} K_{e;j,\dim}^{\mathbf{m},\mathbf{n}} f(u_{\dim}^{\mathbf{m},\mathbf{n}}) = 0$$
(B.16)

Note here that equations of motion (B.15) and (B.16) for the particles in the hexagonal lattice are valid in both x- and z-directions and that the subscripts for the x- and z-directions of the displacements are omitted, because the direction is not of importance for the normalisation.

Replacing the variables for dimensional time and space in equation (B.15) and (B.16) by the corresponding dimensionless parameters according to equation (B.14), as well as dividing by $\frac{\sqrt{3}}{2} \rho \omega_0^2 \ell^3 dy$, we find the system of equations of motion for the hexagonal lattice as:

$$\frac{M_{\text{dim}}^{\text{m,0}}}{\frac{\sqrt{3}}{2}\rho\ell^{2}dy}\ddot{u}^{\text{m,0}} + \sum_{j} \frac{C_{e;j,\text{dim}}^{\text{m,0}}}{\frac{\sqrt{3}}{2}\rho\omega_{0}\ell^{2}dy} f(\dot{u}^{\text{m,0}}) + \sum_{j} \frac{K_{e;j,\text{dim}}^{\text{m,0}}}{\frac{\sqrt{3}}{2}\rho\omega_{0}^{2}\ell^{2}dy} f(u^{\text{m,0}}) = \frac{F_{\text{dim}}^{\text{m,0}}(t)}{\frac{\sqrt{3}}{2}\rho\omega_{0}^{2}\ell^{3}dy}$$
(B.17)

$$\frac{M_{\text{dim}}^{m,n}}{\frac{\sqrt{3}}{2}\rho\ell^{2}dy}\ddot{u}^{m,n} + \sum_{j} \frac{C_{e;j,\text{dim}}^{m,n}}{\frac{\sqrt{3}}{2}\rho\omega_{0}\ell^{2}dy} f(\dot{u}^{m,n}) + \sum_{j} \frac{K_{e;j,\text{dim}}^{m,n}}{\frac{\sqrt{3}}{2}\rho\omega_{0}^{2}\ell^{2}dy} f(u^{m,n}) = 0$$
(B.18)

Evidently, the multiplicator of the dimensionless acceleration $\ddot{u}^{m,n}$ now equals the dimensionless mass previously given in equation (B.14).

Combining the relations in equation (B.13) with the expressions for the particle frequency and the critical particle damping of the lattice, respectively found as $\omega_0 = \sqrt{3K_e/M}$ and $C_{crit} = \frac{2}{3}M\omega_0$, we find the relations $\frac{\sqrt{3}}{2}\rho\omega_0\ell^2dy = \frac{3}{2}C_{crit}$ and $\frac{\sqrt{3}}{2}\rho\omega_0^2\ell^2 = \frac{8\sqrt{3}}{5}E$. Substituting these relations into equations (B.17) and (B.18), the dimensionless system of equations reads:

$$M^{m,0}\ddot{u}^{m,0} + \sum_{i} C_{e;j}^{m,0} f(\dot{u}^{m,0}) + \sum_{i} K_{e;j}^{m,0} f(u^{m,0}) = F^{m,0}(t)$$
(B.19)

$$M^{m,n}ii^{m,n} + \sum_{j} C_{e;j}^{m,n} f(ii^{m,n}) + \sum_{j} K_{e;j}^{m,n} f(u^{m,n}) = 0$$
(B.20)

Here, the dimensionless parameters for respectively the damping and the stiffness of the Kelvin-Voigt elements in the one-dimensional lattice, as well as the expression for the applied dimensionless force are described as:

$$C_{e;j}^{\mathbf{m},\mathbf{n}} = \frac{C_{e;j,\text{dim}}^{\mathbf{m},\mathbf{n}}}{\frac{3}{2}C_{crit}}, \quad K_{e;j}^{\mathbf{m},\mathbf{n}} = \frac{K_{e;j,\text{dim}}^{\mathbf{m},\mathbf{n}}}{\frac{8\sqrt{3}}{5}Edy} = \frac{K_{e;j,\text{dim}}^{\mathbf{m},\mathbf{n}}}{3\frac{8}{5\sqrt{3}}Edy} = \frac{K_{e;j,\text{dim}}^{\mathbf{m},\mathbf{n}}}{3K_e}, \quad F^{\mathbf{m},\mathbf{n}} = \frac{F_{\text{dim}}^{\mathbf{m},\mathbf{n}}}{\frac{8\sqrt{3}}{5}Edy\ell} = \frac{F_{\text{dim}}^{\mathbf{m},\mathbf{n}}}{3K_e\ell}.$$
(B.21)

As stated by equation (B.13), the damping coefficient ζ_e relates the damping and the stiffness of the Kelvin-Voigt elements. In its dimensionless form, the damping is commonly described by means of the damping ratio as $\zeta = C_e/C_{crit}$. As the critical particle damping is expressed as $C_{crit} = \frac{2}{3} M \omega_0$, the relation between the damping ratio and the dimensional damping coefficient follows as:

$$\zeta = \frac{C_e}{C_{crit}} = \frac{\zeta_e}{2\omega_0} \frac{3K_e}{M} = \frac{1}{2} \zeta_e \omega_0 \tag{B.22}$$

Here note that, for a homogeneous lattice, the expressions given by equations (B.14) and (B.21) yield the dimensionless mass, damping and stiffness as $M^{\mathbf{m},\mathbf{n}} = 1$, $C^{\mathbf{m},\mathbf{n}}_{e;j} = \frac{2}{3}\zeta$ and $K^{\mathbf{m},\mathbf{n}}_{e;j} = \frac{1}{3}$ respectively.

B.3 Normalisation in 1D and 2D fully discrete systems

The normalisation for the fully discrete systems is applied in accordance with the normalisation for the discrete-continuous systems. However, as stated in the introduction to Chapter 4, the configuration of the far-field particle system is chosen to match the configuration of the near-field lattice for the case that the near-field lattice is homogeneous. Therefore, considering a fully discrete system comprised of a Kelvin-Voigt lattice and a semi-infinite viscoelastic

discrete particle system of corresponding dimension, the mass of all particles in the interior of the homogeneous far-field system is denoted as M, while the damping and the stiffness of the Kelvin-Voigt elements in the interior of the homogeneous far-field system are denoted as C_e and K_e respectively.

To normalize the system, we introduce the following dimensionless parameters:

$$t = t_{\text{dim}} \omega_0, \quad u^{(\mathbf{m},)\mathbf{n}} = \frac{u_{\text{dim}}^{(\mathbf{m},)\mathbf{n}}}{\ell}, \quad M^{(\mathbf{m},)\mathbf{n}} = \frac{M_{\text{dim}}^{(\mathbf{m},)\mathbf{n}}}{M}.$$
 (B.23)

Here, ω_0 is the particle frequency of both the homogeneous Kelvin-Voigt lattice and the viscoelastic far-field particle system. The subscript dim is here again used to distinguish the dimensional variables from the corresponding dimensionless variables. Furthermore, regarding the superscript notation used in equation (B.23) note that including the part between brackets refers to a particle \mathbf{m} , \mathbf{n} in the two-dimensional system, while neglecting the part between brackets refers to a particle \mathbf{n} in the one-dimensional cascade.

Dimensionless parameters for damping and stiffness of the Kelvin-Voigt elements, as well as that for the applied loading, are derived from the relations given by equation (B.23).

Normalisation in the one-dimensional fully discrete system

The system of equations of motion for the one-dimensional Kelvin-Voigt lattice is previously given by equations (B.3) and (B.4). Replacing the dimensional variables for time and space by their dimensionless counterparts according to equation (B.23), subsequently dividing the remainder by $M \omega_0^2 \ell$ as well as incorporating the expressions for the particle frequency and the critical particle damping of the cascade, respectively found as $\omega_0 = \sqrt{2K_e/M}$ and $C_{crit} = M \omega_0$, the dimensionless system of equations of motion for the one-dimensional Kelvin-Voigt lattice becomes:

$$M^{0}\ddot{u}^{0} + C_{e}^{0,1}(\dot{u}^{0} - \dot{u}^{1}) + K_{e}^{0,1}(u^{0} - u^{1}) = F^{0}(t)$$
(B.24)

$$M^{n}\ddot{u}^{n} + C_{e}^{n,n+1} \left(2\dot{u}^{n} - \dot{u}^{n-1} - \dot{u}^{n+1} \right) + K_{e}^{n,n+1} \left(2u^{n} - u^{n-1} - u^{n+1} \right) = 0$$
(B.25)

Note here that equations (B.24) and (B.25) exactly match equations (B.9) and (B.10) previously obtained for the lattice in the discrete-continuous system. The expressions for the dimensionless parameters in the above system of equations however, are different for the lattice in the one-dimensional fully discrete system; whereas the dimensionless parameter for the mass was previously given by equation (B.23), the dimensionless parameters for respectively the damping and the stiffness of the Kelvin-Voigt elements in the one-dimensional Kelvin-Voigt lattice, as well as the expression for the applied dimensionless force are described as:

$$C_e^{\mathbf{n},\mathbf{n}+1} = \frac{C_{e,\text{dim}}^{\mathbf{n},\mathbf{n}+1}}{C_{crit}}, \quad K_e^{\mathbf{n},\mathbf{n}+1} = \frac{K_{e,\text{dim}}^{\mathbf{n},\mathbf{n}+1}}{M\omega_0^2} = \frac{K_{e,\text{dim}}^{\mathbf{n},\mathbf{n}+1}}{2K_e}, \quad F^{\mathbf{n}} = \frac{F_{\text{dim}}^{\mathbf{n}}}{M\omega_0^2\ell} = \frac{F_{\text{dim}}^{\mathbf{n}}}{2K_e\ell}.$$
(B.26)

Note here that for the homogeneous far-field system, i.e. the one-dimensional semi-infinitie cascade, the dimensionless mass, damping and stiffness in this system are respectively found as $M^n = 1$, $C_e^{n,n+1} = \zeta$ and $K_e^{n,n+1} = \frac{1}{2}$. Here, ζ is the damping ratio, which is commonly described as $\zeta = C_e/C_{crit}$.

Normalisation in the two-dimensional fully discrete system

The system of equations of motion for the hexagonal Kelvin-Voigt lattice is previously given by equations (B.15) and (B.16). Replacing the dimensional variables for time and space by their dimensionless counterparts according to equation (B.23), subsequently dividing the remainder by $M\omega_0^2\ell$ and incorporating the expressions for the particle frequency and the critical particle damping of the cascade, found as $\omega_0 = \sqrt{3K_e/M}$ and $C_{crit} = \frac{2}{3}M\omega_0$ respectively, the dimensionless system of equations of motion for the hexagonal Kelvin-Voigt lattice may now be expressed as:

$$M^{m,0}\ddot{u}^{m,0} + \sum_{j} C_{e;j}^{m,n} f(\dot{u}^{m,0}) + \sum_{j} K_{e;j}^{m,n} f(u^{m,0}) = F^{m,0}(t)$$
(B.27)

$$M^{m,n}ii^{m,n} + \sum_{j} C_{e;j}^{m,n} f(ii^{m,n}) + \sum_{j} K_{e;j}^{m,n} f(u^{m,n}) = 0$$
(B.28)

Note here that equations (B.27) and (B.28) exactly match equations (B.19) and (B.20) previously obtained for the hexagonal lattice in the discrete-continuous system. Here, the expression for the dimensionless mass is given by equation (B.23), while the dimensionless parameters for respectively the damping and the stiffness of the Kelvin-Voigt elements in the one-dimensional Kelvin-Voigt lattice, as well as the expression for the applied dimensionless load are described as:

$$C_{e;j}^{\mathbf{m},\mathbf{n}} = \frac{C_{e;j,\text{dim}}^{\mathbf{m},\mathbf{n}}}{\frac{3}{2}C_{crit}}, \quad K_{e;j}^{\mathbf{m},\mathbf{n}} = \frac{K_{e;j,\text{dim}}^{\mathbf{m},\mathbf{n}}}{M\omega_0^2} = \frac{K_{e;j,\text{dim}}^{\mathbf{m},\mathbf{n}}}{3K_e}, \quad F^{\mathbf{m},\mathbf{n}} = \frac{F_{\text{dim}}^{\mathbf{m},\mathbf{n}}}{M\omega_0^2\ell} = \frac{F_{\text{dim}}^{\mathbf{m},\mathbf{n}}}{3K_e\ell}.$$
(B.29)

Here, the dimensionless mass, damping and stiffness of the homogeneous half-plane of particles are respectively found as $M^{\mathbf{m},\mathbf{n}} = 1$, $C^{\mathbf{m},\mathbf{n}}_{e;j} = \frac{2}{3}\zeta$ and $K^{\mathbf{m},\mathbf{n}}_{e;j} = \frac{1}{3}$, where ζ is the damping ratio that is commonly described as $\zeta = C_e/C_{crit}$.

B.4 Particle natural frequency and critical particle damping

It is commonly known that continuous semi-infinite one-dimensional systems have no natural frequencies. Finite lumped mass systems that consist of several degrees of freedom however, do have natural frequencies that depend on the material parameters and the geometry of the complete system. Additionally, Dieterman and Metrikine [1997] have shown that semi-infinite lumped mass systems, such as the one-dimensional lattices considered in this thesis, may have both real and imaginary natural frequencies depending on the mass of the boundary particle. Next to these natural frequencies of the system, another type of natural frequencies exist in lumped-mass systems that are associated with the motion of a single particle for the

particular case that the motion of all adjacent particles is impeded. These frequencies are sometimes called 'partial frequencies', but in this thesis, we refer to them as 'particle frequencies'. Although in some particular cases, a natural frequency of a system may coincide with a particle frequency, they are not the same; as opposed to the natural frequencies of the enitre system, particle frequencies are independent of whether a system is finite or semi-infinite. In accordance with the particle frequency, also a critical damping may be derived separately for each particle in a system under the condition that the motion of adjacent particles is impeded. In this thesis, we will refer to this damping as the 'critical particle damping'.

For a single mass-spring system, the commonly known natural frequency coincides with the particle frequency and is straightforwardly derived as $\omega_0 = \sqrt{K_e/M}$. Accordingly, for a single mass-spring system, the critical damping coincides with the critical particle damping, which is obtained as $C_{crit} = 2M\,\omega_0 = 2\sqrt{K_eM}$. In this thesis, the particle frequency and the critical particle damping of the homogeneous one- and two-dimensional lattices are used for normalisation of its corresponding systems of equations of motion. Although the derivations of the particle frequency and critical particle damping in one-dimensional lattices are quite straightforward, they are included here for the insight they provide with regard to the corresponding derivations for the hexagonal lattice, in which the particles have two degrees of freedom.

Particle frequency in a homogeneous one-dimensional viscoelastic lattice

Figure B.1a depicts a particle \mathbf{n} in the interior of the homogeneous one-dimensional Kelvin-Voigt lattice, where all masses are equal to M and the stiffness and damping of its elements are respectively equal to K_e and C_e . Defining $u^{\mathbf{n}}$ as the total displacement of the particle \mathbf{n} , the equation of motion for the particle \mathbf{n} is straightforwardly obtained as:

$$M^{n}\ddot{u}^{n} + C_{e}\left(2\dot{u}^{n} - \dot{u}^{n-1} - \dot{u}^{n+1}\right) + K_{e}\left(2u^{n} - u^{n-1} - u^{n+1}\right) = 0$$
(B.30)

To determine the particle frequency for particle $\bf n$, i.e. the natural frequency of particle $\bf n$ for the particular case that the motion of all adjacent particles is impeded, damping is assumed to be equal to zero, i.e. $C_e=0$. The particle frequency is independent of any applied loading and follows from the free-field solution that satisfies the homogeneous equation (B.30). Initially given a certain deflection, the particle $\bf n$ will freely vibrate at its particle frequency and the corresponding displacement $u^{\bf n}$ may then be described by an oscillatory function as $u^{\bf n}(t)=Ae^{i\,\omega_0 t}$, where A is the amplitude and ω_0 is the particle frequency. Substituting the given expression for the displacement $u^{\bf n}$ into the dampingless version of equation (B.30), assuming zero displacement and zero velocity for adjacent particles and solving for ω_0 , then yields the particle frequency as:

$$\omega_0 = \sqrt{\frac{2K_e}{M}} \tag{B.31}$$

For the lattice to be homogeneous, the surface particle, i.e. particle 1 in Figure B.1b, must have the same particle frequency as the particles in the interior of the lattice. Denoting the mass of the surface particle as M^1 , the equation of motion for the surface particle reads:

$$M^{1}\ddot{u}^{1} + C_{e}\left(\dot{u}^{1} - \dot{u}^{2}\right) + K_{e}\left(u^{1} - u^{2}\right) = 0$$
(B.32)

Equation (B.32) yields the particle frequency of the surface particle as $\omega_0 = \sqrt{K_e/M^1}$. Thus, for the surface particle to have the same particle frequency as the interior particles, the mass of the surface particle must be equal to $\frac{1}{2}M$.

Critical particle damping in a homogeneous one-dimensional lattice

The critical particle damping for a particle \mathbf{n} in the one-dimensional lattice may be obtained from its equations of motion that incorporates damping, previously given for an interior and a surface particle by respectively equations (B.30) and (B.32), by assuming that the displacement of the particle \mathbf{n} is of the form $u^{\mathbf{n}}(t) = Ae^{st}$, where s is complex-valued. Substituting the given expression for the displacement $u^{\mathbf{n}}$ of particle \mathbf{n} into equation (B.30) and assuming zero motion of adjacent particles yields the following algebraic equation:

$$Ms^2 + 2C_e s + 2K_e = 0 (B.33)$$

Note here that, for the case that $M^1 = \frac{1}{2}M$, substituting $u^n(t) = Ae^{st}$ into equation (B.32) yields the exact same algebraic equation. Solving equation (B.33) for s using the quadratic formula and rearranging, yields the following solutions:

$$s_{1,2} = -\frac{C_e}{M} \pm \frac{i}{M} \sqrt{2K_e M - C_e^2}$$
 (B.34)

The negative real part of the complex-valued constant s corresponds to an exponential decay of the displacement over time, while the imaginary part describes the oscillatory segment of the displacement response. The damping C_e for which the second term in equation (B.34) is equal to zero corresponds to the critical particle damping C_{crit} in the homogeneous one-dimensional lattice as:

$$C_{crit} = \sqrt{2K_eM} = M\omega_0 \tag{B.35}$$

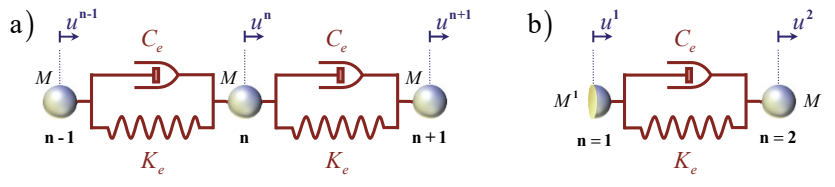


Figure B.1: Particles in the homogeneous one-dimensional lattice: a) particle in the interior; b) surface particle.

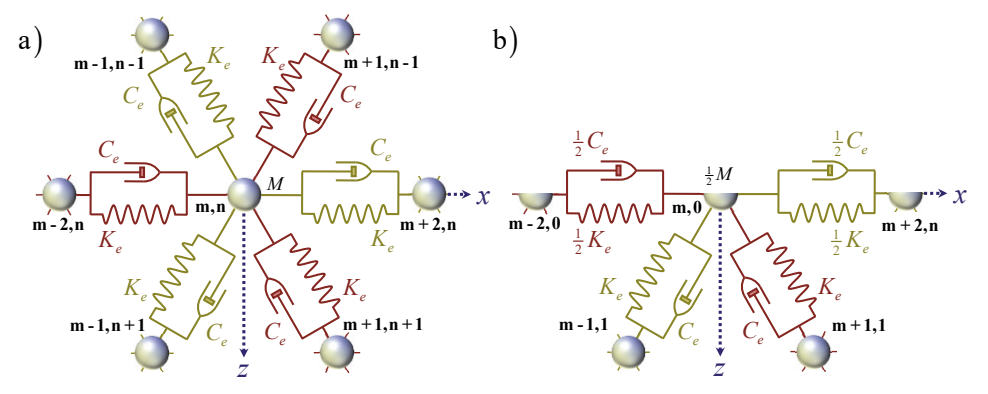


Figure B.2: Particles in the homogeneous hexagonal lattice: a) interior particle; b) surface particle.

Particle frequency in a homogeneous hexagonal lattice

Figure B.2a shows a particle **m,n** in the interior of the homogeneous hexagonal Kelvin-Voigt lattice, where all masses are equal to M and the stiffness and damping of the elements are respectively equal to K_e and C_e . The equations of horizontal and vertical motion for a particle m,n in the homogeneous hexagonal Kelvin-Voigt lattice are obtained as:

$$M\ddot{u}_{x}^{\mathbf{m,n}} - \hat{K}_{e} \sum_{j=1}^{6} \left\{ \left(u_{x}^{\mathbf{m_{j},n_{j}}} - u_{x}^{\mathbf{m,n}} \right) \cos^{2} \alpha_{j}^{\mathbf{m,n}} + \left(u_{z}^{\mathbf{m_{j},n_{j}}} - u_{z}^{\mathbf{m,n}} \right) \sin \alpha_{j}^{\mathbf{m,n}} \cos \alpha_{j}^{\mathbf{m,n}} \right\} = 0$$
 (B.36)

$$M\ddot{u}_{z}^{\mathbf{m},\mathbf{n}} - \hat{K}_{e} \sum_{j=1}^{6} \left\{ \left(u_{x}^{\mathbf{m}_{j},\mathbf{n}_{j}} - u_{x}^{\mathbf{m},\mathbf{n}} \right) \cos \alpha_{j}^{\mathbf{m},\mathbf{n}} \sin \alpha_{j}^{\mathbf{m},\mathbf{n}} + \left(u_{z}^{\mathbf{m}_{j},\mathbf{n}_{j}} - u_{z}^{\mathbf{m},\mathbf{n}} \right) \sin^{2} \alpha_{j}^{\mathbf{m},\mathbf{n}} \right\} = 0$$
 (B.37)

Here, \hat{K}_{e} is an operator that describes the viscoelasticity of the BKV elements in terms of the stiffness and damping as $\hat{K}_e = K_e + C_e \frac{\partial}{\partial t}$. For the angles $\alpha_j^{m,n}$ of the six evenly divided Kelvin-Voigt elements in the cell of particle m,n as depicted in Figure B.2a, the equations of motion for particle **m,n** in the interior of the homogeneous hexagonal lattice become:

$$M\ddot{u}_{x}^{\mathbf{m,n}} + \hat{K}_{e} \begin{pmatrix} 3u_{x}^{\mathbf{m,n}} - u_{x}^{\mathbf{m-2,n}} - u_{x}^{\mathbf{m+2,n}} - \frac{1}{4} \left(u_{x}^{\mathbf{m-1,n+1}} + u_{x}^{\mathbf{m+1,n+1}} + u_{x}^{\mathbf{m-1,n-1}} + u_{x}^{\mathbf{m+1,n-1}} \right) \\ + \frac{\sqrt{3}}{4} \left(u_{z}^{\mathbf{m-1,n+1}} - u_{z}^{\mathbf{m+1,n+1}} - u_{z}^{\mathbf{m-1,n-1}} + u_{z}^{\mathbf{m+1,n-1}} \right) \end{pmatrix} = 0 \quad (B.38)$$

$$M\ddot{u}_{x}^{\mathbf{m},\mathbf{n}} + \hat{K}_{e} \begin{pmatrix} 3u_{x}^{\mathbf{m},\mathbf{n}} - u_{x}^{\mathbf{m}-2,\mathbf{n}} - u_{x}^{\mathbf{m}+2,\mathbf{n}} - \frac{1}{4} \left(u_{x}^{\mathbf{m}-1,\mathbf{n}+1} + u_{x}^{\mathbf{m}+1,\mathbf{n}+1} + u_{x}^{\mathbf{m}-1,\mathbf{n}-1} + u_{x}^{\mathbf{m}+1,\mathbf{n}-1} \right) \\ + \frac{\sqrt{3}}{4} \left(u_{z}^{\mathbf{m}-1,\mathbf{n}+1} - u_{z}^{\mathbf{m}+1,\mathbf{n}+1} - u_{z}^{\mathbf{m}-1,\mathbf{n}-1} + u_{z}^{\mathbf{m}+1,\mathbf{n}-1} \right) \end{pmatrix} = 0 \quad (B.38)$$

$$M\ddot{u}_{z}^{\mathbf{m},\mathbf{n}} + \hat{K}_{e} \begin{pmatrix} 3u_{z}^{\mathbf{m},\mathbf{n}} + \frac{\sqrt{3}}{4} \left(u_{x}^{\mathbf{m}-1,\mathbf{n}+1} - u_{x}^{\mathbf{m}+1,\mathbf{n}+1} - u_{x}^{\mathbf{m}-1,\mathbf{n}-1} + u_{x}^{\mathbf{m}+1,\mathbf{n}-1} \right) \\ -\frac{3}{4} \left(u_{z}^{\mathbf{m}-1,\mathbf{n}+1} + u_{z}^{\mathbf{m}+1,\mathbf{n}+1} + u_{z}^{\mathbf{m}-1,\mathbf{n}-1} + u_{z}^{\mathbf{m}+1,\mathbf{n}-1} \right) \end{pmatrix} = 0 \quad (B.39)$$

To determine the particle frequency of the particle m,n, we consider its equations of motion for the case that all its adjacent particles are fixed. This reduces equations (B.38) and (B.39) to respectively:

$$M\ddot{u}_{x}^{m,n} + 3C_{e}\dot{u}_{x}^{m,n} + 3K_{e}u_{x}^{m,n} = 0$$
 (B.40)

$$M\ddot{u}_{z}^{\mathbf{m,n}} + 3C_{e}\dot{u}_{z}^{\mathbf{m,n}} + 3K_{e}u_{z}^{\mathbf{m,n}} = 0$$
 (B.41)

Comparing equations (B.40) and (B.41) clearly shows that the particle \mathbf{m} , \mathbf{n} behaves the same in both x- and z-direction and therefore has the same particle frequency for both degrees of freedom. To determine the particle frequency, we neglect the damping and describe the displacements of the particle \mathbf{m} , \mathbf{n} as $u_{x/z}^{\mathbf{m},\mathbf{n}}(t) = Ae^{i\,\omega_0 t}$, where A is the amplitude and ω_0 is the particle frequency. Substituting the given displacement for the corresponding degree of freedom into either equation (B.40) or (B.41) and solving for ω_0 , then yields the particle frequency in the hexagonal lattice as:

$$\omega_0 = \sqrt{\frac{3K_e}{M}} \tag{B.42}$$

For the hexagonal lattice to be homogeneous, the surface particle must have the same particle frequency as the particles in the interior of the hexagonal lattice. Describing the viscoelastic behaviour of the Kelvin-Voigt elements at the half-plane surface using the operator \hat{K}_e^0 , while describing the viscoelastic behaviour of the Kelvin-Voigt elements in the interior of the half-plane using the operator \hat{K}_e , the equations of motion for a surface particle $\mathbf{m},\mathbf{0}$ are obtained as:

$$M^{\mathbf{m},0} \dot{u}_{x}^{\mathbf{m},0} + \hat{K}_{e}^{0} \left(2u_{x}^{\mathbf{m},0} - u_{x}^{\mathbf{m}-2,0} - u_{x}^{\mathbf{m}+2,0} \right) + \hat{K}_{e} \begin{cases} \frac{1}{4} \left(2u_{x}^{\mathbf{m},0} - u_{x}^{\mathbf{m}-1,1} - u_{x}^{\mathbf{m}+1,1} \right) \\ + \frac{\sqrt{3}}{4} \left(u_{z}^{\mathbf{m}-1,1} - u_{z}^{\mathbf{m}+1,1} \right) \end{cases} = 0$$
 (B.43)

$$M^{\mathbf{m},0}\ddot{u}_{z}^{\mathbf{m},0} + \hat{K}_{e} \left\{ \frac{3}{4} \left(2u_{z}^{\mathbf{m},0} - u_{z}^{\mathbf{m}-1,1} - u_{z}^{\mathbf{m}+1,1} \right) + \frac{\sqrt{3}}{4} \left(u_{x}^{\mathbf{m}-1,1} - u_{x}^{\mathbf{m}+1,1} \right) \right\} = 0$$
 (B.44)

In accordance with the one-dimensional lattice, any particle at the surface of the hexagonal lattice represents only half the area of a particle in its interior and thus it follows that the mass of a surface particle is equal to half the mass of an interior particle, i.e. $M^{\mathbf{m},0} = \frac{1}{2}M$. Again assuming that the displacements of adjacent particles are equal to zero and additionally describing the viscoelastic behaviour of the surface elements in terms of the viscoelastic behaviour of the interior elements using the operator $\hat{K}_e^0 = \varphi \hat{K}_e$, equations (B.43) and (B.44) reduce to:

$$\frac{1}{2}M\ddot{u}_{x}^{\mathbf{m},\mathbf{0}} + \frac{1}{2}(4\varphi + 1)C_{e}u_{x}^{\mathbf{m},\mathbf{0}} + \frac{1}{2}(4\varphi + 1)K_{e}u_{x}^{\mathbf{m},\mathbf{0}} = 0$$
(B.45)

$$\frac{1}{2}M\ddot{u}_z^{\mathbf{m},0} + \frac{3}{2}C_e\dot{u}_z^{\mathbf{m},0} + \frac{3}{2}K_eu_z^{\mathbf{m},0} = 0$$
(B.46)

In the homogeneous hexagonal lattice, the behaviour of the particle **m,0** must be the same for both degrees of freedom and thus it follows that $\varphi = \frac{1}{2}$. Ergo, the damping and the stiffness of the surface elements are equal to half that of the elements inside the lattice, i.e. $K_e^0 = \frac{1}{2}K_e$ and $C_e^0 = \frac{1}{2}C_e$. The resulting configuration of the surface particle **m,0** is depicted in Figure

B.2b. Note here that multiplying both sides of equations (B.45) and (B.46) by two yields the horizontal and vertical equations of motion for the surface particles that are exactly the same as those previously found for a particle **m,n** in the interior of the hexagonal lattice as equations (B.40) and (B.41). Consequently, the particle frequency of the surface particles must coincide with the particle frequency of the particles in the interior of the hexagonal lattice as given by equation (B.42).

Critical particle damping in a homogeneous hexagonal lattice

The critical particle damping for a particle m,n in the hexagonal lattice may be obtained from the equation of motion for either degree of freedom, given by equations (B.40) and (B.41), by assuming that its displacement is of the form $u_{x/z}^{m,n}(t) = Ae^{st}$, where s is complex-valued. Substituting the given displacement for the corresponding degree of freedom into either equations (B.40) or (B.41) yields the following algebraic equation:

$$Ms^2 + 3C_e s + 3K_e = 0 (B.47)$$

Note here that substituting the given displacement into either equation of motion for the surface particle, described by equations (B.45) and (B.46), yields exactly the same. Solving equation (B.47) using the quadratic formula yields the following solutions for the complex-valued constant s:

$$s_{1,2} = -\frac{3C_e}{2M} \pm \frac{3i}{2M} \sqrt{\frac{4}{3}K_eM - C_e^2}$$
(B.48)

By analogy of the approach for the one-dimensional lattice, the critical particle damping for the response of any particle in the homogeneous hexagonal Kelvin-Voigt lattice is thus found as:

$$C_{crit} = \sqrt{\frac{4}{3} K_e M} = \frac{2}{3} M \omega_0$$
 (B.49)

C Parameters of one- and two-dimensional lattices

C.1 Derivation of material parameters for the hexagonal lattice

Section 2.6.2 shows that the relation between the mass M of a particle in the interior of the hexagonal lattice and the mass density ρ of the material it represents is found as:

$$M = \frac{\sqrt{3}}{2} \rho \ell^2 dy \tag{C.1}$$

Here, ℓ is the unit particle distance in the lattice and dy is the unit third dimension.

To obtain relations between the material parameters of the hexagonal lattice and the macro-material properties, the equations of motion of a particle the homogeneous hexagonal lattice must in the long-wave limit reduce to the equations of motion for a corresponding two-dimensional continuum [Maradudin et al., 1963; Suiker et al., 2001]. The general equations of motion for a particle **m,n** in the interior of the hexagonal Kelvin-Voigt lattice were previously given by equations (B.36) and (B.37). The equations of motion of a particle in the lattice may be obtained in the long-wave limit by replacing the particle displacements $u_x^{m,n}$ and $u_z^{m,n}$ by their continuum counterparts, i.e. $u_x(x,z,t)$ and $u_z(x,z,t)$, and replacing the particle displacements of the adjacent particles by corresponding expressions derived from the given continuum displacements by applying the Taylor expansion [Metrikine and Askes, 2006; Suiker et al., 2001]. The second order Taylor polynomials that are used to replace the adjacent particle displacements $u_x^{m_1,n_2}$ are obtained as:

$$u_{x/z}^{\mathbf{m_{j},n_{j}}} = u_{x/z} \left(x + \ell_{x;j}, z + \ell_{z;j}, t \right) = u_{x/z} \left(x, z, t \right) + \ell_{x;j} \frac{\partial}{\partial x} u_{x/z} \left(x, z, t \right) + \ell_{z;j} \frac{\partial}{\partial z} u_{x/z} \left(x, z, t \right) + \ell_{z;j} \frac{\partial}{\partial z} u_{x/z} \left(x, z, t \right) + \ell_{z;j} \frac{\partial^{2}}{\partial x^{2}} u_{x/z} \left(x, z, t \right) + \ell_{z;j} \ell_{z;j} \frac{\partial^{2}}{\partial x^{2}} u_{x/z} \left(x, z, t \right) + \ell_{z;j} \ell_{z;j} \frac{\partial^{2}}{\partial z^{2}} u_{x/z} \left(x, z, t \right) + \ell_{z;j} \ell_{z;j} \frac{\partial^{2}}{\partial z^{2}} u_{x/z} \left(x, z, t \right) + \ell_{z;j} \ell_{z;j} \frac{\partial^{2}}{\partial z^{2}} u_{x/z} \left(x, z, t \right) + \ell_{z;j} \ell_{z;j} \frac{\partial^{2}}{\partial z^{2}} u_{x/z} \left(x, z, t \right) + \ell_{z;j} \ell_{z;j} \frac{\partial^{2}}{\partial z^{2}} u_{x/z} \left(x, z, t \right) + \ell_{z;j} \ell_{z;j} \frac{\partial^{2}}{\partial z^{2}} u_{x/z} \left(x, z, t \right) + \ell_{z;j} \ell_{z;j} \frac{\partial^{2}}{\partial z^{2}} u_{x/z} \left(x, z, t \right) + \ell_{z;j} \ell_{z;j} \frac{\partial^{2}}{\partial z^{2}} u_{x/z} \left(x, z, t \right) + \ell_{z;j} \ell_{z;j} \frac{\partial^{2}}{\partial z^{2}} u_{x/z} \left(x, z, t \right) + \ell_{z;j} \ell_{z;j} \frac{\partial^{2}}{\partial z^{2}} u_{x/z} \left(x, z, t \right) + \ell_{z;j} \ell_{z;j} \frac{\partial^{2}}{\partial z^{2}} u_{x/z} \left(x, z, t \right) + \ell_{z;j} \ell_{z;j} \frac{\partial^{2}}{\partial z^{2}} u_{x/z} \left(x, z, t \right) + \ell_{z;j} \ell_{z;j} \frac{\partial^{2}}{\partial z^{2}} u_{x/z} \left(x, z, t \right) + \ell_{z;j} \ell_{z;j} \frac{\partial^{2}}{\partial z^{2}} u_{x/z} \left(x, z, t \right) + \ell_{z;j} \ell_{z;j} \frac{\partial^{2}}{\partial z^{2}} u_{x/z} \left(x, z, t \right) + \ell_{z;j} \ell_{z;j} \ell_{z;j} \frac{\partial^{2}}{\partial z^{2}} u_{x/z} \left(x, z, t \right) + \ell_{z;j} \ell_{z;j} \ell_{z;j} \frac{\partial^{2}}{\partial z^{2}} u_{x/z} \left(x, z, t \right) + \ell_{z;j} \ell$$

Here, $\ell_{x;j}$ and $\ell_{z;j}$ are respectively the horizontal and vertical distance between the particle \mathbf{m},\mathbf{n} and the adjacent particle $\mathbf{m}_j,\mathbf{n}_j$, which are respectively expressed in terms of the unit interparticle distance as $\ell_{x;j} = \ell \cos \alpha_j^{\mathbf{m},\mathbf{n}}$ and $\ell_{z;j} = \ell \sin \alpha_j^{\mathbf{m},\mathbf{n}}$. Replacing the particle displacements $u_x^{\mathbf{m},\mathbf{n}}$ and $u_z^{\mathbf{m},\mathbf{n}}$ in equations (B.36) and (B.37) by $u_x(x,z,t)$ and $u_z(x,z,t)$ respectively, as well as incorporating the second order Taylor polynomial given above for adjacent particles and choosing the angles of the Kelvin-Voigt elements to be evenly divided as depicted in Figure B.2, the long-wave limit equations of motion for a particle \mathbf{m},\mathbf{n} in the interior of the hexagonal lattice become:

$$M\ddot{u}_{x}\left(x,z,t\right) - \hat{K}_{e}\ell^{2}\left(\frac{9}{8}\frac{\partial^{2}}{\partial x^{2}}u_{x}\left(x,z,t\right) + \frac{3}{8}\frac{\partial^{2}}{\partial z^{2}}u_{x}\left(x,z,t\right) + \frac{3}{4}\frac{\partial^{2}}{\partial x\partial z}u_{z}\left(x,z,t\right)\right) = 0 \tag{C.2}$$

$$M\ddot{u}_{z}\left(x,z,t\right) - \hat{K}_{e}\ell^{2}\left(\frac{3}{4}\frac{\partial^{2}}{\partial x\partial z}u_{x}\left(x,z,t\right) + \frac{3}{8}\frac{\partial^{2}}{\partial x^{2}}u_{z}\left(x,z,t\right) + \frac{9}{8}\frac{\partial^{2}}{\partial z^{2}}u_{z}\left(x,z,t\right)\right) = 0$$
 (C.3)

The motion of the two-dimensional continuum may be described by the commonly known two-dimensional elastodynamic wave equation [Achenbach, 1973] that respectively describes the horizontal and vertical equations of motion for the continuum as:

$$\rho \ddot{u}_{x}(x,z,t) - (\hat{\lambda} + 2\hat{\mu}) \frac{\partial^{2}}{\partial x^{2}} u_{x}(x,z,t) - \hat{\mu} \frac{\partial^{2}}{\partial z^{2}} u_{x}(x,z,t) - (\hat{\lambda} + \hat{\mu}) \frac{\partial^{2}}{\partial x \partial z} u_{z}(x,z,t) = 0$$
 (C.4)

$$\rho\ddot{u}_{z}(x,z,t) - (\hat{\lambda} + \hat{\mu}) \frac{\partial^{2}}{\partial x \partial z} u_{x}(x,z,t) - \hat{\mu} \frac{\partial^{2}}{\partial x^{2}} u_{z}(x,z,t) - (\hat{\lambda} + 2\hat{\mu}) \frac{\partial^{2}}{\partial z^{2}} u_{z}(x,z,t) = 0$$
 (C.5)

Comparing the long-wave limit equations of motion for a particle inside the lattice, given by equations (C.2) and (C.3), with the corresponding elastodynamic equations (C.4) and (C.5), the relations between the material parameters of the hexagonal Kelvin-Voigt lattice and the two-dimensional continuum are straightforwardly obtained. Accounting for equation (C.1) that gives the relation between the particle mass M and the mass density ρ , the relations between the Lamé operators $\hat{\lambda}$ and $\hat{\mu}$ and the operator \hat{K}_e can be derived. Noting that, as stated in Section 3.5.3, the Lamé operators describe the viscoelastic behavour of the continuum through the damping coefficient ζ_e as $\hat{\lambda} = \lambda \left(1 + \zeta_e \frac{\partial}{\partial t}\right)$ and $\hat{\mu} = \mu \left(1 + \zeta_e \frac{\partial}{\partial t}\right)$, while the operator \hat{K}_e describes the viscoelasticity of the Kelvin-Voigt elements in terms of the stiffness and damping as $\hat{K}_e = K_e + C_e \frac{\partial}{\partial t}$, the relations between the Lamé operators, the stiffness and the damping of the Kelvin-Voigt elements read:

$$\hat{\lambda} = \hat{\mu} = \frac{\sqrt{3}}{4} \frac{\hat{K}_e}{dv} \rightarrow \lambda = \mu = \frac{\sqrt{3}}{4} \frac{K_e}{dv}, \quad C_e = \zeta_e K_e$$
 (C.6)

Because the Lamé constants λ and μ describe the elastic macromaterial properties through the Young's modulus E and the Poisson's ratio ν respectively as $\lambda = \nu E/(1-2\nu)/(1+\nu)$ and $\mu = \frac{1}{2}E/(1+\nu)$, and that according to equation (C.6) the Lamé constants λ and μ must be equal, it follows that the material parameters of the hexagonal lattice only match the macromaterial properties for a Poisson's ratio $\nu = \frac{1}{4}$. For this Poisson's ratio, the Lamé constants are related to the Young's modulus as $\lambda = \mu = \frac{2}{5}E$. Substituting this relationship into equation (C.6) shows that $K_e = \frac{8}{5.5}Edy$.

Furthermore, the corresponding shear and compressional wave velocities then follow as:

$$c_{S} = \sqrt{\frac{\mu}{\rho}} = \sqrt{\frac{2}{5}} \frac{E}{\rho} = \sqrt{\frac{3}{8}} \frac{K_{e}\ell^{2}}{M}, \qquad c_{P} = \sqrt{\frac{\lambda + 2\mu}{\rho}} = \sqrt{\frac{6}{5}} \frac{E}{\rho} = \sqrt{\frac{9}{8}} \frac{K_{e}\ell^{2}}{M} = \sqrt{3}c_{S}. \tag{C.7}$$

Summarizing, the material properties of the Kelvin-Voigt lattice and the macro-material properties are related as:

$$M = \frac{\sqrt{3}}{2} \rho \ell^2 dy, \quad C_e = \frac{8}{5\sqrt{3}} \zeta_e E dy, \quad K_e = \frac{8}{5\sqrt{3}} E dy$$
 (C.8)

C.2 Lock in the one-dimensional BKV lattice by means of a rigid bar

Section 2.3.4 describes lock as the motion state of a rheological element between two adjacent particles during an inelastic collision. Particles in a lattice collide when they move closer to each other than a certain given threshold, i.e. the minimum allowed distance between two particles. Assuming a nonzero threshold, a collision in a one-dimensional lattice can only occur between particles that are adjacent. A collision between two particles $\bf n$ and $\bf n+1$ occurs when the distance $D^{\bf n,n_j}$ between these particles becomes equal to, or is inclined to become smaller than, the threshold distance $D^{\bf n,n_j}_{\rm min}$. Upon reaching this threshold, the relative motion between the two particles is impeded and they continue their motion in unison.

In this thesis, the lock-element is generally modelled by a spring with a stiffness significantly larger than the stiffness of the spring in the BKV elements, but alternatively we can also model lock by using rigid bars. Figure C.1 shows a fragment of the one-dimensional BKV lattice, where a rigid bar lock-element is located parallel to the BKV element between particles $\bf n$ and $\bf n+1$. Figure C.1a shows the situation where the BKV element is not in lock. Here, the distance $D^{{\bf n},{\bf n}+1}$ between particles $\bf n$ and $\bf n+1$ is larger than the threshold distance $D^{{\bf n},{\bf n}+1}_{\min}$ and therefore a certain distance $\Delta D^{{\bf n},{\bf n}+1} = D^{{\bf n},{\bf n}+1} - D^{{\bf n},{\bf n}+1}_{\min}$ remains before the particles $\bf n$ and $\bf n+1$ collide, i.e. $\Delta D^{{\bf n},{\bf n}+1} > 0$. While the BKV element is not in lock, there is no force in the lock element, i.e. $F^{{\bf n},{\bf n}+1}_{lock} = 0$.

The situation where the BKV element is in lock is depicted by Figure C.1b. Here, the distance $D^{\mathbf{n},\mathbf{n}+1}$ between particles \mathbf{n} and $\mathbf{n}+1$ is equal to the threshold distance $D^{\mathbf{n},\mathbf{n}+1}_{\min}$ and thus $\Delta D^{\mathbf{n},\mathbf{n}+1}=0$. The relative movement between particles \mathbf{n} and $\mathbf{n}+1$ is impeded and the lock-element is activated so that it carries an axial compressive load $F^{\mathbf{n},\mathbf{n}+1}_{lock}>0$. Thus, when an element between particles \mathbf{n} and $\mathbf{n}+1$ is in lock, the original rheological element remains intact, while parallel to the original element a lock-element is introduced that impedes the relative motion between particles \mathbf{n} and $\mathbf{n}+1$. Here, note that lock only occurs in compression and for as long as that compression remains.

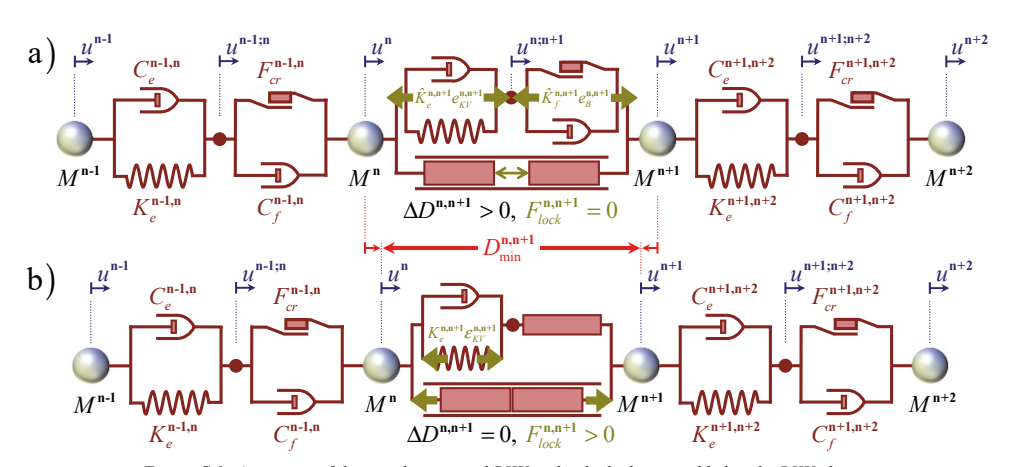


Figure C.1: A segment of the one-dimensional BKV with a lock element added to the BKV element between particles **n** and **n+1**: a) while not in lock-state; b) during lock-state.

Behaviour of the BKV element that remains parallel to the rigid bar during lock

To determine the equations of motion of a particle **n** when the element between particles **n** and **n+1** is in lock, we must first establish what happens in the BKV element that remains parallel to the lock-element. For Hooke or Kelvin-Voigt elements this is rather straightforward, as we only need to account for the force in the spring due to its constant elongation during lock. Due to the dual nature of the BKV element however, we must first determine the response of the node intermediate particles **n** and **n+1**. The response of this node depends on the motion state of the corresponding BKV element right before lock is initiated.

When lock occurs while the BKV element is in stick, the Bingham element that has been inactive during stick will remain inactive during lock. After all, due to the activation of the lock-element, the relative motion between particles **n** and **n+1** stops and, since the compressive force working on the Bingham element did not activate the dry friction element before, it will also not activate the dry friction element during lock. Thus, after a stick-to-lock transition and for the duration that the element remains in lock, the elongation of the Bingham element is constant and equal to its elongation right before the stick-to-lock transition. Consequently, during lock, the displacement of the node intermediate particles **n** and **n+1** is equal to the displacement of particle **n+1** and the BKV element behaves as a Kelvin-Voigt element.

When lock occurs while the BKV element is in slip, the behaviour of the BKV element is less evident. For the case of a slip-to-lock transition, the Bingham element is active during the onset of lock. Clearly as lock sets in, the elongation rate of the BKV element is equal to zero and the elongation of the BKV element becomes constant. If we follow the principles of the slip-to-stick transition as discussed in Section 2.3.5, the Bingham element will remain active and continue to shorten until the node intermediate particles n and n+1 is inclined to change direction. Because the relative motion between the particles n and n+1 stops completely, it follows that the corresponding Kelvin-Voigt element will relax as the Bingham element continues to become shorter. As a result, eventually the force applied by the Kelvin-Voigt element on the Bingham element will reverse and the node intermediate particles n and n+1 wants to change its direction of motion and the BKV element sticks. Now, since the intermediate node has no mass and therefore no inertia, it is quite reasonable to assume that this slip-to-stick-transition occurs quickly after the initiation of lock. Consequently, following a slip-to-lock transition, we assume that the Bingham element is inactive during lock, and therefore, as depicted in Figure C.1b, we generally assume that during lock the BKV element behaves as a Kelvin-Voigt element independent from the motion state before lock.

The position of the node intermediate particles **n** and **n+1**, and thereby the elongation of the Bingham element, at the end of a lock-state are different after a slip-to-lock transition then after a stick-to-lock transition. In this case, the elongation of the Bingham element after a slip-to-lock transition follows from the equilibrium of forces at the time the slip-to-stick transition occurs in the BKV element. For a BKV element under compression, this equilibrium reads:

$$C_e^{\mathbf{n},\mathbf{n}+1}\dot{e}_{KV}^{\mathbf{n},\mathbf{n}+1} + K_e^{\mathbf{n},\mathbf{n}+1}e_{KV}^{\mathbf{n},\mathbf{n}+1} - C_f^{\mathbf{n},\mathbf{n}+1}\dot{e}_B^{\mathbf{n},\mathbf{n}+1} + F_{cr}^{\mathbf{n},\mathbf{n}+1} = 0$$
 (C.9)

At the exact moment that the slip-to-stick transition occurs, it follows that the elongation rate of the Bingham element is equal to zero, i.e. $\dot{e}_B^{n,n+1}=0$. As this transition occurs in a BKV element that is parallel to a rigid bar, the elongation rate of the whole BKV element is equal to zero and therefore the elongation rate of the Kelvin-Voigt element is also equal to zero, i.e. $\dot{e}_{KV}^{n,n+1}=0$. Now noting that the elongation of the Kelvin-Voigt element can be expressed as $e_{KV}^{n,n+1}=e^{n,n+1}-\varepsilon_B^{n,n+1}$ and that the magnitude of the elongation of the BKV element during lock must be equal to the allowed shortening at which lock occurs, we find the elongation of the Bingham element during the lock-state that occurs after a slip-to-lock transition as:

$$K_{\varepsilon}^{\mathbf{n},\mathbf{n}+1}\left(e^{\mathbf{n},\mathbf{n}+1} - \varepsilon_{B}^{\mathbf{n},\mathbf{n}+1}\right) + F_{cr}^{\mathbf{n},\mathbf{n}+1} = 0 \rightarrow \varepsilon_{B}^{\mathbf{n},\mathbf{n}+1} = \frac{F_{cr}^{\mathbf{n},\mathbf{n}+1}}{K_{c}^{\mathbf{n},\mathbf{n}+1}} - \Delta D_{0}^{\mathbf{n},\mathbf{n}+1}$$
 (C.10)

Here, $\Delta D_0^{\mathbf{n},\mathbf{n}+1}$ is the allowed shortening at which lock occurs in the element between particles \mathbf{n} and $\mathbf{n}+1$. This allowed shortening is given by the difference between the initial length of the BKV element, or the initial distance $D_0^{\mathbf{n},\mathbf{n}+1}$ between particles \mathbf{n} and $\mathbf{n}+1$, and the tresh-hold distance $D_{\min}^{\mathbf{n},\mathbf{n}+1}$ at which lock occurs, so that $\Delta D_0^{\mathbf{n},\mathbf{n}+1} = D_0^{\mathbf{n},\mathbf{n}+1} - D_{\min}^{\mathbf{n},\mathbf{n}+1}$.

When modeling the lock-element as a rigid bar, the equations of motion for particles **n** and **n+1** with the BKV element in-between in lock, depend on the motion states of the adjacent BKV elements between respectively particles **n-1** and **n**, and particles **n+1** and **n+2**. Although the motion states of these elements can vary between stick, slip or lock, and are generally not the same, we will here derive the equations of motion for particles **n** and **n+1** with both adjacent BKV elements in either stick- or slip-state. The equations for any other configuration of motion states can be straightforwardly derived from these.

Lock represented by a rigid bar in a BKV element with its adjacent elements in stick

During lock, the distance between particles $\bf n$ and $\bf n+1$ does not change and the elongation $e^{\bf n,n+1}$ of the element in-between is constant. Assuming large elongations, so that the elongation of the element between particles $\bf n$ and $\bf n+1$ is given by equation (A.17), it follows that during lock the elongation $e^{\bf n,n+1}$ is equal to the elongation constant $\varepsilon^{\bf n,n+1}$. As explained above, the Bingham element in a locked BKV element can be considered as a rigid bar with a constant elongation $\varepsilon^{\bf n,n+1}_B$. Consequently, the Kelvin-Voigt element in the locked BKV element between particles $\bf n$ and $\bf n+1$ has a constant elongation $\varepsilon^{\bf n,n+1}_{KV}$ during lock.

When the BKV element between particles $\bf n$ and $\bf n+1$ is in lock, and the BKV element between particles $\bf n-1$ and $\bf n$ is in stick, the equation of motion for particle $\bf n$ follows from the corresponding equation of motion for a particle $\bf n$ in the one-dimensional BKV lattice with all involved BKV elements in stick, previously given in Section 2.3.2. Accounting for the constant elongation of the Kelvin-Voigt element and the non-conservative axial force $F_{lock}^{n,n+1}$ in the lock-element, we find:

$$M^{n}\ddot{u}^{n} + C_{e}^{n-1,n}\dot{e}^{n-1,n} + K_{e}^{n-1,n} \left(e^{n-1,n} - \varepsilon_{B}^{n-1,n}\right) - K_{e}^{n,n+1}\varepsilon_{KV}^{n,n+1} = -F_{lock}^{n,n+1}$$
(C.11)

The equation of motion for particle n+1 with the BKV element between particles n and n+1 in lock and the element between particles n+1 and n+2 in stick is found accordingly as:

$$M^{n+1}\ddot{u}^{n+1} + K_e^{n,n+1} \varepsilon_{KV}^{n,n+1} - C_e^{n+1,n+2} \dot{e}^{n+1,n+2} - K_e^{n+1,n+2} \left(e^{n+1,n+2} - \varepsilon_B^{n+1,n+2} \right) = + F_{lock}^{n,n+1} \quad \text{(C.12)}$$

Note here that the forces working inside the locked BKV element between particles \mathbf{n} and $\mathbf{n+1}$ are depicted in Figure C.1b.

Equations (C.11) and (C.12) may not simply be used to replace the original equations of motion in the system of equations of motion for the one-dimensional BKV lattice as we thereby introduce the unknown lock force $F_{lock}^{\mathbf{n},\mathbf{n}+1}$ into the system. Instead, we remove the unknown lock force $F_{lock}^{\mathbf{n},\mathbf{n}+1}$ from the system of equations of motion by adding equations (C.11) and (C.12), and note that the accelerations $\ddot{u}^{\mathbf{n}}$ and $\ddot{u}^{\mathbf{n}+1}$ are equal since the particles \mathbf{n} and $\mathbf{n}+1$ move together during lock. Consequently, the equation of motion for a particle \mathbf{n} with the BKV element between particles \mathbf{n} and $\mathbf{n}+1$ in lock and the BKV element between particles \mathbf{n} and \mathbf{n} in stick, is ultimately found as:

$$\left(M^{n} + M^{n+1}\right) \ddot{u}^{n} + C_{e}^{n-1,n} \dot{e}^{n-1,n} + K_{e}^{n-1,n} \left(e^{n-1,n} - \varepsilon_{B}^{n-1,n}\right) - C_{e}^{n+1,n+2} \dot{e}^{n+1,n+2} - K_{e}^{n+1,n+2} \left(e^{n+1,n+2} - \varepsilon_{B}^{n+1,n+2}\right) = 0$$
(C.13)

The equation of motion for particle n+1 with the BKV element between particles n and n+1 in lock and the element between particles n+1 and n+2 in stick follows directly from equation (C.13) by substituting $\ddot{u}^n = \ddot{u}^{n+1}$. Note here, that equation (C.13) does not contain any terms related to the forces inside the locked element between particles n and n+1. This makes sense, seeing that the relative movement between these particles is impeded.

The unknown axial force $F_{lock}^{n,n+1}$ in the lock-element is derived by subtracting equations (C.11) and (C.12) from one another instead of adding them. This yields:

$$F_{lock}^{\mathbf{n},\mathbf{n}+1} = K_e^{\mathbf{n},\mathbf{n}+1} \mathcal{E}_{KV}^{\mathbf{n},\mathbf{n}+1} - \frac{1}{2} \begin{pmatrix} \left(M^{\mathbf{n}} - M^{\mathbf{n}+1} \right) \ddot{u}^{\mathbf{n}} + C_e^{\mathbf{n}-1,\mathbf{n}} \dot{e}^{\mathbf{n}-1,\mathbf{n}} + K_e^{\mathbf{n}-1,\mathbf{n}} \left(e^{\mathbf{n}-1,\mathbf{n}} - \mathcal{E}_B^{\mathbf{n}-1,\mathbf{n}} \right) \\ + C_e^{\mathbf{n}+1,\mathbf{n}+2} \dot{e}^{\mathbf{n}+1,\mathbf{n}+2} + K_e^{\mathbf{n}+1,\mathbf{n}+2} \left(e^{\mathbf{n}+1,\mathbf{n}+2} - \mathcal{E}_B^{\mathbf{n}+1,\mathbf{n}+2} \right) \end{pmatrix}$$
(C.14)

Equation (C.14) is required to determine if or when a possible lock-to-stick transition occurs. As the lock element cannot carry tensile loads, the lock-to-stick transition occurs when the axial lock force $F_{lock}^{\mathbf{n},\mathbf{n}+1}$ becomes smaller than or equal to zero. This occurs when the internal force in the BKV element, given by the term $K_e^{\mathbf{n},\mathbf{n}+1} \mathcal{E}_{KV}^{\mathbf{n},\mathbf{n}+1}$, becomes equal to or larger than the external force working on the BKV element, which is given by the second term on the right-hand side of equation (C.14). Note furthermore that the acceleration $\ddot{u}^{\mathbf{n}}$ of particle \mathbf{n} may be freely replaced by the acceleration $\ddot{u}^{\mathbf{n}+1}$ of particle $\mathbf{n}+1$, as they are the same.

'Lock' represented by a rigid bar in a BKV element with its adjacent elements in slip The equations of motion for particles **n** and **n+1**, with the BKV element between particles **n**

and n+1 in lock and both its adjacent BKV elements in slip, are derived in accordance with the equations of motion for the situation with the adjacent BKV elements in stick discussed previously. For the situation where both the BKV elements between respectively particles n-1 and n, and particles n+1 and n+2, are in slip, while the BKV element between particles n and n+1 is in lock, the equation of motion for a particle n may be derived from the equation of motion for particle n with all involved BKV elements in slip, previously given in Section 2.3.3. Adding the non-conservative axial force in the lock-element, $F_{lock}^{n,n+1}$, as well as noting that the elongation of the Kelvin-Voigt element is a constant, yields the equation of motion for particle n as:

$$M^{n}\ddot{u}^{n} + C_{f}^{n-1,n}\dot{e}_{B}^{n-1,n} + F_{cr}^{n-1,n} \operatorname{sgn} F_{B:slip}^{n-1,n} - K_{e}^{n,n+1} \varepsilon_{KV}^{n,n+1} = -F_{lock}^{n,n+1}$$
(C.15)

Accordingly, when the BKV element between particles \mathbf{n} and $\mathbf{n+1}$ is in lock and the element between particles $\mathbf{n+1}$ and $\mathbf{n+2}$ is in slip, the equation of motion for particle $\mathbf{n+1}$ becomes:

$$M^{n+1}\ddot{u}^{n+1} + K_e^{n,n+1} \mathcal{E}_{KV}^{n,n+1} - C_e^{n+1,n+2} \dot{e}_{KV}^{n+1,n+2} - K_e^{n+1,n+2} e_{KV}^{n+1,n+2} = + F_{lock}^{n,n+1}$$
(C.16)

Adding equations (C.15) and (C.16), and taking into account that the accelerations \ddot{u}^{n} and \ddot{u}^{n+1} of particles **n** and **n+1** are the same, yields the equation of motion for a particle **n**, with the BKV element between particles **n** and **n+1** in lock and both its adjacent BKV elements in slip, as:

$$(M^{n} + M^{n+1})\ddot{u}^{n} + C_{f}^{n-1,n}\dot{e}_{B}^{n-1,n} + F_{cr}^{n-1,n} \operatorname{sgn} F_{B;slip}^{n-1,n} - C_{e}^{n+1,n+2}\dot{e}_{KV}^{n+1,n+2} - K_{e}^{n+1,n+2}e_{KV}^{n+1,n+2} = 0$$
(C.17)

The corresponding equation of motion for particle **n+1** follows from equation (C.17) by substituting $\ddot{u}^{n} = \ddot{u}^{n+1}$.

For the situation where its adjacent BKV elements are in slip, the axial lock force $F_{lock}^{\mathbf{n},\mathbf{n}+1}$ in the locked BKV element between particles \mathbf{n} and $\mathbf{n}+1$ is found by subtracting equations (C.15) and (C.16) from one another. This results in:

$$F_{lock}^{\mathbf{n},\mathbf{n}+\mathbf{1}} = K_e^{\mathbf{n},\mathbf{n}+\mathbf{1}} \mathcal{E}_{KV}^{\mathbf{n},\mathbf{n}+\mathbf{1}} - \frac{1}{2} \begin{pmatrix} \left(M^{\mathbf{n}} - M^{\mathbf{n}+\mathbf{1}} \right) \ddot{u}^{\mathbf{n}} + C_f^{\mathbf{n}-\mathbf{1},\mathbf{n}} \dot{e}_B^{\mathbf{n}-\mathbf{1},\mathbf{n}} + F_{cr}^{\mathbf{n}-\mathbf{1},\mathbf{n}} \operatorname{sgn} F_{B:slip}^{\mathbf{n}-\mathbf{1},\mathbf{n}} \\ + C_e^{\mathbf{n}+\mathbf{1},\mathbf{n}+2} \dot{e}_{KV}^{\mathbf{n}+\mathbf{1},\mathbf{n}+2} + K_e^{\mathbf{n}+\mathbf{1},\mathbf{n}+2} e_{KV}^{\mathbf{n}+\mathbf{1},\mathbf{n}+2} \end{pmatrix}$$
(C.18)

It can be seen from comparing equations (C.14) and (C.18), that the motion state of the elements adjacent to locked element only influence the forces applied externally to the locked element, as only the second term on the right-hand side of both equations is different. Evidently, the term $K_e \varepsilon_{KV}^{\mathbf{n},\mathbf{n}+1}$ describing the internal force in the locked BKV element is the same for both equations. Note furthermore that if the masses $M^{\mathbf{n}}$ and $M^{\mathbf{n}+1}$ of particles \mathbf{n} and $\mathbf{n}+1$ are the same, the acceleration terms will not appear in equations (C.14) and (C.18).

C.3 Lock in the hexagonal BKV lattice by means of a rigid bar

As explained in Sections 2.3.4, it is not very straightforward and rather laborious to obtain the equations of motion for the hexagonal BKV lattice for the case that we model the lock-state using rigid bar elements. This is especially true when multiple adjacent BKV elements are in lock. Therefore, instead of using rigid bars, in this thesis the lock-state is modelled by adding a spring with a large stiffness parallel to the BKV element. Nevertheless, to illustrate the approach of using rigid bars to model the lock-state, we here derive the corresponding equations of motion for a particle **m,n**, as well as for an adjacent particle **p,q**, where only the BKV element between particles **m,n** and **p,q** is in lock. Here, we will only consider the equations of motion for the particular case that all other elements are in stick-state. The equations of motion for the case that all adjacent elements are in slip, or for any combination of motion states, may be derived accordingly.

Figure C.2a shows the interior of the hexagonal BKV lattice, where the element between two adjacent particles **m,n** and **p,q** is in lock. Any particles adjacent to **m,n** and **p,q** are referred to by their position relative to **m,n** and **p,q**, so that, for example, the nodal coordinates **m+2,n** and **p+1,q-1** both refer to the same particle. Accordingly, the nodal coordinates **m-1,n+1** and **p-2,q** also refer to the same particle.

For the case where the BKV element between particles **m,n** and **p,q** is in lock, and all other BKV elements in the cell of particle **m,n** are in stick, the equations of motion for that particle can be derived from the corresponding equations of motion for a particle **m,n** in the hexagonal BKV lattice with all involved BKV elements in stick, previously given in Section 2.4.3.

We here have to take into account that the Kelvin-Voigt element in the locked BKV element between particles \mathbf{m} , \mathbf{n} and \mathbf{p} , \mathbf{q} has a constant elongation, i.e. $e_j^{\mathbf{m},\mathbf{n}} - \mathcal{E}_{B;j}^{\mathbf{m},\mathbf{n}} = \mathcal{E}_{KV;j}^{\mathbf{m},\mathbf{n}}$, where the elongation of the Bingham element depends on the motion state of the BKV element between particles \mathbf{m} , \mathbf{n} and \mathbf{p} , \mathbf{q} prior to lock. The elongation of the Bingham element may be determined fully in accordance with the approach for the one-dimensional system discussed in Appendix C.2. This means that after a stick-to-lock transition and for the duration that the

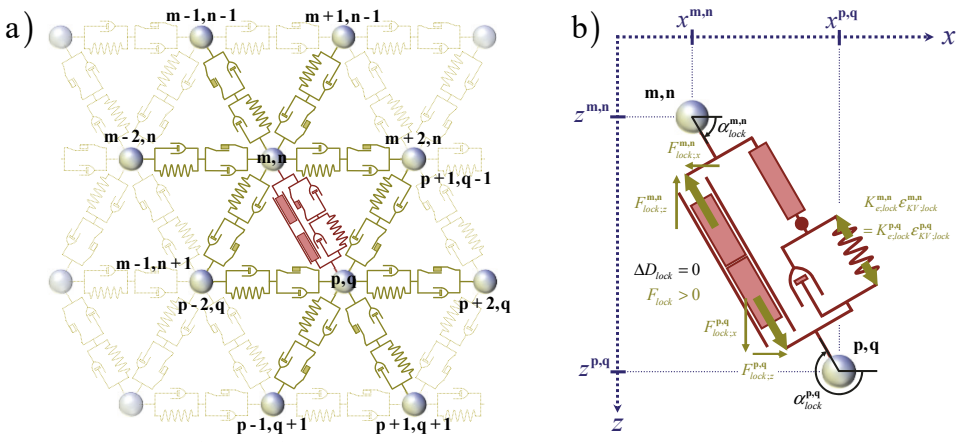


Figure C.2: a) A fragment of the hexagonal BKV lattice with a lock element parallel to the BKV element between particles m,n and p,q; b) The forces in the BKV element between particles m,n and p,q during lock.

element remains in lock, the elongation of the Bingham element is equal to its elongation during the instance of stick prior to lock. Furthermore, after a slip-to-lock transition and for the duration that the element remains in lock, the elongation of the Bingham element is found as:

$$\varepsilon_{B;j}^{\mathbf{m,n}} = \frac{F_{cr;j}^{\mathbf{m,n}}}{K_{e;j}^{\mathbf{m,n}}} - \Delta D_{0;j}^{\mathbf{m,n}} \tag{C.19}$$

Here, $\Delta D_{0;j}^{\mathbf{m},\mathbf{n}}$ is the shortening at which lock in the considered BKV element is induced. This allowed shortening is given by the difference between the initial distance $D_{0;j}^{\mathbf{m},\mathbf{n}}$ between particles \mathbf{m},\mathbf{n} and \mathbf{p},\mathbf{q} , and the treshhold distance $D_{\min,j}^{\mathbf{m},\mathbf{n}}$ at which lock occurs.

Denoting the locked BKV element between particles \mathbf{m} , \mathbf{n} and \mathbf{p} , \mathbf{q} as the element j = J and accounting for the internal forces that work in the locked BKV element between particles \mathbf{m} , \mathbf{n} or \mathbf{p} , \mathbf{q} as depicted in Figure C.2b, we find the equations of motion for the particle \mathbf{m} , \mathbf{n} with all other BKV elements in the cell of particle \mathbf{m} , \mathbf{n} in stick, as:

$$M^{\mathbf{m},\mathbf{n}} \ddot{u}_{x}^{\mathbf{m},\mathbf{n}} - \sum_{j=1}^{5} \hat{K}_{e;j}^{\mathbf{m},\mathbf{n}} \left(e_{j}^{\mathbf{m},\mathbf{n}} - \varepsilon_{B;j}^{\mathbf{m},\mathbf{n}} \right) \cos \alpha_{j}^{\mathbf{m},\mathbf{n}} - K_{e;J}^{\mathbf{m},\mathbf{n}} \varepsilon_{KV;J}^{\mathbf{m},\mathbf{n}} \cos \alpha_{J}^{\mathbf{m},\mathbf{n}} = -F_{lock;J}^{\mathbf{m},\mathbf{n}} \cos \alpha_{J}^{\mathbf{m},\mathbf{n}}$$
 (C.20)

$$M^{m,n} \ddot{u}_{z}^{m,n} - \sum_{j=1}^{5} \hat{K}_{e;j}^{m,n} \left(e_{j}^{m,n} - \varepsilon_{B;j}^{m,n} \right) \sin \alpha_{j}^{m,n} - K_{e;J}^{m,n} \varepsilon_{KV;J}^{m,n} \sin \alpha_{J}^{m,n} = -F_{lock;J}^{m,n} \sin \alpha_{J}^{m,n}$$
 (C.21)

Accordingly, the equations of motion for the particle **p,q** with the BKV element between particles **m,n** and **p,q** in lock and all other BKV elements in the cell of particle **p,q** in stick are found as:

$$M^{\mathbf{p},\mathbf{q}}\ddot{u}_{x}^{\mathbf{p},\mathbf{q}} - \sum_{j=1}^{5} \hat{K}_{e;j}^{\mathbf{p},\mathbf{q}} \left(e_{j}^{\mathbf{p},\mathbf{q}} - \varepsilon_{B;j}^{\mathbf{p},\mathbf{q}} \right) \cos \alpha_{j}^{\mathbf{p},\mathbf{q}} - K_{e;J}^{\mathbf{p},\mathbf{q}} \varepsilon_{KV;J}^{\mathbf{p},\mathbf{q}} \cos \alpha_{J}^{\mathbf{p},\mathbf{q}} = -F_{lock;J}^{\mathbf{p},\mathbf{q}} \cos \alpha_{J}^{\mathbf{p},\mathbf{q}}$$
(C.22)

$$M^{\mathbf{p},\mathbf{q}}\ddot{u}_{z}^{\mathbf{p},\mathbf{q}} - \sum_{j=1}^{5} \hat{K}_{e;j}^{\mathbf{p},\mathbf{q}} \left(e_{j}^{\mathbf{p},\mathbf{q}} - \mathcal{E}_{B;j}^{\mathbf{p},\mathbf{q}} \right) \sin \alpha_{j}^{\mathbf{p},\mathbf{q}} - K_{e;J}^{\mathbf{p},\mathbf{q}} \mathcal{E}_{KV;J}^{\mathbf{p},\mathbf{q}} \sin \alpha_{J}^{\mathbf{p},\mathbf{q}} = -F_{lock;J}^{\mathbf{p},\mathbf{q}} \sin \alpha_{J}^{\mathbf{p},\mathbf{q}}$$
(C.23)

Equations (C.20) to (C.23) may not simply be included in the system of equations of motion for the two-dimensional BKV lattice as this introduces an additional unknown lock force $F_{lock;J}^{\mathbf{m},\mathbf{n}} = F_{lock;J}^{\mathbf{p},\mathbf{q}}$ into the system and thereby requires an additional equation of motion. To keep the dimension of the system of equations of motion the same for all motion states, we combine the equations above to remove the unknown lock force from the system, and subsequently introduce two new equations that follow from the locked element between particles \mathbf{m},\mathbf{n} and \mathbf{p},\mathbf{q} .

Here, the angles $\alpha_J^{\mathbf{m},\mathbf{n}}$ and $\alpha_J^{\mathbf{p},\mathbf{q}}$ of the locked element are related as $\alpha_J^{\mathbf{p},\mathbf{q}} = \alpha_J^{\mathbf{m},\mathbf{n}} \pm \pi$, so that $\cos \alpha_J^{\mathbf{p},\mathbf{q}} = -\cos \alpha_J^{\mathbf{m},\mathbf{n}}$ and $\sin \alpha_J^{\mathbf{p},\mathbf{q}} = -\sin \alpha_J^{\mathbf{m},\mathbf{n}}$. Substituting these relations into respectively equations (C.22) and (C.23), and subsequently adding equations (C.22) and (C.20), as

well as adding equations (C.23) and (C.21), yields the following:

$$M^{\mathbf{m,n}} \ddot{u}_{x}^{\mathbf{m,n}} + M^{\mathbf{p,q}} \ddot{u}_{x}^{\mathbf{p,q}} - \sum_{j=1}^{5} \hat{K}_{e;j}^{\mathbf{m,n}} \left(e_{j}^{\mathbf{m,n}} - \mathcal{E}_{B;j}^{\mathbf{m,n}} \right) \cos \alpha_{j}^{\mathbf{m,n}} - \sum_{j=1}^{5} \hat{K}_{e;j}^{\mathbf{p,q}} \left(e_{j}^{\mathbf{p,q}} - \mathcal{E}_{B;j}^{\mathbf{p,q}} \right) \cos \alpha_{j}^{\mathbf{p,q}} = 0 \quad (C.24)$$

$$M^{\mathbf{m},\mathbf{n}}\ddot{u}_{z}^{\mathbf{m},\mathbf{n}} + M^{\mathbf{p},\mathbf{q}}\ddot{u}_{z}^{\mathbf{p},\mathbf{q}} - \sum_{j=1}^{5} \hat{K}_{e;j}^{\mathbf{m},\mathbf{n}} \left(e_{j}^{\mathbf{m},\mathbf{n}} - \varepsilon_{B;j}^{\mathbf{m},\mathbf{n}} \right) \sin \alpha_{j}^{\mathbf{m},\mathbf{n}} - \sum_{j=1}^{5} \hat{K}_{e;j}^{\mathbf{p},\mathbf{q}} \left(e_{j}^{\mathbf{p},\mathbf{q}} - \varepsilon_{B;j}^{\mathbf{p},\mathbf{q}} \right) \sin \alpha_{j}^{\mathbf{p},\mathbf{q}} = 0 \quad (C.25)$$

Thus, equations (C.24) and (C.25) no longer contain any terms related to the forces inside the locked BKV element between particles **m**,**n** and **p**,**q**.

For the one-dimensional BKV lattice, with a locked BKV element between particles **n** and **n+1**, adding the equations of motion for particles **n** and **n+1** yields one independent equation of motion, while the second required independent equation follows from the identical motion of these particles. In the hexagonal BKV lattice, respectively adding the equations for the horizontal and vertical motion of particles **m,n** and **p,q** yields two independent equations, given by equations (C.24) and (C.25). As each particle in the hexagonal lattice has two degrees of freedom, we require two more equations to properly describe the motion of particles **m,n** and **p,q**. The other two independent equations follow from the relations that must exist between the motions of particles **m,n** and **p,q**. The approach however is not as straightforward as for the corresponding one-dimensional system, because the BKV element between particles **m,n** and **p,q** can still rotate during lock..

The first additional equation follows from the relation between the horizontal and vertical lock forces working on either particle **m,n** or **p,q**. The horizontal and vertical lock forces on particle **m,n** are related by the corresponding angle of the element as:

$$\tan \alpha_J^{\mathbf{m},\mathbf{n}} = \frac{F_{lock;z}^{\mathbf{m},\mathbf{n}}}{F_{lock;x}^{\mathbf{m},\mathbf{n}}} = \frac{F_{lock}^{\mathbf{m},\mathbf{n}} \sin \alpha_J^{\mathbf{m},\mathbf{n}}}{F_{lock}^{\mathbf{m},\mathbf{n}} \cos \alpha_J^{\mathbf{m},\mathbf{n}}}$$

The horizontal and vertical lock forces previously appeared in the right-hand side of equations (C.20) and (C.21), thus combining these equations using the above relation yields the third equation of motion for the particles **m,n** and **p,q** as:

$$\left(M^{\mathbf{m},\mathbf{n}}\ddot{u}_{x}^{\mathbf{m},\mathbf{n}} - \sum_{j=1}^{5} \hat{K}_{e;j}^{\mathbf{m},\mathbf{n}} \left(e_{j}^{\mathbf{m},\mathbf{n}} - \varepsilon_{B;j}^{\mathbf{m},\mathbf{n}}\right) \cos \alpha_{j}^{\mathbf{m},\mathbf{n}}\right) \tan \alpha_{J}^{\mathbf{m},\mathbf{n}}
- M^{\mathbf{m},\mathbf{n}}\ddot{u}_{z}^{\mathbf{m},\mathbf{n}} + \sum_{j=1}^{5} \hat{K}_{e;j}^{\mathbf{m},\mathbf{n}} \left(e_{j}^{\mathbf{m},\mathbf{n}} - \varepsilon_{B;j}^{\mathbf{m},\mathbf{n}}\right) \sin \alpha_{j}^{\mathbf{m},\mathbf{n}} = 0$$
(C.26)

By considering the horizontal and vertical lock forces working on particle **p,q**, we would be able to obtain another equation of motion. The resulting equation however is not independent and may also be found by combining equations (C.24), (C.25) and (C.26).

The second additional equation follows from the distance between particles m,n and p,q

that remains constant during lock. Along the locked BKV element, the relative displacements, velocities and accelerations of particles \mathbf{m} , \mathbf{n} and \mathbf{p} , \mathbf{q} should thus be the same. Accounting for the known relation between the angles $\alpha_J^{\mathbf{p},\mathbf{q}}$ and $\alpha_J^{\mathbf{m},\mathbf{n}}$ yields the last equation of motion from the relation between the displacements of the particles \mathbf{m} , \mathbf{n} and \mathbf{p} , \mathbf{q} as:

$$\left(\ddot{u}_{x}^{m,n} - \ddot{u}_{x}^{p,q}\right)\cos\alpha_{J}^{m,n} + \left(\ddot{u}_{z}^{m,n} - \ddot{u}_{z}^{p,q}\right)\sin\alpha_{J}^{m,n} = 0 \tag{C.27}$$

Here, note that equation (C.27) may also be described in terms of velocity or displacement, but is deliberately described in terms of the acceleration as this is the highest time derivative for which the system of ordinary differential equations is evaluated numerically.

When the BKV element between particles **m,n** and **p,q** is in lock and all other BKV elements in the cells of particles **m,n** and **p,q** are in stick, the motion of the particles **m,n** and **p,q** is described by equations (C.24) to (C.27). None of these equations contain any additional unknowns and they may therefore replace the equations of motion (C.20) to (C.23) in the system of equations of motion for the hexagonal BKV lattice.

To determine when the locked BKV element between particles \mathbf{m} , \mathbf{n} and \mathbf{p} , \mathbf{q} transits from lock to stick, we need to determine the axial lock force $F_{lock}^{\mathbf{m},\mathbf{n}}$. The lock force $F_{lock}^{\mathbf{m},\mathbf{n}}$ can be derived by subtracting equations (C.20) and (C.22) from one another and taking the relation between the angles $\alpha_J^{\mathbf{p},\mathbf{q}}$ and $\alpha_J^{\mathbf{m},\mathbf{n}}$ into account. We thus find the axial lock force $F_{lock}^{\mathbf{m},\mathbf{n}}$ as:

$$F_{lock}^{\mathbf{m,n}} = K_{e;J}^{\mathbf{m,n}} \varepsilon_{KV;J}^{\mathbf{m,n}} - \frac{1}{2\cos\alpha_J^{\mathbf{m,n}}} \begin{pmatrix} M^{\mathbf{m,n}} \ddot{u}_x^{\mathbf{m,n}} - \sum_{j=1}^5 \hat{K}_{e;j}^{\mathbf{m,n}} \left(e_j^{\mathbf{m,n}} - \varepsilon_{B;j}^{\mathbf{m,n}} \right) \cos\alpha_j^{\mathbf{m,n}} \\ -M^{\mathbf{p,q}} \ddot{u}_x^{\mathbf{p,q}} + \sum_{j=1}^5 \hat{K}_{e;j}^{\mathbf{p,q}} \left(e_j^{\mathbf{p,q}} - \varepsilon_{B;j}^{\mathbf{p,q}} \right) \cos\alpha_j^{\mathbf{p,q}} \end{pmatrix}$$
(C.28)

Alternatively, we may also find the lock force $F_{lock}^{m,n}$ by subtracting equations (C.21) and (C.23) from one another. This yields.

$$F_{lock}^{\mathbf{m,n}} = K_{e;J}^{\mathbf{m,n}} \, \varepsilon_{KV;J}^{\mathbf{m,n}} - \frac{1}{2 \sin \alpha_J^{\mathbf{m,n}}} \begin{pmatrix} M^{\mathbf{m,n}} \ddot{u}_z^{\mathbf{m,n}} - \sum_{j=1}^5 \hat{K}_{e;j}^{\mathbf{m,n}} \left(e_j^{\mathbf{m,n}} - \varepsilon_{B;j}^{\mathbf{m,n}} \right) \sin \alpha_j^{\mathbf{m,n}} \\ -M^{\mathbf{p,q}} \ddot{u}_z^{\mathbf{p,q}} + \sum_{j=1}^5 \hat{K}_{e;j}^{\mathbf{p,q}} \left(e_j^{\mathbf{p,q}} - \varepsilon_{B;j}^{\mathbf{p,q}} \right) \sin \alpha_j^{\mathbf{p,q}} \end{pmatrix}$$
(C.29)

In both equations (C.28) and (C.29), the term $K_{e;J}^{\mathbf{m},\mathbf{n}} \varepsilon_{KV;J}^{\mathbf{m},\mathbf{n}}$ gives the internal force in the locked BKV element between particles \mathbf{m},\mathbf{n} and \mathbf{p},\mathbf{q} . The second term on the right-hand side of both equations (C.28) and (C.29) gives the force that is applied to the locked BKV element externally. Although the expressions for these equations are different they must both result in the same axial lock force; whereas equation (C.28) follows from the horizontal components of the externally applied loads working on the locked BKV element, equation (C.29) follows from the corresponding vertical components.

D One-dimensional systems in the time domain

D.1 The one-dimensional discrete-continuous Hooke system

The one-dimensional semi-infinite Hooke system, depicted in Figure D.1, is comprised of a one-dimensional Hooke lattice and a semi-infinite linear-elastic rod. The Hooke lattice consists of **N** particles and features **N-1** Hooke elements, where each particle **n** has a mass M^n , the distance between the particles is ℓ , and the Hooke elements between adjacent particles **n** and **n+1** have a stiffness $K_e^{\mathbf{n},\mathbf{n}+1}$. The one-dimensional Hooke lattice and the semi-infinite linear-elastic rod are connected at the boundary particle **N**, which is fixed to the viscoelastic rod at coordinate $x = x_{lnt}$. The semi-infinite linear-elastic rod has a density ρ , a cross-section area A and a Young's modulus E.

To determine a boundary equation at particle **N** that accounts for the behaviour of the semi-infinite linear-elastic rod, we consider the one-dimensional wave equation of the linear-elastic rod, as well as the balance of forces and the displacement continuity at the lattice-rod interface. In the time domain, these equations read:

$$\rho A\ddot{u}(x,t) - EAu''(x,t) = 0 \tag{D.1}$$

$$M^{N}\ddot{u}^{N} + K_{e}^{N-1,N} e^{N-1,N} = EAu'(x_{lnt},t)$$
(D.2)

$$u^{N} = u\left(x_{Int}, t\right) \tag{D.3}$$

Here, u(x,t) is the displacement in the semi-infinite linear-elastic rod valid for $x > x_{lnt}$.

To correctly describe the one-dimensional semi-infinite Hooke system as a linear-elastic homogeneous medium that is partly modelled by a lattice and partly by a continuum, we match the material parameters of the Hooke lattice with the material properties of the rod by matching the equation of motion for the particles inside the Hooke lattice in the long-wave limit, with the equation of motion for the linear-elastic rod, given by equation (D.1). Here, the mass of the particles and the stiffness of the Hooke elements in the lattice are constant and respectively denoted as M and K_e . Defining the particle displacement u^n as the distance between its current and its initial position, the equation of motion for a particle \mathbf{n} in the interior of the one-dimensional Hooke lattice reads:

$$M\ddot{u}^{n} + K_{e} \left(2u^{n} - u^{n-1} - u^{n+1} \right) = 0 \tag{D.4}$$

To obtain the continualized equation of motion of the lattice in the long-wave limit, we

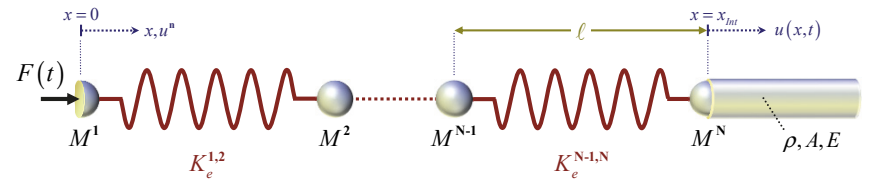


Figure D.1: The one-dimensional semi-infinite discrete-continuous Hooke system.

replace the particle displacement u^n by the continuous displacement u(x,t) and subsequently apply a Taylor series expansion with respect to this displacement. The displacements u^{n-1} and u^{n+1} of adjacent particles n-1 and n+1 are then replaced by the second order Taylor polynomials $u(x \pm \ell, t)$ [Maradudin et al., 1963; Suiker et al., 2001]. Comparing the resulting expression to equation (D.1), and noting that the mass per unit length of both models must match, we find the following relations:

$$M = \rho A \ell, \qquad K_e = \frac{EA}{\ell}.$$

Choosing the interface between the lattice and the continuum according to Figure D.1, the correct distribution of mass over the length of the one-dimensional Hooke system yields the mass of the boundary particle \mathbf{N} as $M^{N} = \frac{1}{2}M$.

Dimensionless boundary equations in the Laplace and in the time domain

To consider the fundamental properties of the Hooke system, we normalize it by introducing the following dimensionless parameters in accordance with Appendix B.1:

$$t = t_{\text{dim}}\omega_0$$
, $u^n = \frac{u_{\text{dim}}^n}{\ell}$, $M^n = \frac{M_{\text{dim}}^n}{\rho A \ell}$, $K_e^{n,n+1} = \frac{K_{e;\text{dim}}^{n,n+1} \ell}{2EA}$.

Here, the particle frequency ω_0 of the homogeneous Hooke lattice reads $\omega_0 = \sqrt{2K_e/M}$.

Application of these dimensionless variables and subsequently applying the Laplace integral transform with respect to time yields the dimensionless wave equation for the linear elastic rod and the two dimensionless interface conditions in the Laplace domain as:

$$s^{2}\tilde{u}(x,s) - \frac{1}{2}\tilde{u}''(x,s) = 0 \tag{D.5}$$

$$M^{\mathsf{N}} s^2 \tilde{u}^{\mathsf{N}} + K_e^{\mathsf{N-1},\mathsf{N}} \tilde{e}^{\mathsf{N-1},\mathsf{N}} = \frac{1}{2} \tilde{u}'(x_{lnt},s)$$
 (D.6)

$$\tilde{u}^{N} = \tilde{u}(x_{lnt}, s) \tag{D.7}$$

Here, s is the complex-valued Laplace parameter and a tilde over a variable denotes that variable in the Laplace domain. Noting that Re(s) > 0, the general solution to equation (D.5) that satisfies the infinity condition, and thus accounts for the proper behaviour of the linear-elastic rod for $x \to \infty$, reads $\tilde{u}(x,s) = Ae^{-s\sqrt{2}x}$, where A is the wave amplitude. Taking its spatial derivative and substituting equation (D.7) then yields $\tilde{u}'(x_{lnt},s) = -s\sqrt{2}\tilde{u}^N$. Consequently, the Laplace domain equation of motion of the boundary particle N reads:

$$M^{\mathsf{N}} s^2 \tilde{u}^{\mathsf{N}} + K_e^{\mathsf{N}-\mathsf{1},\mathsf{N}} \tilde{e}^{\mathsf{N}-\mathsf{1},\mathsf{N}} + \tilde{\chi}(s) \tilde{u}^{\mathsf{N}} = 0$$
 (D.8)

Here, the dynamic stiffness for the linear-elastic rod is found as $\tilde{\chi}(s) = \frac{1}{2}s\sqrt{2}$. Applying the inverse Laplace integral transform to equation (D.8) then yields the equation of motion of the

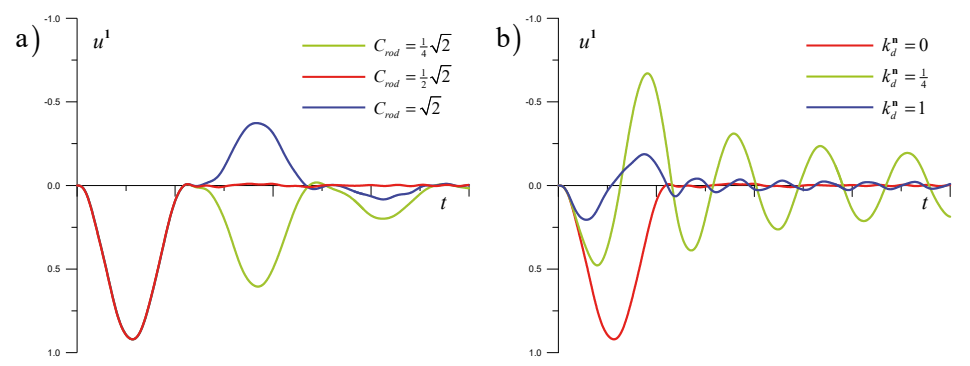


Figure D.2: The influence of: a) the magnitude of the damping C_{rod} ; b) the foundation stiffness k_d ; on the response of the one-dimensional discrete-continuous Hooke system.

boundary particle N in the time domain as:

$$M^{N}\ddot{u}^{N} + K_{e}^{N-1,N} e^{N-1,N} + \frac{1}{2} \sqrt{2} \dot{u}^{N} = 0$$
 (D.9)

Thus, when we model the far-field domain as a semi-infinite linear-elastic rod, the boundary equation is an ordinary differential equation. For systems that include damping or dispersion, this relation is obtained as a boundary integral equation.

Furthermore note that equation (D.9) can alternatively be obtained from equations (D.1) to (D.3) using d'Alembert's solution [D'Alembert, 1747]. However, as soon as damping is included, d'Alembert's solution can no longer be used.

Sensitivity of the dynamic stiffness in the time domain

To review the influence of the dynamic stiffness on the response of discrete-continuous Hooke system, we here derive its complete system of equations of motion. Noting that the load F(t) is applied at the leftmost particle in Figure D.1 and introducing dimensionless parameters, the equations of motion for particles $\mathbf{n} = 1 \dots \mathbf{N} - 1$ read:

$$M^{1}\ddot{u}^{1} - K_{e}^{1,2}e^{1,2} = F(t)$$
(D.10)

$$M^{n}\ddot{u}^{n} + K_{e}^{n-1,n}e^{n-1,n} - K_{e}^{n,n+1}e^{n,n+1} = 0$$
(D.11)

Rewriting the equation of motion for the boundary particle N, given by equation: (D.9), as:

$$M^{N}\ddot{u}^{N} + K_{e}^{N-1,N} e^{N-1,N} + C_{rod}\dot{u}^{N} = 0$$
 (D.12)

Figure D.2a shows how the magnitude of the damping C_{rod} influences the displacement response of particle 1, i.e. the particle at the tip of the Hooke lattice, to a sinusoidal pulse load. Here, the one-dimensional Hooke lattice consists of ten particles and the sinusoidal pulse load at particle 1 is described as $F(t) = \overline{F} \sin(\Omega t) H(T_F - t) H(t)$. Here, \overline{F} , Ω and T_F are respectively the amplitude, the frequency and the period of the sinusoidal pulse.

The red line in Figure D.2a gives the response for the discrete-continuous Hooke system that represents a homogeneous linear-elastic medium and for which the boundary equation is given by equation (D.9), i.e. $C_{rod} = \frac{1}{2}\sqrt{2}$. For this situation, the displacement response almost fully coincides with the applied sinusoidal pulse load. However, after the pulse load a small vibration remains in the displacement response of particle 1. This shows that there is a difference in the dispersive properties of the lattice and the rod, and that the wavelength of the sinusoidal pulse is not very close to the long-wave limit. Compared to the other responses however, the boundary equation (D.9) yields a small reflection from the linear-elastic rod. Changing the value of the damping C_{rod} in equation (D.12) yields a discrete-continuous system that no longer represents a homogeneous medium and therefore yields much larger reflections. Here, note that an infinitely large value for C_{rod} corresponds to a particle N that is fixed, while choosing C_{rod} equal to zero yields the boundary particle N to be unconstrained. In both cases, the pulse will endlessly reflect between particles 1 and N.

Dimensionless boundary equations in terms of the dynamic compliance

For the one-dimensional discrete-continuous Hooke system, the boundary equation may be obtained in the time domain by applying the inverse Laplace transform analytically. For most other media however, the boundary equation can only be obtained in the time domain by numerically evaluating the inverse Laplace transform, which requires the corresponding boundary equation to be expressed in terms of the dynamic compliance.

The Laplace domain boundary equation for the Hooke system in terms of the dynamic compliance may straightforwardly be obtained by multiplying boundary equation (D.8) by the dynamic compliance $\tilde{\beta}(s)$. This yields:

$$\tilde{u}^{N} + \tilde{\beta}(s) \{ M^{N} s^{2} \tilde{u}^{N} + K_{e}^{N-1,N} \tilde{e}^{N-1,N} \} = 0$$
(D.13)

Here, the dynamic compliance follows from the dynamic stiffness as $\tilde{\beta}(s) = s^{-1}\sqrt{2}$. Applying the inverse Laplace transform to equation (D.13) then yields:

$$u^{N} + \int_{0}^{\tau} \beta(t - \tau) \{ M^{N} \ddot{u}^{N} + K_{e}^{N-1,N} e^{N-1,N} \} (\tau) d\tau = 0$$
 (D.14)

Applying differentiation to time to equation (D.14) by using Leibniz' rule for differentiation of integrals [Abramowitz and Stegun, 1972; Woods, 1926], we find:

$$\dot{u}^{N} + \beta(0) \left\{ M^{N} \ddot{u}^{N} + K_{e}^{N-1,N} e^{N-1,N} \right\} + \int_{0}^{t} \dot{\beta}(t-\tau) \left\{ M^{N} \ddot{u}^{N} + K_{e}^{N-1,N} e^{N-1,N} \right\} (\tau) d\tau = 0$$
 (D.15)

Within the domain of the integral in equation (D.14), the inverse Laplace transform of the dynamic compliance is found as $\beta(t) = \sqrt{2}$ and is thus constant, so that its time derivative is equal to zero, i.e. $\dot{\beta}(t) = 0$. Consequently, the integral in the boundary integral equation

(D.15) is zero, yielding the boundary equation for the discrete-continuous Hooke system as:

$$\dot{u}^{N} + \sqrt{2} \left\{ M^{N} \ddot{u}^{N} + K_{e}^{N-1,N} e^{N-1,N} \right\} = 0$$
 (D.16)

Equation (D.16) exactly equals equation (D.9), showing that the use of either the dynamic stiffness or the dynamic compliance leads to the same boundary equation in the time domain.

D.2 The elastically supported 1D discrete-continuous Hooke system

The elastically supported one-dimensional discrete-continuous Hooke system is depicted in Figure D.3. In the lattice, the elastic foundation is incorporated as a founded spring with stiffness $k_d^{\mathbf{n}}$ at each particle \mathbf{n} , while for the rod, the elastic foundation is incorporated as a distributed spring with stiffness k_{rod} . The elastically supported linear-elastic rod is henceforth referred to as the linear-elastic dispersive rod, because the distributed spring causes the wave propagation in the rod to be dispersive.

The other material parameters of the elastically supported Hooke system coincide with the discrete-continuous Hooke system discussed in Appendix D.1. In the time domain, the corresponding wave equation of the dispersive rod and the two interface conditions at the lattice-rod interface read:

$$\rho A \ddot{u}(x,t) - E A u''(x,t) + k_{rod} u(x,t) = 0$$
(D.17)

$$M^{N}\ddot{u}^{N} + K_{e}^{N-1,N} e^{N-1,N} + k_{d}^{N} u^{N} = EAu'(x_{lnt},t)$$
(D.18)

$$u^{N} = u\left(x_{lnt}, t\right) \tag{D.19}$$

Here, u(x,t) is the displacement in the semi-infinite dispersive rod valid for $x > x_{lnt}$.

The material parameters of the elastically supported one-dimensional Hooke lattice match the material properties of the dispersive rod if the following relations are satisfied:

$$M = \rho A \ell, \quad K_e = \frac{EA}{\ell}, \quad k_d = k_{rod} \ell.$$

For an even distribution of the mass and the elastic foundation near the interface, the mass of the boundary particle and the corresponding foundation stiffness are respectively obtained as

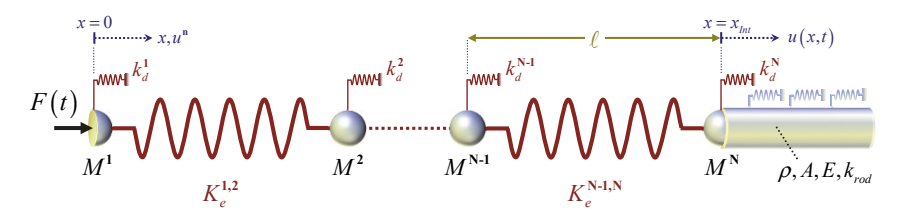


Figure D.3: The elastically supported one-dimensional semi-infinite discrete-continuous Hooke system.

$$M^{N} = \frac{1}{2}M$$
 and $k_d^{N} = \frac{1}{2}k_d$.

Furthermore, we introduce the following set of dimensionless parameters:

$$t = t_{\text{dim}}\omega_0, \quad u^{\mathbf{n}} = \frac{u_{\text{dim}}^{\mathbf{n}}}{\ell}, \quad M^{\mathbf{n}} = \frac{M_{\text{dim}}^{\mathbf{n}}}{\rho A \ell}, \quad K_e^{\mathbf{n},\mathbf{n}+1} = \frac{K_{e;\text{dim}}^{\mathbf{n},\mathbf{n}+1}\ell}{2EA}, \quad k_d^{\mathbf{n}} = \frac{k_{d;\text{dim}}^{\mathbf{n}}\ell}{2EA}, \quad \Omega_d = \frac{\omega_d}{\omega_0}.$$

Here, ω_0 is the particle frequency of the lattice, found as $\omega_0 = \sqrt{2K_e/M}$, and ω_d is the natural frequency of the elastic foundation, found as $\omega_d = \sqrt{k_d/M}$.

Inserting the dimensionless parameters and applying the Laplace integral transform yields the dimensionless wave equation and interface conditions at the lattice-rod interface as:

$$\left(s^{2} + \Omega_{d}^{2}\right)\tilde{u}(x,s) - \frac{1}{2}\tilde{u}''(x,s) = 0 \tag{D.20}$$

$$M^{N}s^{2}\tilde{u}^{N} + K_{e}^{N-1,N}\tilde{e}^{N-1,N} + k_{d}^{N}\tilde{u}^{N} = \frac{1}{2}\tilde{u}'(x_{Int},s)$$
 (D.21)

$$\tilde{u}^N = \tilde{u}(x_{lnt}, s) \tag{D.22}$$

Accounting for the proper behaviour of the rod for $x \to \infty$, the general solution to the wave equation for the dispersive rod reads $\tilde{u}(x,s) = A_1 e^{-\alpha x}$, where $\alpha = \sqrt{2}\sqrt{s^2 + \Omega_d^2}$. Substituting the general solution as well as equation (D.22) into equation (D.21), then yields the boundary equation, i.e. the equation of motion of the boundary particle **N**, in the Laplace domain as:

$$M^{N} s^{2} \tilde{u}^{N} + K_{e}^{N-1,N} \tilde{e}^{N-1,N} + k_{d}^{N} \tilde{u}^{N} + \tilde{\chi}(s) \tilde{u}^{N} = 0$$
(D.23)

Here, the dynamic stiffness of the semi-infinite linear-elastic dispersive rod is found as:

$$\tilde{\chi}(s) = \frac{1}{2}\sqrt{2(s^2 + \Omega_d^2)} \tag{D.24}$$

The inverse Laplace transform of equation (D.24) is known analytically and yields the boundary equation in the time domain as:

$$M^{N}\ddot{u}^{N} + K_{e}^{N-1,N} e^{N-1,N} + k_{d}^{N} u^{N} + \frac{1}{2} \sqrt{2} \left(\dot{u}^{N} + \Omega_{d} \int_{0}^{t} \frac{J_{1} \left(\Omega_{d} \left(t - \tau \right) \right)}{t - \tau} u^{N} \left(\tau \right) d\tau \right) = 0$$
 (D.25)

Here, $J_1(...)$ denotes the first-order Bessel function of the first kind.

The integrand of the convolution integral in equation (D.25) is singular for $\tau = t$. In accordance with the approach applied for the one-dimensional discrete-continuous Kelvin-Voigt system in Section 3.2.3, an approximate solution to the integral in equation (D.25) may be obtained by evaluating the integral numerically for the domain $\tau = 0...t - \Delta t$ and solving the integral analytically on the domain $\tau = t - \Delta t...t$ by assuming that in this domain the displacement $u^{N}(\tau)$ is linear.

Boundary integral equation in terms of the dynamic compliance

Although the boundary integral equation for the elastically supported one-dimensional discrete-continuous Hooke system can be obtained analytically using the dynamic stiffness, an alternative boundary integral equation can be obtained using the dynamic compliance.

For the linear-elastic dispersive rod, the dynamic compliance $\tilde{\beta}(s)$ may straightforwardly be obtained as the inverse of the dynamic stiffness given by equation (D.24):

$$\tilde{\beta}(s) = \frac{2}{\sqrt{2(s^2 + \Omega_d^2)}} \tag{D.26}$$

The boundary integral equation for the elastically supported discrete-continuous Hooke system is found in accordance with the approach for the regular discrete-continuous Hooke system, discussed in Appendix D.1, and given by equation (D.15). Within the domain of the boundary integral equation, i.e. for $t \ge 0$, the inverse Laplace transform of the dynamic compliance given by equation (D.26) and its time derivative are respectively found as:

$$\beta(t) = \sqrt{2}J_0(\Omega_d t), \qquad \dot{\beta}(t) = -\sqrt{2}\Omega_d J_1(\Omega_d t). \tag{D.27}$$

Substituting the above expressions into equation (D.15) then yields:

$$M^{N} \ddot{u}^{N} + K_{e}^{N-1,N} e^{N-1,N} + k_{d}^{N} u^{N} + \frac{1}{2} \sqrt{2} \dot{u}^{N} - \Omega_{d} \int_{0}^{t} J_{1} \left(\Omega_{d} \left(t - \tau\right)\right) F^{N} \left(\tau\right) d\tau = 0$$
 (D.28)

Here, $F^{N}(t)$ is the force that the boundary particle N in the Hooke lattice applies to the linear-elastic dispersive rod at the lattice-rod interface.

Figure D.2b shows how the magnitude of the foundation stiffness k_d influences the displacement response of particle 1, located at the tip of the lattice, to a single-sinus pulse load an amplitude \overline{F} , a frequency Ω and a period T_F . Here, the red line shows the response in the non-dispersive case, i.e. $k_d=0$, that coincides with the red line for $C_{rod}=\frac{1}{2}\sqrt{2}$ in Figure D.2a. The green and blue lines in Figure D.2b respectively show the displacement response for $k_d=\frac{1}{4}$ and $k_d=1$. Note here that by increasing the foundation stiffness, the particle motion is reduced and that in the limit of the foundation stiffness going to infinity, the motion of all particles in the system is impeded.

D.3 The one-dimensional fully discrete Hooke system

Figure D.4 depicts the one-dimensional fully discrete Hooke system that is comprised of a one-dimensional Hooke lattice and a one-dimensional semi-infinite linear-elastic discrete particle system, henceforth referred to as the semi-infinite linear-elastic cascade [Dieterman and Metrikine, 1997]. The one-dimensional lattice consists of N particles, where each particle n has a mass M^n and the distance between any two adjacent particles is denoted as ℓ . Furthermore, the one-dimensional Hooke lattice consists of N-1 Hooke elements in series, where

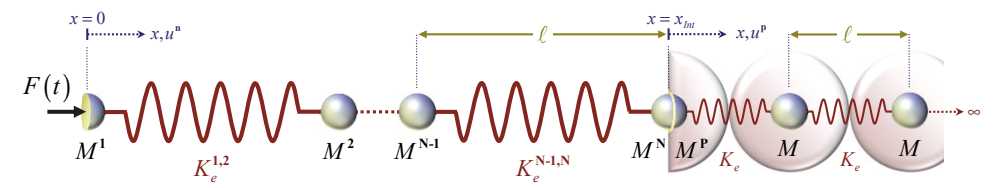


Figure D.4: The one-dimensional fully discrete Hooke system.

any Hooke element between adjacent particles \mathbf{n} and $\mathbf{n+1}$ has a stiffness $K_e^{\mathbf{n},\mathbf{n+1}}$. The parameters of the semi-infinite linear-elastic cascade match those of the lattice, such that the distance is again equal to ℓ , the mass of all particles inside the cascade is equal to M and the interaction between adjacent particles is modelled by springs with a stiffness K_e .

The governing equation of motion for a particle **p** in the semi-infinite linear-elastic cascade and the two interface conditions, respectively describing the balance of forces and the displacement continuity at the lattice-cascade interface, respectively read in the time domain:

$$M\ddot{u}^{p} + K_{e} \left(2u^{p} - u^{p-1} - u^{p+1} \right) = 0$$
 (D.29)

$$M^{N}\ddot{u}^{N} + K_{e}^{N-1,N}e^{N-1,N} = -M^{P}\ddot{u}^{P} - K_{e}\left(u^{P} - u^{P+1}\right)$$
(D.30)

$$u^{N} = u^{P} \tag{D.31}$$

Here, $u^{\mathbf{p}}$ is the axial displacement of a particle \mathbf{p} in the interior of the semi-infinite linear-elastic cascade, where $\mathbf{p} \ge \mathbf{P}$.

By choosing the location of the interface between the near-field and far-field systems at a particle, the masses of the subparticles **N** and **P** must together equal the mass M. Additionally assuming an even distribution of mass over the length of the fully discrete Hooke system, the masses of the subparticles must be equal and are found as $M^{\rm N} = M^{\rm P} = \frac{1}{2}M$.

Dimensionless boundary equations in the Laplace and in the time domain

To consider the fully discrete system in its dimensionless form, we introduce the following dimensionless parameters for time, space, mass and stiffness:

$$t = t_{\text{dim}} \omega_0, \quad u^{n} = \frac{u_{\text{dim}}^{n}}{\ell}, \quad M^{n} = \frac{M_{\text{dim}}^{n}}{M}, \quad K_e^{n,n+1} = \frac{K_{e;\text{dim}}^{n,n+1}}{2K_e}.$$

Here, the particle frequency of the homogeneous Hooke lattice is found as $\omega_0 = \sqrt{2K_e/M}$. Incorporating the dimensionless parameters and applying the Laplace transform with respect to time yields the dimensionless wave equation and interface conditions as:

$$s^{2}\tilde{u}^{p} + \frac{1}{2} \left(2\tilde{u}^{p} - \tilde{u}^{p-1} - \tilde{u}^{p+1} \right) = 0$$
 (D.32)

$$M^{N} s^{2} \tilde{u}^{N} + K_{e}^{N-1,N} \tilde{e}^{N-1,N} = -M^{P} s^{2} \tilde{u}^{P} - \frac{1}{2} (\tilde{u}^{P} - \tilde{u}^{P+1})$$
(D.33)

$$\tilde{u}^{N} = \tilde{u}^{P} \tag{D.34}$$

As before, *s* is the complex-valued Laplace parameter and a tilde denotes that variable in the Laplace domain.

Describing the general solution to the dimensionless wave equation for the linear-elastic cascade in the form of harmonic waves, accounting for the proper behaviour of the linear-elastic cascade for $x \to \infty$ and accounting for the displacement relation (D.34), the Laplace domain displacement of particle \mathbf{p} in the semi-infinite cascade reads $\tilde{u}^{\mathbf{p}} = \tilde{u}^{\mathbf{N}} e^{-i\kappa(\mathbf{p}-\mathbf{P})}$. Here, κ is the dimensionless wavenumber. Substituting the expression for the displacement of particle \mathbf{p} into equation (D.33) yields the Laplace domain equation of motion of particle \mathbf{N} as:

$$M^{N} s^{2} \tilde{u}^{N} + K_{e}^{N-1,N} \tilde{e}^{N-1,N} + \tilde{\chi}(s) \tilde{u}^{N} = 0$$
(D.35)

The dimensionless dynamic stiffness of the semi-infinite linear-elastic cascade is found as:

$$\tilde{\chi}(s) = M^{\mathbf{P}} s^2 + \frac{1}{2} (1 - e^{-i\kappa})$$
 (D.36)

The dispersion relation for the semi-infinite cascade, derived in Appendix E.2, yields the following relations between the Laplace parameter s and the dimensionless wavenumber κ .

$$\cos \kappa = 1 + s^2, \qquad \sin \kappa = -is\sqrt{2 + s^2} \,. \tag{D.37}$$

Using Euler's formula to rearrange equation (D.36), substituting equations (D.37), as well as noting that the dimensionless mass of the subparticle **P** is found as $M^{P} = \frac{1}{2}$, we find the dynamic stiffness of the semi-infinite linear-elastic cascade as:

$$\tilde{\chi}(s) = \frac{1}{2}s\sqrt{2+s^2} \tag{D.38}$$

The dynamic stiffness of the semi-infinite linear-elastic cascade according to equation (D.38) is depicted in Figure D.5a as a function of frequency by substituting $s = i\Omega$.

The inverse Laplace transform of equation (D.38) can be obtained analytically and yields the equation of motion for the boundary particle N at the lattice cascade interface as:

$$\left(M^{N} + \frac{1}{2} \right) \ddot{u}^{N} + K_{e}^{N-1,N} e^{N-1,N} + \frac{1}{2} u^{N} + \int_{0}^{t} \left\{ \frac{J_{0} \left(\sqrt{2} \left(t - \tau \right) \right)}{t - \tau} - \frac{\sqrt{2} J_{1} \left(\sqrt{2} \left(t - \tau \right) \right)}{\left(t - \tau \right)^{2}} \right\} u^{N} \left(\tau \right) d\tau = 0$$
 (D.39)

Here, $J_0(\ldots)$ and $J_1(\ldots)$ are the Bessel functions of the first kind of respectively order zero and order one. The integrand of the convolution integral in equation (D.39) is singular for $\tau = t$. Despite this singularity, the integral in equation (D.39) may be approximated by assuming that, on the domain $\tau = t - \Delta t \ldots t$, the displacement $u^N(\tau)$ is linear and then solving the integral on this segment of its domain analytically.

Dimensionless boundary equations in terms of the dynamic compliance

Alternatively, we may express the Laplace domain boundary equation for the fully discrete Hooke system using the dynamic compliance according to equation (D.13). The dynamic compliance of the semi-infinite linear-elastic cascade follows from equation (D.38) as:

$$\tilde{\beta}(s) = \frac{2}{s\sqrt{2+s^2}} \tag{D.40}$$

In accordance with the approach for the discrete-continuous Hooke system in Appendix D.1, the boundary integral equation for the fully discrete Hooke system may be obtained in the form of equation (D.15). Thus, applying the inverse Laplace transform to equation (D.40), yields the dynamic compliance and its derivative in the time domain for $t \ge 0$ as:

$$\beta(t) = \pi t \mathbf{H}_0\left(\sqrt{2}t\right) J_1\left(\sqrt{2}t\right) + \left(2 - \pi \mathbf{H}_1\left(\sqrt{2}t\right)\right) t J_0\left(\sqrt{2}t\right), \qquad \dot{\beta}(t) = 2J_0\left(\sqrt{2}t\right). \quad (D.41)$$

Here, $\mathbf{H}_0(...)$ and $\mathbf{H}_1(...)$ are respectively the Struve functions of orders zero and one.

Noting that the time domain dynamic compliance of the semi-infinite linear-elastic cascade is equal to zero at t=0, i.e. $\beta(t=0)=0$, and substituting the time domain expression for the admittance $\dot{\beta}(t)$ into equation (D.15) then yields this boundary integral equation as:

$$\dot{u}^{N} + 2 \int_{0}^{t} J_{0} \left(\sqrt{2}t \right) \left\{ M^{N} \ddot{u}^{N} + K_{e}^{N-1,N} e^{N-1,N} \right\} (\tau) d\tau = 0$$
(D.42)

The convolution integral in equation (D.42) may be evaluated numerically in accordance with the approach for the semi-infinite viscoelastic cascade presented in Section 4.1.3.

Comparing the expressions for the dynamic compliance for the semi-infinite linear-elastic

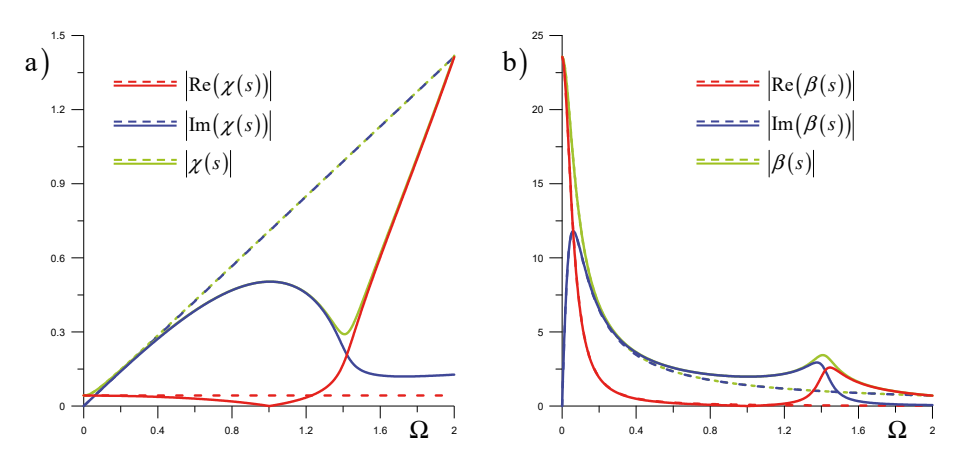


Figure D.5: Comparison of the semi-infinite linear-elastic rod (dashed) and the semi-infinite linear-elastic cascade (continuous) for: a) Dynamic stiffness; b) Dynamic compliance.

rod, previously found as $\tilde{\beta}(s) = s^{-1}\sqrt{2}$, and the dynamic compliance for the semi-infinite linear-elastic cascade, given by equation (D.40), we find that the difference between these two expressions consists of a term s^2 under the square root. The influence of this term is clearly visible in Figure D.5, where Figure D.5a and Figure D.5b respectively compare the dynamic stiffnesses and the dynamic compliances of the semi-infinite linear-elastic rod and the semi-infinite linear-elastic cascade as a function of frequency. Here, the continuous green, red and blue lines respectively give the absolute value, the real part and the imaginary part of the dynamic stiffness and the dynamic compliance for the semi-infinite linear-elastic cascade. The dashed lines in Figure D.5 give the corresponding results for the semi-infinite linear-elastic rod. Both figures show that the response of the rod and the cascade correspond for small frequencies, while the differences are significant for larger frequencies.

Alternative representation of the boundary integral equation in the time domain

In accordance with the approach for the semi-infinite viscoelastic cascade in Section 4.1.3, we can differentiate the equation of motion for the boundary particle a second time to isolate the contribution of the convolution integral to the current integration step more appropriately. This is possible because the time domain admittance, i.e. the time derivative of the dynamic compliance, of the linear-elastic rod is both non-infinite and non-zero at t = 0.

Applying time differentiation to the boundary integral equation given by equation (D.42) using Leibniz' rule for differentiation of integrals and noting that the time domain expression for the admittance of the linear-elastic cascade at t = 0 yields $\dot{\beta}(t = 0) = 2$, the equation of motion for the boundary particle becomes:

$$(2M^{N} + 1)\ddot{u}^{N} + 2K_{e}^{N-1,N}e^{N-1,N} + \int_{0}^{t} \ddot{\beta}(t-\tau) \{M^{N}\ddot{u}^{N} + K_{e}^{N-1,N}e^{N-1,N}\}(\tau)d\tau = 0$$
 (D.43)

Here, $\ddot{\beta}(t)$ is the second time derivative of the time domain expression for the dynamic compliance, or alternatively the time derivative of the time domain admittance. Within the domain of the integral in equation (D.43), i.e. for $t \ge 0$, the expression for the time derivative of the time domain admittance straightforwardly follows from equation (D.41) as:

$$\ddot{\beta}(t) = -2\sqrt{2}J_1(\sqrt{2}t) \tag{D.44}$$

Here, $J_1(...)$ denotes the Bessel functions of the first kind of order one.

Substituting equation (D.44) into equation (D.43) and subsequently dividing the remainder by two then yields the boundary integral equation for the fully discrete Hooke system as:

$$\left(M^{N} + \frac{1}{2} \right) \ddot{u}^{N} + K_{e}^{N-1,N} e^{N-1,N} - \sqrt{2} \int_{0}^{t} J_{1} \left(\sqrt{2} \left(t - \tau \right) \right) \left\{ M^{N} \ddot{u}^{N} + K_{e}^{N-1,N} e^{N-1,N} \right\} \left(\tau \right) d\tau = 0$$
 (D.45)

D.4 The 1D fully discrete Hooke system - alternate interface

In Appendix D.3, the interface between the lattice and the cascade in the fully discrete Hooke system was chosen at a particle. As depicted in Figure D.6, we may alternatively choose the lattice-cascade interface in the middle of a rheological element in-between two particles.

Matching the parameters of the lattice and the cascade for an alternate interface

To determine the stiffness of the interface springs for which the fully discrete Hooke system with the alternate lattice-cascade interface is homogeneous, we first state the equations of motion of the particle **P** and of the massless interface, which respectively read:

$$M^{P}\ddot{u}^{P} + K_{e}^{P} \left(u^{P} - u_{lnt} \right) + K_{e} \left(u^{P} - u^{P+1} \right) = 0$$
 (D.46)

$$K_e^{N}(u_{lnt} - u^{N}) + K_e^{P}(u_{lnt} - u^{P}) = 0$$
 (D.47)

Here, u_{Int} is the axial displacement of the massless lattice-cascade interface at coordinate $x = x_{Int}$ and $K_e^{\rm N}$ and $K_e^{\rm P}$ are the stiffnesses of the springs connected to the lattice-cascade interface respectively in the lattice and in the cascade. Furthermore, assuming an even distribution of the mass and assuming the particles to be equally spaced, they must all have the same mass M, so that $M^{\rm N} = M^{\rm P} = M$. Solving equation (D.47) for the interface displacement u_{Int} and substituting the resulting expression into equation (D.46) then yields:

$$M\ddot{u}^{P} + K_{e}^{P} \left(u^{P} - \frac{K_{e}^{N} u^{N} + K_{e}^{P} u^{P}}{K_{e}^{N} + K_{e}^{P}} \right) + K_{e} \left(u^{P} - u^{P+1} \right) = 0$$
 (D.48)

Given that the response of the system should be independent from the location of the lattice-cascade interface, the equation of motion for particle **P** as given by equation (D.48) must coincide with the equation of motion for any other particle in the interior of the cascade, previously given by equation (D.29). Comparing the two equations shows that:

$$K_e^{\mathbf{P}} \left(u^{\mathbf{P}} - \frac{K_e^{\mathbf{N}} u^{\mathbf{N}} + K_e^{\mathbf{P}} u^{\mathbf{P}}}{K_e^{\mathbf{N}} + K_e^{\mathbf{P}}} \right) = K_e \left(u^{\mathbf{P}} - u^{\mathbf{N}} \right)$$
(D.49)

Let us assume that the relation between the stiffnesses K_e^N and K_e^P of the interface springs

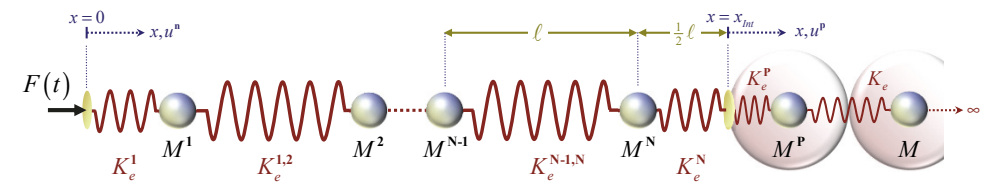


Figure D.6: The one-dimensional fully discrete Hooke lattice with the interface in between particles N and P.

may be described by a ratio φ_e , such that $K_e^{\mathbf{P}} = \varphi_e K_e^{\mathbf{N}}$. Equation (D.49) then yields the stiffnesses of the interface springs in the lattice and the cascade as:

$$K_e^{\mathbf{N}} = \frac{1 + \varphi_e}{\varphi_e} K_e, \qquad K_e^{\mathbf{P}} = (1 + \varphi_e) K_e. \tag{D.50}$$

Choosing equal stiffnesses, i.e. $\varphi_e = 1$, we find $K_e^N = K_e^P = 2K_e$.

Boundary equations for the fully discrete Hooke lattice with an alternate interface

To determine the dynamic stiffness of the linear-elastic cascade for the alternate location of the interface depicted in Figure D.6, we consider the governing equation of motion for a particle **p** inside the semi-infinite linear-elastic cascade, the equation of motion for the particle **P** next to the interface and the force balance between the springs at the massless lattice-cascade interface, previously given by equations (D.46) and (D.47). Substituting the stiffness relation $K_{\varepsilon}^{\mathbf{P}} = 2K_{\varepsilon}$ for the first spring in the cascade, the corresponding equations read:

$$M\ddot{u}^{p} + K_{e} \left(2u^{p} - u^{p-1} - u^{p+1} \right) = 0$$
 (D.51)

$$M\ddot{u}^{P} + K_{e} \left(3u^{P} - 2u_{Int} - u^{P+1}\right) = 0$$
 (D.52)

$$K_e^{\mathbf{N}}\left(u_{lnt} - u^{\mathbf{N}}\right) = -2K_e\left(u_{lnt} - u^{\mathbf{P}}\right) \tag{D.53}$$

Introducing dimensionless parameters for time, space, mass and stiffness in accordance with Appendix D.3, as well as applying the Laplace integral transform with respect to time, the corresponding dimensionless equations read:

$$s^{2}\tilde{u}^{p} + \frac{1}{2} \left(2\tilde{u}^{p} - \tilde{u}^{p-1} - \tilde{u}^{p+1} \right) = 0 \tag{D.54}$$

$$s^2 \tilde{u}^P + \frac{1}{2} (3\tilde{u}^P - 2\tilde{u}_{lnt} - \tilde{u}^{P+1}) = 0$$
 (D.55)

$$K_e^{\mathbf{N}} \left(\tilde{u}_{lnt} - \tilde{u}^{\mathbf{N}} \right) = - \left(\tilde{u}_{lnt} - \tilde{u}^{\mathbf{P}} \right) \tag{D.56}$$

Describing the general solution to the dimensionless wave equation for the semi-infinite linear-elastic cascade in the form of harmonic waves and accounting for the proper behaviour of the cascade for $x \to \infty$, the Laplace domain displacement of a particle **p** in the cascade may be expressed as $\tilde{u}^p = Ae^{-i\kappa p}$. Substituting this expression into the equation of motion for the particle **P**, given by equation (D.55), yields the expression for the unknown wave amplitude A, so that the Laplace domain displacement for a particle **p** in the interior of the semi-infinite cascade reads:

$$\tilde{u}^{\mathbf{p}} = \frac{2}{2s^2 + 3 - e^{-i\kappa}} \tilde{u}_{lnt} e^{-i\kappa(\mathbf{p} - \mathbf{P})}$$
(D.57)

Substituting equation (D.57) into equation (D.56) then yields the equation of motion of the massless lattice-cascade interface as:

$$K_e^{\mathbf{N}} \left(\tilde{u}_{Int} - \tilde{u}^{\mathbf{N}} \right) + \tilde{\chi}(s) \tilde{u}_{Int} = 0 \tag{D.58}$$

Here, the dynamic stiffness of the semi-infinite linear-elastic cascade is found as:

$$\tilde{\chi}(s) = 1 - \frac{2}{2s^2 + 3 - e^{-i\kappa}} = \frac{2s^2 + 1 - e^{-i\kappa}}{2s^2 + 3 - e^{-i\kappa}}$$
(D.59)

Applying Euler's formula and incorporating the dispersion relations (D.37), the dynamic stiffness of the semi-infinite linear-elastic cascade may alternatively be expressed as:

$$\tilde{\chi}(s) = \frac{s^2 + s\sqrt{2 + s^2}}{s^2 + 2 + s\sqrt{2 + s^2}}$$
(D.60)

Consequently, the dynamic compliance of the semi-infinite linear-elastic cascade reads:

$$\tilde{\beta}(s) = 1 + \frac{2}{s^2 + s\sqrt{2 + s^2}}$$
(D.61)

The derivation of the dynamic compliance of the semi-infinite linear-elastic cascade, given by equation (D.61), which is valid for the fully discrete system depicted in Figure D.6, is given here as an example to show that the interface between the near-field and far-field systems may be chosen at any given location. Additionally, this derivation shows how the dynamic compliance between the near-field lattice and the far-field cascade changes depending on the location of the interface.

The expression for the time domain equation of motion of the lattice-cascade interface may again be obtained by applying the inverse Laplace transform to equation (D.58), but its results, either in terms of the dynamic stiffness or in terms of the dynamic compliance, are not further elaborated here.

D.5 The elastically supported 1D discrete-continuous KV-system

Figure D.7 depicts the elastically supported one-dimensional discrete-continuous Kelvin-Voigt system. In the lattice, the elastic support is incorporated as a founded spring with stiffness k_d^n at each particle \mathbf{n} , while the elastic support in the rod, consists of a distributed spring with stiffness k_{rod} . Because the distributed spring causes the wave propagation in the elastically supported viscoelastic rod to be dispersive, it is henceforth referred to as the viscoelastic dispersive rod.

In the time domain, the wave equation for the viscoelastic dispersive rod and the two

interface conditions at the lattice-rod interface respectively read:

$$\rho A\ddot{u}(x,t) - EA\zeta_e \dot{u}''(x,t) - EAu''(x,t) + k_{rod}u(x,t) = 0$$
(D.62)

$$M^{N}\ddot{u}^{N} + C_{e}^{N-1,N}\dot{e}^{N-1,N} + K_{e}^{N-1,N}e^{N-1,N} + k_{d}^{N}u^{N} = EA\zeta_{e}\dot{u}'(x_{lnt},t) + EAu'(x_{lnt},t)$$
(D.63)

$$u^{N} = u(x_{lnt}, t) \tag{D.64}$$

Here, ζ_e and k_{rod} are respectively the damping and the foundation stiffness of the semi-infinite viscoelastic dispersive rod, while u(x,t) denotes its displacement valid for $x > x_{lnt}$.

The material parameters of the elastically supported one-dimensional Kelvin-Voigt lattice match the material properties of the viscoelastic dispersive rod for the following relations:

$$M = \rho A \ell, \quad C_e = \zeta_e \frac{EA}{\ell}, \quad K_e = \frac{EA}{\ell}, \quad k_d = k_{rod} \ell.$$
 (D.65)

For an even distribution of the mass and the elastic foundation along the elastically supported Kelvin-Voigt system, the mass of the boundary particle and the foundation stiffness at the boundary particle are respectively obtained as $M^N = \frac{1}{2}M$ and $k_d^N = \frac{1}{2}k_d$. Furthermore, we introduce the following set of dimensionless parameters:

$$t = t_{\text{dim}}\omega_0, \qquad u^{\mathbf{n}} = \frac{u_{\text{dim}}^{\mathbf{n}}}{\ell}, \qquad M^{\mathbf{n}} = \frac{M_{\text{dim}}^{\mathbf{n}}}{\rho A \ell}, \qquad \zeta = \frac{1}{2}\zeta_e\omega_0,$$

$$C_e^{\mathbf{n},\mathbf{n}+1} = \frac{C_{e;\text{dim}}^{\mathbf{n},\mathbf{n}+1}}{C_{crit}}, \qquad K_e^{\mathbf{n},\mathbf{n}+1} = \frac{K_{e;\text{dim}}^{\mathbf{n},\mathbf{n}+1}\ell}{2EA}, \qquad k_d^{\mathbf{n}} = \frac{k_{d;\text{dim}}^{\mathbf{n}}\ell}{2EA}, \qquad \Omega_d = \frac{\omega_d}{\omega_0}.$$

Here, the particle frequency ω_0 is found as $\omega_0 = \sqrt{2K_e/M}$, and the cutoff frequency ω_d of the elastic foundation reads $\omega_d = \sqrt{k_d/M}$. Furthermore, ζ is the damping ratio, which is defined as $\zeta = C_e/C_{crit}$, where the critical particle damping C_{crit} of the homogeneous Kelvin-Voigt lattice is found as $C_{crit} = M\omega_0$.

Inserting the dimensionless parameters and applying the Laplace integral transform respectively yields the dimensionless wave equation and the interface conditions in the Laplace domain as:

$$\left(s^{2} + \Omega_{d}^{2}\right)\tilde{u}(x,s) - \frac{1}{2}(1 + 2\zeta s)u''(x,s) = 0$$
(D.66)

$$M^{N} s^{2} \tilde{u}^{N} + \left(C_{e}^{N-1,N} s + K_{e}^{N-1,N}\right) \tilde{e}^{N-1,N} + k_{d}^{N} \tilde{u}^{N} = \frac{1}{2} (1 + 2\zeta s) \tilde{u}'(x_{Int}, s)$$
(D.67)

$$\tilde{u}^{N} = \tilde{u}(x_{lnt}, s) \tag{D.68}$$

Accounting for the proper behaviour of the rod for $x \to \infty$, the general solution for the dispersive rod reads $\tilde{u}(x,s) = A_1 e^{-s_\zeta \sqrt{2}x}$, where $s_\zeta = \sqrt{s^2 + \Omega_d^2} / \sqrt{1 + 2\zeta s}$. Substituting the general solution, as well as equation (D.68), into equation (D.67), yields the boundary equation,

i.e. the equation of motion of the boundary particle N, in the Laplace domain as:

$$M^{N} s^{2} \tilde{u}^{N} + \left(C_{e}^{N-1,N} s + K_{e}^{N-1,N}\right) \tilde{e}^{N-1,N} + k_{d}^{N} \tilde{u}^{N} + \tilde{\chi}(s) \tilde{u}^{N} = 0$$
(D.69)

Here, the dynamic stiffness of the semi-infinite viscoelastic dispersive rod is found as:

$$\tilde{\chi}(s) = \frac{1}{2}\sqrt{s^2 + \Omega_d^2}\sqrt{2 + 4\zeta s} \tag{D.70}$$

In correspondence with the dynamic stiffness for the viscoelastic rod, a time domain expression for the dynamic stiffness of the viscoelastic dispersive rod cannot be obtained analytically, because the expression given by equation (D.70) does not tend to zero for for $\omega \to \infty$. Instead, we divide equation (D.69) by the dynamic stiffness, and consider the Laplace domain boundary equation for the elastically supported Kelvin-Voigt system in terms of the dynamic compliance.

Boundary integral equation in terms of the dynamic compliance

The dynamic compliance of the viscoelastic dispersive rod is straightforwardly obtained as the inverse of the dynamic stiffness given by equation (D.70) and thus reads:

$$\tilde{\beta}(s) = \frac{2}{\sqrt{s^2 + \Omega_d^2} \sqrt{2 + 4\zeta s}} \tag{D.71}$$

Following the approach for the discrete-continuous Hooke system in Appendix D.1, the Subboundary integral equation for the elastically supported one-dimensional discrete-continuous Kelvin-Voigt system is described by equation (D.15). For $t \ge 0$, the inverse Laplace transform of equation (D.71) yields the following time domain expression for the dynamic compliance:

$$\beta(t) = \int_{0}^{t} J_{0}\left(\Omega_{d}\left(t-\tau\right)\right) \frac{e^{-\frac{1}{2}\tau/\zeta}}{\sqrt{\pi\zeta\tau}} d\tau = \int_{0}^{t} J_{0}\left(\Omega_{d}t\right) \frac{e^{-\frac{1}{2}(t-\tau)/\zeta}}{\sqrt{\pi\zeta\left(t-\tau\right)}} d\tau \tag{D.72}$$

Then, applying Leibniz' rule for differentiation of integrals, we find the time derivative of

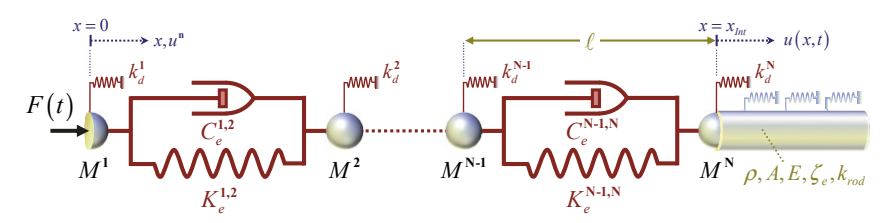


Figure D.7: The elastically supported one-dimensional semi-infinite discrete-continuous Kelvin-Voigt system.

the dynamic compliance, i.e. the time domain expression for the admittance, for $t \ge 0$ as:

$$\dot{\beta}(t) = \frac{e^{-\frac{1}{2}t/\zeta}}{\sqrt{\pi\zeta t}} - \Omega_d \int_0^t J_1(\Omega_d(t-\tau)) \frac{e^{-\frac{1}{2}\tau/\zeta}}{\sqrt{\pi\zeta \tau}} d\tau \tag{D.73}$$

Substituting equations (D.72) and (D.73) into equation (D.15), the boundary integral equation for the elastically supported discrete-continuous Kelvin-Voigt system reads:

$$\dot{u}^{N} + \int_{0}^{t} \dot{\beta}(t-\tau) \Big\{ M^{N} \ddot{u}^{N} + C_{e}^{N-1,N} \dot{e}^{N-1,N} + K_{e}^{N-1,N} e^{N-1,N} + k_{d}^{N} u^{N} \Big\} (\tau) d\tau = 0$$
 (D.74)

In correspondence with the time domain admittance of the viscoelastic rod, the time domain admittance of the viscoelastic dispersive rod, given by equation (D.73) is singular for t = 0. To address this issue, we rearrange the convolution integral in equation (D.73) using its commutativity property and split its integral domain to obtain the time domain admittance as:

$$\dot{\beta}(t) = \frac{e^{-\frac{1}{2}t/\zeta}}{\sqrt{\pi\zeta t}} - \Omega_d \int_0^{t-\Delta t} J_1(\Omega_d \tau) \frac{e^{-\frac{1}{2}(t-\tau)/\zeta}}{\sqrt{\pi\zeta (t-\tau)}} d\tau - \Omega_d \int_{t-\Delta t}^t J_1(\Omega_d \tau) \frac{e^{-\frac{1}{2}(t-\tau)/\zeta}}{\sqrt{\pi\zeta (t-\tau)}} d\tau \qquad (D.75)$$

As all values within the domain of integration $\tau = 0...t - \Delta t$ are known at time t, the corresponding integral in equation (D.75) may be obtained numerically as a constant at time t, here denoted as B_0 . Then, approximating the Bessel function over the domain $\tau = t - \Delta t...t$ by a linear function, i.e. $J_1(\Omega_d t) = at + b$, we can rearrange equation (D.75) as:

$$\dot{\beta}(t) = \frac{e^{-\frac{1}{2}t/\zeta}}{\sqrt{\pi\zeta t}} - \Omega_d B_0 - \Omega_d \int_{t-\Delta t}^t \frac{e^{-\frac{1}{2}(t-\tau)/\zeta}}{\sqrt{\pi\zeta (t-\tau)}} (a\tau + b) d\tau$$
(D.76)

Expressions for the unknowns a and b may be derived by noting that, at time t- Δt , the approximated Bessel function reads $J_1(\Omega_d(t-\Delta t)) = a(t-\Delta t) + b$. This yields:

$$a = \frac{J_1\left(\Omega_d t\right) - J_1\left(\Omega_d \left(t - \Delta t\right)\right)}{\Delta t}, \quad b = \frac{tJ_1\left(\Omega_d \left(t - \Delta t\right)\right) - \left(t - \Delta t\right)J_1\left(\Omega_d t\right)}{\Delta t}.$$

Substituting these expressions for a and b into equation (D.76) and then solving the remaining integral analytically, the time domain expression for the admittance may be obtained as:

$$\dot{\beta}(t) = \frac{e^{-\frac{1}{2}t/\zeta}}{\sqrt{\pi\zeta t}} + f_B(t), \text{ with: } f_B(t) = -\Omega_d\left(B_0 + B_1J_1(\Omega_d t) + B_2J_1(\Omega_d(t - \Delta t))\right) \quad (D.77)$$

Here, the terms B_0 , B_1 and B_2 are respectively found as:

$$B_0 = \int_0^{t-\Delta t} J_1\left(\Omega_d\left(t-\tau\right)\right) \frac{e^{-\frac{1}{2}\tau/\zeta}}{\sqrt{\pi\zeta\tau}} d\tau, \quad B_1 = \sqrt{2}\mathrm{erf}\sqrt{\frac{\Delta t}{2\zeta}} - B_2, \quad B_2 = \frac{\zeta\sqrt{2}}{\Delta t}\mathrm{erf}\sqrt{\frac{\Delta t}{2\zeta}} - 2\sqrt{\frac{\zeta}{\pi\Delta t}}e^{-\frac{\Delta t}{2\zeta}}.$$

Here, erf (...) is the error function, or Gauss error function.

Furthermore, note that the term $f_B(t)$ in equation (D.77) is a known constant at time t, because the three terms B_0 , B_1 and B_2 , all consist of parameters that are either constants, or are known at time t.

Then, substituting equation (D.77) into the integral over the domain $\tau = t - \Delta t \dots t$ allows us to express the boundary integral equation as:

$$\dot{u}^{N} + \int_{t-\Delta t}^{t} \frac{e^{-\frac{1}{2}(t-\tau)/\zeta}}{\sqrt{\pi\zeta(t-\tau)}} F^{N}(\tau) d\tau + \int_{t-\Delta t}^{t} f_{B}(t-\tau) F^{N}(\tau) d\tau + \int_{0}^{t-\Delta t} \dot{\beta}(t-\tau) F^{N}(\tau) d\tau = 0$$
 (D.78)

Here, the force at the boundary reads $F^{N}(t) = M^{N}\ddot{u}^{N} + C_{e}^{N-1,N}\dot{e}^{N-1,N} + K_{e}^{N-1,N}e^{N-1,N} + k_{d}^{N}u^{N}$. Next, we assume that this force is linear over the domain $\tau = t - \Delta t \dots t$ and found as $F^{N}(t) = ct + d$. This yields the expressions for the unknowns c and d respectively as:

$$c = \frac{F^{N}(t) - F^{N}(t - \Delta t)}{\Delta t}, \quad d = \frac{tF^{N}(t - \Delta t) - (t - \Delta t)F^{N}(t)}{\Delta t}.$$

Substituting the above expressions into equation (D.78) and analytically solving the left-most integral then finally yields the interface equation as:

$$\dot{u}^{N} + B_{1}F^{N}\left(t\right) + B_{2}F^{N}\left(t - \Delta t\right) + \int_{t - \Delta t}^{t} f_{B}\left(t - \tau\right)F^{N}\left(\tau\right)d\tau + \int_{0}^{t - \Delta t} \dot{\beta}\left(t - \tau\right)F^{N}\left(\tau\right)d\tau = 0 \qquad (D.79)$$

Note here that $f_B(t)$ is not singular for t = 0 and thus the corresponding integral can be obtained numerically.

E Wave propagation in one-dimensional systems

The performance of any boundary integral equation can be determined by considering the reflection and transmission of an incident wave as it travels through the boundary. Corresponding reflection and transmission coefficients are defined as the absolute value of the ratio between the amplitudes, or the energies, of either the reflected or transmitted waves and the incident wave. The amplitude reflection coefficient R_A , energy reflection coefficient R_E , amplitude transmission coefficient T_A and the energy transmission coefficients T_E thus read:

$$R_A = \left| \frac{A_{ref}}{A_{inc}} \right|, \quad R_E = \left| \frac{E_{ref}}{E_{inc}} \right|, \quad T_A = \left| \frac{A_{tra}}{A_{inc}} \right|, \quad T_E = \left| \frac{E_{tra}}{E_{inc}} \right|.$$

In this appendix, the amplitude and energy reflection and transmission coefficients are derived in their dimensionless forms. Before respectively deriving the dimensionless reflection and transmission coefficients for the linear-elastic and viscoelastic one-dimensional discrete-continuous systems in Appendices 0 and E.5, Appendices E.1 to E.3 present the dimensionless dispersion relations for both one-dimensional continuous systems and one-dimensional discrete particle systems.

E.1 Dispersion in linear-elastic and viscoelastic rods

To determine the dimensionless dispersion relation for the linear-elastic rod, let us consider its dimensionless equation of motion, which is obtained from inserting the dimensionless parameters from Appendix B.1 into its dimensional form as given by equation (D.1):

$$\ddot{u}(x,t) - \frac{1}{2}u''(x,t) = 0 \tag{E.1}$$

Assuming a harmonic wave, with a dimensionless frequency Ω and dimensionless wavenumber κ , that travels through a linear-elastic rod into the direction for which the dimensionless coordinate x increases, the displacement in the rod may be expressed as:

$$u(x,t) = Ae^{i(\Omega t - \kappa x)}$$
 (E.2)

Here, A is the wave amplitude. Furthermore, note that the dimensionless parameters are related to their dimensional counterparts as $\Omega = \omega/\omega_0$, $\kappa = k\ell$ and $x = x_{\rm dim}/\ell$.

Substituting equation (E.2) into equation (E.1) and choosing the branch of the square root that assures the proper behaviour of the linear-elastic rod for $x \to \infty$, yields the dimensionless dispersion relation for a linear-elastic rod as:

$$-\Omega^2 + \frac{1}{2}\kappa^2 = 0 \quad \to \quad \kappa = \sqrt{2\Omega^2} = \Omega\sqrt{2}$$
 (E.3)

To obtain the dispersion relation between the wavenumber κ and the Laplace parameter s, we assume that $u(x,t) = Ae^{st-i\kappa x}$. Choosing the branch of the square root that assures the proper

behaviour for $x \to \infty$, the dimensionless dispersion relation for the linear-elastic rod reads:

$$s^2 + \frac{1}{2}\kappa^2 = 0 \rightarrow \kappa = \sqrt{-2s^2} = \sqrt{2i^2 s^2} = -is\sqrt{2}$$
 (E.4)

Dispersion in the viscoelastic rod

The dimensionless equation of motion for the viscoelastic rod is given in Section 3.2.2 as:

$$\ddot{u}(x,t) - \zeta \dot{u}''(x,t) - \frac{1}{2}u''(x,t) = 0 \tag{E.5}$$

Assuming that the displacement in the rod due to a harmonic wave, with amplitude A, dimensionless frequency Ω and dimensionless wavenumber κ , is expressed as $u(x,t) = Ae^{i(\Omega t - \kappa x)}$ and choosing the square root such that it assures the proper behaviour for $x \to \infty$, the dimensionless dispersion relation is obtained as:

$$-\Omega^{2} + \frac{1}{2} \left(1 + 2i\zeta\Omega \right) \kappa^{2} = 0 \quad \rightarrow \quad \kappa = \frac{\Omega}{1 + 2i\zeta\Omega} \sqrt{2 + 4i\zeta\Omega} = \frac{\Omega\sqrt{2}}{\sqrt{1 + 2i\zeta\Omega}}$$
 (E.6)

Alternatively, we can obtain the dispersion relation as a relation between the wavenumber κ and the Laplace parameter s by assuming that $u(x,t) = Ae^{st-i\kappa x}$. Again, accounting for the proper behaviour for $x \to \infty$, the dispersion relation for the viscoelastic rod reads:

$$s^{2} + \frac{1}{2}(1 + 2\zeta s)\kappa^{2} = 0 \quad \to \quad \kappa = \frac{-is}{1 + 2\zeta s}\sqrt{2 + 4\zeta s} = \frac{-is\sqrt{2}}{\sqrt{1 + 2\zeta s}}$$
 (E.7)

Note here that the dispersion relation for the linear-elastic rod, given by equation (E.4) can be obtained from equation (E.7) by choosing the damping ratio equal to zero, i.e. $\zeta = 0$, and that the dispersion relation according to equation (E.6) can be obtained from equation (E.7) by substituting $s = i\Omega$.

Alternatively, we may describe the dispersion relation in terms of the complex conjugate of the wavenumber κ , denoted as $\bar{\kappa}$. To obtain this dispersion relation, we describe the displacement in the rod due to a harmonic wave as $u(x,t) = Ae^{-i(\Omega t - \bar{\kappa}x)}$. Accounting for the proper behaviour for $x \to \infty$, we find the dispersion relation for the viscoelastic rod as:

$$-\Omega^{2} + \frac{1}{2} (1 - 2i\zeta\Omega) \overline{\kappa}^{2} = 0 \quad \to \quad \overline{\kappa} = \frac{\Omega}{1 - 2i\zeta\Omega} \sqrt{2 - 4i\zeta\Omega} = \frac{\Omega\sqrt{2}}{\sqrt{1 - 2i\zeta\Omega}}$$
 (E.8)

The dispersion relation that describes the relation between the dimensionless complex conjugate wavenumber $\bar{\kappa}$ and the dimensionless Laplace parameter s may straightfowardly be obtained by describing the displacement in the rod as $u(x,t) = Ae^{-st+i\bar{\kappa}x}$.

E.2 Dispersion in one-dimensional linear-elastic particle systems

To determine the dispersion relations for one-dimensional linear-elastic discrete particle systems, let us first consider the dimensionless equation of motion for a particle **p** in its interior. This equation is straightforwardly obtained by inserting the dimensionless parameters from Appendix B.1 into the equation of motion for the linear-elastic cascade, given by equation (D.29). This yields:

$$\ddot{u}^{\mathbf{p}} + \frac{1}{2} \left(2u^{\mathbf{p}} - u^{\mathbf{p}-1} - u^{\mathbf{p}+1} \right) = 0 \tag{E.9}$$

Assuming a forward travelling harmonic incident wave with dimensionless frequency Ω and dimensionless wavenumber κ , the displacement of particle **p** may be expressed as:

$$u^{\mathbf{p}} = Ae^{\mathrm{i}(\Omega t - \kappa \mathbf{p})} \tag{E.10}$$

Here, A is the wave amplitude and the dimensionless frequency and dimensionless wavenumber are respectively found in terms of dimensional variables as $\Omega = \omega/\omega_0$ and $\kappa = k\ell$.

Substituting equation (E.10) into equation (E.9) yields the dispersion relation for a linearelastic discrete particle system, or cascade, that relates frequency and wavenumber as:

$$-\Omega^2 + 2\sin^2\frac{\kappa}{2} = 0\tag{E.11}$$

From this dispersion relation, we find the following useful frequency-wavenumber relations:

$$\cos \kappa = 1 - \Omega^2$$
, $\sin \kappa = \Omega \sqrt{2 - \Omega^2}$. (E.12)

When considering harmonic wave propagation, it is most convenient to assume that the frequency Ω is always real. According to equation (E.12), it then follows that the wavenumber κ is also real for $\Omega \leq \sqrt{2}$, but that the wavenumber is imaginary for $\Omega > \sqrt{2}$.

Alternatively, we may obtain the dispersion relation as a relation between the dimensionless wavenumber κ and the dimensionless Laplace parameter s by assuming that the displacement of particle \mathbf{p} reads $u^{\mathbf{p}} = Ae^{st-i\kappa\mathbf{p}}$. Substituting this expression into equation (E.9), yields:

$$s^{2} + 1 - \cos \kappa = s^{2} + 2\sin^{2}\frac{\kappa}{2} = 0$$
 (E.13)

Accounting for the proper behaviour of the linear-elastic cascade for $x \to \infty$, the dispersion relation yields the following useful relations:

$$\cos \kappa = 1 + s^2, \qquad \sin \kappa = -is\sqrt{2 + s^2} . \tag{E.14}$$

E.3 Dispersion in one-dimensional viscoelastic particle systems

The dispersion relations for the one-dimensional viscoelastic discrete particle systems follow from the dimensionless equation of motion for a particle \mathbf{p} in the interior of a viscoelastic discrete particle system has been obtained in Section 4.1.2 as:

$$\dot{u}^{p} + \zeta \left(2\dot{u}^{p} - \dot{u}^{p-1} - \dot{u}^{p+1} \right) + \frac{1}{2} \left(2u^{p} - u^{p-1} - u^{p+1} \right) = 0$$
 (E.15)

Assuming that the displacement of particle **p** due to a forward travelling harmonic incident wave, with dimensionless amplitude A, dimensionless frequency Ω and dimensionless wavenumber κ , is expressed as $u^{\mathbf{p}} = Ae^{\mathrm{i}(\Omega t - \kappa \mathbf{p})}$, the dimensionless dispersion relation for the viscoelastic particle system reads:

$$-\Omega^2 + \left(1 + 2i\zeta\Omega\right)2\sin^2\frac{\kappa}{2} = 0\tag{E.16}$$

From the dispersion relation given by equation (E.16), the following relations between the dimensionless frequency Ω and dimensionless wavenumber κ can be obtained:

$$\cos \kappa = 1 - \frac{\Omega^2}{1 + 2i\zeta\Omega}, \quad \sin \kappa = \frac{\Omega}{1 + 2i\zeta\Omega} \sqrt{2 + 4i\zeta\Omega - \Omega^2}. \tag{E.17}$$

As for the continuous systems, substituting $\zeta = 0$ reduces the dispersion relations for the viscoelastic system to those for the linear-elastic system, as given by equation (E.12).

When considering the propagation of harmonic waves, it is most convenient to work with real frequencies. From equations (E.17), it then follows that by incorporating damping the wavenumber κ must be complex-valued for any real non-zero frequency Ω .

We can alternatively obtain the dispersion relation as a relation between the wavenumber κ and the Laplace parameter s by assuming that $u^p = Ae^{st-i\kappa p}$. Accounting for the proper behaviour for $x \to \infty$, this dispersion relation reads:

$$s^{2} + 2(1 + 2\zeta s)\sin^{2}\frac{\kappa}{2} = 0$$
 (E.18)

Note that, to obtain the dispersion relation according to equation (E.18), we may alternatively start from the equation of motion for the particle **p** in the Laplace domain, given in Section 4.1.2, by expressing the Laplace domain displacement as $\tilde{u}^{\mathbf{p}} = Ae^{-i\kappa\mathbf{p}}$.

The dispersion relation (E.18) yields the following useful relations:

$$\cos \kappa = 1 + \frac{s^2}{1 + 2\zeta s}, \qquad \sin \kappa = \frac{-is}{1 + 2\zeta s} \sqrt{2 + 4\zeta s + s^2}.$$
 (E.19)

The square root in the expression for the sine of κ in equation (E.19) is chosen such that the forward travelling wave fades for $\mathbf{n} \to \infty$.

Substituting $\kappa = \kappa_R + i\kappa_I$ into the expression for the Laplace domain displacement \tilde{u}^p , then yields:

$$\tilde{u}^{\mathbf{p}} = A e^{-i\kappa_R \mathbf{p}} e^{+\kappa_I \mathbf{p}} \tag{E.20}$$

From equation (E.20) it is evident that the square root must be chosen such that the imaginary part of the wavenumber is negative. This coincides with the sign of the square root chosen to obtain the expression for the sine of κ in equation (E.19).

Dispersion relations for the complex conjugate wavenumbers

To derive the energy reflection and transmission coefficients for an incident wave that travels through a boundary in one-dimensional systems, we additionally require dispersion relations in terms of complex conjugate wavenumbers.

To obtain the dispersion relation between the real-valued frequency Ω and the complex conjugate wavenumber $\bar{\kappa}$, we describe the displacement of particle ${\bf p}$ due to a corresponding harmonic wave with wave amplitude A as:

$$u^{\mathbf{p}} = Ae^{-\mathrm{i}(\Omega t - \bar{\kappa}\mathbf{p})} \tag{E.21}$$

Substituting equation (E.21) into the equation of motion for particle **p**, given by equation (E.15), then yields the dispersion relation for the complex conjugate wavenumber as:

$$-\Omega^2 + \left(1 - 2i\zeta\Omega\right)2\sin^2\frac{\overline{\kappa}}{2} = 0\tag{E.22}$$

From this dispersion relation, we find the following useful relations between the dimensionless frequency and the dimensionless complex conjugate wavenumber as:

$$\cos \bar{\kappa} = 1 - \frac{\Omega^2}{1 - 2i\zeta\Omega}, \quad \sin \bar{\kappa} = \frac{\Omega}{1 - 2i\zeta\Omega} \sqrt{2 - 4i\zeta\Omega - \Omega^2}. \tag{E.23}$$

The corresponding dispersion relation that describes the relation between the dimensionless complex conjugate wavenumber $\bar{\kappa}$ and the dimensionless Laplace parameter s may be obtained in a similar manner by expressing the displacement of particle **p** as $u^{\mathbf{p}} = Ae^{-st+i\bar{\kappa}\mathbf{p}}$.

E.4 Reflection coefficients for discrete-continuous Hooke systems

Amplitude coefficients for the discrete-continuous Hooke system

The amplitude reflection coefficient, defined as the ratio between the amplitude of a reflected and its incident wave, for a wave that reflects from the discrete-continuous interface of the corresponding one-dimensional Hooke system is obtained starting from the equation of motion of its boundary particle **N**, which is found as:

$$M^{N}\ddot{u}^{N} + K_{e}^{N-1,N} \left(u^{N} - u^{N-1} \right) = \frac{1}{2} u'(x_{lnt},t)$$
 (E.24)

Assuming the incident, reflected and transmitted waves to be harmonic, the displacement of an arbitrary particle \mathbf{n} in the one-dimensional Hooke lattice and the displacement at a coordinate x in the linear-elastic rod are respectively described as:

$$u^{\mathbf{n}} = A_{inc}e^{\mathrm{i}(\Omega t - \kappa \mathbf{n})} + A_{ref}e^{\mathrm{i}(\Omega t + \kappa \mathbf{n})}$$
(E.25)

$$u(x,t) = A_{tra}e^{i(\Omega t - \kappa_{rod}x)}$$
 (E.26)

Here, A_{inc} , A_{ref} and A_{tra} are the complex amplitudes of respectively the incident, reflected and transmitted waves and κ_{rod} denotes the wavenumber in the linear-elastic rod that, according to the dispersion relation (E.3), is related to the frequency as $\kappa_{rod} = \Omega\sqrt{2}$. Substituting equation (E.3), the spatial derivate of equation (E.26) reads $u'(x,t) = -i\Omega\sqrt{2}u(x,t)$. Then, noting that the displacement of the linear-elastic rod at the dispersion interface must be equal to the displacement of particle \mathbf{N} , i.e. $u(x_{lnt},t) = u^{\mathbf{N}}$, equation (E.24) becomes:

$$M^{N}\ddot{u}^{N} + K_{e}^{N-1,N} \left(u^{N} - u^{N-1} \right) + \frac{1}{2} i\Omega \sqrt{2} u^{N} = 0$$
 (E.27)

Substituting the displacement of the boundary particle N according to equation (E.25) into equation (E.27) and rearranging the remainder using both Euler's formula and the dispersion relations given by equation (E.12), the ratio between the amplitudes of the reflected and the incident waves may be derived as:

$$\frac{A_{ref} e^{+i\kappa N}}{A_{inc} e^{-i\kappa N}} = \frac{-\left(K_e^{N-1,N} - M^N\right) \Omega + i\left(K_e^{N-1,N} \sqrt{2 - \Omega^2} - \frac{1}{2}\sqrt{2}\right)}{\left(K_e^{N-1,N} - M^N\right) \Omega + i\left(K_e^{N-1,N} \sqrt{2 - \Omega^2} + \frac{1}{2}\sqrt{2}\right)}$$
(E.28)

Noting that A_{inc} and A_{ref} are the complex amplitudes of respectively the incident and reflected waves at the surface particle, i.e. for $\mathbf{n} = 0$, it follows that $A_{inc}e^{-i\kappa \mathbf{N}}$ and $A_{ref}e^{+i\kappa \mathbf{N}}$ are the complex amplitudes of respectively the incident and reflected waves at the boundary particle \mathbf{N} . Equation (E.28) thus describes the amplitude reflection coefficient for an incident wave that reflects from the discrete-continuous interface of the Hooke lattice and the linear-elastic

rod at the boundary particle N.

According to equation (E.28), there will be no wave reflection in the long-wave limit, if the mass of the boundary particle and the stiffness of the attached spring are related as $M^{\rm N}=K_e^{\rm N-1,N}$. Accordingly, the configuration of the lattice boundary for the one-dimensional discrete-continuous systems in this thesis, as discussed in Section 0, yields the dimensionless mass of the boundary particle and the dimensionless stiffness of the springs respectively as $M^{\rm N}=\frac{1}{2}$ and $K_e^{\rm N-1,N}=\frac{1}{2}$. Consequently, the amplitude reflection coefficient at the boundary particle N of the one-dimensional discrete-continuous Hooke system reads:

$$R_{A}^{N} = \left| \frac{A_{ref}^{N}}{A_{inc}^{N}} \right| = \left| \frac{A_{ref}e^{+i\kappa N}}{A_{inc}e^{-i\kappa N}} \right| = \left| \frac{\sqrt{2 - \Omega^{2}} - \sqrt{2}}{\sqrt{2 - \Omega^{2}} + \sqrt{2}} \right|$$
 (E.29)

Energy exchange at the lattice-rod interface in the linear-elastic Hooke system

It is most straightforward to determine the energy reflection and transmission coefficients in a medium by separately considering the energy fluxes of the isolated incident wave, the isolated reflected wave and the isolated transmitted wave. This approach has been presented in Section 3.3.2 for the discrete-continuous Kelvin-Voigt system and, due to the energy flux being independent of the damping, will yield the same results for the discrete-continuous Hooke system.

It is however of interest to review the interaction between the incident wave and the reflected wave near the boundary where these waves are not isolated and possibly interfere. To this purpose, we consider the energy exchange between the incident, the reflected and the transmitted waves at the boundary particle **N** in the discrete-continuous Hooke system. Multiplying the force balance at the lattice-rod interface, i.e. the equation of motion for the boundary particle **N** given by equation (E.24), with the velocity of the interface in their respective models, as well as substituting the dimensionless mass of the boundary particle and the dimensionless stiffness of the springs respectively as $M^N = \frac{1}{2}$ and $K_e^{N-1,N} = \frac{1}{2}$, yields the dimensionless energy balance that describes this energy exchange as:

$$\ddot{u}^{N}\dot{u}^{N} + (u^{N} - u^{N-1})\dot{u}^{N} = \dot{u}(x_{Int}, t)u'(x_{Int}, t)$$
(E.30)

In the energy balance given by equation (E.30), the first term on the left-hand side describes the change in kinetic energy of the boundary particle over time, while the second term on the left-hand side gives the energy flux through the lattice-rod interface applied by the lattice, thus due to the incident and the reflected waves both. The right-hand side of equation (E.30) describes the energy flux through the lattice-rod interface applied by the rod, thus due to the transmitted wave.

Even though the dispersion relation for the Hooke lattice, given by equation (E.12), yields wavenumbers that are either real or imaginary, and the dispersion relation for the linear-elastic rod, given by equation (E.3), yields real wavenumbers, let us here, as a general case,

assume that the wavenumbers in the Hooke lattice and the linear-elastic rod are complexvalued. Then, to assure that the expressions for the displacements in the Hooke lattice and the rod are real-valued, we account for both the complex wavenumbers and their complex conjugates. This yields the expressions for the displacements of the lattice particles and the displacement along the linear-elastic rod as:

$$u^{\mathbf{n}} = \frac{1}{2} \left\{ A_{inc} e^{\mathrm{i}(\Omega t - \kappa \mathbf{n})} + \overline{A}_{inc} e^{-\mathrm{i}(\Omega t - \overline{\kappa} \mathbf{n})} \right\} + \frac{1}{2} \left\{ A_{ref} e^{\mathrm{i}(\Omega t + \kappa \mathbf{n})} + \overline{A}_{ref} e^{-\mathrm{i}(\Omega t + \overline{\kappa} \mathbf{n})} \right\}$$
(E.31)

$$u(x,t) = \frac{1}{2} \left\{ A_{tra} e^{i(\Omega t - \kappa_{rod} x)} + \overline{A}_{tra} e^{-i(\Omega t - \overline{\kappa}_{rod} x)} \right\}$$
 (E.32)

Here, the amplitudes \overline{A}_{inc} , \overline{A}_{ref} and \overline{A}_{tra} are the complex conjugates of the dimensionless amplitudes A_{inc} , A_{ref} and A_{tra} of the incident, reflected and transmitted waves respectively. Furthermore, $\overline{\kappa}$ and $\overline{\kappa}_{rod}$ are the complex conjugates of the dimensionless wavenumbers κ and κ_{rod} in respectively the Hooke lattice and the linear-elastic rod.

Substituting equations (E.31) and (E.32) into equation (E.30), averaging the energy balance over a single period of the harmonic incident wave, and substituting the dispersion relations for the linear-elastic rod, given by equation (E.3), then yields the energy balance as:

$$A_{inc} \overline{A}_{inc} e^{-i(\kappa - \overline{\kappa})N} \left(e^{+i\kappa} - e^{-i\overline{\kappa}} \right) + A_{inc} \overline{A}_{ref} e^{-i(\kappa + \overline{\kappa})N} \left(e^{+i\kappa} - e^{+i\overline{\kappa}} \right)$$

$$+ \overline{A}_{inc} A_{ref} e^{+i(\kappa + \overline{\kappa})N} \left(e^{-i\kappa} - e^{-i\overline{\kappa}} \right) + A_{ref} \overline{A}_{ref} e^{+i(\kappa - \overline{\kappa})N} \left(e^{-i\kappa} - e^{+i\overline{\kappa}} \right) = 2\sqrt{2} i\Omega A_{tra} \overline{A}_{tra} e^{-i(\kappa_{rod} - \overline{\kappa}_{rod})x_{lnt}}$$
(E.33)

Here, note that the particle number N present in the exponents for the incident and reflected waves describes the decay of the wave amplitude at the boundary particle N relative to the wave amplitudes A_{inc} and A_{ref} at the tip of the lattice. Thereby, $A_{inc}e^{-i\kappa N}$ and $A_{ref}e^{+i\kappa N}$ are the wave amplitudes of the incident and reflected waves at the boundary particle N, while $\overline{A}_{inc}e^{+i\kappa N}$ and $\overline{A}_{ref}e^{-i\kappa N}$ are the complex conjugates of the corresponding wave amplitudes at the boundary particle N. Accordingly, the coordinate x_{Int} in the exponent for the transmitted wave describes the decay of the amplitude of the transmitted wave relative to A_{tra} , so that $A_{tra}e^{-i\kappa_{rod}x_{Int}}$ and $\overline{A}_{tra}e^{+i\kappa_{rod}x_{Int}}$ are respectively the wave amplitude of the transmitted wave at the tip of the rod and its complex conjugate. Denoting the wave amplitudes of the incident, reflected and transmitted waves and their complex conjugates at the interface as A_{inc}^N , A_{ref}^N , A_{ref}^N , \overline{A}_{inc}^N , \overline{A}_{ref}^N and $\overline{A}_{tra}^{x_{Int}}$, we can rewrite equation (E.33) as:

$$A_{inc}^{\mathbf{N}} \overline{A}_{inc}^{\mathbf{N}} \left(e^{+i\kappa} - e^{-i\overline{\kappa}} \right) + A_{inc}^{\mathbf{N}} \overline{A}_{ref}^{\mathbf{N}} \left(e^{+i\kappa} - e^{+i\overline{\kappa}} \right)$$

$$+ \overline{A}_{inc}^{\mathbf{N}} A_{ref}^{\mathbf{N}} \left(e^{-i\kappa} - e^{-i\overline{\kappa}} \right) + A_{ref}^{\mathbf{N}} \overline{A}_{ref}^{\mathbf{N}} \left(e^{-i\kappa} - e^{+i\overline{\kappa}} \right) = 2\sqrt{2} \mathbf{i} \Omega A_{tra}^{x_{int}} \overline{A}_{tra}^{x_{int}}$$

$$(E.34)$$

As noted previously, the wavenumber κ in the Hooke lattice is real for $\Omega \leq \sqrt{2}$ and imaginary for $\Omega > \sqrt{2}$. In the following, we will therefore separately consider the energy exchange in the discrete-continuous Hooke system for the two domains for the dimensionless frequency that respectively coincide with real and imaginary wavenumbers.

Energy exchange at the lattice-rod interface for real wavenumbers

For real wavenumbers, the wavenumber and its complex conjugate are equal, i.e. $\bar{\kappa} = \kappa$. Substituting this into equation (E.34) yields the energy balance at the lattice-rod interface as:

$$\left\{ \left| A_{inc}^{\mathbf{N}} \right|^2 - \left| A_{ref}^{\mathbf{N}} \right|^2 \right\} \sin \kappa = \sqrt{2}\Omega \left| A_{tra}^{x_{lat}} \right|^2 \tag{E.35}$$

Substituting the dispersion relation for the linear-elastic particle system, previously given by equation (E.12), the energy balance may be rearranged as:

$$\frac{\left|A_{ref}^{N}\right|^{2}}{\left|A_{inc}^{N}\right|^{2}} + \frac{1}{\sqrt{1 - \frac{1}{2}\Omega^{2}}} \frac{\left|A_{ira}^{N_{int}}\right|^{2}}{\left|A_{inc}^{N}\right|^{2}} = 1$$
(E.36)

The first term in equation (E.36) matches the energy reflection coefficient as derived in Section 3.3.2 for isolated incident and reflected waves. The second term in equation (E.36) relates the energy of the transmitted wave to the energy of the incident wave in a similar manner, and is therefore referred to as the energy transmission coefficient. The energy reflection and transmission coefficients for a harmonic incident wave in the discrete-continuous Hooke system are thus found as:

$$R_{E} = \left| \frac{S_{ref}^{N}}{S_{lnc}^{N}} \right| = \left| \frac{A_{ref}^{N}}{A_{lnc}^{N}} \right|^{2}, \quad T_{E} = \left| \frac{S_{trat}^{x_{lnt}}}{S_{lnc}^{N}} \right| = \frac{1}{\sqrt{1 - \frac{1}{2}\Omega^{2}}} \left| \frac{A_{trat}^{x_{lnt}}}{A_{lnc}^{N}} \right|^{2}.$$
 (E.37)

Substituting the amplitude reflection coefficient, given by equation (E.29), into the expression for the energy reflection coefficient, then yields the energy reflection coefficients as:

$$R_E = \left| \frac{2 - \frac{1}{2}\Omega^2 - \sqrt{4 - 2\Omega^2}}{2 - \frac{1}{2}\Omega^2 + \sqrt{4 - 2\Omega^2}} \right|$$
 (E.38)

For dimensionless frequencies $\Omega \le \sqrt{2}$, note that both the numerator and the denominator in equation (E.38) are real and positive.

The energy transmission coefficient is now straightforwardly determined as $T_E = 1 - R_E$.

Energy exchange at the lattice-rod interface for imaginary wavenumbers

For imaginary wavenumbers, the wavenumber and its complex conjugate are opposite. Thus, substituting $\bar{\kappa} = -\kappa$ into equation (E.34) yields the energy balance at the interface as:

$$\left\{ A_{inc}^{\mathbf{N}} \overline{A}_{ref}^{\mathbf{N}} - \overline{A}_{inc}^{\mathbf{N}} A_{ref}^{\mathbf{N}} \right\} \sin \kappa = \sqrt{2\Omega} \left| A_{tra}^{x_{Int}} \right|^2 \tag{E.39}$$

Noting that for frequencies $\Omega > \sqrt{2}$, the dispersion relation of the linear-elastic particle system follows from equation (E.12) as $\sin \kappa = i\Omega\sqrt{\Omega^2-2}$, the energy balance may be rearranged as:

$$A_{inc}^{N} \bar{A}_{ref}^{N} - \bar{A}_{inc}^{N} A_{ref}^{N} + \frac{1}{\sqrt{1 - \frac{1}{2}\Omega^{2}}} \left| A_{tra}^{x_{int}} \right|^{2} = 0$$
 (E.40)

Because the first two terms in equation (E.40) are cross terms of the amplitudes of the incident and the reflected waves, but are not related to the transmitted wave, these terms must be related to the interference between the incident and the reflected waves.

To interpret equation (E.40) further, let us first consider the energy flux of an isolated incident wave that travels through the one-dimensional Hooke lattice undisturbed. As discussed in Section 3.3.2, the energy flux at a particle $\bf n$ in the interior of one-dimensional lattice, may be obtained as:

$$S_{inc}^{\mathbf{n}} = \frac{1}{2} \left(u_{inc}^{\mathbf{n}} - u_{inc}^{\mathbf{n}-1} \right) \dot{u}_{inc}^{\mathbf{n}} \tag{E.41}$$

Assuming the incident wave to be harmonic, the real-valued displacement of the particle \mathbf{n} is described in terms of the wavenumber κ as well as in terms of its complex conjugate $\bar{\kappa}$ as:

$$u_{inc}^{\mathbf{n}} = \frac{1}{2} \left\{ A_{inc} e^{\mathrm{i}(\Omega t - \kappa \mathbf{n})} + \overline{A}_{inc} e^{-\mathrm{i}(\Omega t - \overline{\kappa} \mathbf{n})} \right\}$$
 (E.42)

Substituting equation (E.42) into equation (E.41) and averaging over a single period of the incident wave, yields the energy flux of the incident wave at a particle **n** as:

$$S_{inc}^{\mathbf{n}} = \frac{1}{8} i \Omega \left(e^{+i\kappa} - e^{-i\overline{\kappa}} \right) A_{inc} \overline{A}_{inc} e^{-i(\kappa - \overline{\kappa})\mathbf{n}}$$
(E.43)

Introducing $A_{inc}^{\mathbf{n}} = A_{inc}e^{-i\kappa\mathbf{n}}$ and $\overline{A}_{inc}^{\mathbf{n}} = \overline{A}_{inc}e^{+i\kappa\overline{\mathbf{n}}}$ as the wave amplitude and its complex conjugate at particle \mathbf{n} , as well as substituting $\overline{\kappa} = \kappa$ for $\Omega \le \sqrt{2}$, and $\overline{\kappa} = -\kappa$ for $\Omega > \sqrt{2}$ respectively, shows that for a harmonic incident wave, the energy flux at a particle \mathbf{n} reads:

$$S_{inc}^{\mathbf{n}} = \begin{cases} -\frac{1}{4}\Omega \sin \kappa \left| A_{inc}^{\mathbf{n}} \right|^2, & \Omega \le \sqrt{2} \\ 0, & \Omega > \sqrt{2} \end{cases}$$
 (E.44)

According to equation (E.44), there is no energy flux, and therefore no transfer of energy through the one-dimensional Hooke lattice for dimensionless frequencies $\Omega > \sqrt{2}$. Therefore, $\Omega_{co} = \sqrt{2}$ is the dimensionless cutoff frequency above which waves do not propagate in the Hooke lattice.

E.5 Reflection coefficients for discrete-continuous KV systems

Amplitude coefficients for the discrete-continuous Kelvin-Voigt system

The amplitude reflection coefficient at the boundary particle **N** of the one-dimensional discrete-continuous Kelvin-Voigt system is obtained starting from its equation of motion, previously obtained in Section 3.2.2 as:

$$M^{N}\ddot{u}^{N} + C_{e}^{N-1,N}\left(\dot{u}^{N} - \dot{u}^{N-1}\right) + K_{e}^{N-1,N}\left(u^{N} - u^{N-1}\right) = \zeta \dot{u}'(x_{lnt},t) + \frac{1}{2}u'(x_{lnt},t)$$
(E.45)

In accordance with the approach for the linear-elastic system in Appendix 0, the displacements in the viscoelastic rod and the Kelvin-Voigt lattice are described by equations (E.25) and (E.26). Substituting equation (E.26) and the dimensionless dispersion relation given by equation (E.6) into equation (E.45), as well as noting that $u(x_{lnt},t)=u^N$ then yields:

$$M^{\rm N} \ddot{u}^{\rm N} + C_e^{\rm N-1,N} \left(\dot{u}^{\rm N} - \dot{u}^{\rm N-1} \right) + K_e^{\rm N-1,N} \left(u^{\rm N} - u^{\rm N-1} \right) + \frac{1}{2} {\rm i} \, \Omega \sqrt{2 + 4 {\rm i} \, \zeta \Omega} \, u^{\rm N} = 0 \eqno(E.46)$$

Then, substituting the displacement of the boundary particle N according to equation (E.25) into equation (E.46), rearranging using Euler's formula and the dispersion relations for the Kelvin-Voigt lattice, given by equation (E.17), as well as introducing $z = 2 + 4i\zeta\Omega$, yields:

$$\frac{A_{ref}e^{+i\kappa N}}{A_{inc}e^{-i\kappa N}} = \frac{-M^{N}\Omega + \frac{K_{e}^{N-1,N} + i\Omega C_{e}^{N-1,N}}{1 + 2i\zeta\Omega} \left(\Omega - i\sqrt{z - \Omega^{2}}\right) + \frac{1}{2}i\sqrt{z}}{M^{N}\Omega - \frac{K_{e}^{N-1,N} + i\Omega C_{e}^{N-1,N}}{1 + 2i\zeta\Omega} \left(\Omega + i\sqrt{z - \Omega^{2}}\right) - \frac{1}{2}i\sqrt{z}}$$
(E.47)

In the discrete-continuous Kelvin-Voigt system, the dimensionless mass of the boundary particle, as well as the dimensionless stiffness and dimensionless damping of the element between particles **N-1** and **N** are respectively found as $M^N = \frac{1}{2}$, $C_e^{N-1,N} = \zeta$ and $K_e^{N-1,N} = \frac{1}{2}$. Substituting these reduces equation (E.47) to:

$$\frac{A_{ref}e^{+i\kappa N}}{A_{lnc}e^{-i\kappa N}} = \frac{\sqrt{z - \Omega^2} - \sqrt{z}}{\sqrt{z - \Omega^2} + \sqrt{z}}$$
(E.48)

Introducing $A_{inc}^{N} = A_{inc}e^{-i\kappa N}$ and $A_{ref}^{N} = A_{ref}e^{+i\kappa N}$ as the complex amplitudes of respectively the incident and the reflected wave at the boundary particle **N**, the amplitude reflection coefficient at the boundary particle **N** of the discrete-continuous Kelvin-Voigt system reads:

$$R_A^{\mathbf{N}} = \left| \frac{A_{ref}^{\mathbf{N}}}{A_{inc}^{\mathbf{N}}} \right| = \left| \frac{A_{ref} e^{+i\kappa \mathbf{N}}}{A_{inc} e^{-i\kappa \mathbf{N}}} \right| = \left| \frac{\sqrt{z - \Omega^2} - \sqrt{z}}{\sqrt{z - \Omega^2} + \sqrt{z}} \right|$$
 (E.49)

Complex conjugate amplitude coefficients for the Kelvin-Voigt system

Alternatively, we may also derive the amplitude reflection coefficient at the boundary particle **N** in the one-dimensional Kelvin-Voigt system by expressing the displacements in the lattice and the rod in terms of their complex conjugate wavenumbers as:

$$u^{\mathbf{n}} = \overline{A}_{inc}e^{-i(\Omega t - \overline{\kappa}\mathbf{n})} + \overline{A}_{ref}e^{-i(\Omega t + \overline{\kappa}\mathbf{n})}$$
(E.50)

$$u(x,t) = \overline{A}_{tra}e^{-i(\Omega t - \overline{\kappa}_{rod}x)}$$
 (E.51)

Substituting equation (E.51) into the equation of motion of the boundary particle **N**, given by equation (E.45), as well as substituting the dimensionless dispersion relation for the complex conjugate wavenumber, given by equation (E.23), and noting that $u(x_{lnt},t) = u^N$ yields:

$$M^{N}\ddot{u}^{N} + C_{e}^{N-1,N} \left(\dot{u}^{N} - \dot{u}^{N-1} \right) + K_{e}^{N-1,N} \left(u^{N} - u^{N-1} \right) - \left(\frac{1}{2} i\Omega \sqrt{2 - 4 i \zeta \Omega} \right) u^{N} = 0$$
 (E.52)

Substituting the dimensionless material parameters of the Kelvin-Voigt lattice, respectively found as $M^N = \frac{1}{2}$, $C_e^{N-1,N} = \zeta$ and $K_e^{N-1,N} = \frac{1}{2}$, as well as equation (E.50) for the displacement of particle **N**, into equation (E.52), and rearranging the remainder using Euler's formula and by introducing $\overline{z} = 2 - 4i\zeta\Omega$, then yields the complex conjugate amplitude ratio as:

$$\frac{\overline{A}_{ref}e^{-i\overline{\kappa}N}}{\overline{A}_{lnc}e^{+i\overline{\kappa}N}} = \frac{\sqrt{\overline{z} - \Omega^2} - \sqrt{\overline{z}}}{\sqrt{\overline{z} - \Omega^2} + \sqrt{\overline{z}}}$$
(E.53)

Introducing $\overline{A}_{inc}^{\mathbf{N}} = \overline{A}_{inc}e^{-i\overline{\kappa}\mathbf{N}}$ and $\overline{A}_{ref}^{\mathbf{N}} = \overline{A}_{ref}e^{+i\overline{\kappa}\mathbf{N}}$ as the complex conjugates of the amplitudes of respectively the incident and the reflected wave at the boundary particle \mathbf{N} , the amplitude reflection coefficient at the boundary particle \mathbf{N} of the discrete-continuous Kelvin-Voigt system in terms of the complex conjugate wavenumber reads:

$$R_{\bar{A}}^{\mathbf{N}} = \left| \frac{\overline{A}_{ref}^{\mathbf{N}}}{\overline{A}_{inc}^{\mathbf{N}}} \right| = \left| \frac{\overline{A}_{ref} e^{-i\bar{\kappa}\mathbf{N}}}{\overline{A}_{inc} e^{+i\bar{\kappa}\mathbf{N}}} \right| = \left| \frac{\sqrt{\overline{z} - \Omega^2} - \sqrt{\overline{z}}}{\sqrt{\overline{z} - \Omega^2} + \sqrt{\overline{z}}} \right|$$
(E.54)

Here, note that it can be shown that the ratio $\overline{A}_{ref}^{N}/\overline{A}_{inc}^{N}$ given by equation (E.54) is, and must be, the complex conjugate of the ratio A_{ref}^{N}/A_{inc}^{N} described by equation (E.48), so that the amplitude reflection coefficients given by equations (E.49) and (E.54) must be equal.

Energy exchange at the lattice-rod interface in the viscoelastic Kelvin-Voigt system

In accordance with the approach for the discrete-continuous Hooke system, we here consider the interaction and possibly the interference between the incident wave and the reflected wave in the vicinity of the boundary particle **N**. To this purpose, we obtain the energy exchange between the incident, the reflected and the transmitted waves at the boundary particle **N** by multiplying its equation of motion, given by equation (E.45), with the velocity of the

interface. Additionally, we substitute the dimensionless material parameters of the boundary particle **N**, respectively as $M^N = \frac{1}{2}$, $C_e^{N-1,N} = \zeta$ and $K_e^{N-1,N} = \frac{1}{2}$. This yields a dimensionless energy balance that describes the energy exchange at the boundary particle **N** as:

$$\ddot{u}^{N}\dot{u}^{N} + 2\zeta(\dot{u}^{N} - \dot{u}^{N-1})\dot{u}^{N} + (u^{N} - u^{N-1})\dot{u}^{N} = 2\zeta\dot{u}'(x_{Int}, t)\dot{u}(x_{Int}, t) + u'(x_{Int}, t)\dot{u}(x_{Int}, t)$$
(E.55)

In the energy balance given by equation (E.55), the first term on the left-hand side describes the change in kinetic energy of the boundary particle over time. Furthermore, the second term on the left-hand side and the first term on the right-hand side describe the energy dissipation due to the damping respectively in the lattice and the rod over time. The third term on the left-hand side and the second term on the right-hand side give the energy fluxes through the lattice-rod interface by respectively the lattice and the rod.

According to the dispersion relations for the one-dimensional viscoelastic particle system and the viscoelastic rod, given in respectively Appendix E.3 and Appendix E.1, the wavenumbers are complex-valued for any real non-zero frequency. To assure real-valued expressions for the displacements in the lattice and the rod, we account for both the wavenumbers and their complex conjugates. This yields the displacements of the lattice particles and along the viscoelastic rod as:

$$u^{\mathbf{n}} = \frac{1}{2} \left\{ A_{inc} e^{\mathrm{i}(\Omega_t - \kappa \mathbf{n})} + \overline{A}_{inc} e^{-\mathrm{i}(\Omega_t - \overline{\kappa} \mathbf{n})} \right\} + \frac{1}{2} \left\{ A_{ref} e^{\mathrm{i}(\Omega_t + \kappa \mathbf{n})} + \overline{A}_{ref} e^{-\mathrm{i}(\Omega_t + \overline{\kappa} \mathbf{n})} \right\}$$
(E.56)

$$u(x,t) = \frac{1}{2} \left\{ A_{tra} e^{i(\Omega t - \kappa_{rod} x)} + \overline{A}_{tra} e^{-i(\Omega t - \overline{\kappa}_{rod} x)} \right\}$$
 (E.57)

Here, the amplitudes \overline{A}_{inc} , \overline{A}_{ref} and \overline{A}_{tra} are the complex conjugates of the dimensionless amplitudes A_{inc} , A_{ref} and A_{tra} of the incident, reflected and transmitted waves respectively. Furthermore, $\overline{\kappa}$ and $\overline{\kappa}_{rod}$ are the complex conjugates of the dimensionless wavenumbers κ and κ_{rod} in respectively the Kelvin-Voigt lattice and the viscoelastic rod.

Substituting equations (E.56) and (E.57) into equation (E.55), and subsequently substituting the dispersion relations for the dimensionless wavenumber κ and its complex conjugate, given by equations (E.17) and (E.23), as well as the dispersion relations for the dimensionless wavenumber κ_{rod} of the viscoelastic rod and its complex conjugate, respectively given by equations (E.6) and (E.8), then averaging the energy balance over a single period of the harmonic incident wave, as well as introducing both $z = 2 + 4i\zeta\Omega$ and its complex conjugate $\bar{z} = 2 - 4i\zeta\Omega$, yields the energy exchange at the boundary particle N as:

$$\left(\sqrt{z-\Omega^{2}} + \sqrt{\overline{z}-\Omega^{2}}\right)\left(A_{inc}\overline{A}_{inc}e^{-\mathrm{i}(\kappa-\overline{\kappa})\mathbf{N}} - A_{ref}\overline{A}_{ref}e^{+\mathrm{i}(\kappa-\overline{\kappa})\mathbf{N}}\right)
+ \left(\sqrt{z-\Omega^{2}} - \sqrt{\overline{z}-\Omega^{2}}\right)\left(A_{inc}\overline{A}_{ref}e^{-\mathrm{i}(\kappa+\overline{\kappa})\mathbf{N}} - A_{ref}\overline{A}_{inc}e^{+\mathrm{i}(\kappa+\overline{\kappa})\mathbf{N}}\right)
= \left(\sqrt{z} + \sqrt{\overline{z}}\right)A_{tra}\overline{A}_{tra}e^{-\mathrm{i}(\kappa_{rod}-\overline{\kappa}_{rod})x_{Int}}$$
(E.58)

Here, note that both the particle number N and the coordinate x_{Int} present in the exponents of the transmitted, incident and reflected waves describe the decay of the wave amplitude at interface relative to the wave amplitudes A_{inc} , A_{ref} and A_{tra} . Thus, introducing the wave amplitudes of the incident, reflected and transmitted waves at the interface as $A_{inc}^{N} = A_{inc}e^{-i\kappa N}$, $A_{ref}^{N} = A_{ref}e^{+i\kappa N}$ and $A_{tra}^{x_{Int}} = A_{tra}e^{-i\kappa_{rod}x_{Int}}$, as well as introducing the corresponding complex conjugate wave amplitudes as $\overline{A}_{inc}^{N} = \overline{A}_{inc}e^{+i\kappa N}$, $\overline{A}_{ref}^{N} = \overline{A}_{ref}e^{-i\kappa N}$ and $\overline{A}_{tra}^{x_{Int}} = \overline{A}_{tra}e^{+i\overline{\kappa}_{rod}x_{Int}}$, we can rewrite equation (E.58) as:

$$\left(\sqrt{z-\Omega^{2}} + \sqrt{\overline{z}-\Omega^{2}}\right)\left(A_{inc}^{N}\overline{A}_{inc}^{N} - A_{ref}^{N}\overline{A}_{ref}^{N}\right) + \left(\sqrt{z-\Omega^{2}} - \sqrt{\overline{z}-\Omega^{2}}\right)\left(A_{inc}^{N}\overline{A}_{ref}^{N} - A_{ref}^{N}\overline{A}_{inc}^{N}\right) = \left(\sqrt{z} + \sqrt{\overline{z}}\right)A_{tra}^{x_{lnt}}\overline{A}_{tra}^{x_{lnt}}$$
(E.59)

Rearranging equation (E.59) by first isolating $\left|A_{inc}^{N}\right|^{2}$ and then dividing by $\left|A_{inc}^{N}\right|^{2}$, we find the energy balance at the discrete-continuous interface of the one-dimensional Kelvin-Voigt system as:

$$\left|\frac{A_{ref}^{N}}{A_{inc}^{N}}\right|^{2} + \frac{\sqrt{z-\Omega^{2}} - \sqrt{\overline{z}-\Omega^{2}}}{\sqrt{z-\Omega^{2}} + \sqrt{\overline{z}-\Omega^{2}}} \left(\frac{\overline{A}_{inc}^{N} A_{ref}^{N}}{\left|A_{inc}^{N}\right|^{2}} - \frac{A_{inc}^{N} \overline{A}_{ref}^{N}}{\left|A_{inc}^{N}\right|^{2}}\right) + \frac{\sqrt{z} + \sqrt{\overline{z}}}{\sqrt{z-\Omega^{2}} + \sqrt{\overline{z}-\Omega^{2}}} \left|\frac{A_{tra}^{x_{int}}}{A_{inc}^{N}}\right|^{2} = 1 \quad (E.60)$$

As explained in Section 3.2.2, the first term in equation (E.60) is the energy reflection coefficient, previously given by equation (E.37), the second term is an interference term that we refer to as the energy interference coefficient and the third term in equation (E.60) gives the energy transmission coefficient. Noting that the energy interference coefficient can be further simplified, the three obtained energy coefficients are separately obtained as:

$$R_E = \left| \frac{A_{ref}^{\rm N}}{A_{inc}^{\rm N}} \right|^2 \tag{E.61}$$

$$I_{E} = \frac{\sqrt{z - \Omega^{2}} - \sqrt{\overline{z} - \Omega^{2}}}{\sqrt{z - \Omega^{2}} + \sqrt{\overline{z} - \Omega^{2}}} \left(\frac{A_{ref}^{N}}{A_{inc}^{N}} - \frac{\overline{A}_{ref}^{N}}{\overline{A}_{inc}^{N}} \right)$$
(E.62)

$$T_E = \frac{\sqrt{z} + \sqrt{\overline{z}}}{\sqrt{z - \Omega^2} + \sqrt{\overline{z} - \Omega^2}} \left| \frac{A_{tra}^{x_{lnt}}}{A_{inc}^{N}} \right|^2$$
 (E.63)

For the particular case that there is no damping, i.e. $\zeta = 0$, it follows that $z = \overline{z} = 2$, so that equations (E.61) and (E.63) for the one-dimensional discrete-continuous Kelvin-Voigt system reduce to equations (E.37) for the one-dimensional discrete-continuous Hooke system. Accordingly, for zero damping, it follows from equation (E.62) that the energy interference coefficient is equal to zero, i.e. $I_E = 0$, thus explaining its absence in the energy balance for the one-dimensional discrete-continuous Hooke system, given by equation (E.36).

F The dynamic compliance of the continuous layer

The expression for the dynamic compliance matrix of the continuous layer with a surface cavity is found in Section 3.5.1 as:

$$\underline{\underline{\tilde{\beta}}}(s) = \underline{\underline{\tilde{T}}}(s)^{-1} \underline{\underline{\tilde{G}}}(s) \left(\underline{\underline{\tilde{T}}}(s)^{-1}\right)^{T}$$
(F.1)

Here, $\underline{\tilde{T}}(s)$ is known as the lumping matrix, while $\underline{\tilde{G}}(s)$ is commonly known as the flexibility matrix. The properties of the lumping and flexibility matrices are discussed in the following two sections of this appendix respectively. Additionally, in Appendix F.2, the symmetry of the flexibility matrix, and thereby the symmetry of the dynamic compliance matrix, is proven mathematically. The terms appearing in the lumping and flexibility matrices follow from the Green's functions for the displacements, tractions and stresses in the continuum. For quick reading, these Green's functions are respectively referred to as Green's displacements, Green's tractions and Green's stresses.

In Appendix F.3, the governing equations for the displacements and stresses are derived using Helmholtz' orthogonal decomposition and transformed to the Laplace-wavenumber domain. Finally, in Appendices F.4 and F.5, the Green's functions for the displacements and stresses are determined for a load inside and for a load at the surface of the continuum respectively.

F.1 Properties of the lumping matrix

The lumping matrix was previously given in Section 3.5.1 as:

$$\underline{\underline{T}}(s) = \int_{\Gamma} \underline{t}_{1}(\xi, s)^{T} \underline{\underline{H}}(\xi) d\xi \tag{F.2}$$

Here, the modified Green's traction matrix $\tilde{t}_{\underline{1}}(\xi, s)$ contains the so-called modified Green's functions for the tractions along the boundary Γ that are due to a unit load distribution along the boundary Γ . Furthermore, $\underline{\underline{H}}(\xi)$ is a matrix that contains Heaviside functions for the subdomains of all boundary particles. In matrix notation, the modified Green's traction matrix and the Heaviside matrix respectively read:

$$\tilde{t}_{1}(\xi,s) = \begin{bmatrix} \tilde{t}_{1;xx}^{1}(\xi,s) & \tilde{t}_{1;xz}^{1}(\xi,s) & \cdots & \tilde{t}_{1;xx}^{N_{\text{Int}}}(\xi,s) & \tilde{t}_{1;xz}^{N_{\text{Int}}}(\xi,s) \\ \tilde{t}_{1;zx}^{1}(\xi,s) & \tilde{t}_{1;zz}^{1}(\xi,s) & \cdots & \tilde{t}_{1;zx}^{N_{\text{Int}}}(\xi,s) & \tilde{t}_{1;zz}^{N_{\text{Int}}}(\xi,s) \end{bmatrix}$$
(F.3)

$$\underline{\underline{H}}(\xi) = \begin{bmatrix} H^{1}(\xi) & 0 & \cdots & H^{N_{\text{Int}}}(\xi) & 0 \\ 0 & H^{1}(\xi) & \cdots & 0 & H^{N_{\text{Int}}}(\xi) \end{bmatrix}$$
 (F.4)

For a two-dimensional system, there are four relations between any two particles and consequently, the lumping matrix is a square matrix with the order $2N_{Int}$, where N_{Int} is the number of particles at the lattice-continuum interface. The four terms in the lumping matrix that

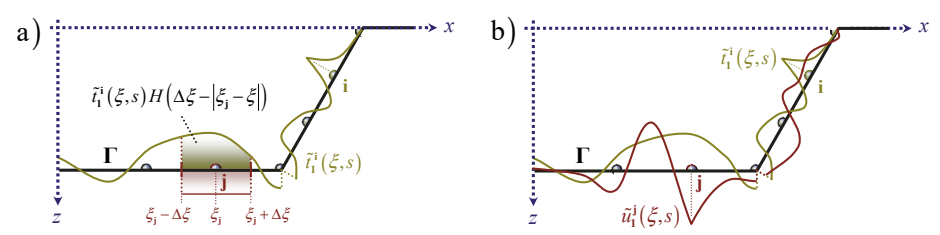


Figure F.1: a) The Green's tractions along Γ due to a unit load distribution at particle i versus the Heaviside function at particle j; b) The Green's tractions and displacements along Γ due to unit load distributions at particles i and j.

describe the lumping relation between two particles **i** and **j** along the boundary Γ are:

$$\tilde{T}_{2i-1,2j-1}(s) = \int_{\Gamma} \tilde{t}_{1;xx}^{i}(\xi,s) H(\Delta \xi - |\xi_{j} - \xi|) d\xi = \int_{\xi_{j} - \Delta \xi}^{\xi_{j} + \Delta \xi} \tilde{t}_{1;xx}^{i}(\xi,s) d\xi$$
 (F.5)

$$\tilde{T}_{2\mathbf{i}-1,2\mathbf{j}}(s) = \int_{\Gamma} \tilde{t}_{1;zx}^{\mathbf{i}}(\xi,s) H(\Delta \xi - |\xi_{\mathbf{j}} - \xi|) d\xi = \int_{\xi_{\mathbf{j}}-\Delta \xi}^{\xi_{\mathbf{j}}+\Delta \xi} \tilde{t}_{1;zx}^{\mathbf{i}}(\xi,s) d\xi$$
(F.6)

$$\tilde{T}_{2i,2j-1}(s) = \int_{\Gamma} \tilde{t}_{1;xz}^{i}(\xi,s) H(\Delta \xi - |\xi_{j} - \xi|) d\xi = \int_{\xi_{j} - \Delta \xi}^{\xi_{j} + \Delta \xi} \tilde{t}_{1;xz}^{i}(\xi,s) d\xi$$
(F.7)

$$\tilde{T}_{2\mathbf{i},2\mathbf{j}}\left(s\right) = \int_{\Gamma} \tilde{t}_{\mathbf{l};zz}^{\mathbf{i}}\left(\xi,s\right) H\left(\Delta\xi - \left|\xi_{\mathbf{j}} - \xi\right|\right) d\xi = \int_{\xi_{\mathbf{j}} - \Delta\xi} \tilde{t}_{\mathbf{l};zz}^{\mathbf{i}}\left(\xi,s\right) d\xi \tag{F.8}$$

Here, the numerator \mathbf{i} refers to the particle at the boundary Γ at which the unit load distribution is applied that generates the modified Green's tractions along Γ . Consequently, the modified Green's traction $\tilde{t}^i_{1;ab}(\xi,s)$ is the traction along the boundary Γ in the direction of the index a due to a unit load distribution at the boundary particle \mathbf{i} in the direction of the index b. For example, $\tilde{t}^i_{1;xz}(\xi,s)$ is the horizontal Green's traction along Γ due to the vertical unit load distribution at particle \mathbf{i} .

The numerator \mathbf{j} denotes the particle on the boundary Γ for which the subdomain along Γ is considered. An example of the integrand of a term in the lumping matrix $\underline{\tilde{I}}(s)$ is depicted in Figure F.1a, where the green line shows an arbitrary modified Green's traction $\tilde{t}_{\mathbf{i}}^{\mathbf{i}}(\xi,s)$ along the boundary Γ , due to a unit load distribution at particle \mathbf{i} and the red line shows the Heaviside function $H(\Delta \xi - |\xi_{\mathbf{j}} - \xi|)$ at particle \mathbf{j} . For example the term $\tilde{T}_{2\mathbf{i},2\mathbf{j}-\mathbf{i}}(s)$ may thus be considered as the result of all horizontal tractions on the domain of particle \mathbf{j} due to the unit load distribution applied at particle \mathbf{i} .

F.2 Properties of the flexibility matrix

The flexibility matrix was previously given in Section 3.5.1 as:

$$\underline{\underline{\underline{G}}}(s) = \int_{\Gamma} \underline{\tilde{t}}_{1}(\xi, s)^{\mathrm{T}} \underline{\tilde{u}}_{1}(\xi, s) d\xi \tag{F.9}$$

In accordance with the modified Green's traction matrix $\tilde{l}_1(\xi,s)$, the modified Green's displacement matrix $\tilde{\underline{u}}_1(\xi,s)$ contains the so-called modified Green's functions for the displacements along the boundary Γ due to a unit load distribution along the boundary Γ , and may be expressed in matrix notation in accordance with equation (F.3).

For a two-dimensional boundary Γ , the flexibility matrix is a square matrix with the order $2N_{\text{Int}}$, where N_{Int} is the number of particles along Γ . The modified Green's tractions and modified Green's displacements compose the terms in the flexibility matrix $\tilde{G}(s)$ as:

$$\tilde{G}_{2i-1,2j-1}(s) = \int_{\Gamma} \tilde{t}_{1;xx}^{i}(\xi,s) \tilde{u}_{1;xx}^{j}(\xi,s) d\xi + \int_{\Gamma} \tilde{t}_{1;zx}^{i}(\xi,s) \tilde{u}_{1;zx}^{j}(\xi,s) d\xi$$
(F.10)

$$\tilde{G}_{2i-1,2j}(s) = \int_{\Gamma} \tilde{t}_{1;xx}^{i}(\xi,s) \tilde{u}_{1;xz}^{j}(\xi,s) d\xi + \int_{\Gamma} \tilde{t}_{1;xx}^{i}(\xi,s) \tilde{u}_{1;zz}^{j}(\xi,s) d\xi$$
(F.11)

$$\tilde{G}_{2i,2j-1}(s) = \int_{\Gamma} \tilde{t}_{1;xx}^{i}(\xi,s) \tilde{u}_{1;xx}^{j}(\xi,s) d\xi + \int_{\Gamma} \tilde{t}_{1;zx}^{i}(\xi,s) \tilde{u}_{1;xx}^{j}(\xi,s) d\xi$$
(F.12)

$$\tilde{G}_{2i,2j}(s) = \int_{\Gamma} \tilde{t}_{1;xz}^{i}(\xi, s) \tilde{u}_{1;xz}^{j}(\xi, s) d\xi + \int_{\Gamma} \tilde{t}_{1;zz}^{i}(\xi, s) \tilde{u}_{1;zz}^{j}(\xi, s) d\xi$$
(F.13)

Here, **i** refers to the particle on the boundary Γ at which the unit load distribution is applied that generates the considered modified Green's tractions, while **j** refers to the particle on the boundary Γ at which the unit load distribution is applied that generates the considered Green's displacement. The modified Green's traction $\tilde{t}^i_{1;ab}\left(\xi,s\right)$ and modified Green's displacement $\tilde{u}^j_{1;ab}\left(\xi,s\right)$ are respectively the traction and the displacement along Γ in the direction of index a due to the unit load distribution applied at respectively particles **i** and **j** in the direction of the index b. For example, the modified Green's displacement $\tilde{u}^i_{1;xz}\left(\xi,s\right)$ is the horizontal displacement along Γ due to a vertical unit load distribution at particle **j**.

An example of the integrand of a term in the flexibility matrix $\underline{\underline{G}}(s)$ is given in Figure F.1b. Here, the green line shows the modified Green's traction $\tilde{t}_1^i(\xi, s)$ along Γ due to a unit load distribution at a particle i, while the red line shows the modified Green's displacement $\tilde{u}_1^i(\xi, s)$ along Γ due to a unit load distribution at particle j.

Proof of symmetry in the flexibility matrix

The symmetry of the flexibility matrix can be mathematically proven by showing that all terms in the flexibility matrix are exactly equal to their symmetric counterparts.

For each combination of the particles **i** and **j**, the flexibility matrix consists of the four terms given by equations (F.10) to (F.13). The flexibility matrix can only be symmetric if each of these terms is equal to its symmetric counterpart, thus its symmetry is proven by showing that:

$$\tilde{G}_{2i-1,2j-1}(s) = \tilde{G}_{2j-1,2i-1}(s)$$
 (F.14)

$$\tilde{G}_{2i-1,2i}(s) = \tilde{G}_{2i,2i-1}(s)$$
 (F.15)

$$\tilde{G}_{2i,2j-1}(s) = \tilde{G}_{2j-1,2i}(s)$$
 (F.16)

$$\tilde{G}_{2i,2j}(s) = \tilde{G}_{2j,2i}(s) \tag{F.17}$$

Substituting equations (F.10) to (F.13) into equations (F.14) to (F.17) yields:

$$\int_{\Gamma} \tilde{t}_{1;xx}^{i}(\xi,s) \tilde{u}_{1;xx}^{j}(\xi,s) d\xi + \int_{\Gamma} \tilde{t}_{1;xx}^{i}(\xi,s) \tilde{u}_{1;xx}^{j}(\xi,s) d\xi
= \int_{\Gamma} \tilde{t}_{1;xx}^{j}(\xi,s) \tilde{u}_{1;xx}^{i}(\xi,s) d\xi + \int_{\Gamma} \tilde{t}_{1;xx}^{j}(\xi,s) \tilde{u}_{1;xx}^{i}(\xi,s) d\xi$$
(F.18)

$$\int_{\Gamma} \tilde{t}_{1;xx}^{i}(\xi,s) \tilde{u}_{1;xz}^{j}(\xi,s) d\xi + \int_{\Gamma} \tilde{t}_{1;xx}^{i}(\xi,s) \tilde{u}_{1;zz}^{j}(\xi,s) d\xi
= \int_{\Gamma} \tilde{t}_{1;xz}^{j}(\xi,s) \tilde{u}_{1;xx}^{i}(\xi,s) d\xi + \int_{\Gamma} \tilde{t}_{1;zz}^{j}(\xi,s) \tilde{u}_{1;zx}^{i}(\xi,s) d\xi$$
(F.19)

$$\int_{\Gamma} \tilde{t}_{1;xz}^{i}(\xi,s) \tilde{u}_{1;xx}^{j}(\xi,s) d\xi + \int_{\Gamma} \tilde{t}_{1;zz}^{i}(\xi,s) \tilde{u}_{1;zx}^{j}(\xi,s) d\xi
= \int_{\Gamma} \tilde{t}_{1;xx}^{j}(\xi,s) \tilde{u}_{1;xz}^{i}(\xi,s) d\xi + \int_{\Gamma} \tilde{t}_{1;zx}^{j}(\xi,s) \tilde{u}_{1;zz}^{i}(\xi,s) d\xi$$
(F.20)

$$\int_{\Gamma} \tilde{t}_{1;xz}^{i}(\xi,s) \tilde{u}_{1;xz}^{j}(\xi,s) d\xi + \int_{\Gamma} \tilde{t}_{1;zz}^{i}(\xi,s) \tilde{u}_{1;zz}^{j}(\xi,s) d\xi
= \int_{\Gamma} \tilde{t}_{1;xz}^{j}(\xi,s) \tilde{u}_{1;xz}^{i}(\xi,s) d\xi + \int_{\Gamma} \tilde{t}_{1;zz}^{j}(\xi,s) \tilde{u}_{1;zz}^{i}(\xi,s) d\xi$$
(F.21)

Each of the modified Green's displacements and tractions can be multiplied by corresponding load magnitudes to obtain displacements and tractions along Γ . Thus, multiplying equation (F.18) by the magnitude of the horizontal loads at both particles \mathbf{i} and \mathbf{j} , i.e. P_x^i and P_x^j , then yields the relations between the actual displacements and tractions along the boundary Γ due to the loads applied at particles \mathbf{i} and \mathbf{j} . Accordingly, we multiply equation (F.19) with P_x^i and P_z^j , equation (F.20) with P_z^i and equation (F.21) with P_z^i and P_z^j . This yields:

$$\int_{\Gamma} \tilde{t}_{:x}^{i} \left(\xi, s\right)^{\mathrm{T}} \underline{\tilde{u}}_{:x}^{j} \left(\xi, s\right) d\xi = \int_{\Gamma} \tilde{t}_{:x}^{j} \left(\xi, s\right)^{\mathrm{T}} \underline{\tilde{u}}_{:x}^{i} \left(\xi, s\right) d\xi \tag{F.22}$$

$$\int_{\Gamma} \underline{\tilde{t}}_{:x}^{i} (\xi, s)^{\mathsf{T}} \underline{\tilde{u}}_{:z}^{j} (\xi, s) d\xi = \int_{\Gamma} \underline{\tilde{t}}_{:z}^{j} (\xi, s)^{\mathsf{T}} \underline{\tilde{u}}_{:x}^{i} (\xi, s) d\xi \tag{F.23}$$

$$\int_{\Gamma} \underline{\tilde{t}}_{:z}^{i} (\xi, s)^{\mathsf{T}} \underline{\tilde{u}}_{:x}^{j} (\xi, s) d\xi = \int_{\Gamma} \underline{\tilde{t}}_{:x}^{j} (\xi, s)^{\mathsf{T}} \underline{\tilde{u}}_{:z}^{i} (\xi, s) d\xi \tag{F.24}$$

$$\left[\tilde{t}_{:z}^{i} \left(\xi, s \right)^{\mathsf{T}} \tilde{u}_{:z}^{j} \left(\xi, s \right) d\xi = \left[\tilde{t}_{:z}^{j} \left(\xi, s \right)^{\mathsf{T}} \tilde{u}_{:z}^{i} \left(\xi, s \right) d\xi \right]$$
 (F.25)

Here, $\underline{\tilde{u}}_{;a}^{\mathbf{n}}(\xi,s)$ and $\underline{\tilde{t}}_{;a}^{\mathbf{n}}(\xi,s)$ respectively describe the displacements and tractions along the boundary Γ due to a load applied at particle \mathbf{n} , where the load is in the direction of index a.

Equations (F.22) to (F.25) all honour the dynamic reciprocal work theorem and since they hold for all combinations of particles i and j, all terms in the flexibility matrix are equal to their symmetric counterparts and the flexibility matrix is thereby proven to be symmetric.

F.3 Displacements and stresses in the Laplace-wavenumber domain

Assuming plane-strain conditions, the displacements and stresses in a continuum due to a dynamic load are derived from the two-dimensional elastodynamic equation that reads:

$$\rho \underline{\ddot{u}}(x,z,t) = (\hat{\lambda} + \hat{\mu}) \nabla_{x,z} (\nabla_{x,z} \cdot \underline{u}(x,z,t)) + \hat{\mu} \nabla_{x,z}^2 \underline{u}(x,z,t)$$
 (F.26)

Applying Helmholtz' orthogonal decomposition, we express the continuum displacement vector as $\underline{u}(x,z,t) = \nabla \times \underline{\psi} + \nabla \phi$. For plane-strain conditions, the Lamé vector potential $\underline{\psi}$ and the Lamé scalar potential ϕ are respectively chosen as $\underline{\psi} = (0, -\psi(x,z,t))$ and $\phi = \phi(x,z,t)$. From Helmholtz' orthogonal decomposition, it then follows directly that the displacements of a continuum may be expressed through the Lamé potentials as:

$$u_{x}(x,z,t) = \frac{\partial \phi}{\partial x} + \frac{\partial \psi}{\partial z}, \qquad u_{z}(x,z,t) = -\frac{\partial \psi}{\partial x} + \frac{\partial \phi}{\partial z}$$
 (F.27)

Using elasticity theory, the stresses inside a continuum may be derived in terms of the Lamé potentials from equation (F.27) as:

$$\sigma_{xx}(x,z,t) = \hat{\lambda} \left(\frac{\partial^2 \phi}{\partial x^2} + \frac{\partial^2 \phi}{\partial z^2} \right) + 2\hat{\mu} \left(\frac{\partial^2 \phi}{\partial x^2} + \frac{\partial^2 \psi}{\partial x \partial z} \right)$$
 (F.28)

$$\sigma_{zx}(x,z,t) = \sigma_{xz}(x,z,t) = \hat{\mu}\left(-\frac{\partial^2 \psi}{\partial x^2} + 2\frac{\partial^2 \phi}{\partial x \partial z} + \frac{\partial^2 \psi}{\partial z^2}\right)$$
 (F.29)

$$\sigma_{zz}(x,z,t) = \hat{\lambda} \left(\frac{\partial^2 \phi}{\partial x^2} + \frac{\partial^2 \phi}{\partial z^2} \right) + 2\hat{\mu} \left(-\frac{\partial^2 \psi}{\partial x \partial z} + \frac{\partial^2 \phi}{\partial z^2} \right)$$
 (F.30)

Applying the Fourier transform with respect to horizontal space and the Laplace transform with respect to time to equations (F.27) to (F.30) yields the displacements and stresses in the Laplace-wavenumber domain as:

$$\tilde{\tilde{u}}_{x}(k,z,s) = ik\tilde{\tilde{\phi}} + \frac{\partial \tilde{\tilde{\psi}}}{\partial z}, \qquad \qquad \tilde{\tilde{u}}_{z}(k,z,s) = -ik\tilde{\tilde{\psi}} + \frac{\partial \tilde{\tilde{\phi}}}{\partial z}$$
(F.31)

$$\tilde{\sigma}_{xx}(k,z,s) = -(\hat{\lambda} + 2\hat{\mu})k^{2}\tilde{\tilde{\phi}} + \hat{\lambda}\frac{\partial^{2}\tilde{\tilde{\phi}}}{\partial z^{2}} + 2\hat{\mu}ik\frac{\partial\tilde{\tilde{\psi}}}{\partial z}$$
(F.32)

$$\tilde{\tilde{\sigma}}_{zx}(k,z,s) = \tilde{\tilde{\sigma}}_{xz}(k,z,s) = \hat{\mu}\left(k^2\tilde{\tilde{\psi}} + \frac{\partial^2\tilde{\tilde{\psi}}}{\partial z^2}\right) + 2ik\hat{\mu}\frac{\partial^2\tilde{\tilde{\phi}}}{\partial z}$$
 (F.33)

$$\tilde{\tilde{\sigma}}_{zz}(k,z,s) = -\hat{\lambda}k^{2}\tilde{\tilde{\phi}} + (\hat{\lambda} + 2\hat{\mu})\frac{\partial^{2}\tilde{\tilde{\phi}}}{\partial z^{2}} - 2\hat{\mu}ik\frac{\partial\tilde{\tilde{\psi}}}{\partial z}$$
(F.34)

Substituting the displacement vector according to Helmholtz' decomposition into equation (F.26), the two-dimensional elastodynamic equation splits into two independent expressions for the Lamé scalar and vector potentials:

$$\ddot{\psi} - \hat{c}_S^2 \left(\frac{\partial^2 \psi}{\partial x^2} + \frac{\partial^2 \psi}{\partial z^2} \right) = 0, \qquad \ddot{\phi} - \hat{c}_P^2 \left(\frac{\partial^2 \phi}{\partial x^2} + \frac{\partial^2 \phi}{\partial z^2} \right) = 0.$$
 (F.35)

Applying the Fourier and Laplace transforms with respect to respectively space and time to equations (F.35) then yields:

$$\frac{\partial^2 \tilde{\tilde{\psi}}}{\partial z^2} - R_S \tilde{\tilde{\psi}} = 0, \qquad \qquad \frac{\partial^2 \tilde{\tilde{\phi}}}{\partial z^2} - R_P \tilde{\tilde{\phi}} = 0.$$
 (F.36)

where R_S and R_P are respectively found as $R_S^2 = k^2 + s^2/\hat{c}_S^2$ and $R_P^2 = k^2 + s^2/\hat{c}_P^2$. The general solutions to equations (F.36) are respectively found as:

$$\tilde{\tilde{\psi}} = A_1 e^{+R_S z} + A_2 e^{-R_S z}, \qquad \qquad \tilde{\tilde{\phi}} = A_3 e^{+R_P z} + A_4 e^{-R_P z}. \tag{F.37}$$

Substituting the Lamé potentials from equation (F.37) into equations (F.31) to (F.34) then gives the displacements and stresses in the continuum as:

$$\tilde{\tilde{u}}_{x}(k,z,s) = R_{S} \left(A_{1} e^{+R_{S}z} - A_{2} e^{-R_{S}z} \right) + ik \left(A_{3} e^{+R_{P}z} + A_{4} e^{-R_{P}z} \right)$$
 (F.38)

$$\tilde{\tilde{u}}_z(k,z,s) = -ik(A_1 e^{+R_S z} + A_2 e^{-R_S z}) + R_P(A_3 e^{+R_P z} - A_4 e^{-R_P z})$$
(F.39)

$$\tilde{\tilde{\sigma}}_{xx}(k,z,s) = 2\hat{\mu}ikR_S \left(A_1 e^{+R_S z} - A_2 e^{-R_S z} \right) - \hat{\mu}\gamma_P \left(A_3 e^{+R_P z} + A_4 e^{-R_P z} \right)$$
 (F.40)

$$\tilde{\tilde{\sigma}}_{zx}(k,z,s) = \tilde{\tilde{\sigma}}_{xz}(k,z,s) = \hat{\mu}\gamma_S(A_1e^{+R_Sz} + A_2e^{-R_Sz}) + 2ik\hat{\mu}R_P(A_3e^{+R_Pz} - A_4e^{-R_Pz})$$
 (F.41)

$$\tilde{\tilde{\sigma}}_{zz}(k,z,s) = -2\hat{\mu}ikR_S\left(A_1e^{+R_Sz} - A_2e^{-R_Sz}\right) + \hat{\mu}\gamma_S\left(A_3e^{+R_Pz} + A_4e^{-R_Pz}\right)$$
(F.42)

Here, γ_S and γ_P are respectively found as $\gamma_S = 2R_S^2 - s^2/\hat{c}_S^2$ and $\gamma_P = 2R_P^2 - s^2/\hat{c}_S^2$.

F.4 Green's functions for a load inside the continuous layer

Substituting the expressions for the displacements of and stresses in the continuous layer, previously obtained in the Laplace-wavenumber domain in Appendix F.3, into the boundary conditions for a load inside the continuous layer, given in Section 3.5.3, yields the system of eight algebraic equations that is to be solved for the wave amplitudes A_1 to A_8 . Thus, at the surface of the continuous layer, we find:

$$\hat{\mu}\gamma_{S}(A_{1} + A_{2}) + 2\hat{\mu}ikR_{P}(A_{3} - A_{4}) = 0$$
(F.43)

$$-2\hat{\mu}ikR_{S}(A_{1}-A_{2})+\hat{\mu}\gamma_{S}(A_{3}+A_{4})=0$$
 (F.44)

Furthermore, at the horizontal level of the applied unit load, substitution of the corresponding displacements and stresses yields the following boundary conditions:

$$R_{S}\left(\left(A_{5}-A_{1}\right)e^{+R_{S}z_{1}}-\left(A_{6}-A_{2}\right)e^{-R_{S}z_{1}}\right)+ik\left(\left(A_{7}-A_{3}\right)e^{+R_{P}z_{1}}+\left(A_{8}-A_{4}\right)e^{-R_{P}z_{1}}\right)=0 \tag{F.45}$$

$$-ik((A_5 - A_1)e^{+R_5z_1} + (A_6 - A_2)e^{-R_5z_1}) + R_P((A_7 - A_3)e^{+R_Pz_1} - (A_8 - A_4)e^{-R_Pz_1}) = 0 \quad (F.46)$$

$$+\hat{\mu}\gamma_{S}\left(\left(A_{5}-A_{1}\right)e^{+R_{S}z_{i}}+\left(A_{6}-A_{2}\right)e^{-R_{S}z_{i}}\right) +2\hat{\mu}ikR_{P}\left(\left(A_{7}-A_{3}\right)e^{+R_{P}z_{i}}-\left(A_{8}-A_{4}\right)e^{-R_{P}z_{i}}\right)=\tilde{\tilde{p}}_{1,x}\left(k\right)e^{-ikx_{i}}$$
(F.47)

$$-2\hat{\mu}ikR_{S}\left(\left(A_{5}-A_{1}\right)e^{+R_{S}z_{i}}-\left(A_{6}-A_{2}\right)e^{-R_{S}z_{i}}\right) + \hat{\mu}\gamma_{S}\left(\left(A_{7}-A_{3}\right)e^{+R_{P}z_{i}}+\left(A_{8}-A_{4}\right)e^{-R_{P}z_{i}}\right) = \tilde{\tilde{p}}_{1,z}\left(k\right)e^{-ikx_{i}}$$
(F.48)

At the bottom of the continuous layer, substitution of the corresponding displacements yield:

$$R_{S}\left(A_{5}e^{+R_{S}z_{b}}-A_{6}e^{-R_{S}z_{b}}\right)+ik\left(A_{7}e^{+R_{P}z_{b}}+A_{8}e^{-R_{P}z_{b}}\right)=0$$
(F.49)

$$-ik\left(A_{5}e^{+R_{5}z_{b}}+A_{6}e^{-R_{5}z_{b}}\right)+R_{L}\left(A_{7}e^{+R_{P}z_{b}}-A_{8}e^{-R_{P}z_{b}}\right)=0$$
(F.50)

In matrix format, the system of algebraic equations (F.43) to (F.50) reads $\underline{\underline{D}}(k)\underline{\underline{A}} = \underline{\underline{P}}$, where the vector $\underline{\underline{A}}$ includes the wave amplitudes A_1 to A_8 . The determinant of $\underline{\underline{D}}(k)$ is found as:

$$\det\left\{\underline{\underline{D}}(k)\right\} = -16\hat{\mu}^4 R_P R_S \left(2k^2 - \gamma_S\right)^2 \Delta(k) \tag{F.51}$$

Here, $\Delta(k)$ is a common denominator that reads:

$$\Delta(k) = 4k^2 R_P R_S \gamma_S + k^2 \left(4R_P^2 R_S^2 + \gamma_S^2\right) \sinh R_P z_b \sinh R_S z_b$$
$$-R_P R_S \left(4k^4 + \gamma_S^2\right) \cosh R_P z_b \cosh R_S z_b$$

The Green's displacements and Green's stresses are obtained separately for horizontal and vertical unit loads. The Green's functions for a horizontal unit load applied at a particle \mathbf{i} are obtained by solving the system of boundary conditions for $\tilde{p}_{1,x}(k) = 1$ and $\tilde{p}_{1,z}(k) = 0$, yielding the wave amplitudes $A_{x;1}^{\mathbf{i}}$ to $A_{x;8}^{\mathbf{i}}$. Accordingly, for a vertical unit load at a particle \mathbf{i} , the system is solved for $\tilde{p}_{1,x}(k) = 0$ and $\tilde{p}_{1,z}(k) = 1$, resulting in the wave amplitudes $A_{z;1}^{\mathbf{i}}$ to $A_{z;8}^{\mathbf{i}}$. Then, substituting the resulting wave amplitudes into the expressions for the displacements and stresses in the Laplace-wavenumber domain given in Section 3.5.2, we find the Green's displacements in the surface layer due to a horizontal load at particle \mathbf{i} as:

$$\tilde{g}_{u,xx,I}^{i}(k,z,s) = R_{S}\left(A_{x;1}^{i}e^{+R_{S}z} - A_{x;2}^{i}e^{-R_{S}z}\right) + ik\left(A_{x;3}^{i}e^{+R_{P}z} + A_{x;4}^{i}e^{-R_{P}z}\right)$$
(F.52)

$$\tilde{g}_{u,x,l}^{i}(k,z,s) = -ik \left(A_{x,1}^{i} e^{+R_{S}z} + A_{x,2}^{i} e^{-R_{S}z} \right) + R_{P} \left(A_{x,3}^{i} e^{+R_{P}z} - A_{x,4}^{i} e^{-R_{P}z} \right)$$
(F.53)

The Green's displacements in the surface layer due to a vertical load at particle i read:

$$\tilde{g}_{u,xz,l}^{i}(k,z,s) = R_{S}\left(A_{z;1}^{i}e^{+R_{S}z} - A_{z;3}^{i}e^{-R_{S}z}\right) + ik\left(A_{z;3}^{i}e^{+R_{P}z} + A_{z;4}^{i}e^{-R_{P}z}\right)$$
(F.54)

$$\tilde{g}_{u,zz,I}^{i}(k,z,s) = -ik\left(A_{z;1}^{i}e^{+R_{S}z} + A_{z;2}^{i}e^{-R_{S}z}\right) + R_{P}\left(A_{z;3}^{i}e^{+R_{P}z} - A_{z;4}^{i}e^{-R_{P}z}\right)$$
(F.55)

Accordingly, the Green's stresses in the surface layer due to a horizontal load at particle i are:

$$\tilde{g}_{\sigma,\text{xxx},I}^{i}(k,z,s) = 2\hat{\mu}ikR_{S}\left(A_{x;1}^{i}e^{+R_{S}z} - A_{x;2}^{i}e^{-R_{S}z}\right) - \hat{\mu}\gamma_{P}\left(A_{x;3}^{i}e^{+R_{P}z} + A_{x;4}^{i}e^{-R_{P}z}\right)$$
(F.56)

$$\tilde{\tilde{g}}_{\sigma,xxx,I}^{i}(k,z,s) = \hat{\mu}\gamma_{S}\left(A_{x;1}^{i}e^{+R_{S}z} + A_{x;2}^{i}e^{-R_{S}z}\right) + 2ik\hat{\mu}R_{P}\left(A_{x;3}^{i}e^{+R_{P}z} - A_{x;4}^{i}e^{-R_{P}z}\right)$$
(F.57)

$$\tilde{g}_{\sigma,zxx,I}^{i}(k,z,s) = -2\hat{\mu}ikR_{S}\left(A_{x;1}^{i}e^{+R_{S}z} - A_{x;2}^{i}e^{-R_{S}z}\right) + \hat{\mu}\gamma_{S}\left(A_{x;3}^{i}e^{+R_{P}z} + A_{x;4}^{i}e^{-R_{P}z}\right)$$
(F.58)

And the Green's stresses in the surface layer due to a vertical load at particle i are found as:

$$\tilde{g}_{\sigma,xxz,I}^{i}(k,z,s) = 2\hat{\mu}ikR_{S}\left(A_{z;1}^{i}e^{+R_{S}z} - A_{z;2}^{i}e^{-R_{S}z}\right) - \hat{\mu}\gamma_{P}\left(A_{z;3}^{i}e^{+R_{P}z} + A_{z;4}^{i}e^{-R_{P}z}\right)$$
(F.59)

$$\tilde{\tilde{g}}_{\sigma,zxz,l}^{i}(k,z,s) = \hat{\mu}\gamma_{S}\left(A_{z;1}^{i}e^{+R_{S}z} + A_{z;2}^{i}e^{-R_{S}z}\right) + 2ik\hat{\mu}R_{P}\left(A_{z;3}^{i}e^{+R_{P}z} - A_{z;4}^{i}e^{-R_{P}z}\right)$$
(F.60)

$$\tilde{\tilde{g}}_{\sigma,zzz,l}^{i}(k,z,s) = -2\hat{\mu}ikR_{S}\left(A_{z;l}^{i}e^{+R_{S}z} - A_{z;2}^{i}e^{-R_{S}z}\right) + \hat{\mu}\gamma_{S}\left(A_{z;3}^{i}e^{+R_{P}z} + A_{z;4}^{i}e^{-R_{P}z}\right)$$
(F.61)

The Green's displacements and Green's stresses in the bottom layer are found in terms of the wave amplitudes $A_{x;5}^{i}$ to $A_{x;8}^{i}$ and $A_{z;5}^{i}$ to $A_{z;8}^{i}$ from the expressions for the displacements and stresses in the Laplace-wavenumber domain given in Section 3.5.2.

Here and in the following, $\tilde{g}_{u,ab,L}^{i}(k,z,s)$ denotes the Green's displacement in the continuous layer L in the direction of a due to a load applied at a particle i in the direction of b. Furthermore, $\tilde{g}_{\sigma,abc,L}^{i}(k,z,s)$ denotes the normal or shear Green's stress, depending on whether indices a and b are equal or not, in the direction of b due to a unit load at particle b in the direction of b.

Green's displacements in the surface layer in the Laplace-wavenumber domain

Solving the system of algebraic equations following from the boundary conditions, and introducing $\Delta = (2k^2 - \gamma_T)\Delta(k)$, the horizontal and vertical Green's displacements in the surface layer due to a horizontal unit load applied at particle **i** are respectively found as:

$$\begin{split} & + k^4 \sinh R_P \left(z_1 - z_b \right) \left(4k^2 R_P R_S \cosh R_P z \cosh R_S z_b - \gamma_S^2 \sinh R_P z \sinh R_S z_b - 2R_P R_S \gamma_S \cosh R_S \left(z - z_b \right) \right) \\ & + k^2 R_P R_S \cosh R_P \left(z_1 - z_b \right) \left(4k^2 R_P R_S \cosh R_P z \cosh R_S z_b - \gamma_S^2 \sinh R_P z \cosh R_S z_b + 2R_P R_S \gamma_S \sinh R_S \left(z - z_b \right) \right) \\ & + k^2 R_P R_S \cosh R_P \left(z_1 - z_b \right) \left(4k^2 R_P R_S \cosh R_P z \sinh R_S z_b - \gamma_S^2 \sinh R_P z \cosh R_S z_b + 2R_P R_S \gamma_S \sinh R_S \left(z - z_b \right) \right) \\ & - k^2 R_P R_S \left(4k^2 R_P R_S \cosh R_P z \sinh R_S z_b - \gamma_S^2 \sinh R_P z \cosh R_S z_b + 2k^2 \gamma_S \cosh R_P \left(z - z_b \right) \right) \\ & + R_P^2 R_S^2 \sinh R_S \left(z_1 - z_b \right) \left(4k^2 R_P R_S \sinh R_S z \cosh R_P z_b - \gamma_S^2 \cosh R_S z \cosh R_P z_b + 2k^2 \gamma_S \cosh R_P \left(z - z_b \right) \right) \\ & + k^2 R_P R_S \cosh R_S \left(z_1 - z_b \right) \left(4k^2 R_P R_S \sinh R_S z \cosh R_P z_b - \gamma_S^2 \cosh R_S z \sinh R_P z_b - 2k^2 \gamma_S \sinh R_P \left(z - z_b \right) \right) \\ & - k^2 R_P R_S \left(4k^2 R_P R_S \sinh R_S z \cosh R_P z_b - \gamma_S^2 \cosh R_S z \sinh R_P z_b - 2k^2 \gamma_S \sinh R_P \left(z - z_b \right) \right) \\ & + k^2 \sinh R_P \left(z_1 - z_b \right) \left(4k^2 R_P R_S \sinh R_P z \cosh R_S z_b - \gamma_S^2 \cosh R_P z \cosh R_S z_b + 2k^2 \gamma_S \cosh R_S \left(z - z_b \right) \right) \\ & + R_P R_S \cosh R_P \left(z_1 - z_b \right) \left(4k^2 R_P R_S \sinh R_P z \sinh R_S z_b - \gamma_S^2 \cosh R_P z \cosh R_S z_b + 2k^2 \gamma_S \cosh R_S \left(z - z_b \right) \right) \\ & + R_P R_S \sinh R_S \left(z_1 - z_b \right) \left(4k^2 R_P R_S \cosh R_S z \sinh R_P z \sinh R_S z_b - \gamma_S^2 \sinh R_S z \cosh R_P z \cosh R_S z_b + 2k^2 \gamma_S \cosh R_S \left(z - z_b \right) \right) \\ & + R_P R_S \sinh R_S \left(z_1 - z_b \right) \left(4k^2 R_P R_S \cosh R_S z \sinh R_P z_b - \gamma_S^2 \sinh R_S z \cosh R_P z \cosh R_S z_b + 2k^2 \gamma_S \cosh R_S \left(z - z_b \right) \right) \\ & + k^2 \cosh R_S \left(z_1 - z_b \right) \left(4k^2 R_P R_S \cosh R_S z \sinh R_P z_b - \gamma_S^2 \sinh R_S z \cosh R_P z_b + 2R_P R_S \gamma_S \sinh R_P \left(z - z_b \right) \right) \\ & + k^2 \cosh R_S \left(z_1 - z_b \right) \left(4k^2 R_P R_S \cosh R_S z \cosh R_P z_b - \gamma_S^2 \sinh R_S z \sinh R_P z_b - 2R_P R_S \gamma_S \cosh R_P \left(z - z_b \right) \right) \\ & + k^2 \cosh R_S \left(z_1 - z_b \right) \left(4k^2 R_P R_S \cosh R_S z \cosh R_P z_b - \gamma_S^2 \sinh R_S z \sinh R_P z_b - 2R_P R_S \gamma_S \cosh R_P \left(z - z_b \right) \right) \\ & + k^2 \cosh R_S \left(z_1 - z_b \right) \left(4k^2 R_P R_S \cosh R_S z \cosh R_P z_b - \gamma_S^2 \sinh R_S z \sinh R_P z_b - 2R_P R_S \gamma_S \cosh R_P \left(z - z_b \right) \right) \\ & + k^2 \cosh R_S \left(z_1 - z_b \right) \left(4k^2 R_P R_S \cosh R_S z \cosh R_P z_b - \gamma_S^2 \sinh R_S z \sinh R$$

The horizontal and vertical Green's displacements in the surface layer due to a vertical unit load at particle i are respectively found as:

$$\tilde{g}_{a,xz,t}^{i}\left(k,z,s\right) = \frac{-\mathrm{i}ke^{-\mathrm{i}kn_{t}}}{\hat{\mu}\Delta} \\ \begin{pmatrix} +R_{P}R_{S}\sinh R_{P}\left(z_{1}-z_{b}\right)\left(4k^{2}R_{P}R_{S}\cosh R_{F}z\sinh R_{S}z_{b}-\gamma_{S}^{2}\sinh R_{P}z\cosh R_{S}z_{b}+2R_{P}R_{S}\gamma_{S}\sinh R_{S}\left(z-z_{b}\right)\right) \\ +k^{2}\cosh R_{P}\left(z_{1}-z_{b}\right)\left(4k^{2}R_{P}R_{S}\cosh R_{F}z\cosh R_{S}z_{b}-\gamma_{S}^{2}\sinh R_{P}z\sinh R_{S}z_{b}-2R_{P}R_{S}\gamma_{S}\cosh R_{S}\left(z-z_{b}\right)\right) \\ -k^{2}\left(4k^{2}R_{P}R_{S}\cosh R_{F}z\cosh R_{S}z_{b}-\gamma_{S}^{2}\sinh R_{P}z\sinh R_{S}z_{b}-2R_{P}R_{S}\gamma_{S}\cosh R_{S}\left(z-z_{b}\right)\right) \\ +k^{2}\sinh R_{S}\left(z_{1}-z_{b}\right)\left(4k^{2}R_{P}R_{S}\cosh R_{F}z\cosh R_{F}z\cosh R_{F}z-\gamma_{S}^{2}\cosh R_{S}z\sinh R_{F}z_{b}-2k^{2}\gamma_{S}\sinh R_{P}\left(z-z_{b}\right)\right) \\ +R_{P}R_{S}\cosh R_{S}\left(z_{1}-z_{b}\right)\left(4k^{2}R_{P}R_{S}\sinh R_{S}z\cosh R_{P}z_{b}-\gamma_{S}^{2}\cosh R_{S}z\cosh R_{P}z_{b}+2k^{2}\gamma_{S}\cosh R_{P}\left(z-z_{b}\right)\right) \\ -R_{P}R_{S}\left(4k^{2}R_{P}R_{S}\sinh R_{S}z\sinh R_{F}z\sinh R_{S}z\cosh R_{F}z\cosh R_{S}z\cosh R_{P}z_{b}+2k^{2}\gamma_{S}\cosh R_{F}\left(z-z_{b}\right)\right) \\ +k^{2}R_{P}R_{S}\cosh R_{P}\left(z_{1}-z_{b}\right)\left(4k^{2}R_{P}R_{S}\sinh R_{P}z\cosh R_{S}z_{b}-\gamma_{S}^{2}\cosh R_{P}z\cosh R_{S}z_{b}+2k^{2}\gamma_{S}\cosh R_{S}\left(z-z_{b}\right)\right) \\ +k^{2}R_{P}R_{S}\cosh R_{P}\left(z_{1}-z_{b}\right)\left(4k^{2}R_{P}R_{S}\sinh R_{P}z\cosh R_{S}z_{b}-\gamma_{S}^{2}\cosh R_{P}z\sinh R_{S}z_{b}-2k^{2}\gamma_{S}\sinh R_{S}\left(z-z_{b}\right)\right) \\ +k^{2}R_{P}R_{S}\cosh R_{P}\left(z_{1}-z_{b}\right)\left(4k^{2}R_{P}R_{S}\sinh R_{P}z\cosh R_{S}z_{b}-\gamma_{S}^{2}\cosh R_{P}z\sinh R_{S}z_{b}-2k^{2}\gamma_{S}\sinh R_{S}\left(z-z_{b}\right)\right) \\ +k^{2}R_{P}R_{S}\cosh R_{S}z\cosh R_{S}z\cosh R_{S}z\cosh R_{S}z \cosh R_{S}z_{b}+2k^{2}\gamma_{S}\cosh R_{S}\left(z-z_{b}\right)\right) \\ +k^{2}R_{P}R_{S}\cosh R_{S}\left(2k^{2}R_{P}R_{S}\cosh R_{S}z\cosh R_{P}z_{b}-\gamma_{S}^{2}\sinh R_{S}z\cosh R_{P}z_{b}-2k^{2}\gamma_{S}\sinh R_{S}\left(z-z_{b}\right)\right) \\ +k^{2}R_{P}R_{S}\cosh R_{S}\left(2k^{2}R_{P}R_{S}\cosh R_{S}z\cosh R_{S}z \cosh R_{P}z_{b}-\gamma_{S}^{2}\sinh R_{S}z\cosh R_{P}z_{b}-2k^{2}\gamma_{S}\sinh R_{S}\left(z-z_{b}\right)\right) \\ +k^{2}R_{P}R_{S}\cosh R_{S}\left(2k^{2}R_{P}R_{S}\cosh R_{S}z\cosh R_{S}z\cosh R_{P}z_{b}-\gamma_{S}^{2}\sinh R_{S}z\cosh R_{P}z_{b}-2k^{2}\gamma_{S}\sinh R_{F}\left(z-z_{b}\right)\right) \\ +k^{2}R_{P}R_{S}\cosh R_{S}\left(2k^{2}R_{P}R_{S}\cosh R_{S}z\cosh R_{S}z\sinh R_{P}z_{b}-\gamma_{S}^{2}\sinh R_{S}z\cosh R_{P}z_{b}+2k^{2}R_{P}R_{S}\gamma_{S}\sinh R_{F}\left(z-z_{b}\right)\right) \\ -k^{2}R_{P}R_{S}\left(4k^{2}R_{P}R_{S}\cosh R_{S}z\sinh R_{P}z_{b}-\gamma_{S}^{2}\sinh R_{S}z\cosh R_{P}z_{b}+2k^{2}R_{P}R_{S}\gamma_{S}\sinh R_{F}\left(z-z_{b}\right)\right) \\ -k^{2}R_{P}R_$$

Green's displacements in the bottom layer in the Laplace-wavenumber domain

Again using $\Delta = (2k^2 - \gamma_T)\Delta(k)$, the horizontal and vertical Green's displacements in the bottom layer due to a horizontal unit load at particle **i** are respectively found as:

$$\tilde{g}_{u,xx,H}^{1}\left(k,z,s\right) = \frac{-e^{-ikx_{1}}}{\hat{\mu}R_{D}} \left(+k^{4} \sinh R_{P}\left(z-z_{b}\right) \left(4k^{2}R_{P}R_{S}\cosh R_{P}z_{1}\cosh R_{S}z_{b} - y_{S}^{2}\sinh R_{P}z_{1}\sinh R_{S}z_{b} - 2R_{P}R_{S}\gamma_{S}\cosh R_{S}\left(z_{1}-z_{b}\right) \right) \\ +k^{2}R_{P}R_{S}\cosh R_{P}\left(z-z_{b}\right) \left(4k^{2}R_{P}R_{S}\cosh R_{P}z_{1}\sinh R_{S}z_{b} - y_{S}^{2}\sinh R_{P}z_{1}\cosh R_{S}z_{b} + 2R_{P}R_{S}\gamma_{S}\sinh R_{S}\left(z_{1}-z_{b}\right) \right) \\ -k^{2}R_{P}R_{S}\cosh R_{P}\left(z-z_{b}\right) \left(4k^{2}R_{P}R_{S}\cosh R_{P}z_{1}\sinh R_{S}z_{b} - y_{S}^{2}\sinh R_{P}z_{1}\cosh R_{S}z_{b} + 2R_{P}R_{S}\gamma_{S}\sinh R_{S}\left(z_{1}-z_{b}\right) \right) \\ +R_{P}^{2}R_{S}^{2}\sinh R_{S}\left(z-z_{b}\right) \left(4k^{2}R_{P}R_{S}\sinh R_{S}z_{1}\sinh R_{P}z_{b} - y_{S}^{2}\cosh R_{S}z_{1}\cosh R_{P}z_{b} + 2k^{2}\gamma_{S}\cosh R_{P}\left(z_{1}-z_{b}\right) \right) \\ +k^{2}R_{P}R_{S}\cosh R_{S}\left(z-z_{b}\right) \left(4k^{2}R_{P}R_{S}\sinh R_{S}z_{1}\cosh R_{P}z_{b} - y_{S}^{2}\cosh R_{S}z_{1}\sinh R_{P}z_{b} - 2k^{2}\gamma_{S}\sinh R_{P}\left(z_{1}-z_{b}\right) \right) \\ -k^{2}R_{P}R_{S}\left(4k^{2}R_{P}R_{S}\sinh R_{S}z_{1}\cosh R_{P}z_{b} - y_{S}^{2}\cosh R_{S}z_{1}\sinh R_{P}z_{b} - 2k^{2}\gamma_{S}\sinh R_{P}\left(z_{1}-z_{b}\right) \right) \\ +k^{2}\cosh R_{P}\left(z-z_{b}\right) \left(4k^{2}R_{P}R_{S}\cosh R_{P}z_{1}\cosh R_{S}z_{b} - y_{S}^{2}\sinh R_{P}z_{1}\cosh R_{S}z_{b} + 2R_{P}R_{S}\gamma_{S}\cosh R_{S}\left(z_{1}-z_{b}\right) \right) \\ +k^{2}\cosh R_{P}\left(z-z_{b}\right) \left(4k^{2}R_{P}R_{S}\cosh R_{P}z_{1}\cosh R_{S}z_{b} - y_{S}^{2}\sinh R_{P}z_{1}\sinh R_{S}z_{b} - 2R_{P}R_{S}\gamma_{S}\cosh R_{S}\left(z_{1}-z_{b}\right) \right) \\ +k^{2}\cosh R_{S}\left(z-z_{b}\right) \left(4k^{2}R_{P}R_{S}\cosh R_{P}z_{1}\cosh R_{S}z_{b} - y_{S}^{2}\sinh R_{P}z_{1}\sinh R_{S}z_{b} - 2R_{P}R_{S}\gamma_{S}\cosh R_{S}\left(z_{1}-z_{b}\right) \right) \\ +k^{2}\sinh R_{S}\left(z-z_{b}\right) \left(4k^{2}R_{P}R_{S}\cosh R_{P}z_{1}\cosh R_{S}z_{b} - y_{S}^{2}\sinh R_{P}z_{1}\sinh R_{S}z_{b} - 2R_{P}R_{S}\gamma_{S}\cosh R_{S}\left(z_{1}-z_{b}\right) \right) \\ +k^{2}\sinh R_{S}\left(z-z_{b}\right) \left(4k^{2}R_{P}R_{S}\sinh R_{S}z_{1}\cosh R_{P}z_{b} - y_{S}^{2}\cosh R_{S}z_{1}\sinh R_{P}z_{b} - 2k^{2}\gamma_{S}\cosh R_{S}\left(z_{1}-z_{b}\right) \right) \\ +R_{P}R_{S}\cosh R_{S}\left(z-z_{b}\right) \left(4k^{2}R_{P}R_{S}\sinh R_{S}z_{1}\sinh R_{S}z_{1}\cosh R_{S}z_{1}\sinh R_{P}z_{b} - 2k^{2}\gamma_{S}\cosh R_{F}\left(z_{1}-z_{b}\right) \right) \\ -R_{P}R_{S}\left(4k^{2}R_{P}R_{S}\sinh R_{S}z_{1}\sinh R_{S}z_{1}\sinh R_{P}z_{b} - y_{S}^{2}\cosh R_{S}z_{1}\cosh R_{P}z_{b} + 2k^{2}\gamma_{S}\cosh R_{P}\left(z_{1}-z_{b}\right) \right) \\ -R_{P}R_{S}\left(4k^{2}R_{P}R_{S}\sinh R_{S}z$$

The horizontal and vertical Green's displacements in the bottom layer due to a vertical unit load at particle i are respectively found as:

$$\tilde{g}_{a,xz,H}^{1}\left(k,z,s\right) = \frac{-ike^{-ikx_{1}}}{\hat{\mu}\Delta} \left(+ k^{2}\sinh R_{F}\left(z-z_{b}\right)\left(4k^{2}R_{F}R_{S}\sinh R_{F}z_{i}\cosh R_{S}z_{b} - \gamma_{S}^{2}\cosh R_{F}z_{i}\sinh R_{S}z_{b} - 2k^{2}\gamma_{S}\sinh R_{S}\left(z_{i}-z_{b}\right)\right) + R_{F}R_{S}\cosh R_{F}\left(z-z_{b}\right)\left(4k^{2}R_{F}R_{S}\sinh R_{F}z_{i}\sinh R_{S}z_{b} - \gamma_{S}^{2}\cosh R_{F}z_{i}\cosh R_{S}z_{b} + 2k^{2}\gamma_{S}\cosh R_{S}\left(z_{i}-z_{b}\right)\right) + R_{F}R_{S}\cosh R_{F}\left(z-z_{b}\right)\left(4k^{2}R_{F}R_{S}\sinh R_{F}z_{i}\sinh R_{S}z - \gamma_{S}^{2}\cosh R_{F}z_{i}\cosh R_{S}z + 2k^{2}\gamma_{S}\cosh R_{S}\left(z_{i}-z_{b}\right)\right) + R_{F}R_{S}\sinh R_{S}\left(z-z_{b}\right)\left(4k^{2}R_{F}R_{S}\cosh R_{S}z_{i}\sinh R_{F}z_{b} - \gamma_{S}^{2}\sinh R_{S}z_{i}\cosh R_{F}z_{b} + 2R_{F}R_{S}\gamma_{S}\sinh R_{F}\left(z_{i}-z_{b}\right)\right) + k^{2}\cosh R_{S}\left(z-z_{b}\right)\left(4k^{2}R_{F}R_{S}\cosh R_{S}z_{i}\cosh R_{F}z_{b} - \gamma_{S}^{2}\sinh R_{S}z_{i}\sinh R_{F}z_{b} - 2R_{F}R_{S}\gamma_{S}\cosh R_{F}\left(z_{i}-z_{b}\right)\right) - k^{2}\left(4k^{2}R_{F}R_{S}\cosh R_{S}z_{i}\cosh R_{F}z_{b} - \gamma_{S}^{2}\sinh R_{S}z_{i}\sinh R_{F}z_{b} - 2R_{F}R_{S}\gamma_{S}\cosh R_{F}\left(z_{i}-z_{b}\right)\right) + k^{2}\cosh R_{S}z_{i}\cosh R_{S}z_{i}\cosh R_{S}z_{i}\cosh R_{F}z_{b} - 2R_{F}R_{S}\gamma_{S}\cosh R_{F}\left(z_{i}-z_{b}\right)\right) + k^{2}\cosh R_{S}z_{i}\cosh R_{S}z_{i}\cosh R_{S}z_{i}\cosh R_{S}z_{i}\cosh R_{F}z_{b} + 2k^{2}\gamma_{S}\cosh R_{F}\left(z_{i}-z_{b}\right)\right) + k^{2}\cosh R_{S}z_{i}\cosh R_{S}z_{i}\cosh R_{S}z_{i}\cosh R_{S}z_{i}\cosh R_{S}z_{i}\cosh R_{S}z_{i}\cosh R_{S}z_{i}\cosh R_{F}z_{b} + 2k^{2}\gamma_{S}\cosh R_{F}z_{b}\right)$$

```
 \tilde{g}_{u,z,H}^{1}\left(k,z,s\right) = \frac{-e^{-ikz_{1}}}{\hat{\mu}R_{S}\Delta} \left( \begin{array}{l} +R_{P}^{2}R_{S}^{2}\sinh R_{L}\left(z-z_{b}\right)\left(4k^{2}R_{P}R_{S}\sinh R_{P}z_{1}\sinh R_{S}z_{b}-\gamma_{S}^{2}\cosh R_{P}z_{1}\cosh R_{S}z_{b}+2k^{2}\gamma_{S}\cosh R_{S}\left(z_{1}-z_{b}\right)\right) \\ +k^{2}R_{P}R_{S}\cosh R_{L}\left(z-z_{b}\right)\left(4k^{2}R_{P}R_{S}\sinh R_{P}z_{1}\cosh R_{S}z_{b}-\gamma_{S}^{2}\cosh R_{P}z_{1}\sinh R_{S}z_{b}-2k^{2}\gamma_{S}\sinh R_{S}\left(z_{1}-z_{b}\right)\right) \\ -k^{2}R_{P}R_{S}\left(4k^{2}R_{P}R_{S}\sinh R_{P}z_{1}\cosh R_{S}z-\gamma_{S}^{2}\cosh R_{P}z_{1}\sinh R_{S}z_{b}-2k^{2}\gamma_{S}\sinh R_{S}\left(z_{1}-z_{b}\right)\right) \\ +k^{4}\sinh R_{S}\left(z-z_{b}\right)\left(4k^{2}R_{P}R_{S}\cosh R_{S}z_{1}\cosh R_{P}z_{b}-\gamma_{S}^{2}\sinh R_{S}z_{1}\sinh R_{P}z_{b}-2R_{P}R_{S}\gamma_{S}\cosh R_{P}\left(z_{1}-z_{b}\right)\right) \\ +k^{2}R_{P}R_{S}\cosh R_{S}\left(z-z_{b}\right)\left(4k^{2}R_{P}R_{S}\cosh R_{S}z_{1}\sinh R_{P}z_{b}-\gamma_{S}^{2}\sinh R_{S}z_{1}\cosh R_{P}z_{b}+2R_{P}R_{S}\gamma_{S}\sinh R_{P}\left(z_{1}-z_{b}\right)\right) \\ -k^{2}R_{P}R_{S}\left(4k^{2}R_{P}R_{S}\cosh R_{S}z_{1}\sinh R_{P}z_{b}-\gamma_{S}^{2}\sinh R_{S}z_{1}\cosh R_{P}z_{b}+2R_{P}R_{S}\gamma_{S}\sinh R_{P}z_{b}\right) \\ +k^{2}R_{P}R_{S}\left(4k^{2}R_{P}R_{S}\cosh R_{S}z_{1}\sinh R_{P}z_{2}-\gamma_{S}^{2}\sinh R_{S}z_{1}\cosh R_{P}z_{b}\right) \\ +k^{2}R_{P}R_{S}\left(4k^{2}R_{P}R_{S}\cosh R_{S}z_{1}\sinh R_{S}z_{1}-2R_{P}R_{S}\gamma_{S}\sinh
```

Green's stresses in the surface layer in the Laplace-wavenumber domain

The Green's stresses in the surface layer due to a horizontal unit load at particle i read:

```
+k^2 \sinh R_P (z_1-z_b) (4k^2 R_P R_S \gamma_P \cosh R_P z \cosh R_S z_b - \gamma_P \gamma_S^2 \sinh R_P z \sinh R_S z_b - 4k^2 R_P R_S \gamma_S \cosh R_S (z-z_b))
                                                                         +R_PR_S \cosh R_P (z_1-z_b) (4k^2R_PR_S\gamma_P \cosh R_Pz \sinh R_Sz_b-\gamma_P\gamma_S^2 \sinh R_Pz \cosh R_Sz_b+4k^2R_PR_S\gamma_S \sinh R_S (z-z_b))
\tilde{g}_{\sigma,\text{xxx},I}^{i}\left(k,z,s\right) = \frac{-\mathrm{i}ke^{-\mathrm{i}kr_{1}}}{R_{P}\Delta} \begin{bmatrix} -R_{P}R_{S}\left(4k^{2}R_{P}R_{S}\gamma_{P}\cosh R_{P}z\sinh R_{S}z_{1} - \gamma_{P}\gamma_{S}^{2}\sinh R_{P}z\cosh R_{S}z_{1} + 4k^{2}R_{P}R_{S}\gamma_{S}\sinh R_{S}\left(z-z_{1}\right)\right) \\ +2R_{P}^{2}R_{S}^{2}\sinh R_{S}\left(z_{1}-z_{b}\right)\left(4k^{2}R_{P}R_{S}\sinh R_{S}z\sinh R_{P}z\cosh R_{P}z_{b} + \gamma_{P}\gamma_{S}\cosh R_{P}z - z_{b}\right)\right) \end{bmatrix}
                                                                                         +2k^2R_PR_S\cosh R_S\left(z_1-z_b\right)\left(4k^2R_PR_S\sinh R_Sz\cosh R_Pz_b-\gamma_S^2\cosh R_Sz\sinh R_Pz_b-\gamma_P\gamma_S\sinh R_P\left(z-z_b\right)\right)
                                                                                                                                     -2k^2R_PR_S\left(4k^2R_PR_S\sinh R_Sz\cosh R_Pz_i-\gamma_S^2\cosh R_Sz\sinh R_Pz_i-\gamma_P\gamma_S\sinh R_P\left(z-z_i\right)\right)
                                                                                           +2k^4 \sinh R_P (z_1-z_b) (4k^2 R_P R_S \sinh R_P z \cosh R_S z_b - \gamma_S^2 \cosh R_P z \sinh R_S z_b - \gamma_S^2 \sinh R_S (z-z_b))
                                                                           +2k^2R_PR_S\cosh R_P(z_1-z_b)(4k^2R_PR_S\sinh R_Pz\sinh R_Sz_b-\gamma_S^2\cosh R_Pz\cosh R_Sz_b+\gamma_S^2\cosh R_S(z-z_b))
\frac{+2k^2R_PR_S\cosh R_P\left(z_1-z_b\right)\left(4k^2R_PR_S\sinh R_Pz\sinh R_Sz_b-\gamma_S^2\cosh R_Pz\cosh R_Sz_b+\gamma_S^2\cosh R_S\left(z-z_b\right)\right)}{-2k^2R_PR_S\left(4k^2R_PR_S\sinh R_Pz\sinh R_Sz_i-\gamma_S^2\cosh R_Pz\cosh R_Sz_i+\gamma_S^2\cosh R_S\left(z-z_b\right)\right)}\\ +R_PR_S\gamma_S\sinh R_S\left(z_1-z_b\right)\left(4k^2R_PR_S\cosh R_Sz\sinh R_Pz\sinh R_Sz_i-\gamma_S^2\cosh R_Pz\cosh R_Sz_i+\gamma_S^2\cosh R_Sz_i-\gamma_S^2\cosh R_Sz_i\right)\\ +R_PR_S\gamma_S\sinh R_S\left(z_1-z_b\right)\left(4k^2R_PR_S\cosh R_Sz_i+R_Sz_i\right)\\ +R_PR_S\gamma_S\sinh R_S\left(z_1-z_b\right)\left(4k^2R_PR_S\cosh R_Sz_i+R_Sz_i\right)\\ +R_PR_S\gamma_S\sinh R_S\left(z_1-z_b\right)\left(4k^2R_PR_S\cosh R_Sz_i\right)\\ +R_PR_S\gamma_S\sinh R_Sz_i\right)\\ +R_PR_S\gamma_S\sinh R_S\left(z_1-z_b\right)\left(4k^2R_PR_S\cosh R_Sz_i\right)\\ +R_PR_S\gamma_S\sinh R_Sz_i\right)\\ +R_PR_S\gamma_S\sinh R_Sz_i\right)
                                                                        +k^2\gamma_S \cosh R_S (z_1-z_b)(4k^2R_PR_S \cosh R_Sz \cosh R_Pz_b-\gamma_S^2 \sinh R_Sz \sinh R_Pz_b-4k^2R_PR_S \cosh R_P(z-z_b))
                                                                                                                   -k^2 \gamma_S \left(4k^2 R_P R_S \cosh R_S z \cosh R_P z_1 - \gamma_S^2 \sinh R_S z \sinh R_P z_1 - 4k^2 R_P R_S \cosh R_P (z-z_1)\right)
                                                                       +k^2\gamma_S \sinh R_P (z_1-z_b)(4k^2R_PR_S\cosh R_Pz\cosh R_Sz_b-\gamma_S^2\sinh R_Pz\sinh R_Sz_b-4k^2R_PR_S\cosh R_S(z-z_b))
                                                                 +R_PR_S\gamma_S\cosh R_P(z_1-z_b)(4k^2R_PR_S\cosh R_Pz\sinh R_Sz_b-\gamma_S^2\sinh R_Pz\cosh R_Sz_b+4k^2R_PR_S\sinh R_S(z-z_b))
\tilde{\tilde{g}}_{\sigma,=x,I}^{i}\left(k,z,s\right) = \frac{ike^{-ikx_{i}}}{R_{P}\Delta}
                                                                                                              -R_P R_S \gamma_S \left(4k^2 R_P R_S \cosh R_P z \sinh R_S z_i - \gamma_S^2 \sinh R_P z \cosh R_S z_i + 4k^2 R_P R_S \sinh R_S (z-z_i)\right)
                                                                                  +2R_P^2R_S^2\sinh R_S\left(z_1-z_b\right)\left(4k^2R_PR_S\sinh R_Sz\sinh R_Pz_b-\gamma_S^2\cosh R_Sz\cosh R_Pz_b+\gamma_S^2\cosh R_P\left(z-z_b\right)\right)
                                                                              +2k^2R_PR_S\cosh R_S(z_1-z_b)(4k^2R_PR_S\sinh R_Sz\cosh R_Pz_b-\gamma_S^2\cosh R_Sz\sinh R_Pz_b-\gamma_S^2\sinh R_P(z-z_b))
                                                                                                                           -2k^2R_PR_S\left(4k^2R_PR_S\sinh R_Sz\cosh R_Pz_1-\gamma_S^2\cosh R_Sz\sinh R_Pz_1-\gamma_S^2\sinh R_P\left(z-z_1\right)\right)
```

The Green's stresses in the surface layer due to a vertical unit load at particle i are found as:

```
 \tilde{g}_{\sigma,xxz,I}^{1}(k,z,s) = \frac{e^{-ikx_{1}}}{\Delta} \\ \begin{pmatrix} +R_{\rho}R_{S} \sinh R_{\rho} \left(z_{1}-z_{b}\right) \left(4k^{2}R_{\rho}R_{S}\gamma_{\rho} \cosh R_{\rho}z \sinh R_{\rho}z \cosh R_{\rho}z \sinh R_{\rho}z \cosh R_{S}z_{b} + 4k^{2}R_{\rho}R_{S}\gamma_{S} \sinh R_{S} \left(z-z_{b}\right) \right) \\ +k^{2} \cosh R_{\rho} \left(z_{1}-z_{b}\right) \left(4k^{2}R_{\rho}R_{S}\gamma_{\rho} \cosh R_{\rho}z \cosh R_{S}z_{b} - \gamma_{\rho}\gamma_{S}^{2} \sinh R_{\rho}z \sinh R_{S}z_{b} - 4k^{2}R_{\rho}R_{S}\gamma_{S} \cosh R_{S} \left(z-z_{b}\right) \right) \\ -k^{2} \left(4k^{2}R_{\rho}R_{S}\gamma_{\rho} \cosh R_{\rho}z \cosh R_{S}z_{b} - \gamma_{\rho}\gamma_{S}^{2} \sinh R_{\rho}z \sinh R_{S}z_{b} - 4k^{2}R_{\rho}R_{S}\gamma_{S} \cosh R_{S} \left(z-z_{b}\right) \right) \\ +2k^{4} \sinh R_{S} \left(z_{1}-z_{b}\right) \left(4k^{2}R_{\rho}R_{S} \sinh R_{S}z \cosh R_{\rho}z_{b} - \gamma_{S}^{2} \cosh R_{S}z \sinh R_{\rho}z_{b} - \gamma_{\rho}\gamma_{S} \sinh R_{\rho}z_{b} - \gamma_{\rho}\gamma_{S} \sinh R_{\rho}z_{b} - \gamma_{\rho}\gamma_{S} \sinh R_{\rho}z_{b} \right) \\ +2k^{2}R_{\rho}R_{S} \cosh R_{S} \left(z_{1}-z_{b}\right) \left(4k^{2}R_{\rho}R_{S} \sinh R_{S}z \sinh R_{\rho}z_{b} - \gamma_{S}^{2} \cosh R_{S}z \cosh R_{\rho}z_{b} + \gamma_{\rho}\gamma_{S} \cosh R_{\rho} \left(z-z_{b}\right) \right) \\ -2k^{2}R_{\rho}R_{S} \left(4k^{2}R_{\rho}R_{S} \sinh R_{\rho}z \sinh R_{\rho}z_{b} - \gamma_{S}^{2} \cosh R_{\rho}z \cosh R_{\rho}z_{b} + \gamma_{\rho}\gamma_{S} \cosh R_{\rho} \left(z-z_{b}\right) \right) \\ +2k^{2}R_{\rho}R_{S} \cosh R_{\rho} \left(z_{1}-z_{b}\right) \left(4k^{2}R_{\rho}R_{S} \sinh R_{\rho}z \cosh R_{S}z_{b} - \gamma_{S}^{2} \cosh R_{\rho}z \sinh R_{S}z_{b} - \gamma_{S}^{2} \sinh R_{S}z_{b} - \gamma_{S}^{2
```

```
 \tilde{g}_{\sigma,zzz,I}^{1}\left(k,z,s\right) = \frac{-e^{-ikz_{1}}}{\Delta} \\ \begin{pmatrix} +R_{F}R_{S}\gamma_{S}\sinh R_{F}\left(z_{1}-z_{b}\right)\left(4k^{2}R_{F}R_{S}\cosh R_{F}z\sinh R_{S}z_{b}-\gamma_{S}^{2}\sinh R_{F}z\cosh R_{S}z_{b}+4k^{2}R_{F}R_{S}\sinh R_{S}\left(z-z_{b}\right)\right) \\ +k^{2}\gamma_{S}\cosh R_{F}\left(z_{1}-z_{b}\right)\left(4k^{2}R_{F}R_{S}\cosh R_{F}z\cosh R_{S}z_{b}-\gamma_{S}^{2}\sinh R_{F}z\sinh R_{S}z_{b}-4k^{2}R_{F}R_{S}\cosh R_{S}\left(z-z_{b}\right)\right) \\ -k^{2}\gamma_{S}\left(4k^{2}R_{F}R_{S}\cosh R_{F}z\cosh R_{S}z_{b}-\gamma_{S}^{2}\sinh R_{F}z\sinh R_{S}z_{b}-4k^{2}R_{F}R_{S}\cosh R_{S}\left(z-z_{b}\right)\right) \\ +2k^{4}\sinh R_{S}\left(z_{1}-z_{b}\right)\left(4k^{2}R_{F}R_{S}\sinh R_{S}z\cosh R_{F}z_{b}-\gamma_{S}^{2}\cosh R_{S}z\sinh R_{F}z_{b}-\gamma_{S}^{2}\cosh R_{F}\left(z-z_{b}\right)\right) \\ +2k^{2}R_{F}R_{S}\cosh R_{S}\left(z_{1}-z_{b}\right)\left(4k^{2}R_{F}R_{S}\sinh R_{S}z\sinh R_{F}z_{b}-\gamma_{S}^{2}\cosh R_{S}z\cosh R_{F}z_{b}+\gamma_{S}^{2}\cosh R_{F}\left(z-z_{b}\right)\right) \\ -2k^{2}R_{F}R_{S}\left(4k^{2}R_{F}R_{S}\sinh R_{S}z\sinh R_{F}z_{1}-\gamma_{S}^{2}\cosh R_{S}z\cosh R_{F}z_{1}+\gamma_{S}^{2}\cosh R_{F}\left(z-z_{b}\right)\right) \\ +2k^{2}R_{F}R_{S}\left(4k^{2}R_{F}R_{S}\sinh R_{S}z\sinh R_{F}z_{2}-\gamma_{S}^{2}\cosh R_{S}z\cosh R_{F}z_{1}+\gamma_{S}^{2}\cosh R_{F}z_{2}+\gamma_{S}^{2}\cosh R_{F}z_{1}+\gamma_{S}^{2}\cosh R_{F}z_{2}+\gamma_{S}^{2}\cosh R_{F}z_{2}
```

Green's stresses in the bottom layer in the Laplace-wavenumber domain

The Green's stresses in the bottom layer due to a horizontal unit load at particle i read:

```
 \tilde{g}_{\sigma,xxx,H}^{1}(k,z,s) = \frac{-ike^{-iks_{1}}}{R_{P}\Delta} \begin{cases} +k^{2}\gamma_{F}\sinh R_{F}\left(z-z_{b}\right)\left(4k^{2}R_{F}R_{S}\cosh R_{F}z_{1}\cosh R_{S}z_{b}-\gamma_{S}^{2}\sinh R_{F}z_{1}\sinh R_{S}z_{b}-2R_{F}R_{S}\gamma_{S}\cosh R_{S}\left(z_{1}-z_{b}\right)\right) \\ +R_{F}R_{S}\gamma_{F}\cosh R_{F}\left(z-z_{b}\right)\left(4k^{2}R_{F}R_{S}\cosh R_{F}z_{1}\sinh R_{S}z_{b}-\gamma_{S}^{2}\sinh R_{F}z_{1}\cosh R_{S}z_{b}+2R_{F}R_{S}\gamma_{S}\sinh R_{S}\left(z_{1}-z_{b}\right)\right) \\ -2k^{2}R_{F}R_{S}\left(4k^{2}R_{F}R_{S}\cosh R_{F}z_{1}\sinh R_{S}z-\gamma_{S}^{2}\sinh R_{F}z_{1}\cosh R_{S}z_{b}+2R_{F}R_{S}\gamma_{S}\sinh R_{S}\left(z_{1}-z_{b}\right)\right) \\ +2R_{F}R_{S}\gamma_{F}\cosh R_{S}\left(2-z_{b}\right)\left(4k^{2}R_{F}R_{S}\sinh R_{S}z_{1}\cosh R_{F}z_{b}-\gamma_{S}^{2}\cosh R_{S}z_{1}\sinh R_{F}z_{b}-2k^{2}\gamma_{S}\cosh R_{F}\left(z_{1}-z_{b}\right)\right) \\ +2k^{2}R_{F}R_{S}\cosh R_{S}\left(z-z_{b}\right)\left(4k^{2}R_{F}R_{S}\sinh R_{S}z_{1}\cosh R_{F}z_{b}-\gamma_{S}^{2}\cosh R_{S}z_{1}\sinh R_{F}z_{b}-2k^{2}\gamma_{S}\sinh R_{F}\left(z_{1}-z_{b}\right)\right) \\ +2k^{2}R_{F}R_{S}\cosh R_{S}\left(z-z_{b}\right)\left(4k^{2}R_{F}R_{S}\sinh R_{S}z_{1}\cosh R_{F}z_{b}-\gamma_{S}^{2}\cosh R_{S}z_{1}\sinh R_{F}z_{b}-2k^{2}\gamma_{S}\sinh R_{F}\left(z_{1}-z_{b}\right)\right) \\ +2k^{2}R_{F}R_{S}\cosh R_{F}\left(z-z_{b}\right)\left(4k^{2}R_{F}R_{S}\cosh R_{F}z_{1}\sinh R_{S}z_{b}-\gamma_{S}^{2}\sinh R_{F}z_{1}\cosh R_{S}z_{b}+2R_{F}R_{S}\gamma_{S}\cosh R_{S}\left(z_{1}-z_{b}\right)\right) \\ +2k^{2}R_{F}R_{S}\sinh R_{F}\left(z-z_{b}\right)\left(4k^{2}R_{F}R_{S}\cosh R_{F}z_{1}\cosh R_{S}z_{b}-\gamma_{S}^{2}\sinh R_{F}z_{1}\sinh R_{S}z_{b}-2R_{F}R_{S}\gamma_{S}\cosh R_{S}\left(z_{1}-z_{b}\right)\right) \\ +2k^{2}\cosh R_{F}\left(z-z_{b}\right)\left(4k^{2}R_{F}R_{S}\cosh R_{F}z_{1}\cosh R_{S}z_{b}-\gamma_{S}^{2}\sinh R_{F}z_{1}\sinh R_{S}z_{b}-2R_{F}R_{S}\gamma_{S}\cosh R_{S}\left(z_{1}-z_{b}\right)\right) \\ +2k^{2}\gamma_{S}\sinh R_{S}\left(z-z_{b}\right)\left(4k^{2}R_{F}R_{S}\sinh R_{S}z_{1}\cosh R_{F}z_{b}-\gamma_{S}^{2}\cosh R_{S}z_{1}\sinh R_{F}z_{b}-2k^{2}\gamma_{S}\cosh R_{F}\left(z_{1}-z_{b}\right)\right) \\ +2k^{2}\gamma_{S}\sinh R_{F}\left(z-z_{b}\right)\left(4k^{2}R_{F}R_{S}\sinh R_{S}z_{1}\cosh R_{F}z_{b}-\gamma_{S}^{2}\cosh R_{S}z_{1}\cosh R_{F}z_{b}-2k^{2}\gamma_{S}\cosh R_{F}\left(z_{1}-z_{b}\right)\right) \\ +2k^{2}\gamma_{S}\sinh R_{F}\left(z-z_{b}\right)\left(4k^{2}R_{F}R_{S}\cosh R_{F}z_{1}\sinh R_{S}z_{b}-\gamma_{S}^{2}\sinh R_{F}z_{1}\cosh R_{S}z_{b}+2R_{F}S\gamma_{S}\cosh R_{F}\left(z_{1}-z_{b}\right)\right) \\ +2k^{2}\gamma_{S}\cosh R_{F}\left(z-z_{b}\right)\left(4k^{2}R_{F}R_{S}\cosh R_{F}z_{1}\sinh R_{S}z_{b}-\gamma_{S}^{2}\sinh R_{F}z_{1}\cosh R_{S}z_{b}+2R_{F}S\gamma_{S}\cosh R_{S}\left(z_{1}-z_{b}\right)\right) \\ +2k^{2}\gamma_{S}\cosh R_{S}\left(z-z_{b}\right)\left(4k^{2}R_{F}R_{S}\cosh R_{F}z_{1}\sinh R
```

The Green's stresses in the bottom layer due to a vertical unit load at particle i are found as:

```
 \tilde{g}_{\sigma,xxz,H}^{1}\left(k,z,s\right) = \frac{e^{-ikx_{1}}}{\Delta} \\ \begin{pmatrix} +k^{2}\gamma_{F}\sinh R_{F}\left(z-z_{b}\right)\left(4k^{2}R_{F}R_{S}\sinh R_{F}z_{i}\cosh R_{S}z_{b} - \gamma_{S}^{2}\cosh R_{F}z_{i}\sinh R_{S}z_{b} - 2k^{2}\gamma_{S}\sinh R_{S}\left(z_{i}-z_{b}\right)\right) \\ +R_{F}R_{S}\gamma_{F}\cosh R_{F}\left(z-z_{b}\right)\left(4k^{2}R_{F}R_{S}\sinh R_{F}z_{i}\sinh R_{S}z_{b} - \gamma_{S}^{2}\cosh R_{F}z_{i}\cosh R_{S}z_{b} + 2k^{2}\gamma_{S}\cosh R_{S}\left(z_{i}-z_{b}\right)\right) \\ -2k^{2}R_{F}R_{S}\left(4k^{2}R_{F}R_{S}\sinh R_{F}z_{i}\sinh R_{S}z_{b} - \gamma_{S}^{2}\cosh R_{F}z_{i}\cosh R_{S}z_{b} + 2k^{2}\gamma_{S}\cosh R_{S}\left(z_{i}-z_{b}\right)\right) \\ +2k^{2}R_{F}R_{S}\sinh R_{S}\left(z-z_{b}\right)\left(4k^{2}R_{F}R_{S}\cosh R_{S}z_{i}\sinh R_{F}z_{b} - \gamma_{S}^{2}\sinh R_{S}z_{i}\cosh R_{F}z_{b} + 2R_{F}R_{S}\gamma_{S}\sinh R_{F}\left(z_{i}-z_{b}\right)\right) \\ +2k^{4}\cosh R_{S}\left(z-z_{b}\right)\left(4k^{2}R_{F}R_{S}\cosh R_{S}z_{i}\cosh R_{F}z_{b} - \gamma_{S}^{2}\sinh R_{S}z_{i}\sinh R_{F}z_{b} - 2R_{F}R_{S}\gamma_{S}\cosh R_{F}\left(z_{i}-z_{b}\right)\right) \\ -k^{2}\gamma_{F}\left(4k^{2}R_{F}R_{S}\cosh R_{S}z_{i}\cosh R_{F}z_{b} - \gamma_{S}^{2}\sinh R_{S}z_{i}\sinh R_{F}z_{b} - 2R_{F}R_{S}\gamma_{S}\cosh R_{F}\left(z_{i}-z_{b}\right)\right) \\ +2k^{2}R_{F}R_{S}\cosh R_{F}\left(z-z_{b}\right)\left(4k^{2}R_{F}R_{S}\sinh R_{F}z_{i}\cosh R_{S}z_{i}\cosh R_{F}z_{i}\sinh R_{S}z_{b} - 2k^{2}\gamma_{S}\sinh R_{S}\left(z_{i}-z_{b}\right)\right) \\ +2k^{2}R_{F}R_{S}\cosh R_{F}\left(z-z_{b}\right)\left(4k^{2}R_{F}R_{S}\sinh R_{F}z_{i}\cosh R_{S}z_{b} - \gamma_{S}^{2}\cosh R_{F}z_{i}\sinh R_{S}z_{b} - 2k^{2}\gamma_{S}\sinh R_{S}\left(z_{i}-z_{b}\right)\right) \\ +2k^{2}R_{F}R_{S}\cosh R_{F}\left(z-z_{b}\right)\left(4k^{2}R_{F}R_{S}\sinh R_{F}z_{i}\cosh R_{S}z_{b} - \gamma_{S}^{2}\cosh R_{F}z_{i}\sinh R_{S}z_{b} - 2k^{2}\gamma_{S}\sinh R_{S}\left(z_{i}-z_{b}\right)\right) \\ +2k^{2}R_{F}R_{S}\cosh R_{F}\left(z-z_{b}\right)\left(4k^{2}R_{F}R_{S}\sinh R_{F}z_{i}\cosh R_{S}z_{i}\cosh R_{F}z_{i}\sinh R_{S}z_{b} - 2k^{2}\gamma_{S}\sinh R_{S}\left(z_{i}-z_{b}\right)\right) \\ +2k^{2}R_{F}R_{S}\cosh R_{F}\left(z-z_{b}\right)\left(4k^{2}R_{F}R_{S}\sinh R_{F}z_{i}\cosh R_{S}z_{i}\cosh R_{F}z_{i}\sinh R_{S}z_{i}\cosh R_{F}z_{i}\sinh R_{S}z_{b}\right) \\ +2k^{2}R_{F}R_{S}\cosh R_{S}\left(z-z_{b}\right)\left(4k^{2}R_{F}R_{S}\cosh R_{S}z_{i}\cosh R_{F}z_{b}-\gamma_{S}^{2}\sinh R_{S}z_{i}\cosh R_{F}z_{b}\right) \\ +2k^{2}R_{F}R_{S}\cosh R_{S}\left(z-z_{b}\right)\left(4k^{2}R_{F}R_{S}\cosh R_{S}z_{i}\sinh R_{F}z_{b}-\gamma_{S}^{2}\sinh R_{S}z_{i}\cosh R_{F}z_{b}\right) \\ +2k^{2}R_{F}R_{S}\cosh R_{S}\left(z-z_{b}\right)\left(4k^{2}R_{F}R_{S}\cosh R_{S}z_{i}\sinh R_{F}z_{b}-\gamma_{S}^{2}\sinh R_{S}z_{i}\cosh R_{F}z_{b}\right) \\ +2k^{2}R_{F}R_{S}\cosh R_{S}\left(z-z_{b}\right)\left(4k^
```

F.5 Green's functions for a load at the surface of the continuum

The displacements and stresses in the continuous layer due to a load applied at its surface are obtained from equations (F.38) to (F.42) following the same approach as for a load inside the continuous layer. The expressions for these displacements and stresses due to a load at a particle i at the surface of the continuum, and thus with z-coordinate $z_i = 0$, coincide with the expressions for the displacements and stresses in the bottom layer given in Section 3.5.3.

The expressions for the wave amplitudes follow from the boundary conditions of the continuous layer for a unit load applied at a particle **i** located at its surface. The boundary conditions at respectively the surface and the bottom of the continuous layer are found as:

$$\left. \tilde{\tilde{\sigma}}_{zx,H} \left(k,z,s \right) \right|_{z=z_{1}=0} = \tilde{\tilde{p}}_{x}^{i} \left(k \right) e^{-ikx_{i}} \tag{F.62}$$

$$\left. \tilde{\sigma}_{zz,II} \left(k, z, s \right) \right|_{z=\tau_i=0} = \tilde{p}_z^{i} \left(k \right) e^{-ikx_i} \tag{F.63}$$

$$\left. \tilde{\tilde{u}}_{x,II} \left(k, z, s \right) \right|_{z=z_h} = \left. \tilde{\tilde{u}}_{z,II} \left(k, z, s \right) \right|_{z=z_h} = 0 \tag{F.64}$$

Substituting the corresponding expressions for the displacements and stresses into the boundary conditions above yields the following system of four algebraic equations:

$$\hat{\mu}\gamma_{S}\left(A_{5}+A_{6}\right)+2\hat{\mu}ikR_{P}\left(A_{7}-A_{8}\right)=\tilde{\tilde{p}}_{x}^{i}\left(k\right)e^{-ikx_{i}}$$
(F.65)

$$-2\hat{\mu}ikR_{S}(A_{5}-A_{6})+\hat{\mu}\gamma_{S}(A_{7}+A_{8})=\tilde{\tilde{p}}_{z}^{i}(k)e^{-ikx_{i}}$$
(F.66)

$$R_{s}\left(A_{5}e^{+R_{S}z_{b}}-A_{6}e^{-R_{S}z_{b}}\right)+ik\left(A_{7}e^{+R_{P}z_{b}}+A_{8}e^{-R_{P}z_{b}}\right)=0$$
(F.67)

$$-ik(A_5e^{+R_5z_b} + A_6e^{-R_5z_b}) + R_P(A_7e^{+R_Pz_b} - A_8e^{-R_Pz_b}) = 0$$
(F.68)

In matrix format, the system of algebraic equations (F.65) to (F.68) reads $\underline{\underline{D}}(k)\underline{\underline{A}} = \underline{\underline{P}}$, where the vector $\underline{\underline{A}}$ consists of the wave amplitudes A_5 to A_8 . The determinant of $\underline{\underline{D}}(k)$ reads:

$$\det\left\{\underline{D}(k)\right\} = 4\hat{\mu}^2 \Delta(k) \tag{F.69}$$

Where, $\Delta(k)$ is the single-valued common denominator, previously given in Section 3.5.3. For a horizontal unit load at the surface of the continuum, we find the wave amplitudes $A_{x;5}^{i}$ to $A_{x;8}^{i}$ by solving the system of boundary conditions for $\tilde{\tilde{p}}_{1,x}(k) = 1$ and $\tilde{\tilde{p}}_{1,z}(k) = 0$.

Accordingly, we find the wave amplitudes $A_{z;5}^{i}$ to $A_{z;8}^{i}$ by solving the system for $\tilde{p}_{1,x}(k) = 0$ and $\tilde{p}_{1,z}(k) = 1$. The expressions for the displacements and stresses in the Laplace-wave-number domain given in Section 3.5.2 then yield the Green's displacements in the continuous layer due to respectively a horizontal and a vertical load at a particle **i** as:

$$\tilde{\tilde{g}}_{u,xx,II}^{i}(k,z,s) = R_{S}\left(A_{x;5}^{i}e^{+R_{S}z} - A_{x;6}^{i}e^{-R_{S}z}\right) + ik\left(A_{x;7}^{i}e^{+R_{P}z} + A_{x;8}^{i}e^{-R_{P}z}\right)$$
(F.70)

$$\tilde{g}_{u,zx,H}^{i}(k,z,s) = -ik(A_{x;5}^{i}e^{+R_{S}z} + A_{x;6}^{i}e^{-R_{S}z}) + R_{P}(A_{x;7}^{i}e^{+R_{P}z} - A_{x;8}^{i}e^{-R_{P}z})$$
(F.71)

$$\tilde{g}_{u,xz,H}^{i}(k,z,s) = R_{S}\left(A_{z;5}^{i}e^{+R_{S}z} - A_{z;6}^{i}e^{-R_{S}z}\right) + ik\left(A_{z;7}^{i}e^{+R_{P}z} + A_{z;8}^{i}e^{-R_{P}z}\right)$$
(F.72)

$$\tilde{\tilde{g}}_{u,zz,II}^{i}(k,z,s) = -ik \left(A_{z;5}^{i} e^{+R_{S}z} + A_{z;6}^{i} e^{-R_{S}z} \right) + R_{P} \left(A_{z;7}^{i} e^{+R_{P}z} - A_{z;8}^{i} e^{-R_{P}z} \right)$$
 (F.73)

Accordingly, the Green's stresses in the surface layer due to respectively a horizontal and a vertical load at a particle **i** are:

$$\tilde{g}_{\sigma,xxx,H}^{i}(k,z,s) = 2\hat{\mu}ikR_{S}\left(A_{x;5}^{i}e^{+R_{S}z} - A_{x;6}^{i}e^{-R_{S}z}\right) - \hat{\mu}\gamma_{P}\left(A_{x;7}^{i}e^{+R_{P}z} + A_{x;8}^{i}e^{-R_{P}z}\right)$$
(F.74)

$$\tilde{g}_{\sigma,zxx,H}^{i}(k,z,s) = \hat{\mu}\gamma_{S}\left(A_{x;5}^{i}e^{+R_{S}z} + A_{x;6}^{i}e^{-R_{S}z}\right) + 2\hat{\mu}ikR_{P}\left(A_{x;7}^{i}e^{+R_{P}z} - A_{x;8}^{i}e^{-R_{P}z}\right)$$
(F.75)

$$\tilde{\tilde{g}}_{\sigma,zzx,II}^{i}(k,z,s) = -2\hat{\mu}ikR_{S}\left(A_{x;5}^{i}e^{+R_{S}z} - A_{x;6}^{i}e^{-R_{S}z}\right) + \hat{\mu}\gamma_{S}\left(A_{x;7}^{i}e^{+R_{P}z} + A_{x;8}^{i}e^{-R_{P}z}\right)$$
(F.76)

$$\tilde{\tilde{g}}_{\sigma,xxz,II}^{i}(k,z,s) = 2\hat{\mu}ikR_{S}\left(A_{z;5}^{i}e^{+R_{S}z} - A_{z;6}^{i}e^{-R_{S}z}\right) - \hat{\mu}\gamma_{P}\left(A_{z;7}^{i}e^{+R_{P}z} + A_{z;8}^{i}e^{-R_{P}z}\right)$$
(F.77)

$$\tilde{\tilde{g}}_{\sigma,zxz,H}^{i}(k,z,s) = \hat{\mu}\gamma_{S}\left(A_{z;5}^{i}e^{+R_{S}z} + A_{z;6}^{i}e^{-R_{S}z}\right) + 2\hat{\mu}ikR_{P}\left(A_{z;7}^{i}e^{+R_{P}z} - A_{z;8}^{i}e^{-R_{P}z}\right)$$
(F.78)

$$\tilde{\tilde{g}}_{\sigma,zzz,II}^{i}(k,z,s) = -2\hat{\mu}ikR_{S}\left(A_{z;5}^{i}e^{+R_{S}z} - A_{z;6}^{i}e^{-R_{S}z}\right) + \hat{\mu}\gamma_{S}\left(A_{z;7}^{i}e^{+R_{P}z} + A_{z;8}^{i}e^{-R_{P}z}\right)$$
(F.79)

Here, $\tilde{g}^{i}_{u,ab,II}(k,z,s)$ denotes the Green's displacement in the continuum in the direction of a due to a unit load applied at particle i in the direction of b. Accordingly $\tilde{g}^{i}_{\sigma,abc,II}(k,z,s)$ denotes the normal or shear Green's stress, depending on whether indices a and b are equal or not, in the direction of b due to a load at particle i in the direction of c.

Green's displacements in the Laplace-wavenumber domain

Solving the algebraic system of boundary conditions for the wave amplitudes and substituting the resulting expressions into equations (F.70) and (F.71), the horizontal and vertical Green's displacements due to a horizontal unit load at a surface particle **i** are respectively found as:

$$\begin{split} \tilde{\tilde{g}}_{u,xx,H}^{i}\left(k,z,s\right) &= \frac{-R_{S}e^{-ikx_{l}}}{\hat{\mu}\Delta\left(k\right)} \left(+2k^{2}\left(k^{2}\sinh R_{P}\left(z-z_{b}\right)\cosh R_{S}z_{b} + R_{P}R_{S}\cosh R_{P}\left(z-z_{b}\right)\sinh R_{S}z_{b}\right) \right) \\ &+ \gamma_{S}\left(R_{P}R_{S}\sinh R_{S}\left(z-z_{b}\right)\cosh R_{P}z_{b} + k^{2}\cosh R_{S}\left(z-z_{b}\right)\sinh R_{P}z_{b}\right) \\ &- k^{2}\gamma_{S}\sinh R_{P}z - 2k^{2}R_{P}R_{S}\sinh R_{S}z\right) \\ \tilde{\tilde{g}}_{u,zx,H}^{i}\left(k,z,s\right) &= \frac{ike^{-ikx_{l}}}{\hat{\mu}\Delta\left(k\right)} \left(+2R_{P}R_{S}\left(R_{P}R_{S}\sinh R_{P}\left(z-z_{b}\right)\sinh R_{S}z_{b} + k^{2}\cosh R_{P}\left(z-z_{b}\right)\cosh R_{S}z_{b}\right) \\ &+ \gamma_{S}\left(k^{2}\sinh R_{S}\left(z-z_{b}\right)\sinh R_{P}z_{b} + R_{P}R_{S}\cosh R_{S}\left(z-z_{b}\right)\cosh R_{P}z_{b}\right) \\ &- R_{P}R_{S}\gamma_{S}\cosh R_{P}z - 2k^{2}R_{P}R_{S}\cosh R_{S}z \end{split}$$

Accordingly, the horizontal and vertical Green's displacements due to a vertical unit load at a surface particle **i** are respectively found as:

$$\begin{split} \tilde{\tilde{g}}_{u,xz,H}^{i}\left(k,z,s\right) &= \frac{-\mathrm{i}ke^{-\mathrm{i}kx_{l}}}{\hat{\mu}\Delta\left(k\right)} \\ &+ \gamma_{S}\left(k^{2}\sinh R_{P}\left(z-z_{b}\right)\sinh R_{S}z_{b} + R_{P}R_{S}\cosh R_{P}\left(z-z_{b}\right)\cosh R_{S}z_{b}\right) \\ &+ 2R_{P}R_{S}\left(R_{P}R_{S}\sinh R_{S}\left(z-z_{b}\right)\sinh R_{P}z_{b} + k^{2}\cosh R_{S}\left(z-z_{b}\right)\cosh R_{P}z_{b}\right) \\ &- 2k^{2}R_{P}R_{S}\cosh R_{P}z - R_{P}R_{S}\gamma_{S}\cosh R_{P}z \\ &- 2k^{2}R_{P}R_{S}\cosh R_{P}z - R_{P}R_{S}\gamma_{S}\cosh R_{S}z_{b} \\ &+ \gamma_{S}\left(R_{P}R_{S}\sinh R_{P}\left(z-z_{b}\right)\cosh R_{S}z_{b} + k^{2}\cosh R_{P}\left(z-z_{b}\right)\sinh R_{S}z_{b}\right) \\ &+ 2k^{2}\left(k^{2}\cosh R_{P}z_{b}\sinh R_{S}\left(z-z_{b}\right) + R_{P}R_{S}\cosh R_{S}\left(z-z_{b}\right)\sinh R_{P}z_{b}\right) \\ &- 2k^{2}R_{P}R_{S}\sinh R_{P}z - k^{2}\gamma_{S}\sinh R_{S}z \end{split}$$

Green's stresses in the Laplace-wavenumber domain

The Green's stresses due to a horizontal unit load at a surface particle i are found as:

$$\begin{split} \tilde{\tilde{g}}_{\sigma,\text{xxx},H}^{i}\left(k,z,s\right) &= \frac{-\mathrm{i}kR_{S}e^{-\mathrm{i}k\alpha_{l}}}{\Delta(k)} \begin{pmatrix} +2\gamma_{P}\left(k^{2}\sinh R_{P}\left(z-z_{b}\right)\cosh R_{S}z_{b} + R_{P}R_{S}\cosh R_{P}\left(z-z_{b}\right)\sinh R_{S}z_{b}\right) \\ +2\gamma_{S}\left(R_{P}R_{S}\sinh R_{S}\left(z-z_{b}\right)\cosh R_{P}z_{b} + k^{2}\cosh R_{S}\left(z-z_{b}\right)\sinh R_{P}z_{b}\right) \\ -\gamma_{P}\gamma_{S}\sinh R_{P}z - 4k^{2}R_{P}R_{S}\sinh R_{S}z \end{pmatrix} \\ \tilde{\tilde{g}}_{\sigma,\text{xxx},H}^{i}\left(k,z,s\right) &= \frac{-e^{-\mathrm{i}k\alpha_{l}}}{\Delta(k)} \begin{pmatrix} +4k^{2}R_{P}R_{S}\left(R_{P}R_{S}\sinh R_{P}\left(z-z_{b}\right)\sinh R_{S}z_{b} + k^{2}\cosh R_{P}\left(z-z_{b}\right)\cosh R_{S}z_{b}\right) \\ +\gamma_{S}^{2}\left(k^{2}\sinh R_{S}\left(z-z_{b}\right)\sinh R_{P}z_{b} + R_{P}R_{S}\cosh R_{S}\left(z-z_{b}\right)\cosh R_{P}z_{b}\right) \\ -2k^{2}R_{P}R_{S}\gamma_{S}\left(\cosh R_{P}z + \cosh R_{S}z\right) \end{pmatrix} \\ \tilde{\tilde{g}}_{\sigma,\text{xxx},H}^{i}\left(k,z,s\right) &= \frac{\mathrm{i}kR_{S}e^{-\mathrm{i}k\alpha_{l}}}{\Delta(k)} \begin{pmatrix} +2\gamma_{S}\left(k^{2}\sinh R_{P}\left(z-z_{b}\right)\cosh R_{S}z_{b} + R_{P}R_{S}\cosh R_{F}\left(z-z_{b}\right)\sinh R_{S}z_{b}\right) \\ +2\gamma_{S}\left(k^{2}\sinh R_{S}\left(z-z_{b}\right)\cosh R_{P}z_{b} + R_{P}R_{S}\cosh R_{S}\left(z-z_{b}\right)\sinh R_{P}z_{b}\right) \\ -\gamma_{S}^{2}\sinh R_{P}z - 4k^{2}R_{P}R_{S}\sinh R_{S}z \end{pmatrix} \end{split}$$

The Green's stresses due to a vertical unit load at a surface particle i are found as:

$$\begin{split} \tilde{\tilde{g}}_{\sigma,\text{XXZ},H}^{i}\left(k,z,s\right) &= \frac{e^{-ik\alpha_{l}}}{\Delta(k)} \\ &+ \gamma_{P}\gamma_{S}\left(k^{2}\sinh R_{P}\left(z-z_{b}\right)\sinh R_{S}z_{b} + R_{P}R_{S}\cosh R_{P}\left(z-z_{b}\right)\cosh R_{S}z_{b}\right) \\ &+ 4k^{2}R_{P}R_{S}\left(R_{P}R_{S}\sinh R_{S}\left(z-z_{b}\right)\sinh R_{P}z_{b} + k^{2}\cosh R_{S}\left(z-z_{b}\right)\cosh R_{P}z_{b}\right) \\ &- 2k^{2}R_{P}R_{S}\left(\gamma_{P}\cosh R_{P}z + \gamma_{S}\cosh R_{S}z\right) \\ &- 2k^{2}R_{P}R_{S}\left(\gamma_{P}\cosh R_{P}z + \gamma_{S}\cosh R_{S}z\right) \\ &\tilde{\tilde{g}}_{\sigma,\text{ZZZ},H}^{i}\left(k,z,s\right) &= \frac{-ikR_{P}e^{-ik\alpha_{l}}}{\Delta(k)} \\ &+ 2\gamma_{S}\left(R_{P}R_{S}\sinh R_{P}\left(z-z_{b}\right)\cosh R_{S}z_{b} + k^{2}\cosh R_{P}\left(z-z_{b}\right)\sinh R_{S}z_{b}\right) \\ &- 4k^{2}R_{P}R_{S}\sinh R_{P}z - \gamma_{S}^{2}\sinh R_{S}z\right) \\ &- 4k^{2}R_{P}R_{S}\sinh R_{P}z - \gamma_{S}^{2}\sinh R_{S}z\right) \\ &\tilde{\tilde{g}}_{\sigma,\text{ZZZ},H}^{i}\left(k,z,s\right) &= \frac{-e^{-ik\alpha_{l}}}{\Delta(k)} \\ &+ 4k^{2}R_{P}R_{S}\left(R_{P}R_{S}\sinh R_{S}\left(z-z_{b}\right)\sinh R_{S}z_{b} + R_{P}R_{S}\cosh R_{P}\left(z-z_{b}\right)\cosh R_{P}z_{b}\right) \\ &- 2k^{2}R_{P}R_{S}\gamma_{S}\left(\cosh R_{P}z + \cosh R_{S}z\right) \\ &- 2k^{2}R_{P}R_{S}\gamma_{S}\left(\cosh R_{P}z + \cosh R_{S}z\right) \end{split}$$

G The dynamic compliance of the half-plane of particles

In Section 4.3.2, the expression for the dynamic compliance matrix of the half-plane of particles with a surface cavity is obtained as:

$$\underline{\underline{\tilde{\beta}}}(s) = \left(\underline{\underline{\tilde{g}}_R}(s)^{-1}\underline{\underline{\tilde{g}}_u}(s)\right)^{\mathsf{T}} \tag{G.1}$$

Here, $\underline{\tilde{g}}_{u}(s)$ and $\underline{\tilde{g}}_{R}(s)$ are matrices that respectively contain the Green's functions for the displacements and $\overline{\text{the}}$ reaction forces of all particles \mathbf{j} along the boundary Γ due to unit loads applied at any particle \mathbf{i} along the boundary Γ . For quick reading, these Green's functions are respectively referred to as Green's displacements and Green's reaction forces.

In Section 4.4.2, the boundary conditions for the half-plane of particles are given in terms of displacements and reaction forces. In the following, the system of boundary conditions is derived in terms of the wave amplitudes. First, in Appendix G.1, the system of six boundary conditions is derived for a load inside the half-plane of particles, while in Appendix G.2, the system of two boundary conditions is derived for a load at the surface of the half-plane.

The expressions for the Green's displacements are given in Section 4.4.3 in terms of the wave amplitudes and require no further investigation. The general expressions for the Green's reaction forces at the particles along Γ have previously been given in Section 4.4.4. As stated in that section, the expressions for $\varphi_{x,r}^{(h)}$ and $\varphi_{z,r}^{(h)}$, with r=1...3 and h=1...2, are found depending on the location of the particles \mathbf{i} and \mathbf{j} and on the cell configuration of particle \mathbf{j} along Γ . The expressions for $\varphi_{x,r}^{(h)}$ and $\varphi_{z,r}^{(h)}$ are derived for seven existing cell configurations along the boundary Γ in respectively Appendices G.3 to G.9. Appendix G.10 addresses the reaction forces in the half-plane of particles for the equivalent one-dimensional response of the half-plane of particles to an infinitely-long uniform vertical load.

G.1 Boundary conditions for a load inside the half-plane of particles

When a load is applied at a particle i in the interior of the half-plane, we divide the half-plane into two subsystems, a layer of particles that ranges from the surface to the horizontal level of particle i, referred to as subsystem I, and the remaining subsystem, referred to as subsystem II, which is a half-plane with its surface at the horizontal level of the loaded particle i.

The first two boundary conditions follow from the force equilibrium at the unloaded surface of the half-plane. These boundary conditions thus read:

$$R_{x,I}^{\mathbf{m},0} = R_{z,I}^{\mathbf{m},0} = 0 \tag{G.2}$$

Note here that at the free surface of any system of particles, the horizontal and vertical reaction forces follow directly from respectively the horizontal and vertical force equilibrium, i.e. the equation of motion, of that particle. Note furthermore that, in accordance with a surface particle in the hexagonal lattice, the mass of a particle at the surface of the half-plane of particles is half the mass of a particle in the interior of the half-plane, i.e. $M^{\mathbf{m},\mathbf{0}} = \frac{1}{2}M$. Accordingly, the stiffness and the damping of the elements at the surface are respectively equal

to half the stiffness and half the damping of the elements in the interior of the half-plane. In terms of the operator \hat{K}_e that describes the viscoelastic behaviour of the rheological elements as $\hat{K}_e = K_e + C_e \frac{\partial}{\partial t}$, this yields $\hat{K}_{e;1}^{\mathbf{m},0} = \hat{K}_{e;2}^{\mathbf{m},0} = \frac{1}{2}\hat{K}_e$ and $\hat{K}_{e;3}^{\mathbf{m},0} = \hat{K}_{e;4}^{\mathbf{m},0} = \hat{K}_e$. The dimensional equations of motion for a surface particle, and thereby the first two boundary conditions for a load applied inside the half-plane of particles, are thus found in the time domain as:

$$\frac{1}{2}M\ddot{u}_{x,l}^{\mathbf{m},\mathbf{0}} + \frac{1}{2}\hat{K}_{e}\left\{3u_{x,l}^{\mathbf{m},\mathbf{0}} - u_{x,l}^{\mathbf{m}-2,\mathbf{0}} - u_{x,l}^{\mathbf{m}+2,\mathbf{0}} - \frac{1}{2}\left(u_{x,l}^{\mathbf{m}-1,1} + u_{x,l}^{\mathbf{m}+1,1}\right) + \frac{\sqrt{3}}{2}\left(u_{z,l}^{\mathbf{m}-1,1} - u_{z,l}^{\mathbf{m}+1,1}\right)\right\} = 0 \quad (G.3)$$

$$\frac{1}{2}M\ddot{u}_{z,l}^{\mathbf{m},0} + \frac{1}{2}\hat{K}_{e}\left\{3u_{z,l}^{\mathbf{m},0} - \frac{3}{2}\left(u_{z,l}^{\mathbf{m}-1,1} + u_{z,l}^{\mathbf{m}+1,1}\right) + \frac{\sqrt{3}}{2}\left(u_{x,l}^{\mathbf{m}-1,1} - u_{x,l}^{\mathbf{m}+1,1}\right)\right\} = 0 \tag{G.4}$$

To obtain the corresponding dimensionless boundary conditions, we here introduce the following dimensionless parameters for time and space:

$$t = t_{\text{dim}} \omega_0, \quad x = \frac{x_{\text{dim}}}{\ell}, \quad z = \frac{z_{\text{dim}}}{\ell}.$$

Inserting the dimensionless parameters into equations (G.3) and (G.4), inserting the expressions for the operator \hat{K}_e , as well as dividing by $M\omega_0^2\ell$, applying the Laplace transform and introducing the operator $K_{\zeta}=1+2\zeta s$, we find the Laplace domain boundary conditions at the surface of the half-plane of particles as:

$$s^{2}\tilde{u}_{x,I}^{\mathbf{m},0} + K_{\zeta} \left\{ \tilde{u}_{x,I}^{\mathbf{m},0} - \frac{1}{3} \left(\tilde{u}_{x,I}^{\mathbf{m}-2,0} + \tilde{u}_{x,I}^{\mathbf{m}+2,0} \right) - \frac{1}{6} \left(\tilde{u}_{x,I}^{\mathbf{m}-1,1} + \tilde{u}_{x,I}^{\mathbf{m}+1,1} \right) + \frac{\sqrt{3}}{6} \left(\tilde{u}_{z,I}^{\mathbf{m}-1,1} - \tilde{u}_{z,I}^{\mathbf{m}+1,1} \right) \right\} = 0$$
 (G.5)

$$s^{2}\tilde{u}_{z,I}^{\mathbf{m},0} + K_{\zeta} \left\{ \tilde{u}_{z,I}^{\mathbf{m},0} + \frac{\sqrt{3}}{6} \left(\tilde{u}_{x,I}^{\mathbf{m}-1,1} - \tilde{u}_{x,I}^{\mathbf{m}+1,1} \right) - \frac{1}{2} \left(\tilde{u}_{z,I}^{\mathbf{m}-1,1} + \tilde{u}_{z,I}^{\mathbf{m}+1,1} \right) \right\} = 0$$
 (G.6)

In Section 4.4.1, the horizontal and vertical displacements of a particle \mathbf{m} , \mathbf{n} in subsystem I were expressed in terms of the horizontal wave amplitudes as:

$$\tilde{u}_{x,I}^{\mathbf{m},\mathbf{n}}(s) = \int_{-2\pi}^{+2\pi} \left(\sum_{h=1}^{2} A_{1}^{\mathbf{i},(h)} e^{+\frac{\sqrt{2}}{2} \mathbf{i} \kappa_{z}^{(h)} \mathbf{n}} + \sum_{h=1}^{2} A_{2}^{\mathbf{i},(h)} e^{-\frac{\sqrt{2}}{2} \mathbf{i} \kappa_{z}^{(h)} \mathbf{n}} \right) e^{-\frac{1}{2} \mathbf{i} \kappa_{x} \mathbf{m}} d\kappa_{x}$$
(G.7)

$$\tilde{u}_{z,I}^{\mathbf{m},\mathbf{n}}(s) = \int_{-2\pi}^{+2\pi} \left(\sum_{h=1}^{2} D^{(h)} A_{1}^{\mathbf{i},(h)} e^{+\frac{\sqrt{5}}{2} i \kappa_{z}^{(h)} \mathbf{n}} - \sum_{h=1}^{2} D^{(h)} A_{2}^{\mathbf{i},(h)} e^{-\frac{\sqrt{5}}{2} i \kappa_{z}^{(h)} \mathbf{n}} \right) e^{-\frac{1}{2} i \kappa_{x} \mathbf{m}} d\kappa_{x}$$
(G.8)

Substituting equations (G.7) and (G.8) into equations (G.5) and (G.6) yields the horizontal and vertical boundary conditions at the half-plane surface as:

$$\int_{-2\pi}^{+2\pi} \sum_{h=1}^{2} \left(s^{2} + K_{\zeta} \left(1 - \frac{2}{3} \cos \kappa_{x} - \frac{1}{3} \left(\cos \frac{\kappa_{x}}{2} - D^{(h)} i \sqrt{3} \sin \frac{\kappa_{x}}{2} \right) e^{+\frac{\sqrt{5}}{2} i \kappa_{z}^{(h)}} \right) \right) A_{1}^{\mathbf{i},(h)} e^{-\frac{1}{2} i \kappa_{x} \mathbf{m}} d\kappa_{x} \\
+ \int_{-2\pi}^{+2\pi} \sum_{h=1}^{2} \left(s^{2} + K_{\zeta} \left(1 - \frac{2}{3} \cos \kappa_{x} - \frac{1}{3} \left(\cos \frac{\kappa_{x}}{2} + D^{(h)} i \sqrt{3} \sin \frac{\kappa_{x}}{2} \right) e^{-\frac{\sqrt{5}}{2} i \kappa_{z}^{(h)}} \right) \right) A_{2}^{\mathbf{i},(h)} e^{-\frac{1}{2} i \kappa_{x} \mathbf{m}} d\kappa_{x} = 0 \tag{G.9}$$

$$\int_{-2\pi}^{+2\pi} \sum_{h=1}^{2} \left(s^{2} + K_{\zeta} \left(1 - \left(\cos \frac{\kappa_{x}}{2} - \frac{i}{D^{(h)} \sqrt{3}} \sin \frac{\kappa_{x}}{2} \right) e^{+\frac{\sqrt{5}}{2} i \kappa_{z}^{(h)}} \right) \right) D^{(h)} A_{1}^{\mathbf{i},(h)} e^{-\frac{1}{2} i \kappa_{x} \mathbf{m}} d\kappa_{x} \\
- \int_{-2\pi}^{+2\pi} \sum_{h=1}^{2} \left(s^{2} + K_{\zeta} \left(1 - \left(\cos \frac{\kappa_{x}}{2} + \frac{i}{D^{(h)} \sqrt{3}} \sin \frac{\kappa_{x}}{2} \right) e^{-\frac{\sqrt{5}}{2} i \kappa_{z}^{(h)}} \right) \right) D^{(h)} A_{1}^{\mathbf{i},(h)} e^{-\frac{1}{2} i \kappa_{x} \mathbf{m}} d\kappa_{x} = 0$$
(G.10)

When their integrands are equal to zero, the integrals in equations (G.9) and (G.10) must also be equal to zero, and thus we find:

$$\sum_{h=1}^{2} \left(s^{2} + K_{\zeta} \left(1 - \frac{2}{3} \cos \kappa_{x} - \frac{1}{3} \left(\cos \frac{\kappa_{x}}{2} - D^{(h)} i \sqrt{3} \sin \frac{\kappa_{x}}{2} \right) e^{+\frac{\sqrt{5}}{2} i \kappa_{z}^{(h)}} \right) \right) A_{l}^{i,(h)}$$

$$+ \sum_{h=1}^{2} \left(s^{2} + K_{\zeta} \left(1 - \frac{2}{3} \cos \kappa_{x} - \frac{1}{3} \left(\cos \frac{\kappa_{x}}{2} + D^{(h)} i \sqrt{3} \sin \frac{\kappa_{x}}{2} \right) e^{-\frac{\sqrt{5}}{2} i \kappa_{z}^{(h)}} \right) \right) A_{2}^{i,(h)} = 0$$

$$\sum_{h=1}^{2} \left(s^{2} + K_{\zeta} \left(1 - \frac{2}{3} \cos \kappa_{x} - \frac{1}{3} \left(\cos \frac{\kappa_{x}}{2} + D^{(h)} i \sqrt{3} \sin \frac{\kappa_{x}}{2} \right) e^{-\frac{\sqrt{5}}{2} i \kappa_{z}^{(h)}} \right) \right) D_{h}^{(h)} A_{2}^{i,(h)} = 0$$

$$(G.11)$$

$$\sum_{h=1}^{2} \left\{ s^{2} + K_{\zeta} \left\{ 1 - \left(\cos \frac{\kappa_{x}}{2} - \frac{i}{D^{(h)} \sqrt{3}} \sin \frac{\kappa_{x}}{2} \right) e^{+\frac{\sqrt{5}}{2} i \kappa_{z}^{(h)}} \right\} \right\} D^{(h)} A_{1}^{\mathbf{i},(h)} \\
- \sum_{h=1}^{2} \left\{ s^{2} + K_{\zeta} \left\{ 1 - \left(\cos \frac{\kappa_{x}}{2} + \frac{i}{D^{(h)} \sqrt{3}} \sin \frac{\kappa_{x}}{2} \right) e^{-\frac{\sqrt{5}}{2} i \kappa_{z}^{(h)}} \right\} \right\} D^{(h)} A_{2}^{\mathbf{i},(h)} = 0$$
(G.12)

Equations (G.11) and (G.12) are the first two boundary conditions for a load at a particle in the interior of the half-plane of particles expressed in terms of the wave amplitudes $A_{1:2}^{i,(h)}$.

The other four boundary conditions are found at the interface between subsystems I and II, i.e. at the horizontal level of the loaded particle **i**. As the displacements of the upper and lower half-particles at the level with vertical nodal coordinate $\mathbf{n} = \mathbf{n}_i$ must coincide, we find:

$$u_{x,II}^{\mathbf{m},\mathbf{n}_i} - u_{x,I}^{\mathbf{m},\mathbf{n}_i} = 0 (G.13)$$

$$u_{z,II}^{\mathbf{m},\mathbf{n}_i} - u_{z,I}^{\mathbf{m},\mathbf{n}_i} = 0 (G.14)$$

The remaining two boundary conditions follow from the force equilibrium at $\mathbf{n} = \mathbf{n}_i$ as:

$$R_{r,II}^{\mathbf{m},\mathbf{n}_{i}} - R_{r,I}^{\mathbf{m},\mathbf{n}_{i}} = P_{x}\delta_{\mathbf{m}_{i}\mathbf{m}} \tag{G.15}$$

$$R_{z,II}^{\mathbf{m},\mathbf{n}_i} - R_{z,I}^{\mathbf{m},\mathbf{n}_i} = P_z \delta_{\mathbf{m}_i \mathbf{m}}$$
 (G.16)

The horizontal and vertical displacements of a particle \mathbf{m} , \mathbf{n} in subsystem I are given in the Laplace domain by equations (G.7) and (G.8). In Section 4.4.1, the horizontal and vertical displacements of a particle \mathbf{m} , \mathbf{n} in subsystem II were obtained in the Laplace domain as:

$$\tilde{u}_{x,H}^{\mathbf{m,n}}(s) = \int_{-2\pi}^{+2\pi} \left(\sum_{h=1}^{2} A_3^{\mathbf{i},(h)} e^{+\frac{\sqrt{5}}{2} \mathbf{i} \kappa_z^{(h)} \mathbf{n}} \right) e^{-\frac{1}{2} \mathbf{i} \kappa_x \mathbf{m}} d\kappa_x$$
(G.17)

$$\tilde{u}_{z,H}^{\mathbf{m},\mathbf{n}}(s) = \int_{-2\pi}^{+2\pi} \left(\sum_{h=1}^{2} D^{(h)} A_3^{\mathbf{i},(h)} e^{+\frac{\sqrt{5}}{2} \mathrm{i} \kappa_z^{(h)} \mathbf{n}} \right) e^{-\frac{1}{2} \mathrm{i} \kappa_x \mathbf{m}} d\kappa_x$$
(G.18)

Thus, applying the Laplace transform to equations (G.13) and (G.14), and substituting equations (G.7) and (G.8), as well as equations (G.17) and (G.18), into the remainder yields the two displacement boundary conditions at the interface of the two subsystems in terms of the wave amplitudes as:

$$\sum_{h=1}^{2} \left(A_{3}^{\mathbf{i},(h)} - A_{1}^{\mathbf{i},(h)} \right) e^{+\frac{\sqrt{2}}{2} i \kappa_{z}^{(h)} \mathbf{n}_{i}} - \sum_{h=1}^{2} A_{2}^{\mathbf{i},(h)} e^{-\frac{\sqrt{2}}{2} i \kappa_{z}^{(h)} \mathbf{n}_{i}} = 0$$
 (G.19)

$$\sum_{h=1}^{2} D^{(h)} \left(A_3^{\mathbf{i},(h)} - A_1^{\mathbf{i},(h)} \right) e^{+\frac{\sqrt{5}}{2} \mathbf{i} \kappa_z^{(h)} \mathbf{n}_{\mathbf{i}}} + \sum_{h=1}^{2} D^{(h)} A_2^{\mathbf{i},(h)} e^{-\frac{\sqrt{5}}{2} \mathbf{i} \kappa_z^{(h)} \mathbf{n}_{\mathbf{i}}} = 0$$
 (G.20)

As the interface between subsystems I and II is by definition horizontal, the expressions for the reaction forces at the lower half-particle in subsystem II coincide with the equations of motion for a particle at the surface of the half-plane of particles, previously given by equations (G.3) and (G.4). Adapting the subscript to denote a half-particle located in subsystem II, the horizontal and vertical reaction forces at the lower half-particle are found as:

$$R_{x,II}^{\mathbf{m},\mathbf{n_{i}}} = \frac{1}{2} M \ddot{u}_{x,II}^{\mathbf{m},\mathbf{n_{i}}} + \frac{1}{2} \hat{K}_{e} \begin{cases} 3u_{x,II}^{\mathbf{m},\mathbf{n_{i}}} - u_{x,II}^{\mathbf{m}-2,\mathbf{n_{i}}} - u_{x,II}^{\mathbf{m}+2,\mathbf{n_{i}}} - \frac{1}{2} \left(u_{x,II}^{\mathbf{m}-1,\mathbf{n_{i}}+1} + u_{x,II}^{\mathbf{m}+1,\mathbf{n_{i}}+1} \right) \\ + \frac{\sqrt{3}}{2} \left(u_{z,II}^{\mathbf{m}-1,\mathbf{n_{i}}+1} - u_{z,II}^{\mathbf{m}+1,\mathbf{n_{i}}+1} \right) \end{cases}$$
(G.21)

$$R_{z,II}^{\mathbf{m},\mathbf{n_i}} = \frac{1}{2} M \ddot{u}_{z,II}^{\mathbf{m},\mathbf{n_i}} + \frac{1}{2} \hat{K}_e \left\{ 3 u_{z,II}^{\mathbf{m},\mathbf{n_i}} - \frac{3}{2} \left(u_{z,II}^{\mathbf{m}-\mathbf{1},\mathbf{n_i}+\mathbf{1}} + u_{z,II}^{\mathbf{m}+\mathbf{1},\mathbf{n_i}+\mathbf{1}} \right) + \frac{\sqrt{3}}{2} \left(u_{x,II}^{\mathbf{m}-\mathbf{1},\mathbf{n_i}+\mathbf{1}} - u_{x,II}^{\mathbf{m}+\mathbf{1},\mathbf{n_i}+\mathbf{1}} \right) \right\} \quad (G.22)$$

The reaction forces at the upper half-particle at the interface between subsystems I and II are derived in the same manner. The mass of the half-particles at the interface between subsystems I and II are equal to half the mass of a particle in the interior of either subsystem, i.e. $M^{\mathbf{m},\mathbf{n}_i} = \frac{1}{2}M$, and the stiffness and the damping of the elements at the half-plane surface are respectively equal to half the stiffness and half the damping of the elements in the interior, so that $\hat{K}^{\mathbf{m},\mathbf{n}_i}_{e:1} = \hat{K}^{\mathbf{m},\mathbf{n}_i}_{e:2} = \frac{1}{2}\hat{K}_e$ and $\hat{K}^{\mathbf{m},\mathbf{n}_i}_{e:5} = \hat{K}^{\mathbf{m},\mathbf{n}_i}_{e:6} = \hat{K}_e$.

Noting that the direction of the reaction forces of the upper half-particle is opposite to those of the lower half-particle, the horizontal and vertical reaction forces at the upper half-particle respectively become:

$$R_{x,I}^{\mathbf{m},\mathbf{n_{i}}} = -\frac{1}{2}M\ddot{u}_{x,I}^{\mathbf{m},\mathbf{n_{i}}} - \frac{1}{2}\hat{K}_{e} \left\{ 3u_{x,I}^{\mathbf{m},\mathbf{n_{i}}} - u_{x,I}^{\mathbf{m}-2,\mathbf{n_{i}}} - u_{x,I}^{\mathbf{m}+2,\mathbf{n_{i}}} - \frac{1}{2} \left(u_{x,I}^{\mathbf{m}-1,\mathbf{n_{i}}-1} + u_{x,I}^{\mathbf{m}+1,\mathbf{n_{i}}-1} \right) - \frac{\sqrt{3}}{2} \left(u_{z,I}^{\mathbf{m}-1,\mathbf{n_{i}}-1} - u_{z,I}^{\mathbf{m}+1,\mathbf{n_{i}}-1} \right) \right\}$$
(G.23)

$$R_{z,l}^{\mathbf{m},\mathbf{n}_{i}} = -\frac{1}{2}M\ddot{u}_{z,l}^{\mathbf{m},\mathbf{n}_{i}} - \frac{1}{2}\hat{K}_{e}\left\{3u_{z,l}^{\mathbf{m},\mathbf{n}_{i}} - \frac{3}{2}\left(u_{z,l}^{\mathbf{m}-\mathbf{1},\mathbf{n}_{i}-\mathbf{1}} + u_{z,l}^{\mathbf{m}+\mathbf{1},\mathbf{n}_{i}-\mathbf{1}}\right) - \frac{\sqrt{3}}{2}\left(u_{x,l}^{\mathbf{m}-\mathbf{1},\mathbf{n}_{i}-\mathbf{1}} - u_{x,l}^{\mathbf{m}+\mathbf{1},\mathbf{n}_{i}-\mathbf{1}}\right)\right\}$$
(G.24)

Substituting equations (G.21) to (G.24) into equations (G.15) and (G.16) yields the reaction

force boundary conditions at the interface between subsystems I and II, as:

$$\hat{K}_{e} \left\{ 3u_{x,ll}^{\mathbf{m},\mathbf{n}_{i}} - u_{x,ll}^{\mathbf{m}-2,\mathbf{n}_{i}} - u_{x,ll}^{\mathbf{m}+2,\mathbf{n}_{i}} - \frac{1}{2} \left(u_{x,ll}^{\mathbf{m}-1,\mathbf{n}_{i}+1} + u_{x,ll}^{\mathbf{m}+1,\mathbf{n}_{i}+1} \right) + \frac{\sqrt{3}}{2} \left(u_{z,ll}^{\mathbf{m}-1,\mathbf{n}_{i}+1} - u_{z,ll}^{\mathbf{m}+1,\mathbf{n}_{i}+1} \right) \right\} \\
+ \hat{K}_{e} \left\{ 3u_{x,l}^{\mathbf{m},\mathbf{n}_{i}} - u_{x,l}^{\mathbf{m}-2,\mathbf{n}_{i}} - u_{x,l}^{\mathbf{m}+2,\mathbf{n}_{i}} - \frac{1}{2} \left(u_{x,l}^{\mathbf{m}-1,\mathbf{n}_{i}-1} + u_{x,l}^{\mathbf{m}+1,\mathbf{n}_{i}-1} \right) - \frac{\sqrt{3}}{2} \left(u_{z,l}^{\mathbf{m}-1,\mathbf{n}_{i}-1} - u_{z,l}^{\mathbf{m}+1,\mathbf{n}_{i}-1} \right) \right\} \\
+ M \ddot{u}_{x,ll}^{\mathbf{m},\mathbf{n}_{i}} + M \ddot{u}_{x,l}^{\mathbf{m},\mathbf{n}_{i}} = 2P_{x} \delta_{\mathbf{m}_{i}\mathbf{m}} \\
\hat{K}_{e} \left\{ 3u_{z,ll}^{\mathbf{m},\mathbf{n}_{i}} - \frac{3}{2} \left(u_{z,ll}^{\mathbf{m}-1,\mathbf{n}_{i}+1} + u_{z,ll}^{\mathbf{m}+1,\mathbf{n}_{i}+1} \right) + \frac{\sqrt{3}}{2} \left(u_{x,ll}^{\mathbf{m}-1,\mathbf{n}_{i}+1} - u_{x,ll}^{\mathbf{m}+1,\mathbf{n}_{i}+1} \right) \right\} \\
+ \hat{K}_{e} \left\{ 3u_{z,l}^{\mathbf{m},\mathbf{n}_{i}} - \frac{3}{2} \left(u_{z,l}^{\mathbf{m}-1,\mathbf{n}_{i}-1} + u_{z,ll}^{\mathbf{m}+1,\mathbf{n}_{i}-1} \right) - \frac{\sqrt{3}}{2} \left(u_{x,l}^{\mathbf{m}-1,\mathbf{n}_{i}-1} - u_{x,ll}^{\mathbf{m}+1,\mathbf{n}_{i}-1} \right) \right\} \\
+ M \ddot{u}_{x,ll}^{\mathbf{m},\mathbf{n}_{i}} + M \ddot{u}_{x,ll}^{\mathbf{m},\mathbf{n}_{i}} = 2P_{c} \delta_{\mathbf{m}_{i}\mathbf{m}_{i}} \\
+ M \ddot{u}_{x,ll}^{\mathbf{m},\mathbf{n}_{i}} + M \ddot{u}_{x,ll}^{\mathbf{m},\mathbf{n}_{i}} = 2P_{c} \delta_{\mathbf{m}_{i}\mathbf{m}_{i}}$$
(G.26)

To obtain the corresponding dimensionless boundary conditions, we introduce the following dimensionless parameters for time, space and force:

$$t = t_{\text{dim}}\omega_0, \quad x = \frac{x_{\text{dim}}}{\ell}, \quad z = \frac{z_{\text{dim}}}{\ell}, \quad P = \frac{P_{\text{dim}}}{M\omega_0^2\ell} = \frac{P_{\text{dim}}}{3K_e\ell}. \tag{G.27}$$

Noting that $\hat{K}_e = K_e + C_e \frac{\partial}{\partial t}$, substituting the dimensionless parameters into equations (G.25) and (G.26), as well as dividing by $M\omega_0^2\ell$, applying the Laplace transform and introducing the operator $K_{\zeta} = 1 + 2\zeta s$, the Laplace domain reaction force boundary conditions read:

$$K_{\zeta} \left\{ \tilde{u}_{x,ll}^{\mathbf{m},\mathbf{n}_{i}} - \frac{1}{3} \left(\tilde{u}_{x,ll}^{\mathbf{m}-2,\mathbf{n}_{i}} + \tilde{u}_{x,ll}^{\mathbf{m}+2,\mathbf{n}_{i}} \right) - \frac{1}{6} \left(\tilde{u}_{x,ll}^{\mathbf{m}-1,\mathbf{n}_{i}+1} + \tilde{u}_{x,ll}^{\mathbf{m}+1,\mathbf{n}_{i}+1} \right) + \frac{\sqrt{3}}{6} \left(\tilde{u}_{z,ll}^{\mathbf{m}-1,\mathbf{n}_{i}+1} - \tilde{u}_{z,ll}^{\mathbf{m}+1,\mathbf{n}_{i}+1} \right) \right\} \\ + K_{\zeta} \left\{ \tilde{u}_{x,l}^{\mathbf{m},\mathbf{n}_{i}} - \frac{1}{3} \left(\tilde{u}_{x,l}^{\mathbf{m}-2,\mathbf{n}_{i}} + \tilde{u}_{x,l}^{\mathbf{m}+2,\mathbf{n}_{i}} \right) - \frac{1}{6} \left(\tilde{u}_{x,l}^{\mathbf{m}-1,\mathbf{n}_{i}-1} + \tilde{u}_{x,l}^{\mathbf{m}+1,\mathbf{n}_{i}-1} \right) - \frac{\sqrt{3}}{6} \left(\tilde{u}_{z,l}^{\mathbf{m}-1,\mathbf{n}_{i}-1} - \tilde{u}_{z,l}^{\mathbf{m}+1,\mathbf{n}_{i}-1} \right) \right\} \\ + s^{2} \tilde{u}_{x,ll}^{\mathbf{m},\mathbf{n}_{i}} + s^{2} \tilde{u}_{x,l}^{\mathbf{m},\mathbf{n}_{i}} = 2 \tilde{P}_{x} \delta_{\mathbf{m}_{i}\mathbf{m}} \\ K_{\zeta} \left\{ \tilde{u}_{z,ll}^{\mathbf{m},\mathbf{n}_{i}} - \frac{1}{2} \left(\tilde{u}_{z,ll}^{\mathbf{m}-1,\mathbf{n}_{i}+1} + \tilde{u}_{z,ll}^{\mathbf{m}+1,\mathbf{n}_{i}+1} \right) + \frac{\sqrt{3}}{6} \left(\tilde{u}_{x,ll}^{\mathbf{m}-1,\mathbf{n}_{i}+1} - \tilde{u}_{x,ll}^{\mathbf{m}+1,\mathbf{n}_{i}+1} \right) \right\}$$

$$K_{\zeta} \left\{ \tilde{u}_{z,ll}^{\mathbf{m},\mathbf{n}_{i}} - \frac{1}{2} \left(\tilde{u}_{z,ll}^{\mathbf{m}-1,\mathbf{n}_{i}+1} + \tilde{u}_{z,ll}^{\mathbf{m}-1,\mathbf{n}_{i}+1} \right) + \frac{3\delta}{6} \left(\tilde{u}_{x,ll}^{\mathbf{m}-1,\mathbf{n}_{i}+1} - \tilde{u}_{x,ll}^{\mathbf{m}+1,\mathbf{n}_{i}+1} \right) \right\}$$

$$+ K_{\zeta} \left\{ \tilde{u}_{z,l}^{\mathbf{m},\mathbf{n}_{i}} - \frac{1}{2} \left(\tilde{u}_{z,l}^{\mathbf{m}-1,\mathbf{n}_{i}-1} + \tilde{u}_{z,l}^{\mathbf{m}+1,\mathbf{n}_{i}-1} \right) - \frac{\sqrt{3}}{6} \left(\tilde{u}_{x,l}^{\mathbf{m}-1,\mathbf{n}_{i}-1} - \tilde{u}_{x,l}^{\mathbf{m}+1,\mathbf{n}_{i}-1} \right) \right\}$$

$$+ s^{2} \tilde{u}_{z,ll}^{\mathbf{m},\mathbf{n}_{i}} + s^{2} \tilde{u}_{z,l}^{\mathbf{m},\mathbf{n}_{i}} = 2 \tilde{P}_{z} \delta_{\mathbf{m}_{i}\mathbf{m}}$$

$$(G.29)$$

Substituting equations (G.7), (G.8), (G.17) and (G.18) into equations (G.28) and (G.29), as well as incorporating the integral representation for the Kronecker Delta, we ultimately find:

$$\sum_{h=1}^{2} \left(s^{2} + K_{\zeta} \left\{ 1 - \frac{2}{3} \cos \kappa_{x} - \frac{1}{3} \left(\cos \frac{\kappa_{x}}{2} + D^{(h)} i \sqrt{3} \sin \frac{\kappa_{x}}{2} \right) e^{-\frac{\sqrt{3}}{2} i \kappa_{z}^{(h)}} \right\} \right) A_{1}^{\mathbf{i},(h)} e^{+\frac{\sqrt{3}}{2} i \kappa_{z}^{(h)} \mathbf{n}_{\mathbf{i}}} \\
+ \sum_{h=1}^{2} \left(s^{2} + K_{\zeta} \left\{ 1 - \frac{2}{3} \cos \kappa_{x} - \frac{1}{3} \left(\cos \frac{\kappa_{x}}{2} - D^{(h)} i \sqrt{3} \sin \frac{\kappa_{x}}{2} \right) e^{+\frac{\sqrt{3}}{2} i \kappa_{z}^{(h)}} \right\} \right) A_{2}^{\mathbf{i},(h)} e^{-\frac{\sqrt{5}}{2} i \kappa_{z}^{(h)} \mathbf{n}_{\mathbf{i}}} \\
+ \sum_{h=1}^{2} \left(s^{2} + K_{\zeta} \left\{ 1 - \frac{2}{3} \cos \kappa_{x} - \frac{1}{3} \left(\cos \frac{\kappa_{x}}{2} - D^{(h)} i \sqrt{3} \sin \frac{\kappa_{x}}{2} \right) e^{+\frac{\sqrt{5}}{2} i \kappa_{z}^{(h)}} \right\} \right) A_{3}^{\mathbf{i},(h)} e^{+\frac{\sqrt{5}}{2} i \kappa_{z}^{(h)} \mathbf{n}_{\mathbf{i}}} = \frac{\tilde{P}_{x}}{2\pi} e^{\frac{1}{2} i \kappa_{x} \mathbf{m}_{\mathbf{i}}}$$
(G.30)

$$\begin{split} &\sum_{h=1}^{2} \left(s^{2} + K_{\zeta} \left\{ 1 - \left(\cos \frac{\kappa_{x}}{2} + \frac{\mathrm{i}}{D^{(h)} \sqrt{3}} \sin \frac{\kappa_{x}}{2} \right) e^{-\frac{\sqrt{5}}{2} \mathrm{i} \kappa_{z}^{(h)}} \right\} \right) D^{(h)} A_{\mathbf{l}}^{\mathbf{i},(h)} e^{+\frac{\sqrt{5}}{2} \mathrm{i} \kappa_{z}^{(h)} \mathbf{n}_{\mathbf{i}}} \\ &- \sum_{h=1}^{2} \left(s^{2} + K_{\zeta} \left\{ 1 - \left(\cos \frac{\kappa_{x}}{2} - \frac{\mathrm{i}}{D^{(h)} \sqrt{3}} \sin \frac{\kappa_{x}}{2} \right) e^{+\frac{\sqrt{5}}{2} \mathrm{i} \kappa_{z}^{(h)}} \right\} \right) D^{(h)} A_{2}^{\mathbf{i},(h)} e^{-\frac{\sqrt{5}}{2} \mathrm{i} \kappa_{z}^{(h)} \mathbf{n}_{\mathbf{i}}} \\ &+ \sum_{h=1}^{2} \left(s^{2} + K_{\zeta} \left\{ 1 - \left(\cos \frac{\kappa_{x}}{2} - \frac{\mathrm{i}}{D^{(h)} \sqrt{3}} \sin \frac{\kappa_{x}}{2} \right) e^{+\frac{\sqrt{5}}{2} \mathrm{i} \kappa_{z}^{(h)}} \right\} \right) D^{(h)} A_{3}^{\mathbf{i},(h)} e^{+\frac{\sqrt{5}}{2} \mathrm{i} \kappa_{z}^{(h)} \mathbf{n}_{\mathbf{i}}} = \frac{\tilde{P}_{z}}{2\pi} e^{\frac{1}{2} \mathrm{i} \kappa_{x} \mathbf{m}_{\mathbf{i}}} \end{split}$$

$$(G.31)$$

Together, equations (G.11), (G.12), (G.19), (G.20), (G.30) and (G.31), give the complete system of boundary conditions in terms of the wave amplitudes. Solving this system for $\tilde{P}_x = 1$ and $\tilde{P}_z = 0$ yields the wave amplitudes $A_{x;1}^{\mathbf{i},(h)}$, $A_{x;2}^{\mathbf{i},(h)}$ and $A_{x;3}^{\mathbf{i},(h)}$ for h = 1...2. Accordingly, solving the given system for $\tilde{P}_x = 0$ and $\tilde{P}_z = 1$ yields the wave amplitudes $A_{z;1}^{\mathbf{i},(h)}$ to $A_{z;3}^{\mathbf{i},(h)}$ for h = 1...2.

G.2 Boundary conditions for a load at the half-plane surface

For a load applied at the surface of the half-plane of particles, we consider the half-plane as a single system that, comparing it with the approach for a load inside the half-plane of particles, coincides with subsystem II for the case that $\mathbf{n_i} = 0$. In this case, we only require the two boundary conditions at the surface of the half-plane of particles. Incorporating the horizontal and vertical components of a load applied at a particle \mathbf{i} at the surface of the half-plane by means of the Kronecker Delta, the force balance at the surface of the half-plane of particles yields the two boundary conditions as:

$$R_{x,H}^{\mathbf{m},0} = P_x \delta_{\mathbf{m},\mathbf{m}} \tag{G.32}$$

$$R_{z,II}^{\mathbf{m},0} = P_z \delta_{\mathbf{m},\mathbf{m}} \tag{G.33}$$

As stated previously, at a free surface of the system of particles, the reaction forces follow directly from the respective force equilibria, i.e. the equations of motion, of that particle. The expressions for the horizontal and vertical reaction forces for a half-particle in subsystem II were previously given by equations (G.21) and (G.22). Adapting the given expressions for the reaction forces to denote a surface particle by substituting $\mathbf{n}_i = 0$ and incorporating them into equations (G.32) and (G.33) yields the following boundary conditions at the surface of the half-plane:

$$M\ddot{u}_{x,II}^{\mathbf{m},0} + \hat{K}_{e} \begin{cases} 3u_{x,II}^{\mathbf{m},0} - u_{x,II}^{\mathbf{m}-2,0} - u_{x,II}^{\mathbf{m}+2,0} - \frac{1}{2} \left(u_{x,II}^{\mathbf{m}-1,1} + u_{x,II}^{\mathbf{m}+1,1} \right) \\ + \frac{\sqrt{3}}{2} \left(u_{z,II}^{\mathbf{m}-1,1} - u_{z,II}^{\mathbf{m}+1,1} \right) \end{cases} = 2P_{x}\delta_{\mathbf{m}_{i}\mathbf{m}}$$
(G.34)

$$M\ddot{u}_{z,H}^{\mathbf{m},0} + \hat{K}_{e} \left\{ 3u_{z,H}^{\mathbf{m},0} - \frac{3}{2} \left(u_{z,H}^{\mathbf{m}-1,1} + u_{z,H}^{\mathbf{m}+1,1} \right) + \frac{\sqrt{3}}{2} \left(u_{x,H}^{\mathbf{m}-1,1} - u_{x,H}^{\mathbf{m}+1,1} \right) \right\} = 2P_{z}\delta_{\mathbf{m}_{i}\mathbf{m}}$$
(G.35)

To obtain the corresponding dimensionless boundary conditions, we introduce the dimensionless parameters for time, space and force previously given by equation (G.27). Then,

noting that $\hat{K}_e = K_e + C_e \frac{\partial}{\partial t}$, as well as dividing by $M \omega_0^2 \ell$, applying the Laplace transform and introducing the operator $K_{\zeta} = 1 + 2\zeta s$, the Laplace domain reaction force boundary conditions at the half-plane surface read:

$$s^{2}\tilde{u}_{x,H}^{\mathbf{m},\mathbf{0}} + K_{\zeta} \left\{ \tilde{u}_{x,H}^{\mathbf{m},\mathbf{0}} - \frac{1}{3} \left(\tilde{u}_{x,H}^{\mathbf{m}-\mathbf{2},\mathbf{0}} + \tilde{u}_{x,H}^{\mathbf{m}+\mathbf{2},\mathbf{0}} \right) - \frac{1}{6} \left(\tilde{u}_{x,H}^{\mathbf{m}-\mathbf{1},\mathbf{1}} + \tilde{u}_{x,H}^{\mathbf{m}+\mathbf{1},\mathbf{1}} \right) + \frac{\sqrt{3}}{6} \left(\tilde{u}_{z,H}^{\mathbf{m}-\mathbf{1},\mathbf{1}} - \tilde{u}_{z,H}^{\mathbf{m}+\mathbf{1},\mathbf{1}} \right) \right\} = 2\tilde{P}_{x}\delta_{\mathbf{m}_{i}\mathbf{m}}$$
 (G.36)

$$s^{2}\tilde{u}_{z,H}^{\mathbf{m},0} + K_{\zeta} \left\{ \tilde{u}_{z,H}^{\mathbf{m},0} - \frac{1}{2} \left(\tilde{u}_{z,H}^{\mathbf{m}-1,1} + \tilde{u}_{z,H}^{\mathbf{m}+1,1} \right) + \frac{\sqrt{3}}{6} \left(\tilde{u}_{x,H}^{\mathbf{m}-1,1} - \tilde{u}_{x,H}^{\mathbf{m}+1,1} \right) \right\} = 2\tilde{P}_{z}\delta_{\mathbf{m};\mathbf{m}}$$
(G.37)

Substituting the horizontal and vertical displacements of a particle **m,n** in subsystem *II*, previously given by equations (G.17) and (G.18), into equations (G.36) and (G.37), as well as incorporating the integral representation for the Kronecker Delta, we ultimately find:

$$\sum_{h=1}^{2} \left\{ s^{2} + K_{\zeta} \left\{ 1 - \frac{2}{3} \cos \kappa_{x} - \frac{1}{3} \left(\cos \frac{\kappa_{x}}{2} - D^{(h)} i \sqrt{3} \sin \frac{\kappa_{x}}{2} \right) e^{+\frac{\sqrt{5}}{2} i \kappa_{z}^{(h)}} \right\} \right\} A_{3}^{i,(h)} = \frac{\tilde{P}_{x}}{2\pi} e^{\frac{1}{2} i \kappa_{x} \mathbf{m}_{i}} \quad (G.38)$$

$$\sum_{h=1}^{2} \left\{ s^{2} + K_{\zeta} \left\{ 1 - \left(\cos \frac{\kappa_{x}}{2} - \frac{i}{D^{(h)} \sqrt{3}} \sin \frac{\kappa_{x}}{2} \right) e^{+\frac{\sqrt{E}}{2} i \kappa_{z}^{(h)}} \right\} \right\} D^{(h)} A_{3}^{\mathbf{i},(h)} = \frac{\tilde{P}_{z}}{2\pi} e^{\frac{1}{2} i \kappa_{x} \mathbf{m}_{\mathbf{i}}}$$
(G.39)

G.3 Green's reaction forces at the left surface particle

The cell configuration for the left surface particle j at the boundary Γ is depicted in Figure G.1. As stated in Section 4.4.4, the reaction forces must be obtained for the subparticles along the boundary Γ of the far-field body V, rather than along the boundary Γ_{cav} of the near-field, or cavity, body V_{cav} .

Disregarding the involved subsystems that follow from the location of the loaded particle **i**, the horizontal and vertical reaction forces at the left surface particle are found as:

$$\tilde{R}_{x}^{j,i}(s) = \frac{1}{3}s^{2}\tilde{u}_{x}^{m_{j},0} + \frac{1}{6}K_{\zeta}\begin{pmatrix} \frac{7}{4}\tilde{u}_{x}^{m_{j},0} - \tilde{u}_{x}^{m_{j}-2,0} - \frac{1}{4}(\tilde{u}_{x}^{m_{j}+1,1} + 2\tilde{u}_{x}^{m_{j}-1,1}) \\ -\frac{\sqrt{3}}{4}(\tilde{u}_{z}^{m_{j},0} + \tilde{u}_{z}^{m_{j}+1,1} - 2\tilde{u}_{z}^{m_{j}-1,1}) \end{pmatrix}$$
(G.40)

$$\tilde{R}_{z}^{\mathbf{j},\mathbf{i}}\left(s\right) = \frac{1}{3}s^{2}\tilde{u}_{z}^{\mathbf{m}_{j},0} + \frac{1}{6}K_{\zeta}\begin{pmatrix} \frac{9}{4}\tilde{u}_{z}^{\mathbf{m}_{j},0} - \frac{\sqrt{3}}{4}\left(\tilde{u}_{x}^{\mathbf{m}_{j},0} + \tilde{u}_{x}^{\mathbf{m}_{j}+1,1} - 2\tilde{u}_{x}^{\mathbf{m}_{j}-1,1}\right) \\ -\frac{3}{4}\left(\tilde{u}_{z}^{\mathbf{m}_{j}+1,1} + 2\tilde{u}_{z}^{\mathbf{m}_{j}-1,1}\right) \end{pmatrix}$$
(G.41)

The corresponding Green's reaction forces are obtained from equations (G.40) and (G.41) by substituting the given Laplace domain displacements by the corresponding Green's displacements.

In the following, the expressions for $\varphi_{x;r}^{(h)}$ and $\varphi_{z;r}^{(h)}$, with r = 1..3, will first be obtained for a loaded particle in the interior of the half-plane and, subsequently, for a loaded particle at the surface of the half-plane.

For a load at a particle in the interior of the half-plane

When the loaded particle $\bf i$ is located in inside the half-plane of particles, i.e. $\bf n_i > \bf n_j$, it follows that all displacements in equations (G.40) and (G.41) may be considered as degrees of freedom of subsystem $\bf I$. Substituting the Green's displacements for a particle $\bf j$ in subsystem $\bf I$, previously given in Section 4.4.3, into equations (G.40) and (G.41), thus yields the corresponding Green's reaction forces. The expressions for $\varphi_{x;r}^{(h)}$ with r=1...3 are in this case found as:

$$\begin{split} \varphi_{x;1}^{(h)} &= \frac{1}{3}s^2 + \frac{1}{6}K_{\zeta} \begin{pmatrix} \frac{3}{2} - e^{+i\kappa_{x}} + \frac{1}{4}\left(1 - D^{(h)}\sqrt{3}\right) \\ -\frac{1}{4}\left(\left(1 - D^{(h)}\sqrt{3}\right)e^{+\frac{1}{2}i\kappa_{x}} + 2\left(\cos\frac{\kappa_{x}}{2} - D^{(h)}i\sqrt{3}\sin\frac{\kappa_{x}}{2}\right)\right)e^{+\frac{\sqrt{5}}{2}i\kappa_{z}^{(h)}} \end{pmatrix} \\ \varphi_{x;2}^{(h)} &= \frac{1}{3}s^2 + \frac{1}{6}K_{\zeta} \begin{pmatrix} \frac{3}{2} - e^{+i\kappa_{x}} + \frac{1}{4}\left(1 + D^{(h)}\sqrt{3}\right) \\ -\frac{1}{4}\left(\left(1 + D^{(h)}\sqrt{3}\right)e^{+\frac{1}{2}i\kappa_{x}} + 2\left(\cos\frac{\kappa_{x}}{2} + D^{(h)}i\sqrt{3}\sin\frac{\kappa_{x}}{2}\right)\right)e^{-\frac{\sqrt{5}}{2}i\kappa_{z}^{(h)}} \end{pmatrix} \\ \varphi_{x;3}^{(h)} &= 0 \end{split}$$

Accordingly, the expressions for $\varphi_{z,r}^{(h)}$ with r = 1..3 are respectively found as:

$$\begin{split} \varphi_{z;1}^{(h)} &= \frac{1}{3} s^2 D^{(h)} + \frac{1}{6} K_{\zeta} \begin{pmatrix} \frac{3}{2} D^{(h)} - \frac{\sqrt{3}}{4} \left(1 - D^{(h)} \sqrt{3}\right) \\ + \left(\frac{\sqrt{3}}{4} \left(1 - D^{(h)} \sqrt{3}\right) e^{+\frac{1}{2} i \kappa_{x}} - \frac{3}{2} \left(D^{(h)} \cos \frac{\kappa_{x}}{2} - \frac{i}{\sqrt{3}} \sin \frac{\kappa_{x}}{2}\right) \right) e^{+\frac{\sqrt{5}}{2} i \kappa_{z}^{(h)}} \end{pmatrix} \\ \varphi_{z;2}^{(h)} &= -\frac{1}{3} s^2 D^{(h)} - \frac{1}{6} K_{\zeta} \begin{pmatrix} \frac{3}{2} D^{(h)} + \frac{\sqrt{3}}{4} \left(1 + D^{(h)} \sqrt{3}\right) \\ - \left(\frac{\sqrt{3}}{4} \left(1 + D^{(h)} \sqrt{3}\right) e^{+\frac{1}{2} i \kappa_{x}} + \frac{3}{2} \left(D^{(h)} \cos \frac{\kappa_{x}}{2} + \frac{i}{\sqrt{3}} \sin \frac{\kappa_{x}}{2}\right) \right) e^{-\frac{\sqrt{5}}{2} i \kappa_{z}^{(h)}} \end{pmatrix} \\ \varphi_{z;3}^{(h)} &= 0 \end{split}$$

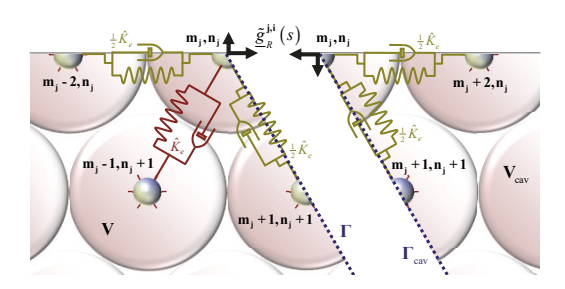


Figure G.1: Cell configuration of the left surface particle.

For a load at a particle at the half-plane surface

When the loaded particle $\bf i$ is located at the surface of the half-plane, i.e. for $\bf n_i=0$, the half-plane is considered as a single system and consists of degrees of freedom of subsystem $\it II$. Substituting the Green's displacements from Section 4.4.3 specifically for a particle $\bf j$ in subsystem $\it II$, into equations (G.40) and (G.41) yields the expressions for $\varphi_{x,r}^{(h)}$ with r=1..3 respectively as:

$$\begin{split} & \varphi_{x;1}^{(h)} = \varphi_{x;2}^{(h)} = 0 \\ & \varphi_{x;3}^{(h)} = \frac{1}{3} s^2 + \frac{1}{6} K_{\zeta} \left(\frac{\frac{3}{2} - e^{+i\kappa_x} + \frac{1}{4} \left(1 - D^{(h)} \sqrt{3} \right)}{-\left(\frac{1}{4} \left(1 - D^{(h)} \sqrt{3} \right) e^{+\frac{1}{2}i\kappa_x} + \frac{1}{2} \left(\cos \frac{\kappa_x}{2} - D^{(h)} i \sqrt{3} \sin \frac{\kappa_x}{2} \right) \right) e^{+\frac{\sqrt{6}}{2}i\kappa_z^{(h)}} \end{split}$$

Accordingly, the expressions for $\varphi_{z,r}^{(h)}$ with r = 1..3 are respectively found as:

$$\begin{split} & \varphi_{z;1}^{(h)} = \varphi_{z;2}^{(h)} = 0 \\ & \varphi_{z;3}^{(h)} = \frac{1}{3} s^2 D^{(h)} + \frac{1}{6} K_{\zeta} \begin{pmatrix} \frac{3}{2} D^{(h)} - \frac{\sqrt{3}}{4} \left(1 - D^{(h)} \sqrt{3}\right) \\ & + \left(\frac{\sqrt{3}}{4} \left(1 - D^{(h)} \sqrt{3}\right) e^{+\frac{1}{2} i \kappa_{x}} - \frac{3}{2} \left(D^{(h)} \cos \frac{\kappa_{x}}{2} - \frac{i}{\sqrt{3}} \sin \frac{\kappa_{x}}{2}\right) \right) e^{+\frac{\sqrt{3}}{2} i \kappa_{z}^{(h)}} \end{pmatrix} \end{split}$$

G.4 Green's reaction forces at a particle along the left slope

The cell configuration for a particle j along the left slope of the interface Γ is depicted in Figure G.2a. Disregarding the involved subsystems, the horizontal and vertical reaction forces at a particle along the left slope of the interface Γ are obtained as:

$$\tilde{R}_{x}^{j,i}(s) = \frac{1}{2}s^{2}\tilde{u}_{x}^{\mathbf{m}_{j},\mathbf{n}_{j}} + \frac{1}{6}K_{\zeta} \begin{pmatrix} 3\tilde{u}_{x}^{\mathbf{m}_{j},\mathbf{n}_{j}} - \frac{1}{4}\left(\tilde{u}_{x}^{\mathbf{m}_{j}+\mathbf{1},\mathbf{n}_{j}+1} + 2\tilde{u}_{x}^{\mathbf{m}_{j}-\mathbf{1},\mathbf{n}_{j}+1} + \tilde{u}_{x}^{\mathbf{m}_{j}-\mathbf{1},\mathbf{n}_{j}-1}\right) \\ -2\tilde{u}_{x}^{\mathbf{m}_{j}-\mathbf{2},\mathbf{n}_{j}} - \frac{\sqrt{3}}{4}\left(\tilde{u}_{z}^{\mathbf{m}_{j}+\mathbf{1},\mathbf{n}_{j}+1} - 2\tilde{u}_{z}^{\mathbf{m}_{j}-\mathbf{1},\mathbf{n}_{j}+1} + \tilde{u}_{z}^{\mathbf{m}_{j}-\mathbf{1},\mathbf{n}_{j}-1}\right) \end{pmatrix} \tag{G.42}$$

$$\tilde{R}_{z}^{\mathbf{j},\mathbf{i}}(s) = \frac{1}{2}s^{2}\tilde{u}_{z}^{\mathbf{m}_{j},\mathbf{n}_{j}} + \frac{1}{6}K_{\zeta} \begin{pmatrix} 3\tilde{u}_{z}^{\mathbf{m}_{j},\mathbf{n}_{j}} - \frac{\sqrt{3}}{4} \left(\tilde{u}_{x}^{\mathbf{m}_{j}+1,\mathbf{n}_{j}+1} - 2\tilde{u}_{x}^{\mathbf{m}_{j}-1,\mathbf{n}_{j}+1} + \tilde{u}_{x}^{\mathbf{m}_{j}-1,\mathbf{n}_{j}-1} \right) \\ -\frac{3}{4} \left(\tilde{u}_{z}^{\mathbf{m}_{j}+1,\mathbf{n}_{j}+1} + 2\tilde{u}_{z}^{\mathbf{m}_{j}-1,\mathbf{n}_{j}+1} + \tilde{u}_{z}^{\mathbf{m}_{j}-1,\mathbf{n}_{j}-1} \right) \end{pmatrix} \tag{G.43}$$

The corresponding Green's reaction forces are obtained from equations (G.42) and (G.43) by replacing the given Laplace domain displacements by the corresponding Green's displacements.

For a load at a particle further from the surface of the half-plane

When the loaded particle **i** is located further from the surface of the half-plane than particle **j**, i.e. when $\mathbf{n_i} > \mathbf{n_j}$, all displacements in equations (G.42) and (G.43) may be considered as

degrees of freedom of subsystem *I*. Substituting the Green's displacements for a particle **j** in subsystem *I* from Section 4.4.3 into equations (G.42) and (G.43), we find the expressions for $\varphi_{x:r}^{(h)}$ with r = 1..3 as:

$$\begin{split} \varphi_{x;1}^{(h)} &= \frac{1}{2} s^2 + \frac{1}{6} K_{\zeta} \begin{pmatrix} 3 - 2 e^{+i\kappa_{x}} - \frac{1}{4} \left(1 + D^{(h)} \sqrt{3} \right) e^{+\frac{1}{2}i\kappa_{x}} e^{-\frac{\sqrt{5}}{2}i\kappa_{z}^{(h)}} \\ - \frac{1}{4} \left(\left(1 - D^{(h)} \sqrt{3} \right) e^{+\frac{1}{2}i\kappa_{x}} + 2 \left(\cos \frac{\kappa_{x}}{2} - D^{(h)} i \sqrt{3} \sin \frac{\kappa_{x}}{2} \right) \right) e^{+\frac{\sqrt{5}}{2}i\kappa_{z}^{(h)}} \\ \varphi_{x;2}^{(h)} &= \frac{1}{2} s^2 + \frac{1}{6} K_{\zeta} \begin{pmatrix} 3 - 2 e^{+i\kappa_{x}} - \frac{1}{4} \left(1 - D^{(h)} \sqrt{3} \right) e^{+\frac{1}{2}i\kappa_{x}} e^{+\frac{\sqrt{5}}{2}i\kappa_{z}^{(h)}} \\ - \frac{1}{4} \left(\left(1 + D^{(h)} \sqrt{3} \right) e^{+\frac{1}{2}i\kappa_{x}} + 2 \left(\cos \frac{\kappa_{x}}{2} + D^{(h)} i \sqrt{3} \sin \frac{\kappa_{x}}{2} \right) \right) e^{-\frac{\sqrt{5}}{2}i\kappa_{z}^{(h)}} \\ \varphi_{x;3}^{(h)} &= 0 \end{split}$$

Accordingly, we find the expressions for $\varphi_{z;r}^{(h)}$ with r = 1..3 respectively as:

$$\begin{split} \varphi_{z;1}^{(h)} &= \frac{1}{2} s^2 D^{(h)} + \frac{1}{6} K_{\zeta} \begin{pmatrix} 3D^{(h)} - \frac{\sqrt{3}}{4} \left(1 + D^{(h)} \sqrt{3}\right) e^{+\frac{1}{2} i \kappa_{x}} e^{-\frac{\sqrt{5}}{2} i \kappa_{z}^{(h)}} \\ + \left(\frac{\sqrt{3}}{4} \left(1 - D^{(h)} \sqrt{3}\right) e^{+\frac{1}{2} i \kappa_{x}} - \frac{3}{2} \left(D^{(h)} \cos \frac{\kappa_{x}}{2} - \frac{i}{\sqrt{3}} \sin \frac{\kappa_{x}}{2}\right) \right) e^{+\frac{\sqrt{5}}{2} i \kappa_{z}^{(h)}} \end{pmatrix} \\ \varphi_{z;2}^{(h)} &= \frac{1}{2} s^2 D^{(h)} + \frac{1}{6} K_{\zeta} \begin{pmatrix} 3D^{(h)} + \frac{\sqrt{3}}{4} \left(1 - D^{(h)} \sqrt{3}\right) e^{-\frac{1}{2} i \kappa_{x}} e^{-\frac{\sqrt{5}}{2} i \kappa_{z}^{(h)}} \\ - \left(\frac{\sqrt{3}}{4} \left(1 + D^{(h)} \sqrt{3}\right) e^{-\frac{1}{2} i \kappa_{x}} + \frac{3}{2} \left(D^{(h)} \cos \frac{\kappa_{x}}{2} - \frac{i}{\sqrt{3}} \sin \frac{\kappa_{x}}{2}\right) \right) e^{+\frac{\sqrt{5}}{2} i \kappa_{z}^{(h)}} \end{pmatrix} \\ \varphi_{z;3}^{(h)} &= 0 \end{split}$$

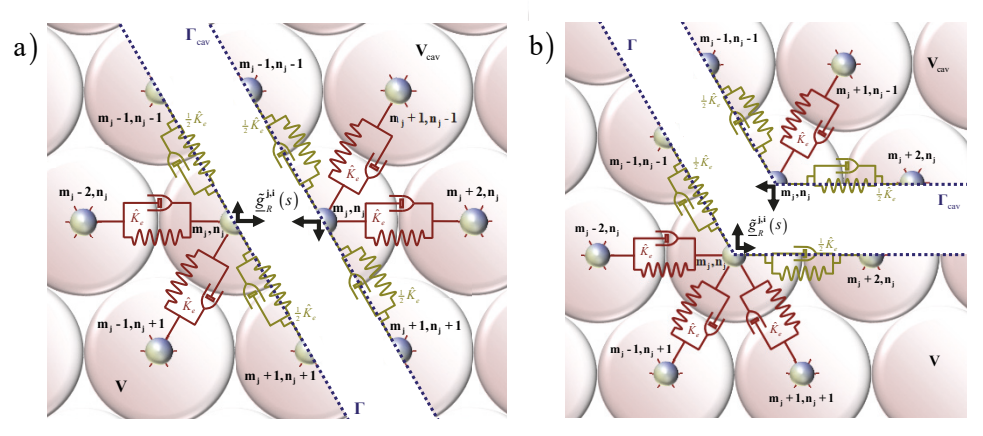


Figure G.2: a) Cell configuration of a particle along the left slope; b) Cell configuration of the left corner particle.

For a load at a particle closer to the surface of the half-plane

When the loaded particle **i** is located closer to the surface of the half-plane of particles than the particle **j**, i.e. for $\mathbf{n_i} < \mathbf{n_j}$, the Green's displacements in equations (G.42) and (G.43) are all degrees of freedom of subsystem *II*. Substituting the Green's displacements for a particle **j** in subsystem *II* from Section 4.4.3 into equations (G.42) and (G.43), the expressions for $\phi_{vr}^{(h)}$ and $\phi_{vr}^{(h)}$ with r = 1...3 are:

$$\begin{split} \varphi_{x;1}^{(h)} &= \varphi_{x;2}^{(h)} = \varphi_{z;1}^{(h)} = \varphi_{z;2}^{(h)} = 0 \\ \varphi_{x;3}^{(h)} &= \frac{1}{2} s^2 + \frac{1}{6} K_{\zeta} \begin{pmatrix} 3 - 2 e^{+i\kappa_x} - \frac{1}{4} \left(1 + D^{(h)} \sqrt{3} \right) e^{+\frac{1}{2}i\kappa_x} e^{-\frac{\sqrt{5}}{2}i\kappa_z^{(h)}} \\ -\frac{1}{4} \left(\left(1 - D^{(h)} \sqrt{3} \right) e^{+\frac{1}{2}i\kappa_x} + 2 \left(\cos \frac{\kappa_x}{2} - D^{(h)} i \sqrt{3} \sin \frac{\kappa_x}{2} \right) \right) e^{+\frac{\sqrt{5}}{2}i\kappa_z^{(h)}} \\ \varphi_{z;3}^{(h)} &= \frac{1}{2} s^2 D^{(h)} + \frac{1}{6} K_{\zeta} \begin{pmatrix} 3 D^{(h)} - \frac{\sqrt{3}}{4} \left(1 + D^{(h)} \sqrt{3} \right) e^{+\frac{1}{2}i\kappa_x} e^{-\frac{\sqrt{5}}{2}i\kappa_z^{(h)}} \\ + \left(\frac{\sqrt{3}}{4} \left(1 - D^{(h)} \sqrt{3} \right) e^{+\frac{1}{2}i\kappa_x} - \frac{3}{2} \left(D^{(h)} \cos \frac{\kappa_x}{2} - \frac{i}{\sqrt{3}} \sin \frac{\kappa_x}{2} \right) \right) e^{+\frac{\sqrt{5}}{2}i\kappa_z^{(h)}} \end{split}$$

For a load at the same level of the considered particle

When the loaded particle i is located at the same level of the half-plane of particles as particle j, i.e. when $n_i = n_j$, the displacements appearing in equations (G.42) and (G.43) no longer all belong to the same subsystem. The particles with horizontal nodal coordinate $n_j - 1$ belong to subsystem I, while the particles with nodal coordinate $n_j + 1$ belong to subsystem II. The particles with horizontal nodal coordinate n_j are located at the interface of the subsystems, and their displacements are therefore degrees of freedom that exist in both subsystems. In this case, we choose to let the corresponding subsystem of a particle at the interface of the two susbsystems depend on the location of its associated rheological element. This means that when a rheological element is for example located in subsystem I, the degrees of freedom associated with the elongation of that element are also considered to be part of subsystem I.

Substituting the corresponding Green's displacements into equations (G.42) and (G.43) yields the expressions for $\varphi_{x,r}^{(h)}$ and $\varphi_{z,r}^{(h)}$ with r = 1..3 respectively as:

$$\begin{split} & \varphi_{x;1}^{(h)} = \frac{1}{6} \, s^2 + \frac{1}{6} \, K_{\zeta} \left(1 - e^{+i\kappa_x} + \frac{1}{4} \left(1 + D^{(h)} \sqrt{3} \right) \left(1 - e^{+\frac{1}{2}i\kappa_x} e^{-\frac{\sqrt{5}}{2}i\kappa_z^{(h)}} \right) \right) \\ & \varphi_{x;2}^{(h)} = \frac{1}{6} \, s^2 + \frac{1}{6} \, K_{\zeta} \left(1 - e^{+i\kappa_x} + \frac{1}{4} \left(1 - D^{(h)} \sqrt{3} \right) \left(1 - e^{+\frac{1}{2}i\kappa_x} e^{+\frac{\sqrt{5}}{2}i\kappa_z^{(h)}} \right) \right) \\ & \varphi_{x;3}^{(h)} = \frac{1}{3} \, s^2 + \frac{1}{6} \, K_{\zeta} \left(\frac{\frac{3}{2} - e^{+i\kappa_x} + \frac{1}{4} \left(1 - D^{(h)} \sqrt{3} \right)}{1 - \frac{1}{4} \left(\left(1 - D^{(h)} \sqrt{3} \right) e^{+\frac{1}{2}i\kappa_x} + 2 \left(\cos \frac{\kappa_x}{2} - D^{(h)} i \sqrt{3} \sin \frac{\kappa_x}{2} \right) \right) e^{+\frac{\sqrt{5}}{2}i\kappa_z^{(h)}} \end{split}$$

$$\begin{split} \varphi_{z;1}^{(h)} &= \frac{1}{6} s^2 D^{(h)} + \frac{1}{6} K_{\zeta} \frac{\sqrt{3}}{4} \left(1 + D^{(h)} \sqrt{3} \right) \left(1 - e^{+\frac{1}{2} i \kappa_x} e^{-\frac{\sqrt{2}}{2} i \kappa_z^{(h)}} \right) \\ \varphi_{z;2}^{(h)} &= -\frac{1}{6} s^2 D^{(h)} + \frac{1}{6} K_{\zeta} \frac{\sqrt{3}}{4} \left(1 - D^{(h)} \sqrt{3} \right) \left(1 - e^{+\frac{1}{2} i \kappa_x} e^{+\frac{\sqrt{2}}{2} i \kappa_z^{(h)}} \right) \\ \varphi_{z;3}^{(h)} &= \frac{1}{3} s^2 D^{(h)} + \frac{1}{6} K_{\zeta} \left(\frac{\frac{3}{2}}{2} D^{(h)} - \frac{\sqrt{3}}{4} \left(1 - D^{(h)} \sqrt{3} \right) + \left(\frac{\sqrt{3}}{4} \left(1 - D^{(h)} \sqrt{3} \right) e^{+\frac{1}{2} i \kappa_x} - \frac{3}{2} \left(D^{(h)} \cos \frac{\kappa_x}{2} - \frac{i}{\sqrt{3}} \sin \frac{\kappa_x}{2} \right) \right) e^{+\frac{\sqrt{2}}{2} i \kappa_z^{(h)}} \end{split}$$

G.5 Green's reaction forces at the left corner particle

The cell configuration for the left corner particle \mathbf{j} along Γ is depicted in Figure G.2b. Disregarding the involved subsystems, the reaction forces at the left corner particle \mathbf{j} are:

$$\tilde{R}_{x}^{\mathbf{j},\mathbf{i}}\left(s\right) = \frac{2}{3}s^{2}\tilde{u}_{x}^{\mathbf{m}_{j},\mathbf{n}_{j}} + \frac{1}{6}K_{\zeta} \left\{ \begin{cases}
\frac{17}{4}\tilde{u}_{x}^{\mathbf{m}_{j},\mathbf{n}_{j}} - 2\tilde{u}_{x}^{\mathbf{m}_{j}-2,\mathbf{n}_{j}} - \tilde{u}_{x}^{\mathbf{m}_{j}+2,\mathbf{n}_{j}} \\
-\frac{1}{4}\left(2\tilde{u}_{x}^{\mathbf{m}_{j}+1,\mathbf{n}_{j}+1} + 2\tilde{u}_{x}^{\mathbf{m}_{j}-1,\mathbf{n}_{j}+1} + \tilde{u}_{x}^{\mathbf{m}_{j}-1,\mathbf{n}_{j}-1}\right) \\
+\frac{\sqrt{3}}{4}\left(\tilde{u}_{z}^{\mathbf{m}_{j},\mathbf{n}_{j}} - 2\tilde{u}_{z}^{\mathbf{m}_{j}+1,\mathbf{n}_{j}+1} + 2\tilde{u}_{z}^{\mathbf{m}_{j}-1,\mathbf{n}_{j}+1} - \tilde{u}_{z}^{\mathbf{m}_{j}-1,\mathbf{n}_{j}-1}\right)
\end{cases} \tag{G.44}$$

$$\tilde{R}_{z}^{\mathbf{j},\mathbf{i}}\left(s\right) = \frac{2}{3} s^{2} \tilde{u}_{z}^{\mathbf{m}_{j},\mathbf{n}_{j}} + \frac{1}{6} K_{\zeta} \left\{ -\frac{\sqrt{3}}{4} \left(-\tilde{u}_{x}^{\mathbf{m}_{j},\mathbf{n}_{j}} + 2\tilde{u}_{x}^{\mathbf{m}_{j}+1,\mathbf{n}_{j}+1} - 2\tilde{u}_{x}^{\mathbf{m}_{j}-1,\mathbf{n}_{j}+1} + \tilde{u}_{x}^{\mathbf{m}_{j}-1,\mathbf{n}_{j}-1} \right) + \frac{15}{4} \tilde{u}_{z}^{\mathbf{m}_{j},\mathbf{n}_{j}} - \frac{3}{4} \left(2\tilde{u}_{z}^{\mathbf{m}_{j}+1,\mathbf{n}_{j}+1} + 2\tilde{u}_{z}^{\mathbf{m}_{j}-1,\mathbf{n}_{j}+1} + \tilde{u}_{z}^{\mathbf{m}_{j}-1,\mathbf{n}_{j}-1} \right) \right\}$$
(G.45)

Since particles i and j are both located along Γ and the left corner particle is at the bottom, the loaded particle i is either at the same level as particle j, or closer to the half-plane surface.

For a load at a particle closer to the surface of the half-plane

When the loaded particle **i** is closer to the surface of the half-plane than particle **j**, i.e. for $\mathbf{n_i} < \mathbf{n_j}$, the displacements in equations (G.44) and (G.45) may all be considered degrees of freedom of subsystem *II*. Substituting the corresponding Green's displacements for a particle **j** in subsystem *II*, the expressions for $\varphi_{x,r}^{(h)}$ and $\varphi_{z,r}^{(h)}$ with r = 1...3 are obtained as:

$$\begin{split} \varphi_{x;1}^{(h)} &= \varphi_{x;2}^{(h)} = \varphi_{z;1}^{(h)} = \varphi_{z;2}^{(h)} = 0 \\ \varphi_{x;3}^{(h)} &= \frac{2}{3} s^2 + \frac{1}{6} K_{\zeta} \begin{cases} 4 - 2 \cos \kappa_x - e^{+i\kappa_x} + \frac{1}{4} \left(1 + D^{(h)} \sqrt{3} \right) \left(1 - e^{+\frac{1}{2} i \kappa_x} e^{-\frac{\sqrt{5}}{2} i \kappa_z^{(h)}} \right) \\ - \left(\cos \frac{\kappa_x}{2} - D^{(h)} i \sqrt{3} \sin \frac{\kappa_x}{2} \right) e^{+\frac{\sqrt{5}}{2} i \kappa_z^{(h)}} \end{cases} \\ \varphi_{z;3}^{(h)} &= \frac{2}{3} s^2 D^{(h)} + \frac{1}{6} K_{\zeta} \begin{cases} 3 D^{(h)} + \frac{\sqrt{3}}{4} \left(1 + D^{(h)} \sqrt{3} \right) \left(1 - e^{+\frac{1}{2} i \kappa_x} e^{-\frac{\sqrt{5}}{2} i \kappa_z^{(h)}} \right) \\ - 3 \left(D^{(h)} \cos \frac{\kappa_x}{2} - \frac{i}{\sqrt{3}} \sin \frac{\kappa_x}{2} \right) e^{+\frac{\sqrt{5}}{2} i \kappa_z^{(h)}} \end{cases} \end{split}$$

For a load at the same level of the considered particle

When the loaded particle **i** is located at the same level as particle **j**, i.e. when $\mathbf{n_i} = \mathbf{n_j}$, all displacements in equations (G.44) and (G.45) may be considered as degrees of freedom of subsystem *I*. Substituting the corresponding Green's displacements for a particle **j** in subsystem *I*, the expressions for $\varphi_{x,r}^{(h)}$ and $\varphi_{z,r}^{(h)}$ with r = 1...3 are respectively found as:

$$\begin{split} & \varphi_{x;1}^{(h)} = \frac{1}{6} \, s^2 + \frac{1}{6} \, K_{\zeta} \left(1 - e^{+\mathrm{i} \kappa_x} + \frac{1}{4} \left(1 + D^{(h)} \sqrt{3} \right) \left(1 - e^{+\frac{1}{2} \mathrm{i} \kappa_x} e^{-\frac{\sqrt{5}}{2} \mathrm{i} \kappa_z^{(h)}} \right) \right) \\ & \varphi_{x;2}^{(h)} = \frac{1}{6} \, s^2 + \frac{1}{6} \, K_{\zeta} \left(1 - e^{+\mathrm{i} \kappa_x} + \frac{1}{4} \left(1 - D^{(h)} \sqrt{3} \right) \left(1 - e^{+\frac{1}{2} \mathrm{i} \kappa_x} e^{+\frac{\sqrt{5}}{2} \mathrm{i} \kappa_z^{(h)}} \right) \right) \\ & \varphi_{x;3}^{(h)} = \frac{1}{2} \, s^2 + \frac{1}{6} \, K_{\zeta} \left(3 - 2 \cos \kappa_x - \left(\cos \frac{\kappa_x}{2} - D^{(h)} \mathrm{i} \sqrt{3} \sin \frac{\kappa_x}{2} \right) e^{+\frac{\sqrt{5}}{2} \mathrm{i} \kappa_z^{(h)}} \right) \\ & \varphi_{z;1}^{(h)} = \frac{1}{6} \, s^2 D^{(h)} + \frac{1}{6} \, K_{\zeta} \, \frac{\sqrt{3}}{4} \left(1 + D^{(h)} \sqrt{3} \right) \left(1 - e^{+\frac{1}{2} \mathrm{i} \kappa_x} e^{-\frac{\sqrt{5}}{2} \mathrm{i} \kappa_z^{(h)}} \right) \\ & \varphi_{z;2}^{(h)} = -\frac{1}{6} \, s^2 D^{(h)} + \frac{1}{6} \, K_{\zeta} \, \frac{\sqrt{3}}{4} \left(1 - D^{(h)} \sqrt{3} \right) \left(1 - e^{+\frac{1}{2} \mathrm{i} \kappa_x} e^{+\frac{\sqrt{5}}{2} \mathrm{i} \kappa_z^{(h)}} \right) \\ & \varphi_{z;3}^{(h)} = \frac{1}{2} \, s^2 D^{(h)} + \frac{1}{2} \, K_{\zeta} \left(D^{(h)} - \left(D^{(h)} \cos \frac{\kappa_x}{2} - \frac{\mathrm{i}}{\sqrt{3}} \sin \frac{\kappa_x}{2} \right) e^{+\frac{\sqrt{5}}{2} \mathrm{i} \kappa_z^{(h)}} \right) \end{split}$$

G.6 Green's reaction forces at a particle along the horizontal domain

The cell configuration for a particle **j** located at the horizontal domain of the interface Γ is depicted in Figure G.3a. Disregarding the involved subsystems, the horizontal and vertical reaction forces at a particle located on the horizontal domain of the interface Γ are found as:

$$\tilde{R}_{x}^{j,i}(s) = \frac{1}{2}s^{2}\tilde{u}_{x}^{\mathbf{m}_{j},\mathbf{n}_{j}} + \frac{1}{6}K_{\zeta} \begin{cases} 3\tilde{u}_{x}^{\mathbf{m}_{j},\mathbf{n}_{j}} - \tilde{u}_{x}^{\mathbf{m}_{j}+2,\mathbf{n}_{j}} - \tilde{u}_{x}^{\mathbf{m}_{j}-2,\mathbf{n}_{j}} \\ -\frac{1}{2}(\tilde{u}_{x}^{\mathbf{m}_{j}+1,\mathbf{n}_{j}+1} + \tilde{u}_{x}^{\mathbf{m}_{j}-1,\mathbf{n}_{j}+1}) - \frac{\sqrt{3}}{2}(\tilde{u}_{z}^{\mathbf{m}_{j}+1,\mathbf{n}_{j}+1} - \tilde{u}_{z}^{\mathbf{m}_{j}-1,\mathbf{n}_{j}+1}) \end{cases}$$
(G.46)

$$R_z^{\mathbf{j},\mathbf{i}}(s) = \frac{1}{2}s^2 \tilde{u}_z^{\mathbf{m}_{\mathbf{j}},\mathbf{n}_{\mathbf{j}}} + \frac{1}{6}K_{\zeta} \left\{ 3\tilde{u}_z^{\mathbf{m}_{\mathbf{j}},\mathbf{n}_{\mathbf{j}}} - \frac{\sqrt{3}}{2} \left(\tilde{u}_x^{\mathbf{m}_{\mathbf{j}}+\mathbf{1},\mathbf{n}_{\mathbf{j}}+\mathbf{1}} - \tilde{u}_x^{\mathbf{m}_{\mathbf{j}}-\mathbf{1},\mathbf{n}_{\mathbf{j}}+\mathbf{1}} \right) - \frac{3}{2} \left(u_z^{\mathbf{m}_{\mathbf{j}}+\mathbf{1},\mathbf{n}_{\mathbf{j}}+\mathbf{1}} + \tilde{u}_z^{\mathbf{m}_{\mathbf{j}}-\mathbf{1},\mathbf{n}_{\mathbf{j}}+\mathbf{1}} \right) \right\}$$
(G.47)

Since both particles \mathbf{i} and \mathbf{j} are located at the horizontal segment of the boundary Γ , the loaded particle \mathbf{i} is located either at the same horizontal level as the particle \mathbf{j} , or at a particle closer to the half-plane surface. For both cases, i.e. for $\mathbf{n_i} \leq \mathbf{n_j}$, the displacements in equations (G.46) and (G.47) are all degrees of freedom of subsystem II. Substituting the Green's displacements for particle \mathbf{j} in subsystem II from Section 4.4.3, we obtain the expressions for $\varphi_{x;r}^{(h)}$ and $\varphi_{z;r}^{(h)}$ with r=1...3 as:

$$\varphi_{x:1}^{(h)} = \varphi_{x:2}^{(h)} = \varphi_{z:1}^{(h)} = \varphi_{z:2}^{(h)} = 0$$

$$\begin{split} & \varphi_{x;3}^{(h)} = \frac{1}{2} s^2 + \frac{1}{6} K_{\zeta} \left(3 - 2\cos \kappa_x - \left(\cos \frac{\kappa_x}{2} - D^{(h)} i \sqrt{3} \sin \frac{\kappa_x}{2} \right) e^{+\frac{\sqrt{2}}{2} i \kappa_z^{(h)}} \right) \\ & \varphi_{z;3}^{(h)} = \frac{1}{2} s^2 D^{(h)} + \frac{1}{2} K_{\zeta} \left(D^{(h)} - \left(D^{(h)} \cos \frac{\kappa_x}{2} - \frac{i}{\sqrt{3}} \sin \frac{\kappa_x}{2} \right) e^{+\frac{\sqrt{2}}{2} i \kappa_z^{(h)}} \right) \end{split}$$

G.7 Green's reaction forces at the right corner particle

The configuration for the right corner particle \mathbf{j} along Γ is depicted in Figure G.3b. Disregarding the involved subsystems, the reaction forces at the right corner particle \mathbf{j} read:

$$\tilde{R}_{x}^{\mathbf{j},\mathbf{i}}\left(s\right) = \frac{2}{3}s^{2}\tilde{u}_{x}^{\mathbf{m}_{j},\mathbf{n}_{j}} + \frac{1}{6}K_{\zeta} \begin{cases}
\frac{17}{4}\tilde{u}_{x}^{\mathbf{m}_{j},\mathbf{n}_{j}} - 2\tilde{u}_{x}^{\mathbf{m}_{j}+2,\mathbf{n}_{j}} - \tilde{u}_{x}^{\mathbf{m}_{j}-2,\mathbf{n}_{j}} \\
-\frac{1}{4}\left(2\tilde{u}_{x}^{\mathbf{m}_{j}+1,\mathbf{n}_{j}+1} + 2\tilde{u}_{x}^{\mathbf{m}_{j}-1,\mathbf{n}_{j}+1} + \tilde{u}_{x}^{\mathbf{m}_{j}+1,\mathbf{n}_{j}-1}\right) \\
-\frac{\sqrt{3}}{4}\left(\tilde{u}_{z}^{\mathbf{m}_{j},\mathbf{n}_{j}} + 2\tilde{u}_{z}^{\mathbf{m}_{j}+1,\mathbf{n}_{j}+1} - 2\tilde{u}_{z}^{\mathbf{m}_{j}-1,\mathbf{n}_{j}+1} - \tilde{u}_{z}^{\mathbf{m}_{j}+1,\mathbf{n}_{j}-1}\right)
\end{cases} (G.48)$$

$$R_{z}^{\mathbf{j},\mathbf{i}}\left(s\right) = \frac{2}{3}s^{2}\tilde{u}_{z}^{\mathbf{m}_{j},\mathbf{n}_{j}} + \frac{1}{6}K_{\zeta} \begin{cases} -\frac{\sqrt{3}}{4}\left(\tilde{u}_{x}^{\mathbf{m}_{j},\mathbf{n}_{j}} + 2\tilde{u}_{x}^{\mathbf{m}_{j}+\mathbf{1},\mathbf{n}_{j}+1} - 2\tilde{u}_{x}^{\mathbf{m}_{j}-\mathbf{1},\mathbf{n}_{j}+1} - \tilde{u}_{x}^{\mathbf{m}_{j}+\mathbf{1},\mathbf{n}_{j}-1}\right) \\ +\frac{15}{4}\tilde{u}_{z}^{\mathbf{m}_{j},\mathbf{n}_{j}} - \frac{3}{4}\left(2u_{z}^{\mathbf{m}_{j}+\mathbf{1},\mathbf{n}_{j}+1} + 2\tilde{u}_{z}^{\mathbf{m}_{j}-\mathbf{1},\mathbf{n}_{j}+1} + \tilde{u}_{z}^{\mathbf{m}_{j}+\mathbf{1},\mathbf{n}_{j}-1}\right) \end{cases}$$
(G.49)

Since both particles **i** and **j** are located at the interface Γ and the right corner particle is at the bottom of the interface Γ , the loaded particle **i** is located either at the same horizontal level as the particle **j**, or at a particle closer to the surface of the half-plane.

For a load at a particle closer to the surface of the half-plane

When particle **i**, at which the load is applied, is located closer to the surface of the half-plane than particle **j**, i.e. for $\mathbf{n_i} < \mathbf{n_j}$, the displacements in equations (G.48) and (G.49) may all be considered degrees of freedom of subsystem *II*. This yields the expressions for $\varphi_{x;r}^{(h)}$ and $\varphi_{z;r}^{(h)}$

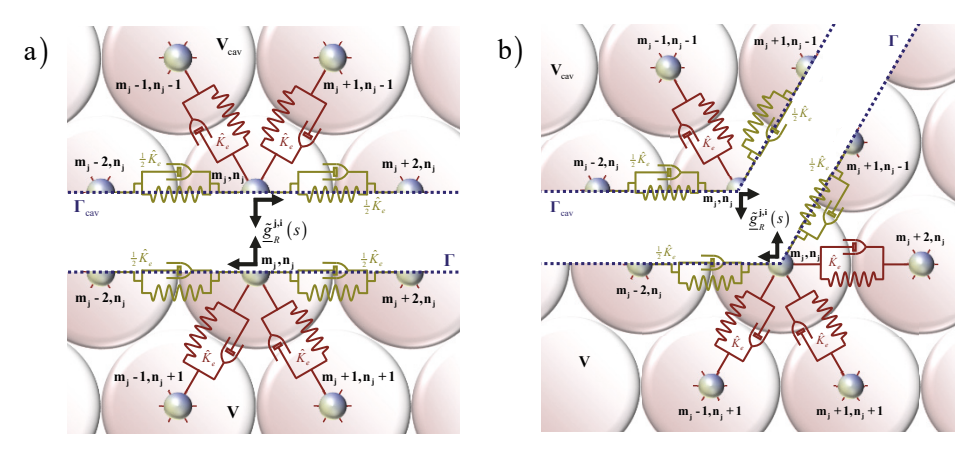


Figure G.3: a) Cell configuration of a particle along the horizontal domain; b) Cell configuration of the right corner particle.

with r = 1...3 as:

$$\begin{split} \varphi_{x;1}^{(h)} &= \varphi_{x;2}^{(h)} = \varphi_{z;1}^{(h)} = \varphi_{z;2}^{(h)} = 0 \\ \varphi_{x;3}^{(h)} &= \frac{2}{3} s^2 + \frac{1}{6} K_{\zeta} \begin{cases} 4 - 2 \cos \kappa_x - e^{-i\kappa_x} + \frac{1}{4} \left(1 - D^{(h)} \sqrt{3} \right) \left(1 - e^{-\frac{1}{2} i\kappa_x} e^{-\frac{\sqrt{5}}{2} i\kappa_z^{(h)}} \right) \\ - \left(\cos \frac{\kappa_x}{2} - D^{(h)} i\sqrt{3} \sin \frac{\kappa_x}{2} \right) e^{+\frac{\sqrt{5}}{2} i\kappa_z^{(h)}} \end{cases} \\ \varphi_{z;3}^{(h)} &= \frac{2}{3} s^2 D^{(h)} + \frac{1}{6} K_{\zeta} \begin{cases} 3D^{(h)} - \frac{\sqrt{3}}{4} \left(1 - D^{(h)} \sqrt{3} \right) \left(1 - e^{-\frac{1}{2} i\kappa_x} e^{-\frac{\sqrt{5}}{2} i\kappa_z^{(h)}} \right) \\ - 3 \left(D^{(h)} \cos \frac{\kappa_x}{2} - \frac{i}{\sqrt{3}} \sin \frac{\kappa_x}{2} \right) e^{+\frac{\sqrt{5}}{2} i\kappa_z^{(h)}} \end{cases} \end{split}$$

For a load at the level of the considered particle

When the loaded particle **i** is located at the same level as particle **j**, i.e. when $\mathbf{n_i} = \mathbf{n_j}$, all displacements in equations (G.48) and (G.49) may be considered as degrees of freedom of subsystem *I*. Substituting the corresponding Green's displacements for a particle **j** in subsystem *I*, the corresponding expressions for $\varphi_{x:r}^{(h)}$ and $\varphi_{z:r}^{(h)}$ with r = 1..3 are found as:

$$\varphi_{x;1}^{(h)} = \frac{1}{6}s^{2} + \frac{1}{6}K_{\zeta}\left(1 - e^{-i\kappa_{x}} + \frac{1}{4}\left(1 - D^{(h)}\sqrt{3}\right)\left(1 - e^{-\frac{1}{2}i\kappa_{x}}e^{-\frac{\sqrt{2}}{2}i\kappa_{z}^{(h)}}\right)\right) \\
\varphi_{x;2}^{(h)} = \frac{1}{6}s^{2} + \frac{1}{6}K_{\zeta}\left(1 - e^{-i\kappa_{x}} + \frac{1}{4}\left(1 + D^{(h)}\sqrt{3}\right)\left(1 - e^{-\frac{1}{2}i\kappa_{x}}e^{+\frac{\sqrt{2}}{2}i\kappa_{z}^{(h)}}\right)\right) \\
\varphi_{x;3}^{(h)} = \frac{1}{2}s^{2} + \frac{1}{6}K_{\zeta}\left(3 - 2\cos\kappa_{x} - \left(\cos\frac{\kappa_{x}}{2} - D^{(h)}i\sqrt{3}\sin\frac{\kappa_{x}}{2}\right)e^{+\frac{\sqrt{2}}{2}i\kappa_{z}^{(h)}}\right) \\
\varphi_{z;1}^{(h)} = \frac{1}{6}s^{2}D^{(h)} - \frac{1}{6}K_{\zeta}\frac{\sqrt{3}}{4}\left(1 - D^{(h)}\sqrt{3}\right)\left(1 - e^{-\frac{1}{2}i\kappa_{x}}e^{-\frac{\sqrt{2}}{2}i\kappa_{z}^{(h)}}\right) \\
\varphi_{z;1}^{(h)} = \frac{1}{6}s^{2}D^{(h)} - \frac{1}{6}K_{\zeta}\frac{\sqrt{3}}{4}\left(1 - D^{(h)}\sqrt{3}\right)\left(1 - e^{-\frac{1}{2}i\kappa_{x}}e^{-\frac{\sqrt{2}}{2}i\kappa_{z}^{(h)}}\right) \\
\varphi_{z;1}^{(h)} = \frac{1}{6}s^{2}D^{(h)} - \frac{1}{6}K_{\zeta}\frac{\sqrt{3}}{4}\left(1 - D^{(h)}\sqrt{3}\right)\left(1 - e^{-\frac{1}{2}i\kappa_{x}}e^{-\frac{\sqrt{2}}{2}i\kappa_{z}^{(h)}}\right) \\
\varphi_{z;1}^{(h)} = \frac{1}{6}s^{2}D^{(h)} - \frac{1}{6}K_{\zeta}\frac{\sqrt{3}}{4}\left(1 - D^{(h)}\sqrt{3}\right)\left(1 - e^{-\frac{1}{2}i\kappa_{x}}e^{-\frac{\sqrt{2}}{2}i\kappa_{z}^{(h)}}\right) \\
\varphi_{z;1}^{(h)} = \frac{1}{6}s^{2}D^{(h)} - \frac{1}{6}K_{\zeta}\frac{\sqrt{3}}{4}\left(1 - D^{(h)}\sqrt{3}\right)\left(1 - e^{-\frac{1}{2}i\kappa_{x}}e^{-\frac{\sqrt{2}}{2}i\kappa_{z}^{(h)}}\right) \\
\varphi_{z;1}^{(h)} = \frac{1}{6}s^{2}D^{(h)} - \frac{1}{6}K_{\zeta}\frac{\sqrt{3}}{4}\left(1 - D^{(h)}\sqrt{3}\right)\left(1 - e^{-\frac{1}{2}i\kappa_{x}}e^{-\frac{\sqrt{2}}{2}i\kappa_{z}^{(h)}}\right) \\
\varphi_{z;1}^{(h)} = \frac{1}{6}s^{2}D^{(h)} - \frac{1}{6}K_{\zeta}\frac{\sqrt{3}}{4}\left(1 - D^{(h)}\sqrt{3}\right)\left(1 - e^{-\frac{1}{2}i\kappa_{x}}e^{-\frac{\sqrt{2}}{2}i\kappa_{z}^{(h)}}\right) \\
\varphi_{z;1}^{(h)} = \frac{1}{6}s^{2}D^{(h)} - \frac{1}{6}K_{\zeta}\frac{\sqrt{3}}{4}\left(1 - D^{(h)}\sqrt{3}\right)\left(1 - e^{-\frac{1}{2}i\kappa_{x}}e^{-\frac{\sqrt{2}}{2}i\kappa_{z}^{(h)}}\right) \\
\varphi_{z;1}^{(h)} = \frac{1}{6}s^{2}D^{(h)} - \frac{1}{6}K_{\zeta}\frac{\sqrt{3}}{4}\left(1 - D^{(h)}\sqrt{3}\right)\left(1 - e^{-\frac{1}{2}i\kappa_{x}}e^{-\frac{\sqrt{2}}{2}i\kappa_{z}^{(h)}}\right) \\
\varphi_{z;1}^{(h)} = \frac{1}{6}s^{2}D^{(h)} - \frac{1}{6}K_{\zeta}\frac{\sqrt{3}}{4}\left(1 - D^{(h)}\sqrt{3}\right)\left(1 - e^{-\frac{1}{2}i\kappa_{x}}e^{-\frac{\sqrt{2}}{2}i\kappa_{z}^{(h)}}\right) \\
\varphi_{z;1}^{(h)} = \frac{1}{6}s^{2}D^{(h)} - \frac{1}{6}K_{\zeta}\frac{\sqrt{3}}{4}\left(1 - D^{(h)}\sqrt{3}\right)\left(1 - e^{-\frac{1}{2}i\kappa_{x}}e^{-\frac{\sqrt{2}}{2}i\kappa_{z}^{(h)}}\right) \\
\varphi_{z;2}^{(h)} = \frac{1}{6}s^{2}D^{(h)} - \frac{1}{6}s^{2}D^{(h)} - \frac{1}{6}s^{2}D^{(h)} - \frac{1}{6}s^{2}D^{(h)} - \frac{1}{6}s^{2}D^{(h)}\right) \\
\varphi_$$

Figure G.4: a) Cell configuration of a particle along the right slope; b) Cell configuration of the right surface particle.

$$\begin{split} & \varphi_{z;2}^{(h)} = -\frac{1}{6} s^2 D^{(h)} - \frac{1}{6} K_{\zeta} \frac{\sqrt{3}}{4} \Big(1 + D^{(h)} \sqrt{3} \Big) \Big(1 - e^{-\frac{1}{2} i \kappa_{x}} e^{+\frac{\sqrt{2}}{2} i \kappa_{z}^{(h)}} \Big) \\ & \varphi_{z;3}^{(h)} = \frac{1}{2} s^2 D^{(h)} + \frac{1}{2} K_{\zeta} \left(D^{(h)} - \left(D^{(h)} \cos \frac{\kappa_{x}}{2} - \frac{i}{\sqrt{3}} \sin \frac{\kappa_{x}}{2} \right) e^{+\frac{\sqrt{2}}{2} i \kappa_{z}^{(h)}} \right) \end{split}$$

G.8 Green's reaction forces at a particle along the right slope

The configuration for a particle **j** along the right slope of the boundary Γ is depicted in Figure G.4a. Disregarding the involved subsystems, the reaction forces at a particle along the right slope of the boundary Γ are respectively derived as:

$$\tilde{R}_{x}^{\mathbf{j},\mathbf{i}}\left(s\right) = \frac{1}{2}s^{2}\tilde{u}_{x}^{\mathbf{m}_{j},\mathbf{n}_{j}} + \frac{1}{6}K_{\zeta}\left(3\tilde{u}_{x}^{\mathbf{m}_{j},\mathbf{n}_{j}} - \frac{1}{4}\left(2\tilde{u}_{x}^{\mathbf{m}_{j}+1,\mathbf{n}_{j}+1} + \tilde{u}_{x}^{\mathbf{m}-1,\mathbf{n}_{j}+1} + \tilde{u}_{x}^{\mathbf{m}_{j}+1,\mathbf{n}_{j}-1}\right) - 2\tilde{u}_{x}^{\mathbf{m}_{j}+2,\mathbf{n}_{j}} - \frac{\sqrt{3}}{4}\left(2\tilde{u}_{z}^{\mathbf{m}_{j}+1,\mathbf{n}_{j}+1} - \tilde{u}_{z}^{\mathbf{m}_{j}-1,\mathbf{n}_{j}+1} - \tilde{u}_{z}^{\mathbf{m}_{j}+1,\mathbf{n}_{j}-1}\right)\right) \tag{G.50}$$

$$\widetilde{R}_{z}^{j,i}\left(s\right) = \frac{1}{2}s^{2}\widetilde{u}_{z}^{\mathbf{m}_{j},\mathbf{n}_{j}} + \frac{1}{6}K_{\zeta}\left(3\widetilde{u}_{z}^{\mathbf{m}_{j},\mathbf{n}_{i}} - \frac{\sqrt{3}}{4}\left(2\widetilde{u}_{x}^{\mathbf{m}_{j}+1,\mathbf{n}_{j}+1} - \widetilde{u}_{x}^{\mathbf{m}_{j}-1,\mathbf{n}_{j}+1} - \widetilde{u}_{x}^{\mathbf{m}_{j}+1,\mathbf{n}_{j}-1}\right) - \frac{3}{4}\left(2\widetilde{u}_{z}^{\mathbf{m}_{j}+1,\mathbf{n}_{j}+1} + \widetilde{u}_{z}^{\mathbf{m}_{j}-1,\mathbf{n}_{j}+1} + \widetilde{u}_{z}^{\mathbf{m}_{j}+1,\mathbf{n}_{j}-1}\right)\right) \tag{G.51}$$

For a load at a particle further from the surface of the half-plane

When $\mathbf{n_i} > \mathbf{n_j}$, all displacements in equations (G.50) and (G.51) are degrees of freedom of subsystem *I*. The expressions for $\varphi_{x;r}^{(h)}$ and $\varphi_{z;r}^{(h)}$ with r = 1..3 now respectively become:

$$\begin{split} & \varphi_{x;1}^{(h)} = \frac{1}{2}s^2 + \frac{1}{6}K_{\zeta} \begin{pmatrix} 3 - 2e^{-i\kappa_{x}} - \frac{1}{4}\left(1 - D^{(h)}\sqrt{3}\right)e^{-\frac{1}{2}i\kappa_{x}}e^{-\frac{\sqrt{5}}{2}i\kappa_{z}^{(h)}} \\ -\frac{1}{4}\left(\left(1 + D^{(h)}\sqrt{3}\right)e^{-\frac{1}{2}i\kappa_{x}} + 2\left(\cos\frac{\kappa_{x}}{2} - D^{(h)}i\sqrt{3}\sin\frac{\kappa_{x}}{2}\right)\right)e^{+\frac{\sqrt{5}}{2}i\kappa_{z}^{(h)}} \end{pmatrix} \\ & \varphi_{x;2}^{(h)} = \frac{1}{2}s^2 + \frac{1}{6}K_{\zeta} \begin{pmatrix} 3 - 2e^{-i\kappa_{x}} - \frac{1}{4}\left(1 + D^{(h)}\sqrt{3}\right)e^{-\frac{1}{2}i\kappa_{x}}e^{+\frac{\sqrt{5}}{2}i\kappa_{z}^{(h)}} \\ -\frac{1}{4}\left(\left(1 - D^{(h)}\sqrt{3}\right)e^{-\frac{1}{2}i\kappa_{x}} + 2\left(\cos\frac{\kappa_{x}}{2} + D^{(h)}i\sqrt{3}\sin\frac{\kappa_{x}}{2}\right)\right)e^{-\frac{\sqrt{5}}{2}i\kappa_{z}^{(h)}} \end{pmatrix} \\ & \varphi_{z;1}^{(h)} = \frac{1}{2}s^2D^{(h)} + \frac{1}{6}K_{\zeta} \begin{pmatrix} 3D^{(h)} + \frac{\sqrt{3}}{4}\left(1 - D^{(h)}\sqrt{3}\right)e^{-\frac{1}{2}i\kappa_{x}}e^{-\frac{\sqrt{5}}{2}i\kappa_{z}^{(h)}} \\ -\left(\frac{\sqrt{3}}{4}\left(1 + D^{(h)}\sqrt{3}\right)e^{-\frac{1}{2}i\kappa_{x}} + \frac{3}{2}\left(D^{(h)}\cos\frac{\kappa_{x}}{2} - \frac{i}{\sqrt{3}}\sin\frac{\kappa_{x}}{2}\right)\right)e^{+\frac{\sqrt{5}}{2}i\kappa_{z}^{(h)}} \end{pmatrix} \\ & \varphi_{z;2}^{(h)} = -\frac{1}{2}s^2D^{(h)} - \frac{1}{6}K_{\zeta} \begin{pmatrix} 3D^{(h)} - \frac{\sqrt{3}}{4}\left(1 + D^{(h)}\sqrt{3}\right)e^{-\frac{1}{2}i\kappa_{x}} - \frac{3}{2}\left(D^{(h)}\cos\frac{\kappa_{x}}{2} + \frac{i}{\sqrt{3}}\sin\frac{\kappa_{x}}{2}\right)\right)e^{-\frac{\sqrt{5}}{2}i\kappa_{z}^{(h)}} \\ +\left(\frac{\sqrt{3}}{4}\left(1 - D^{(h)}\sqrt{3}\right)e^{-\frac{1}{2}i\kappa_{x}} - \frac{3}{2}\left(D^{(h)}\cos\frac{\kappa_{x}}{2} + \frac{i}{\sqrt{3}}\sin\frac{\kappa_{x}}{2}\right)\right)e^{-\frac{\sqrt{5}}{2}i\kappa_{z}^{(h)}} \end{pmatrix} \\ & \varphi_{x;3}^{(h)} = \varphi_{z;3}^{(h)} = 0 \end{pmatrix}$$

For a load at a particle closer to the surface of the half-plane

When the loaded particle **i** is closer to the surface of the half-plane than particle **j**, i.e. for $\mathbf{n_i} < \mathbf{n_j}$, the displacements in equations (G.50) and (G.51) are all degrees of freedom of subsystem *II*. This yields the expressions for $\varphi_{x,r}^{(h)}$ and $\varphi_{z,r}^{(h)}$ with r = 1...3 as:

$$\begin{split} \varphi_{x;1}^{(h)} &= \varphi_{x;2}^{(h)} = \varphi_{z;1}^{(h)} = \varphi_{z;2}^{(h)} = 0 \\ \varphi_{x;3}^{(h)} &= \frac{1}{2} s^2 + \frac{1}{6} K_{\zeta} \left(3 - 2 e^{-i\kappa_x} - \frac{1}{4} \left(1 - D^{(h)} \sqrt{3} \right) e^{-\frac{1}{2} i\kappa_x} e^{-\frac{\sqrt{3}}{2} i\kappa_z^{(h)}} \\ - \frac{1}{4} \left(\left(1 + D^{(h)} \sqrt{3} \right) e^{-\frac{1}{2} i\kappa_x} + 2 \left(\cos \frac{\kappa_x}{2} - D^{(h)} i\sqrt{3} \sin \frac{\kappa_x}{2} \right) \right) e^{+\frac{\sqrt{5}}{2} i\kappa_z^{(h)}} \\ \varphi_{z;3}^{(h)} &= \frac{1}{2} s^2 D^{(h)} + \frac{1}{6} K_{\zeta} \left(3 D^{(h)} + \frac{\sqrt{3}}{4} \left(1 - D^{(h)} \sqrt{3} \right) e^{-\frac{1}{2} i\kappa_x} e^{-\frac{\sqrt{5}}{2} i\kappa_z^{(h)}} \\ - \left(\frac{\sqrt{3}}{4} \left(1 + D^{(h)} \sqrt{3} \right) e^{-\frac{1}{2} i\kappa_x} + \frac{3}{2} \left(D^{(h)} \cos \frac{\kappa_x}{2} - \frac{i}{\sqrt{3}} \sin \frac{\kappa_x}{2} \right) \right) e^{+\frac{\sqrt{5}}{2} i\kappa_z^{(h)}} \end{split}$$

For a load at the same level of the considered particle

If the loaded particle **i** is located at the same level as particle **j**, i.e. when $\mathbf{n_i} = \mathbf{n_j}$, the displacements in equations (G.50) and (G.51) belong to different subsystems. The particles with horizontal nodal coordinate $\mathbf{n_j} - \mathbf{1}$ belong to subsystem *I*, while the particles with nodal coordinate $\mathbf{n_j} + \mathbf{1}$ belong to subsystem *II*. In this case, we let the corresponding subsystem of the particles at the interface of the two susbsystems depend on the location of its associated rheological element. This yields the expressions for $\varphi_{x,r}^{(h)}$ and $\varphi_{z,r}^{(h)}$ with r = 1...3 as:

$$\begin{split} & \varphi_{x;1}^{(h)} = \frac{1}{6} s^2 + \frac{1}{6} K_{\zeta} \left(1 - e^{-i\kappa_x} + \frac{1}{4} \left(1 - D^{(h)} \sqrt{3} \right) \left(1 - e^{-\frac{1}{2}i\kappa_x} e^{-\frac{\sqrt{5}}{2}i\kappa_z^{(h)}} \right) \right) \\ & \varphi_{x;2}^{(h)} = \frac{1}{6} s^2 + \frac{1}{6} K_{\zeta} \left(1 - e^{-i\kappa_x} + \frac{1}{4} \left(1 + D^{(h)} \sqrt{3} \right) \left(1 - e^{-\frac{1}{2}i\kappa_x} e^{+\frac{\sqrt{5}}{2}i\kappa_z^{(h)}} \right) \right) \\ & \varphi_{x;3}^{(h)} = \frac{1}{3} s^2 + \frac{1}{6} K_{\zeta} \left(\frac{3}{2} - e^{-i\kappa_x} + \frac{1}{4} \left(1 + D^{(h)} \sqrt{3} \right) - \frac{1}{4} \left(\left(1 + D^{(h)} \sqrt{3} \right) e^{-\frac{1}{2}i\kappa_x} + 2 \left(\cos \frac{\kappa_x}{2} - D^{(h)} i \sqrt{3} \sin \frac{\kappa_x}{2} \right) \right) e^{+\frac{\sqrt{5}}{2}i\kappa_z^{(h)}} \right) \\ & \varphi_{z;1}^{(h)} = \frac{1}{6} s^2 D^{(h)} - \frac{1}{6} K_{\zeta} \frac{\sqrt{3}}{4} \left(1 - D^{(h)} \sqrt{3} \right) \left(1 - e^{-\frac{1}{2}i\kappa_x} e^{-\frac{\sqrt{5}}{2}i\kappa_z^{(h)}} \right) \\ & \varphi_{z;2}^{(h)} = -\frac{1}{6} s^2 D^{(h)} - \frac{1}{6} K_{\zeta} \frac{\sqrt{3}}{4} \left(1 + D^{(h)} \sqrt{3} \right) \left(1 - e^{-\frac{1}{2}i\kappa_x} e^{+\frac{\sqrt{5}}{2}i\kappa_z^{(h)}} \right) \\ & \varphi_{z;3}^{(h)} = \frac{1}{3} s^2 D^{(h)} + \frac{1}{6} K_{\zeta} \left(\frac{3}{2} D^{(h)} + \frac{\sqrt{3}}{4} \left(1 + D^{(h)} \sqrt{3} \right) \right) \\ & - \left(\frac{\sqrt{3}}{4} \left(1 + D^{(h)} \sqrt{3} \right) e^{-\frac{1}{2}i\kappa_x} + \frac{3}{2} \left(D^{(h)} \cos \frac{\kappa_x}{2} - \frac{i}{\sqrt{3}} \sin \frac{\kappa_x}{2} \right) \right) e^{+\frac{\sqrt{5}}{2}i\kappa_z^{(h)}} \end{split}$$

G.9 Green's reaction forces at the right surface particle

The cell configuration for a right surface particle \mathbf{j} along Γ is depicted in Figure G.4b. Disregarding the involved subsystems, the reaction forces at the left surface particle read:

$$\tilde{R}_{x}^{\mathbf{j},\mathbf{i}}\left(s\right) = \frac{1}{3}s^{2}\tilde{u}_{x}^{\mathbf{m}_{j},0} + \frac{1}{6}K_{\zeta} \begin{pmatrix} \frac{7}{4}\tilde{u}_{x}^{\mathbf{m}_{j},0} - \tilde{u}_{x}^{\mathbf{m}_{j}+2,0} - \frac{1}{4}\left(2\tilde{u}_{x}^{\mathbf{m}_{j}+1,1} + \tilde{u}_{x}^{\mathbf{m}-1,1}\right) \\ + \frac{\sqrt{3}}{4}\left(\tilde{u}_{z}^{\mathbf{m}_{j},0} - 2\tilde{u}_{z}^{\mathbf{m}_{j}+1,1} + \tilde{u}_{z}^{\mathbf{m}_{j}-1,1}\right) \end{pmatrix} \tag{G.52}$$

$$\tilde{R}_{z}^{j,i}(s) = \frac{1}{3}s^{2}\tilde{u}_{z}^{m_{j},0} + \frac{1}{6}K_{\zeta} \begin{pmatrix} \frac{9}{4}\tilde{u}_{z}^{m_{j},0} + \frac{\sqrt{3}}{4}\left(\tilde{u}_{x}^{m_{j},0} - 2\tilde{u}_{x}^{m_{j}+1,1} + \tilde{u}_{x}^{m_{j}-1,1}\right) \\ -\frac{3}{4}\left(2\tilde{u}_{z}^{m_{j}+1,1} + \tilde{u}_{z}^{m_{j}-1,1}\right) \end{pmatrix}$$
(G.53)

As the particle \mathbf{j} is located at the surface, the loaded particle \mathbf{i} is either located in the interior of the half-plane, or at the same horizontal level as the particle \mathbf{j} .

For a load at a particle in the interior of the half-plane

When the loaded particle **i** is located inside the half-plane of particles, i.e. $\mathbf{n_i} > \mathbf{n_j}$, it follows that the displacements in equations (G.52) and (G.53) are degrees of freedom of subsystem *I*. This yields the expressions for $\varphi_{x:r}^{(h)}$ and $\varphi_{z:r}^{(h)}$ with r = 1..3 respectively as:

$$\begin{split} \varphi_{x;1}^{(h)} &= \frac{1}{3}s^2 + \frac{1}{6}K_{\zeta} \begin{pmatrix} \frac{3}{2} - e^{-i\kappa_{x}} + \frac{1}{4}\left(1 + D^{(h)}\sqrt{3}\right) \\ -\frac{1}{4}\left(\left(1 + D^{(h)}\sqrt{3}\right)e^{-\frac{1}{2}i\kappa_{x}} + 2\left(\cos\frac{\kappa_{x}}{2} - D^{(h)}i\sqrt{3}\sin\frac{\kappa_{x}}{2}\right)\right)e^{+\frac{\sqrt{5}}{2}i\kappa_{z}^{(h)}} \end{pmatrix} \\ \varphi_{x;2}^{(h)} &= \frac{1}{3}s^2 + \frac{1}{6}K_{\zeta} \begin{pmatrix} \frac{3}{2} - e^{-i\kappa_{x}} + \frac{1}{4}\left(1 - D^{(h)}\sqrt{3}\right) \\ -\frac{1}{4}\left(\left(1 - D^{(h)}\sqrt{3}\right)e^{-\frac{1}{2}i\kappa_{x}} + 2\left(\cos\frac{\kappa_{x}}{2} + D^{(h)}i\sqrt{3}\sin\frac{\kappa_{x}}{2}\right)\right)e^{-\frac{\sqrt{5}}{2}i\kappa_{z}^{(h)}} \end{pmatrix} \\ \varphi_{z;1}^{(h)} &= \frac{1}{3}s^2D^{(h)} + \frac{1}{6}K_{\zeta} \begin{pmatrix} \frac{3}{2}D^{(h)} + \frac{\sqrt{3}}{4}\left(1 + D^{(h)}\sqrt{3}\right) \\ -\left(\frac{\sqrt{3}}{4}\left(1 + D^{(h)}\sqrt{3}\right)e^{-\frac{1}{2}i\kappa_{x}} + \frac{3}{2}\left(D^{(h)}\cos\frac{\kappa_{x}}{2} - \frac{i}{\sqrt{3}}\sin\frac{\kappa_{x}}{2}\right)\right)e^{+\frac{\sqrt{5}}{2}i\kappa_{z}^{(h)}} \end{pmatrix} \\ \varphi_{z;2}^{(h)} &= -\frac{1}{3}s^2D^{(h)} - \frac{1}{6}K_{\zeta} \begin{pmatrix} \frac{3}{2}D^{(h)} - \frac{\sqrt{3}}{4}\left(1 - D^{(h)}\sqrt{3}\right) \\ +\left(\frac{\sqrt{3}}{4}\left(1 - D^{(h)}\sqrt{3}\right)e^{-\frac{1}{2}i\kappa_{x}} - \frac{3}{2}\left(D^{(h)}\cos\frac{\kappa_{x}}{2} + \frac{i}{\sqrt{3}}\sin\frac{\kappa_{x}}{2}\right)\right)e^{-\frac{\sqrt{5}}{2}i\kappa_{z}^{(h)}} \end{pmatrix} \\ \varphi_{x;3}^{(h)} &= \varphi_{x;3}^{(h)} &= 0 \end{pmatrix}$$

For a load at a particle at the half-plane surface

When the loaded particle **i** is located at the surface of the half-plane, i.e. for $\mathbf{n_i} = \mathbf{n_j}$, the displacements in equations (G.52) and (G.53) are all degrees of freedom of subsystem II.

This yields the corresponding expressions for $\varphi_{x;r}^{(h)}$ and $\varphi_{z;r}^{(h)}$ with r = 1..3 respectively as:

$$\begin{split} & \varphi_{x;1}^{(h)} = \varphi_{x;2}^{(h)} = \varphi_{z;1}^{(h)} = \varphi_{z;2}^{(h)} = 0 \\ & \varphi_{x;3}^{(h)} = \frac{1}{3} s^2 + \frac{1}{6} K_{\zeta} \begin{pmatrix} \frac{3}{2} - e^{-i\kappa_{x}} + \frac{1}{4} \left(1 + D^{(h)} \sqrt{3} \right) \\ & -\frac{1}{4} \left(\left(1 + D^{(h)} \sqrt{3} \right) e^{-\frac{1}{2}i\kappa_{x}} + 2 \left(\cos \frac{\kappa_{x}}{2} - D^{(h)} i \sqrt{3} \sin \frac{\kappa_{x}}{2} \right) \right) e^{+\frac{\sqrt{2}}{2} i \kappa_{z}^{(h)}} \end{pmatrix} \\ & \varphi_{z;3}^{(h)} = \frac{1}{3} s^2 D^{(h)} + \frac{1}{6} K_{\zeta} \begin{pmatrix} \frac{3}{2} D^{(h)} + \frac{\sqrt{3}}{4} \left(1 + D^{(h)} \sqrt{3} \right) \\ & - \left(\frac{\sqrt{3}}{4} \left(1 + D^{(h)} \sqrt{3} \right) e^{-\frac{1}{2}i\kappa_{x}} + \frac{3}{2} \left(D^{(h)} \cos \frac{\kappa_{x}}{2} - \frac{i}{\sqrt{3}} \sin \frac{\kappa_{x}}{2} \right) \right) e^{+\frac{\sqrt{2}}{2} i \kappa_{z}^{(h)}} \end{split}$$

G.10 Equivalent 1D Green's reaction forces in the half-plane of particles

For the equivalent one-dimensional response of the half-plane of particles, discussed in Section 4.5, we consider the Green's reaction forces at a particle in the half-plane. While Section 4.5 considers the particular case of an applied vertical uniform load at the half-plane surface, this appendix considers the more general case of a uniform vertical load along any horizontal level of the half-plane. The corresponding Green's reaction forces are thus obtained as:

$$\widetilde{g}_{R,zz}^{0,\mathbf{n}_{even}}(s) = \int_{-2\pi}^{+2\pi} \left(\sum_{h=1}^{1,3} \sum_{h=1}^{2} \varphi_{z;r}^{(h)} A_{z;r}^{\mathbf{i},(h)} e^{+\frac{\sqrt{5}}{2} \mathbf{i} \kappa_{z}^{(h)} \mathbf{n}_{j}} + \sum_{h=1}^{2} \varphi_{z;2}^{(h)} A_{z;2}^{\mathbf{i},(h)} e^{-\frac{\sqrt{5}}{2} \mathbf{i} \kappa_{z}^{(h)} \mathbf{n}_{j}} \right) d\kappa_{x}
+ 2 \sum_{\mathbf{i}=1}^{\mathbf{i}_{max}} \int_{-2\pi}^{+2\pi} \left(\sum_{r} \sum_{h=1}^{1,3} \varphi_{z;r}^{(h)} A_{z;r}^{\mathbf{i},(h)} e^{+\frac{\sqrt{5}}{2} \mathbf{i} \kappa_{z}^{(h)} \mathbf{n}_{j}} + \sum_{h=1}^{2} \varphi_{z;2}^{(h)} A_{z;2}^{\mathbf{i},(h)} e^{-\frac{\sqrt{5}}{2} \mathbf{i} \kappa_{z}^{(h)} \mathbf{n}_{j}} \right) e^{-\frac{1}{2} \mathbf{i} \kappa_{x} \mathbf{m}_{i}} d\kappa_{x}$$

$$\mathbf{G}.54)$$

$$\tilde{g}_{R,zz}^{0,\mathbf{n}_{odd}}\left(s\right) = 2\sum_{i=1}^{i_{\max}} \int_{-2\pi}^{2\pi} \left(\sum_{r}\sum_{h=1}^{1,3} \varphi_{z;r}^{(h)} A_{z;r}^{i,(h)} e^{+\frac{\sqrt{3}}{2}i\kappa_{z}^{(h)}\mathbf{n}_{j}} + \sum_{h=1}^{2} \varphi_{z;2}^{(h)} A_{z;2}^{i,(h)} e^{-\frac{\sqrt{5}}{2}i\kappa_{z}^{(h)}\mathbf{n}_{j}}\right) e^{-\frac{1}{2}i\kappa_{x}\mathbf{m}_{i}} d\kappa_{x}$$
(G.55)

To obtain the equivalent one-dimensional Green's reaction forces, we make the assumption that for the equivalent one-dimensional response, the Green's reaction forces are determined along the horizontal line that divides the considered particle into two exact halves. The resulting cell configuration for a particle \mathbf{m} , \mathbf{n} located in the half-plane, depicted in Figure G.5, then exactly corresponds to that of a particle along the horizontal domain of the boundary Γ , previously discussed in Appendix G.6. Disregarding the involved subsystems, the corresponding horizontal and vertical reaction forces

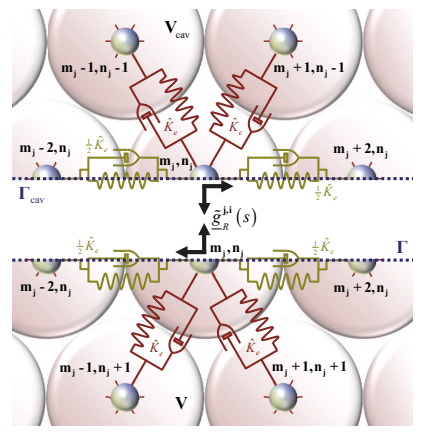


Figure G.5: Cell configuration of a particle along a horizontal domain;

at the particle \mathbf{j} with nodal coordinates $\mathbf{m_j}$, $\mathbf{n_j}$ due to a load applied at particle \mathbf{i} are then described by equations (G.46) and (G.47). Replacing the Laplace domain displacements in these equations by the corresponding Green's displacements then yields the corresponding Green's reaction forces.

As the loaded particle **i** and particle **j**, at which the Green's reaction forces are considered, can be anywhere, note that, next to the case that $\mathbf{n_i} \leq \mathbf{n_j}$ considered in Appendix G.6, for the equivalent one-dimensional response we must also consider the case that $\mathbf{n_i} > \mathbf{n_i}$.

For a load at a particle further from the surface of the half-plane

When the loaded particle **i** is located further from the surface of the half-plane than the particle **j** at which the reaction forces are to be determined, i.e. if $\mathbf{n_i} > \mathbf{n_j}$, the Laplace domain displacements in equations (G.46) and (G.47) are all degrees of freedom of subsystem *I*. Susbtituting the corresponding Green's displacements from Section 4.4.3, then yields the expressions for $\varphi_{xy}^{(n)}$ and $\varphi_{xy}^{(n)}$ for r = 1...3 as:

$$\begin{split} \varphi_{x;1}^{(h)} &= \frac{1}{2}s^{2} + \frac{1}{6}K_{\zeta}\left(3 - 2\cos\kappa_{x} - \left(\cos\frac{\kappa_{x}}{2} - D^{(h)} i\sqrt{3}\sin\frac{\kappa_{x}}{2}\right)e^{+\frac{\sqrt{5}}{2}i\kappa_{z}^{(h)}}\right) \\ \varphi_{x;2}^{(h)} &= \frac{1}{2}s^{2} + \frac{1}{6}K_{\zeta}\left(3 - 2\cos\kappa_{x} - \left(\cos\frac{\kappa_{x}}{2} + D^{(h)} i\sqrt{3}\sin\frac{\kappa_{x}}{2}\right)e^{-\frac{\sqrt{5}}{2}i\kappa_{z}^{(h)}}\right) \\ \varphi_{z;1}^{(h)} &= \frac{1}{2}s^{2}D^{(h)} + \frac{1}{2}K_{\zeta}\left(D^{(h)} - \left(D^{(h)}\cos\frac{\kappa_{x}}{2} - \frac{i}{\sqrt{3}}\sin\frac{\kappa_{x}}{2}\right)e^{+\frac{\sqrt{5}}{2}i\kappa_{z}^{(h)}}\right) \\ \varphi_{z;2}^{(h)} &= -\frac{1}{2}s^{2}D^{(h)} - \frac{1}{2}K_{\zeta}\left(D^{(h)} - \left(D^{(h)}\cos\frac{\kappa_{x}}{2} + \frac{i}{\sqrt{3}}\sin\frac{\kappa_{x}}{2}\right)e^{-\frac{\sqrt{5}}{2}i\kappa_{z}^{(h)}}\right) \\ \varphi_{x;3}^{(h)} &= 0 \end{split}$$

For a load at a particle closer to the surface of the half-plane

When the loaded particle **i** is located at the same level as, or is located closer to the surface of the half-plane than, the particle **j** at which the reaction forces are to be determined, i.e. if $\mathbf{n_i} \ge \mathbf{n_j}$, the Laplace domain displacements in equations (G.46) and (G.47) are all degrees of freedom of subsystem *II*. In correspondence with Appendix G.6, this yields the expressions for $\varphi_{xir}^{(h)}$ and $\varphi_{zir}^{(h)}$ with r = 1...3 respectively as:

$$\begin{split} & \varphi_{x;1}^{(h)} = \varphi_{x;2}^{(h)} = \varphi_{z;1}^{(h)} = \varphi_{z;2}^{(h)} = 0 \\ & \varphi_{x;3}^{(h)} = \frac{1}{2} s^2 + \frac{1}{6} K_{\zeta} \left(3 - 2 \cos \kappa_x - \left(\cos \frac{\kappa_x}{2} - D^{(h)} i \sqrt{3} \sin \frac{\kappa_x}{2} \right) e^{+\frac{\sqrt{h}}{2} i \kappa_z^{(h)}} \right) \\ & \varphi_{z;3}^{(h)} = \frac{1}{2} s^2 D^{(h)} + \frac{1}{2} K_{\zeta} \left(D^{(h)} - \left(D^{(h)} \cos \frac{\kappa_x}{2} - \frac{i}{\sqrt{3}} \sin \frac{\kappa_x}{2} \right) e^{+\frac{\sqrt{h}}{2} i \kappa_z^{(h)}} \right) \end{split}$$

H Wave propagation in two-dimensional systems

H.1 Dispersion in the half-plane of particles

In this appendix, we consider the dispersion relations for the shear and compressional waves propagating through the half-plane of particles in its principal directions, i.e. in x- and z-direction, for comparison with the corresponding one-dimensional system, discussed in Section 4.5.1, and with the continuous layer, discussed in Section 4.6.

In Section 4.4, the dimensionless dispersion relation for the viscoelastic half-plane of particles with a hexagonal configuration is obtained as:

$$\left(3\left(1+\frac{s^2}{1+2\zeta s}\right)-2\cos\kappa_x-\cos\frac{\kappa_x}{2}\cos\frac{\kappa_z\sqrt{3}}{2}\right)\left(1+\frac{s^2}{1+2\zeta s}-\cos\frac{\kappa_x}{2}\cos\frac{\kappa_z\sqrt{3}}{2}\right) -\sin^2\frac{\kappa_x}{2}\sin^2\frac{\kappa_z\sqrt{3}}{2} = 0$$
(H.1)

Equation (H.1) is the general dispersion relation for wave propagation in the viscoelastic halfplane of particles in all directions. The dispersion relation for waves propagating in z-direction follows from equation (H.1) by substituting $\kappa_x = 0$. This yields:

$$\left(1 + \frac{3s^2}{1 + 2\zeta s} - \cos\frac{\kappa_z \sqrt{3}}{2}\right) \left(1 + \frac{s^2}{1 + 2\zeta s} - \cos\frac{\kappa_z \sqrt{3}}{2}\right) = 0$$
(H.2)

The above dispersion relation has two solutions that are obtained as:

$$\cos\frac{\kappa_{z,1}\sqrt{3}}{2} = 1 + \frac{3s^2}{1 + 2\zeta s}, \qquad \cos\frac{\kappa_{z,2}\sqrt{3}}{2} = 1 + \frac{s^2}{1 + 2\zeta s}.$$
 (H.3)

As discussed in Section 4.5.1, the second dispersion relation in equation (H.3) must be related to the propagation of compressional waves in z-direction, i.e. $\kappa_{z,2} \to \kappa_{z,P}$. As a consequence, the first dispersion relation in equation (H.3) must be related to the propagation of shear waves in z-direction, i.e. $\kappa_{z,1} \to \kappa_{z,S}$. Alternatively, solving these dispersions relations for the Laplace parameter s and for zero damping shows that the phase speeds of the two waves are related as $c_{z,2} = c_{z,1}\sqrt{3}$. Then, noting that the shear and compressional wave velocities in the two-dimensional continuum are known to be related as $c_P = c_S\sqrt{3}$ and that this must also be the case for the half-plane of particles in the long wave limit, yields the same conclusion.

Substituting $\kappa_z = 0$ into equation (H.1), yields the dispersion relation for waves propagating in x-direction as:

$$\left(3\left(1+\frac{s^2}{1+2\zeta s}\right)-2\cos\kappa_x-\cos\frac{\kappa_x}{2}\right)\left(1+\frac{s^2}{1+2\zeta s}-\cos\frac{\kappa_x}{2}\right)=0$$
(H.4)

The two solutions to the above dispersion relation are obtained as:

$$\cos\frac{\kappa_{x,1}}{2} = 1 + \frac{s^2}{1 + 2\zeta s}, \qquad \cos\frac{\kappa_{x,2}}{2} + 2\cos\kappa_{x,2} - 2 = 1 + \frac{3s^2}{1 + 2\zeta s}. \tag{H.5}$$

Solving both dispersion relations for the Laplace parameter s assuming zero damping shows that the phase speeds for the two dispersion relations in equation (H.5) are related as $c_{x,2} = c_{x,1}\sqrt{3}$. Assuming that the phase speeds of shear and compressional waves are the same in x- and z- direction, the first dispersion relation in equation (H.5) must be related to the propagation of shear waves, i.e. $\kappa_{x,1} \to \kappa_{x,S}$, while the second dispersion relation in equation (H.5) appears to correspond to the propagation of compressional waves, i.e. $\kappa_{x,2} \to \kappa_{x,P}$.

Using trigonometry to rewrite and rearrange the second relation in equation (H.5) exclusively in terms of $\cos \frac{1}{2} \kappa_x$, and solving the remainder for $\cos \frac{1}{2} \kappa_x$ using the quadratic equation, we find:

$$\cos\frac{\kappa_{x,P}}{2} = -\frac{1}{8} \pm \frac{9}{8} \sqrt{1 + \frac{48}{81} \frac{s^2}{1 + 2\zeta s}}$$
 (H.6)

The dispersion equation (H.6) for the propagation of compressional waves in x-direction has two solutions that correspond to two segments within the first Brillouin zone. These two segments are depicted in Figure H.1 for zero damping. Here, the continuous blue line gives the frequency-wavenumber relation that follows from equation (H.6) by substituting $s = i\Omega$ and using a positive sign for the square root, while the dashed blue line gives the correspond-

ing relation using a negative sign for the square root. Furthermore, the red line gives the frequency-wavenumber relation for the shear wave in *x*-direction. Figure H.1 shows that for a certain frequency range within the first Brillouin zone, a single frequency corresponds to two wavenumbers.

Note here that the shear wave has a frequency range $\Omega=0...\sqrt{2}$, while for the compressional wave the frequency ranges from zero to $\Omega=\sqrt{\frac{81}{48}}\approx 1,229$. The dispersion curve for the compressional wave has a local minimum at $\Omega=\sqrt{\frac{2}{3}}\approx 0,8165$. The maximum frequency in the dispersion curve for the compressional wave corresponds to $\cos\frac{1}{2}\kappa_{x,P}=-\frac{1}{8}$.

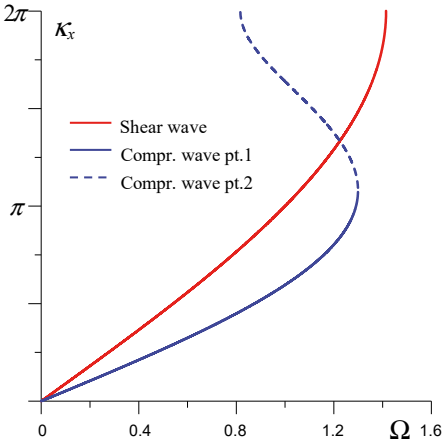


Figure H.1: Dispersion relation for wave propagation in x-direction for the 1st Brillouin zone.

H.2 Dispersion in the continuous layer

Although the derivation of the dispersion relation for a two-dimensional continuum can be considered as commonly known textbook material, we here shortly address this derivation in the appendix specifically for the case that the material properties of the continuum coincide with the material parameters of the half-plane of particles with a hexagonal configuration

The dispersion relation for two-dimensional continuum under plane-strain conditions is derived starting from the commonly known two-dimensional elastodynamic wave equation [Achenbach, 1973]. To this purpose, we divide the horizontal and vertical equations of motion for the continuum, previously given by equations (C.4) and (C.5), by the density ρ and note that the viscoelastic shear and compressional wave velocities may respectively be expressed in terms of the Lamé operators as $\hat{c}_s^2 = \hat{\mu}/\rho$ and $\hat{c}_P^2 = (\hat{\lambda} + 2\hat{\mu})/\rho$. Applying the Fourier transform with respect to horizontal space and the Laplace transform with respect to time then yields:

$$\left(s^{2}+\hat{c}_{P}^{2}k_{x}^{2}\right)\tilde{\tilde{u}}_{x}\left(k_{x},z,s\right)-\hat{c}_{S}^{2}\frac{\partial^{2}}{\partial z^{2}}\tilde{\tilde{u}}_{x}\left(k_{x},z,s\right)+\mathrm{i}k_{x}\left(\hat{c}_{S}^{2}-\hat{c}_{P}^{2}\right)\frac{\partial}{\partial z}\tilde{\tilde{u}}_{z}\left(k_{x},z,s\right)=0\tag{H.7}$$

$$ik_{x}\left(\hat{c}_{S}^{2}-\hat{c}_{P}^{2}\right)\frac{\partial}{\partial z}\tilde{\tilde{u}}_{x}\left(k_{x},z,s\right)+\left(s^{2}+\hat{c}_{S}^{2}k_{x}^{2}\right)\tilde{\tilde{u}}_{z}\left(k_{x},z,s\right)-\hat{c}_{P}^{2}\frac{\partial^{2}}{\partial z^{2}}\tilde{\tilde{u}}_{z}\left(k_{x},z,s\right)=0$$
(H.8)

Here, k_x denotes the horizontal wavenumber. Note that in Section 3.5.3 and in Appendix F.3, the horizontal wavenumber was simply expressed as the wavenumber k, while in this appendix the subscript x is used to emphasize its horizontal orientation as opposed to the vertical wavenumber.

To find a general solution to equations (H.7) and (H.8), we assume plane harmonic waves and describe the horizontal and vertical displacements of the continuum in the Laplace-wavenumber domain in terms of the vertical wavenumber k_z as:

$$\tilde{\tilde{u}}_{x}(k_{x},z,s) = Ae^{-ik_{z}z}, \qquad \tilde{\tilde{u}}_{z}(k_{x},z,s) = Be^{-ik_{z}z}$$
(H.9)

Substituting equations (H.9) into equations (H.7) and (H.8), and noting that the determinant of the resulting system of equations of motion must be equal to zero, shows that the shear and compressional waves in the continuum are decoupled, and that we find separate dispersion relations for the propagation of the shear and compressional waves as:

$$s^{2} + \hat{c}_{S}^{2} \left(k_{x}^{2} + k_{z}^{2} \right) = 0,$$
 $s^{2} + \hat{c}_{P}^{2} \left(k_{x}^{2} + k_{z}^{2} \right) = 0.$ (H.10)

To compare the dispersion in the continuum with the dispersion in the half-plane of particles, we replace the Laplace parameter and wavenumber in equation (H.10) by the dimensionless Laplace parameter as $s = s_{\text{dim}}/\omega_0$ and the dimensionless wavenumber as $\kappa = k\ell$ respectively. Subsequently, we express the shear and compressional wave velocities in terms of the Lamé parameters, and note that the Lamé operators describe the viscoelastic behavour of the

continuum in terms of the damping ratio as $\hat{\lambda} = \lambda (1 + 2\zeta s)$ and $\hat{\mu} = \mu (1 + 2\zeta s)$. Then, matching the material parameters of the hexagonal lattice with the material properties of the continuous layer, so that the Lamé operators are related to the Young's modulus as $\lambda = \mu = \frac{2}{5}E$, and additionally, taking into account the relation $\rho \omega_0^2 \ell^2 = \frac{16}{5}E$ previously obtained in Appendix B.2, the dimensionless dispersion relations for the propagation of shear and compressional waves in the continuum are respectively found as:

$$\frac{s^2}{\hat{c}_x^2} + \kappa_x^2 + \kappa_z^2 = 0, \qquad \frac{s^2}{\hat{c}_P^2} + \kappa_x^2 + \kappa_z^2 = 0.$$
 (H.11)

Here, the dimensionless shear and compressional wave velocities are respectively found as:

$$\hat{c}_S = \pm \sqrt{\frac{1}{8}(1 + 2\zeta s)}, \qquad \hat{c}_P = \pm \sqrt{\frac{3}{8}(1 + 2\zeta s)}.$$
 (H.12)

The dispersion relations for wave propagation in either x- or z-direction are obtained from equation (H.11) by substituting $\kappa_z = 0$ and $\kappa_x = 0$ respectively. Evidently, the dispersion relations for the propagation of shear and compressional waves in the continuum are the same for both directions. In fact, expressing these dispersion relations in polar coordinates by introducing $\kappa_x = \kappa_r \cos \theta$ and $\kappa_z = \kappa_r \sin \theta$, where κ_r is the wavenumber magnitude and θ gives the direction of wave propagation, it follows that $\kappa_x^2 + \kappa_z^2 = \kappa_r^2$, so that both dispersion relations are independent of the direction of wave propagation. Noting that the first dispersion relation in equation (H.11) is related to the propagation of shear waves, and the second dispersion relation is related to the propagation of compressional waves, the direction-independent dispersion relations for the propagation of shear and compressional waves in the continuum are respectively obtained as:

$$\kappa_S = \pm i s \sqrt{\frac{8}{1 + 2\zeta s}}, \qquad \kappa_P = \pm \frac{i s}{\sqrt{3}} \sqrt{\frac{8}{1 + 2\zeta s}}. \tag{H.13}$$

Corresponding inverse dispersion relations for the continuous layer are obtained by rearranging and solving equation (H.11) for the Laplace parameter s using the quadratic formula. Then, expressing the Laplace parameter in terms of frequency using $s = i\Omega + \sigma$, with $\sigma = 0$, we find the direction-independent dispersion relations for the propagation of the shear and compressional waves as:

$$\Omega_{S} = i\frac{1}{8}\kappa_{r}^{2}\zeta \pm \frac{1}{8}\kappa_{r}\sqrt{8 - \kappa_{r}^{2}\zeta^{2}}, \qquad \Omega_{P} = i\frac{3}{8}\kappa_{r}^{2}\zeta \pm \frac{3}{8}\kappa_{r}\sqrt{\frac{8}{3} - \kappa_{r}^{2}\zeta^{2}}.$$
(H.14)

Here, κ_r is the magnitude of the dimensionless wavenumber in the continuous layer in the direction of wave propagation.

I Contour integration and the residue theorem

I.1 Contour integration to evaluate the inverse Fourier transform

Consider a complex-valued function $\tilde{f}(k)$ in the wavenumber domain. To obtain the corresponding function f(x) in the space domain, we apply the inverse Fourier transform with respect to the wavenumber k as:

$$f(x) = \frac{1}{2\pi} \int_{-\infty}^{+\infty} \tilde{f}(k)e^{ikx}dk$$
 (I.1)

To evaluate the inverse Fourier transform according to equation (I.1), we apply contour integration and the residue theorem [Ahlfors, 1966]. The residue theorem states that the line integral over the closed contour of a complex-valued function $\tilde{g}(k)$ is obtained through its residues as:

$$\oint \tilde{g}(k)dk = \pm 2\pi i \sum_{j} \underset{k=k_{j}^{x}}{\text{Res}} \left(\tilde{g}(k) \right) \tag{I.2}$$

Here, k_j^* denotes a pole, or singularity, of the function $\tilde{g}(k)$ in the complex wavenumber domain within the closed contour. Provided that k_j^* is a simple pole, the residue of a complex-valued function at a complex wavenumber k_j^* is found as:

$$\operatorname{Res}_{k=k_{j}^{\times}}\left(\tilde{g}\left(k\right)\right) = \frac{\operatorname{N}\left(\tilde{g},k_{j}^{\times}\right)}{\frac{\partial}{\partial k}\operatorname{\Delta}\left(\tilde{g},k\right)\Big|_{k=k_{j}^{\times}}}\tag{I.3}$$

Where $N(\tilde{g}, k)$ and $\Delta(\tilde{g}, k)$ respectively denote the numerator and denominator of the function $\tilde{g}(k)$ in the wavenumber domain that must both be single-valued.

While the inverse Fourier transform in equation (I.1) is an integral over the real domain of the wavenumber k, the contour integral in equation (I.2) is applied over a contour in the complex wavenumber domain. Therefore, to be able to evaluate the inverse Fourier transform by means of the integration over a closed contour in the complex wavenumber domain, the contour must include the real axis, and the direction of the contour integration must match the direction of the considered integral transform. Next to the real axis, the closed contour consist of a semicircle over either the upper or lower half of the complex k-plane. The sign of the right-hand side of equation (I.2) is then determined by the half of the complex k-plane that is included in the contour; if the contour is closed over the upper half of the complex k-plane, as depicted in Figure I.1, the line integration along the contour is applied in a counterclockwise, i.e. mathematically positive, direction yielding a positive sign. The sign of the right-hand side of equation (I.2) becomes negative when the contour is closed over the lower half of the complex k-plane and the line integration along the contour is applied in clockwise direction. Consequently, the contour integral over $\tilde{g}(k)$ may be expressed as a set of separate

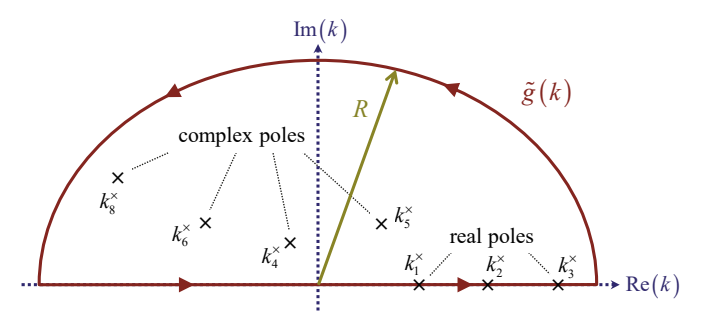


Figure I.1: A closed contour over the upper half of the complex k-plane.

line integrals over respectively the real axis and the semicircle with radius R over either half of the complex k-plane as:

$$\oint \tilde{g}(k)dk = \int_{-R}^{+R} \tilde{g}(k)dk + \int_{R(0)}^{R(\pi)} \tilde{g}(k)dk \tag{I.4}$$

Note here that the closed contour as shown in Figure I.1, is only valid if the function $\tilde{g}(k)$ in the complex k-plane is single-valued. If the function $\tilde{g}(k)$ is multi-valued, the contour must be adapted by applying a so-called branch cut. An example of a contour integral that involves a branch cut is discussed in Appendix I.5.

For the case that the function $\tilde{g}(k)$ goes to zero for infinitely large complex wavenumbers, it logically follows that in the limit of $R \to \infty$, the result of the line integral over the semicircle goes to zero. It then follows from equation (I.4) that:

$$\lim_{R \to \infty} \oint \tilde{g}(k) dk = \int_{-\infty}^{+\infty} \tilde{g}(k) dk \tag{I.5}$$

Substituting $\tilde{g}(k) = \tilde{f}(k)e^{ikx}$, as well as noting that the exponent e^{ikx} itself does not contain any poles, it follows from combining equations (I.2), (I.3) and (I.5) that the inverse Fourier transform may be obtained as:

$$f(x) = \frac{1}{2\pi} \int_{-\infty}^{+\infty} \tilde{f}(k)e^{ikx}dk = \pm i \sum_{j} \underset{k=k_{j}^{\times}}{\operatorname{Res}} \left(\tilde{f}(k)e^{ikx}\right) = \pm i \sum_{j} \frac{N(f,k_{j}^{\times})}{\frac{\partial}{\partial k} \Delta(\tilde{f},k)\Big|_{k=k_{j}^{\times}}} e^{ik_{j}^{\times}x}$$
(I.6)

Here, the summation over j must include all existing poles of the function $\tilde{f}(k)$ within either the upper or lower half of the complex k-plane. Note furthermore that, as depicted in Figure I.1, the poles of a complex-valued function $\tilde{g}(k)$ may either be real or complex.

1.2 Algorithm to find the roots of a function in the complex plane

To evaluate the contour integration of a complex-valued function by means of Cauchy's residue theorem, we must estimate the locations of the poles, or singularities, of that function, and thus we must estimate the locations of the roots, or zeroes, of its denominator in the complex plane. For the two-dimensional system considered here, the Green's functions for the displacements and the stresses all have the same determinant, yielding the common denominator $\Delta(k)$, that has infinitely many roots. Consequently, depending on the expression for the denominator, the size of the complex domain required to obtain sufficient convergence may differ. Therefore, let us emphasize here that to apply the residue theorem correctly, the radius of the semicircle-segment of the contour, and thus the domain for which the roots of the denominator are to be considered, must be chosen large enough to assure that the contribution of an additional root to the integration result is negligible.

The domain of the complex *k*-plane for which the roots, or zeroes, of the common denominator are considered, has in this case been established empirically.

Determining the number of roots within the complex *k*-plane

Once the domain of the complex *k*-plane has been established, we apply Cauchy's Argument Principle [Krantz, 1999] to determine the number of roots that exist within this domain of the complex *k*-plane. According to the Argument Principle, the winding number about the origin of the complex *k*-plane of the common denominator along a closed contour *C* yields the difference between the number of roots and the number of poles inside that contour. We may write this as:

$$\frac{1}{2\pi i} \oint_C \frac{\Delta'(k)}{\Delta(k)} dk = N - P \tag{I.7}$$

Here, N and P respectively denote the number of roots and poles inside the closed contour C. Thus, choosing the denominator $\Delta(k)$ such that it has no poles or singularities, the Argument Principle exactly yields the number of roots within the closed contour C. For the Argument Principle to hold, note that the closed contour may not intersect itself. Numerically, we determine the winding number by considering the denominator $\Delta(k)$ at small increments along the contour C. To make sure that we do not miss a single wind, we determine the winding number along the contour multiple times, each time significantly decreasing the step-size along the closed contour up to the point that the calculated number of roots no longer changes.

Division of the complex k-plane into single-root subdomains

Once the total number of roots in the considered domain of the complex k-plane is established, we divide this domain into subdomains such that each subdomain contains exactly one root. To manage this, the considered domain is arbitrarily divided into a number of subdomains, after which the Argument Principle is applied for each subdomain to determine the number of roots within using the winding number of the denominator $\Delta(k)$ along the closed subcontours of each subdomain. As the denominator $\Delta(k)$ is a single-valued function, each

root has a multiplicity of one. Thus, when the amount of roots in a subdomain is found to be larger than one, that subdomain contains multiple roots and is therefore again divided into smaller segments. When there are no roots found within a subdomain, this subdomain is disregarded. This process is repeated until the number of subdomains that remain is exactly equal to the amount of roots found within the domain of the complex *k*-plane originally considered. Note here that care should be taken that the division of the full domain into single-root subdomains is applied correctly such that each subdomain contains exactly one wind around the origin of the complex plane. If the subdomains are chosen such that the considered function contains partial winds along the subcontours, the number of single-root subdomains found, and thus the total amount of roots found in all subdomains together, may no longer coincide with the number of roots found in the full domain.

Finding the locations of the roots within each single-root subdomain

The exact position of the root in each subdomain of the complex k-plane is found by applying the Nelder-Mead algorithm [Nelder and Mead, 1965]. The Nelder-Mead algorithm is an optimized simplex method to find the minimum of a given two-dimensional function, in this case the absolute value of the complex denominator $\Delta(k)$. As a first step of the Nelder-Mead algorithm, the values of the considered function are calculated at the vertices of a simplex, i.e. a triangle in the complex k-plane. The vertex that gives the largest value for the considered function is then replaced by a new point in the complex k-plane that is found by reflecting the original vertex in the opposite face of the vertex. This new point in the complex k-plane is then used to construct a new simplex together with the two smallest values of the initial simplex. This process is repeated until the algorithm no longer finds a new minimum and thus a new simplex. The minimum vertex of the final simplex then gives the minimum of the supplied function.

It is possible that the minimum obtained by the Nelder-Mead algorithm is a local minimum and does not yield the intended root. When this occurs, there are two possible remedies. Either the vertices of the initial simplex are chosen differently, or the considered subdomain is divided into a set of smaller subdomains, after which the Nelder-Mead algorithm is reapplied to a simplex in the subdomain that contains the root. This process is repeated for each single-root subdomain until all roots within the original domain of the complex *k*-plane are obtained.

To make sure that the complex-valued roots located closest to the origin of the complex k-plane are considered first and those furthest away are considered last, the roots are sorted using the heapsort method [Williams, 1964]. The heapsort method is a comparison-based sorting algorithm with a worst-case runtime order of $n \log n$ where n is the number of roots considered.

Path of the roots in the complex *k*-plane as a function of frequency

Independent of whether we apply a frequency or time domain approach to obtain the displacements and stresses in the two-dimensional continuum, we do require its Green's functions for the displacements and the stresses and thus the roots of the denominator $\Delta(k)$ for

a range of frequencies. In this appendix, we have so far only considered an algorithm to find the roots in complex k-plane for a single given frequency. Although it works well and this algorithm can be applied to any frequency, considering every frequency separately is numerically elaborate and rather inefficient. Instead, noting that each root only shifts slightly in the complex k-plane for one frequency to the next, the locations of the roots in the complex k-plane for any frequency may be determined using the roots of a nearby frequency. As the roots of a nearby frequency are close, using them as a starting point for the Nelder-Mead algorithm is a numerically efficient way to find the roots for a set or range of frequencies. Effectively, we thus only need to apply the root-finder algorithm to find the location of all roots in the complex k-plane only for a single frequency, after which the roots for all frequencies can be derived from the path that each root travels through the complex k-plane as a function of frequency.

Figure I.2a and Figure I.2b show the path of the first six roots of the denominator $\Delta(k)$ in both the upper and the lower half of the complex k-plane, for respectively damping ratios $\zeta = 0.1$ and $\zeta = 0.75$. For both damping ratio's, the starting position of the roots, i.e. the location of the roots in the complex k-plane for zero frequency, here given by the black crosses, is the same. Note here that in both the upper and lower halves of the complex k-plane, the root located closest to the origin is nonzero only due to the nonzero real part of the Laplace parameter s. For increasing frequency, the complex-valued roots first move closer to the real axis and subsequently, with an increase of their real values slowly deviate from the real axis. For a damping ratio $\zeta = 0.75$, this effect is much more pronounced then for a damping ratio of $\zeta = 0.1$. Note here that for a linear-elastic material, i.e. for a damping ratio $\zeta = 0$, the roots become real as the frequency increases.

I.3 Green's functions of the linear-elastic rod

For the particular case of nonzero initial conditions (ICs), the Laplace domain equation of motion for the linear-elastic rod may be written as:

$$s^{2}\tilde{u}(x,s) - \frac{1}{2}\tilde{u}''(x,s) = \tilde{f}(x,s) = \int_{x_{lm}}^{+\infty} \tilde{f}(\xi,s)\delta(x-\xi)d\xi$$
 (I.8)

Here, the variable of integration ξ gives a coordinate along the linear-elastic rod and the integration is therefore applied over the domain $\xi = x_{lnt} \dots + \infty$. The function $\tilde{f}(x,s)$, and therefore also the function $\tilde{f}(\xi,s)$, contains the contribution of the initial conditions to the equation of motion. The particular solution to equation (I.8), is then found as:

$$\tilde{u}_{p}(x,s) = \int_{x_{lu}}^{\infty} \tilde{f}(\xi,s) \tilde{g}_{u}(x-\xi,s) d\xi$$
(I.9)

Here, $\tilde{g}_u(x-\xi,s)$ denotes the Green's function for the displacement of the linear-elastic rod, henceforth referred to as the Green's displacement of the rod, and found as the solution

to equation (I.8) for the case that $\tilde{f}(x,s)$ is equal to the Dirac delta function $\delta(x-\xi)$. The Green's displacement $\tilde{g}_u(x-\xi,s)$ is thus found as the solution to the following equation:

$$s^{2}\tilde{g}_{u}(x-\xi,s) - \frac{1}{2}\tilde{g}''_{u}(x-\xi,s) = \delta(x-\xi)$$
(I.10)

Note here that the Green's displacement $\tilde{g}_u(x-\xi,s)$ is valid for an infinitely long rod so that the boundary conditions of the rod in the discrete-continuous system are not accounted for. Applying the Fourier transform with respect to space to equation (I.10) then yields:

$$s^{2}\tilde{\tilde{g}}_{u}(k,s) - \frac{1}{2} \int_{-\infty}^{+\infty} \tilde{g}''_{u}(x - \xi, s) e^{-ik(x - \xi)} dx = \int_{-\infty}^{+\infty} \delta(x - \xi) e^{-ik(x - \xi)} dx$$
 (I.11)

The Fourier transform of $\tilde{g}_{u}''(x-\xi,s)$ is obtained by applying integration by parts as:

$$\int_{-\infty}^{+\infty} \tilde{g}_{u}''(x-\xi,s)e^{-\mathrm{i}k(x-\xi)}dx = -k^{2}\int_{-\infty}^{+\infty} \tilde{g}_{u}(x-\xi,s)e^{-\mathrm{i}k(x-\xi)}dx = -k^{2}\tilde{\tilde{g}}_{u}(k,s)$$

Substituting the above into equation (I.11) and noting that the Fourier transform over a Dirac delta function is by definition equal to one, the Green's displacement in the Laplace-wavenumber domain may be straightforwardly derived as:

$$\tilde{\tilde{g}}_{u}(k,s) = \frac{2}{2s^{2} + k^{2}}$$
 (I.12)

Applying the inverse Fourier transform to equation (I.12) yields the Green's displacement of the linear-elastic rod in the Laplace domain. The resulting integral equation is evaluated using

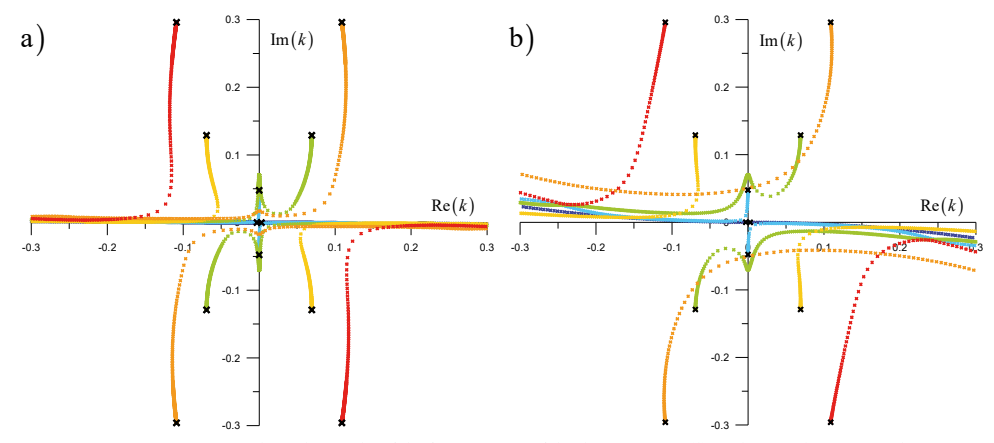


Figure I.2: Frequency-dependent paths of the first six roots of the denominator $\Delta(k)$ in the complex wavenumber domain: a) for a damping ratio $\zeta = 0.1$; b) for a damping ratio $\zeta = 0.75$.

contour integration and the residue theorem as previously discussed in Appendix I.1.

To assure that equation (I.5) holds, i.e. to assure that the contribution of the complex part of the contour that is not on the real axis reduces to zero in the limit of $\operatorname{Im}(k) \to |\infty|$, the contour is chosen over the upper half of the complex k-plane when $x-\xi>0$ and the contour integration is applied in mathematically positive, i.e. counter-clockwise, direction. Accordingly, for the situation that $x-\xi<0$, the contour is chosen over the lower half of the complex k-plane and the contour integration is applied in the mathematically negative, i.e. clockwise, direction. Using the contour integration and the residue theorem to apply the inverse Fourier transform, thus yields the Green's displacement in the Laplace domain as:

$$\tilde{g}_{u}(x-\xi,s) = \frac{1}{2\pi} \int_{-\infty}^{+\infty} \tilde{\tilde{g}}_{u}(k,s) e^{ik(x-\xi)} dk = \pm 2i \sum_{j} \underset{k=k_{j}^{*}}{\text{Res}} \left(\frac{e^{ik(x-\xi)}}{2s^{2}+k^{2}} \right)$$
(I.13)

Respectively choosing the numerator and denominator of the inverse Fourier integrand in a straightforward manner as $N\left(\tilde{\tilde{f}},k\right) = e^{ik(x-\xi)}$ and $\Delta\left(\tilde{\tilde{f}},k\right) = 2s^2 + k^2$, we find the residue at a pole k_j^{\times} as:

$$\operatorname{Res}_{k=k_{j}^{c}}\left(\frac{e^{\mathrm{i}k(x-\xi)}}{2s^{2}+k^{2}}\right) = \frac{N\left(\tilde{\tilde{f}},k_{j}^{\times}\right)}{\frac{\partial}{\partial k}\Delta\left(\tilde{\tilde{f}},k\right)\Big|_{k=k_{j}^{\times}}} = \frac{1}{2k_{j}^{\times}}e^{\mathrm{i}k_{j}^{\times}(x-\xi)}$$
(I.14)

The denominator $\Delta\left(\tilde{f},k\right)$ yields poles at the wavenumbers $k_1^\times=+\mathrm{i} s\sqrt{2}$ and $k_2^\times=-\mathrm{i} s\sqrt{2}$, where k_1^\times is the only pole in the upper half of the complex k-plane, while k_2^\times is the only pole in the lower half of the complex k-plane. Thus, we find the Green's displacements for respectively $x-\xi>0$ and $x-\xi<0$ in respectively the upper and lower half of the complex k-planes as:

$$\tilde{g}_{u}(x-\xi,s)\Big|_{x-\xi>0} = +2i\operatorname{Res}_{k=k_{1}^{x}}\left(\frac{e^{ik(x-\xi)}}{2s^{2}+k^{2}}\right) = \frac{+i}{k_{1}^{x}}e^{ik_{1}^{x}(x-\xi)} = \frac{1}{s\sqrt{2}}e^{-s\sqrt{2}(x-\xi)}$$
(I.15)

$$\tilde{g}_{u}\left(x-\xi,s\right)\Big|_{x-\xi<0} = -2i\operatorname{Res}_{k=k_{2}^{\times}}\left(\frac{e^{ik(x-\xi)}}{2s^{2}+k^{2}}\right) = \frac{-i}{k_{2}^{\times}}e^{ik_{2}^{\times}(x-\xi)} = \frac{1}{s\sqrt{2}}e^{+s\sqrt{2}(x-\xi)}$$
(I.16)

Thus, applying the residue theorem, the Green's displacement of the linear-elastic rod may generally be expressed in the Laplace domain as:

$$\tilde{g}_u\left(x-\xi,s\right) = \frac{1}{s\sqrt{2}}e^{-s\sqrt{2}|x-\xi|}\tag{I.17}$$

I.4 Green's functions of the viscoelastic rod

Taking into account nonzero initial conditions (ICs), the equation of motion for the viscoelastic rod may, in the Laplace domain, be written as:

$$s_{\zeta}^{2}\tilde{u}(x,s) - \frac{1}{2}\tilde{u}''(x,s) = \tilde{f}(x,s) = \int_{x_{tot}}^{+\infty} \tilde{f}(\xi,s)\delta(x-\xi)d\xi$$
 (I.18)

Here, we find $s_{\zeta} = s/\sqrt{1+2\zeta s}$. Again, the variable of integration ξ gives a coordinate along the viscoelastic rod, therefore the integration is applied over the domain $\xi = x_{lnt} \dots + \infty$, and the particular solution to equation (I.18) may be obtained as:

$$\tilde{u}_{p}(x,s) = \int_{x_{lnt}}^{\infty} \tilde{f}(\xi,s) \tilde{g}_{u}(x-\xi,s) d\xi$$
(I.19)

Here, $\tilde{g}_u(x-\xi,s)$ denotes the Green's function for the displacement along the viscoelastic rod, henceforth referred to as the Green's displacement, which is obtained in accordance with the approach for the linear-elastic rod. In fact, the equation of motion for the viscoelastic rod may be obtained from that of the linear-elastic rod by substituting $s = s_{\zeta}$. Since the Green's displacement in the Laplace-wavenumber domain is obtained by applying the Fourier transform with respect to space, the dependency on s is not altered and the Green's displacement for the viscoelastic rod in the Laplace-wavenumber domain follows from substituting $s = s_{\zeta}$ into equation (I.12) as:

$$\tilde{\tilde{g}}_u(k,s) = \frac{2}{2s_{\zeta}^2 + k^2} \tag{I.20}$$

The Green's displacement in the Laplace domain is now obtained by applying the inverse Fourier transform to equation (I.20) with respect to the wavenumber. During this operation the dependency on s is again not altered and therefore applying contour integration and the residue theorem will show that the Laplace domain Green's displacement of the viscoelastic rod follows from substituting $s = s_{\zeta}$ into equation (I.17) as:

$$\tilde{g}_{u}\left(x-\xi,s\right) = \frac{1}{s_{\zeta}\sqrt{2}}e^{-s_{\zeta}\sqrt{2}|x-\xi|} \tag{I.21}$$

Substituting equation (I.21) into equation (I.19), we then find the particular solution as:

$$\tilde{u}_{p}(x,s) = \frac{1}{s_{\zeta}\sqrt{2}} \int_{x_{tot}}^{x} \tilde{f}(\xi,s) e^{-s_{\zeta}\sqrt{2}(x-\xi)} d\xi + \frac{1}{s_{\zeta}\sqrt{2}} \int_{x}^{+\infty} \tilde{f}(\xi,s) e^{-s_{\zeta}\sqrt{2}(\xi-x)} d\xi$$
(I.22)

I.5 Convolution term in the Green's function for the viscoelastic rod

As discussed in Section 5.3.1, the equation of motion for the particle **N** at the lattice-rod interface of the one-dimensional discrete-continuous Kelvin-Voigt lattice that accounts for nonzero initial conditions contains an expression that reads:

$$\tilde{f}_0(s) = \zeta s_{\zeta} \sqrt{2} u_0^{N} + \int_0^{t_0} f(\tau) \left(\frac{s_{\zeta}^2}{s} v^{N} (t_0 - \tau) + a^{N} (t_0 - \tau) \right) d\tau$$
(I.23)

Here, the function $f(\tau)$ is found as the inverse Laplace transform of the Laplace domain function $\tilde{f}(\hat{s})$ that is applied with respect to the complex-valued Laplace parameter \hat{s} to obtain the time domain displacement and time domain velocity along the viscoelastic rod at time t_0 , rather than at time t. The complex-valued Laplace parameter \hat{s} is expressed in terms of frequency as $\hat{s} = i\hat{\omega} + \hat{\sigma}$. The corresponding inverse Laplace transform is generally expressed by the Bromwich integral as:

$$f(\tau) = \mathcal{L}_{\hat{s}}^{-1} \left\{ \tilde{f}(\hat{s}) \right\} (\tau) = \frac{1}{2\pi i} \int_{\hat{\sigma}^{-i\infty}}^{\hat{\sigma}^{+i\infty}} \tilde{f}(\hat{s}) e^{\hat{s}\tau} d\hat{s}$$
 (I.24)

Here, the expression for $\tilde{f}(\hat{s})$ is found as:

$$\tilde{f}(\hat{s}) = \frac{1}{\sqrt{2}} \frac{1}{\hat{s}(\hat{s}_{\zeta} + s_{\zeta})} \tag{I.25}$$

Noting that $s_{\zeta} = s/\sqrt{1+2\zeta s}$ and $\hat{s}_{\zeta} = \hat{s}/\sqrt{1+2\zeta \hat{s}}$, and multiplying both the denominator and the numerator of equation (I.25) first by respectively the square roots $\sqrt{1+2\zeta s}$ and $\sqrt{1+2\zeta \hat{s}}$, and subsequently by the expression $s\sqrt{2+4\zeta \hat{s}} - \hat{s}\sqrt{2+4\zeta s}$ yields:

$$\tilde{f}(\hat{s}) = \frac{s\sqrt{2+4\zeta s} (1+2\zeta \hat{s})}{\hat{s}(s^2(2+4\zeta \hat{s})-\hat{s}^2(2+4\zeta s))} - \frac{(1+2\zeta s)\sqrt{2+4\zeta \hat{s}}}{(s^2(2+4\zeta \hat{s})-\hat{s}^2(2+4\zeta s))}$$
(I.26)

Here, note that the square roots in equation (I.26) are chosen such that their real parts are positive, i.e. $Re(s_{\zeta}) > 0$, and that the general solution for the displacement in the rod satisfies the infinity condition.

Then, respectively denoting the first and second terms on the right-hand side of equation (I.26) as $\tilde{f}_1(\hat{s})$ and $\tilde{f}_2(\hat{s})$, the corresponding expression in terms of the time domain operator τ may be obtained from applying the inverse Laplace transform as:

$$f(\tau) = \mathcal{L}_{\hat{s}}^{-1} \left\{ \tilde{f}_1(\hat{s}) \right\} - \mathcal{L}_{\hat{s}}^{-1} \left\{ \tilde{f}_2(\hat{s}) \right\} \tag{I.27}$$

To evaluate the inverse Laplace transform according to equation (I.24), we apply contour integration and the residue theorem. As stated by equation (I.2), the residue theorem allows us to obtain the contour integral of a complex-valued function through the residues of that complex-valued function within the contour.

First consider the inverse Laplace transform of $\tilde{f}_2(\hat{s})$, i.e. the second term on the right-hand side of equation (I.26). Due to the square root in its numerator, $\tilde{f}_2(\hat{s})$ is generally a multi-valued function, unless the argument of the square root is equal to zero. In other words, the function $\tilde{f}_2(\hat{s})$ has a branch point when $2+4\zeta\hat{s}=0$. Within the complex \hat{s} -plane, this branch point is found as $\hat{s}^*=-1/(2\zeta)$. Additionally, we find that the function $\tilde{f}_2(\hat{s})$ has two poles, respectively found as $\hat{s}_1^*=-s/(1+2\zeta s)$ and $\hat{s}_2^*=s$.

Here, first of all note that the integration involved with applying the inverse Laplace transform is applied over a line parallel to the imaginary axis. According to the range of the convolution integral in equation (I.23) the time parameter τ is always equal to or larger than zero. To make sure that the contribution of the corresponding part of the contour integral is equal to zero, we close the contour by a semicircle with an infinite radius over the left half of the complex \hat{s} -plane, i.e. for $\text{Re}(\hat{s}) \to -\infty$. Additionally, both poles of the function $f_2(\hat{s})$ must be located within the contour. As the pole \hat{s}_1^{x} is located in the left half of the complex \hat{s} -plane, it is apparent that this pole lies within the chosen contour. The pole \hat{s}_2^{\times} however has a positive real part equal to σ and therefore, to include this pole, the line parallel to the imaginary axis, must be chosen at a positive real value that is larger than σ , i.e. $\hat{\sigma} > \sigma$. Finally, to assure that the contour integration is applied over a single-valued domain of the function $\tilde{f}_2(\hat{s})$ in the complex \hat{s} -plane, we apply a branch cut along the real axis of the complex \hat{s} plane from minus infinity to the branch point, i.e. on the domain $\hat{s} = -\infty \dots -1/(2\zeta)$. This results in the contour depicted in Figure I.3. The contour integral over the inverse Laplace integrand is then found as the summation of the line integrals over all segments of the closed contour. Note here that, as previously stated, the contribution of the line integral over the segments of the contour for which $Re(\hat{s}) \rightarrow -\infty$ are equal to zero. Furthermore, as the radius

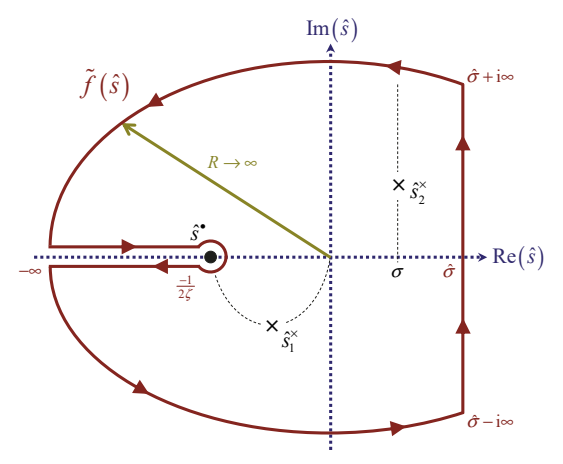


Figure I.3: The closed contour applied to obtain the inverse Laplace transform.

of the segment of the contour around the branch point is infinitesimal, its contribution is equal to zero as well. Consequently, we find the contour integral over the inverse Laplace integrand as:

$$\frac{1}{2\pi i} \oint \tilde{f}_{2}(\hat{s}) e^{\hat{s}r} d\hat{s} = \mathcal{L}_{\hat{s}}^{-1} \left\{ \tilde{f}_{2}(\hat{s}) \right\} + \frac{1}{2\pi i} \int_{-\infty}^{-\frac{1}{2\zeta}} \tilde{f}_{2}(\hat{s}) e^{\hat{s}r} d\hat{s} + \frac{1}{2\pi i} \int_{-\frac{1}{2\zeta}}^{\infty} \tilde{f}_{2}(\hat{s}) e^{\hat{s}r} d\hat{s}$$
 (I.28)

Note here that the contour integration is applied in counter-clockwise, i.e. mathematically positive, direction to account for the proper domain of integration of the inverse Laplace transform. According to the residue theorem, we find the above contour integral in terms of its residues as:

$$\frac{1}{2\pi i} \oint \tilde{f}_2(\hat{s}) e^{\hat{s}r} d\hat{s} = + \sum_{\hat{s} = \hat{s}_j^*} \operatorname{Res}_{\hat{s} = \hat{s}_j^*} \left(\tilde{f}_2(\hat{s}) e^{\hat{s}r} \right)$$
(I.29)

From combining equations (I.28) and (I.29), the inverse Laplace transform of $\tilde{f}_2(\hat{s})$ may now be obtained as:

$$\mathcal{L}_{\hat{s}}^{-1}\left\{\tilde{f}_{2}\left(\hat{s}\right)\right\} = +\sum_{j} \underset{\hat{s}=\hat{s}_{j}^{*}}{\text{Res}}\left(\tilde{f}_{2}\left(\hat{s}\right)e^{\hat{s}\tau}\right) - \frac{1}{2\pi i} \int_{-\infty}^{\frac{1}{2-\xi}} \tilde{f}_{2}\left(\hat{s}\right)e^{\hat{s}\tau}d\hat{s} - \frac{1}{2\pi i} \int_{-\frac{1}{2-\xi}}^{\infty} \tilde{f}_{2}\left(\hat{s}\right)e^{\hat{s}\tau}d\hat{s}$$

$$(I.30)$$

Choosing the numerator and denominator of the inverse Laplace integrand in accordance with the second term on the right-hand side of equation (I.26), the residue at a pole \hat{s}_j^{\times} is found as:

$$\operatorname{Res}_{\hat{s}=\hat{s}_{j}^{s}}\left(\tilde{f}_{2}\left(\hat{s}\right)e^{\hat{s}\tau}\right) = \frac{N\left(\tilde{f}_{2},\hat{s}_{j}^{x}\right)e^{\hat{s}_{j}^{s}\tau}}{\frac{\partial}{\partial\hat{s}}\Delta\left(\tilde{f}_{2},\hat{s}\right)\Big|_{\hat{s}=\hat{s}_{j}^{s}}} = \frac{e^{\hat{s}_{j}^{s}\tau}\left(1+2\zeta s\right)\sqrt{2+4\zeta \hat{s}_{j}^{x}}}{4\zeta s^{2}-2\hat{s}_{j}^{x}\left(2+4\zeta s\right)}$$
(I.31)

We previously found that $\tilde{f}_2(\hat{s})$ has two poles at $\hat{s}_1^x = -s/(1+2\zeta s)$ and $\hat{s}_2^x = s$ respectively. The corresponding residues are respectively found as:

$$\operatorname{Res}_{\hat{s}=\hat{s}_{1}^{\kappa}}\left(\tilde{f}_{2}\left(\hat{s}\right)e^{\hat{s}\tau}\right) = \frac{N\left(\tilde{f}_{2},\hat{s}_{1}^{\kappa}\right)e^{\hat{s}_{1}^{\kappa}\tau}}{\frac{\partial}{\partial\hat{s}}\Delta\left(\tilde{f}_{2},\hat{s}\right)\Big|_{\hat{s}=\hat{s}^{\kappa}}} = e^{\frac{-s\tau}{1+2\zeta s}}\frac{\sqrt{2+4\zeta s}}{4s\left(1+\zeta s\right)}$$
(I.32)

$$\operatorname{Res}_{\hat{s}=\hat{s}_{2}^{c}}\left(\tilde{f}_{2}\left(\hat{s}\right)e^{\hat{s}\tau}\right) = \frac{N\left(\tilde{f}_{2},\hat{s}_{2}^{\times}\right)e^{\hat{s}_{2}^{\times}\tau}}{\frac{\partial}{\partial\hat{s}}\Delta\left(\tilde{f}_{2},\hat{s}\right)\Big|_{\hat{s}=\hat{s}_{2}^{\times}}} = -e^{s\tau}\left(1+2\zeta s\right)\frac{\sqrt{2+4\zeta s}}{4s\left(1+\zeta s\right)}$$
(I.33)

The integrals remaining in equation (I.30) correspond to the segments of the contour integral along the branch cut that are applied at the real axis of the complex \hat{s} -plane. To assure that the square root in the numerator of the function $\tilde{f}_2(\hat{s})$ itself is always real on the considered domain of the contour integral, we write the square root as $\sqrt{2+4\zeta\hat{s}}=\pm i\sqrt{-2-4\zeta\hat{s}}$. Then, for the line integral along the real axis in the upper half of the complex \hat{s} -plane, with the domain $\hat{s}=-\infty...-1/(2\zeta)$, we substitute $\sqrt{2+4\zeta\hat{s}}$ by $+i\sqrt{-2-4\zeta\hat{s}}$, and accordingly along the real axis in the lower half plane, on the domain $\hat{s}=-1/(2\zeta)...-\infty$, we substitute $\sqrt{2+4\zeta\hat{s}}$ by $-i\sqrt{-2-4\zeta\hat{s}}$. Evaluating the line integrals along the branch cut that appear in equation (I.30), we find:

$$\frac{1}{2\pi i} \int_{-\infty}^{\frac{1}{2\zeta}} \tilde{f}_2(\hat{s}) e^{\hat{s}r} d\hat{s} = \frac{1}{2\pi i} \int_{-\frac{1}{2\zeta}}^{\infty} \tilde{f}_2(\hat{s}) e^{\hat{s}r} d\hat{s} = \frac{1}{2\pi} \int_{-\infty}^{\frac{1}{2\zeta}} \frac{e^{\hat{s}r} (1 + 2\zeta s) \sqrt{-2 - 4\zeta \hat{s}}}{s^2 (2 + 4\zeta \hat{s}) - \hat{s}^2 (2 + 4\zeta s)} d\hat{s}$$
 (I.34)

Substituting equations (I.32), (I.33) and (I.34) into equation (I.30), now yields:

$$\mathcal{L}_{\hat{s}}^{-1}\left\{\tilde{f}_{2}\left(\hat{s}\right)\right\} = \frac{\sqrt{2+4\zeta s}}{4s\left(1+\zeta s\right)} \left(e^{\frac{-sr}{1+2\zeta s}} - e^{sr}\left(1+2\zeta s\right)\right) - \frac{1}{\pi} \int_{-\infty}^{\frac{1}{2\zeta}} \frac{e^{\hat{s}r}\left(1+2\zeta s\right)\sqrt{-2-4\zeta \hat{s}}}{s^{2}\left(2+4\zeta \hat{s}\right) - \hat{s}^{2}\left(2+4\zeta s\right)} d\hat{s}$$
 (I.35)

Note here that the integral remaining in equation (I.35) is an integral over the real domain of \hat{s} that quickly decays for $\omega \to \infty$ and can be straightforwardly evaluated numerically.

Now, since $\tilde{f}_1(\hat{s})$ is a polynomial function with regard to \hat{s} , and has no branch points, its inverse Laplace transform with respect to \hat{s} can be obtained analytically by applying the contour integration in accordance with Appendix I.1. Using the same contour as for the function $\tilde{f}_2(\hat{s})$ but without the branch cut, the inverse Laplace transform of $\tilde{f}_1(\hat{s})$ may be obtained as:

$$\mathcal{L}_{\hat{s}}^{-1}\left\{\tilde{f}_{1}\left(\hat{s}\right)\right\} = +\sum_{j} \underset{\hat{s}=\hat{s}_{j}^{*}}{\operatorname{Res}}\left(\tilde{f}_{1}\left(\hat{s}\right)e^{\hat{s}r}\right) \tag{I.36}$$

Choosing the numerator and denominator of the inverse Laplace integrand in accordance with the numerator and denominator of $\tilde{f}_1(\hat{s})$ as stated by the first term on the right-hand side of equation (I.26), the corresponding residue at a pole \hat{s}_j^* in the complex \hat{s} -plane is found as:

$$\operatorname{Res}_{\hat{s}=\hat{s}_{j}^{c}}\left(\tilde{f}_{1}\left(\hat{s}\right)e^{\hat{s}\tau}\right) = \frac{N\left(\tilde{f}_{1},\hat{s}_{j}^{\times}\right)e^{\hat{s}_{j}^{\times}\tau}}{\frac{\partial}{\partial\hat{s}}\Delta\left(\tilde{f}_{1},\hat{s}\right)\Big|_{\hat{s}=\hat{s}_{j}^{\times}}} = \frac{s\sqrt{2+4\zeta s}\left(1+2\zeta\hat{s}_{j}^{\times}\right)e^{\hat{s}_{j}^{\times}\tau}}{2s^{2}\left(1+4\zeta\hat{s}_{j}^{\times}\right)-6\left(\hat{s}_{j}^{\times}\right)^{2}\left(1+2\zeta s\right)}$$
(I.37)

Here, $\tilde{f}_1(\hat{s})$ has three poles; of which two are the same as the poles found for $\tilde{f}_2(\hat{s})$, i.e. $\hat{s}_1^{\times} = -s/(1+2\zeta s)$ and $\hat{s}_2^{\times} = s$, while the third pole is found as $\hat{s}_3^{\times} = 0$. Their residues are

respectively found as:

$$\operatorname{Res}_{\hat{s}=\hat{s}_{1}^{s}}\left(\tilde{f}_{1}\left(\hat{s}\right)e^{\hat{s}\tau}\right) = -e^{\frac{-s\tau}{1+2\zeta s}}\frac{\sqrt{2+4\zeta s}}{4s\left(1+\zeta s\right)}\tag{I.38}$$

$$\operatorname{Res}_{\hat{s}=\hat{s}_{s}^{\kappa}}\left(\tilde{f}_{1}\left(\hat{s}\right)e^{\hat{s}\tau}\right) = -e^{s\tau}\left(1+2\zeta s\right)\frac{\sqrt{2+4\zeta s}}{4s\left(1+\zeta s\right)}\tag{I.39}$$

$$\operatorname{Res}_{\hat{s}=\hat{s}_{s}^{*}}\left(\tilde{f}_{1}\left(\hat{s}\right)e^{\hat{s}r}\right)=2\left(1+\zeta s\right)\frac{\sqrt{2+4\zeta s}}{4s\left(1+\zeta s\right)}\tag{I.40}$$

Substituting equation (I.38) to (I.40) into equation (I.36) then yields the inverse Laplace transform of $\tilde{f}_1(\hat{s})$ as:

$$\mathcal{L}_{\hat{s}}^{-1} \left\{ \tilde{f}_{1} \left(\hat{s} \right) \right\} = \frac{\sqrt{2 + 4\zeta s}}{4s \left(1 + \zeta s \right)} \left(2 \left(1 + \zeta s \right) - e^{\frac{-sr}{1 + 2\zeta s}} - e^{sr} \left(1 + 2\zeta s \right) \right) \tag{I.41}$$

Substituting equations (I.35) and (I.41) into equation (I.27), we ultimately find the convolution term $f(\tau)$, in terms of the time domain operator τ , as:

$$f(\tau) = \frac{\sqrt{2 + 4\zeta s}}{2s(1 + \zeta s)} \left(1 + \zeta s - e^{\frac{-s\tau}{1 + 2\zeta s}} \right) + \frac{1}{\pi} \int_{-\infty}^{-\frac{1}{2\zeta}} \frac{e^{\hat{s}\tau} (1 + 2\zeta s) \sqrt{-2 - 4\zeta \hat{s}}}{s^2 (2 + 4\zeta \hat{s}) - \hat{s}^2 (2 + 4\zeta s)} d\hat{s}$$
 (I.42)

J The Laplace transform and nonzero initial conditions

J.1 Identities of the Laplace transform

The Laplace transform of an arbitrary but locally integrable function of time f(t) reads:

$$\tilde{f}(s) = \mathcal{L}\left\{f(t)\right\} = \int_{0}^{+\infty} f(t)e^{-st}dt \tag{J.1}$$

Here, *s* is the complex-valued Laplace parameter.

When applying the Laplace transform to an equation of motion, we may also have to apply it to any time derivatives of the function f(t). The Laplace transform of the first time derivative of f(t) may be derived from equation (J.1) using integration by parts as:

$$\mathcal{L}\left\{\dot{f}\left(t\right)\right\} = \int_{0}^{+\infty} \dot{f}\left(t\right)e^{-st}dt = f\left(t\right)e^{-st}\Big|_{0}^{+\infty} + s\int_{0}^{+\infty} f\left(t\right)e^{-st}dt = \lim_{t \to \infty} f\left(t\right)e^{-st} - f\left(t\right)\Big|_{t=0} + s\tilde{f}\left(s\right)$$

As the Laplace parameter s is found as $s=i\omega+\sigma$, where σ is a small positive real value, and noting that the function f(t) is not infinite at $t\to\infty$, it follows that $\lim_{t\to\infty} f(t)e^{-st}=0$. Thus, the Laplace transform of the first time derivative of a function $f(t)^\infty$ with nonzero initial condition $f(t=0)=f_0$, reads:

$$\mathcal{L}\left\{\dot{f}\left(t\right)\right\} = s\tilde{f}\left(s\right) - f_0 \tag{J.2}$$

Accordingly, the Laplace transform of the second derivative of a function f(t) with nonzero initial conditions $f(t=0) = f_0$ and $\dot{f}(t=0) = \dot{f_0}$, reads:

$$\mathcal{L}\left\{\ddot{f}(t)\right\} = s^2 \tilde{f}(s) - sf_0 - \dot{f}_0 \tag{J.3}$$

Equations (J.1) to (J.3) show that the application of the Laplace transform to a time domain function f(t) and its derivatives accounts for its initial conditions in the time domain, as opposed to, for example, the bilateral Fourier transform.

J.2 The inverse Laplace transform in terms of frequency

A common representation of the inverse Laplace transform is given by the Bromwich integral, also known as the Fourier-Mellin Integral or Mellin's inverse formula, and reads:

$$f(t) = \mathcal{L}^{-1}\left\{\tilde{f}(s)\right\} = \frac{1}{2\pi i} \lim_{\alpha \to \infty} \int_{\sigma - i\alpha}^{\sigma + i\alpha} \tilde{f}(s)e^{st}ds \tag{J.4}$$

The inverse Laplace transform is obtained by applying the integration along the vertical line

 $\Re(s) = \sigma$ in the complex s-plane, where σ is a positive real value chosen larger than the real part of the singularities of $\tilde{f}(s)$ to assure that the integration is in the region of convergence.

For further applications, we choose to write the Bromwich integral as an equivalent integral in the frequency domain. The relation between the complex-valued Laplace parameter s and frequency ω reads $s = i\omega + \sigma$, where σ is a small positive real value. And thus, it straightforwardly follows that $ds = id\omega$. Additionally, by noting that $\omega = -i(s - \sigma)$, the domain of integration of the Bromwich integral in terms of frequency becomes bilaterally infinite and the inverse Laplace transform may therefore be expressed as:

$$f(t) = \mathcal{L}^{-1}\left\{\tilde{f}(s)\right\} = \frac{e^{\sigma t}}{2\pi} \int_{-\infty}^{+\infty} \tilde{f}(s)e^{i\omega t}d\omega \tag{J.5}$$

Note here that if the singularities of $\tilde{f}(s)$ are all located left of the imaginary axis, the Laplace parameter σ may be set to zero and the inverse Laplace transform reduces to the inverse Fourier transform.

Splitting the integrand of the inverse Laplace transform into its real and imaginary parts and rearranging equation (J.5) yields:

$$\frac{2\pi}{e^{\sigma t}} f(t) = \int_{-\infty}^{+\infty} \text{Re}\left\{\tilde{f}(s)e^{i\omega t}\right\} d\omega + i\int_{-\infty}^{+\infty} \text{Im}\left\{\tilde{f}(s)e^{i\omega t}\right\} d\omega \tag{J.6}$$

As the left-hand side of equation (J.6) is a real-valued function, it follows directly that:

$$\frac{2\pi}{e^{\sigma t}}f(t) = \int_{-\infty}^{+\infty} \text{Re}\left\{\tilde{f}(s)e^{i\omega t}\right\}d\omega \tag{J.7}$$

$$\int_{-\infty}^{+\infty} \operatorname{Im}\left\{\tilde{f}(s)e^{i\omega t}\right\}d\omega = 0 \tag{J.8}$$

Expanding the integrands in equations (J.7) and (J.8) using Euler's formula and separately considering the real and imaginary parts of $\tilde{f}(s)$, we can rewrite these equations as:

$$\frac{2\pi}{e^{\sigma t}} f(t) = \int_{-\infty}^{+\infty} \left(\text{Re}\left\{\tilde{f}(s)\right\} \cos \omega t - \text{Im}\left\{\tilde{f}(s)\right\} \sin \omega t \right) d\omega \tag{J.9}$$

$$\int_{-\infty}^{+\infty} \left(\operatorname{Re} \left\{ \tilde{f}(s) \right\} \sin \omega t + \operatorname{Im} \left\{ \tilde{f}(s) \right\} \cos \omega t \right) d\omega = 0$$
(J.10)

Noting that $\sin \omega t$ and $\cos \omega t$ are respectively anti-symmetric and symmetric, it follows that the real and imaginary parts of $\tilde{f}(s)$ must respectively be symmetric and anti-symmetric for equation (J.10) to hold.

Taking into account that the real and imaginary parts of the expression for $\tilde{f}(s)$, as well

as the terms $\cos \omega t$ and $\sin \omega t$, are respectively symmetric and anti-symmetric, the integrand in equation (J.9) must be symmetric, so that:

$$\frac{\pi}{e^{\sigma t}} f(t) = \int_{0}^{+\infty} \left(\text{Re} \left\{ \tilde{f}(s) \right\} \cos \omega t - \text{Im} \left\{ \tilde{f}(s) \right\} \sin \omega t \right) d\omega = \int_{0}^{+\infty} \text{Re} \left\{ \tilde{f}(s) e^{i\omega t} \right\} d\omega$$
 (J.11)

Thus, the inverse Laplace transform may be expressed in terms of the frequency ω as:

$$f(t) = \frac{e^{\sigma t}}{\pi} \int_{0}^{\infty} \operatorname{Re}\left\{\tilde{f}(s)e^{i\omega t}\right\} d\omega = \frac{e^{\sigma t}}{\pi} \int_{0}^{+\infty} \left(\operatorname{Re}\left\{\tilde{f}(s)\right\}\cos\omega t - \operatorname{Im}\left\{\tilde{f}(s)\right\}\sin\omega t\right) d\omega \quad (J.12)$$

J.3 The causality principle and the Laplace transform

A causal system is a system that obeys the rules of cause and effect. For any process that starts at t = 0 and is at rest for t < 0, the integral over the domain $\langle -\infty, 0 \rangle$ has no contribution to the total integral. In the following, the causality principle is used to derive a relation between the real and imaginary parts of a Laplace domain function $\tilde{f}(s)$.

Substituting $s = i\omega + \sigma$ into equation (J.1) and employing Euler's formula, the real and imaginary parts of the Laplace domain function f(s) may be separately expressed as:

$$\operatorname{Re}\left\{\tilde{f}(s)\right\} = \int_{0}^{+\infty} f(t)e^{-\sigma t} \cos \omega t dt \tag{J.13}$$

$$\operatorname{Im}\left\{\tilde{f}(s)\right\} = -\int_{0}^{+\infty} f(t)e^{-\sigma t} \sin \omega t dt \tag{J.14}$$

To find a relation between the real and imaginary parts of f(s), we first use the Hilbert transform to express a relation between $\sin \omega t$ and $\cos \omega t$. Applying the Hilbert transform with respect to frequency ω , the following relations are known to exist:

$$H_{\omega}\left(\cos\omega't\right) = \frac{1}{\pi}PV\int_{-\infty}^{+\infty} \frac{\cos\omega't}{\omega'-\omega}d\omega' = -\sin\omega t \tag{J.15}$$

$$H_{\omega}\left(\sin\omega't\right) = \frac{1}{\pi}PV\int_{-\infty}^{+\infty} \frac{\sin\omega't}{\omega'-\omega}d\omega' = +\cos\omega t \tag{J.16}$$

Here, the notation *PV* means that the Cauchy principle value is taken in the integral. Substituting equation (J.16) into equation (J.13) and rearranging the resulting expression by changing the order of integration yields:

$$\operatorname{Re}\left\{\tilde{f}(s)\right\} = \int_{0}^{+\infty} f(t)e^{-\sigma t} \frac{1}{\pi} PV \int_{-\infty}^{+\infty} \frac{\cos \omega' t}{\omega' - \omega} d\omega' dt = \frac{1}{\pi} PV \int_{-\infty}^{+\infty} \frac{1}{\omega' - \omega} \int_{0}^{+\infty} f(t)e^{-\sigma t} \sin \omega' t dt d\omega' \qquad (J.17)$$

Substituting equation (J.14), where ω is replaced by ω' , it follows from equation (J.17) that we can now express the real part of $\tilde{f}(s)$ as:

$$\operatorname{Re}\left\{\tilde{f}\left(s\right)\right\} = -\frac{1}{\pi}PV\int_{-\infty}^{+\infty} \frac{\operatorname{Im}\left\{\tilde{f}\left(s'\right)\right\}}{\omega' - \omega} d\omega' \tag{J.18}$$

Here, the variable s' is described as $s' = i\omega' + \sigma$.

Alternatively, substituting equation (J.15) into equation (J.14), rearranging the result and substituting equation (J.13) with ω substituted by ω' , yields the imaginary part of $\tilde{f}(s)$ as:

$$\operatorname{Im}\left\{\tilde{f}(s)\right\} = \frac{1}{\pi} P V \int_{-\infty}^{+\infty} \frac{\operatorname{Re}\left\{\tilde{f}(s')\right\}}{\omega' - \omega} d\omega' \tag{J.19}$$

Equation (J.18) and (J.19) are commonly known as the Kramers-Krönig relations.

If we multiply both sides of equation (J.19) by respectively $\sin \omega t$ and $\cos \omega t$ and apply bilateral integration over the frequency ω , we obtain:

$$\int_{-\infty}^{+\infty} \operatorname{Im}\left\{\tilde{f}\left(s\right)\right\} \sin \omega t d\omega = \int_{-\infty}^{+\infty} \operatorname{Re}\left\{\tilde{f}\left(s'\right)\right\} \frac{1}{\pi} P V \int_{-\infty}^{+\infty} \frac{\sin \omega t}{\omega' - \omega} d\omega d\omega' \tag{J.20}$$

$$\int_{-\infty}^{+\infty} \operatorname{Im}\left\{\tilde{f}(s)\right\} \cos \omega t d\omega = \int_{-\infty}^{+\infty} \operatorname{Re}\left\{\tilde{f}(s')\right\} \frac{1}{\pi} PV \int_{-\infty}^{+\infty} \frac{\cos \omega t}{\omega' - \omega} d\omega d\omega'$$
(J.21)

Substituting the Hilbert transforms of $\sin \omega t$ and $\cos \omega t$ with respect to the operator ω' , which are found from equations (J.15) and (J.16) by interchanging ω and ω' , into respectively equations (J.20) and (J.21) shows that:

$$\int_{-\infty}^{+\infty} \operatorname{Im}\left\{\tilde{f}(s)\right\} \sin \omega t d\omega = -\int_{-\infty}^{+\infty} \operatorname{Re}\left\{\tilde{f}(s')\right\} \cos \omega' t d\omega' \tag{J.22}$$

$$\int_{-\infty}^{+\infty} \operatorname{Im}\left\{\tilde{f}(s)\right\} \cos \omega t d\omega = + \int_{-\infty}^{+\infty} \operatorname{Re}\left\{\tilde{f}(s')\right\} \sin \omega' t d\omega' \tag{J.23}$$

Without loss of generality, the variable of integration ω' on the right-hand side of equations (J.22) and (J.23) may be replaced by the frequency ω . This yields:

$$\int_{-\infty}^{+\infty} \operatorname{Im}\left\{\tilde{f}(s)\right\} \sin \omega t d\omega = -\int_{-\infty}^{+\infty} \operatorname{Re}\left\{\tilde{f}(s)\right\} \cos \omega t d\omega \tag{J.24}$$

$$\int_{-\infty}^{+\infty} \operatorname{Im}\left\{\tilde{f}(s)\right\} \cos \omega t d\omega = + \int_{-\infty}^{+\infty} \operatorname{Re}\left\{\tilde{f}(s)\right\} \sin \omega t d\omega \tag{J.25}$$

In Appendix J.2, we found that the real and imaginary parts of the function $\tilde{f}(s)$, as well as $\cos \omega t$ and $\sin \omega t$, are respectively symmetric and anti-symmetric. Therefore, the above integral relations may be more specifically expressed using unilateral integrals as:

$$\int_{0}^{+\infty} \operatorname{Im}\left\{\tilde{f}(s)\right\} \sin \omega t d\omega = -\int_{0}^{+\infty} \operatorname{Re}\left\{\tilde{f}(s)\right\} \cos \omega t d\omega \tag{J.26}$$

$$\int_{0}^{+\infty} \operatorname{Im}\left\{\tilde{f}(s)\right\} \cos \omega t d\omega = + \int_{0}^{+\infty} \operatorname{Re}\left\{\tilde{f}(s)\right\} \sin \omega t d\omega \tag{J.27}$$

J.4 Identities of the inverse Laplace transform

Substituting equation (J.26) into equation (J.12) shows that it follows from the causality principle that the inverse Laplace transform may be expressed as either one of:

$$f(t) = \mathcal{L}^{-1}\left\{\tilde{f}(s)\right\} = \frac{e^{\sigma t}}{\pi} \int_{0}^{+\infty} \operatorname{Re}\left\{\tilde{f}(s)e^{i\omega t}\right\} d\omega \tag{J.28}$$

$$= \frac{2e^{\sigma t}}{\pi} \int_{0}^{+\infty} \operatorname{Re}\left\{\tilde{f}(s)\right\} \cos \omega t d\omega \tag{J.29}$$

$$= \frac{-2e^{\sigma t}}{\pi} \int_{0}^{+\infty} \operatorname{Im}\left\{\tilde{f}(s)\right\} \sin \omega t d\omega \tag{J.30}$$

To obtain the first and second time derivatives of the time domain function f(t), we differentiate equation (J.28), (J.29) or (J.30) to time respectively once and twice. This however is only allowed if these integrals are uniformly convergent.

Assuming that the integral in equation (J.28) is uniformly convergent, time differentiation yields the first and second time derivatives of the time domain function f(t) as:

$$\dot{f}(t) = \frac{e^{\sigma t}}{\pi} \int_{0}^{+\infty} \text{Re}\left\{s\tilde{f}(s)e^{i\omega t}\right\} d\omega \tag{J.31}$$

$$\ddot{f}(t) = \frac{e^{\sigma t}}{\pi} \int_{0}^{+\infty} \text{Re}\left\{s^{2} \tilde{f}(s) e^{i\omega t}\right\} d\omega \tag{J.32}$$

Using the form of the inverse Laplace transform according to equation (J.29), and assuming that its integral is uniformly convergent, the first and second time derivatives of f(t) read:

$$\dot{f}(t) = \frac{2e^{\sigma t}}{\pi} \int_{0}^{+\infty} \text{Re}\left\{\tilde{f}(s)\right\} (\sigma \cos \omega t - \omega \sin \omega t) d\omega$$
 (J.33)

$$\ddot{f}(t) = \frac{2e^{\sigma t}}{\pi} \int_{0}^{+\infty} \text{Re}\left\{\tilde{f}(s)\right\} \left(\left(\sigma^{2} - \omega^{2}\right)\cos\omega t - 2\sigma\omega\sin\omega t\right) d\omega \tag{J.34}$$

Using the form of the inverse Laplace transform according to equation (J.30), and assuming that its integral is uniformly convergent, the first and second time derivatives of f(t) read:

$$\dot{f}(t) = \frac{-2e^{\sigma t}}{\pi} \int_{0}^{+\infty} \operatorname{Im}\left\{\tilde{f}(s)\right\} (\sigma \sin \omega t + \omega \cos \omega t) d\omega \tag{J.35}$$

$$\ddot{f}(t) = \frac{-2e^{\sigma t}}{\pi} \int_{0}^{+\infty} \operatorname{Im}\left\{\tilde{f}(s)\right\} \left(\left(\sigma^{2} - \omega^{2}\right) \sin \omega t + 2\sigma\omega \cos \omega t\right) d\omega \tag{J.36}$$

Instead of applying time differentiation to equation (J.12), we may also obtain the time derivatives of $\dot{f}(t)$ by applying the inverse Laplace transform to the Laplace transforms of $\dot{f}(t)$ and $\ddot{f}(t)$, previously given by equations (J.2) and (J.3) respectively. This yields:

$$\dot{f}(t) = \mathcal{L}^{-1}\left\{\mathcal{L}\left\{\dot{f}(t)\right\}\right\} = \frac{e^{\sigma t}}{\pi} \int_{0}^{+\infty} \operatorname{Re}\left\{\left(s\tilde{f}(s) - f_{0}\right)e^{i\omega t}\right\}d\omega \tag{J.37}$$

$$\ddot{f}(t) = \mathcal{L}^{-1}\left\{\mathcal{L}\left\{\ddot{f}(t)\right\}\right\} = \frac{e^{\sigma t}}{\pi} \int_{0}^{+\infty} \operatorname{Re}\left\{\left(s^{2}\tilde{f}(s) - sf_{0} - \dot{f}_{0}\right)e^{i\omega t}\right\} d\omega \tag{J.38}$$

Here, f_0 and \dot{f}_0 are the initial conditions of f(t), where $f_0 = f(t=0)$ and $\dot{f}_0 = \dot{f}(t=0)$. Furthermore, note here that for zero initial conditions, i.e. $f_0 = \dot{f}_0 = 0$, equations (J.37) and (J.38) coincide with equations (J.31) and (J.32).

Alternatively, we can derive the first and second time derivatives of f(t) in the form of either equations (J.29) or (J.30) by expanding the integrands in equations (J.37) and (J.38) and respectively substituting equations (J.26) and (J.27). Using the form according to equation (J.29), the first and second time derivatives of f(t) are found as:

$$\dot{f}(t) = \frac{e^{\sigma t}}{\pi} \int_{0}^{+\infty} \left(2\operatorname{Re}\left\{ \tilde{f}(s) \right\} \left(\sigma \cos \omega t - \omega \sin \omega t \right) - f_0 \cos \omega t \right) d\omega \tag{J.39}$$

$$\ddot{f}(t) = \frac{e^{\sigma t}}{\pi} \int_{0}^{+\infty} \left(2\operatorname{Re}\left\{ \tilde{f}(s) \right\} \left(\left(\sigma^{2} - \omega^{2} \right) \cos \omega t - 2\sigma \omega \sin \omega t \right) - f_{0} \cos \omega t - \omega \sin \omega t \right) - f_{0} \cos \omega t \right) d\omega$$
(J.40)

Using the form of the inverse Laplace transform according to equation (J.30), the first and second time derivatives of the time domain function f(t) are found as:

$$\dot{f}(t) = \frac{-e^{\sigma t}}{\pi} \int_{0}^{+\infty} \left(2\operatorname{Im}\left\{ \tilde{f}(s) \right\} \left(\sigma \sin \omega t + \omega \cos \omega t \right) + f_0 \cos \omega t \right) d\omega \tag{J.41}$$

$$\ddot{f}(t) = \frac{-e^{\sigma t}}{\pi} \int_{0}^{+\infty} \left(2\operatorname{Im}\left\{\tilde{f}(s)\right\} \left(\left(\sigma^{2} - \omega^{2}\right) \sin \omega t + 2\sigma\omega \cos \omega t \right) + f_{0}\left(\sigma \cos \omega t - \omega \sin \omega t\right) + \dot{f}_{0}\cos \omega t \right) d\omega$$
(J.42)

J.5 Laplace domain expressions for applied loads

In this appendix, the Laplace domain expression for three types of loads are derived: a singlesinus pulse load, a continuous harmonic load and a half sinus pulse with a carrier frequency.

A single sinus pulse load

Let us consider a pulse load that consists of a single sinus period that starts at a time t = 0, then the time domain expression for this single sinus pulse reads:

$$F(t) = \overline{F}\sin(\Omega t)H(T_F - t)H(t)$$
(J.43)

Here, \overline{F} is the load amplitude, Ω is the load frequency and T_F is the period. The single sinus pulse load corresponding to equation (J.43) is depicted in Figure J.1a.

Now, let us consider the same pulse load for a certain time period where the time parameter t has been reset at a time t_0 , where t_0 is chosen as $0 < t_0 < T_F$ as depicted in Figure J.1b. The loading applied prior to time t_0 is then included in the system response by the nonzero initial conditions, while the load is considered to start at time t_0 . In global time, i.e. in terms of the original time parameter that has not been reset, the single sinus pulse load that starts at time t_0 is then found as:

$$F(t) = \overline{F}\sin(\Omega t)H(T_F - t)H(t - t_0)$$
(J.44)

To obtain the Laplace domain expression for this load in the new time period, i.e. in terms of the new time parameter that has been reset at time t_0 and thus starts at t=0, we replace the time parameter t in equation (J.44) by t_0+t . This yields:

$$F(t) = \overline{F}\sin(\Omega(t_0 + t))H(T_F - (t_0 + t))H(t)$$
(J.45)

Applying the Laplace transform to equation (J.45) now yields:

$$\tilde{F}(s) = \bar{F} \int_{0}^{T_{F}-t_{0}} \sin(\Omega(t_{0}+t))e^{-st}dt$$
(J.46)

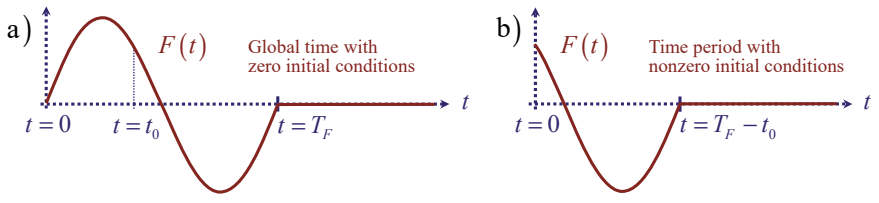


Figure J.1: A single sinus pulse load: a) in global time with zero initial conditions, b) for a new time period with nonzero initial conditions.

The above integral can be solved analytically as:

$$\tilde{F}(s) = \bar{F} \frac{s \sin \Omega t_0 + \Omega \cos \Omega t_0 - \Omega e^{-s(T_F - t_0)}}{s^2 + \Omega^2} H(T_F - t_0)$$
(J.47)

Here, the Heaviside function is maintained to assure that, for $t_0 \ge T_F$, the resultant Laplace domain load is equal to zero. For the particular case that $t_0 = 0$, we then find:

$$\tilde{F}(s) = \overline{F} \frac{\Omega}{s^2 + \Omega^2} \left(1 - e^{-sT_F} \right) \tag{J.48}$$

Here, note that equation (J.48) corresponds to the Laplace transform for the single sinus pulse load given by equation (J.43).

A continuous harmonic load

The continuous harmonic load that starts at a time t = 0 is expressed in the time domain as:

$$F(t) = \overline{F}\sin(\Omega t)H(t) \tag{J.49}$$

Here, the Heaviside function H(t) is included to indicate that the load is equal to zero for t < 0. Assuming that the time parameter t is reset at a certain time t_0 , where t_0 is chosen as $0 < t_0 < T_F$, so that t_0 is the starting point of a new time period. The time domain expression for the continuous harmonic load in this new time period then becomes:

$$F(t) = \overline{F}\sin(\Omega(t+t_0))H(t)$$
(J.50)

Applying the Laplace transform and analytically solving the resulting integral then yields the Laplace domain expression for a continuous harmonic load in the new time period as:

$$\tilde{F}(s) = \bar{F} \frac{s \sin \Omega t_0 + \Omega \cos \Omega t_0}{s^2 + \Omega^2}$$
(J.51)

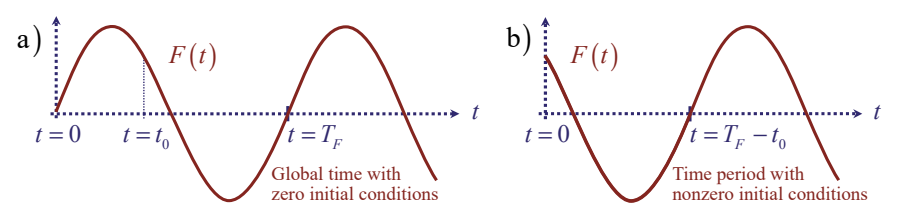


Figure J.2: A continuous harmonic load: a) in global time with zero initial conditions; b) for a new time period with nonzero initial conditions.

Here, note that for $t_0 = 0$ equation (J.51) reduces to the expression for the continuous harmonic load in global time, which is the Laplace transform of equation (J.49) and reads:

$$\tilde{F}(s) = \bar{F} \frac{\Omega}{s^2 + \Omega^2} \tag{J.52}$$

A half-sinus pulse with a carrier frequency

The half-sinus pulse load with a carrier frequency that starts at a time t = 0 is expressed in the time domain as:

$$F(t) = \overline{F}\sin(\Omega t)\sin(\Omega_{car}t)H(\frac{1}{2}T_F - t)H(t)$$
(J.53)

Here, Ω_{car} is the carrier frequency. Assuming that the time parameter t is reset at a certain time t_0 , where t_0 is chosen as $0 < t_0 < T_F$, so that t_0 is the starting point of a new time period. The time domain expression for the pulse load with a carrier frequency in this new time period then becomes:

$$F(t) = \overline{F}\sin(\Omega(t+t_0))\sin(\Omega_{car}(t+t_0))H(\frac{1}{2}T_F - (t+t_0))H(t)$$
(J.54)

Applying the Laplace transform and analytically solving the resulting integral yields the Laplace domain expression for the pulse load in the new time period as:

$$\tilde{F}(s) = \frac{\bar{F}\Omega}{\left(s^2 + \Omega^2 + \Omega_{car}^2\right)^2 - 4\Omega^2\Omega_{car}^2} \begin{pmatrix} \left(\left(s^2 + \Omega^2 - \Omega_{car}^2\right)\cos\Omega t_0 + \frac{s^2 + \Omega^2 + \Omega_{car}^2}{\Omega}s\sin\Omega t_0\right) \sin\Omega_{car} t_0 \\ + \left(2s\cos\Omega t_0 + \frac{s^2 - \Omega^2 + \Omega_{car}^2}{\Omega}\sin\Omega t_0\right)\Omega_{car}\cos\Omega_{car} t_0 \\ + \left(2s\Omega_{car}\cos\frac{\pi\Omega_{car}}{\Omega} + \left(s^2 + \Omega^2 - \Omega_{car}^2\right)\sin\frac{\pi\Omega_{car}}{\Omega}\right)e^{-s\left(\frac{1}{2}T_F - t_0\right)} \end{pmatrix} \tag{J.55}$$

Here, note that if we choose $t_0 = 0$, equation (J.55) reduces to the expression for the halfsinus pulse load with a carrier frequency in global time that has zero initial conditions, which

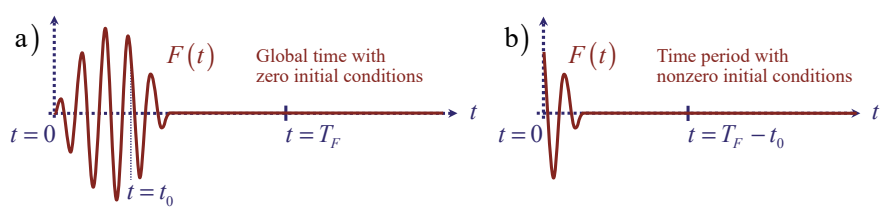


Figure J.3: A half-sinus pulse load with a carrier frequency: a) in global time with zero initial conditions; b) for a new time period with nonzero initial conditions.

corresponds to the Laplace transform of equation (J.53) and reads:

$$\tilde{F}(s) = \frac{\overline{F}\Omega}{\left(s^2 + \Omega^2 + \Omega_{car}^2\right)^2 - 4\Omega^2\Omega_{car}^2} \left(2s\Omega_{car} + \left(2s\Omega_{car}\cos\frac{\pi\Omega_{car}}{\Omega} + \left(s^2 + \Omega^2 - \Omega_{car}^2\right)\sin\frac{\pi\Omega_{car}}{\Omega}\right)e^{-s\frac{1}{2}T_F}\right) (J.56)$$

J.6 The MTFD-method applied to a one-mass-spring-system

As an example, we here apply the MTFD-method to a one-mass-spring system with mass M and spring stiffness K_e , subjected to a single sinus pulse load F(t). In the time domain, the equation of motion for this one -mass-spring system reads:

$$M\ddot{u} + K_{\varepsilon}u = F(t) \tag{J.57}$$

Here, u is the displacement of the mass M. The expression for the single-sinus pulse load depends on whether the time parameter t has been reset or not. When the time parameter has not been reset, or if we consider time globally, the single sinus period is fully included and the expression for the pulse load is given by equation (J.43). Otherwise, when a new time period is considered for which the time parameter has been reset at time t_0 , where t_0 is chosen as $0 < t_0 < T_F$, and that has nonzero initial conditions, the expression for the single-sinus pulse load is given by equation (J.45).

Applying the Laplace transform to equation (J.57), as well as introducing dimensionless parameters for time and space as $t = t_{\text{dim}}\omega_0$ and $u = u_{\text{dim}}/\ell$ respectively, where ω_0 is the natural frequency of the one-mass-spring system, i.e. $\omega_0 = \sqrt{K_e/M}$, and ℓ is the initial length of the spring, yields the dimensionless equation of motion for the one-mass-spring-system with nonzero initial conditions in the Laplace domain as:

$$(s^2+1)\tilde{u} = \tilde{F}(s) + su_0 + v_0$$
 (J.58)

Here, F(s) is the Laplace domain expression for the applied load, which is previously given by equation (J.47) for any time t_0 , where $0 \le t_0 < T_F$, and s is the complex-valued Laplace parameter. Furthermore, u_0 and v_0 are respectively the initial displacement and the initial velocity of the mass for the considered time period.

Laplace domain expressions for the displacement, the velocity and the acceleration The Laplace domain expression for the displacement of the mass may be directly derived from equation (J.58) as:

$$\tilde{u} = \frac{su_0 + v_0}{s^2 + 1} + \frac{\tilde{F}(s)}{s^2 + 1} \tag{J.59}$$

Substituting equation (J.59) into equations (J.2) and (J.3) that account for nonzero initial

conditiosn, the Laplace domain expressions for the velocity and the acceleration of the mass M are respectively found as:

$$\tilde{v} = s\tilde{u} - u_0 = \frac{-u_0 + sv_0}{s^2 + 1} + \frac{s\tilde{F}(s)}{s^2 + 1}$$
(J.60)

$$\tilde{a} = s^2 \tilde{u} - s u_0 - v_0 = \frac{-s u_0 - v_0}{s^2 + 1} + \frac{s^2 \tilde{F}(s)}{s^2 + 1}$$
(J.61)

Because the Laplace domain expression for the applied load, given by equation (J.47), itself already tends to zero with a rate ω^{-1} for $\omega \to \infty$, it follows that the first terms on the right-hand sides of equations (J.59) to (J.61) govern the decay of the Laplace domain expressions for the displacement, velocity and acceleration of the mass and that each of these expressions decays with a rate ω^{-1} for $\omega \to \infty$.

Numerical evaluation of the inverse Laplace transform

To determine the displacements, velocities and accelerations of the mass in the one-mass-spring system, we can now apply the inverse Laplace transform according to either one of the expressions given by equations (J.28), (J.29) and (J.30), where equations (J.29) and (J.30) are derived from equation (J.28) by employing the causality principle. Analytically, i.e. when the full semi-infinite domain of the involved integrals is taken into account, each of these equations yields the exact same response in the time domain. When evaluating the inverse Laplace transforms numerically however, the semi-infinite domains of integration must be truncated, causing equations (J.28), (J.29) and (J.30) to yield different results.

Figure J.4, Figure J.5 and Figure J.6 respectively present the displacements, velocities and accelerations of the mass in the one-mass-spring system due to a single sinus pulse load by numerically evaluating the inverse Laplace transforms given by equations (J.28), (J.29) and (J.30) using a truncated, and thus finite, domain of integration. The applied single sinus pulse has a dimensionless angular frequency that is arbitrarily chosen as $\Omega = 0.2$, so that its dimensionless period is found as $T_F = 10\pi$. The dimensional mass and stiffness of the one-mass-spring system are respectively chosen as $M = 392 \, \mathrm{kg}$ and $K_e = 98 \, \mathrm{MN/m}$.

Figure J.4 shows the different displacements of the mass in the one-mass-spring system that result from numerically evaluating the different instances of the inverse Laplace transforms. Here, Figure J.4a shows the displacements due to the applied load as a function of the global time parameter t, where the time domain simulation was manually reset at respectively time t_0 , t_1 and t_2 . Furthermore, Figure J.4b shows the displacements of the mass in the time period for which the time parameter has been reset at time t_0 . As shown in Figure J.4a, each time the time parameter t is reset and new nonzero initial conditions are introduced, the numerical evaluation of the inverse Laplace transform according to either of equations (J.28), (J.29) and (J.30) leads to erroneous behaviour near the reinitiation point. The result of equation (J.29), which employs the real part of the Laplace domain displacement \tilde{u} , is given by the blue line and leads to the most accurate displacements, while the result of employing the imaginary part of the Laplace domain displacement \tilde{u} according to equation (J.30), given by

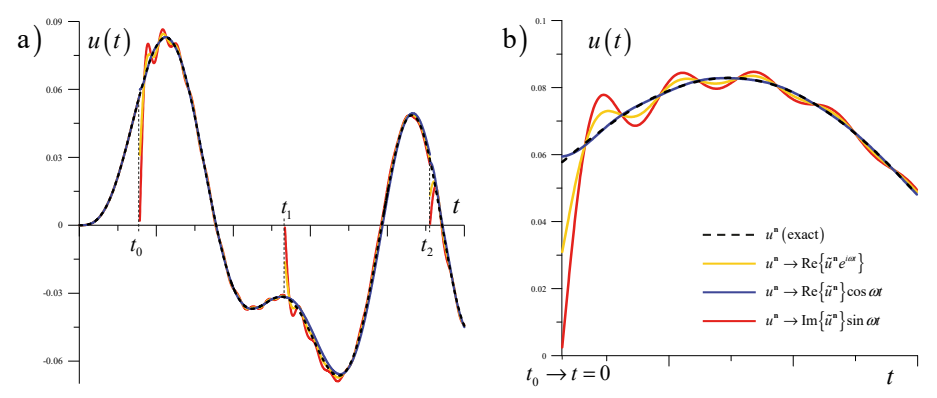


Figure J.4: Error in the time domain displacement due to the truncation of the semi-infinite integral domain of the inverse Laplace transform: a) As a function of global time; b) In the time period reset at t₀.

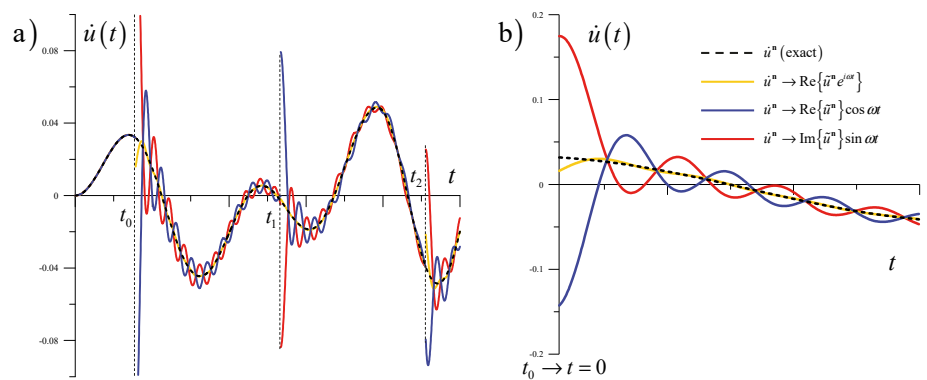


Figure J.5: Error in the time domain velocity due to the truncation of the semi-infinite integral domain of the inverse Laplace transform: a) As a function of global time; b) In the time period reset at t₀.

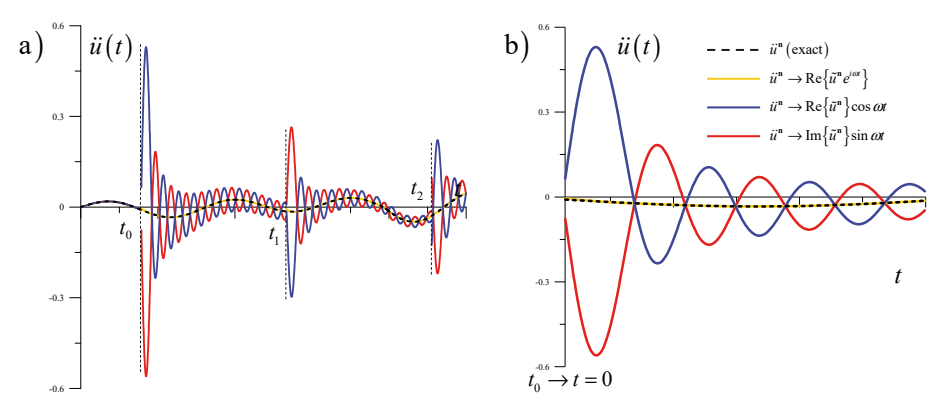


Figure J.6: Error in the time domain acceleration due to the truncation of the semi-infinite integral domain of the inverse Laplace transform: a) As a function of global time; b) In the time period reset at to.

the red line, yields the largest error. The reason that equation (J.30) gives the largest error is due to the term $\sin \omega t$ in its integrand. Due to this term, numerically evaluating equation (J.30) for a finite domain of integration always yields a zero displacement at time t=0. This is independent of the chosen truncation frequency and therefore occurs for any size and any resolution of the truncated domain of integration. Evidently, this is only an issue for nonzero initial conditions. The oscillation of the obtained displacement around the correct displacement as a function of time is a logical consequence of the error at the start of the considered time period.

Note here that the result of applying the inverse Laplace transform according to equation (J.28) must always give the exact average of the red and blue lines, respectively giving the results of equations (J.29) and (J.30). This can easily be verified by expanding the integrand of equation (J.28) using Euler's formula, which yields:

$$f(t) = \frac{e^{\sigma t}}{\pi} \int_{0}^{+\infty} \left(\text{Re}\left\{ \tilde{f}(s) \right\} \cos \omega t - \text{Im}\left\{ \tilde{f}(s) \right\} \sin \omega t \right) d\omega$$
 (J.62)

Because equation (J.62) incorporates both the real and imaginary parts of the Laplace domain displacement equally, the displacement according to this expression is numerically found as the exact average of equations (J.29) and (J.30).

Figure J.5 and Figure J.6 respectively show the velocities and accelerations for the one-mass-spring system that result from numerically evaluating the different instances of the inverse Laplace transforms derived in Appendix J.4. Figure J.5 and Figure J.6 clearly show that the erroneous behaviour after each reset of the time parameter *t* are much worse for the velocities and the accelerations than for the displacements. Additionally, the resulting velocities in Figure J.5 do not seem to correspond to the time derivative of the displacements given in Figure J.4 and accordingly, the accelerations in Figure J.6 do not seem to correspond to the time derivative of the velocities given in Figure J.5.

Thus, although analytically the instances of the inverse Laplace transforms that are given by equations (J.28), (J.29) and (J.30) are all valid and must yield the same displacements, velocities and accelerations, numerically evaluating these inverse Laplace transforms for a truncated, and thus finite, domain of integration leads to severe problems. The mismatch between the analytically and numerically obtained responses is most severe near the time of reinitiation, i.e. the time moment at which the time parameter t is reset and new nonzero initial conditions are introduced.

Response obtained using an improved statement for the inverse Laplace transform

To improve the results for the numerical evaluation of the inverse Laplace transform when using a truncated, and thus finite, domain of integration for a system that, in the time domain, has nonzero initial conditions, we extract the contribution of the initial conditions from the corresponding Laplace domain expression and separately include their contribution in time domain.

In Section 5.2.3, it was shown that if we extract a nonzero initial condition f_0 from a

Laplace domain function \tilde{f} , applying the inverse Laplace transform then yields the corresponding time domain expression as:

$$f(t) = \mathcal{L}^{-1}\left\{\tilde{f}\right\} = \mathcal{L}^{-1}\left\{\tilde{f} - \frac{f_0}{s}\right\} + \mathcal{L}^{-1}\left\{\frac{f_0}{s}\right\} = \mathcal{L}^{-1}\left\{\tilde{f}_{imp}\right\} + f_0H(t)$$
(J.63)

If we separately introduce the improved Laplace domain expressions for the displacement, velocity and acceleration of the mass in the one-mass-spring system in accordance to equation (J.63), we find the improved Laplace domain displacement, velocity and acceleration of the mass M as:

$$\tilde{u}_{imp} = \tilde{u} - \frac{u_0}{s}, \qquad \tilde{v}_{imp} = \tilde{v} - \frac{v_0}{s}, \qquad \tilde{a}_{imp} = \tilde{a} - \frac{a_0}{s}.$$

Here note that previously, the Laplace domain velocity and acceleration were given for non-zero initial conditions by respectively equations (J.60) and (J.61) as $\tilde{v} = s\tilde{u} - u_0$ and $\tilde{a} = s^2\tilde{u} - su_0 - v_0$.

Applying the inverse Laplace transform, we respectively find the displacement, velocity and acceleration of the mass in the one-mass-spring-system in the time domain for $t \ge 0$ as:

$$u = \frac{e^{\sigma t}}{\pi} \int_{0}^{+\infty} \operatorname{Re}\left\{\tilde{u}_{imp}e^{i\omega t}\right\} d\omega + u_{0}$$
(J.64)

$$\dot{u} = \frac{e^{\sigma t}}{\pi} \int_{0}^{+\infty} \text{Re}\left\{\tilde{v}_{imp} e^{i\omega t}\right\} d\omega + v_0 \tag{J.65}$$

$$\ddot{u} = \frac{e^{\sigma t}}{\pi} \int_{0}^{+\infty} \text{Re}\left\{\tilde{a}_{imp}e^{i\omega t}\right\} d\omega + a_0 \tag{J.66}$$

When numerically evaluating the inverse Laplace transform according to equations (J.64) to (J.66) for a truncated domain of integration, each equation will yield reasonable results in the time domain as the contribution of the respective initial conditions have been extracted from the Laplace domain expressions. Nevertheless, although equations (J.64) to (J.66) do respectively describe the displacement, velocity and acceleration for the mass in the one-mass-spring-system, the expressions for the velocity and the acceleration, respectively given by equations (J.65) and (J.66), cannot be obtained from time differentiation of equation (J.64).

Thus, to further improve the expressions for the inverse Laplace transforms, we do not only extract the contribution of the initial displacement from the corresponding Laplace domain expression, but also the contributions of the initial velocity and the initial acceleration. Furthermore, next to extracting the contribution of the initial velocity, we also extract the contribution of the initial acceleration from the Laplace domain velocity. The improved Laplace domain expressions for the displacement, velocity and acceleration of the mass in the

one-mass-spring-system then become:

$$\tilde{u}_{imp} = \tilde{u} - \frac{u_0}{s} - \frac{v_0}{s^2} - \frac{a_0}{s^3} \tag{J.67}$$

$$\tilde{v}_{imp} = s\tilde{u}_{imp} = \tilde{v} - \frac{v_0}{s} - \frac{a_0}{s^2} \tag{J.68}$$

$$\tilde{a}_{imp} = s^2 \tilde{u}_{imp} = \tilde{a} - \frac{a_0}{s} \tag{J.69}$$

The corresponding time domain expressions for the displacement, velocity and acceleration are then obtained for $t \ge 0$ as:

$$u = \frac{e^{\sigma t}}{\pi} \int_{0}^{+\infty} \operatorname{Re}\left\{\tilde{u}_{imp}e^{i\omega t}\right\} d\omega + u_0 + v_0 t + \frac{1}{2}a_0 t^2$$
(J.70)

$$\dot{u} = \frac{e^{\sigma t}}{\pi} \int_{0}^{+\infty} \text{Re}\left\{s\tilde{u}_{imp}e^{i\omega t}\right\} d\omega + v_0 + a_0 t \tag{J.71}$$

$$\ddot{u} = \frac{e^{\sigma t}}{\pi} \int_{0}^{+\infty} \operatorname{Re}\left\{s^{2} \tilde{u}_{imp} e^{i\omega t}\right\} d\omega + a_{0} \tag{J.72}$$

Equations (J.71) and (J.72) may be found directly from equation (J.70) by applying time differentiation once and twice respectively. Additionally, the displacement and velocity according to equations (J.70) and (J.71) yield more exact results than the expressions for the displacements and velocities given by equations (J.64) and (J.65) because the improved Laplace domain expressions decay much faster for $\omega \to \infty$ than the original Laplace domain expressions. This can easily be verified by comparing the involved Laplace domain expressions. For example, substituting equation (J.59) into equation (J.67) and rearranging yields:

$$\tilde{u}_{imp} = -\frac{su_0 + v_0}{s^2 \left(s^2 + 1\right)} - \frac{a_0}{s^3} + \frac{\tilde{F}(s)}{s^2 + 1} \tag{J.73}$$

Noting that the applied load decays with a rate ω^{-1} for $\omega \to \infty$, equation (J.73) shows that the improved Laplace domain displacement \tilde{u}_{imp} decays with a rate ω^{-3} for $\omega \to \infty$. As the improved Laplace domain velocity and acceleration of the one-mass-spring-system are respectively obtained as $\tilde{v}_{imp} = s\tilde{u}_{imp}$ and $\tilde{a}_{imp} = s^2\tilde{u}_{imp}$, the resulting expressions for the velocity and acceleration respectively decay with a rate ω^{-2} and ω^{-1} for $\omega \to \infty$. Furthermore, since the contribution of the initial conditions in equations (J.70) to (J.72) has been taken out of the integral, the improved Laplace domain expressions to which the inverse Laplace transform is to be applied may be considered to have zero initial conditions. As such, the erroneous behaviour in the time domain due to applying the inverse Laplace transforms with a truncated domain of integration for a set of nonzero initial conditions is virtually removed.

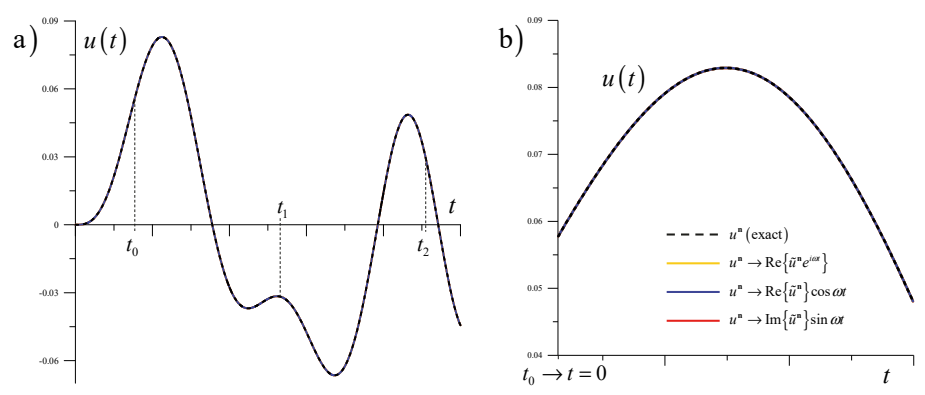


Figure J.7: Displacements in the time domain obtained from applying the inverse Laplace transform to the improved Laplace domain expressions a) As a function of global time; b) In the time period reset at to.

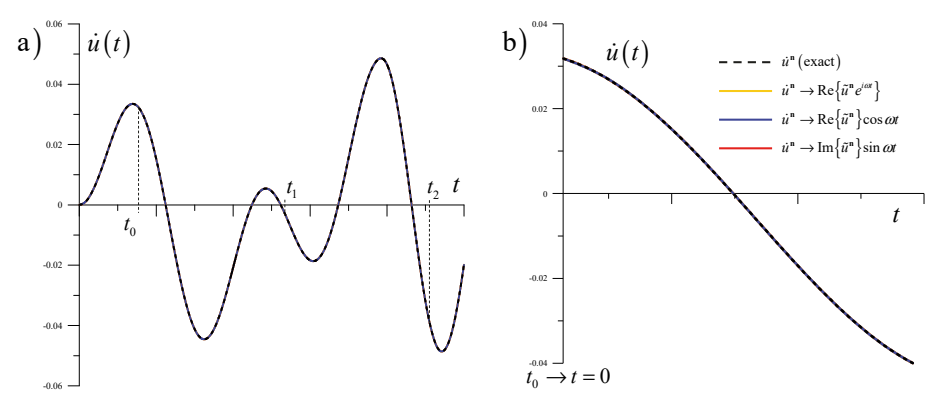


Figure J.8: Velocities in the time domain obtained from applying the inverse Laplace transform to the improved Laplace domain expressions a) As a function of global time; b) In the time period reset at t₀.

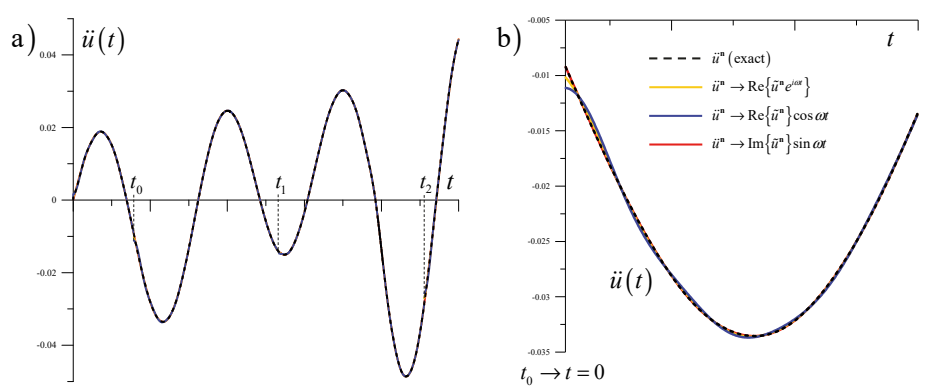


Figure J.9: Accelerations in the time domain obtained from applying the inverse Laplace transform to the improved Laplace domain expressions a) As a function of global time; b) In the time period reset at t₀.

Figure J.7, Figure J.8 and Figure J.9 respectively show the time domain displacements, velocities and accelerations obtained by applying the improved statements for the inverse Laplace transform, but still for a truncated, and thus finite, domain of integration. In each of these figures, the yellow line shows the results obtained by applying the inverse Laplace transform according to respectively equations (J.70) to (J.72). Alternative expressions to equations (J.70) to (J.72) that are exclusively expressed in terms of either the real or imaginary part of the improved Laplace domain displacement \tilde{u}_{imp} can be obtained by employing the causality principle. In terms of the real part of the improved Laplace domain displacement \tilde{u}_{imp} , we may thus respectively obtain the displacement, velocity and acceleration of the one-mass-spring system as:

$$u = \frac{2e^{\sigma t}}{\pi} \int_{0}^{+\infty} \operatorname{Re}\left\{\tilde{u}_{imp}\right\} \cos \omega t d\omega + u_0 + v_0 t + \frac{1}{2}a_0 t^2$$
(J.74)

$$\dot{u} = \frac{2e^{\sigma t}}{\pi} \int_{0}^{+\infty} \text{Re}\left\{\tilde{u}_{imp}\right\} \left(\sigma\cos\omega t - \omega\sin\omega t\right) d\omega + v_0 + a_0 t \tag{J.75}$$

$$\ddot{u} = \frac{2e^{\sigma t}}{\pi} \int_{0}^{+\infty} \text{Re}\left\{\tilde{u}_{imp}\right\} \left(\left(\sigma^{2} - \omega^{2}\right)\cos\omega t - 2\sigma\omega\sin\omega t\right) d\omega + a_{0}$$
(J.76)

The displacement, velocity and acceleration according to respectively equations (J.74), (J.75) and (J.76) are given in respectively Figure J.7, Figure J.8 and Figure J.9 by the blue line.

In terms of the imaginary part of the improved Laplace domain displacement \tilde{u}_{imp} , we respectively obtain the displacement, velocity and acceleration of the one-mass-spring system as:

$$u = \frac{-2e^{\sigma t}}{\pi} \int_{0}^{+\infty} \operatorname{Im}\{\tilde{u}_{imp}\}\sin\omega t d\omega \tag{J.77}$$

$$\dot{u} = \frac{-2e^{\sigma t}}{\pi} \int_{0}^{+\infty} \operatorname{Im}\left\{\tilde{u}_{imp}\right\} \left(\sigma \sin \omega t + \omega \cos \omega t\right) d\omega + v_0 + a_0 t \tag{J.78}$$

$$\ddot{u} = \frac{-2e^{\sigma t}}{\pi} \int_{0}^{+\infty} \text{Im} \left\{ \tilde{u}_{imp} \right\} \left(\left(\sigma^{2} - \omega^{2} \right) \sin \omega t + 2\sigma \omega \cos \omega t \right) d\omega \tag{J.79}$$

Applying the inverse Laplace transform according to respectively equations (J.77), (J.78) and (J.79) yields the displacement, velocity and acceleration of the one-mass-spring-system given in respectively Figure J.7, Figure J.8 and Figure J.9 by the red line.

Comparing Figure J.7, Figure J.8 and Figure J.9 to respectively Figure J.4, Figure J.5 and Figure J.6, shows that extracting the nonzero initial conditions from the corresponding Laplace domain expressions yields a spectacular improvement of the time domain displacement, velocity and acceleration. Only Figure J.9b, depicting a close-up of the acceleration after reinitiation of the time domain at t_0 , visibly shows a small error near the point where new nonzero initial conditions have been introduced.

J.7 Alternative derivation of the convolution for the linear-elastic rod

Accounting for nonzero initial conditions, the equation of motion for particle N at the lattice-rod interface of the one-dimensional discrete-continuous Hooke system reads:

$$M^{N} s^{2} \tilde{u}^{N} + K_{e}^{N-1,N} \tilde{e}^{N-1,N} + \chi(s) \tilde{u}^{N} = M^{N} (s u_{0}^{N} + v_{0}^{N}) + \tilde{f}_{0}(s)$$
(J.80)

Here, the dynamic stiffness is found as $\tilde{\chi}(s) = \frac{1}{2}s\sqrt{2}$ and the expression for $\tilde{f}_0(s)$ contains the contribution of the rod's initial conditions to the interface equation, which is found as:

$$\tilde{f}_0(s) = \int_{x_{lmt}}^{+\infty} e^{-s\sqrt{2}(\xi - x_{lmt})} \left(su_0(\xi) + v_0(\xi) \right) d\xi \tag{J.81}$$

In Section 5.2.1, this expression is analysed further by finding a Laplace domain relation that describes the response of the rod in terms of the response of the boundary particle and subsequently applying the inverse Laplace transform analytically. For the viscoelastic rod however, discussed in Section 5.3.1, the involved inverse Laplace transforms cannot be solved analytically and an alternate approach was used to describe $\tilde{f}_0(s)$ in terms of the response of boundary particle. This appendix applies this alternate approach to show that it yields the same convolution integral for the linear-elastic rod as derived in Section 5.2.1 before.

First, let us suppose that equation (J.81) is valid for a time period where the time parameter t was reset at a global time t_0 . The initial displacement $u_0(\xi)$ and the initial velocity $v_0(\xi)$ along the linear-elastic rod of this new time period, then correspond to the displacement $u(\xi,t_0)$ and the velocity $v(\xi,t_0)$ at time t_0 in global time. Within the integral of equation (J.81), we then express this displacement and this velocity by the inverse Laplace transforms of their Laplace domain expressions. This yields:

$$\tilde{f}_0(s) = \int_{x_{loc}}^{+\infty} e^{-s\sqrt{2}(\xi - x_{lnt})} \left(s\mathcal{L}_{\hat{s}}^{-1} \left\{ \tilde{u}\left(\xi, \hat{s}\right) \right\} + \mathcal{L}_{\hat{s}}^{-1} \left\{ \tilde{v}\left(\xi, \hat{s}\right) \right\} \right) d\xi \tag{J.82}$$

Here, \hat{s} is the complex-valued Laplace parameter that corresponds to the application of the inverse Laplace transform with respect to time t_0 . The applied inverse Laplace transform thus reads:

$$f_0(\xi) = f(\xi, t_0) = \mathcal{L}_{\hat{s}}^{-1} \left\{ \tilde{f}(\xi, \hat{s}) \right\} = \frac{e^{\hat{\sigma}t_0}}{\pi} \int_{0}^{+\infty} \operatorname{Re}\left\{ \tilde{f}(\hat{s}) e^{i\hat{\omega}t_0} \right\} d\omega$$
 (J.83)

Because we here consider the response along the linear-elastic rod at a time t_0 in terms of the full history of the response of the boundary particle **N**, we consider time globally and with zero initial conditions. Thus, accounting for the proper behaviour of the rod at $\xi \to \infty$, the Laplace domain displacement along the linear-elastic rod is found as $\tilde{u}(\xi,\hat{s}) = Ae^{-\hat{s}\sqrt{2}\xi}$,

where the constant A is found as $A = \tilde{u}^{N}(\hat{s})e^{+\hat{s}\sqrt{2}x_{int}}$ from the displacement relation at the lattice-rod interface. For zero initial conditions, the Laplace domain relation for the velocity along the rod follows from the corresponding displacement as $\tilde{v}(\xi,\hat{s}) = \hat{s}\tilde{u}(\xi,\hat{s})$ and therefore $\tilde{v}^{N}(\hat{s}) = \hat{s}\tilde{u}^{N}(\hat{s})$. The relations between the displacement and velocity along the linear-elastic rod and, respectively, the displacement and velocity of the boundary particle N, are thus found in the Laplace domain as:

$$\tilde{u}(\xi,\hat{s}) = \tilde{u}^{N}(\hat{s})e^{-\hat{s}\sqrt{2}(\xi-x_{lnt})}$$
(J.84)

$$\tilde{v}(\xi,\hat{s}) = \tilde{v}^{N}(\hat{s})e^{-\hat{s}\sqrt{2}(\xi-x_{Int})}$$
(J.85)

Substituting equations (J.84) and (J.85) into equation (J.82) and changing the order of integration then yields the expression for $f_0(s)$ as:

$$\tilde{f}_{0}\left(s\right) = \mathcal{L}_{\hat{s}}^{-1} \left\{ e^{+(s+\hat{s})\sqrt{2}x_{Int}} \int_{x_{Int}}^{\infty} e^{-(s+\hat{s})\sqrt{2}\xi} d\xi \left(s\tilde{u}^{N}\left(\hat{s}\right) + \tilde{v}^{N}\left(\hat{s}\right)\right) \right\}$$
(J.86)

The integral over the semi-infinite domain of the linear-elastic rod in equation (J.86) may be straightforwardly obtained analytically. This yields the expression for $\tilde{f}_0(s)$ as:

$$\tilde{f}_0(s) = \frac{1}{2}\sqrt{2}\mathcal{L}_{\hat{s}}^{-1} \left\{ \frac{1}{s+\hat{s}} \left(s\tilde{u}^{N}(\hat{s}) + \tilde{v}^{N}(\hat{s}) \right) \right\}$$
(J.87)

The inverse Laplace transform of two Laplace domain equations may always be found as the convolution of the corresponding time domain expressions, so that equation (J.87) becomes:

$$\tilde{f}_0(s) = \frac{1}{2} \sqrt{2} \int_0^{t_0} \mathcal{L}_{\hat{s}}^{-1} \left\{ \frac{1}{s+\hat{s}} \right\} (\tau) (su^{N}(t_0 - \tau) + v^{N}(t_0 - \tau)) d\tau$$
(J.88)

The remaining inverse Laplace transform is found analytically as:

$$\mathcal{L}_{\hat{s}}^{-1} \left\{ \frac{1}{s+\hat{s}} \right\} (\tau) = \frac{1}{2\pi i} \lim_{\alpha \to \infty} \int_{\hat{\sigma} - i\alpha}^{\hat{\sigma} + i\alpha} \frac{1}{s+\hat{s}} e^{\hat{s}\tau} d\hat{s} \stackrel{q=s+\hat{s}}{=} \frac{1}{2\pi i} \lim_{\alpha \to \infty} \int_{\hat{\sigma} - i\alpha}^{\hat{\sigma} + i\alpha} \frac{e^{q\tau}}{q} dq e^{-s\tau} = H(\tau) e^{-s\tau}$$
 (J.89)

And substitution of equation (J.89) into equation (J.88) then gives:

$$\tilde{f}_0(s) = \frac{1}{2} \sqrt{2} \int_0^{t_0} e^{-s\tau} \left(su^{\mathbf{N}} \left(t_0 - \tau \right) + v^{\mathbf{N}} \left(t_0 - \tau \right) \right) d\tau \tag{J.90}$$

Which is exactly equal to the equation previously given at the end of Section 5.2.1.

Samenvatting

De dynamische interactie tussen constructies en het omringende medium speelt een cruciale rol in tal van technische toepassingen. In gevallen waarin een dynamisch belast medium zich niet-lineair gedraagt, zoals bij dynamische interacties tussen constructies en de ondergrond of tussen ijs en constructies op zee, moet een model voor dat medium met niet-lineaire verschijnselen kunnen omgaan om de respons van het medium accuraat weer te geven. Om de rekentijd te minimaliseren is het wenselijk om het domein van het model dat deze niet-lineariteiten meeneemt zo klein mogelijk te houden. Dit proefschrift behandelt de ontwikkeling van een methodologie waarmee de niet-gelijkmatige dynamische respons van een vast medium in het tijdsdomein efficiënt en robuust kan worden beschreven, waarbij tegelijkertijd op juiste wijze rekening wordt gehouden met het omringende lineaire verre veld.

Daartoe wordt het medium opgedeeld in twee domeinen: een geavanceerd domein in de regio van interactie met een dynamische belasting waarin niet-lineaire fenomenen kunnen worden gemodelleerd, en een omringend domein op zodanige afstand van de dynamische bron dat de respons lineair is. Het nabij veld wordt gemodelleerd met behulp van discrete lattices, die in staat zijn niet-gelijkmatig dynamisch gedrag te beschrijven door het toepassen van niet-lineaire reologische elementen. Het verre veld wordt beschreven met behulp van een randintegraalvergelijking, die de respons van het verre veld uitsluitend op de grenslijn met het nabije veld beschrijft, terwijl het gedrag van het volledige verre veld achter deze grenslijn meegenomen wordt. Deze aanpak maakt een accurate en efficiënte modellering mogelijk van eindige, oneindige en semi-oneindige verre velden, waarbij golven zich zonder verstoring over de grens tussen beide domeinen kunnen propageren.

De discrete lattice-modellering in het nabije veld maakt gebruik van zogenoemde Bingham-Kelvin-Voigt (BKV)-elementen, bestaande uit een combinatie van veren, dempers en droge-frictiecomponenten. Door de aanwezigheid van deze droge-frictiecomponenten, evenals het beschouwen van mogelijke inelastische botsingen, wordt het gedrag van deze lattices gekenmerkt door overgangen tussen verschillende bewegingsmodes, zoals stick, slip en lock, die worden gestuurd door de dynamische belasting en de drempelwaarden van de reologische elementen.

Om de lineaire respons van het verre veld te modelleren, zijn de randintegraalvergelijkingen (RIVs) afgeleid voor zowel continue als discrete representaties van het verre veld. Waar RIVs voor continue media goed gedocumenteerd zijn in de literatuur, presenteert dit proefschrift een van de eerste afleidingen van RIVs voor een domein dat bestaat uit een eindig of semi-oneindig discrete systeem van massa's en veren. Deze RIVs worden doorgaans uitgedrukt in termen van de dynamische stijfheid of, omgekeerd, in termen van de dynamische flexibiliteit, die de kracht-verplaatsingsrelatie in het Laplace-domein beschrijven. Voor eendimensionale systemen kunnen deze relaties vaak analytisch worden afgeleid, maar tijdsdomeinanalyses vereisen doorgaans numerieke evaluatie, waardoor het gebruik van de dynamische flexibiliteit de voorkeur heeft. Voor tweedimensionale systemen is de formulering van

de RIVs gebaseerd op de Greense functies van het betreffende medium en zijn numerieke randmethoden nodig om de corresponderende dynamische flexibiliteitsmatrices te verkrijgen. Aangezien deze Greense functies niet altijd bekend zijn en vaak niet eenvoudig verkregen kunnen worden, vormt het bepalen ervan doorgaans de grootste uitdaging bij het afleiden van RIVs.

Gezien de rekenkundige uitdagingen bij tijdsdomeinsimulaties van niet-lineaire systemen, is een gemengde tijd-frequentie-domein (MTFD) methode ontwikkeld. Deze hybride benadering benut de efficiëntie van frequentiedomeintechnieken tijdens perioden van lineair gedrag, terwijl elke keer dat er niet-lineair gedrag optreedt gebeurt, de eigenschappen van het medium in de tijd worden aangepast. De voorgestelde methodologie heeft de potentie om de rekentijd aanzienlijk te verkorten, vooral in systemen waarin niet-lineair gedrag instantaan optreedt.

De resultaten die in dit proefschrift worden gepresenteerd tonen aan dat discrete lattice-modellen uitermate geschikt zijn voor het beschrijven van niet-gelijkmatige dynamische fenomenen, en onderstrepen het belang van een accurate modellering van het grensvlak met het verre veld. De vergelijking tussen discrete-continue en volledig discrete systemen laat zien dat de representatie van het verre veld een significante invloed heeft op de totale dynamische respons. In combinatie met discrete lattice modellen, presteren RIVs die zijn gebaseerd op een discreet verre veld veel beter dan RIVs gebaseerd op een verre veld dat gemodelleerd is als een continuum, met name op het gebied van compatibiliteit en ongestoorde golfvoortplanting door de grenslijn. Eventueel vervolgonderzoek zou zich moeten toespitsen op de invloed van variaties in de lattice-configuratie op de formulering van RIVs, bijvoorbeeld door over te stappen van een hexagonaal naar een vierkant rooster, interacties met tweede buren te modelleren of aanvullende reologische elementen toe te voegen voor transversale en roterende interacties. De prestaties van RIVs gebaseerd op discrete modellen worden daarnaast sterk beïnvloed door de kwaliteit van de numerieke implementatie, en verdere verbeteringen daarin zijn nodig om deze aanpak robuuster en breder toepasbaar te maken.

Hoewel algemeen wordt aangenomen dat modellen die niet-lineair gedrag beschrijven noodzakelijkerwijs in het tijdsdomein geëvalueerd moeten worden, laat de niet-iteratieve MTFD-methode zien dat het mogelijk is om frequentiedomeintechnieken uit te breiden naar toepassingen waarin niet-lineair gedrag in het tijdsdomein wordt gemodelleerd.

Tot slot biedt dit proefschrift zowel de theoretische grondslagen als de numerieke instrumenten voor het efficiënt modelleren van niet-lineaire golfvoortplanting in vaste media. Daarmee levert dit werk een bijdrage aan de verdere ontwikkeling van modelleringstechnieken voor niet-gelijkmatige dynamisch gedrag in het tijdsdomein, met potentiële toepassingen in uit-eenlopende civieltechnische, geotechnische en offshore engineeringvraagstukken.

Curriculum Vitae

24-07-1979 Born in Den Helder, the Netherlands

Education and Supplementary knowledge

1997-2003: MSc Civil Engineering, TU Delft, faculty CEG.

Thesis: Vibrations of Buildings on (Soft) Soil; A parametric study to

the effect of chosen interface conditions.

Supervisors: Prof.ir. A.C.W.M. Vrouwenvelder, Dr. A.V. Metrikine,

Prof.dr.ir. F. Molenkamp, Ir. J.M.J. Spijkers.

2017-2018: CEG-TQ, a portfolio-based university teaching qualification (BKO/UTQ). 2021-2022: LDE Leergang Onderwijskundig Leiderschap (LOL) for EUR, UL and TUD.

2023-2024: Senior Examination Qualification (SEQ) 2004-2025: PhD Research, TU Delft, faculty CEG.

Dissertation: Boundary formulations for discrete lattices to describe the non-

smooth dynamic response of solid media in the time domain,

Promotors: Prof.dr. A.V. Metrikine, dr.ir. K. van Dalen.

Positions at Delft University of Technology

2000-2003: Student-assistant Civil Engineering Informatics, TU Delft, faculty CEG.

2009-2018: Researcher/Lecturer/Assistant Professor Offshore & Arctic Engineering,

TU Delft, faculty CEG, section Offshore Engineering.

2011-2018: Track-coordinator Bottom Founded Offshore Structures, Arctic & Wind,

Interfaculty MSc Offshore & Dredging Engineering (ODE).

2018-2026: Director of Studies for the Interfaculty 4TU MSc Construction Management

and Engineering (CME), TU Delft, faculty CEG, section Integral Design &

Management (IDM).

2018-: Senior Lecturer Offshore & Arctic Engineering (0.6 fte), TU Delft, faculty

CEG, section Offshore Engineering.

Other Experience & Affiliations

2006: Co-organiser EuroMech Colloq. 484: Wave Mechanics and stability of long

flexible structures subject to moving loads and flows, Sept. 19-22, 2006, Delft.

2010-2011: Org. committee OMAE 2011, Rotterdam, the Netherlands, June 19-24, 2011.

2014-2020: Member Dutch Arctic Circle; Networking platform connecting companies,

governmental and knowledge institutes for sustainable Dutch Arctic opera-

tions.

2020-2021: Member NWO-ENW strategy committee for the Netherlands Polar Pro-

gramme 2021-2025.

2017-2019: Chairman local org. committee POAC2019: 25th Intern. Conference on Port

and Ocean Engineering under Arctic Conditions 2019, June 9-13, 2019, Delft.

Publications

Journal Publications

Dalen, K.N. van, Tsouvalas, A., Metrikine, A.V., & Hoving, J.S. (2015).

Transition radiation excited by a surface load that moves over the interface of two elastic layers. International Journal of Solids and Structures, 73-74, p. 99-112.

Metrikine, A.V., Kudarova, A.M., Hoving, J.S., & van Vliet, R. (2015).

On the minimization of wave reflection at the interface of a discrete system and a dispersively-similar continuum. Journal of Sound and Vibration, 346, p. 191-199.

Conference Proceedings

Nuus, N., Bruneau, S.E., & Hoving, J.S. (2019).

Estimation of static and kinetic friction coefficients for ice interacting with concrete surfaces. Proc. of the 25th Int. conf. on Port and Ocean engineering under Arctic Conditions (POAC), June 9-13, Delft, the Netherlands.

Aalbers, A.B., & Hoving, J.S. (2019).

Marine spray from wave run-up to a hull as input to icing models. Proc. of the 25th Int. conf. on Port and Ocean engineering under Arctic Conditions (POAC), June 9-13, Delft, the Netherlands.

Hoving, J.S., Marquart, R., & Pisano, F. (2017).

Modelling the Dynamics of Iceberg-Soil Interaction during Seabed Gouging. Proc. of the 24th Int. conf. on Port and Ocean engineering under Arctic Conditions (POAC), June 11-16, Busan, Korea.

Hoving, J.S., & Metrikine, A.V. (2017).

Wave reflection at the interface between a nonlinear discrete lattice and a matching linear system. Proc. of the ICSV24 – Int. Congress on Sound and Vibration, July 23-27, London, UK.

de Jong, M., Candy, A., Hoving, J.S., Kleute, B., & Pietrzak, J. (2017).

Ocean Current Patterns and Variability around Curaçao: An Analysis for Ocean Thermal Energy Conversion. Proc. of the 5th OTEC Symposium, Nov. 7, France.

Hoes, C.M., Aalbers, A.B., & Hoving, J.S. (2016).

Modelling the ballistics and thermodynamics of bow spray droplets for marine icing. Proceedings of the Arctic Technology Conference 2016, Oct. 24-26, St. John's, Canada.

Hoving, J.S., & Metrikine, A.V. (2015).

A mixed time-frequency domain method to describe the non-smooth dynamic behaviour of a nonlinear medium bounded by a linear continuum. Proc. of the XXXXIII Summer School - Conf. on Adv. Problems in Mechanics, St. Petersburg, Russia.

Hoving, J.S., Vermeulen, R., Mesu, A.W., & Cammaert, A.B. (2013).

Experiment-based relations between level ice loads and managed ice loads on an Arctic jack-up structure. Proc. of the 22nd Int. conf. on Port and Ocean engineering under Arctic Conditions (POAC), Espoo, Finland.

Cammaert, A.B., Metrikine, A.V., & Hoving, J.S. (2011).

Performance of minimal offshore platforms in ice environments. Proc. of the 21st Int. conf. on Port and Ocean engineering under Arctic Conditions (POAC), July 10-14, Montréal, Canada.

Versteijlen, W.G., Metrikine, A., Hoving, J.S., Smidt, E.H., & De Vries, W.E. (2011).

Estimation of the vibration decrement of an offshore wind turbine support structure caused by its interaction with soil. Proc. of the EWEA Offshore 2011, Nov. 29 to Dec. 1, 2011, Amsterdam, The Netherlands

Hoving, J.S., & Metrikine, A.V. (2010).

On the coupling of nonlinear discrete element models with continua in the time domain. Proc. of the XXXVIII Summer School – Conf. on Adv. Problems in Mechanics, St. Petersburg, Russia.

Koopman, A., Lentzen, S.S.K., Steenbergen, R.D.J.M., Metrikine, A.V., & Hoving, J.S. (2009).

SRM-T: The Dutch standardized prediction model for railway vibration and induced noise. Proc. of the 4th Int. Symposium on Environmental Vibrations – Prediction, Monitoring, Mitigation and Evaluation, October 28-30, 2009, Beijing, China.

Hoving, J.S., Molenkamp, F., Metrikine, A.V., & Vrouwenvelder, A.C.W.M. (2005).

The dynamic response of a discrete lattice containing dry-friction elements to a surface load. Proc. of the XXXIII Summer School - Conf. on Adv. Problems in Mechanics, St. Petersburg, Russia.

Technical reports

Cammaert, A.B., Hoving, J.S., & Vermeulen, R. (2014).

Experimental program for ice loads on an Arctic jack-up structure. Proceedings of the HYDRALAB IV Joint User Meeting, Lisbon, Portugal.

Hoving, J.S., & Metrikine, A.V. (2008).

Evaluation of the effect of embankment on the transfer functions for soil vibrations. Delft: TNO & Delft Cluster.